PAIN MECHANISMS AND MODULATORS EDITOR'S PICKS 2021

EDITED BY: Robert John Vandenberg

PUBLISHED IN: Frontiers in Molecular Neuroscience

frontiers Research Topics

frontiers

ISSN 1664-8714
ISBN 978-2-88971-064-5
DOI 10.3389/978-2-88971-064-5

About Frontiers

Frontiers is more than just an open-access publisher of scholarly articles: it is a pioneering approach to the world of academia, radically improving the way scholarly research is managed. The grand vision of Frontiers is a world where all people have an equal opportunity to seek, share and generate knowledge. Frontiers provides immediate and permanent online open access to all its publications, but this alone is not enough to realize our grand goals.

Frontiers Journal Series

The Frontiers Journal Series is a multi-tier and interdisciplinary set of open-access, online journals, promising a paradigm shift from the current review, selection and dissemination processes in academic publishing. All Frontiers journals are driven by researchers for researchers; therefore, they constitute a service to the scholarly community. At the same time, the Frontiers Journal Series operates on a revolutionary invention, the tiered publishing system, initially addressing specific communities of scholars, and gradually climbing up to broader public understanding, thus serving the interests of the lay society, too.

Dedication to Quality

Each Frontiers article is a landmark of the highest quality, thanks to genuinely collaborative interactions between authors and review editors, who include some of the world's best academicians. Research must be certified by peers before entering a stream of knowledge that may eventually reach the public - and shape society; therefore, Frontiers only applies the most rigorous and unbiased reviews.
Frontiers revolutionizes research publishing by freely delivering the most outstanding research, evaluated with no bias from both the academic and social point of view. By applying the most advanced information technologies, Frontiers is catapulting scholarly publishing into a new generation.

What are Frontiers Research Topics?

Frontiers Research Topics are very popular trademarks of the Frontiers Journals Series: they are collections of at least ten articles, all centered on a particular subject. With their unique mix of varied contributions from Original Research to Review Articles, Frontiers Research Topics unify the most influential researchers, the latest key findings and historical advances in a hot research area! Find out more on how to host your own Frontiers Research Topic or contribute to one as an author by contacting the Frontiers Editorial Office: frontiersin.org/about/contact

PAIN MECHANISMS AND MODULATORS EDITOR'S PICKS 2021

Topic Editor:
Robert John Vandenberg, The University of Sydney Darlington, Australia

Citation: Vandenberg, R. J., ed. (2021). Pain Mechanisms and Modulators Editor's Picks 2021. Lausanne: Frontiers Media SA. doi: 10.3389/978-2-88971-064-5

Table of Contents

04 ***Circular RNA Expression Alteration and Bioinformatics Analysis in Rats After Traumatic Spinal Cord Injury***
Chuan Qin, Chang-Bin Liu, De-Gang Yang, Feng Gao, Xin Zhang, Chao Zhang, Liang-Jie Du, Ming-Liang Yang and Jian-Jun Li

17 ***Transcriptome Analysis of the Human Tibial Nerve Identifies Sexually Dimorphic Expression of Genes Involved in Pain, Inflammation, and Neuro-Immunity***
Pradipta R. Ray, Jawad Khan, Andi Wangzhou, Diana Tavares-Ferreira, Armen N. Akopian, Gregory Dussor and Theodore J. Price

32 ***TRPA1 Activation-Induced Myelin Degradation Plays a Key Role in Motor Dysfunction After Intracerebral Hemorrhage***
Min Xia, Weixiang Chen, Jie Wang, Yi Yin, Chao Guo, Chengcheng Li, Mingxi Li, Xiaoqin Tang, Zhengcai Jia, Rong Hu, Xin Liu and Hua Feng

43 ***Role of Long Noncoding RNAs and Circular RNAs in Nerve Regeneration***
Chun Yao and Bin Yu

53 ***The Role of TRESK in Discrete Sensory Neuron Populations and Somatosensory Processing***
Greg A. Weir, Philippa Pettingill, Yukyee Wu, Galbha Duggal, Andrei-Sorin Ilie, Colin J. Akerman and M. Zameel Cader

64 **PIEZO1** ***Is Selectively Expressed in Small Diameter Mouse DRG Neurons Distinct From Neurons Strongly Expressing*** **TRPV1**
Jigong Wang, Jun-Ho La and Owen P. Hamill

79 ***Tissue Specific Reference Genes for MicroRNA Expression Analysis in a Mouse Model of Peripheral Nerve Injury***
Theodora Kalpachidou, Kai K. Kummer, Miodrag Mitrić and Michaela Kress

94 ***Modulation of Glycine Receptor-Mediated Pain Signaling*** **in vitro** ***and*** **in vivo** ***by Glucose***
Rama Ashraf Hussein, Marwa Ahmed, Hans-Georg Breitinger and Ulrike Breitinger

102 ***Transcriptional Profiling of Non-injured Nociceptors After Spinal Cord Injury Reveals Diverse Molecular Changes***
Jessica R. Yasko, Isaac L. Moss and Richard E. Mains

121 ***Differential Expression Profiles and Functional Prediction of tRNA-Derived Small RNAs in Rats After Traumatic Spinal Cord Injury***
Chuan Qin, Hao Feng, Chao Zhang, Xin Zhang, Yi Liu, De-Gang Yang, Liang-Jie Du, Ying-Chun Sun, Ming-Liang Yang, Feng Gao and Jian-Jun Li

136 ***Identification of Differentially Expressed Genes and Key Pathways in the Dorsal Root Ganglion After Chronic Compression***
Zhanhui Du, Sen Yin, Xiuhui Song, Lechi Zhang, Shouwei Yue, Xiaofeng Jia and Yang Zhang

145 ***Inhibition of M/K_V7 Currents Contributes to Chloroquine-Induced Itch in Mice***
Dong Zhang, Hongchao Men, Ludi Zhang, Xiangxin Gao, Jingjing Wang, Leying Li, Qiaoying Zhu, Hailin Zhang, and Zhanfeng Jia

frontiers in Molecular Neuroscience

ORIGINAL RESEARCH
published: 14 January 2019
doi: 10.3389/fnmol.2018.00497

Circular RNA Expression Alteration and Bioinformatics Analysis in Rats After Traumatic Spinal Cord Injury

*Chuan Qin[1,2,3,4,5], Chang-Bin Liu[1,2,3,4,5], De-Gang Yang[1,2,3,4,5], Feng Gao[1,2,3,4,5], Xin Zhang[1,2,3,4,5], Chao Zhang[1,2,3,4,5], Liang-Jie Du[1,2,3,4,5], Ming-Liang Yang[1,2,3,4,5] and Jian-Jun Li[1,2,3,4,5]**

[1] School of Rehabilitation Medicine, Capital Medical University, Beijing, China, [2] China Rehabilitation Science Institute, Beijing, China, [3] Center of Neural Injury and Repair, Beijing Institute for Brain Disorders, Beijing, China, [4] Department of Spinal and Neural Functional Reconstruction, China Rehabilitation Research Center, Beijing, China, [5] Beijing Key Laboratory of Neural Injury and Rehabilitation, Beijing, China

Spinal cord injury (SCI) is mostly caused by trauma. As primary mechanical injury is unavoidable in SCI, a focus on the pathophysiology and underlying molecular mechanisms of SCI-induced secondary injury is necessary to develop promising treatments for SCI patients. Circular RNAs (circRNAs) are associated with various diseases. Nevertheless, studies to date have not yet determined the functional roles of circRNAs in traumatic SCI. We examined circRNA expression profiles in the contused spinal cords of rats using microarray and quantitative reverse transcription-PCR (qRT-PCR) then predict their potential roles in post-SCI pathophysiology with bioinformatics. We found a total of 1676 differentially expressed circRNAs (fold change $\geq$ 2.0; $P < 0.05$) in spinal cord 3 days after contusion using circRNA microarray; 1261 circRNAs were significantly downregulated, whereas the remaining 415 were significantly upregulated. Then, five selected circRNAs, namely, rno_circRNA_005342, rno_circRNA_015513, rno_circRNA_002948, rno_circRNA_006096, and rno_circRNA_013017 were all significantly downregulated in the SCI group after verification by qRT-PCR, demonstrating a similar expression pattern in both microarray and PCR data. The next section of the study was concerned with the prediction of circRNA/miRNA/mRNA interactions using bioinformatics analysis. In the final part of the study, Gene Ontology (GO) and Kyoto Encyclopedia of Genes and Genomes analyses indicated carbohydrate metabolic process was one of the most significant enrichments and meaningful terms after GO analysis, and the top two signaling pathways affected by the circRNAs-miRNAs axes were the AMP-activated protein kinase signaling pathway and the peroxisome related pathway. In summary, this study showed an altered circRNA expression pattern that may be involved in physiological and pathological processes in rats after traumatic SCI, providing deep insights into numerous possibilities for SCI treatment targets by regulating circRNAs.

Keywords: circular RNA, spinal cord injury, microarray, bioinformatics, rats

OPEN ACCESS

Edited by:
Guilherme Lucas, University of São Paulo, Brazil

Reviewed by:
Orion Furmanski, Uniformed Services University of the Health Sciences, United States
Paolo Follesa, Università degli Studi di Cagliari, Italy

****Correspondence:***
Jian-Jun Li
crrclijj@163.com

Received: *23 September 2018*
Accepted: *28 December 2018*
Published: *14 January 2019*

Citation:
Qin C, Liu C-B, Yang D-G, Gao F, Zhang X, Zhang C, Du L-J, Yang M-L and Li J-J (2019) Circular RNA Expression Alteration and Bioinformatics Analysis in Rats After Traumatic Spinal Cord Injury. Front. Mol. Neurosci. 11:497. doi: 10.3389/fnmol.2018.00497

Abbreviations: AMPK, AMP-activated protein kinase; ceRNAs, competing endogenous RNAs; circRNAs, circular RNAs; FCs, fold changes; FDR, false discovery rate; GAPDH, glyceraldehyde 3-phosphate dehydrogenase; GO, Gene Ontology; KEGG, Kyoto Encyclopedia of Genes and Genomes database; lncRNA, long non-coding RNA; miRNA, microRNA; MREs, miRNA response elements; ncRNAs, non-coding RNAs; qRT-PCR, quantitative reverse transcription-PCR; SCI, spinal cord injury.

INTRODUCTION

Spinal cord injury is a growing public health concern worldwide that is accompanied by permanent neurological impairment and attendant social and economic losses (Yang et al., 2014; Manohar et al., 2017). SCI is mostly caused by trauma (Fan et al., 2017), which involves primary mechanical injury due to rapid direct compression and contusion on the cord and secondary injury, such as hemorrhage, edema, ischemia, cell death and oxidative stress, during the following hours (Zhu et al., 2017b). It is well-known that primary mechanical injury is hardly avoidable. As a result, concentrating on the pathophysiology and underlying molecular mechanisms of SCI-induced secondary injury is necessary to develop promising diagnosis and treatment approaches for SCI patients (Liu et al., 2017a). However, no neuroprotective and regenerative therapies are currently available that can directly produce beneficial effects. Although past decades have seen the rapid development of stem cell transplantation (Nagoshi and Okano, 2017), surgical decompression (Yang et al., 2013; Hu et al., 2015) and high-dose methylprednisolone (Hextrum and Bennett, 2018) in the field of SCI, a multitude of controversies on the efficacy of these approaches remains.

Recent advances in ncRNAs, including lncRNA and miRNA, may be at the point of breaking this impasse. Increasing studies in this field have examined an outstanding outcome that neurologic damage can be alleviated by normalizing the expression levels of certain lncRNAs and miRNAs in rats after SCI (Hwang et al., 2016; Lv, 2017; Zhu et al., 2017a; Zhou et al., 2018a). Circular RNAs (circRNAs) are a special type of endogenous non-coding RNAs formed by back-splicing events via protein-coding exons (Qu et al., 2015). Notably, they have been attracting a wealth of interest because growing research has found that the altered expression of specific circRNAs was closely related to human diseases, such as cancer (Zhou et al., 2018b), neurological diseases (Bai et al., 2018), and cardiac diseases (Salgado-Somoza et al., 2017). In recent years, a selection of studies stated that circRNA expression profiles were significantly altered after traumatic brain injury in mice and rats (Xie et al., 2018; Zhao et al., 2018). Nevertheless, there are no data concerning circRNAs in traumatic SCI so far, and their molecular and intermolecular interactions and key signaling pathways remain to be elucidated. Although the physiological functions of circRNAs are largely unknown, they are expected to regulate the transcription of parent genes, promote rolling circle translation, and help form alternatively spliced mRNAs and sponge miRNAs, namely, ceRNAs (Memczak et al., 2013; Liu et al., 2017b).

We used high-throughput microarray analysis to screen circRNAs expression patterns in the spinal cord of adult rats after traumatic SCI to determine whether the expression levels of circRNAs were altered and lay a foundation for future work. Subsequently, we selected five differentially expressed circRNAs for low-throughput validation by qRT-PCR. Then, we used bioinformatics tools to predict their putative biological functions with miRNA and mRNA by establishing circRNA/miRNA/mRNA networks and to identify feasible functions of all mRNAs regulated by these specific circRNAs in traumatic SCI.

The purpose of this investigation was to explore the circRNA expression profiles in rats after traumatic SCI, to determine the potential roles of these differentially expressed circRNAs in post-SCI pathophysiology processes.

MATERIALS AND METHODS

Animals and Experimental Groups

This study was carried out in accordance with the principles of the Basel Declaration and recommendations of the National Institute of Health Guide for the Care and Use of Laboratory Animals (NIH Publications No. 8023, revised 1978). The protocol was approved by the Institutional Animal Care and Use Committee of Capital Medical University. Female Sprague–Dawley rats (age: 10–12 weeks; weight: 250–300 g) were purchased from the Animal Care Center of Academy of Military Medical Sciences (Beijing, China). Rats were housed in a temperature-controlled (20–28°C) and light-controlled (12-h light/dark cycle) room. They were habituated to the housing conditions for at least 7 days before SCI. Additionally, the animals had free access to standard rat chow and tap water; however, food was withheld overnight before surgery.

Twelve rats were randomly assigned to two groups using a computer-generated randomization schedule: rats in the sham control group (n = 6) were treated with laminectomy alone without contusion, and rats in the SCI group (n = 6) were subjected to laminectomy plus contusion. The operators performing the surgeries were blinded to the experimental groups. Before and after surgery, our two experienced researchers performed a behavioral test of rats in the two groups using the BBB (Basso, Beattie, and Bresnahan) score, which is frequently used to observe the locomotor function of rats (Scheff et al., 2002). The BBB score ranges from 0 (no hindlimb movement) to 21 (normal movement), and the final score was given by consensus.

Contusion SCI Model and Tissue Collection

In this study, the contusion injury method was adopted to trigger moderate injuries in rat models. Briefly, all rats were anesthetized by intraperitoneal injection of 0.4 mg/g body weight 10% chloral hydrate (Kermel, Tianjing, China), and their backs were shaved and sterilized. After suspending the rats in a stereotaxic frame, a 4-cm-long longitudinal midline incision was made to expose the T9–T11 spinal column. Following stripping of the paraspinal muscles, laminectomy was performed at the T10 level to expose the spinal dura mater without tearing it in a sterile condition. Subsequently, rats were clamped by their spinous processes at T9 and T11 with sterilizing forceps, which was followed by spinal cord contusions induced by an Infinite Horizon Impactor (IH-0400 Impactor, Precision Systems and Instrumentation, LLC, United States), leading to a moderate injury at the T10 level. For parameter setting, a standard rat tip impactor size (2.5 mm in diameter), programmable dwell time (1 s) and programmable force levels (225 kDynes) were applied to induce moderate intensity injuries with the NYU weight-drop device

(2.5 mm in diameter, 10 g rod, height of 12.5 mm) according to the conversion equation (Basso et al., 1996; Khuyagbaatar et al., 2015). Errors greater than 3% in terms of force levels and fracture of spinal dura mater were not accepted.

After inducing contusions, the operative region was washed gently with warm 0.9% normal saline twice (37°C, 2 mL) to avoid local infection. The cord surface showed signs of subarachnoid hematoma and an intense dark brown/purple color. The rats with swinging tails that quickly retracted their lower limbs immediately after SCI were regarded as eligible as described previously (Hu et al., 2015). Finally, the wound was then sutured in layers. A warm environment was established to maintain body temperature during surgery. Notably, 4 mL of Ringer lactate solution was administered intraperitoneally to supplement electrolytes and body fluids. Rats were then housed in individual cages. Animals were fed with free access to food and water. Penicillin (40000 U, intramuscular injection) was administered daily for 3 days to prevent systemic infection. The bladders were emptied manually every 8 h until the rats were killed.

At 3 days post-surgery, rats in all groups were euthanized with an overdose of 10% chloral hydrate (10 mL/kg), and a 1-cm long segment of spinal cord, including the injury epicenter, was quickly dissected and collected without transcardial perfusion in advance and was then fresh frozen in liquid nitrogen to prevent RNA degradation similarly to a previously reported method (Pang et al., 2016).

RNA Extraction and Quality Control

Briefly, total RNA was isolated with TRIzol reagent (Invitrogen, Carlsbad, CA, United States) based on the manufacturer's instructions. After identifying the purity and concentration of total RNA from each sample with a NanoDrop ND-1000 (NanoDrop, Wilmington, DE, United States), the integrity of RNA and gDNA contamination was tested using denaturing agarose gel electrophoresis.

CircRNA Microarray

Cord tissue samples from rats in the SCI (n = 3) and sham groups (n = 3) were used in the microarray experiment. As shown in **Supplementary Figure 1A**, the sample preparations, sample labeling, and microarray hybridizations were performed based on the manufacturer's standard protocols (Arraystar). First, total RNAs were digested with Rnase R (Epicentre, Inc.) to remove linear RNAs and enrich circRNAs. Second, the enriched circRNAs were amplified and transcribed into fluorescent cRNA using a random priming method (Arraystar Super RNA Labeling Kit; Arraystar). Third, the labeled cRNAs were purified by a RNeasy Mini Kit according to the manufacturer's instructions (Qiagen). Then, the concentration and specific activity of the labeled cRNAs (pmol Cy3/μg cRNA) were accessed by a NanoDrop ND-1000. Afterward, 1 μg of each labeled cRNA was fragmented by adding 5 μL of 10× blocking agent and 1 μL of 25× fragmentation buffer, and then, the mixture was heated at 60°C for 30 min; finally, 25 μL of 2× hybridization buffer was added to dilute the labeled cRNA. Approximately 50 μL of hybridization solution was dispensed into the gasket slide and assembled onto the circRNA expression microarray slide. Lastly, the slides were incubated for 17 h at 65°C in an Agilent Hybridization Oven. The hybridized arrays were washed, fixed and scanned with an Agilent Scanner G2505C. The microarray experiments in our study were performed by KangChen Bio-tech, Shanghai, China. This standard procedure was also used in other publications (Xie et al., 2018).

CircRNA Data Analysis

Acquired array images were analyzed using Agilent Feature Extraction software (version 11.0.1.1). As shown in **Supplementary Figure 1B**, quantile normalization and subsequent data processing were performed with the R software limma package. After quantile normalization of the raw data, low intensity filtering was performed. When comparing two groups for profile differences (SCI versus sham control), the "fold change" (i.e., the ratio of the group averages) between the groups of each circRNA was computed. The statistical significance of the difference was conveniently estimated by a t-test. False discovery rate was calculated from Benjamini Hochberg FDR to correct the P.

Differentially expressed circRNAs with statistical significance (fold changes $\geq$ 2.0, $P < 0.05$) between the groups were identified through volcano plot filtering or fold change filtering. Hierarchical clustering was used to show distinguishable circRNAs expression patterns among tissue samples using MeV (Multiple Experiment Viewer[1]). Additionally, the distribution of differentially expressed circRNAs in rat chromosomes and the bar diagram of circRNA categories were performed by GraphPad prism 6.

Next, we first predicted the potential sponging miRNAs for each differentially expressed circRNA with Arraystar's homemade miRNA target prediction software according to TargetScan (Enright et al., 2003) and miRanda (Pasquinelli, 2012) in order to investigate the functions of dysregulated circRNAs. We ranked miRNA candidates based on the mirSVR and listed the five highest-ranking miRNA candidates for each circRNA.

qRT-PCR Assay

The expression of five circRNAs randomly selected from microarray analysis was validated using a qRT-PCR assay. Cord tissue samples from rats in the SCI (n = 6) and sham groups (n = 6) were used in the PCR experiment. As previously reported (Xie et al., 2018), total RNA was isolated using TRIzol reagent according to the manufacturer's standard protocols (Invitrogen). RNA quantification and quality were accessed by a NanoDrop ND-1000, and RNA integrity was identified by electrophoresis on a denaturing agarose gel. Next, we synthesized cDNA in line with the manufacturer's instructions. qRT-PCR was performed in a ViiA 7 Real-time PCR System (Applied Biosystems) with PCR master mix (2×, Arraystar). The parameter settings were 95°C denaturation (10 min), 95°C (10 s), and 60°C (60 s), which was repeated for 40 cycles. After the amplification reaction was finished, the procedure was performed as follows: 95°C (10 s), 60°C (60 s), and 95°C (15 s). Glyceraldehyde 3-phosphate dehydrogenase (GAPDH) acted as an internal control to normalize the data. The relative expression levels

[1]https://sourceforge.net/projects/mev-tm4/files/mev-tm4/

of circRNAs were calculated using the relative standard curve method (Larionov et al., 2005).

Prediction for CircRNA/miRNA/mRNA Interactions

The ceRNA hypothesis is that RNA transcripts can crosstalk by competing for common miRNAs, where MREs are the foundation of this interaction (Salmena et al., 2011). Any RNA transcript with MREs might act as a ceRNA, and ceRNAs include pseudogene transcripts, circRNAs and mRNAs; these transcripts can compete for the same MER to mutually regulate it. We constructed the ceRNA network by merging common targeted miRNAs. The circRNA/miRNA/mRNA interactions were predicted in combination with in-house miRNA target prediction software according to TargetScan and miRanda software (Friedman et al., 2009; Huang et al., 2016) to identify the potential targets of miRNAs. Three conditions must exist for the ceRNA network to occur (Salmena et al., 2011). First, the relative concentration of ceRNAs and their miRNAs is clearly important; second, the effectiveness of a ceRNA depends on the number of miRNAs that it can "sponge"; third, not all of the MREs on ceRNAs are equal. Therefore, we accept only the ceRNA-pair relations that passed filtering measures ($P < 0.05$). A graph of the circRNA/miRNA/mRNA network was made using Cytoscape software (version 3.5.1) to visualize these relationships.

Next, we used Gene Ontology (GO[2]) to reveal the biological process, cellular component and molecular function of the target mRNAs. Significant pathways were identified using pathways in the Kyoto Encyclopedia of Genes and Genomes database (KEGG[3]). A $P < 0.05$ indicates the significance of GO and KEGG pathway terms. The FDR was calculated to correct the *P*.

Statistical Analysis

Statistical analysis was performed using SPSS software (version 21.0, Chicago, IL, United States). The results were shown as the mean ± SEM. Student's *t*-test was used to compare significant differences between the two groups. A $P < 0.05$ was considered to be statistically significant.

Database and Accession Numbers

CircRNA microarray data in our study were deposited at the NCBI Gene Expression Omnibus (GEO) under the Accession No. GSE114426.

RESULTS

Expression Pattern of CircRNAs in Spinal Cord Tissues After SCI

Prior to injury, the BBB scores of all rats were 21. Rats in the sham group remained at 21, indicating the integrity of the spinal cord during the experimental period. However, in the SCI group, no hindlimb motor performance was observed immediately after anesthesia recovery, which indicates a loss of locomotive function due to the contusion (data not shown).

The first set of questions aimed to identify circRNAs expression levels in the two groups, so a high-throughput microarray assay was used. It can be seen from the box plot (**Supplementary Figure 2A**) that the normalized intensity values in all samples were not significantly different, suggesting a similar distribution of circRNAs expression profiles in each group. **Supplementary Figure 2B** showed RNA integrity and the gDNA contamination test. After microarray scanning and normalization, the dysregulated expression of all 13279 circRNAs between groups was detected. A total of 1676 circRNAs were differentially expressed (fold change ≥ 2; $P < 0.05$) between the groups, 1261 of which were significantly downregulated and 415 of which were significantly upregulated in the SCI group. Then, **Table 1** provides experimental data on the top 10 upregulated and downregulated circRNAs ranked by fold changes after microarray analysis. Two graphs of hierarchical clustering of circRNAs expression were performed (shown in **Figure 1**) to visualize these data. Next, volcano plots were constructed using fold change values and P values to visualize differential expression between the two different conditions (**Figure 2A**), and scatter plots presented the circRNA expression variation (or reproducibility) between the SCI and sham control groups (**Figure 2B**). Additionally, the distribution of differentially expressed circRNAs in chromosomes is presented in **Figure 2C**. What stands out in **Figure 2D** is that the bar diagram of the circRNA category based on gene sources revealed 325 exonic, 6 antisense, 7 intronic, 9 intergenic, and 68 sense overlapping circRNAs that were upregulated. In contrast, 1012 exonic, 4 antisense, 5 intronic, 33 intergenic, and 207 sense overlapping circRNAs were downregulated.

Lastly, we predicted the five most likely potential target miRNAs for each differentially expressed circRNA. The five highest-ranking miRNA candidates as binding targets of each circRNA are listed in **Table 2** (for the top 10 upregulated and downregulated circRNAs).

Verification of qRT-PCR

Overall, 1261 differentially expressed circRNAs were listed after we filtered the high-throughput microarray assay data; therefore, the accuracy of the data needed verification. Next, five circRNAs with relatively high fold changes and similar tissue sample distributions within each group were randomly selected for low-throughput verification with qRT-PCR. Compared with the sham control, rno_circRNA_005342, rno_circRNA_015513, rno_circRNA_002948, rno_circRNA_006096, and rno_circRNA_013017 in the SCI group were all significantly downregulated after SCI, suggesting a similar expression pattern in these candidate circRNAs in both the microarray and PCR data, as shown in **Figures 3A–E**. **Table 3** provides the fold change and *P*-value for each candidate circRNA between groups in terms of microarray and PCR analysis to make data interpretation more straightforward. As presented in **Table 4**, the sequences of the primers used for qRT-PCR analysis of circRNA are listed. We also provided amplification plots and melt curve plots of these candidate circRNAs and GAPDH in **Supplementary Figures 3**, **4**.

[2]http://www.geneontology.org

[3]www.genome.jp/kegg

TABLE 1 | The top 10 up-regulated and down-regulated circRNAs ranked by fold changes after SCI.

CircRNA	FC	*P*-value	FDR	Chrom	Strand	CircRNA type	Best transcript	GeneSymbol	Regulation
circRNA_005554	17.4927581	0.00249	0.07049	chr15	–	Exonic	NM_031783	Nefl	Down
circRNA_011688	11.0787102	0.00326	0.07374	chr4	+	Exonic	NM_001047116	Rundc3b	Down
circRNA_001668	10.3034657	0.00027	0.05619	chr1	–	Exonic	NM_012506	Atp1a3	Down
circRNA_015152	9.6814247	0.01177	0.09248	chr7	+	Exonic	NM_001271371	Anks1b	Down
circRNA_003787	9.6707443	0.01306	0.09515	chr12	+	Sense overlapping	NM_001105937	Sgsm1	Down
circRNA_005536	9.6595211	0.00082	0.06066	chr15	–	Exonic	XM_003751491	LOC691889	Down
circRNA_013612	9.5445837	0.00081	0.06066	chr6	–	Sense overlapping	NM_078620	Slc8a3	Down
circRNA_013610	9.4741174	0.00040	0.05971	chr6	–	Exonic	NM_078620	Slc8a3	Down
circRNA_015151	9.4653558	0.01049	0.09061	chr7	+	Sense overlapping	NM_001271371	Anks1b	Down
circRNA_009608	9.316022	0.00098	0.06066	chr20	–	Sense overlapping	NM_013189	Gnaz	Down
circRNA_014299	10.2046519	0.04402	0.15222	chr6	+	Exonic	NM_053888	Myt1l	Up
circRNA_014620	9.9983039	0.04890	0.16031	chr6	–	Exonic	NM_020083	Ralgapa1	Up
circRNA_31436	9.258806	0.03142	0.13033	chr18	+	Sense overlapping	NM_012499	Apc	Up
circRNA_002187	9.0443039	0.03409	0.13447	chr10	–	Exonic	XM_002727722	Dnah9	Up
circRNA_017723	9.0003643	0.02898	0.12586	chrX	–	Exonic	XM_229124	Smarca1	Up
circRNA_008695	8.8206292	0.02831	0.12445	chr2	+	Exonic	NM_001013200	Anp32e	Up
circRNA_002186	8.4481357	0.03361	0.13388	chr10	–	Exonic	XM_002727722	Dnah9	Up
circRNA_23780	7.577899	0.00934	0.08796	chr10	+	Exonic	NM_001013117	Phf12	Up
circRNA_014301	7.0536658	0.02369	0.11557	chr6	+	Exonic	NM_053888	Myt1l	Up
circRNA_005470	6.6801172	0.00001	0.02228	chr15	+	Sense overlapping	NM_031056	Mmp14	Up

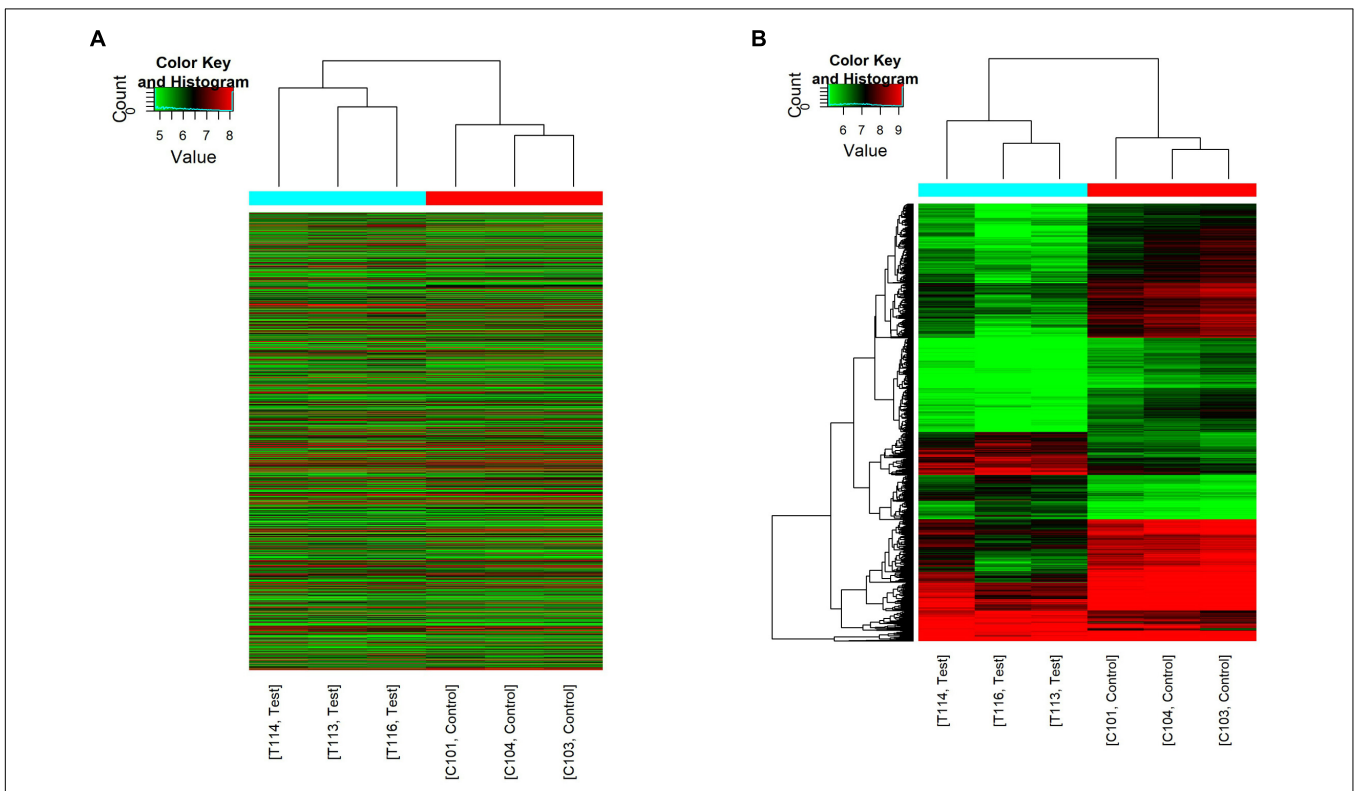

FIGURE 1 | Hierarchical clustering of circRNA expression. C101/103/104 refers to the cord samples from the sham control group, and T113/114/116 refers to the cord samples from the SCI group. **(A)** Hierarchical clustering analysis included all 13279 circRNAs between the sham control and the SCI groups. **(B)** Hierarchical clustering analysis included differentially expressed circRNAs (fold change ≥ 2; $P < 0.05$) between the sham control and the SCI groups.

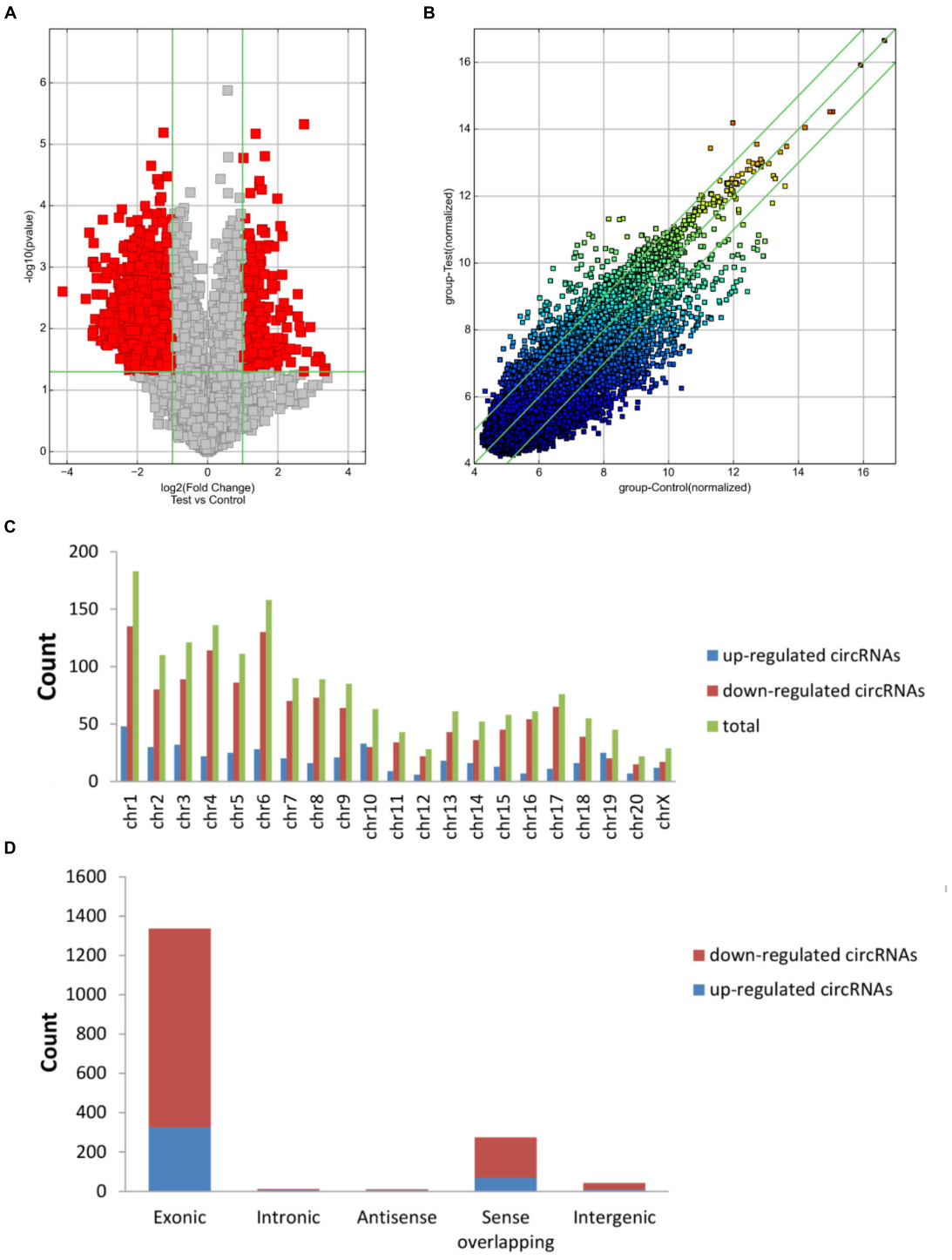

FIGURE 2 | Differences in the circRNA expression profiles between the two groups. **(A)** The scatter plot showed the differences in circRNA expression between the SCI and sham groups. The values of the X and Y axes in the scatter plot are the normalized signal values of the samples (log2 scaled) or the averaged normalized signal values of groups of samples (log2 scaled). The green lines are fold change lines. The circRNAs above the top green line and below the bottom green line indicated more than twofold changes of circRNAs between the two compared samples. **(B)** Volcano plots show the differentially expressed circRNAs with statistical significance (fold change ≥ 2; $P < 0.05$). The vertical lines correspond to 2.0-fold up and down, respectively, and the horizontal line represents a P of 0.05; the red point in the plot represents differentially expressed circRNAs with statistical significance. **(C)** The distribution of differentially expressed circRNAs in chromosomes is presented, showing that the dysregulated circRNAs stem from every chromosome. **(D)** The bar diagram of circRNA categories based on gene sources is shown, revealing that most of the circRNAs altered after SCI are exonic.

TABLE 2 | The five highest-ranking miRNA candidates for top 10 up-regulated and down-regulated circRNAs.

CircRNA	Predicted miRNA response elements (MREs)				
	MRE1	MRE2	MRE3	MRE4	MRE5
circRNA_005554	rno-miR-547-3p	rno-miR-216a-5p	rno-miR-141-5p	rno-miR-615	rno-miR-328a-3p
circRNA_011688	rno-miR-26b-3p	rno-miR-667-5p	rno-miR-133c	rno-miR-540-3p	rno-miR-18a-5p
circRNA_001668	rno-miR-494-5p	rno-miR-410-5p	rno-miR-205	rno-miR-496-5p	rno-miR-377-5p
circRNA_015152	rno-miR-22-5p	rno-miR-485-5p	rno-miR-488-3p	rno-miR-431	rno-miR-187-3p
circRNA_003787	rno-miR-370-5p	rno-miR-151-5p	rno-miR-346	rno-miR-485-5p	rno-miR-1843b-5p
circRNA_005536	rno-miR-23b-3p	rno-miR-23a-3p	rno-miR-495	rno-miR-493-3p	rno-miR-7a-1-3p
circRNA_013612	rno-miR-182	rno-miR-107-5p	rno-miR-298-5p	rno-miR-31a-5p	rno-miR-6314
circRNA_013610	rno-miR-182	rno-miR-140-3p	rno-miR-17-2-3p	rno-miR-298-5p	rno-miR-6216
circRNA_015151	rno-miR-466b-5p	rno-miR-363-5p	rno-miR-466b-3p	rno-miR-466d	rno-miR-297
circRNA_009608	rno-miR-3084b-5p	rno-miR-3084c-5p	rno-miR-3558-3p	rno-miR-3541	rno-miR-336-5p
circRNA_014299	rno-miR-673-5p	rno-miR-3575	rno-miR-370-3p	rno-miR-466c-5p	rno-miR-672-5p
circRNA_014620	rno-miR-329-5p	rno-miR-22-5p	rno-miR-3568	rno-miR-760-3p	rno-miR-185-3p
circRNA_31436	rno-miR-466b-3p	rno-miR-466c-3p	rno-miR-466b-4-3p	rno-miR-466b-2-3p	rno-miR-297
circRNA_002187	rno-miR-207	rno-miR-27a-3p	rno-miR-135b-5p	rno-miR-484	rno-miR-27b-3p
circRNA_017723	rno-miR-216b-5p	rno-miR-153-5p	rno-miR-28-5p	rno-miR-130a-5p	rno-miR-329-5p
circRNA_008695	rno-miR-880-5p	rno-let-7g-5p	rno-miR-1306-3p	rno-miR-3084a-3p	rno-miR-3084d
circRNA_002186	rno-miR-6331	rno-miR-207	rno-miR-135b-5p	rno-miR-3583-3p	rno-miR-320-5p
circRNA_23780	rno-miR-204-3p	rno-miR-328a-5p	rno-miR-423-5p	rno-miR-138-5p	rno-miR-3573-5p
circRNA_014301	rno-miR-672-5p	rno-miR-3593-5p	rno-miR-3575	rno-miR-1306-5p	rno-miR-466b-5p

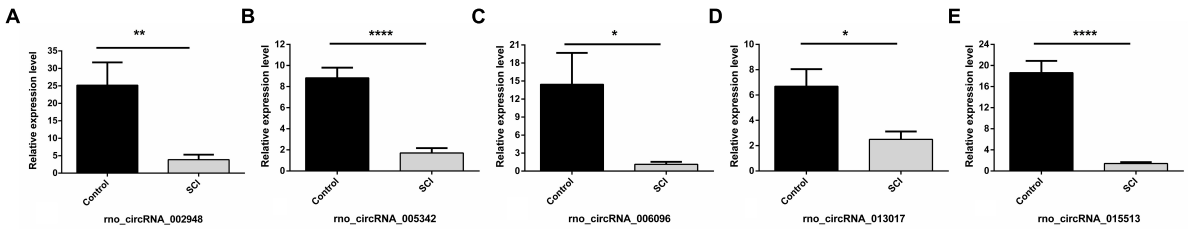

FIGURE 3 | Validation of five selected circRNAs using qRT-PCR. Compared with the sham control, rno_circRNA_005342, rno_circRNA_015513, rno_circRNA_002948, rno_circRNA_006096, and rno_circRNA_013017 in the SCI group were all significantly downregulated after SCI after validation by PCR assay in 12 samples **(A–E).** The data were normalized using the mean ± SEM (n = 6 per group). *P < 0.05, **P < 0.01, ****P < 0.0001.

Bioinformatic Predictions of CircRNA/miRNA/mRNA Interactions

The five candidate circRNAs validated by qRT-PCR were next selected to construct circRNA/mRNA of miRNA interactions using bioinformatics tools. Notably, an entire network of these interactions was depicted (shown in **Figure 4**). The results showed that a total of 5 circRNAs, 60 miRNAs and 253 mRNAs were included, presenting a large interaction network. CircRNAs can serve as ceRNA for miRNAs, and miRNAs usually inhibit target mRNAs; therefore, circRNAs may indirectly upregulate target mRNAs by inhibiting the negative regulation of miRNAs.

TABLE 3 | Comparison for candidate circRNAs expression in microarray and PCR.

CircRNAs	Microarray			PCR		
	FC	*P*-value	Regulation	FC	*P*-value	Regulation
rno_circRNA_002948	5.72	0.0064	Down	6.52	0.0096	Down
rno_circRNA_005342	5.59	0.0023	Down	5.18	<0.0001	Down
rno_circRNA_006096	6.36	0.0048	Down	12.77	0.0296	Down
rno_circRNA_013017	4.54	0.0097	Down	2.68	0.0184	Down
rno_circRNA_015513	5.98	0.0130	Down	13.12	<0.0001	Down

GO and Pathway Analysis of Putative Target mRNAs

Based on these interactions, five candidate circRNAs may play an important role in molecular mechanisms by regulating target miRNAs/mRNAs. As a result, we performed GO and pathway analysis of all target mRNAs to provide strong evidence for the further functional verification of these circRNAs.

First, GO bioinformatic analysis covers three domains: biological process, cellular component and molecular function. For each part, we showed the following classifications for significantly enriched terms: top 10 counts, top 10-fold enrichment value, top 10 enrichment score value and gene ratio values. The results indicated the following: (1) in terms of biological processes, the most significant enrichment and meaningful terms are metabolic process and RNA splicing,

TABLE 4 | Sequences of primers used for qRT-PCR assay.

Gene name	Primer sequence	Ta Opt (°C)	Product size (bp)
GAPDH (RAT)	F: 5′-GCTCTCTGCTCCTCCCTGTTCTA-3′ R: 5′-TGGTAACCAGGCGTCCGATA-3′	60	124
rno_circRNA_002948	F: 5′-GGACTTGGAGTCTTCCGATGAG-3′ R: 5′-CAGAAGAAAGCAAAAACCCGTA-3′	60	140
rno_circRNA_005342	F: 5′-CCTCCTCTTCTTCCTTCTTCTG-3′ R: 5′-AGGTACAAAACCACAGTCCTGG-3′	60	110
rno_circRNA_006096	F: 5′-GGAACAGTCTTCAGAAAATGCT-3′ R: 5′-GGGTTGAAGGAAAAGCAGTATA-3′	60	64
rno_circRNA_013017	F: 5′-ATATTTGCTGCTCGTGAATTTA-3′ R: 5′-TGGGAGTTGTGGACCTTGT-3′	60	88
rno_circRNA_015513	F: 5′-GAAGCGGCGATCTAGCATT-3′ R: 5′-TATCTGCCCCTCTATGTGGAT-3′	60	126

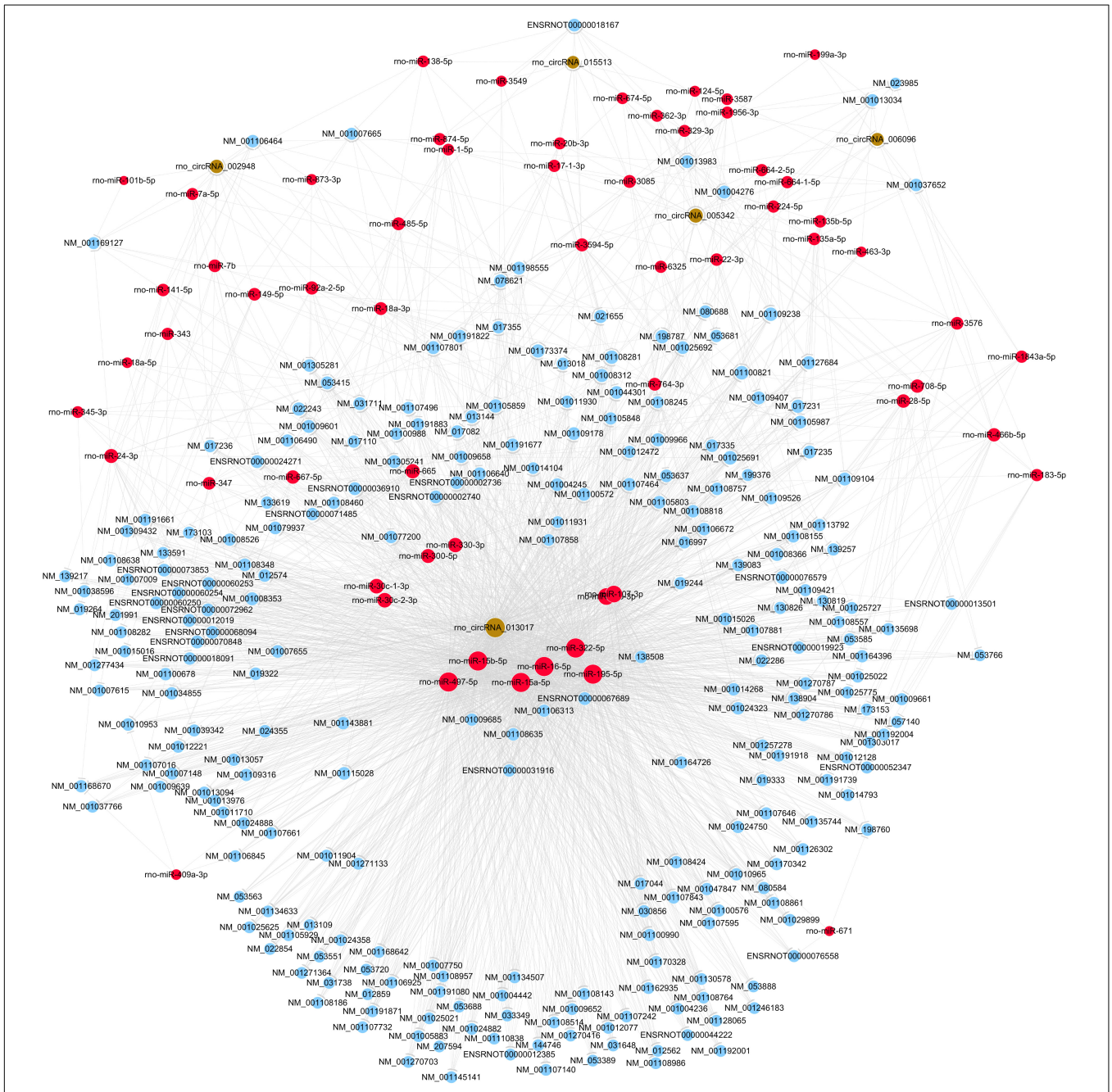

FIGURE 4 | The circRNA/miRNA/mRNA network analysis. The network included the 5 circRNAs, 60 miRNAs, and 253 mRNAs (Nodes with red color are miRNAs; nodes with light-blue color are mRNAs; nodes with brown color are circRNAs).

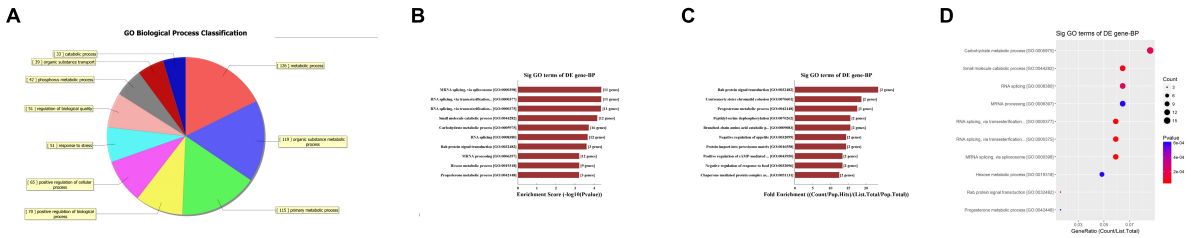

FIGURE 5 | The GO annotations for biological process of target mRNAs regulated by the five candidate circRNAs. **(A)** The pie chart above shows the top 10 counts of the significant enrichment terms. **(B)** The bar plot shows the top 10 enrichment score values of the significant enrichment terms. **(C)** The bar plot shows the top 10-fold enrichment values of the significant enrichment terms. **(D)** The dot plot shows the gene ratio values of the top 10 most significant enrichment terms. Gene ratio: the GOID's gene ratio value, which equals (Count/List.Total).

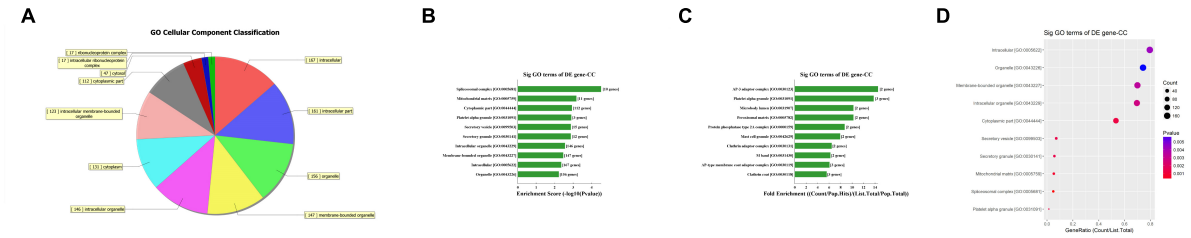

FIGURE 6 | The GO annotations for cellular component of target mRNAs regulated by the five candidate circRNAs. **(A)** The pie chart above shows the top 10 counts of the significant enrichment terms. **(B)** The bar plot shows the top 10 Enrichment Score values of the significant enrichment terms. **(C)** The bar plot shows the top 10-fold enrichment values of the significant enrichment terms. **(D)** The dot plot shows the gene ratio values of the top 10 most significant enrichment terms. Gene ratio: GOID's gene ratio value, which equals (Count/List.Total).

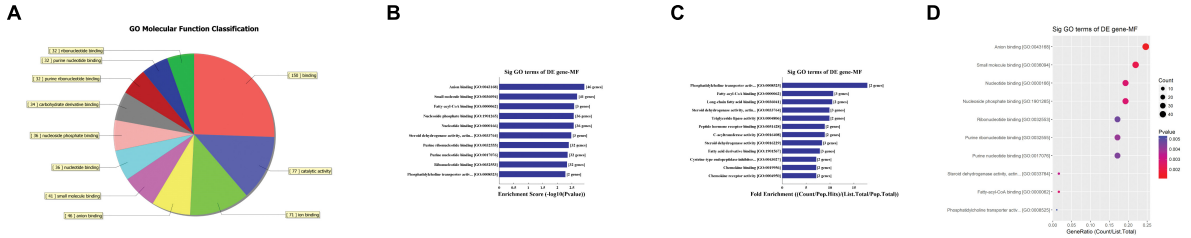

FIGURE 7 | The GO annotations for molecular function of target mRNAs regulated by the five candidate circRNAs. **(A)** The pie chart above shows the top 10 counts of the significant enrichment terms. **(B)** The bar plot shows the top 10 enrichment score values of the significant enrichment terms. **(C)** The bar plot shows the top 10-fold enrichment values of the significant enrichment terms. **(D)** The dot plot shows the gene ratio values of the top 10 most significant enrichment terms. Gene ratio: the GOID's gene ratio value, which equals (Count/List.Total).

describing a series of biological events (**Figures 5A–D**). (2) In terms of cellular component, the most significant enrichment and meaningful terms are intracellular parts and complexes, describing the components of a cell (**Figures 6A–D**). (3) In terms of molecular function, the most significant enrichment and meaningful terms are binding events, suggesting a functional role at the molecular level (**Figures 7A–D**).

Second, the top 10 enrichment score value of significantly enriched pathways based on KEGG pathway analysis is presented in **Figure 8A**. In addition, the dot plot showed the gene ratio value of the top 10 most significantly enriched pathways (**Figure 8B**). The results suggest that these target genes may play a vital role in multiple metabolic activities, and the top two significant pathways are the AMPK signaling pathway and the peroxisome related pathway (**Figures 8C,D**).

DISCUSSION

In the present study, we found that an array of circRNAs were differentially expressed in the early stage after SCI based on circRNA microarray detection. After validation by qRT-PCR, five candidate circRNAs were selected for further prediction. Next, using bioinformatics tools, circRNA/miRNA/mRNA interactions were constructed according to ceRNA mechanisms, indicating a close relationship between circRNAs, miRNAs, and their target mRNAs. Notably, we predicted that the target mRNAs of these confirmed circRNAs may regulate various biological processes, cellular components and molecular functions, suggesting the functional roles of these circRNAs in pathophysiologic processes. Lastly, target mRNAs were revealed to participate in multiple cell signaling pathways of metabolism, including the AMPK

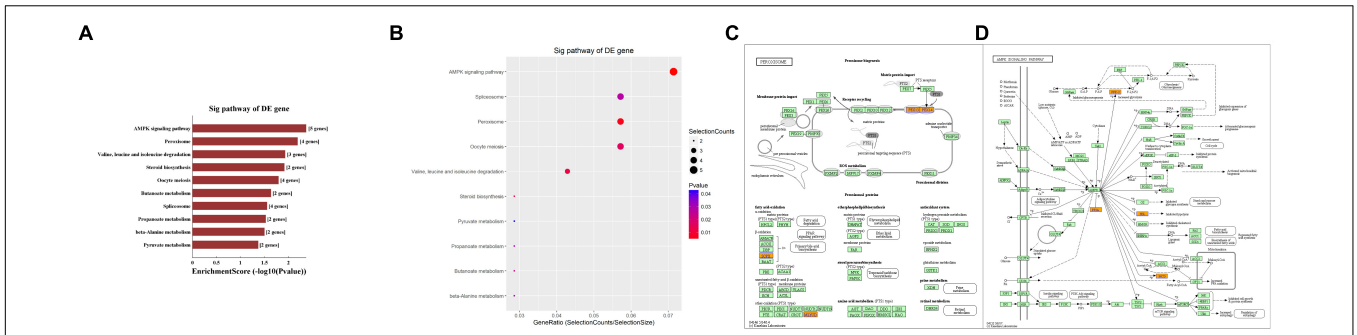

FIGURE 8 | KEGG pathway analysis of target mRNAs regulated by the five candidate circRNAs. **(A)** The bar plot shows the top 10 enrichment score values of the significantly enriched pathway. **(B)** The dot plot shows the gene ratio values of the top 10 most significantly enriched pathways. **(C)** The AMP-activated protein kinase (AMPK) signaling pathway and **(D)** the peroxisome related pathway are shown. Yellow marked nodes are associated with downregulated genes, orange marked nodes are associated with upregulated or only whole dataset genes, and green nodes have no significance.

signaling pathway and peroxisome activity, which play a pivotal role in the regulation of cell energy homeostasis, significantly affecting cell survival, death, differentiation, proliferation, and inflammation (Chen et al., 2018b; Di Cara et al., 2018). Taken together, the observations from this study suggest that these altered circRNAs are extensively involved in pathophysiologic processes after traumatic SCI. In reviewing the literature, no studies have focused on screening circRNA expression patterns in any model with traumatic SCI. Given this finding, the present study, to the best of our knowledge, provides the first comprehensive assessment of circRNA expression patterns and subsequent functional prediction after traumatic SCI, which offers strong evidence for further investigation.

Most of the human genome is composed of ncRNAs, which are widely involved in physiological and pathological activities and are closely related to many diseases (Dimartino et al., 2018; Sun et al., 2018). miRNAs and lincRNAs, two important types of ncRNAs, have caused interest due to their multiple functions in diverse pathophysiological events (Nicolas, 2017). Prior studies have noted that miRNAs and lincRNAs, as key factors, regulate the molecular mechanisms behind secondary injury after SCI, including inflammation, blood–brain damage, apoptosis, autophagy, oxidative stress, edema, endoplasmic reticulum stress, and demyelination (Shi et al., 2017). Interestingly, normalizing the level of dysregulated miRNAs and lincRNAs can alleviate the pathological changes after SCI (Hu et al., 2013). circRNAs, a recent rising star of ncRNAs, are endogenously expressed as single-stranded and covalently closed circular molecules that are enriched in mammals. Compared to miRNAs and lincRNAs, they are more stable due to their unique covalently closed loop and specific tertiary structures, which offer more possibilities to act as ideal biomarkers or novel therapeutic targets. Recent growing evidence has shown that circRNAs are implicated in various biological processes and human illness, such as cancers, cardiovascular diseases, and neurological disorders (Floris et al., 2017; Chen et al., 2018a; Hu et al., 2018). As an example, in Alzheimer's disease, Cdr1as is downregulated, thus regulating the downstream target gene and ultimately affecting the progression of disease (Zhao et al., 2016). In terms of trauma to the central nervous system, an report stated for the first time that a total of 192 circRNAs were observed to be differentially expressed (FC $\geq$ 1.5 and $P < 0.05$) after traumatic brain injury, 98 of which were upregulated and 94 of which were downregulated, indicating the potential roles of these altered circRNAs in pathophysiologic processes after traumatic brain injury[19]. Another study (Zhao et al., 2018) provided evidence concerning circRNA expression alteration in exosomes from the brain extracellular space after traumatic brain injury in mice, which broadens the horizon of research on circRNAs. However, no previous studies have profiled circRNA expression in the spinal cord after SCI. As a result, we put forward a hypothesis that circRNAs expression is significantly altered after traumatic SCI in rats. Finally, after validation, the striking results in our study indicated that circRNAs were altered significantly in rat spinal cord after SCI compared to sham controls.

The relationship between circRNAs and their potential target genes was examined to investigate the functions of these dysregulated circRNAs after screening their expression patterns. Mounting evidence has reported that circRNA can serve as ceRNAs for miRNAs, namely, as miRNA sponges (Liu et al., 2017b; Bai et al., 2018). A circRNA may contain multiple miRNA binding sites and may have adsorptive and suppressive effects on miRNAs. Thus, circRNAs can remove the inhibitory effect of miRNAs on their target mRNAs, indirectly upregulating these target mRNAs. As an example, in the plasma of acute ischemic stroke patients and in a mouse stroke model, circDLGAP4 was significantly downregulated, functioning as an endogenous miR-143 sponge to inhibit miR-143 activity and leading to the inhibition of target gene expression (Bai et al., 2018). In addition, in bladder carcinoma, it has been demonstrated that over-expression of circTCF25 could sponge miR-103a-3p and miR-107, increase CDK6 expression, and promote proliferation and migration *in vitro* and *in vivo* (Zhong et al., 2016). Interestingly, several studies stated that a protein can be translated from circRNAs in human cells driven by N6-methyladenosine22, suggesting a possible translatable function of circRNAs (Du et al., 2017; Yang et al., 2017). However, the number of relevant studies is quite limited, and further studies should be conducted to validate these novel results. As a consequence, based on the function of circRNAs as ceRNAs in regulating the activity of corresponding linear mRNAs by binding miRNAs, we first predicted the potential sponging miRNAs

for each differentially expressed circRNA by conserved seed sequence matches. We ranked miRNA candidates based on the mirSVR and listed the five highest-ranking miRNA candidates for each circRNA, including the five candidate circRNAs. Then, target-binding mRNAs for miRNA candidates were calculated and filtered with bioinformatics tools. In our study, a total of 5 circRNAs, 60 miRNAs, and 253 mRNAs were included to construct circRNA/mRNA of miRNA interactions, which presented a large interaction network for bioinformatic analysis. These results together lay the groundwork for future research into the specific circRNA/miRNA/mRNA network, which is beneficial for investigating the role of circRNAs in regulating the expression of target genes. We will next validate the selected interaction.

In addition, GO analysis and KEGG pathway analysis were performed to functionally annotate the predicted target mRNAs of circRNAs-miRNAs axes. First, the goal of the Gene Ontology Consortium is to produce a dynamic, controlled vocabulary that can be applied to all eukaryotes, even as knowledge of gene and protein roles in cells is accumulating and changing (Ashburner et al., 2000); thus, three independent ontologies accessible on the World Wide Web[4] are being constructed: biological process, molecular function, and cellular component. Briefly, we found that the target mRNAs are involved in multiple biological processes, cellular signaling pathways, protein activities and gene splicing in rat with SCI. As an example, the carbohydrate metabolic process was found to be one of the most significantly enriched and meaningful terms of biological processes after GO analysis. In addition, one previous study confirmed the central adiposity associations to carbohydrate and lipid metabolism in individuals with complete motor SCI (Gorgey et al., 2011). Thus, the results together suggested the functional roles of the circRNA/miRNA/mRNA network in regulating pathophysiology after SCI. Second, we used KEGG pathway analysis to reveal the potential roles of the target mRNAs regulated by circRNAs-miRNAs axes in diverse biological pathways. According to our annotation, the top two signaling pathways affected by the circRNAs-miRNAs axes were the AMPK signaling pathway and the peroxisome related pathway. Previous studies have explored the relationships between these pathways and pathophysiological processes after SCI. As an example, AMPK is a pivotal regulator of energy homeostasis, and after assessing the influence of longstanding and recent SCI on protein abundance of AMPK isoforms in human skeletal muscle, researchers found that physical/neuromuscular activity is an important determinant of isoform abundance of AMPK (Kostovski et al., 2013). Additionally, another report described the pharmacological activation of peroxisome proliferator-activated receptors due to their anti-inflammatory/antioxidant/anti-excitotoxic/pro-energetic profile in SCI (Esposito and Cuzzocrea, 2011). After pathway analysis, we performed pathway diagrams of the AMPK signaling pathway and the peroxisome related pathway (**Figures 8A,B**), presenting the most significant core downstream pathways of the circRNAs-miRNAs axes directly.

However, several questions remain to be answered. First and most importantly, the reader should bear in mind that this study was unable to validate the circRNA/miRNA/mRNA network predicted by bioinformatics, and our future work is to identify their functions. Next, the relatively small group size for the PCR experiments may limit the interpretation for candidate circRNAs and subsequent bioinformatics. Thus, the enlarged group size is needed to improve the scientific rigor. Then, it was beyond the scope of this study to examine the potential effect of different time points on the possible dynamic changes in circRNA expression patterns in the contused spinal cords of rats with SCI. Last but not least, we strongly recommend that future research should focus on different animal models and types of SCI to study the expression and functions of circRNAs.

Taken together, the current findings of this study were greatly significant in at least two major respects. On one hand, this study explored, for the first time, the significant alteration of circRNA expression profiles after traumatic SCI in rats. On the other hand, these differentially expressed circRNAs were predicted to closely correlate with post-SCI pathophysiology processes based on bioinformatics analysis. Despite its exploratory nature, this study offered deep insights into many possible treatment targets of SCI by regulating circRNAs.

DATA AVAILABILITY STATEMENT

The raw data supporting the conclusions of this manuscript will be made available by the authors, without undue reservation, to any qualified researcher.

AUTHOR CONTRIBUTIONS

CQ, C-BL, and M-LY performed the research. J-JL designed the research study. D-GY and FG contributed essential reagents or tools. CZ and L-JD analyzed the data. CQ wrote the manuscript. All authors read and approved the final manuscript.

FUNDING

This work was supported by a grant from the Special Fund for Basic Scientific Research of Central Public Research Institutes (2018CZ-1), the National Natural Science Foundation of China (General Program 81870979 and 81271366), Basic Scientific Research Foundation of China Rehabilitation Research Center (2018ZX-30), the Scientific Research Foundation of CRRC (2012C-1), the Beijing Science and Technology Major Project (D161100002816004), and the Capital Health Research and Development of Special (2018-1-6011).

ACKNOWLEDGMENTS

Special thanks to Pei-Pei Xu for her animal care.

SUPPLEMENTARY MATERIAL

The Supplementary Material for this article can be found online at: https://www.frontiersin.org/articles/10.3389/fnmol.2018.00497/full#supplementary-material

[4]http://www.geneontology.org

REFERENCES

Ashburner, M., Ball, C. A., Blake, J. A., Botstein, D., Butler, H., Cherry, J. M., et al. (2000). Gene ontology: tool for the unification of biology. the gene ontology consortium. *Nat. Genet.* 25, 25–29. doi: 10.1038/75556

Bai, Y., Zhang, Y., Han, B., Yang, L., Chen, X., Huang, R., et al. (2018). Circular RNA DLGAP4 ameliorates ischemic stroke outcomes by targeting mir-143 to regulate endothelial-mesenchymal transition associated with blood-brain barrier integrity. *J. Neurosci.* 38, 32–50. doi: 10.1523/JNEUROSCI.1348-17.2017

Basso, D. M., Beattie, M. S., and Bresnahan, J. C. (1996). Graded histological and locomotor outcomes after spinal cord contusion using the NYU weight-drop device versus transection. *Exp. Neurol.* 139, 244–256. doi: 10.1006/exnr.1996.0098

Chen, S., Zhang, L., Su, Y., and Zhang, X. (2018a). Screening potential biomarkers for colorectal cancer based on circular RNA chips. *Oncol. Rep.* 39, 2499–2512. doi: 10.3892/or.2018.6372

Chen, X. L., Wang, Y., Peng, W. W., Zheng, Y. J., Zhang, T. N., Wang, P. J., et al. (2018b). Effects of interleukin-6 and IL-6/AMPK signaling pathway on mitochondrial biogenesis and astrocytes viability under experimental septic condition. *Int. Immunopharmacol.* 59, 287–294. doi: 10.1016/j.intimp.2018.04.020

Di Cara, F., Sheshachalam, A., Braverman, N. E., Rachubinski, R. A., and Simmonds, A. J. (2018). Peroxisome-mediated metabolism is required for immune response to microbial infection. *Immunity* 48, 832–833. doi: 10.1016/j.immuni.2018.03.035

Dimartino, D., Colantoni, A., Ballarino, M., Martone, J., Mariani, D., Danner, J., et al. (2018). The Long non-coding RNA lnc-31 interacts with rock1 MRNA and mediates its YB-1-dependent translation. *Cell Rep.* 23, 733–740. doi: 10.1016/j.celrep.2018.03.101

Du, W. W., Zhang, C., Yang, W., Yong, T., Awan, F. M., and Yang, B. B. (2017). Identifying and characterizing circRNA-protein interaction. *Theranostics* 7, 4183–4191. doi: 10.7150/thno.21299

Enright, A. J., John, B., Gaul, U., Tuschl, T., Sander, C., and Marks, D. S. (2003). MicroRNA targets in drosophila. *Genome Biol.* 5:R1.

Esposito, E., and Cuzzocrea, S. (2011). Targeting the peroxisome proliferator-activated receptors (PPARs) in spinal cord injury. *Expert Opin. Ther. Targets* 15, 943–959. doi: 10.1517/14728222.2011.581231

Fan, X., Wang, J. Z., Lin, X. M., and Zhang, L. (2017). Stem cell transplantation for spinal cord injury: a meta-analysis of treatment effectiveness and safety. *Neural Regen. Res.* 12, 815–825. doi: 10.4103/1673-5374.206653

Floris, G., Zhang, L., Follesa, P., and Sun, T. (2017). Regulatory role of circular RNAs and neurological disorders. *Mol. Neurobiol.* 54, 5156–5165. doi: 10.1007/s12035-016-0055-4

Friedman, R. C., Farh, K. K., Burge, C. B., and Bartel, D. P. (2009). Most mammalian mRNAs are conserved targets of microRNAs. *Genome Res.* 19, 92–105. doi: 10.1101/gr.082701.108

Gorgey, A. S., Mather, K. J., and Gater, D. R. (2011). Central adiposity associations to carbohydrate and lipid metabolism in individuals with complete motor spinal cord injury. *Metabolism* 60, 843–851. doi: 10.1016/j.metabol.2010.08.002

Hextrum, S., and Bennett, S. (2018). A critical examination of subgroup analyses: the national acute spinal cord injury studies and beyond. *Front. Neurol.* 9:11. doi: 10.3389/fneur.2018.00011

Hu, A. M., Li, J. J., Sun, W., Yang, D. G., Yang, M. L., Du, L. J., et al. (2015). Myelotomy reduces spinal cord edema and inhibits aquaporin-4 and aquaporin-9 expression in rats with spinal cord injury. *Spinal Cord* 53, 98–102. doi: 10.1038/sc.2014.209

Hu, J. Z., Huang, J. H., Zeng, L., Wang, G., Cao, M., and Lu, H. B. (2013). Anti-apoptotic effect of microRNA-21 after contusion spinal cord injury in rats. *J. Neurotrauma* 30, 1349–1360. doi: 10.1089/neu.2012.2748

Hu, W., Bi, Z. Y., Chen, Z. L., Liu, C., Li, L. L., Zhang, F., et al. (2018). Emerging landscape of circular RNAs in lung cancer. *Cancer Lett.* 427, 18–27. doi: 10.1016/j.canlet.2018.04.006

Huang, M., Zhong, Z., Lv, M., Shu, J., Tian, Q., and Chen, J. (2016). Comprehensive analysis of differentially expressed profiles of lncRNAs and circRNAs with associated co-expression and ceRNA networks in bladder carcinoma. *Oncotarget* 7, 47186–47200. doi: 10.18632/oncotarget.9706

Hwang, T., Park, C. K., Leung, A. K., Gao, Y., Hyde, T. M., Kleinman, J. E., et al. (2016). Dynamic regulation of RNA editing in human brain development and disease. *Nat. Neurosci.* 19, 1093–1099. doi: 10.1038/nn.4337

Khuyagbaatar, B., Kim, K., and Kim, Y. H. (2015). Conversion equation between the drop height in the New York university impactor and the impact force in the infinite horizon impactor in the contusion spinal cord injury model. *J. Neurotrauma* 32, 1987–1993. doi: 10.1089/neu.2015.3875

Kostovski, E., Boon, H., Hjeltnes, N., Lundell, L. S., Ahlsen, M., Chibalin, A. V., et al. (2013). Altered content of AMP-activated protein kinase isoforms in skeletal muscle from spinal cord injured subjects. *Am. J. Physiol. Endocrinol. Metab.* 305, E1071–E1080. doi: 10.1152/ajpendo.00132.2013

Larionov, A., Krause, A., and Miller, W. (2005). A standard curve based method for relative real time PCR data processing. *BMC Bioinformatics* 6:62. doi: 10.1186/1471-2105-6-62

Liu, C., Zhang, C., Yang, J., Geng, X., Du, H., Ji, X., et al. (2017a). Screening circular RNA expression patterns following focal cerebral ischemia in mice. *Oncotarget* 8, 86535–86547. doi: 10.18632/oncotarget.21238

Liu, J., Liu, T., Wang, X., and He, A. (2017b). Circles reshaping the RNA world: from waste to treasure. *Mol. Cancer* 16:58. doi: 10.1186/s12943-017-0630-y

Lv, H. R. (2017). lncRNA-Map2k4 sequesters miR-199a to promote FGF1 expression and spinal cord neuron growth. *Biochem. Biophys. Res. Commun.* 490, 948–954. doi: 10.1016/j.bbrc.2017.06.145

Manohar, A., Foffani, G., Ganzer, P. D., Bethea, J. R., and Moxon, K. A. (2017). Cortex-dependent recovery of unassisted hindlimb locomotion after complete spinal cord injury in adult rats. *eLife* 6:e23532. doi: 10.7554/eLife.23532

Memczak, S., Jens, M., Elefsinioti, A., Torti, F., Krueger, J., Rybak, A., et al. (2013). Circular RNAs are a large class of animal RNAs with regulatory potency. *Nature* 495, 333–338. doi: 10.1038/nature11928

Nagoshi, N., and Okano, H. (2017). Applications of induced pluripotent stem cell technologies in spinal cord injury. *J. Neurochem.* 141, 848–860. doi: 10.1111/jnc.13986

Nicolas, F. E. (2017). Role of ncRNAs in development, diagnosis and treatment of human cancer. *Recent Pat. Anticancer Drug Discov.* 12, 128–135. doi: 10.2174/1574892812666170105113415

Pang, X., Tang, Y., and Zhang, D. (2016). Role of miR-145 in chronic constriction injury in rats. *Exp. Ther. Med.* 12, 4121–4127. doi: 10.3892/etm.2016.3900

Pasquinelli, A. E. (2012). MicroRNAs and their targets: recognition, regulation and an emerging reciprocal relationship. *Nat. Rev. Genet.* 13, 271–282. doi: 10.1038/nrg3162

Qu, S., Yang, X., Li, X., Wang, J., Gao, Y., Shang, R., et al. (2015). Circular RNA: a new star of noncoding RNAs. *Cancer Lett.* 365, 141–148. doi: 10.1016/j.canlet.2015.06.003

Salgado-Somoza, A., Zhang, L., Vausort, M., and Devaux, Y. (2017). The circular RNA MICRA for risk stratification after myocardial infarction. *Int. J. Cardiol. Heart Vasc.* 17, 33–36. doi: 10.1016/j.ijcha.2017.11.001

Salmena, L., Poliseno, L., Tay, Y., Kats, L., and Pandolfi, P. P. (2011). A ceRNA hypothesis: the rosetta stone of a hidden RNA language? *Cell* 146, 353–358. doi: 10.1016/j.cell.2011.07.014

Scheff, S. W., Saucier, D. A., and Cain, M. E. (2002). A statistical method for analyzing rating scale data: the BBB locomotor score. *J. Neurotrauma* 19, 1251–1260. doi: 10.1089/08977150260338038

Shi, Z., Zhou, H., Lu, L., Li, X., Fu, Z., Liu, J., et al. (2017). The roles of microRNAs in spinal cord injury. *Int. J. Neurosci.* 127, 1104–1115. doi: 10.1080/00207454.2017.1323208

Sun, N., Zhang, G., and Liu, Y. (2018). Long non-coding RNA XIST sponges miR-34a to promotes colon cancer progression via Wnt/beta-catenin signaling pathway. *Gene* 665, 141–148. doi: 10.1016/j.gene.2018.04.014

Xie, B., Wang, Y., Lin, Y., Zhao, C. C., Mao, Q., Feng, J. F., et al. (2018). Circular RNA Expression profiles alter significantly after traumatic brain injury in rats. *J. Neurotrauma* 35, 1659–1666. doi: 10.1089/neu.2017.5468

Yang, D. G., Li, J. J., Gu, R., Yang, M. L., Zhang, X., Du, L. J., et al. (2013). Optimal time window of myelotomy in rats with acute traumatic spinal cord injury: a preliminary study. *Spinal Cord* 51, 673–678. doi: 10.1038/sc.2013.56

Yang, M. L., Li, J. J., Gao, F., Du, L. J., Zhao, H. P., Wang, Y. M., et al. (2014). A preliminary evaluation of the surgery to reconstruct thoracic breathing in patients with high cervical spinal cord injury. *Spinal Cord* 52, 564–569. doi: 10.1038/sc.2014.64

Yang, Y., Fan, X., Mao, M., Song, X., Wu, P., Zhang, Y., et al. (2017). Extensive translation of circular RNAs driven by N(6)-methyladenosine. *Cell Res.* 27, 626–641. doi: 10.1038/cr.2017.31

Zhao, R., Zhou, J., Dong, X., Bi, C., Jiang, R., Dong, J., et al. (2018). Circular RNA expression alteration in exosomes from the brain extracellular space after traumatic brain injury in mice. *J. Neurotrauma* 35, 2056–2066. doi: 10.1089/neu.2017.5502

Zhao, Y., Alexandrov, P. N., Jaber, V., and Lukiw, W. J. (2016). Deficiency in the ubiquitin conjugating enzyme UBE2A in alzheimer's disease (AD) is Linked to deficits in a natural circular miRNA-7 sponge (circRNA; ciRS-7). *Genes* 7:116. doi: 10.3390/genes7120116

Zhong, Z., Lv, M., and Chen, J. (2016). Screening differential circular RNA expression profiles reveals the regulatory role of circTCF25-miR-103a-3p/miR-107-CDK6 pathway in bladder carcinoma. *Sci. Rep.* 6:30919. doi: 10.1038/srep30919

Zhou, H. J., Wang, L. Q., Wang, D. B., Yu, J. B., Zhu, Y., Xu, Q. S., et al. (2018a). Long non-coding RNA MALAT1 contributes to inflammatory response of microglia following spinal cord injury via modulating miR-199b/IKKbeta/NF-kappaB signaling pathway. *Am. J. Physiol. Cell Physiol.* 315, C52–C61. doi: 10.1152/ajpcell.00278.2017

Zhou, R., Wu, Y., Wang, W., Su, W., Liu, Y., Wang, Y., et al. (2018b). Circular RNAs (circRNAs) in cancer. *Cancer Lett.* 425, 134–142. doi: 10.1016/j.canlet.2018.03.035

Zhu, H., Xie, R., Liu, X., Shou, J., Gu, W., Gu, S., et al. (2017a). MicroRNA-494 improves functional recovery and inhibits apoptosis by modulating PTEN/AKT/mTOR pathway in rats after spinal cord injury. *Biomed. Pharmacother.* 92, 879–887. doi: 10.1016/j.biopha.2017.05.143

Zhu, L. L., Li, M. Q., He, F., Zhou, S. B., and Jiang, W. (2017b). Mitochondria targeted peptide attenuates mitochondrial dysfunction, controls inflammation and protects against spinal cord injury-induced lung injury. *Cell Physiol. Biochem.* 44, 388–400. doi: 10.1159/000484919

Conflict of Interest Statement: The authors declare that the research was conducted in the absence of any commercial or financial relationships that could be construed as a potential conflict of interest.

frontiers in Molecular Neuroscience

BRIEF RESEARCH REPORT
published: 05 March 2019
doi: 10.3389/fnmol.2019.00037

Transcriptome Analysis of the Human Tibial Nerve Identifies Sexually Dimorphic Expression of Genes Involved in Pain, Inflammation, and Neuro-Immunity

Pradipta R. Ray[1,2]*, *Jawad Khan*[1,2], *Andi Wangzhou*[1,2], *Diana Tavares-Ferreira*[1,2], *Armen N. Akopian*[3], *Gregory Dussor*[1,2] *and Theodore J. Price*[1,2]

[1] School of Behavioral and Brain Sciences, The University of Texas at Dallas, Richardson, TX, United States, [2] Center for Advanced Pain Studies, The University of Texas at Dallas, Richardson, TX, United States, [3] Department of Endodontics, University of Texas Health San Antonio, San Antonio, TX, United States

Sex differences in gene expression are important contributors to normal physiology and mechanisms of disease. This is increasingly apparent in understanding and potentially treating chronic pain where molecular mechanisms driving sex differences in neuronal plasticity are giving new insight into why certain chronic pain disorders preferentially affect women vs. men. Large transcriptomic resources are now available and can be used to mine for sex differences to gather insight from molecular profiles using donor cohorts. We performed in-depth analysis of 248 human tibial nerve (hTN) transcriptomes from the GTEx Consortium project to gain insight into sex-dependent gene expression in the peripheral nervous system (PNS). We discover 149 genes with sex differential gene expression. Many of the more abundant genes in men are associated with inflammation and appear to be primarily expressed by glia or immune cells, with some genes downstream of Notch signaling. In women, we find the differentially expressed transcription factor SP4 that is known to drive a regulatory program, and may impact sex differences in PNS physiology. Many of these 149 differentially expressed (DE) genes have some previous association with chronic pain but few of them have been explored thoroughly. Additionally, using clinical data in the GTEx database, we identify a subset of DE, sexually dimorphic genes in diseases associated with chronic pain: arthritis and Type II diabetes. Our work creates a unique resource that identifies sexually dimorphic gene expression in the human PNS with implications for discovery of sex-specific pain mechanisms.

Keywords: sex-differential gene expression, human peripheral nerve transcriptome, peripheral nervous system sex differences, pain genes, pro-inflammatory genes

OPEN ACCESS

Edited by:
Guilherme Lucas,
University of São Paulo, Brazil

Reviewed by:
Alexandre Henriques,
Neuro-Sys, France
Sangsu Bang,
Duke University, United States

***Correspondence:**
Pradipta R. Ray
pradiptaray@gmail.com

Received: *26 October 2018*
Accepted: *31 January 2019*
Published: *05 March 2019*

Citation:
Ray PR, Khan J, Wangzhou A, Tavares-Ferreira D, Akopian AN, Dussor G and Price TJ (2019) Transcriptome Analysis of the Human Tibial Nerve Identifies Sexually Dimorphic Expression of Genes Involved in Pain, Inflammation, and Neuro-Immunity. Front. Mol. Neurosci. 12:37. doi: 10.3389/fnmol.2019.00037

INTRODUCTION

Sex-differential gene regulation and resultant changes in transcriptome, proteome, and metabolome shape sexually dimorphic physiology and behavior in animals. Sex-differential molecular profiles in human tissues have a profound effect on health, resulting in disease susceptibility, prevalence and pathophysiology differences between sexes. Acute and chronic pain

have a staggering global disease burden, and prevalence of many chronic pain conditions like fibromyalgia and neuralgia have been shown to be higher in women (De Toledo et al., 2016), and sex-differential molecular changes in the peripheral and central nervous system (CNS) have been implicated in preclinical models (Mogil, 2012). Transcriptome profiles of human Dorsal Root Ganglia (DRG) and Trigeminal Ganglia have been characterized previously (Flegel et al., 2015; LaPaglia et al., 2018; Ray et al., 2018) but these studies are underpowered for capturing subtle transcriptional changes between sexes. Human tibial nerve (hTN) transcriptomes, which contains axons from DRG neurons, along with a panel of other harvested tissues, have been profiled using RNA-sequencing (RNA-seq) in hundreds of male and female donors as part of the GTEx project (Lonsdale et al., 2013). Some studies have characterized sex-differential gene expression changes (Chen et al., 2016; Gershoni and Pietrokovski, 2017) and investigated the evolutionary and regulatory basis of such changes across the repertoire of GTEx tissues, but none have focused on the hTN.

We cataloged sex differences in the hTN transcriptome under baseline conditions focusing on potential functional impact in the context of pain, inflammation and neuro-immunity. Previous analysis of the human peripheral nerve transcriptome has focused on changes in disease pathologies like nerve sheath tumors (Lee et al., 2014), or diabetic neuropathy (Hur et al., 2011; Luo et al., 2017). To our knowledge, sexual dimorphism studies on mammalian peripheral nerves is limited to a single microarray study in a rodent model of Type II diabetes (O'Brien et al., 2016). Our work thus fills an important gap in transcriptome studies of the human PNS and we created an online database (https://www.utdallas.edu/bbs/painneurosciencelab/sensoryomics/sexdiffnerve/) identifying sex differentially expressed genes in the hTN, and identified potentially functionally important genes by intersectional analysis with relevant databases. We further analyzed the cell type of expression of these genes, putatively identifying axonally localized transcripts. We also investigated the possible regulatory role of sex hormones in the sexual dimorphic genes by analyzing correlation of age with gene expression.

MATERIALS AND METHODS

Data Use Policy

We only analyzed anonymized samples for which the corresponding donor consent information was available in the GTEx dataset (dbGAP phs000424.v7.p2) at the time of analysis. All of the datasets we analyzed were approved for General Research Use (GRU) and thus have no further limitations outside of those in the NIH model Data Use Certification Agreement. Our work was further approved by the UT Dallas IRB (protocol number 15-237).

Abbreviations: hTN, human tibial nerve; CJP, chronic joint pain cohort; T2D, Type II diabetes cohort; BSL, baseline cohort; DE, differentially expressed; BHP, Benjamini-Hochberg procedure; MFR, male:female ratio; PIN, protein interaction network; DRG, dorsal root ganglion; PNS, peripheral nervous system; PAR: pseudo-autosomal region; TPM, transcripts per million; BMI, body mass index; PCA, principal components analysis.

Donor Selection by GTEx Consortium

The Genotype Tissue Expression (GTEx) consortium performed RNA-seq on a panel of harvested tissues, including the hTN, in a large cohort of consented tissue, organ or post-mortem donors. Donors of both sexes, from all ancestry groups between the ages of 21–70, and with Body Mass Index (BMI) between 18.5 and 35 were eligible. Post-mortem donors were also constrained to have had no whole blood transfusion within 48 h prior to death, and time between death and tissue collection was constrained to be $<$24 h. Donors were further restricted to have no history of metastatic cancer, no chemotherapy or radiation therapy within 2 years prior to death, and no communicable diseases that disqualify people for organ or tissue donation.

Sample Processing by GTEx Consortium

This provided a diverse dataset that is uniquely suitable for studying differences across sub-cohorts, such as sex differences in our study. Post-excision, aliquots were stabilized in a solution containing ethanol and methanol, acetic acid and Paxgene Tissue fixative (Qiagen). A portion of each tissue was then subject to RNA extraction and quantification. Next Generation sequencing (RNA-seq) was performed using the Illumina TruSeq platform, averaging $\sim$50 million reads per sample. Sequenced reads were mapped to the human reference genome and transcriptome using the STAR toolkit (Dobin et al., 2013) and relative abundance quantified as Transcripts per Million (TPM) using the RSEM tool (Li and Dewey, 2011). RNA quality was checked using the RNA Integrity Number, and sequencing quality was analyzed using the RNA-SeqC toolkit (DeLuca et al., 2012). Donor level data included basic demographics, use of medication, medical history, results of laboratory tests, and circumstances of death were collected from the donor or next of kin and compared with the medical record. Donor level data and sample level data (which includes ischemic time, and comments from prosector and pathology reviewer) were analyzed for completeness and quality before release by the consortium. Further details of bench protocols and computational pipelines used by the GTEx consortium can be obtained from Lonsdale et al. (2013).

GTEx Data Requantification

PAXgene preserved hTN RNA-seq samples (dbGAP phs000424.v7.p2) with total RNA sequenced on the Illumina Truseq platform (and available donor consent information at the time of analysis) were identified. Samples noted to have sepsis, HIV infection, Type I diabetes or having both chronic joint pain and Type II diabetes were not used. The GTEx uniform processing pipeline provided relative abundance of genes in the form of normalized read counts as Transcripts per Million (TPM). GTEx RNA-seq assays used rRNA-depleted total RNA libraries containing reads from non-polyA transcripts with the proportion of such reads potentially varying between samples (Cui et al., 2010). We thus limited our analysis to validated coding genes by re-constraining the TPMs of coding genes [based on GENCODE annotation (Harrow et al., 2012)] to sum to a million.

Separation Into Cohorts

We mined the associated clinical information for samples to classify donors into three cohorts based on well-understood phenotypic changes in peripheral nerves: those noted to have arthritis or rheumatoid arthritis (chronic joint pain cohort, CJP), those noted to suffer from Type II diabetes (Type II diabetes cohort, T2D, which often causes diabetic neuropathic pain), and those without either of these diseases (baseline cohort, BSL) based on studies in the literature that suggested phenotypic and molecular profile changes in peripheral nerves in arthritic and diabetic patients (Hur et al., 2011; Pongratz and Straub, 2013). We then studied whether these cohorts could be analyzed together, or needed to be analyzed separately.

For the entire dataset including all three cohorts, only stably expressed genes (filtering out genes with median TPM across cohorts <0.5 or maximum TPM across cohorts <1.0) were analyzed, and each gene's normalized entropy score e_i (based on Ray et al., 2018) using samples from all cohorts was calculated as a measure of its variability:

$$e_i = -\frac{1}{log_2(N)} \sum_j \frac{t_{i,j}}{\sum_k t_i,k} log_2 \frac{t_{i,j}}{\sum_k t_i,k}.$$

where $t_{i,j}$ is the TPM of the ith gene in the jth sample, with i indexing genes and j and k indexing samples, N being the total number of samples, and log 0 being defined as 0. Principal Components Analysis (PCA) was performed for samples (**Figure 1A**) using stably expressed, highly variable genes (with normalized entropy using samples in all three cohorts in the 90th percentile or above). The top two principal components were found to account for 72% of the total variance in the dataset but did not spatially segregate the samples on the basis of sex or membership in the three cohorts, which is expected since sex differences or disease pathologies like arthritis or diabetes are not expected to cause transcriptome-wide changes (like cancer). Based on the first two PCA dimensions, we performed outlier analysis to identify samples that were two standard deviations or further away from the origin (around

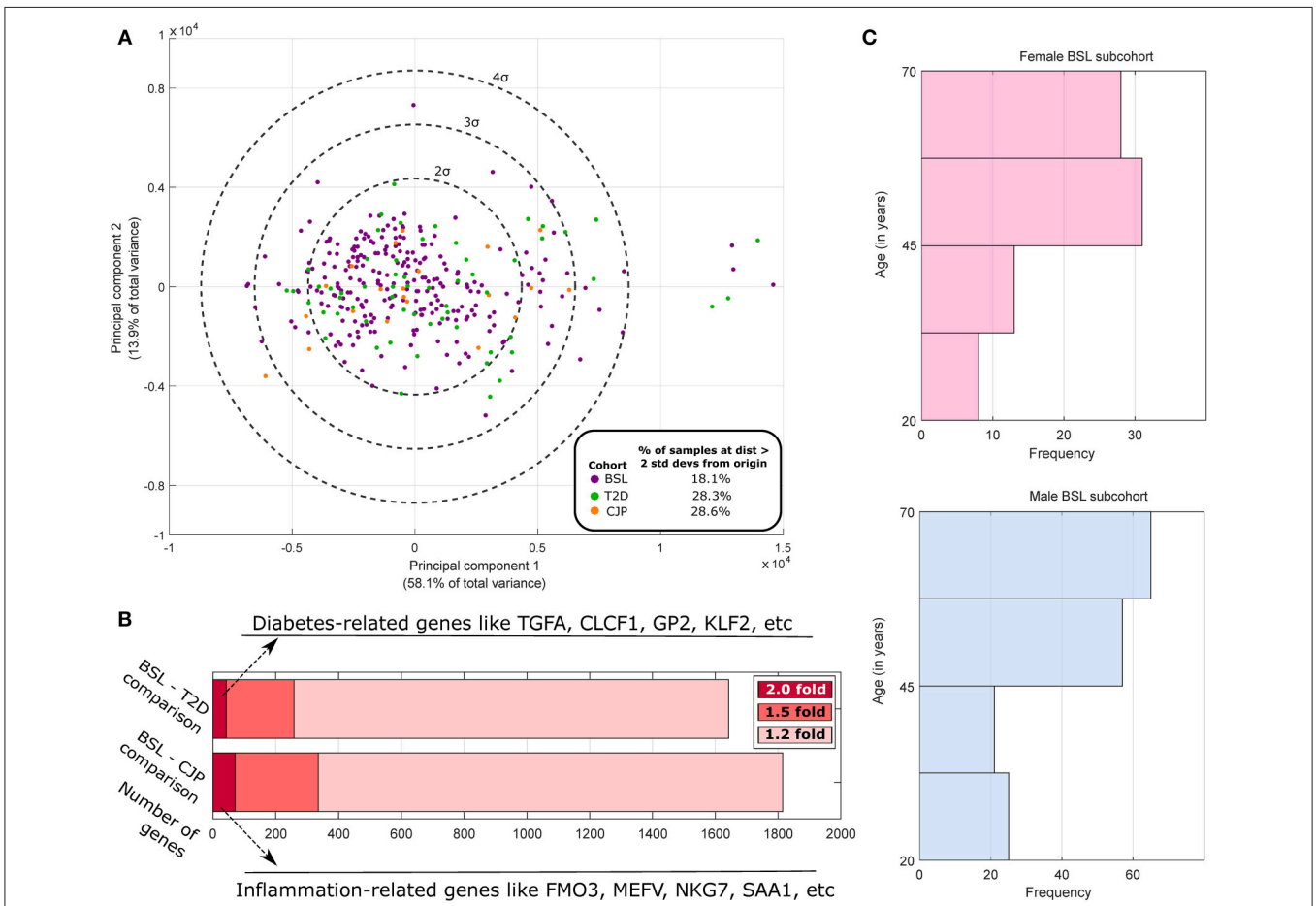

FIGURE 1 | Population analysis of GTEx human tibial nerve samples. **(A)** PCA of the gene expression profile across all three cohorts of highly variable genes and subsequent plotting of the top 2 principal components show a larger fraction of outlier samples in CJP and T2D with respect to BSL. **(B)** The number of genes that are DE at 1.2-fold, 1.5-fold, and 2-fold when comparing the BSL with CJP and T2D are shown, along with some of the strongest DE genes. **(C)** The histogram of age in male and female BSL subcohorts show a similar distribution.

which the principal component values are centered). We note an ∼50% increase in the proportion of outlier samples in the CJP and T2D cohorts (both >28%) as compared to the BSL cohort (18.1%). Additionally, a preliminary analysis finds that over 250 genes are differentially expressed at the effect size of 1.5-fold change or above for both BSL–CJP and BSL–T2D comparisons (**Figure 1B**). These include genes well-known to be implicated in inflammation (for BSL–CJP comparison) and diabetes (for BSL–T2D comparison). These findings suggest very distinct phenotypes in the three cohorts, and any sex difference studies in the cohorts are thus more suited for analysis separately due to the large inter-cohort differences.

However, while rigorous statistical hypotheses testing to identify DE genes was performed on BSL (168:80 Male: Female Ratio/MFR) to characterize sex differences in healthy hTN (**Supplementary Table 1**), hypotheses testing was not performed in CJP (11:10 MFR) or T2D (44:16 MFR) due to these cohorts being underpowered for DE gene identification. Expression values, median fold change and Strictly Standardized Mean Differences for male–female gene expression changes in the two cohorts are shown in **Supplementary Tables 2**, **3** as a starting point for future studies. Strictly standardized mean difference (s_i) (Zhang, 2010) is a sample statistic that is often used to look at differences in effect size, while controlling for dispersion of data, under limited replication.

$$s_i = \frac{\mu_{F,i} - \mu_{M,i} + \in}{\sqrt{\sigma^2_{F,i} + \sigma^2_{M,i}} + \in}$$

where $\mu_{F,i}$ and $\mu_{M,i}$ are mean TPMs for female and male member of a cohort for the ith gene, $\sigma_{F,i}$ and $\sigma_{M,I}$ are the corresponding standard deviations with covariance assumed to be 0, with i indexing genes, and ε being a small smoothing factor (0.001) added to both the numerator and denominator.

Analysis of Potential Confounding Factors in Male and Female BSL Subcohorts

Based on donor level data, we performed a thorough analysis of documented variables that could potentially be a confounding factor in our analysis (results shown in **Table 1**). We identified several variables that were potentially confounding factors, including demographic (age, race), anatomical (BMI), and medical history based (presence of autoimmune disease like lupus or scleroderma, and inflammatory diseases like sarcoidosis or cellulites) variables. We find no appreciable difference in the breakup of BSL male and female subcohorts by race, and distribution of age (**Figure 1C**) and BMI are also comparable. Examined disease conditions were either completely absent in both subcohorts, or present in a small number of males (sarcoidosis). Height and weight distributions for the male and female subcohorts are noted to be different, as expected.

DE Gene Identification

We performed non-parametric statistical hypotheses testing to identify DE genes. To minimize effects of multiple testing, we filtered out lowly expressed or undetectable genes (based on

TABLE 1 | Statistics for BSL cohort.

	Male	Female
Cohort size	168	80
CONSENT VARIABLES		
Consent group (phv00169057.v7.p2.c1)		
General research use	100.0%	100.0%
No consent available	0.0%	0.0%
VARIABLES DEFINING COHORT		
Male	100.0%	0.0%
Female	0.0%	100.0%
Type I/II diabetes (MHT1D or MHT2D)		
Yes	0.0%	0.0%
No	100.0%	100.0%
Arthritis (MHARTHTS or MHRA)		
Yes	0.0%	0.0%
No	100.0%	100.0%
Sepsis (MHSEPSIS)		
Yes	0.0%	0.0%
No	100.0%	100.0%
HIV serology testing outcome (LBHIV1NT)		
Positive	0.0%	0.0%
Negative	94.6%	97.5%
Not performed	5.4%	2.5%
DEMOGRAPHIC VARIABLES		
Race (RACE)		
Asian	2.4%	2.5%
African American/Black	8.9%	11.3%
White	86.3%	86.3%
Am. Indian/Alaska Native	0.0%	0.0%
Unknown	2.4%	0.0%
Age in years (AGE)		
Mean	50.9	52.0
Standard deviation	14.0	12.9
BMI/HEIGHT/WEIGHT		
Body mass index (BMI)		
Mean	27.2	27.3
Standard deviation	3.9	3.9
Height in inches (HGHT)		
Mean	69.8	64.8
Standard deviation	3.1	2.8
Weight in pounds (WGHT)		
Mean	188.8	163.6
Standard deviation	32.3	26.8
POTENTIALLY CONFOUNDING CLINICAL VARIABLES		
Lupus (MHLUPUS)		
Yes	0.0%	0.0%
No	100.0%	100.0%
Cellulites (MHCLLULTS)		
Yes	0.0%	0.0%
No	100.0%	100.0%
Scleroderma (MHSCLRDRM)		
Yes	0.0%	0.0%
No	100.0%	100.0%
Sarcoidosis (MHSRCDSS)		
Yes	1.2%	0.0%
No	98.8%	100.0%

Sample Characteristics. Distribution of relevant demographic, anatomical, clinical and medical history variables for the male and female subcohorts in BSL show no significant differences for potentially confounding variables.

the conservative filtering criterion of median gene TPM <0.5 or maximum gene TPM <1.0 in both males and females in a cohort). We also filtered out genes that were ubiquitously expressed in BSL by calculating the normalized entropy (defined previously) across all samples in the BSL cohort. Since higher normalized entropy signifies more ubiquitous expression, we retained only those expressed genes in our analysis whose normalized entropy was less than the 75th percentile of normalized entropies of expressed coding genes, thus performing gene filtering in a manner agnostic to the sex of the samples. Wilcoxon rank-sum test (Wilcoxon, 1945) was used to calculate *p*-values for differences in the male and female sub-cohorts in BSL for the median (50th percentile) and the upper quartile (75th percentile), which can be robustly estimated given the cohort size. To test for differences at the 50th percentile (median), the entire male and female BSL sub-cohorts were used for comparison. In order to identify differences at the 75th percentile (upper quartile), only values greater than or equal to the medians of the male and female BSL sub-cohorts were used. To account for multiple testing, the Benjamini–Hochberg Procedure (BHP) (Benjamini and Hochberg, 1995) was used for both the 50th and 75th percentile tests with a False Discovery Rate (FDR) threshold of 0.05 for both tests (suggesting a combined FDR of 0.1). Since test statistics for the two tests are well-correlated due to overlap of data, the empirical FDR is effectively in the range (0.05, 0.1).

Age–TPM Correlational Analysis

In order to understand how age affects gene abundances on the sex differentially expressed gene set, we first performed PCA on the BSL samples using only the 149 sex-DE genes. Correlation [Pearsons' Correlational Coefficient R (Pearson, 1895)] was calculated between the principal components and age. We also calculated Pearson's R separately for the male and female subcohorts of BSL for the sex-DE genes. For the male subcohort, BHP was performed on the corresponding *p*-values to identify $R > 0.20$ or $R < -0.20$ as a statistically significant correlation. For the female subcohort, while the number of samples were less, and the number of comparisons also less (Y chromosomal genes not tested), we used the same thresholds for consistency.

The list of sex differentially expressed genes are present in **Table 2**, and a searchable public database with gene expression values for all genes, as well as all code and data for the analyses can be found online at the companion website https://www.utdallas.edu/bbs/painneurosciencelab/sensoryomics/sexdiffnerve/.

RESULTS

We identified 29 genes in males, and 19 in females that were statistically significantly DE at ≥1.2-fold change (in their relative abundance/TPM) between the sexes in BSL at the 50th percentile. Additionally, we identified an additional 74 genes in males (**Figure 2**; **Table 2**), and 27 genes in females that were DE at the 75th percentile (**Figure 3**; **Table 2**). While several of these genes (including the 24 DE sex chromosomal genes) have been previously identified in the literature (Chen et al., 2016; Gershoni and Pietrokovski, 2017), our analysis identified new DE genes not identified in previous studies (Chen et al., 2016; Gershoni and Pietrokovski, 2017) including several that are potentially relevant to PNS function and pain mechanisms, including ISLR2, SP4, and TPPP2 (Chu et al., 2011; Aoki et al., 2014; Panza et al., 2015).

Neural Tissue Enriched Genes

We found several genes that are sex-differential in expression and are enriched in expression in neural tissues. To identify neural tissue enriched genes, we identified genes in our DE gene list with high (≥0.5) Neural Proportion Scores (quantified in Ray et al., 2018) suggesting that they are primarily expressed in neurons or glia (in the CNS and PNS). NTRK1, which is known to be enriched in mammalian sensory neurons, was more abundant in males at both the 50th and 75th percentiles (**Figure 2**), suggesting sex-differential axonal mRNA trafficking. RNF165, involved in axonal growth, was also more abundant in male samples at the 75th percentile (**Figure 2**), and is another putative axonally transported mRNA. Well-known Schwann cell genes like Sonic Hedgehog (SHH) (Babcock et al., 2011) and Artemin (ARTN) (Lippoldt et al., 2013), that have been shown to be involved in pain, were also DE and higher in males at the 75th percentile (**Figure 2**). ISLR2 and MEGF11, known to be involved in axonal pathfinding, were differentially expressed in subsets of males and females, respectively (**Figures 2**, **3**), and are potentially expressed in neurons and glia, respectively. Other neurally enriched genes that were DE in our datasets include PGBD5 and RNA helicase MOV10L1 in females [whose ortholog MOV10 has been shown to be implicated in nerve injury response in rodents (Melemedjian et al., 2011)], and AGAP2, NXPH3, and NRGN in males (**Table 2**). A small number of genes (SHH, *EFCAB5, FABP7*), which were neural tissue enriched, showed stronger or comparable sex-dependent expression in the hTN with respect to other tissues we examined (**Supplementary Table 4**).

To potentially identify the cell type of expression of neural tissue enriched genes, we analyzed the mouse nervous system single cell gene expression database at mousebrain.org (Zeisel et al., 2018) as well as the literature. Despite species' divergence of transcriptional regulation, we identified 15 genes whose murine orthologs were distinctly expressed in neuronal or glial cells in the mouse PNS (**Figure 4A**). Several of the neuronally expressed genes (NTRK1, ATP8A2, SRRM3, TMEM255A, RNF165, ISLR2) are expressed in the human DRG and have been shown in the literature to be important for axonal viability and routing or neurite outgrowth, suggesting that these are likely candidates for axonal mRNA transport and local translation.

Pro-inflammatory Gene Signatures

The DE gene set with higher expression in subsets of male BSL sub-cohort showed a different pro-inflammatory gene signature (ARTN, HP, NOTCH1, CCL2, DIO2, and others), with respect to the female BSL sub-cohort (SULF1, GPR64, KRT4), suggesting sex-differential expression patterns of inflammatory gene markers under normal conditions (**Table 2**). This agrees with studies showing sex differences in clinical markers of inflammation (Casimir et al., 2010). Interestingly, the ratio of DE pro-inflammatory to anti-inflammatory genes in males

TABLE 2 | Statistically significant DE genes for BSL male vs. female subcohort analysis (statistically significant outcomes in boldface).

Gene #	Gene	Log2 Fold change at 50th percentile (female:male, smoothing factor 0.0001)	*P*-value for 50th percentile rank-sum test	Log2 Fold change at 75th percentile (female:male, smoothing factor 0.0001)	*P*-value for 75th percentile rank-sum test	Normalized entropy	Pearsons R (male age with TPM)	Pearsons R (fem age with TPM)	Gene #	Gene	Log2 Fold change at 50th percentile (female:male, smoothing factor 0.0001)	*P*-value for 50th percentile rank-sum test	Log2 Fold change at 75th percentile (female:male, smoothing factor 0.0001)	*P*-value for 75th percentile rank-sum test	Normalized entropy	Pearsons R (male age with TPM)	Pearsons R (fem age with TPM)
		Thresholds: >0.26, or <-0.26	BHP based *p*-value threshold for 0.05 FDR: 2.38E-04	Thresholds: >0.26, or <-0.26	BHP based *p*-value threshold for 0.05 FDR: 3.50E-03	Normalized entropy threshold: <0.9895	Pearsons R threshold >0.20 or <-0.20	Same threshold used as in male dataset			Thresholds : >0.26, or <-0.26	BHP based *p*-value threshold for 0.05 FDR: 2.38E-04	Thresholds: >0.26, or <-0.26	BHP based *p*-value threshold for 0.05 FDR: 3.50E-03	Normalized entropy threshold: <0.9895	Pearsons R 0.05 FDR threshold (>0.20 or <-0.20)	Same threshold used as in male dataset
1	ZFX	**0.59**	**1.28E-31**	**0.59**	**1.42E-18**	0.9889	0.16	−0.13	41	TF	0.20	2.72E-02	**0.35**	**5.49E-04**	0.9625	0.11	0.03
2	EIF1AX	**0.59**	**4.36E-29**	**0.58**	**3.90E-19**	0.9888	−0.07	−0.19	42	C5orf64	0.27	3.11E-02	**0.30**	**3.38E-04**	0.9619	−0.15	0.05
3	KDM6A	**0.65**	**2.14E-25**	**0.58**	**3.24E-17**	0.9859	**0.27**	0.13	43	MOV10L1	0.19	4.04E-02	**0.32**	**7.96E-04**	0.9543	−0.07	0.02
4	RPS4X	**0.53**	**1.62E-15**	**0.56**	**6.72E-17**	0.9838	−0.09	−0.01	44	TMEM125	0.67	4.53E-02	**0.29**	**2.46E-03**	0.8652	0.01	−0.16
5	MAP7D2	**1.40**	**2.02E-14**	**1.48**	**1.25E-15**	0.9065	0.01	−0.06	45	CD8B	0.16	7.16E-02	**0.35**	**2.75E-04**	0.9530	0.13	0.12
6	DDX3X	**0.55**	**2.07E-13**	**0.53**	**5.71E-16**	0.9803	**0.23**	−0.16	46	C17orf97	0.37	7.53E-02	**0.30**	**2.25E-03**	0.9162	−0.03	0.09
7	OFD1	**0.50**	**2.40E-12**	**0.41**	**2.84E-15**	0.9862	0.08	0.17	47	KCNRG	0.17	NA	**−0.51**	**1.60E-03**	0.8630	0.06	−0.08
8	PNPLA4	**0.37**	**2.50E-12**	**0.34**	**5.63E-15**	0.9887	−0.10	−0.05	48	ATAD3C	−0.27	2.70E-01	**−0.40**	**1.35E-03**	0.9428	0.16	−0.02
9	EIF2S3	**0.40**	**2.52E-09**	**0.45**	**2.38E-12**	0.9843	**0.31**	0.10	49	ASB8	−0.08	2.60E-01	**−0.28**	**3.25E-04**	0.9815	**0.23**	0.07
10	TXLNG	**0.34**	**1.84E-08**	**0.39**	**5.73E-11**	0.9859	0.08	0.00	50	CYP4A22	−0.01	2.10E-01	**−0.31**	**1.08E-03**	0.9431	0.06	0.06
11	PRSS16	**0.92**	**2.44E-07**	**0.57**	**8.44E-09**	0.8479	0.04	0.02	51	UBBP4	−0.15	2.04E-01	**−0.27**	**5.38E-04**	0.9533	0.05	−0.18
12	CA5B	**0.34**	**7.83E-07**	**0.27**	**3.27E-07**	0.9811	0.14	−0.17	52	REEP1	−0.16	1.88E-01	**−0.29**	**1.12E-03**	0.9600	−0.04	−0.16
13	ZRSR2	**0.63**	**7.36E-06**	**0.43**	**2.13E-07**	0.9614	0.11	−0.04	53	ISLR2	−0.09	1.81E-01	**−0.29**	**1.35E-03**	0.9559	0.12	−0.11
14	SEZ6L2	**0.34**	**1.33E-05**	**0.28**	**7.13E-07**	0.9759	−0.19	−0.04	54	RARRES1	−0.31	1.62E-01	**−0.65**	**1.17E-03**	0.8621	**−0.26**	**−0.25**
15	PRKX	**0.43**	**2.59E-05**	**0.28**	**2.66E-06**	0.9773	0.14	0.08	55	GMCL1	−0.17	1.38E-01	**−0.28**	**1.81E-04**	0.9588	**0.23**	−0.12
16	CPZ	**0.73**	**8.35E-05**	**0.57**	**5.56E-07**	0.9164	0.01	**0.26**	56	FLT1	−0.82	9.39E-02	**−0.40**	**1.43E-03**	0.8864	0.18	−0.09
17	ASMT	**0.54**	**1.33E-04**	**0.32**	**2.17E-05**	0.9494	−0.11	−0.03	57	STRA6	−0.10	9.07E-02	**−0.30**	**7.81E-04**	0.9684	**0.35**	0.16
18	SNRPG	**0.49**	**2.04E-04**	**0.32**	**1.12E-03**	0.9702	**−0.24**	0.15	58	ADCY1	−0.18	8.96E-02	**−0.32**	**1.51E-03**	0.9552	0.03	0.13
19	MCOLN3	**0.35**	**2.38E-04**	**0.33**	**2.95E-05**	0.9730	−0.14	−0.09	59	DHRS3	−0.26	8.75E-02	**−0.30**	**2.14E-04**	0.9606	0.14	0.03
20	SLC27A6	0.30	4.85E-04	**0.39**	**2.68E-07**	0.9760	**−0.35**	−0.19	60	CCL2	−0.22	8.54E-02	**−0.44**	**3.55E-03**	0.8938	−0.06	0.13
21	PGBD5	0.29	5.62E-04	**0.33**	**2.02E-05**	0.9722	**−0.22**	0.06	61	MUSTN1	−0.38	7.84E-02	**−0.38**	**1.37E-05**	0.9543	−0.12	**−0.31**
22	CD3G	0.65	8.17E-04	**0.26**	**7.51E-04**	0.9358	0.15	−0.03	62	SRRM3	−0.12	7.65E-02	**−0.31**	**6.36E-06**	0.9814	−0.03	−0.10
23	GYG2	0.72	9.55E-04	**0.67**	**2.33E-06**	0.9043	−0.10	**−0.25**	63	CAMK1G	−0.44	7.65E-02	**−0.48**	**2.99E-03**	0.8322	−0.18	−0.08
24	IGSF10	0.47	1.85E-03	**0.29**	**1.35E-03**	0.9348	−0.03	−0.07	64	SHH	−0.24	6.54E-02	**−0.37**	**5.60E-04**	0.9495	**0.33**	**0.24**
25	SULF1	0.19	2.38E-03	**0.27**	**2.38E-04**	0.9811	**−0.20**	**−0.30**	65	COMP	−0.54	6.16E-02	**−0.86**	**7.21E-06**	0.8862	−0.02	−0.15
26	CD2	0.36	2.70E-03	**0.29**	**1.56E-04**	0.9522	0.14	0.15	66	LZTS1	−0.27	6.02E-02	**−0.32**	**2.17E-03**	0.9607	**0.26**	0.19
27	MEGF11	0.81	3.96E-03	**0.38**	**2.33E-04**	0.9316	**−0.33**	−0.19	67	RALGPS2	−0.18	5.79E-02	**−0.36**	**1.20E-04**	0.9730	**0.24**	−0.01
28	TMEM97	0.44	4.67E-03	**0.38**	**5.28E-04**	0.9419	−0.16	−0.03	68	SCRG1	−0.26	5.51E-02	**−0.55**	**1.00E-03**	0.9292	−0.12	0.12
29	DRP2	0.32	5.49E-03	**0.27**	**4.80E-05**	0.9772	**−0.39**	**−0.23**	69	NXPH3	−0.11	5.21E-02	**−0.30**	**3.25E-04**	0.9674	0.08	−0.13
30	GPR64	0.45	5.68E-03	**0.44**	**1.63E-03**	0.9433	−0.18	−0.14	70	DMRTC1B	−0.44	5.08E-02	**−0.47**	**4.15E-04**	0.9084	**0.20**	0.04
31	KRT4	0.99	6.83E-03	**0.57**	**1.12E-04**	0.8086	−0.12	−0.17	71	C4A	−0.17	5.01E-02	**−0.33**	**5.14E-05**	0.9741	0.07	0.18
32	GLYAT	0.47	7.03E-03	**0.39**	**3.67E-04**	0.9411	−0.11	−0.15	72	PDGFRA	−0.09	4.90E-02	**−0.30**	**3.60E-04**	0.9788	0.06	**−0.21**
33	MORN2	0.29	1.06E-02	**0.35**	**3.56E-05**	0.9530	−0.03	0.00	73	LRRC16B	−0.20	4.69E-02	**−0.31**	**5.07E-04**	0.9609	−0.07	0.17
34	GIPR	0.45	1.54E-02	**0.41**	**6.68E-04**	0.9349	−0.04	−0.15	74	GRIK3	−0.24	4.00E-02	**−0.50**	**6.30E-04**	0.9298	**0.30**	**0.26**
35	NCAPH	0.42	1.89E-02	**0.50**	**2.07E-05**	0.9412	−0.06	−0.06	75	TANGO6	−0.37	3.87E-02	**−0.28**	**2.10E-03**	0.9252	−0.01	0.00
36	CD3E	0.24	2.04E-02	**0.28**	**2.02E-03**	0.9523	0.13	0.11	76	WWC3	−0.31	3.09E-02	**−0.36**	**1.17E-03**	0.9443	0.02	−0.02
37	SP4	1.72	2.08E-02	**0.44**	**4.41E-04**	0.8549	−0.06	−0.02	77	FST	−0.13	2.96E-02	**−0.35**	**3.73E-05**	0.9651	−0.17	**0.25**
38	SPRR3	0.66	2.10E-02	**0.69**	**5.71E-04**	0.6949	−0.07	−0.14	78	RNF165	−0.32	2.87E-02	**−0.41**	**3.25E-04**	0.9604	0.01	−0.03
39	DSC3	0.53	2.15E-02	**0.34**	**1.60E-03**	0.8951	0.11	0.04	79	CPAMD8	−0.17	2.81E-02	**−0.33**	**1.37E-05**	0.9672	−0.14	**−0.28**
40	FH	0.28	2.63E-02	**0.35**	**3.32E-05**	0.9556	0.06	0.08	80	TMEM255A	−0.14	2.51E-02	**−0.42**	**3.02E-05**	0.9601	**0.32**	0.08

(Continued)

TABLE 2 | Continued

Gene #	Gene	Log2 Fold change at 50th percentile (female:male, smoothing factor 0.0001)	*P*-value for 50th percentile rank-sum test	Log2 Fold change at 75th percentile (female:male, smoothing factor 0.0001)	*P*-value for 75th percentile rank-sum test	Normalized entropy	Pearsons R (male age with TPM)	Pearsons R (fem age with TPM)	Gene #	Gene	Log2 Fold change at 50th percentile (female:male, smoothing factor 0.0001)	*P*-value for 50th percentile rank-sum test	Log2 Fold change at 75th percentile (female:male, smoothing factor 0.0001)	*P*-value for 75th percentile rank-sum test	Normalized entropy	Pearsons R (male age with TPM)	Pearsons R (fem age with TPM)
		Thresholds: >0.26, or <-0.26	BHP based *p*-value threshold for 0.05 FDR: 2.38E-04	Thresholds: >0.26, or <-0.26	BHP based *p*-value threshold for 0.05 FDR: 3.50E-03	Normalized entropy threshold: <0.9895	Pearsons R threshold >0.20 or <-0.20	Same threshold used as in male dataset			Thresholds : >0.26, or <-0.26	BHP based *p*-value threshold for 0.05 FDR: 2.38E-04	Thresholds: >0.26, or <-0.26	BHP based *p*-value threshold for 0.05 FDR: 3.50E-03	Normalized entropy threshold: <0.9895	Pearsons R 0.05 FDR threshold (>0.20 or <-0.20)	Same threshold used as in male dataset
81	CA8	−0.32	2.47E-02	**−0.27**	**4.59E-04**	0.9645	−0.05	−0.09	116	PMEPA1	−0.18	7.68E-04	**−0.33**	**5.21E-08**	0.9777	**0.24**	0.11
82	FABP7	−0.37	2.46E-02	**−0.46**	**4.32E-04**	0.8988	0.14	**0.20**	117	HBA2	−0.86	5.89E-04	**−0.87**	**1.63E-04**	0.7814	−0.18	−0.17
83	PDE4C	−0.30	2.36E-02	**−0.40**	**4.13E-06**	0.9534	0.11	−0.08	118	ICAM5	−0.34	5.74E-04	**−0.47**	**7.97E-06**	0.9547	−0.06	0.01
84	NOTCH1	−0.15	2.05E-02	**−0.32**	**5.38E-04**	0.9668	0.15	0.02	119	PLCXD1	−0.40	5.17E-04	**−0.36**	**7.21E-06**	0.9683	0.19	0.03
85	C1orf101	−0.30	2.04E-02	**−0.31**	**3.38E-04**	0.9701	0.16	0.08	120	DDX43	−0.56	4.02E-04	**−0.48**	**3.03E-06**	0.9348	0.09	0.03
86	HP	−0.58	1.94E-02	**−0.93**	**8.17E-06**	0.7888	0.02	0.07	121	PPP2R3B	**−0.52**	**1.96E-04**	**−0.35**	**5.03E-05**	0.9724	**0.31**	**0.21**
87	KIAA1279	−12.60	1.83E-02	**−0.71**	**9.22E-05**	0.8143	0.13	−0.15	122	OOEP	**−0.59**	**1.40E-04**	**−0.50**	**6.05E-07**	0.9420	−0.01	−0.04
88	DIO2	−0.38	1.73E-02	**−0.42**	**1.04E-03**	0.9471	0.12	0.08	123	AGAP2	**−0.42**	**1.40E-04**	**−0.45**	**1.64E-07**	0.9570	0.08	0.13
89	SSC5D	−0.24	1.61E-02	**−0.31**	**2.55E-03**	0.9619	**0.21**	0.01	124	MMEL1	**−0.53**	**1.27E-04**	**−0.31**	**3.81E-05**	0.9690	−0.03	0.09
90	PTPN9	−0.20	1.60E-02	**−0.30**	**3.64E-05**	0.9725	**0.20**	−0.11	125	NTRK1	**−0.58**	**1.11E-04**	**−0.59**	**4.90E-08**	0.9573	−0.01	0.08
91	TPPP2	−0.29	1.30E-02	**−0.34**	**1.15E-04**	0.9194	0.08	−0.03	126	SEL1L2	**−1.73**	**1.08E-04**	**−0.83**	**1.55E-05**	0.8889	−0.03	**−0.23**
92	FAM228A	−0.40	1.27E-02	**−0.37**	**2.10E-04**	0.9216	−0.08	0.08	127	PTGFR	**−0.34**	**6.53E-05**	**−0.43**	**4.48E-08**	0.9781	−0.10	−0.13
93	ADAMTS8	−0.22	1.23E-02	**−0.45**	**9.13E-07**	0.9632	0.07	**0.25**	128	WISP2	**−0.65**	**3.35E-05**	**−0.52**	**2.10E-06**	0.9634	−0.03	0.12
94	ANKFN1	−0.38	1.16E-02	**−0.30**	**1.56E-04**	0.9421	0.04	0.11	129	SV2A	**−0.36**	**2.46E-05**	**−0.23**	**4.94E-06**	0.9792	−0.03	−0.12
95	VWA3B	−0.38	1.11E-02	**−0.29**	**1.85E-03**	0.9550	0.16	0.04	130	KCND3	**−0.34**	**2.14E-05**	**−0.55**	**7.67E-08**	0.9696	−0.16	−0.11
96	EFCAB5	−0.42	9.15E-03	**−0.29**	**2.02E-03**	0.9517	**0.22**	0.05	131	DYNC1I1	**−0.31**	**1.56E-05**	**−0.33**	**8.90E-08**	0.9850	0.10	0.10
97	C10orf67	−0.31	8.60E-03	**−0.27**	**4.50E-04**	0.9507	**0.37**	**0.26**	132	WDR62	**−0.49**	**3.32E-06**	**−0.54**	**2.35E-10**	0.9653	0.12	0.04
98	SHC3	−0.34	8.00E-03	**−0.37**	**4.48E-05**	0.9537	0.11	0.10	133	NUDT4	**−0.29**	**1.27E-06**	**−0.35**	**4.09E-08**	0.9882	0.09	0.02
99	MED13	−0.32	7.65E-03	**−0.27**	**2.05E-04**	0.9589	0.08	**0.20**	134	IGF1	**−1.01**	**1.14E-06**	**−0.95**	**9.44E-08**	0.9260	**−0.20**	**−0.32**
100	KLK4	−0.33	5.36E-03	**−0.43**	**5.51E-05**	0.9423	0.05	0.06	135	ADA	**−0.59**	**7.99E-08**	**−0.64**	**6.34E-10**	0.9683	−0.02	−0.06
101	LUM	−0.36	5.33E-03	**−0.36**	**5.14E-05**	0.9555	**0.26**	0.06	136	FRG1B	**−0.38**	**4.31E-10**	**−0.37**	**8.19E-11**	0.9857	0.11	**−0.22**
102	GREB1L	−0.35	4.28E-03	**−0.34**	**5.03E-05**	0.9679	0.05	−0.01	137	NOX5	**−1.08**	**4.72E-11**	**−0.80**	**1.30E-13**	0.9630	0.05	−0.09
103	TP53INP2	−0.41	4.21E-03	**−0.39**	**1.89E-04**	0.9620	**0.38**	**0.30**	138	SLITRK4	**−1.13**	**4.22E-16**	**−1.23**	**1.01E-15**	0.9439	−0.11	0.00
104	ATP8A2	−0.24	3.82E-03	**−0.41**	**8.08E-05**	0.9513	0.04	0.03	139	HSD11B1	**−1.61**	**6.83E-17**	**−1.42**	**7.35E-17**	0.9138	**−0.23**	−0.10
105	CYB561	−0.19	3.73E-03	**−0.30**	**2.66E-06**	0.9809	**0.22**	0.15	140	CADPS	**−2.31**	**2.96E-22**	**−2.16**	**6.13E-17**	0.9145	0.00	−0.14
106	COL4A6	−0.34	3.69E-03	**−0.28**	**1.12E-04**	0.9559	−0.04	0.01	141	HSFY2	**−12.91**	**3.76E-36**	**−13.52**	**9.12E-20**	0.8888	0.12	Y chrom
107	FAM20A	−0.32	3.64E-03	**−0.40**	**8.59E-06**	0.9641	−0.03	0.01	142	RPS4Y1	**−9.00**	**4.34E-37**	**−8.68**	**2.77E-19**	0.9257	**−0.35**	Y chrom
108	ARTN	−0.53	3.58E-03	**−0.44**	**5.14E-05**	0.9329	0.14	**−0.23**	143	KDM5D	**−8.89**	**4.34E-37**	**−8.36**	**2.77E-19**	0.9224	0.07	Y chrom
109	UPB1	−0.70	3.51E-03	**−0.46**	**1.18E-04**	0.9351	0.12	0.08	144	USP9Y	**−9.19**	**4.23E-37**	**−8.19**	**2.77E-19**	0.9227	**0.23**	Y chrom
110	NRGN	−0.35	2.85E-03	**−0.28**	**7.78E-06**	0.9687	−0.06	−0.03	145	EIF1AY	**−7.93**	**3.91E-37**	**−6.88**	**2.77E-19**	0.9247	−0.06	Y chrom
111	RAP1GAP2	−0.36	2.44E-03	**−0.31**	**3.27E-06**	0.9783	**0.44**	**0.23**	146	DDX3Y	**−8.57**	**3.91E-37**	**−7.12**	**2.77E-19**	0.9187	**0.23**	Y chrom
112	C4B	−0.27	2.26E-03	**−0.41**	**4.18E-09**	0.9743	0.10	0.15	147	UTY	**−9.99**	**3.81E-37**	**−8.53**	**2.77E-19**	0.9239	0.15	Y chrom
113	GREB1	−0.22	1.78E-03	**−0.37**	**2.70E-04**	0.9589	0.06	−0.06	148	NLGN4Y	**−8.46**	**3.76E-37**	**−7.01**	**2.77E-19**	0.9195	−0.02	Y chrom
114	MKX	−0.47	1.22E-03	**−0.33**	**2.14E-04**	0.9576	−0.06	−0.15	149	ZFY	**−15.68**	**3.00E-37**	**−8.55**	**2.77E-19**	0.9118	0.04	Y chrom
115	SYNM	−0.13	8.75E-04	**−0.27**	**1.70E-06**	0.9855	**0.25**	−0.01									

Differentially expressed genes in human tibial nerve. Fold changes at the 50 and 75th percentile between males and females in BSL for 149 DE genes and p-values for Wilcoxon Rank Sum test are shown.
Dark red (DE in females) and dark blue boxes (DE in males) with boldface correspond to BHP-corrected statistically significant outcomes. Pearson's R for correlation with age in both male and female BSL subcohorts are shown with purple and green bars corresponding to negative and positive correlation with age, respectively, and boldface corresponding to effect sizes that are BHP-corrected statistically significant in males in BSL. Normalized entropy based on the BSL cohort values are shown.

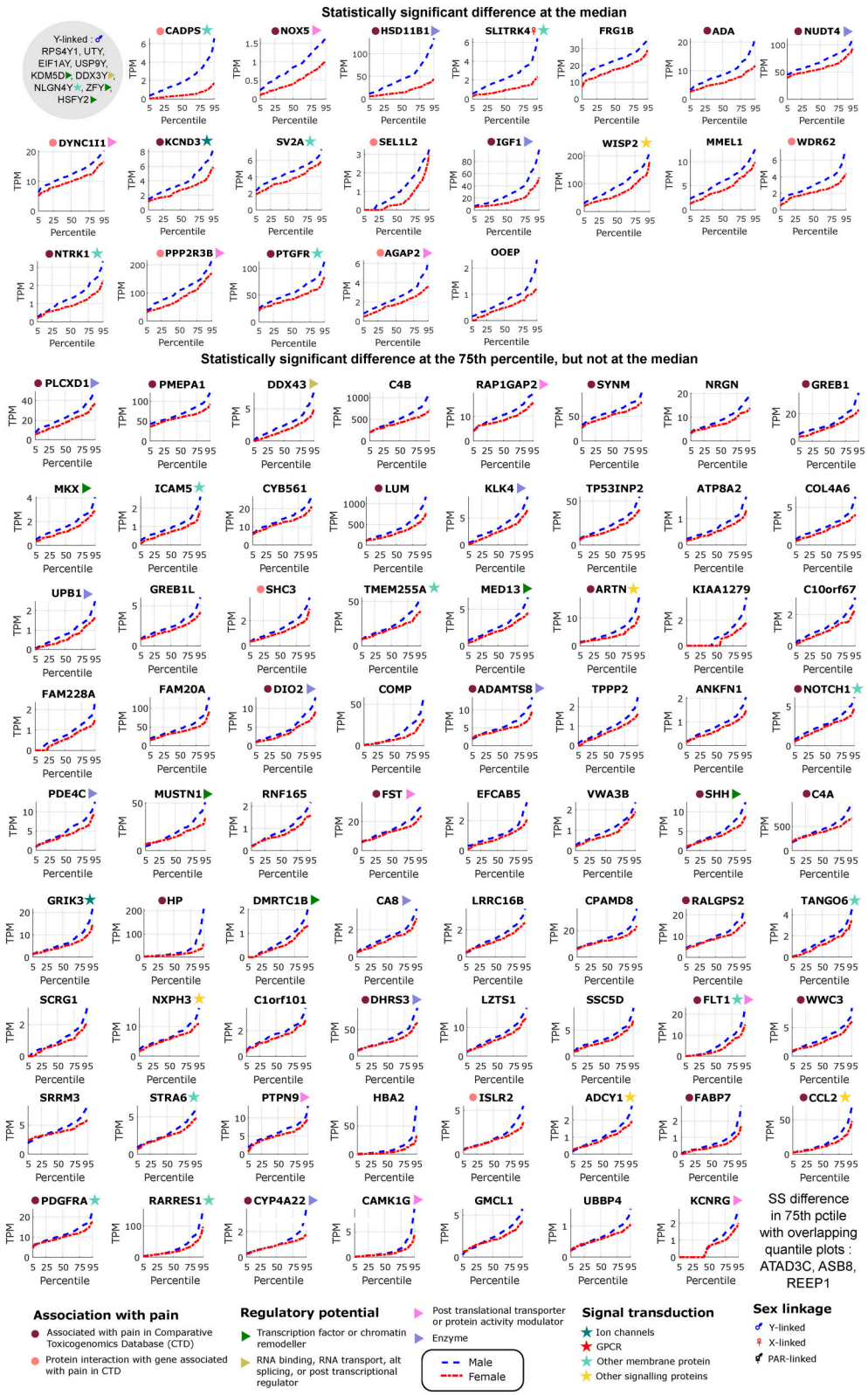

FIGURE 2 | Differentially expressed genes in male tibial nerves. Quantile values for TPMs of sex-differentially expressed genes in BSL that are more abundant in males. Sex linkage, signal transduction and regulatory potential, and association with pain are also shown. Genes are shown in decreasing order of the area between the curves.

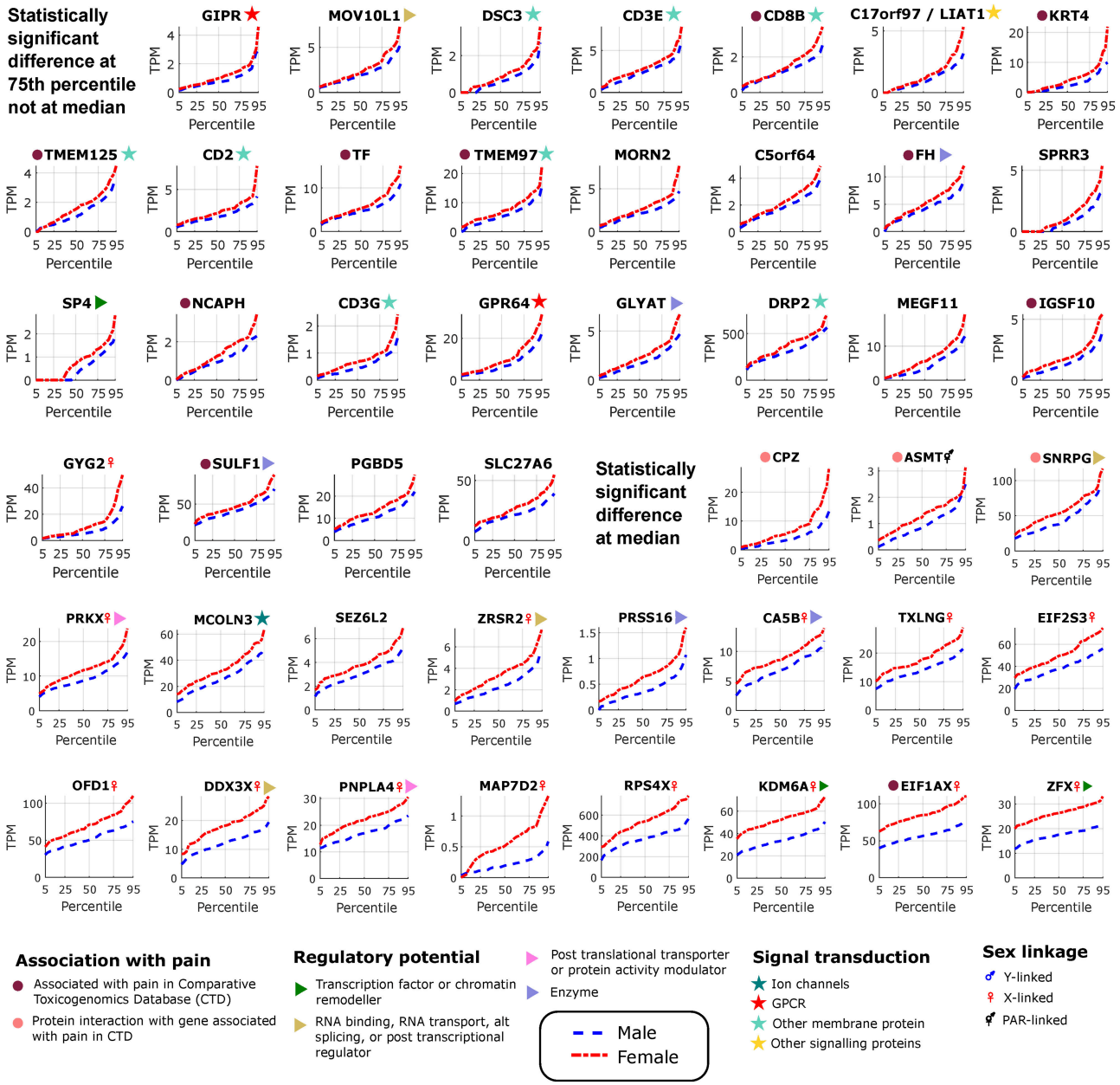

FIGURE 3 | Differentially expressed genes in female tibial nerves. Quantile values for TPMs of sex-differentially expressed genes in BSL that are more abundant in females. Sex linkage, signal transduction and regulatory potential, and association with pain are also shown. Genes are shown in increasing order of the area between the curves.

were higher than in females, also in agreement with studies on human endothelial cells showing greater pro-inflammatory effects of androgens over estrogens (Annibalini et al., 2014). We analyzed the BSL male sub-cohort pro-inflammatory genes in T2D and CJP, and found only 3 inflammatory genes (LUM, WISP2, ARTN) with sex-dimorphic expression at comparable effect sizes in either T2D or CJP with respect to BSL (**Figure 4B**) suggesting that the pro-inflammatory gene signature is unlikely to be caused solely by a subset of donors in BSL that are suffering from inflammatory conditions unreported in the clinical record. The larger number of genes detected as more abundant in the male BSL sub-cohort can potentially be attributed to a combination of Y-chromosomal gene expression and downstream regulatory effects, and a larger set of DE pro-inflammatory genes.

We mined the set of pro-inflammatory protein that were more abundant in males for protein interaction based on both the literature and the StringDB database (Szklarczyk

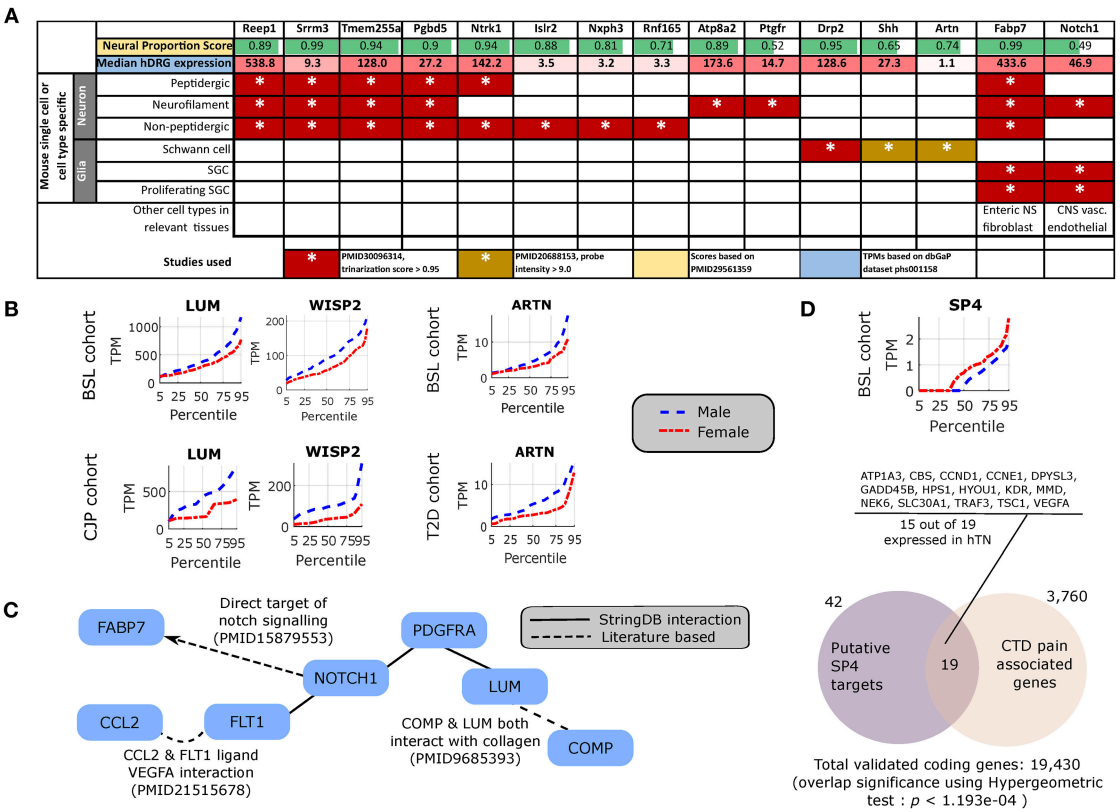

FIGURE 4 | Cellular enrichment and functional roles of differentially expressed genes. **(A)** For DE genes that are expressed in the human DRG, enriched in neural tissues, and detected in murine PNS single cell RNA-sequencing, median expression in TPMs in the human DRG, enrichment of expression in human neural tissues [based on the human neural proportion score (Ray et al., 2018)], and murine cell types of expression in the DRG (based on Zeisel et al., 2018) are shown. **(B)** LUM and WISP2 show similar sex-differential expression trends in BSL and CJP, and ARTN shows similar trends in BSL and T2D. **(C)** Protein Interaction Network for pro-inflammatory genes that are more abundant in the male cohort, suggesting a central role of NOTCH1. **(D)** Quantile plot for SP4 male and female sub-cohorts, and gene set enrichment analysis showing overlap of known SP4 targets from TRANSFAC (Matys et al., 2006) expressed in the hTN and present in Comparative Toxicogenomics Database (Davis et al., 2012) based pain associated gene list.

et al., 2016). We identified a Protein Interaction Network (PIN) connected through NOTCH1 (**Figure 4C**), known to be involved in neuropathic pain (Xie et al., 2015). This suggests that some of the pro-inflammatory genes more abundant in males (FABP7, FLT1, CCL2, PDGFRA, LUM, COMP) are potentially transcriptionally regulated by Notch signaling, or are co-regulated with NOTCH1. This is consistent with our knowledge of Notch signaling which is understood to drive a pro-inflammatory phenotype (Quillard and Charreau, 2013) in multiple tissues.

DE Regulatory Genes

Underlying causes for such sex-differential gene expression include Y chromosome gene expression, incomplete X inactivation in females (Gershoni and Pietrokovski, 2017), differential androgen and estrogen receptor driven regulation between sexes (Chen et al., 2016) and transcription regulatory programs controlled directly or indirectly by sex chromosomal gene products. Additionally, we find DE transcriptional regulators on autosomes including DMRTC1B and MED13 in males, and SP4 in females. SP4 is known to regulate pain-related genes, including several expressed in hTN (**Figure 4D**). While fold changes in these autosomal genes under baseline conditions are unlikely to affect transcription in their regulatory targets, the presence of sex-differential expression in a subset of samples suggests that under pathological conditions like inflammation and pain, more prominent sex-differential expression of these transcriptional regulators could potentially drive sex-specific regulatory programs.

Correlation of Gene Abundance With Age

We performed a principal components analysis of only the 149 sex differentially expressed genes, with the top two components clearly spatially separating male and female samples (**Figure 5A**). We also find that the top six principal components accounted for >90% of the variance (**Figure 5B**), but more interestingly four of the top six components are correlated with age (**Figure 5C**), both positively and negatively, showing that different parts of sex differential gene expression are both positively and negatively

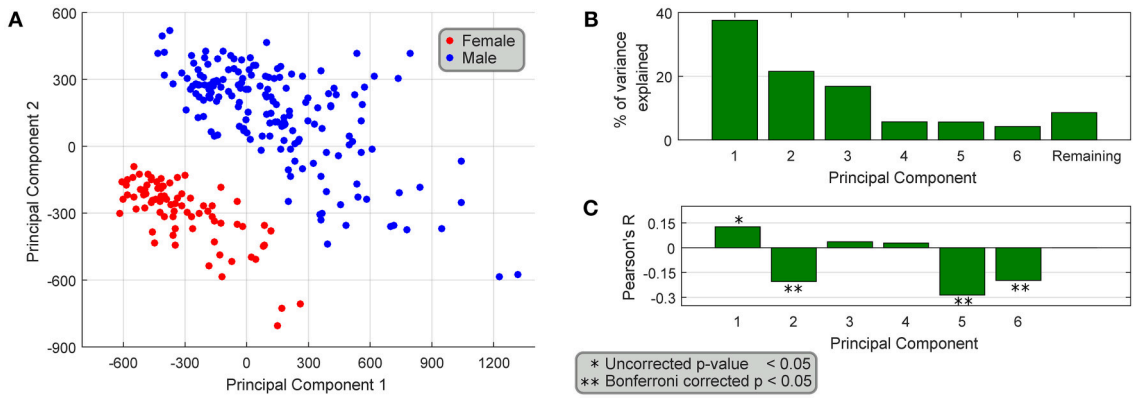

FIGURE 5 | Association of differentially expressed genes with age. **(A)** PCA of the 149 sex-differentially expressed genes in BSL yields top two principal components that spatially segregate male and female samples. **(B)** The top six principal components explain >90% of the variance, and **(C)** 4 out of the top 6 principal components are weakly correlated with age of the samples.

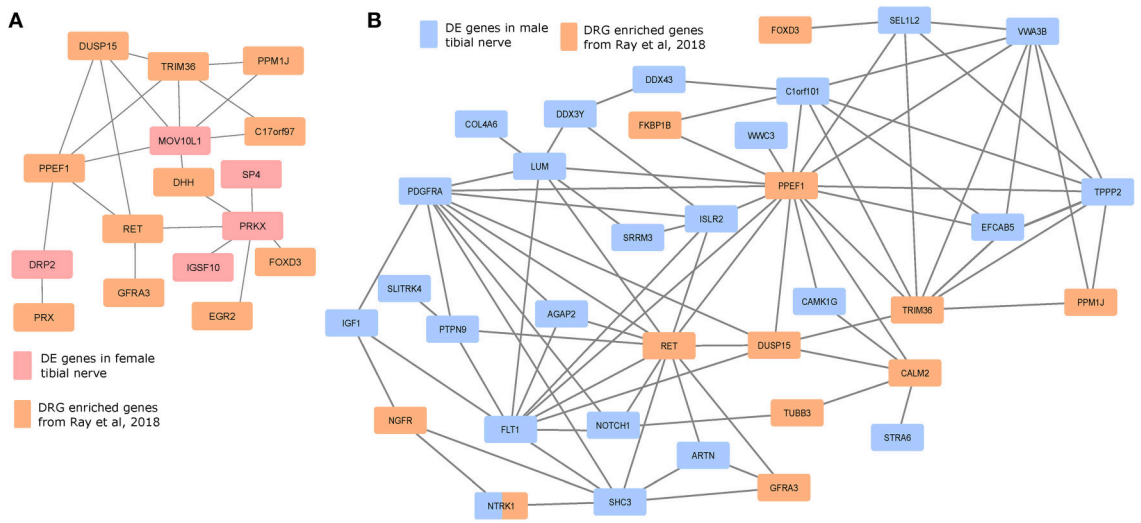

FIGURE 6 | Protein interaction networks of sex differentially expressed genes and human DRG enriched genes. Largest connected components of PINs based on known StringDB interactions between mammalian DRG-enriched genes (based on Ray et al., 2018), and DE genes that are more abundant in the **(A)** female BSL sub-cohort, and **(B)** male sub-cohort.

correlated with age. At the level of individual genes, we find that several genes have very different (weak) correlational patterns in males and females (**Table 2**). One possible explanation for this is regulation (direct or indirect) by sex hormones, especially via ESRA and ESRB, which have been studied in GTEx datasets (Chen et al., 2016). In fact, we find genes in our datasets (DDX3X, SULF1, TMEM125, and others more abundant in females; FLT1, MUSTN1, COMP, ARTN, REEP1, SEL1L2, and others more abundant in males) with negative correlation between female BSL gene abundance values and age, and a smaller correlative effect (or positive correlation) in male BSL samples. Several genes in our dataset like MUSTN1, REEP1, and FLT1 have been shown to be regulated by estrogen in the literature.

Potential Protein Interaction Networks (PINs)

We investigated whether the gene products of the DE gene sets potentially interacted with genes whose expression is enriched in mammalian DRGs, which would help identify candidate sex-differential PINs in the PNS (**Figures 6A,B**). We used DRG-enriched genes from Ray et al. (2018) and our DE gene sets to identify putative PINs. The largest connected components from PINs generated using the StringDB database (Szklarczyk et al., 2016) show multiple DRG-enriched and male-preferentially expressed genes known to be expressed in glia (DUSP15, PRX, EGR2, DHH, FOXD3, ARTN), and involved in pain and inflammation, which points to a potential role for glia in sex differential pain processing

in human peripheral nerves [shown in preclinical models (Averitt et al., 2018)]. Additionally, the presence of several neuronally expressed genes in the PIN among the set of DRG-enriched genes (GFRA3, NTRK1, NGFR, RET, and PPM1J) also suggests sex-differential glia-neuron crosstalk, which in turn can affect neuronal plasticity and excitability differently between the sexes.

Roles in Pain and Neuro-Immunity

Out of 149 DE genes we identified, 56 (>33%) genes have known roles in pain, inflammation, innate immunity and other neuro-immune functions (**Table 3**). Sex differences in mammalian neuro-immune systems have been studied and linked to disease prevalence and susceptibility (Osborne et al., 2018), with PNS and CNS immune response sex differences studied in rodent pain models (Sorge et al., 2015; Mapplebeck et al., 2016; Lopes et al., 2017). In hTN, we find that DE genes involved in the innate immune system (C4A/B, CPAMD8 in males; DDX3X, TF in females) as well as genes known to be expressed in infiltrating or resident immune cells (ADA, PDGFRA in males; CD2, CD8B in females). We also found 34 genes that were associated with pain based on either the Comparative Toxicogenomics Database (Davis et al., 2012) or the Human Pain Genetics Database (Meloto et al., 2018), including genes that are central to pain pathways like NTRK1, and CCL2 in males and TMEM97 in females (Sahn et al., 2017; Ray et al., 2018).

DISCUSSION

Our work provides a biostatistical framework, and thoroughly catalogs sex-differential gene expression in hTN. The public resource (https://www.utdallas.edu/bbs/painneurosciencelab/sensoryomics/sexdiffnerve/) we generated provides a starting point for sex difference studies in human peripheral nerve drug target discovery, gene regulation and pathophysiology. We cataloged sex differences in gene expression in the PNS finding that many sexually dimorphic genes have known associations with pain, inflammation and neuro-immune interactions. This resource can be used for hypothesis-driven work to identify cell type and sub-compartment specificity of gene expression (e.g., NTRK1, LUM) by *in situ* hybridization or other techniques. These types of experiments will be important in identifying whether neuron-specific transcripts found in the tibial nerve are *bona-fide* axonally-localized transcripts or if they represent low level expression in other cell types that have not been recognized in single cell datasets to date. For genes like NTRK1 we favor the hypothesis that this is an axonally localized mRNA. From that perspective, it is likewise interesting that some of these genes are DE suggesting that sex hormones may drive mRNA localization in neurons. We are not aware of any previous studies that describe sex hormone-mediated control of axonal mRNA localization.

Our study can also be used to back-translate into transgenic preclinical models to identify potential sex differences in mechanisms of PNS physiology that may be relevant to pain therapeutics. While studies of molecular mechanism in human cohorts are difficult, sex differences in regulatory programs, signaling cascades and pathophysiological and behavioral changes can be studied in rodent-based perturbation models. Both SP4 and NOTCH1 are known to play key regulatory roles with respect to gene products that drive pain pathways (Chu et al., 2011; Xie et al., 2015), and are good candidates for further study.

While there are no rodent studies of baseline transcriptome sex differences in peripheral nerves, O'Brien et al. (2016) found sex differences in transcriptomes of sciatic nerves of diabetic mouse models show clear differences in the inflammasome. It is possible that the baseline differences in molecular profiles that we identified drive greater sexual dimorphisms under neuropathic conditions. While our study was underpowered for identifying sex-DE genes in the CJP and T2D cohorts, it can be expanded as GTEx cohort sizes continue to grow to potentially identify clinically relevant sex differences in CJP or T2D. Moreover, co-expressed (and putatively co-regulated) gene modules based on Whole Genome Correlation Network Analysis (Langfelder and Horvath, 2008) can be identified by finding correlated expression changes across cohorts and sexes. Given that sex differences in gene expression likely contribute to sexual dimorphism in neurological disease, such as chronic pain, exploiting these transcriptomic resources will be increasingly important for mechanism and drug discovery.

There are limitations to our work. As mentioned in the previous paragraph, our study was not able to identify sex-differential expression in Type II diabetes or arthritis, largely due to the small sample size. However, our work does identify some putative targets for future prospective studies. Most prominently, our findings suggest differential expression of immune-regulatory genes in tibial nerve of males and females. It may be reasonable to hypothesize that these differences will become more pronounced in chronic pain disorders. It is striking that we observed higher expression of some macrophage-expressed and/or macrophage recruiting genes (CCL2, NOTCH1) at higher levels in males given that many recent studies have identified macrophages and microglia as important contributors to pain specifically in male rodents (Mapplebeck et al., 2016; Lopes et al., 2017; Averitt et al., 2018; Inyang et al., 2018). We also observed higher expression of a well-known T cell gene in female TN, CD8B. This is interesting because T cells have been associated both with pain promotion (Sorge et al., 2015) and pain resolution (Krukowski et al., 2016) in female mice. Another shortcoming is that we have not addressed any specific hypotheses with interventional, prospective studies. This will be a future goal using rodent models. Finally, there is a potential confound of age in our analysis of sexual dimorphisms in gene expression. Our detailed analysis of this confound shows that age cannot explain all of the differences observed, and even when it does, it may be explained by changes in sex hormones across the lifespan.

In conclusion, our work demonstrates robust sexual dimorphisms in gene expression in the human tibial nerve. Some of these dimorphisms are likely important for understanding how the immune system interacts with the peripheral nervous system. Insofar as this is a major focus of current research into

TABLE 3 | Functionally relevant genes that are sex-differentially expressed in the human tibial nerve.

DE genes in females	Pain genes	Inflammation genes	Immune genes	Axon-related genes	Related publications	DE genes in males	Pain genes	Inflammation genes	Immune genes	Axon-related genes
EIF1AX	✪					**DDX3Y**	✪			
NCAPH	✪					CADPS	✪			
FH	✪					NOX5	✪			
TMEM97	✪					HSD11B1	✪			
TMEM125	✪					NUDT4	✪			
DRP2	✪					PTGFR	✪			✪
SP4	✪✪				← PMID21645329	KCND3				
IGSF10	✪		✪		← PMID27137492	PLCXD1				
CD8B	✪		✪			PMEPA1	✪			
CD3E			✪			FST	✪			
CD2			✪			WWC3	✪			
CD3G			✪			ADAMTS8	✪			
PRSS16			✪		← PMID25543139	NTRK1	✪✪			✪
MORN2			✪			SYNM	✪			
DDX3X			✪			GREB1	✪			
TF			✪		PMID27320922→	ADA	✪		✪	
PRKX		✪	✪			SSC5D			✪	
SULF1		✪				C4A			✪	
GPR64		✪				C4B			✪	
KRT4	✪	✪				CPAMD8			✪	
CA5B		✪				FLT1*		✪	✪	
GIPR		✪				PDGFRA		✪	✪	
MEGF11				✪		CCL2		✪		
						LUM		✪		
Sex linked genes in boldface : X-linked, Y-linked						ARTN		✪		
						DIO2		✪		
✪ Pain-gene association in Comparative Toxicogenomics Database						NOTCH1		✪		
✪ Pain-gene association in Human Pain Gene Database and literature						FABP7		✪		
✪ Gene involved in pain pathways in literature (PUBMED id provided)						CYP4A22		✪		
						IGF1		✪		
✪ Pro-inflammatory gene						WISP2		✪		
✪ Anti-inflammatory gene						KLK4		✪		
						COMP		✪		
✪ Involved in innate immune system function						SHH		✪		✪
✪ Cell surface receptor signaling in immune cells						RNF165				✪✪
✪ Other role in immune or nervous system (PUBMED id provided)						SRRM3				✪✪
						ISLR2				✪✪
✪ Potentially axonally transported						TMEM255A				✪✪
✪ Axonal growth, positioning, and wayfinding						ICAM5				✪✪
✪ Neurite outgrowth						ATP8A2				✪✪

**Primarily expressed in endothelial cells, also reported in immune cells.*

Functional annotation of sex differentially expressed genes. Functional annotations for sex-differentially expressed genes in BSL showing whether they are involved in pain, inflammation, immune system functions, axonal growth/neurite outgrowth or are potentially axonally transported, based on literature. ICAM5 is known to be present in dendrites, and has not been shown to be present in axons. Other potentially axonally transported transcripts have known roles in axonal viability, growth and wayfinding or neurite outgrowth.

acute and chronic pain mechanisms (Mapplebeck et al., 2016; Lopes et al., 2017; Averitt et al., 2018; Inyang et al., 2018), these findings give new insight into translating findings from animal models into humans, as well as potential back-translation for testing of new hypotheses in animal models based on human molecular data.

AUTHOR CONTRIBUTIONS

PR, AA, GD, and TP conceived the project. PR designed and performed experiments, analyzed and interpreted the data. JK performed exon-level analysis. DT-F performed pilot experiments. AW performed experiments for **Supplementary Table 4**. PR drew all figures. PR and TP wrote the paper, with input from GD.

FUNDING

NIH/NINDS grants R01NS065926 (to TP), R01NS102161 (to TP and AA) and R01NS098826 (to TP and GD).

ACKNOWLEDGMENTS

A preprint of this work is deposited in biorXiv at https://doi.org/10.1101/450197.

SUPPLEMENTARY MATERIAL

The Supplementary Material for this article can be found online at: https://www.frontiersin.org/articles/10.3389/fnmol.2019.00037/full#supplementary-material

REFERENCES

Annibalini, G., Agostini, D., Calcabrini, C., Martinelli, C., Colombo, E., Guescini, M., et al. (2014). Effects of sex hormones on inflammatory response in male and female vascular endothelial cells. *J. Endocrinol. Invest.* 37, 861–869. doi: 10.1007/s40618-014-0118-1

Aoki, M., Segawa, H., Naito, M., and Okamoto, H. (2014). Identification of possible downstream genes required for the extension of peripheral axons in primary sensory neurons. *Biochem. Biophys. Res. Commun.* 445, 357–362. doi: 10.1016/j.bbrc.2014.01.193

Averitt, D. L., Eidson, L. N., Doyle, H. H., and Murphy, A. Z. (2018). Neuronal and glial factors contributing to sex differences in opioid modulation of pain. *Neuropsychopharmacology* 44, 155–165. doi: 10.1038/s41386-018-0127-4

Babcock, D. T., Shi, S., Jo, J., Shaw, M., Gutstein, H. B., and Galko, M. J. (2011). Hedgehog signaling regulates nociceptive sensitization. *Curr. Biol.* 21, 1525–1533. doi: 10.1016/j.cub.2011.08.020

Benjamini, Y., and Hochberg, Y. (1995). Controlling the false discovery rate: a practical and powerful approach to multiple testing. *J. R. Stat. Soc. B Methodol.* 289–300. doi: 10.1111/j.2517-6161.1995.tb02031.x

Casimir, G. J., Mulier, S., Hanssens, L., Zylberberg, K., and Duchateau, J. (2010). Gender differences in inflammatory markers in children. *Shock* 33, 258–262. doi: 10.1097/SHK.0b013e3181b2b36b

Chen, C.-Y., Lopes-Ramos, C. M., Kuijjer, M. L., Paulson, J. N., Sonawane, A. R., Fagny, M., et al. (2016). Sexual dimorphism in gene expression and regulatory networks across human tissues. *bioRxiv [preprint]*. doi: 10.1101/082289

Chu, C., Zavala, K., Fahimi, A., Lee, J., Xue, Q., Eilers, H., et al. (2011). Transcription factors Sp1 and Sp4 regulate TRPV1 gene expression in rat sensory neurons. *Mol. Pain* 7:44. doi: 10.1186/1744-8069-7-44

Cui, P., Lin, Q., Ding, F., Xin, C., Gong, W., Zhang, L., et al. (2010). A comparison between ribo-minus RNA-sequencing and polyA-selected RNA-sequencing. *Genomics* 96, 259–265. doi: 10.1016/j.ygeno.2010.07.010

Davis, A. P., Murphy, C. G., Johnson, R., Lay, J. M., Lennon-Hopkins, K., Saraceni-Richards, C., et al. (2012). The comparative toxicogenomics database: update 2013. *Nucleic Acids Res.* 41, D1104–D1114. doi: 10.1093/nar/gks994

De Toledo, I. P., Réus, J. C., Fernandes, M., Porporatti, A. L., Peres, M. A., Takaschima, A., et al. (2016). Prevalence of trigeminal neuralgia: a systematic review. *J. Am. Dental Assoc.* 147, 570–576.e2. doi: 10.1016/j.adaj.2016.02.014

DeLuca, D. S., Levin, J. Z., Sivachenko, A., Fennell, T., Nazaire, M.-D., Williams, C., et al. (2012). RNA-SeQC: RNA-seq metrics for quality control and process optimization. *Bioinformatics* 28, 1530–1532. doi: 10.1093/bioinformatics/bts196

Dobin, A., Davis, C. A., Schlesinger, F., Drenkow, J., Zaleski, C., Jha, S., et al. (2013). STAR: ultrafast universal RNA-seq aligner. *Bioinformatics* 29, 15–21. doi: 10.1093/bioinformatics/bts635

Flegel, C., Schöbel, N., Altmuller, J., Becker, C., Tannapfel, A., Hatt, H., et al. (2015). RNA-seq analysis of human trigeminal and dorsal root ganglia with a focus on chemoreceptors. *PLoS ONE* 10:e0128951. doi: 10.1371/journal.pone.0128951

Gershoni, M., and Pietrokovski, S. (2017). The landscape of sex-differential transcriptome and its consequent selection in human adults. *BMC Biol.* 15:7. doi: 10.1186/s12915-017-0352-z

Harrow, J., Frankish, A., Gonzalez, J. M., Tapanari, E., Diekhans, M., Kokocinski, F., et al. (2012). GENCODE: the reference human genome annotation for The ENCODE Project. *Genome Res.* 22, 1760–1774. doi: 10.1101/gr.135350.111

Hur, J., Sullivan, K. A., Pande, M., Hong, Y., Sima, A. A., Jagadish, H. V., et al. (2011). The identification of gene expression profiles associated with progression of human diabetic neuropathy. *Brain* 134, 3222–3235. doi: 10.1093/brain/awr228

Inyang, K. E., Szabo-Pardi, T., Wentworth, E., McDougal, T. A., Dussor, G., Burton, M. D., et al. (2018). The antidiabetic drug metformin prevents and reverses neuropathic pain and spinal cord microglial activation in male but not female mice. *Pharmacol. Res.* 139, 1–16. doi: 10.1016/j.phrs.2018.10.027

Krukowski, K., Eijkelkamp, N., Laumet, G., Hack, C. E., Li, Y., Dougherty, P. M., et al. (2016). $CD8^+$ T cells and endogenous IL-10 are required for resolution of chemotherapy-induced neuropathic pain. *J. Neurosci.* 36, 11074–11083. doi: 10.1523/JNEUROSCI.3708-15.2016

Langfelder, P., and Horvath, S. (2008). WGCNA: an R package for weighted correlation network analysis. *BMC Bioinformatics* 9:559. doi: 10.1186/1471-2105-9-559

LaPaglia, D. M., Sapio, M. R., Burbelo, P. D., Thierry-Mieg, J., Thierry-Mieg, D., Raithel, S. J., et al. (2018). RNA-Seq investigations of human post-mortem trigeminal ganglia. *Cephalalgia* 38, 912–932. doi: 10.1177/0333102417720216

Lee, W., Teckie, S., Wiesner, T., Ran, L., Granada, C. N. P., Lin, M., et al. (2014). PRC2 is recurrently inactivated through EED or SUZ12 loss in malignant peripheral nerve sheath tumors. *Nat. Genet.* 46:1227. doi: 10.1038/ng.3095

Li, B., and Dewey, C. N. (2011). RSEM: accurate transcript quantification from RNA-Seq data with or without a reference genome. *BMC Bioinformatics* 12:323. doi: 10.1186/1471-2105-12-323

Lippoldt, E. K., Elmes, R. R., McCoy, D. D., Knowlton, W. M., and McKemy, D. D. (2013). Artemin, a glial cell line-derived neurotrophic factor family member, induces TRPM8-dependent cold pain. *J. Neurosci.* 33, 12543–12552. doi: 10.1523/JNEUROSCI.5765-12.2013

Lonsdale, J., Thomas, J., Salvatore, M., Phillips, R., Lo, E., Shad, S., et al. (2013). The genotype-tissue expression (GTEx) project. *Nat. Genet.* 45:580. doi: 10.1038/ng.2653

Lopes, D. M., Malek, N., Edye, M., Jager, S. B., McMurray, S., McMahon, S. B., et al. (2017). Sex differences in peripheral not central immune responses to pain-inducing injury. *Sci. Rep.* 7:16460. doi: 10.1038/s41598-017-16664-z

Luo, L., Zhou, W. H., Cai, J.-J., Feng, M., Zhou, M., Hu, S.-P., et al. (2017). Gene expression profiling identifies downregulation of the neurotrophin-MAPK signaling pathway in female diabetic peripheral neuropathy patients. *J. Diabetes Res.* 2017:8103904. doi: 10.1155/2017/8103904

Mapplebeck, J. C., Beggs, S., and Salter, M. W. (2016). Sex differences in pain: a tale of two immune cells. *Pain* 157, S2–S6. doi: 10.1097/j.pain.0000000000000389

Matys, V., Kel-Margoulis, O. V., Fricke, E., Liebich, I., Land, S., Barre-Dirrie, A., et al. (2006). TRANSFAC® and its module TRANSCompel®: transcriptional gene regulation in eukaryotes. *Nucleic Acids Res.* 34, D108–D110. doi: 10.1093/nar/gkj143

Melemedjian, O. K., Asiedu, M. N., Tillu, D. V., Sanoja, R., Yan, J., Lark, A., et al. (2011). Targeting adenosine monophosphate-activated protein kinase (AMPK) in preclinical models reveals a potential mechanism for the treatment of neuropathic pain. *Mol. Pain* 7:70. doi: 10.1186/1744-8069-7-70

Meloto, C. B., Benavides, R., Lichtenwalter, R. N., Wen, X., Tugarinov, N., Zorina-Lichtenwalter, K., et al. (2018). Human pain genetics database: a resource dedicated to human pain genetics research. *Pain* 159, 749–763. doi: 10.1097/j.pain.0000000000001135

Mogil, J. S. (2012). Sex differences in pain and pain inhibition: multiple explanations of a controversial phenomenon. *Nat. Rev. Neurosci.* 13:859. doi: 10.1038/nrn3360

O'Brien, P. D., Hur, J., Robell, N. J., Hayes, J. M., Sakowski, S. A., and Feldman, E. L. (2016). Gender-specific differences in diabetic neuropathy in BTBR ob/ob mice. *J. Diabetes Complicat.* 30, 30–37. doi: 10.1016/j.jdiacomp.2015.09.018

Osborne, B. F., Turano, A., and Schwarz, J. M. (2018). Sex differences in the neuroimmune system. *Curr. Opin. Behav. Sci.* 23, 118–123. doi: 10.1016/j.cobeha.2018.05.007

Panza, P., Sitko, A. A., Maischein, H.-M., Koch, I., Flötenmeyer, M., Wright, G. J., et al. (2015). The LRR receptor Islr2 is required for retinal axon routing at the vertebrate optic chiasm. *Neural Dev.* 10, 23. doi: 10.1186/s13064-015-0050-x

Pearson, K. (1895). Note on regression and inheritance in the case of two parents. *Proc. R. Soc. Lond.* 58, 240–242. doi: 10.1098/rspl.1895.0041

Pongratz, G., and Straub, R. H. (2013). Role of peripheral nerve fibres in acute and chronic inflammation in arthritis. *Nat. Rev. Rheumatol.* 9:117. doi: 10.1038/nrrheum.2012.181

Quillard, T., and Charreau, B. (2013). Impact of notch signaling on inflammatory responses in cardiovascular disorders. *Int. J. Mol. Sci.* 14, 6863–6888. doi: 10.3390/ijms14046863

Ray, P., Torck, A., Quigley, L., Wangzhou, A., Neiman, M., Rao, C., et al. (2018). Comparative transcriptome profiling of the human and mouse dorsal root ganglia: an RNA-seq–based resource for pain and sensory neuroscience research. *Pain* 159, 1325–1345. doi: 10.1097/j.pain.0000000000001217

Sahn, J. J., Mejia, G. L., Ray, P. R., Martin, S. F., and Price, T. J. (2017). Sigma 2 receptor/Tmem97 agonists produce long lasting antineuropathic pain effects in mice. *ACS Chem. Neurosci.* 8, 1801–1811. doi: 10.1021/acschemneuro.7b00200

Sorge, R. E., Mapplebeck, J. C., Rosen, S., Beggs, S., Taves, S., Alexander, J. K., et al. (2015). Different immune cells mediate mechanical pain hypersensitivity in male and female mice. *Nat. Neurosci.* 18, 1081. doi: 10.1038/nn.4053

Szklarczyk, D., Morris, J. H., Cook, H., Kuhn, M., Wyder, S., Simonovic, M., et al. (2016). The STRING database in 2017: quality-controlled protein–protein association networks, made broadly accessible. *Nucleic acids research, gkw*937.

Wilcoxon, F. (1945). Individual comparisons by ranking methods. *Biometr. Bull.* 1, 80–83. doi: 10.2307/3001968

Xie, K., Qiao, F., Sun, Y., Wang, G., and Hou, L. (2015). Notch signaling activation is critical to the development of neuropathic pain. *BMC Anesthesiol.* 15:41. doi: 10.1186/s12871-015-0021-0

Zeisel, A., Hochgerner, H., Lönnerberg, P., Johnsson, A., Memic, F., van der Zwan, J., et al. (2018). Molecular architecture of the mouse nervous system. *Cell* 174, 999–1014.e22. doi: 10.1016/j.cell.2018.06.021

Zhang, X. D. (2010). Strictly standardized mean difference, standardized mean difference and classical *t*-test for the comparison of two groups. *Stat. Biopharm. Res.* 2, 292–299. doi: 10.1198/sbr.2009.0074

Conflict of Interest Statement: The authors declare that the research was conducted in the absence of any commercial or financial relationships that could be construed as a potential conflict of interest.

frontiers in Molecular Neuroscience

ORIGINAL RESEARCH
published: 17 April 2019
doi: 10.3389/fnmol.2019.00098

TRPA1 Activation-Induced Myelin Degradation Plays a Key Role in Motor Dysfunction After Intracerebral Hemorrhage

Min Xia†, Weixiang Chen†, Jie Wang, Yi Yin, Chao Guo, Chengcheng Li, Mingxi Li, Xiaoqin Tang, Zhengcai Jia, Rong Hu, Xin Liu and Hua Feng**

Department of Neurosurgery, Southwest Hospital, Third Military Medical University, Chongqing, China

Intracerebral hemorrhage (ICH) is a devastating disease that is characterized by high morbidity and high mortality. ICH has an annual incidence of 10–30/100,000 people and accounts for approximately 10%–30% of all types of stroke. ICH mostly occurs at the basal ganglia, which is rich in nerve fibers; thus, hemiplegia is quite common in ICH patients with partial sensory disturbance and ectopic blindness. In the clinic, those symptoms are considered to originate from the white matter injury in the area, but the exact mechanisms are unknown, and currently, no effective drug treatments are available to improve the prognosis. Clarifying the mechanisms will contribute to the development of new treatment methods for patients. The transient receptor potential ankyrin 1 (TRPA1) channel is a non-selective cation channel that plays a role in inflammatory pain sensation and nociception and may be a potential regulator in emotion, cognition and social behavior. Here, we report that TRPA1 is involved in myelin damage and oxidative stress injury in a mouse ICH model. Intervention with the TRPA1 channel may be a new method to improve the motor function of patients in the early stage of ICH.

Keywords: transient receptor potential ankyrin 1 channel (TRPA1), myelin damage, nerve conduction, motor dysfunction, intracerebral hemorrhage

OPEN ACCESS

Edited by:
Felix Viana, Institute of Neurosciences of Alicante (IN), Spain

Reviewed by:
Hugo Cabedo, Universidad Miguel Hernández de Elche, Spain
Antti Pertovaara, University of Helsinki, Finland

***Correspondence:**
Xin Liu
shenwai@tmmu.edu.cn
Hua Feng
fenghua8888@vip.163.com

†These authors have contributed equally to this work

Received: *11 December 2018*
Accepted: *03 April 2019*
Published: *17 April 2019*

Citation:
Xia M, Chen W, Wang J, Yin Y, Guo C, Li C, Li M, Tang X, Jia Z, Hu R, Liu X and Feng H (2019) TRPA1 Activation-Induced Myelin Degradation Plays a Key Role in Motor Dysfunction After Intracerebral Hemorrhage. Front. Mol. Neurosci. 12:98. doi: 10.3389/fnmol.2019.00098

INTRODUCTION

Intracerebral hemorrhage (ICH) comprises 10%–30% of all stroke cases (Balami and Buchan, 2012). After ICH, the case fatality rate is approximately 55% at 1 year and 70% at 5 years, and a few survivors regain functional independence (Joseph et al., 2016). Most instances of ICH occur in basal nuclei, which are rich in neural tracts (Zuo et al., 2017). Therefore, white matter injury is considered the major cause of hemiplegia with partial sensory disturbance and ectopic blindness, which are quite common symptoms in ICH patients. In fact, significant myelin and axonal injury were shown to occur in both an animal model and ICH patients. Severe myelin destruction and swelling axons are typical in the ICH animal model, but the exact mechanisms contributing to the loss of motor function are uncertain. This lack of understanding has hampered efforts to develop a therapeutic strategy aimed at protecting and repairing the damaged white matter of the ICH patients (Cheng et al., 2015; Tao et al., 2017).

The transient receptor potential ankyrin 1 (TRPA1) channel is a type of nonselective transmembrane cation channel that contains a large number of N-terminal ankyrin repeats and has high permeability to calcium (Ca^{2+}; De Logu et al., 2017). This channel is best known as a sensor of pain, cold, and environmental irritants and is expressed in sensory neurons, astrocytes,

oligodendrocytes, ependymal cells located at ventricles and cardiomyocytes (Andrei et al., 2017; Lee et al., 2017). Recent studies have indicated that TRPA1 is involved in the myelin Ca^{2+} accumulation process and regulation of emotion, cognition, learning, memory, and social behavior (Hamilton et al., 2016; Lee et al., 2017). Previous research has shown that decreased pH and increased reactive oxygen species (ROS) production can activate the TRPA1, causing an inflow of Ca^{2+} (Andersson et al., 2008; Wang et al., 2011). The increase in Ca^{2+} activates NADPH oxidase 1 (NOX1), which acts by releasing oxidant molecules and increasing their expression, to produce more ROS, eventually exacerbating oxidative stress (Lee et al., 2009; De Logu et al., 2017). TRPA1 can promote the synaptic dysfunction mediated by the oligomeric forms of amyloid-β peptide in Alzheimer's disease (AD; Bosson et al., 2017). TRPA1 deficiency has also been shown to attenuate cuprizone-induced demyelination (Sághy et al., 2016).

In this study, we investigated whether the TRPA1 channel was involved in white matter injury and motor function deficits in a mouse ICH model.

MATERIALS AND METHODS

Animals

Adult male C57BL/6 mice (aged 8–10-weeks-old, 22–30 g) were used in this study. The mice were provided by the Experimental Animal Centre at the Third Military Medical University (Army Medical University). The mice were housed in a specific temperature-controlled room under a 12-h light/dark cycle and provided free access to food and water throughout the experimental period.

ICH Model

All experimental protocols were approved by the Ethics Committee of the Third Military Medical University (Army Medical University) were performed according to the eighth edition of the National Institutes of Health Guide for the Care and Use of Laboratory Animals. The detailed procedures used to construct the ICH model were established in a previous study (Krafft et al., 2012). Briefly, the mice were anesthetized intraperitoneally with 1% phenobarbital sodium and were immobilized on the stereotaxic frame in a prone position. Then, a small cranial burr hole was made at a precise location in the mice (Bregma coordinates: 0.8 mm anterior and 2.1 mm lateral to the midline) under stereotactic guidance. The mice received 25 μl of autologous blood at a depth of 3 mm into the right basal ganglia at a rate of 2 μl/min using a sterile Hamilton syringe needle (Cat: RN1702) and a microinfusion pump (KD Scientific, Holliston, MA, USA). The mice were randomly divided into the following groups: Sham, ICH, ICH + HC-030031, ICH + A-967079, and ICH + polygodial. According to previous studies (Mendes et al., 2000; McNamara et al., 2007; Sałat and Filipek, 2015), the ICH mice received HC-030031 [30 mg/kg i.p. dissolved in isotonic saline with 4% dimethyl sulfoxide (DMSO) and 4% Tween 80], A-967079 (5 mg/kg s.c. dissolved in isotonic saline with 4% DMSO and 4% Tween 80) or polygodial (20 mg/kg s.c. dissolved in isotonic saline with 4% ethanol and 4% Tween 80) 1 h after the ICH procedure. On days 1, 3, 7, and 14 after surgery, the mice were euthanized, and their brains were collected for morphological and biochemical experiments. The TRPA1 antagonists HC-030031 and A-967079 and agonist polygodial were obtained from Sigma-Aldrich. According to the previous research method (Duncan et al., 2017), L-α-lysophosphatidylcholine purchased from Sigma-Aldrich was used to construct a demyelinating model under stereotactic guidance, which was used as a comparison of myelin morphology with that of the ICH mice. The mice received 2 μl of 1% L-α-lysophosphatidylcholine at a depth of 3 mm into the right basal ganglia at a rate of 50 nl/min using a sterile Hamilton syringe needle and a microinfusion pump. There were two preadministrated ICH groups to evaluate the effect of pretreatment (ICH* group represents the group given HC-030031 1 day before constructing ICH model, and ICH# group represents the group given A-967079 1 day before constructing ICH model).

Immunofluorescence

The mice were deeply anesthetized with 1% pentobarbital sodium and transcardially perfused with 4% paraformaldehyde in 0.01 M phosphate-buffered saline (PBS) after an initial flush with isotonic saline. The brains were collected and post-fixed with 4% paraformaldehyde in 0.01 M PBS overnight, and then these tissues were dehydrated in 30% sucrose in 0.01 M PBS for 2 days. The brains were embedded in optimal cutting temperature compound (O.C.T. Compound, SAKURA, Whittier, CA, USA) and then sliced coronally (35 μm) on a cryostat microtome (CM1860UV, Leica, Wetzlar, Germany). For immunofluorescence staining, the cryostat floating sections were blocked with 5% bovine serum albumin (BSA) and 0.3% Triton X-100 for 1.5 h at room temperature and then sequentially incubated with primary antibodies overnight at 4°C and fluorescent secondary antibodies overnight at 4°C. The primary antibodies included rabbit anti-Neurofilament 200 (anti-NF200; 1:200; Sigma-Aldrich; Cat: N4142), goat anti-myelin basic protein (anti-MBP; 1:250; Santa Cruz; Cat: sc-13914), rabbit anti-degraded MBP (anti-DMBP; 1:250; Millipore; Cat: AB5864), rabbit anti-TRPA1 (1:250; Abcam; Cat: ab58844), rabbit anti-TRPA1 (1:250; Millipore; Cat: ABN1009), rabbit anti-NOX1 (1:500; Abcam; Cat: ab131088), and mouse anti-Calpain1 (1:250; Santa Cruz; Cat: sc-390677; Ottens et al., 2008; Deshmukh et al., 2013; Zou et al., 2017). The secondary antibodies included the following: AlexaFluor-488-, AlexaFluor-555-, or AlexaFluor-594-conjugated secondary antibodies against goat, rabbit and mouse (1:1,000; Invitrogen) antibodies. The nuclei were counterstained with 4′-6-diamidino-2-phenylindole (DAPI; Santa Cruz Biotechnology). Peri-hematoma region was defined as the surrounding white matter of the hematoma produced by the stereotactic injection of blood. Fluorescent images in the white matter adjacent to the hematoma were photographed using a Zeiss confocal microscope (Zeiss, LSM780).

Western Blot Analysis

The western blot (WB) method was described in a previous study (Xie et al., 2017). The ipsilateral hematoma was removed

by a magnifying glass using a microscopic instrument, and then the white matter surrounding the hematoma was collected for extraction. The entire process was completed at low temperatures. Equivalent amounts of a protein sample (50 μg) were loaded onto an SDS-PAGE gel after sample preparation. After gel electrophoresis was completed, the proteins were transferred to PVDF membranes, and the membranes were blocked in 5% BSA for 2 h at room temperature. Then, they were incubated with the following primary antibodies at 4°C overnight: goat anti-MBP (1:250; Santa Cruz; Cat: sc-13914), rabbit anti-NOX1 (1:500; Abcam; Cat: ab131088), mouse anti-Calpain1 (1:250; Santa Cruz; Cat: sc-390677), and rabbit anti-TRPA1 (1:2,000; Millipore; Cat: ABN1009; Das et al., 2013; Lee et al., 2017). β-actin was used as an internal loading control. Then, the membranes were probed with specific horseradish peroxidase-conjugated secondary antibodies (1:2,000; Invitrogen) for 2 h at room temperature. Finally, an enhanced chemiluminescence reagent kit (Thermo Scientific, Rockford, IL, USA) for western blotting was used to visualize the immunoreactive bands, which were detected with a bioimaging system (ChemiDoc XRS+; Bio-Rad, Hercules, CA, USA). The blot bands were quantified by densitometry using the Image Lab software (Image Lab 3.0; Bio-Rad, Hercules, CA, USA). Three animals per group and at least three repetitions of each treatment condition were used for the WB analysis.

Transmission Electron Microscopy

For transmission electron microscopy (TEM), the animals were perfused with 1.25% glutaraldehyde and 2% paraformaldehyde in 0.1 M PB after an initial flush with isotonic saline. Then, the brains were rapidly removed and postfixed for at least 3 days at 4°C. The tissues were rinsed, postfixed with 1% OsO_4 in PB for 2 h, counterstained with uranyl acetate, dehydrated with a graded acetone series, infiltrated with propylene oxide, and embedded in Epon. Ultrathin sections (∼60 nm) were cut by using an ultramicrotome (LKB-V, LKB Produkter AB, Bromma) and observed under a transmission electron microscope (TECNAI10; Philips; Wang et al., 2018). A random image with 12 different fields of view was selected for each group for statistical analysis of the myelinated axons. The G-ratios of the myelinated fibers were calculated as the ratio of the axon diameter to the axon diameter with the myelin sheath using the ImageJ software (ImageJ 1.8; NIH, Bethesda, MD, USA), and at least 60 myelinated fibers per group were calculated (Chomiak and Hu, 2009). The grading system for focal myelin injury was described in a previous study (3 = complete myelin breakdown; 2 = myelin bubbling involving multiple lamella; 1 = one layer of myelin splitting; and 0 = normal compact myelin). A total of 100 myelinated fibers per group were used to assess myelin injury (Doyle et al., 2018). At least three mice per group were used in TEM analysis. The image of sham (D0) was derived from the tissue of the sham-operated group on the day of surgery, and the image of sham (D3) was derived from the tissue of the sham-operated group on the third day after surgery. The images of the two sham groups were used as controls for the treatment groups at the corresponding time points.

Electrophysiologic Recording

To record the motor evoked potentials (MEPs) elicited by transcranial electrical stimulation, three mice per group were anesthetized with 1% pentobarbital sodium (25 mg/kg i.p.). Previous studies showed that this dose of pentobarbital sodium did not significantly affect the amplitude and waveform of MEPs in dogs and rodents (Redondo-Castro et al., 2016; Wu et al., 2017). The electrode placement was described in a previous study (Redondo-Castro et al., 2016). The stimulation needle electrodes were placed subcutaneously with the tip touching the scalp. The cathode was placed at the midpoint of an imaginary line connecting the two ears and the anode at the base of the nose. The hindlimbs of mice were exposed to enable insertion of recording electrodes into the gastrocnemius muscles. A ground electrode was placed subcutaneously in the back. Electrical stimulation was applied to excite the brain using a stimulator (Keypoint, Medtronic, USA). A single pulse of stimulation (7.8 mA, 0.1 ms, 1 Hz) was delivered *via* stimulation needle electrodes (DSN1620, Medtronic, USA). The electrical stimulation was repeated five times at intervals of 15 s in each mouse, and a trace of one of the five stimuli was presented as a representative in the figure (**Supplementary Figure S1D**). The trace represented the potential change that occurred after a single transcranial electrical stimulation, and two wave groups appeared after the stimuli. The two wave groups were regarded as the short-latency MEPs and the long-latency MEPs after transcranial electrical stimulation respectively. The short-latency MEPs were reported to involve brainstem reticulospinal tract, while long-latency MEPs mainly involved primary motor cortex and dorsal corticospinal tract (Wu et al., 2017). The long latency of MEPs was recorded for analysis, and it was measured from the onset of the transcranial electrical stimulation to the beginning of the evoked-event. An average long latency of these five stimuli was used for statistics. D-1 indicates the day before the ICH surgery, and D0 indicates the day the mice underwent ICH surgery.

Behavioral Assessments

All tests were monitored by a digital video camera and analyzed in a blinded manner. The mice were weighed before the daily behavioral test. The behavioral tests were performed at the specified time, during the light cycle. D-1 indicates the day before the ICH surgery, and D0 indicates the day the mice underwent ICH surgery.

Beam Balance Test

The mice had to cross a round wooden beam that was 1.5 cm in diameter and 70 cm in length and was elevated 30 cm from the ground for 1 min. The score (0–4) was decided by the walking distance. The average score of three consecutive trials was calculated (Schneider et al., 2016; Yin et al., 2017).

Basso Mouse Scale (BMS)

This open-field locomotor scoring system consisted of scores from 0 (no ankle movement) to 9 (frequent or consistent plantar stepping, mostly coordinated, paws parallel at initial contact and lift off, normal trunk stability and tail always up; Wu et al., 2017).

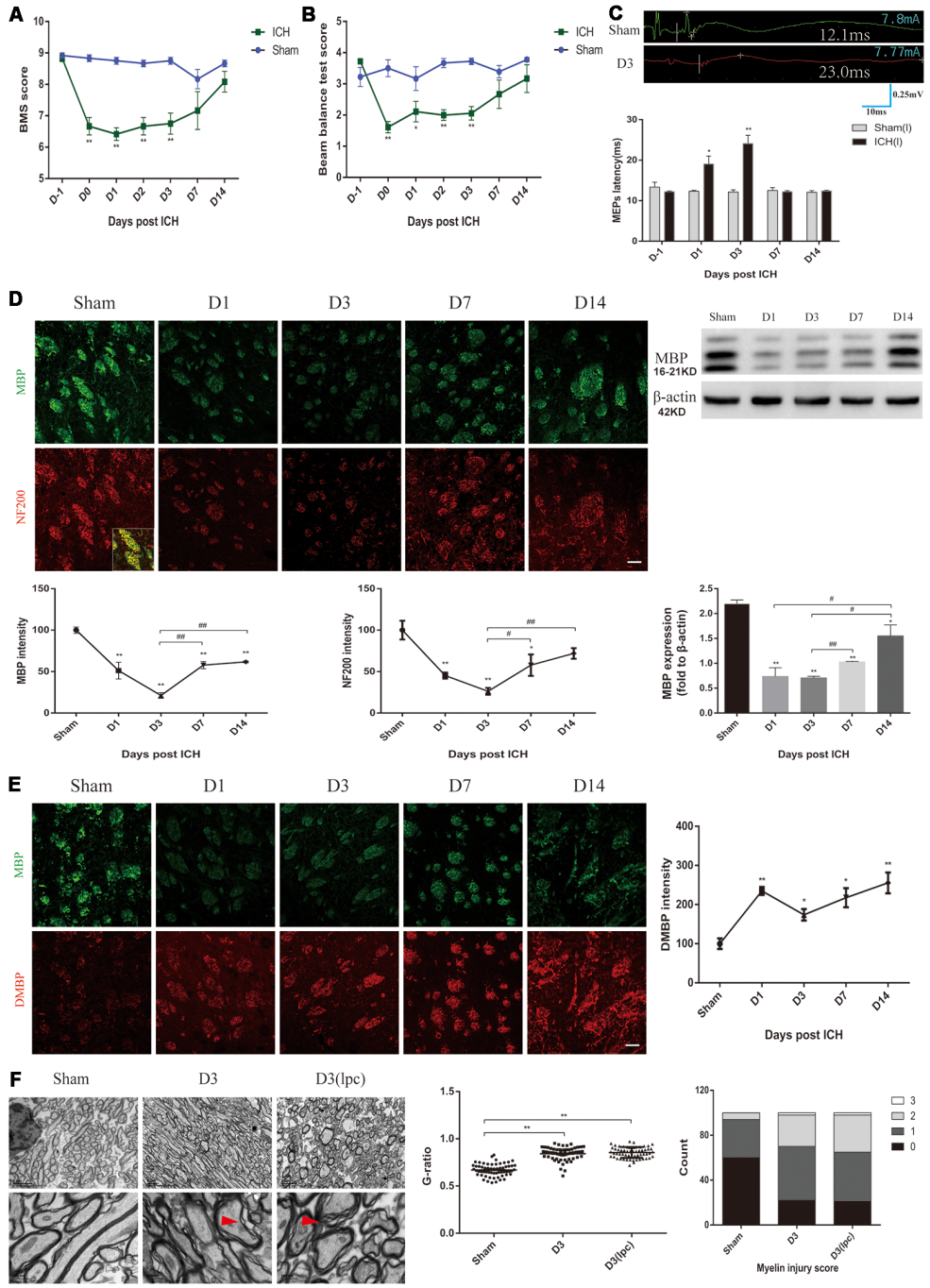

FIGURE 1 | Motor dysfunction, nerve conduction damage and histological changes of the intracerebral hemorrhage (ICH) mice. **(A,B)** The behavioral scores of the ICH mice first decreased and then gradually increased after ICH ($n = 6$). **(C)** The motor evoked potentials (MEPs) latency was prolonged on days 1 and 3 after ICH, and the left MEPs was detected ($n = 3$). **(D)** Myelin basic protein (MBP) and neurofilament 200 (NF200) expression were significantly reduced in the acute phase of ICH ($n \geq 3$). **(E)** Degraded MBP (DMBP) expression was increased after ICH ($n \geq 3$). **(F)** After ICH, transmission electron microscopy (TEM) showed that the myelin sheath around the hematoma thinned and disintegrated. The time before white vertical lines represents the long latency of MEPs, and the moment of using electrical stimulation is at the beginning of the trace. Crossbars are the markers of the amplitude of MEPs detected by software. Unless specified, scale bars represent 50 μm. The red arrows mark the phenomenon of demyelination (*$P < 0.05$ vs. sham group, **$P < 0.01$ vs. sham group, $^{\#}P < 0.05$, $^{\#\#}P < 0.01$).

Mouse Forelimb Muscle Strength

The mouse forelimb muscle strength was detected by the Grip Strength Meter (1027SM Columbus Instruments).

Statistical Analysis

All statistical analyses were performed using the SPSS 18.0 software. The data are expressed as the mean ± SEM.

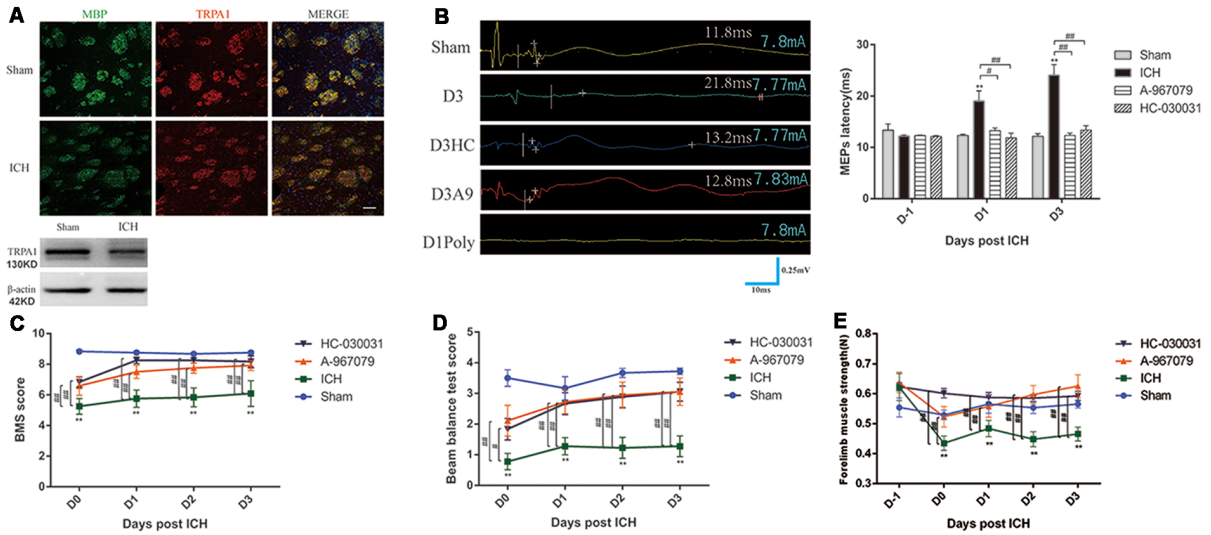

FIGURE 2 | Transient receptor potential ankyrin 1 (TRPA1) blockers improved motor dysfunction and nerve conduction in the ICH mice. **(A)** TRPA1 was expressed on the myelin. The sham group was assessed on D1 after sham surgery. **(B)** The extended MEPs latency was restored by TRPA1 blockers, and the left MEPs was detected ($n = 3$). **(C,D)** The TRPA1 blockers (HC-030031 and A-967079) increased the basso mouse scale (BMS) and beam balance test scores of the ICH mice ($n = 6$). **(E)** The TRPA1 blockers improved muscle strength in the ICH mice ($n = 6$). Unless specified, scale bars represent 50 μm. The time before white vertical lines represents the long latency of MEPs, and the moment of using electrical stimulation is at the beginning of the trace. Crossbars are the markers of the amplitude of MEPs detected by software (**$P < 0.01$ vs. sham group, $^{\#}P < 0.05$, $^{\#\#}P < 0.01$).

Comparisons between two groups were analyzed using a two-tailed Student's *t*-tests. The behavioral data, weights and electrophysiological data from the different groups collected at different time points were analyzed using a mixed design two-way ANOVA. The G-ratio, WB results, fluorescence intensity and axon diameters were analyzed using one-way repeated measures ANOVA, followed by Scheffe's *post hoc* test. The survival rate was analyzed by log-rank (Mantel-Cox) test. Differences were considered statistically significant at $P < 0.05$.

RESULTS

Neuronal Tract Damage and Motor Dysfunction in the ICH Mice

In this study, changes in locomotion, muscle strength and balance in the ICH mice were characterized by using various behavioral mouse models. First, compared with those of the sham group mice, the ICH mice showed a lower score in the basso mouse scale (BMS) and beam balance tests on D0-D3 (**Figures 1A,B**). The forelimb muscle strength of the ICH mice was lower than that of the sham group mice on D0-D3 (**Supplementary Figure S1A**). However, no significant differences were observed in the BMS score, the beam balance test score and forelimb muscle strength between the two groups on D7 and D14 (**Figures 1A,B**; **Supplementary Figure S1A**). No significant difference in weight was noted between the two groups throughout the experimental period (**Supplementary Figure S1B**). The MEPs latency was used to test nerve conduction function (**Figure 1C**). In contrast to that of the sham group mice, the latency of the ICH mice was significantly extended on D1 and D3 and returned to the sham group level on D7 and D14 (**Figure 1C**). These results suggested the ICH mice had significant motor dysfunction and nerve conduction damage during the acute phase of ICH.

MBP, DMBP and NF200 were used to assess the condition of the white matter after ICH. The coronal sections showed a progressive, overt decrease based on staining for normal MBP expression in the peri-hematoma region on D1 and D3 after ICH, and the immunofluorescence gradually recovered on D7 and D14 (**Figure 1D**). MBP protein expression showed a similar trend (**Figure 1D**). Simultaneously, the DMBP immunofluorescence was enhanced after ICH, which indicated that myelin degradation was increased (**Figure 1E**). Moreover, the decrease in NF200 was parallel with that of MBP (**Figure 1D**). Myelin damage can lead to slowed or reduced action potential conduction (Armstrong et al., 2016). Therefore, the severe myelin degradation of the ICH mice may be related to the prolonged MEPs latency.

Then, the white matter of the sham group mice and ICH group mice was compared using TEM. We noted oedema of the axons and disintegration of myelin in the peri-hematoma white matter, and an increased G-ratio indicated thinning of the myelin sheath (**Figure 1F**, **Supplementary Figure S1C**). The demyelinating model is a classic myelin injury model (Plemel et al., 2018). The myelin sheath of the ICH mice was compared to that of the demyelinating model, which was generated by stereotactically injecting L-α-lysophosphatidylcholine into the inner capsule. Interestingly, the pathological changes of the white matter were similar, probably because the two models shared some common myelin damage signaling pathways (**Figure 1F**). These results indicated severe neuronal tract

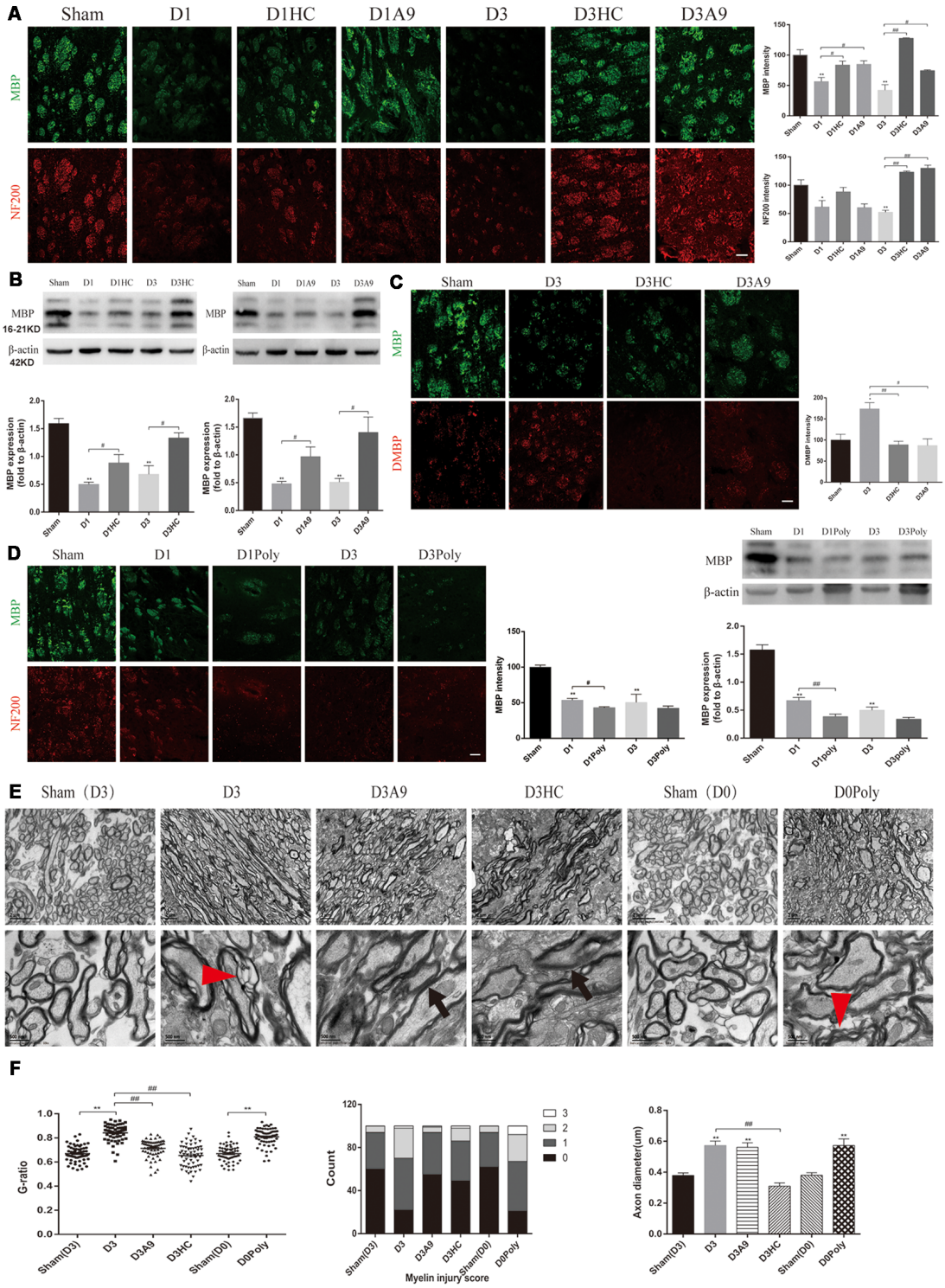

FIGURE 3 | Changes in the white matter after application of the TRPA1 blockers and agonist to the ICH mice. **(A)** The TRPA1 blockers significantly enhanced the immunofluorescence intensity of NF200 and MBP on D1 and D3 in the ICH mice ($n \geq 3$). **(B)** MBP expression was increased after application of the TRPA1 blockers. The sham group was assessed on D3 after sham surgery ($n \geq 3$). **(C)** The TRPA1 blockers reduced the immunofluorescence intensity of DMBP on D3 in the ICH mice ($n \geq 3$). **(D)** The TRPA1 agonist aggravated the myelin damage. The sham group was assessed on D3 after sham surgery ($n \geq 3$). **(E)** The thinning and disintegration of myelin were reduced by the TRPA1 blockers. **(F)** The TRPA1 blocker HC-030031 could reduce axonal oedema. The red arrows mark the phenomenon of demyelination, and the black arrows indicate the reduction of demyelination. Unless specified, scale bars represent 50 μm (*$P < 0.05$ vs. sham group, **$P < 0.01$ vs. sham group, $^{\#}P < 0.05$, $^{\#\#}P < 0.01$).

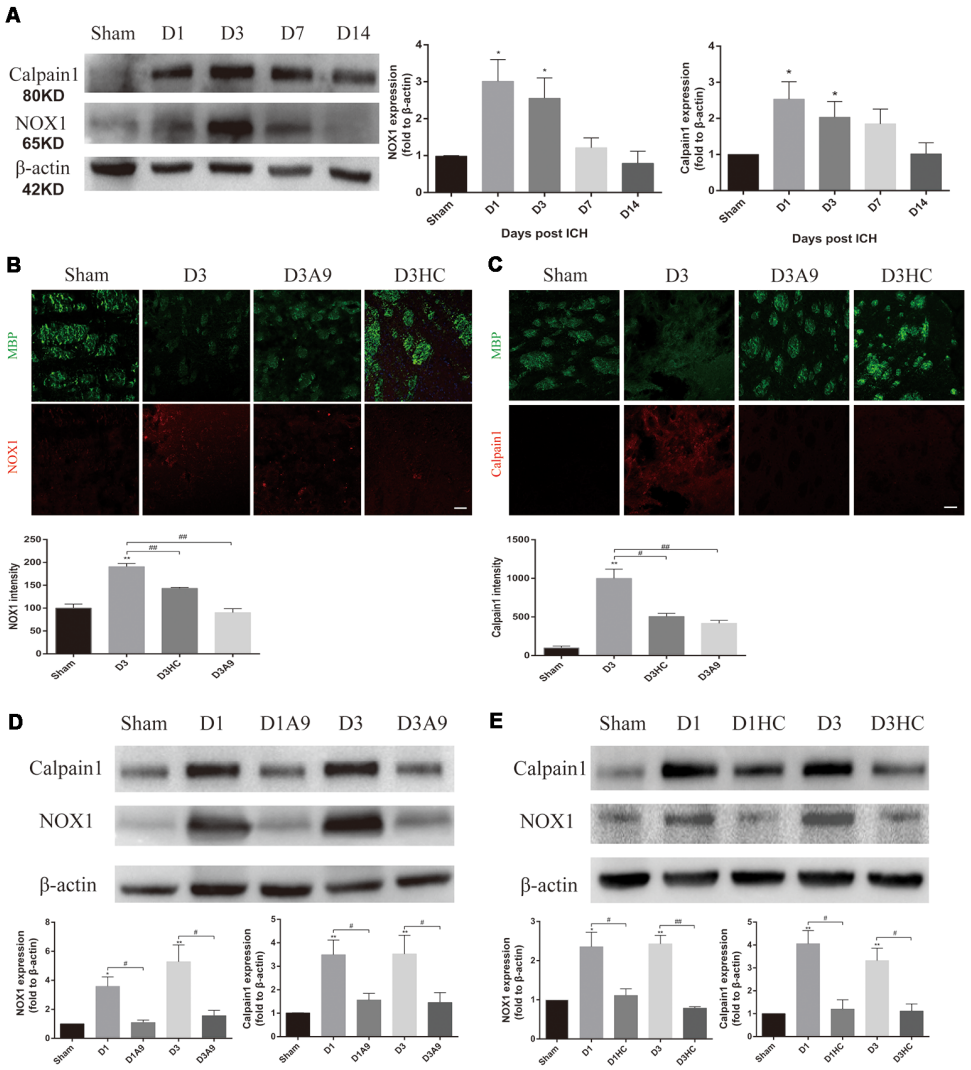

FIGURE 4 | The signal pathway downstream of TRPA1 induced myelin injury. **(A)** NADPH oxidase 1 (NOX1) and Calpain1 expression were enhanced in the ICH mice. The sham group was assessed on D3 after sham surgery ($n \geq 3$). **(B,C)** The TRPA1 blockers reduced the immunofluorescence intensity of NOX1 and Calpian1 on D3 in the ICH mice ($n \geq 3$). **(D,E)** NOX1 and Calpain1 expression were reduced in the ICH mice after application of the TRPA1 blockers. The sham group was assessed on D3 after sham surgery ($n \geq 3$). Scale bars represent 50 μm (*$P < 0.05$ vs. sham group, **$P < 0.01$ vs. sham group, $^{\#}P < 0.05$, $^{\#\#}P < 0.01$).

damage and motor dysfunction in the acute phase after ICH in mice.

Improved Nerve Conduction and Behavioral Performance of the ICH Mice After TRPA1 Blockade

TRPA1 expression on myelin was investigated. The immunofluorescence and WB analyses demonstrated that TRPA1 was expressed in the white matter and was co-labeled with the MBP (**Figure 2A**, **Supplementary Figure S2A**). The TRPA1 blockers (HC-030031 and A-967079) and the agonist polygodial were applied to the ICH mice to observe their impacts on the MEPs latency. The experimental results showed that HC-030031 and A-967079 shortened the MEPs latency of the ICH mice on D1 and D3. In contrast, in the ICH mice using the TRPA1 agonist polygodial, transcranial electrical stimulation did not induce MEPs (**Figure 2B**). Moreover, polygodial significantly increased the mortality of the ICH mice. The first three mice given TRPA1 agonist died in the afternoon after constructing ICH model (about 6 h after surgery), one mouse died on the second and third day respectively, and no mice died after 3 days. There was a significant difference in survival rate between the two groups (**Supplementary Figure S2B**). Further research indicated that HC-030031 and A-967079 obviously improved the BMS, beam balance test and the forelimb muscle strength scores in the first 3 days of ICH (**Figures 2C–E**). But there was no significant difference between the preadministrated ICH group and the ICH group, except for ICH group and ICH* group on D3 in the forelimb muscle strength test (**Supplementary Figure S2C**). The above findings suggested that TRPA1 blockers

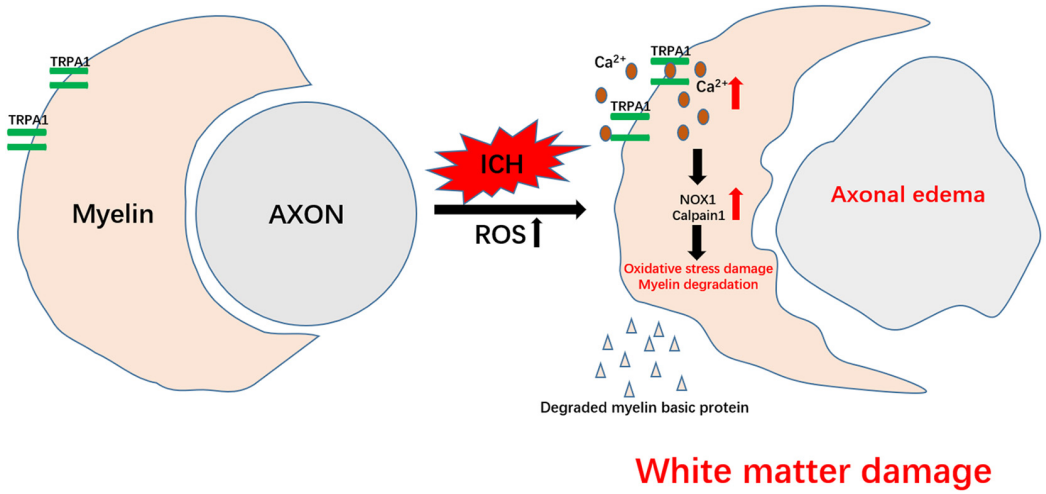

FIGURE 5 | Schematic representation of TRPA1-mediated myelin damage after ICH. TRPA1 is activated by the increased reactive oxygen species (ROS) after ICH, leading to an increase in the TRPA1-mediated Ca^{2+} influx. The increased Ca^{2+} further contributes to the rise in NOX1 and Calpain1, causing oxidative stress damage and myelin degradation. Axons that lose myelin protection are more susceptible to ICH injury. The damaged white matter eventually aggravates motor dysfunction in the mice.

could significantly ameliorate nerve conduction and motor dysfunction during the acute phase in ICH mice.

Improvement of the Neuronal Tract After Application of a TRPA1 Blocker in the ICH Mice

The NF200 and MBP immunofluorescence were significantly enhanced on D1 and D3 after HC-030031 and A-967079 application in the ICH mice (**Figure 3A**). The improved MBP protein expression indicated that HC-030031 and A-967079 reduced the degradation of myelin skeletal proteins (**Figure 3B**). The reduced fluorescence intensity of DMBP showed that HC-030031 and A-967079 also reduced MBP degradation (**Figure 3C**). Conversely, we found that polygodial deteriorated myelin damage with a decreased fluorescence intensity and reduced MBP expression on D1 (**Figure 3D**). TEM showed that HC-030031 and A967079 reduced the degree of demyelination in the acute phase of ICH, leading to a decline in the G-ratio and the improvement of the myelin injury score (**Figure 3E**). Additionally, HC-030031 could ameliorate the axonal oedema (**Figure 3F**), whereas application of polygodial showed severe myelin damage and axonal oedema (**Figures 3E,F**). These findings suggested that TRPA1 played a vital role in myelin damage after ICH.

TRPA1-Induced Myelin Degradation Was Mediated by Upregulation of NOX1 and Calpain1

Considerable amounts of oxygen free radicals are released after ICH and may activate the TRPA1 signaling pathway (Qureshi et al., 2009; Qu et al., 2016). Therefore, we examined the NOX1 level after ICH and the changes in NOX1 expression after the application of TRPA1 blockers. The results demonstrated that NOX1 expression was increased after ICH (**Figures 4A,B**). A significant decrease of NOX1 was observed after application of HC-030031 and A-967079 (**Figures 4B,D,E**).

Moreover, according to previous studies, elevated Ca^{2+} can activate Calpain1 and increase its expression; this protein is involved in myelin degradation (Liu et al., 2006; Qureshi et al., 2009; Zhao et al., 2017; Baraban et al., 2018). Hence, changes in Calpain1 expression in the ICH mice were examined before and after use of the TRPA1 blockers. The results implied that Calpain1 expression was increased in the ICH mice (**Figures 4A,C**) and that its expression was significantly down-regulated after administration of HC-030031 and A-967079. These findings proved that TRPA1 blockers could reduce the amount of Calpain1 and thus reduce MBP degradation (**Figures 4C–E**). These results indicated that up-regulation of NOX1 and Calpain1 mediated the myelin degradation induced by TRPA1 activation. The TRPA1 blockers reduced the oxidative stress response of the white matter and the myelin damage after ICH.

DISCUSSION

Although white matter injury has long been considered the major cause of hemiplegia, partial sensory disturbance and ectopic blindness in ICH patients, our understanding of the mechanisms of white matter injury is still quite limited. Indeed, little is known about the effects on the neural fibers in the damaged area (Tao et al., 2017).

In this study, we observed that the neuronal tract damage and motor dysfunction of the ICH mice were severe in the acute phase and gradually improved after 7 days. The nonselective TRPA1 cation channel was involved in myelin injury after ICH, and inhibition of TRPA1 during the acute phase of ICH could ease the peri-hematoma white matter injury, nerve

impulse conduction disorder and motor dysfunction in the mice. However, the preadministration of TRPA1 antagonism did not produce an obvious protective effect on motor function in ICH mice. This may be due to the metabolism of the TRPA1 antagonism by the mouse, resulting in the TRPA1 antagonism for pretreatment that is insufficiently concentrated after ICH to provide protection. ROS increases have been widely reported in ischemic stroke and hemorrhagic stroke, and the increase in ROS has also been found to activate TRPA1 (Hamilton et al., 2016; Qu et al., 2016; Arenas et al., 2017; **Figure 5**).

Axonal injury and demyelination at the edge of the hematoma were first described in a collagenase-induced ICH rat model (Wasserman and Schlichter, 2008). Significant demyelination and axonal damage were observed on D3 after ICH and were highly associated with motor dysfunction. Our group and others observed the same phenomena in the autologous blood infusion ICH mouse model (Barratt et al., 2014; Tao et al., 2016). Our data showed that the white matter injury severity peaked on D3 after ICH together with the obvious motor function deficits detected with several motor function tests; however, the axon demyelination lasted at least 2 weeks after ICH, whereas most of the motor function tests returned to normal on D7 after ICH. Data from other groups were consistent with our observation (Ni et al., 2015; Yang et al., 2018). Most of the motor function tests used here were adapted from an ischemic stroke mouse model; therefore, we assumed that the discordance of demyelination with the motor function tests was partially caused by inadequate sensitivity of the test. We developed a modified motor function test that could distinguish motor function deficits on day 28 after ICH [modified behavioral tests to detect white matter injury-induced motor deficits after intracerebral hemorrhage in mice (under review)]. Therefore, the improved function test could more accurately assess the relationship between white matter injury and motor dysfunction.

Using TEM to evaluate the white matter damage, we found that the morphological changes of the axons in the ICH mice were almost the same as those in the L-α-lysophosphatidylcholine-induced demyelinating mice. Sághy et al. (2016) and Bölcskei et al. (2018) showed that cuprizone-treated TRPA1 KO animals had reduced myelin damage and attenuated accumulation of astrocytes and microglia in 2016 and 2018, respectively. In the absence of the TRPA1 receptor, the release of astrocyte factors is altered, which significantly increases ERK1/2 and decreases both p38-MAPK and c-Jun activation, resulting in less oligodendrocyte apoptosis (Sághy et al., 2016; Bölcskei et al., 2018). Our results suggested that the increases in NOX1 and Calpain1 were associated with TRPA1 activation-induced myelin degradation and that blockade of TRPA1 could reduce NOX1 and Calpain1 expression. These studies also demonstrate that the myelin and oligodendrocyte damage begins with the increase in Ca^{2+} that is apparent with TRPA1. Together, these investigations indicate that TRPA1 is involved in myelin damage through a variety of mechanisms. In addition, destruction of the myelin sheath was more serious and the mortality rate of the ICH mice was distinctly increased by the TRPA1 agonist, the related mechanism needs further exploration. Collectively, interventions for TRPA1-mediated myelin damage may represent a new and hopeful target to save patients' motor functions.

ETHICS STATEMENT

All experimental protocols were approved by the Ethics Committee of the Third Military Medical University (Army Medical University) and performed according to the eighth edition of the National Institutes of Health Guide for the Care and Use of Laboratory Animals.

AUTHOR CONTRIBUTIONS

HF and XL were responsible for experimental design. MX and WC conducted the experiments and wrote the manuscript. RH, YY, JW, CG, XT, CL, and ML collected the data. XL and ZJ revised the manuscript. MX and WC have contributed equally to this work.

FUNDING

This work was supported by the National Basic Research Program of China (973 Program, Grant No. 2014CB541600), the Major Innovation Project of Southwest Hospital (Grant number SWH2016ZDCX1011) and National Natural Science Foundation of China (Grant numbers 81802509).

SUPPLEMENTARY MATERIAL

The Supplementary Material for this article can be found online at: https://www.frontiersin.org/articles/10.3389/fnmol.2019.00098/full#supplementary-material

FIGURE S1 | The changes in muscle strength, weight and the axons of the ICH mice. **(A)** The muscle strength was lower in the ICH mice than that in the sham group mice on D0–D3 ($n = 6$). **(B)** Comparison of weights between the two groups did not show a significant difference ($n = 6$). **(C)** Axonal oedema was observed around the hematoma in the ICH mice. **(D)** The five traces of D3 as an example of the MEPs approach ($^{*}P < 0.05$ vs. sham group, $^{**}P < 0.01$ vs. sham group).

FIGURE S2 | **(A)** TRPA1 was expressed on the myelin. The sham group was on D1 after sham surgery. **(B)** The TRPA1 agonist (polygodial) significantly increased the mortality of the ICH mice ($n = 8$; $P < 0.05$). **(C)** There was no significant difference between the preadministrated ICH group and the ICH group, except for ICH group and ICH* group on D3 in the forelimb muscle strength test ($n = 3$). Scale bars represent 50 μm ($^{\#}P < 0.05$).

REFERENCES

Andersson, D. A., Gentry, C., Moss, S., and Bevan, S. (2008). Transient receptor potential A1 is a sensory receptor for multiple products of oxidative stress. *J. Neurosci.* 28, 2485–2494. doi: 10.1523/JNEUROSCI.5369-07.2008

Andrei, S. R., Ghosh, M., Sinharoy, P., Dey, S., Bratz, I. N., and Damron, D. S. (2017). TRPA1 ion channel stimulation enhances cardiomyocyte contractile

function via a CaMKII-dependent pathway. *Channels* 11, 587–603. doi: 10.1080/19336950.2017.1365206

Arenas, O. M., Zaharieva, E. E., Para, A., Vásquez-Doorman, C., Petersen, C. P., and Gallio, M. (2017). Activation of planarian TRPA1 by reactive oxygen species reveals a conserved mechanism for animal nociception. *Nat. Neurosci.* 20, 1686–1693. doi: 10.1038/s41593-017-0005-0

Armstrong, R. C., Mierzwa, A. J., Sullivan, G. M., and Sanchez, M. A. (2016). Myelin and oligodendrocyte lineage cells in white matter pathology and plasticity after traumatic brain injury. *Neuropharmacology* 110, 654–659. doi: 10.1016/j.neuropharm.2015.04.029

Balami, J. S., and Buchan, A. M. (2012). Complications of intracerebral haemorrhage. *Lancet Neurol.* 11, 101–118. doi: 10.1016/S1474-4422(11)70264-2

Baraban, M., Koudelka, S., and Lyons, D. A. (2018). Ca^{2+} activity signatures of myelin sheath formation and growth *in vivo*. *Nat. Neurosci.* 21, 19–23. doi: 10.1038/s41593-017-0040-x

Barratt, H. E., Lanman, T. A., and Carmichael, S. T. (2014). Mouse intracerebral hemorrhage models produce different degrees of initial and delayed damage, axonal sprouting and recovery. *J. Cereb. Blood Flow Metab.* 34, 1463–1471. doi: 10.1038/jcbfm.2014.107

Bölcskei, K., Kriszta, G., Sághy, É., Payrits, M., Sipos, É., Vranesics, A., et al. (2018). Behavioural alterations and morphological changes are attenuated by the lack of TRPA1 receptors in the cuprizone-induced demyelination model in mice. *J. Neuroimmunol.* 320, 1–10. doi: 10.1016/j.jneuroim.2018.03.020

Bosson, A., Paumier, A., Boisseau, S., Jacquier-Sarlin, M., Buisson, A., and Albrieux, M. (2017). TRPA1 channels promote astrocytic Ca^{2+} hyperactivity and synaptic dysfunction mediated by oligomeric forms of amyloid-β peptide. *Mol. Neurodegener.* 12:53. doi: 10.1186/s13024-017-0194-8

Cheng, C.-Y., Hsu, C.-Y., Huang, Y.-C., Tsai, Y.-H., Hsu, H.-T., Yang, W.-H., et al. (2015). Motor outcome of deep intracerebral haemorrhage in diffusion tensor imaging: comparison of data from different locations along the corticospinal tract. *Neurol. Res.* 37, 774–781. doi: 10.1179/1743132815y.0000000050

Chomiak, T., and Hu, B. (2009). What is the optimal value of the g-ratio for myelinated fibers in the rat CNS? A theoretical approach. *PLoS One* 4:e7754. doi: 10.1371/journal.pone.0007754

Das, A., Guyton, M. K., Smith, A., Wallace, G. T., McDowell, M. L., Matzelle, D. D., et al. (2013). Calpain inhibitor attenuated optic nerve damage in acute optic neuritis in rats. *J. Neurochem.* 124, 133–146. doi: 10.1111/jnc.12064

De Logu, F., Nassini, R., Materazzi, S., Carvalho Gonçalves, M., Nosi, D., Rossi Degl'Innocenti, D., et al. (2017). Schwann cell TRPA1 mediates neuroinflammation that sustains macrophage-dependent neuropathic pain in mice. *Nat. Commun.* 8:1887. doi: 10.1038/s41467-017-01739-2

Deshmukh, V. A., Tardif, V., Lyssiotis, C. A., Green, C. C., Kerman, B., Kim, H. J., et al. (2013). A regenerative approach to the treatment of multiple sclerosis. *Nature* 502, 327–332. doi: 10.1038/nature12647

Doyle, S., Hansen, D. B., Vella, J., Bond, P., Harper, G., Zammit, C., et al. (2018). Vesicular glutamate release from central axons contributes to myelin damage. *Nat. Commun.* 9:1032. doi: 10.1038/s41467-018-03427-1

Duncan, G. J., Plemel, J. R., Assinck, P., Manesh, S. B., Muir, F. G. W., Hirata, R., et al. (2017). Myelin regulatory factor drives remyelination in multiple sclerosis. *Acta Neuropathol.* 134, 403–422. doi: 10.1007/s00401-017-1741-7

Hamilton, N. B., Kolodziejczyk, K., Kougioumtzidou, E., and Attwell, D. (2016). Proton-gated Ca^{2+}-permeable TRP channels damage myelin in conditions mimicking ischaemia. *Nature* 529, 523–527. doi: 10.1038/nature16519

Joseph, M. J., Caliaperumal, J., and Schlichter, L. C. (2016). After intracerebral hemorrhage, oligodendrocyte precursors proliferate and differentiate inside white-matter tracts in the rat striatum. *Transl. Stroke Res.* 7, 192–208. doi: 10.1007/s12975-015-0445-3

Krafft, P. R., Rolland, W. B., Duris, K., Lekic, T., Campbell, A., Tang, J., et al. (2012). Modeling intracerebral hemorrhage in mice: injection of autologous blood or bacterial collagenase. *J. Vis. Exp.* 67:e4289. doi: 10.3791/4289

Lee, K. I., Lin, H. C., Lee, H. T., Tsai, F. C., and Lee, T. S. (2017). Loss of transient receptor potential ankyrin 1 channel deregulates emotion, learning and memory, cognition, and social behavior in mice. *Mol. Neurobiol.* 54, 3606–3617. doi: 10.1007/s12035-016-9908-0

Lee, S. H., Park, D. W., Park, S. C., Park, Y. K., Hong, S. Y., Kim, J. R., et al. (2009). Calcium-independent phospholipase A2β-Akt signaling is involved in lipopolysaccharide-induced NADPH oxidase 1 expression and foam cell formation. *J. Immunol.* 183, 7497–7504. doi: 10.4049/jimmunol.0900503

Liu, M. C., Akle, V., Zheng, W., Kitlen, J., O'Steen, B., Larner, S. F., et al. (2006). Extensive degradation of myelin basic protein isoforms by calpain following traumatic brain injury. *J. Neurochem.* 98, 700–712. doi: 10.1111/j.1471-4159.2006.03882.x

McNamara, C. R., Mandel-Brehm, J., Bautista, D. M., Siemens, J., Deranian, K. L., Zhao, M., et al. (2007). TRPA1 mediates formalin-induced pain. *Proc. Natl. Acad. Sci. U S A* 104, 13525–13530. doi: 10.1073/pnas.0705924104

Mendes, G. L., Santos, A. R., Malheiros, A., Filho, V. C., Yunes, R. A., and Calixto, J. B. (2000). Assessment of mechanisms involved in antinociception caused by sesquiterpene polygodial. *J. Pharmacol. Exp. Ther.* 292, 164–172.

Ni, W., Okauchi, M., Hatakeyama, T., Gu, Y., Keep, R. F., Xi, G., et al. (2015). Deferoxamine reduces intracerebral hemorrhage-induced white matter damage in aged rats. *Exp. Neurol.* 272, 128–134. doi: 10.1016/j.expneurol.2015.02.035

Ottens, A. K., Golden, E. C., Bustamante, L., Hayes, R. L., Denslow, N. D., and Wang, K. K. (2008). Proteolysis of multiple myelin basic protein isoforms after neurotrauma: characterization by mass spectrometry. *J. Neurochem.* 104, 1404–1414. doi: 10.1111/j.1471-4159.2007.05086.x

Plemel, J. R., Michaels, N. J., Weishaupt, N., Caprariello, A. V., Keough, M. B., Rogers, J. A., et al. (2018). Mechanisms of lysophosphatidylcholine-induced demyelination: a primary lipid disrupting myelinopathy. *Glia* 66, 327–347. doi: 10.1002/glia.23245

Qu, J., Chen, W., Hu, R., and Feng, H. (2016). The injury and therapy of reactive oxygen species in intracerebral hemorrhage looking at mitochondria. *Oxid. Med. Cell. Longev.* 2016:2592935. doi: 10.1155/2016/2592935

Qureshi, A. I., Mendelow, A. D., and Hanley, D. F. (2009). Intracerebral haemorrhage. *Lancet* 373, 1632–1644. doi: 10.1016/S0140-6736(09)60371-8

Redondo-Castro, E., Navarro, X., and García-Alías, G. (2016). Longitudinal evaluation of residual cortical and subcortical motor evoked potentials in spinal cord injured rats. *J. Neurotrauma* 33, 907–916. doi: 10.1089/neu.2015.4140

Sághy, É., Sipos, É., Ács, P., Bölcskei, K., Pohóczky, K., Kemény, Á., et al. (2016). TRPA1 deficiency is protective in cuprizone-induced demyelination-A new target against oligodendrocyte apoptosis. *Glia* 64, 2166–2180. doi: 10.1002/glia.23051

Sałat, K., and Filipek, B. (2015). Antinociceptive activity of transient receptor potential channel TRPV1, TRPA1, and TRPM8 antagonists in neurogenic and neuropathic pain models in mice. *J. Zhejiang Univ. Sci. B* 16, 167–178. doi: 10.1631/jzus.b1400189

Schneider, S., Gruart, A., Grade, S., Zhang, Y., Kröger, S., Kirchhoff, F., et al. (2016). Decrease in newly generated oligodendrocytes leads to motor dysfunctions and changed myelin structures that can be rescued by transplanted cells. *Glia* 64, 2201–2218. doi: 10.1002/glia.23055

Tao, C., Hu, X., Li, H., and You, C. (2017). White matter injury after intracerebral hemorrhage: pathophysiology and therapeutic strategies. *Front. Hum. Neurosci.* 11:422. doi: 10.3389/fnhum.2017.00422

Tao, C., Zhang, R., Hu, X., Song, L., Wang, C., Gao, F., et al. (2016). A novel brainstem hemorrhage model by autologous blood infusion in rat: white matter injury, magnetic resonance imaging, and neurobehavioral features. *J. Stroke Cerebrovasc. Dis.* 25, 1102–1109. doi: 10.1016/j.jstrokecerebrovasdis.2016.01.025

Wang, Y. Y., Chang, R. B., Allgood, S. D., Silver, W. L., and Liman, E. R. (2011). A TRPA1-dependent mechanism for the pungent sensation of weak acids. *J. Gen. Physiol.* 137, 493–505. doi: 10.1085/jgp.201110615

Wang, F., Yang, Y. J., Yang, N., Chen, X. J., Huang, N. X., Zhang, J., et al. (2018). Enhancing oligodendrocyte myelination rescues synaptic loss and improves functional recovery after chronic hypoxia. *Neuron* 99, 689.e5–701.e5. doi: 10.1016/j.neuron.2018.07.017

Wasserman, J. K., and Schlichter, L. C. (2008). White matter injury in young and aged rats after intracerebral hemorrhage. *Exp. Neurol.* 214, 266–275. doi: 10.1016/j.expneurol.2008.08.010

Wu, W., Xiong, W., Zhang, P., Chen, L., Fang, J., Shields, C., et al. (2017). Increased threshold of short-latency motor evoked potentials in transgenic mice

expressing Channelrhodopsin-2. *PLoS One* 12:e0178803. doi: 10.1371/journal.pone.0178803

Xie, Z., Enkhjargal, B., Reis, C., Huang, L., Wan, W., Tang, J., et al. (2017). Netrin-1 preserves blood-brain barrier integrity through deleted in colorectal cancer/focal adhesion kinase/RhoA signaling pathway following subarachnoid hemorrhage in rats. *J. Am. Heart Assoc.* 6:e005198. doi: 10.1161/jaha.116.005198

Yang, Y., Zhang, X., Ge, H., Liu, W., Sun, E., Ma, Y., et al. (2018). Epothilone B benefits nigrostriatal pathway recovery by promoting microtubule stabilization after intracerebral hemorrhage. *J. Am. Heart Assoc.* 7:e007626. doi: 10.1161/jaha.117.007626

Yin, C., Huang, G. F., Sun, X. C., Guo, Z., and Zhang, J. H. (2017). DLK silencing attenuated neuron apoptosis through JIP3/MA2K7/JNK pathway in early brain injury after SAH in rats. *Neurobiol. Dis.* 103, 133–143. doi: 10.1016/j.nbd.2017.04.006

Zhao, H., Xu, M., and Chu, G. (2017). Association between myocardial cell apoptosis and calpain-1/caspase-3 expression in rats with hypoxic-ischemic brain damage. *Mol. Med. Rep.* 15, 2727–2731. doi: 10.3892/mmr.2017.6341

Zuo, S., Pan, P., Li, Q., Chen, Y., and Feng, H. (2017). White matter injury and recovery after hypertensive intracerebral hemorrhage. *Biomed Res. Int.* 2017:6138424. doi: 10.1155/2017/6138424

Zou, X., Wu, Z., Zhu, W., Chen, L., Mao, Y., and Zhao, F. (2017). Effectiveness of minocycline in acute white matter injury after intracerebral hemorrhage. *J. Neurosurg.* 126, 1855–1862. doi: 10.3171/2016.5.jns152670

Conflict of Interest Statement: The authors declare that the research was conducted in the absence of any commercial or financial relationships that could be construed as a potential conflict of interest.

frontiers in Molecular Neuroscience

REVIEW
published: 28 June 2019
doi: 10.3389/fnmol.2019.00165

Role of Long Noncoding RNAs and Circular RNAs in Nerve Regeneration

Chun Yao and Bin Yu*

Key Laboratory of Neuroregeneration of Jiangsu and Ministry of Education, Co-innovation Center of Neuroregeneration, Nantong University, Nantong, China

Nerve injuries may cause severe disability and affect the quality of life. It is of great importance to get a full understanding of the biological processes and molecular mechanisms underlying nerve injuries to find and target specific molecules for nerve regeneration. Numerous studies have shown that noncoding RNAs (ncRNAs) participate in diverse biological processes and diseases. Long noncoding RNAs (lncRNAs) and circular RNAs (circRNAs) are two major groups of ncRNAs, which attract growing attention. The altered expression patterns of lncRNAs and circRNAs following nerve injury suggest that these ncRNAs might be associated with nerve regeneration. This review will give a brief introduction of lncRNAs and circRNAs. We then summarize the current studies on lncRNAs and circRNAs following peripheral nerve injury and spinal cord injury (SCI). Typical lncRNAs and circRNAs are introduced to illustrate the diverse molecular mechanisms for nerve regeneration. In addition, we also discuss some issues to be addressed in future investigations on lncRNAs and circRNAs.

Keywords: long noncoding RNA, circular RNA, peripheral nerve injury, spinal cord injury, nerve regeneration

OPEN ACCESS

Edited by:
Jaewon Ko,
Daegu Gyeongbuk Institute of Science and Technology (DGIST), South Korea

Reviewed by:
Jinju Han,
Korea Advanced Institute of Science & Technology (KAIST), South Korea
Je-Hyun Yoon,
Medical University of South Carolina, United States

****Correspondence:***
Chun Yao
yaochun@ntu.edu.cn

Received: *10 April 2019*
Accepted: *14 June 2019*
Published: *28 June 2019*

Citation:
Yao C and Yu B (2019) Role of Long Noncoding RNAs and Circular RNAs in Nerve Regeneration. Front. Mol. Neurosci. 12:165. doi: 10.3389/fnmol.2019.00165

INTRODUCTION

Injuries to the central nervous system (CNS) or peripheral nervous system (PNS) are a common clinical problem and cause inconvenience in daily life. Although PNS has an intrinsic regenerative ability following nerve injury compared with CNS, the axon regeneration speed is slow and the functional recovery is poor. To explore the complex biological processes underlying nerve injury and identify specific molecules in nerve regeneration will provide new therapeutic targets for nerve injury (Chan et al., 2014).

More than three-quarters of the human genome is transcribed with only less than 2% is coding for proteins, suggesting a potential RNA-based regulation network (Djebali et al., 2012; Fatica and Bozzoni, 2014). These RNAs that do not encode a protein, but have other cellular functions were termed as noncoding RNAs (ncRNAs; Cech and Steitz, 2014). In addition to ribosomal RNAs (rRNAs) and transfer RNAs (tRNAs), new classes of ncRNAs have been identified over the last two decades, including microRNAs (miRNAs), long noncoding RNAs (lncRNAs) and circular RNAs (circRNAs; Cech and Steitz, 2014; Qu et al., 2015).

NcRNAs could guide DNA synthesis, genome rearrangement and regulate gene expression during transcription, RNA processing and translation, emerging as a major source of biomarkers and targets for therapeutics in numerous diseases (Cech and Steitz, 2014; St Laurent et al., 2015). Previously, the role of miRNAs in nerve regeneration has been summarized (Yu et al., 2015). Recently, the dynamic alterations and functions of lncRNAs and circRNAs after nerve injury were also uncovered. LncRNA Kcna2 AS is increased in dorsal root ganglion (DRG) after peripheral

nerve injury. Blocking Kcna2 AS expression could attenuate the development and maintenance of neuropathic pain by increasing Kcna2 (Zhao et al., 2013). Rat sciatic chronic constriction injury (CCI) induced a comprehensive expression profile of circRNAs, suggesting a potential role of circRNAs in neuropathic pain (Cao et al., 2017). In addition to neuropathic pain (Li et al., 2019; Wu et al., 2019), lncRNAs and circRNAs could also regulate nerve regeneration after nerve injury.

Here, we review the recent studies on lncRNAs and circRNAs following nerve injuries (peripheral nerve injury and spinal cord injury, SCI; **Table 1**) and summarize some key lncRNAs and circRNAs (**Table 2** and **Figure 1**) to illustrate their functional mechanisms in nerve regeneration.

A BRIEF GLANCE AT LncRNAs AND CircRNAs

Origins, Characteristics and Classifications

LncRNAs are a class of ncRNAs longer than 200 nt, usually capped, polyadenylated and spliced without significant protein-coding capacity (Rinn and Chang, 2012). The origins of lncRNAs are diverse. Besides metamorphosis from pre-existing protein-coding sequence, lncRNAs can also emerge from chromosome rearrangement, retrotransposition, tandem duplication and transposable element sequences insertion (Ponting et al., 2009). LncRNAs have been found to be transcribed from various genome regions, including promoter upstream regions, enhancers, intergenic regions and the opposite strand of protein-coding genes. Some lncRNA species are generated by unique biogenesis pathways, such as RNase P cleavage and capping by small nucleolar RNA (snoRNA)-protein (snoRNP) complexes at their ends (Wu et al., 2017). Previously, based on the genomic location relative to neighboring protein-coding genes, lncRNAs are classified into sense, antisense, bidirectional, intronic and intergenic lncRNAs (Peng et al., 2018). In addition, there are new lncRNA species according to the association with other DNA elements or based on unique structures, including the promoter up-stream transcripts (PROMPTs), enhancer-associated RNAs (eRNAs), sno-lncRNAs and so on (St Laurent et al., 2015).

Circular RNAs (circRNAs) are an increasingly appreciated class of ncRNA. Unlike linear RNAs, circRNAs are characterized by a covalently closed continuous loop without 5′-3′ polarity or a polyadenylated tail (Qu et al., 2015). Compared to the diverse origins of lncRNAs, circRNAs usually originate from protein-coding genes and complete exons (Pamudurti et al., 2017). Eukaryotic circRNAs are mainly produced during splicing, catalyzed by either the spliceosomal machinery or by groups I and II ribozymes (Vicens and Westhof, 2014). In addition to circRNAs formed from exon back-splicing circularization, there are various types of circRNAs existed according to different biogenesis mechanisms, such as circular viral RNA genomes, circRNA intermediates, spliced introns and exons production (Qu et al., 2015; Chen, 2016). Due to the lack of free ends, circRNAs are resistant toward exonucleases (Vicens and Westhof, 2014). Besides that property, circRNAs also have potentials for rolling circle amplification, rearranging genomic sequences and constraining RNA folding (Vicens and Westhof, 2014). As the first known function of a circRNA is miRNA sponge, circRNAs are predicted as ncRNAs regulating miRNAs. However, some of the circRNAs are translated into polypeptides (Legnini et al., 2017; Pamudurti et al., 2017).

Functions and Mechanisms

Numerous studies have revealed the role of lncRNAs and circRNAs in disease pathological progress, diagnosis, and prognosis (Wan et al., 2017; Han et al., 2018). In the nervous system, lncRNAs could take part in brain development, neuron maintenance and differentiation, as well as synaptic plasticity,

TABLE 1 | List of studies on long noncoding RNA (lncRNA) and circular RNA (circRNA) alteration after nerve injury.

Injury model	Tissue	Time points post injury	Methods	Reference
LncRNA				
•Peripheral nerve injury				
Rat sciatic nerve transection	L4-L6 DRGs	0, 1, 4, 7 days	Microarray	Yu et al. (2013)
Mouse sciatic nerve crush	DRGs	0, 1, 4, 7 days	RNA-Seq	Perry et al. (2018)
Mouse sciatic nerve crush	Distal sciatic nerve	0, 3, 7, 14 days	Microarray	Pan et al. (2017b)
Mouse sciatic nerve transection itransection	Distal sciatic nerve	uncut, 7 days	RNA-Seq	Arthur-Farraj et al. (2017)
IL-22 treated rat SCs	SCs		RNA-Seq	Xu et al. (2017)
Rat sciatic nerve transection	Sciatic nerve	8 weeks	Microarray	Wang et al. (2018)
Rat sciatic nerve crush	Sciatic nerve	0, 1, 4, 7 days	Microarray	Yao et al. (2018)
•Spinal cord injury				
Rat contusion SCI	Epicenter spinal cord	0, 1, 4 and 7 days	RNA-Seq	Wang J. et al. (2015)
Mouse contusion SCI	Epicenter spinal cord	0, 1, 3 days, 1 and 3 weeks	Microarray	Ding et al. (2016)
Rat contusion SCI	Epicenter spinal cord	0, 1, 3, 6 months	RNA-Seq	Duran et al. (2017)
Rat contusion SCI	Epicenter spinal cord	2 days	Microarray	Shi et al. (2019)
CircRNA				
Rat traumatic SCI	Spinal cord	3 days	Microarray	Qin et al. (2018)
Rat traumatic SCI	Spinal cord	6 h	RNA-Seq	Zhou et al. (2019)
Mice sciatic nerve injury	Gastrocnemius muscles	0, 1, 2, 4, 8 weeks	RNA-Seq	Weng et al. (2018)
Rat sciatic nerve compression	Sciatic nerve	1 day	RNA-Seq	Zhou Z.-B. et al. (2018)

TABLE 2 | Summary of the functions and mechanisms of lncRNAs and circRNAs in nerve injury.

LncRNA	Injury model	Expression	Function	Mechanism	Reference
•Peripheral nerve injury					
BC089918	Rat sciatic nerve transection	down	Negatively regulate neurite outgrowth	Unclear	Yu et al. (2013)
Uc.217	Rat sciatic nerve transection	down	Negatively regulate neurite outgrowth	Affect the expressions of genes involved in nerve regeneration	Yao et al. (2015)
Silc1	Mouse sciatic nerve crush	up	Depletion of Silc1 impair neurite outgrowth	Activate in *cis* the expression of transcription factor Sox11	Perry et al. (2018)
NONMMUG014387	Rat sciatic nerve transection	up	Promote SC proliferation	Increase Cthrc1 expression and activate Wnt/PCP pathway	Pan et al. (2017a)
BC088327	Rat sciatic nerve transection	up	Promote SC proliferation	Synergic with heregulin-1β	Wang et al. (2018)
TNXA-PS1	Rat sciatic nerve crush	down	Downregulation of TNXA-PS1 promote SC migration	Act as a ceRNA to affect Dusp1 expression	Yao et al. (2018)
Egr2-AS-RNA	Mouse sciatic nerve transection	up	Induce demyelination	Inhibit Egr2 expression	Martinez-Moreno et al. (2017)
•Spinal cord injury					
lncSCIR1	Rat contusion SCI	down	Negatively regulate astrocyte proliferation and migration.	Affect the expressions of Adm, Bmp7, Snca and Wnt3	Wang J. et al. (2015)
lncSNHG5	Rat contusion SCI	up	Enhance astrocytes and microglia viability	Interact with KLF4	Jiang and Zhang (2018)
lncRNA-Map2k4	Mouse contusion SCI	down	Promote neuron proliferation and inhibit apoptosis	Through an miR-199a/FGF1 pathway	Lv (2017)
XIST	Rat contusion SCI	up	Induce neuronal apoptosis	Negatively modulate PI3K/AKT pathway by decreasing miR-494 and increasing PTEN expression	Gu et al. (2017)
BDNF-AS	Rat ASCI and hypoxia cellular model	up	Promote neuronal cell apoptosis	Sponge miR-130b-5p to regulate PRDM5	Zhang et al. (2018a)
DGCR5	Rat ASCI and hypoxia cellular model	down	Suppress neuronal apoptosis	Bind and negatively regulate PRDM5	Zhang et al. (2018b)
MALAT1	Rat ASCI	up	Regulate inflammatory response of microglia	*Via* miR-199b/ IKKβ/NF-κB pathway	Zhou H.-J. et al. (2018)
CircRNA					
circRNA 2837	Rat sciatic nerve compression	down	Regulate autophagy in neurons	Serve as a miRNA sponge for the miR-34 family	Zhou Z.-B. et al. (2018)

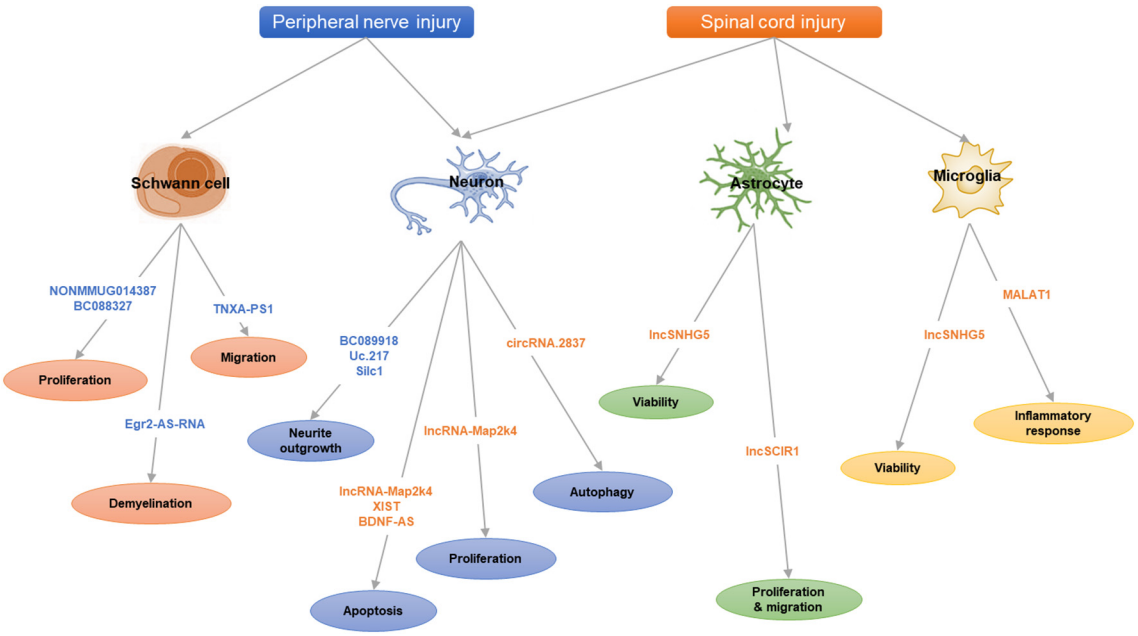

FIGURE 1 | The scheme of long noncoding RNAs (lncRNAs) and circular RNAs (circRNAs) in nerve injury.

cognitive function and memory (Wu et al., 2013). In addition, dysregulated lncRNAs were also found in neurodegenerative diseases in human, such as lncRNA BACE1-AS and BC200 (Alzheimer's disease, AD), PINK1-AS (Parkinson's disease), NEAT1 and MEG3 (Huntington's disease), AS C9ORF72 (amyotrophic lateral sclerosis) and so on (Wan et al., 2017).

CircRNAs are enriched in mammalian brain, conserved and dynamically expressed during neuronal differentiation (Rybak-Wolf et al., 2015). Expressions of circRNAs in mouse hippocampus and prefrontal cortex, regions involved in memory formation and learning, were illustrated (Chen B.-J. et al., 2018). In adult rat subventricular zone (SVZ), one SVZ-specific circRNA (rat_circ:chr15:9915223-9915671) was identified to bind miR-138-5p as a potential negative regulator in neural stem cell proliferation (Xie et al., 2018). CircRNA CDR1as (ciRS-7) was exclusively highly expressed in brain tissues and served as a potential circular miR-7 sponge in neuronal tissues (Memczak et al., 2013). In human AD brain tissues, ciRS-7 was decreased with increased expression of miR-7 and could downregulate expression of several AD-relevant genes, such as the ubiquitin conjugase (UBE2A) protein (Zhao et al., 2016).

The functional mechanisms of lncRNAs and circRNAs are complicated. Briefly, lncRNAs localized in nucleus could interact with chromatin complexes, modulate proteins and enzyme cofactors, bind DNA/RNA-binding proteins or interact directly with DNA to form R-loops and triple helixes, working as key regulators for transcriptional programs (Marchese et al., 2017). On the other hand, cytoplasmic lncRNAs could also interact with proteins to form complex, regulating a set of cytoplasmic events (e.g., protein localization and turnover, mRNA translation and stability). Cytoplasmic lncRNAs can also act as sponges of miRNAs (competing endogenous RNA, ceRNA) and alleviate the negative effects of miRNAs on its target genes (Noh et al., 2018).

Comparing with lncRNAs, the large majority of circRNAs are in the cytoplasm. These circRNAs can function as miRNA or lncRNA sponges to indirectly regulate mRNA expression through a complex RNA communication network (Wang Y.-H. et al., 2015; Chen, 2016; Adams et al., 2017). Gene regulatory axis of lncRNAs-miRNAs-circRNAs has been described in the brain recently (Kleaveland et al., 2018). It reported that lncRNA Cyrano could bind with miR-7 to trigger miR-7 degradation, preventing repression of miR-7 targeted mRNAs and promoting circRNA Cdr1as accumulation. On the other hand, miR-7 could lead to destruction of Cdr1as with another miRNA miR-671. These ncRNAs collaborated to establish a sophisticated regulatory network. In addition, some exon-intron circRNAs could also interact with transcription complexes to affect gene transcription (Barrett and Salzman, 2016).

LncRNAs IN NERVE INJURY

Peripheral Nerve Injury

Injuries to peripheral nerves by trauma or acute compression may lead to axon continuity interruption, nerve degeneration and neuron death, resulting in partial or total loss of nerve functions (Navarro et al., 2007). Unlike CNS, the PNS has a regenerate ability after injury due to the intrinsic growth capacity of neurons and a permissive microenvironment mainly provided by Schwann cells (SCs; Barton et al., 2017). The sciatic nerve injury model is a classic model for investigating effects of peripheral nerve regeneration. After sciatic nerve injury, in the distal segment of the lesion, a progressive

degeneration (Wallerian degeneration) is occurring, breaking down both axons and myelin. This process is accompanied by the dedifferentiation of SCs and activation of immune response (Chen et al., 2015). The dedifferentiated SCs could replenish the damaged tissues by proliferation, clear myelin debris, secrete neurotrophic factors and form Bungner band, providing a favorable environment for axon regeneration and ensuing remyelination (Jessen and Mirsky, 2016). In the proximal nerve stump, the damaged neurons shift their states from neurotransmission to regeneration, which is triggered by a sequence of molecular responses, including calcium influx, activation of protein kinase pathways and gene expression by transcription factors (Wu and Murashov, 2013). Nerve regeneration following peripheral nerve injury is a complicated process, accompanied with multiple signaling pathways and genes, such as Neuregulin 1 signaling, Gpr126 signaling, Erk signaling, PI3K-GSK3 signaling, DLK-JNK signaling, Wnt signaling and so on (Glenn and Talbot, 2013; Zhang and Zhou, 2013).

Intrinsic Regeneration Ability of Neurons

The survival and transition into a regenerative state of injured neurons are critical for nerve regeneration. DRG neurons provide a favorable model for mammalian axon regeneration investigation among PNS neurons (Zhang and Zhou, 2013). Yu et al. (2013) reported the altered lncRNA expressions in DRGs after rat sciatic nerve injury. By lncRNA microarray, they identified 105 lncRNAs dysregulated in L4-L6 DRGs at 0, 1, 4 and 7 days post sciatic nerve transection. In a mouse sciatic nerve crush model, Perry et al. (2018) identified dysregulated lncRNAs expressed during neuroregeneration in DRGs by RNA-Seq.

From these lncRNA profiles after peripheral nerve injury, BC089918 was identified to have a negative effect on neurite outgrowth *in vitro*. However, its regulatory mechanism is unclear (Yu et al., 2013). Another lncRNA, uc.217, was also selected for validation. The data showed that uc.217 was down-regulated in DRG neurons after sciatic nerve injury and could regulate neurite outgrowth in cultured DRG neurons by affecting the expressions of regeneration-associated genes, Gal and Vip. Besides that, uc.217 could serve as a sponge RNA to regulate Sema3d and Smad7 expressions, which are genes involved in nerve regeneration (Yao et al., 2015). Experiments suggested that lncRNAs, Silc1 and Norris1, could affect neurite outgrowth *in vitro*. In addition, mice with Silc1 deletion had a delayed regeneration after sciatic nerve crush. Further investigations showed that Silc1 could affect neuroregeneration by activating in *cis* the expression of Sox11, which is a well-known transcription factor that could modulate peripheral nerve regeneration (Jankowski et al., 2009; Perry et al., 2018).

Schwann Cell Phenotype Modulation

As the major glial cells in PNS, SCs also play an important role in peripheral nerve regeneration. Upon injury, SCs will dedifferentiate, proliferate and migrate to form bands of Bungner, providing guidance cues for regeneration. In addition, SCs will also clear myelin debris and secrete neurotrophic factors to facilitate nerve injury repair (Glenn and Talbot, 2013). Previously, numerous studies have confirmed the role of miRNAs in SC modulation, such as miR-221-3p, miR-182, miR-9 and miR-132 (Yao et al., 2016; Zhao L. et al., 2018). Similar to miRNAs, lncRNAs also take part in regulating SCs. Profiles of lncRNA expression alterations in sciatic nerve after injury or in SCs were identified in different conditions (**Table 1;** Arthur-Farraj et al., 2017; Pan et al., 2017b; Xu et al., 2017; Yao et al., 2018; Wang et al., 2018).

Further investigation identified several potential lncRNAs for SC modulation. LncRNA NONMMUG014387 was upregulated after peripheral nerve injury and could promote SC proliferation by increasing collagen triple helix repeat containing 1 (Cthrc1) and activating Wnt/PCP pathway (Pan et al., 2017a). LncRNA BC088327 was increased with the exposure time of heregulin-1β in SCs under hypoxic conditions. Knockdown of BC088327 expression could significantly suppress cell viability in the presence of heregulin-1β. This suggested that BC088327 could play a synergistic role with heregulin1β in SC proliferation during peripheral nerve repair (Wang et al., 2018). Recently, our group identified that lncRNA TNXA-PS1 (NR_024118) could affect SC migration by acting as a sponge RNA for miR-24-3p/miR-152-3p. After sciatic nerve injury, TNXA-PS1 was down-regulated, releasing miR-24-3p and miR-152-3p previously bound. These miRNAs could interact with the 3′-UTR of Dual specificity phosphatase 1 (Dusp1) and reduce Dusp1 expression, promoting SC migration (Yao et al., 2018).

Besides modulating SC proliferation and migration, lncRNAs could also take part in SC myelination. Previous studies have shown the crucial role of transcription factor Egr2 in the control of SC myelination (Ghislain et al., 2002; Le et al., 2005). The expression of lncRNA Egr2-AS-RNA, an anti-sense RNA to the promoter of Egr2, was increased after peripheral nerve injury. This will lead to the decline of Egr2 expression and induce demyelination by recruiting H3K27ME3, AGO1, AGO2 and EZH2 on Egr2 promoter (Martinez-Moreno et al., 2017). Upstream exploration indicated that Egr2-AS-RNA expression is regulated by ERK1/2 signaling. Nerve injury inhibits the NRG1-ERK1/2 signaling axis, which dephosphorizes YY1 and elevating Egr2-AS-RNA expression.

Spinal Cord Injury

Comparing to the PNS, the CNS has limited regeneration ability. It was estimated that about 3 million people suffered from traumatic SCI, with about 180,000 new cases annually in the worldwide (Lee et al., 2014). SCI is much more complicated due to extensive cell loss, axonal disruption, glial scar and a shortage of growth-permissive factors (Estrada and Müller, 2014). After a primary mechanical injury (damage to neurons, axons, and glia at injury sites), a subsequent secondary injury will develop within hours or days, including ischemia, edema, inflammation and vascular changes (Silva et al., 2014). During this phage, inflammatory cells, such as macrophages, microglia, T-cells and neutrophils, will infiltrate the injury site and release inflammatory cytokines. The architectural disruption and glial scarring formed by uncontrolled reactive astrogliosis impair directed axonal regrowth (Ahuja and Fehlings, 2016). Extensive temporal gene expression changes were occurred during these processes. In addition, the role and implication of miRNAs in

SCI have been widely investigated (Bhalala et al., 2013; Ning et al., 2014). Recent years, the alterations of lncRNAs after SCI at different time points were extensively identified (Wang J. et al., 2015; Ding et al., 2016; Duran et al., 2017; Shi et al., 2019), suggesting that lncRNAs might also take part in SCI.

Reactive Astrocytes

One of the main barriers to SCI regeneration is glial scar, which is composed primarily of astrocytes (Silver and Miller, 2004). In response to nerve injury, the astrocytes are hypertrophic reactivated. The enlarged and entangled reactive astrocytes will develop then into a rubbery, tenacious barrier for nerve regeneration. On the other hand, astrocyte gliosis might also provide permissive functions for CNS injury, such as neuroprotection, facilitating blood brain barrier repair, limiting the spread of inflammatory cells and so on (Sofroniew and Vinters, 2010).

LncSCIR1 was down-regulated post SCI and knockdown of lncSCIR1 could promote astrocyte proliferation and migration (Wang J. et al., 2015). However, the regulatory mechanism of lncSCIR1 was unclear. LncRNA SNHG5 (small nucleolar RNA host gene5) has been widely studied in tumorigenesis (Damas et al., 2016; Zhao et al., 2017). It can regulate gene expression by sponging miRNAs (He et al., 2017) or stabilizing target transcripts (Damas et al., 2016). Recently, lncSNHG5 was also identified to enhance the viability of astrocytes and microglia after SCI through SNHG5/KLF4/eNOS axis (Jiang and Zhang, 2018). Kruppel-like factor 4 (KLF4), an inflammation associated molecule induced in reactive astrocytes and microglia, might be positively regulated by SNHG5 as a sponge RNA for miR-32 (Zhao et al., 2017).

Neuron Survival

Neuronal survival and axon regeneration are two key decisions of injured neurons (He and Jin, 2016). A number of neurotrophins (NGF, BDNF and NT-3) and miRNAs (miR-486, miR-20a, miR-21) have been identified to regulate neuronal survival after SCI (Bhalala et al., 2013; Ning et al., 2014; Keefe et al., 2017).

Fibroblast growth factor 1 (FGF1) is a powerful neurotrophic factor for nerve regeneration (Tsai et al., 2015). LncRNA-Map2k4 (ENSMUST00000138093) was declined after SCI and could affect neuron proliferation and apoptosis through an miR-199a/FGF1 pathway. Knockdown of LncRNA-Map2k4 will inhibit FGF1 expression by up-regulating miR-199a (Lv, 2017). Some classical lncRNAs involved in cancer progress and neurological diseases can also affect neuronal survival after SCI. By retrieving the microarray data in the GEO dataset, lncRNA XIST was found significantly increased after SCI. Down-regulating lncRNA XIST could improve locomotor activity and attenuate neuronal apoptosis after SCI by activating PI3K/AKT pathway through mopping up of miR-494 (Gu et al., 2017). After acute spinal cord injury (ASCI), lncRNA BDNF-AS were up-regulated. BDNF-AS will then sponge miR-130b-5p and increase PRDM5 expression, leading to neuronal apoptosis (Zhang et al., 2018a). LncRNA DGCR5 is a significant neural lncRNA involved in a number of neurological disorders, such as Huntington's disease (Johnson, 2012). Recent studies found that DGCR5 was also down-regulated in ASCI model and in neurons treated with hypoxia. DGCR5 could inhibit neuronal apoptosis by directly binding and negatively regulating PRDM5 expression. Overexpression of DRCR5 could ameliorate ASCI in rats with elevated BBB score (Zhang et al., 2018b).

Inflammation

After SCI, inflammation is triggered with activated microglia, hematogenous macrophages and other inflammatory cells recruited to the lesion site, leading to secondary injury (Assinck et al., 2017). The activated immune cells will secret proinflammatory factors and contribute to cell death by producing ROS (Tran et al., 2018). On the other hand, some macrophages can promote nerve regeneration by secretion of anti-inflammatory factors. Besides lncSNHG5, which we have discussed above, lncRNA MALAT1 also take part in microglia activation. After acute SCI, MALAT1 expression was significantly increased, resulting in the activation of IKKβ/NF-κB signaling pathway. MALAT1 could also promote the secretion of proinflammatory cytokines TNF-α and IL-1β in microglia through down-regulating miR-199b (Zhou H.-J. et al., 2018).

CircRNAs IN NERVE INJURY

Recently, the investigation of circRNAs in nerve injury is increasing. A number of studies have revealed circRNA expression patterns in the models of traumatic brain injury and neuropathic pain by microarray and RNA-seq (Zhou et al., 2017; Chen Z. et al., 2018; Zhao R.-T. et al., 2018). One-hundred and eighty-eight differentially expressed circRNAs (68 up-regulated and 120 down-regulated) were identified in rat spinal cord at 14 days after spared nerve injury. Among them, circ_0006928 was found might regulate neuron apoptosis by binding miR-184 (Zhou et al., 2017). circRNAs-Filipi1l, which was negatively regulated by miRNA-1224 *via* binding and splicing in the Ago2-dependent manner, was increased in chronic inflammation pain and could regulate nociception by targeting Ubr5 (Pan et al., 2019).

However, the roles of circRNAs in nerve regeneration remain unknown. The expression profiles of circRNAs in rat spinal cord after traumatic SCI have been identified (Qin et al., 2018; Zhou et al., 2019). As for peripheral nerve injury, there is one report for the whole transcriptome involved in denervated muscle atrophy after peripheral nerve injury (Weng et al., 2018). In addition, differentially expressed circRNAs in a rat sciatic nerve compression model were identified and one down-regulated circRNA, circRNA.2837, was found to regulate autophagy in neurons by serving as a miRNA sponge for the miR-34 family (Zhou Z.-B. et al., 2018). Silencing circRNAs.2837 could induce autophagy in primary spinal neurons by targeting miR-34a.

CONCLUSION AND PERSPECTIVE

This review aims to summarize the recent progress of lncRNAs and circRNAs in nerve regeneration. From this review article, we could find that at present, most of the studies on lncRNAs and circRNAs in nerve regeneration were focused on microarray and RNA-sequencing data analysis.

These studies always first conduct an animal model of nerve injury and then dissect nerve tissue or cells for microarray or RNA-sequencing to obtain significantly differentially expressed lncRNAs and circRNAs. Further, bioinformatic analyses will be performed to obtain enriched biological processes and signaling pathways of these ncRNAs and their regulated genes. In addition, one or two dysregulated ncRNAs will be selected for further qRT-PCR expression validation and lncRNAs/circRNAs-miRNA-gene regulated networks will be constructed to find target genes of certain lncRNA/circRNA.

Though a set of dysregulated lncRNAs after peripheral nerve injury and SCI has been reported, a few lncRNAs among them received further investigation and the mechanisms underlying the regulation role of lncRNAs in nerve injury are still unclear. A few number of studies got a deep investigation of certain lncRNA/circRNA to explore their characteristics, function and regulation mechanisms. Serving as a sponge RNA or binding proteins directly are two major mechanisms involved in the regulation role of lncRNAs in nerve regeneration till now.

In future investigation, there are some issues to be addressed: (1) The detailed mechanisms underlying the role of lncRNAs/circRNAs. We need to illustrate how lncRNAs/circRNAs regulate certain genes. Which segment of lncRNAs/circRNAs plays the critical regulatory role? (2) The interaction networks between lncRNAs-miRNAs-circRNAs and circRNAs-miRNAs-mRNAs. Recently, gene regulatory axis of lncRNAs-miRNAs-circRNAs has been described in the brain (Kleaveland et al., 2018). The possibility of interaction between circRNAs and lncRNAs after nerve injury deserves our further attention. In addition, more solid evidence should be provided to confirm the interaction between lncRNAs/circRNAs, miRNAs and target genes, such as Ago2 immunoprecipitation. (3) The upstream of lncRNAs/circRNAs. From what we have reviewed, the majority of these studies are focused on the function of lncRNAs/circRNAs after nerve injury. However, how nerve injuries trigger the expression alteration of lncRNAs/circRNAs? Which signaling or genes affect the dysregulation of lncRNAs/circRNAs? These upstream regulators of lncRNAs/circRNAs will be another interesting research topic. (4) The application of lncRNAs/circRNAs in nerve injury repair. Preclinical and clinical trials based on miRNA therapeutics have been conducted (Wahid et al., 2010). Some lncRNAs/circRNAs have been identified as prognostic markers in cancers (Tian and Xu, 2015; Lyu and Huang, 2017; Xiong et al., 2017). How could we apply lncRNAs/circRNAs to clinical nerve injury repair? Till now, the majority of studies on lncRNAs and circRNAs in nerve regeneration were based on animal models. Could these ncRNAs be used in clinical therapeutics? A recent study reported synthetically conserved lncRNAs in human, mouse, and rat by analyzing lncRNAs expressed in injured nerves of animal models and lncRNAs in human sensory neurons derived from iPSCs (Baskozos et al., 2019). In addition, circRNAs are also expected to be conserved between species (Rybak-Wolf et al., 2015). These studies showed the conservation of lncRNAs and circRNAs between species, which will facilitate the clinical transformation for lncRNAs and circRNAs in nerve injury. More efforts are needed to develop lncRNAs/circRNAs based clinical therapeutics for nerve injury.

AUTHOR CONTRIBUTIONS

CY conceived and wrote the review article. BY revised the article.

FUNDING

This work was supported by National Major Project of Research and Development (2017YFA0104701 to BY), National Natural Science Foundation of China (31500823 to CY, 81771326 and 31371062 to BY), Jiangsu Provincial Natural Science Foundation (BK20150403 to CY).

REFERENCES

Adams, B. D., Parsons, C., Walker, L., Zhang, W. C., and Slack, F. J. (2017). Targeting noncoding RNAs in disease. *J. Clin. Invest.* 127, 761–771. doi: 10.1172/JCI84424

Ahuja, C. S., and Fehlings, M. (2016). Concise review: bridging the gap: novel neuroregenerative and neuroprotective strategies in spinal cord injury. *Stem Cells Transl. Med.* 5, 914–924. doi: 10.5966/sctm.2015-0381

Arthur-Farraj, P. J., Morgan, C. C., Adamowicz, M., Gomez-Sanchez, J. A., Fazal, S. V., Beucher, A., et al. (2017). Changes in the coding and non-coding transcriptome and DNA methylome that define the schwann cell repair phenotype after nerve injury. *Cell Rep.* 20, 2719–2734. doi: 10.1016/j.celrep.2017.08.064

Assinck, P., Duncan, G. J., Hilton, B. J., Plemel, J. R., and Tetzlaff, W. (2017). Cell transplantation therapy for spinal cord injury. *Nat. Neurosci.* 20, 637–647. doi: 10.1038/nn.4541

Barrett, S. P., and Salzman, J. (2016). Circular RNAs: analysis, expression and potential functions. *Development* 143, 1838–1847. doi: 10.1242/dev.128074

Barton, M. J., John, J. S., Clarke, M., Wright, A., and Ekberg, J. (2017). The glia response after peripheral nerve injury: a comparison between schwann cells and olfactory ensheathing cells and their uses for neural regenerative therapies. *Int. J. Mol. Sci.* 18:E287. doi: 10.3390/ijms18020287

Baskozos, G., Dawes, J. M., Austin, J. S., Antunes-Martins, A., McDermott, L., Clark, A. J., et al. (2019). Comprehensive analysis of long noncoding RNA expression in dorsal root ganglion reveals cell-type specificity and dysregulation after nerve injury. *Pain* 160, 463–485. doi: 10.1097/j.pain.0000000000001416

Bhalala, O. G., Srikanth, M., and Kessler, J. A. (2013). The emerging roles of microRNAs in CNS injuries. *Nat. Rev. Neurol.* 9, 328–339. doi: 10.1038/nrneurol.2013.67

Cao, S., Deng, W., Li, Y., Qin, B., Zhang, L., Yu, S., et al. (2017). Chronic constriction injury of sciatic nerve changes circular RNA expression in rat spinal dorsal horn. *J. Pain Res.* 10, 1687–1696. doi: 10.2147/jpr.s139592

Cech, T. R., and Steitz, J. A. (2014). The noncoding RNA revolution-trashing old rules to forge new ones. *Cell* 157, 77–94. doi: 10.1016/j.cell.2014.03.008

Chan, K. M., Gordon, T., Zochodne, D. W., and Power, H. A. (2014). Improving peripheral nerve regeneration: from molecular mechanisms to potential therapeutic targets. *Exp. Neurol.* 261, 826–835. doi: 10.1016/j.expneurol.2014.09.006

Chen, L. L. (2016). The biogenesis and emerging roles of circular RNAs. *Nat. Rev. Mol. Cell Biol.* 17, 205–211. doi: 10.1038/nrm.2015.32

Chen, P., Piao, X., and Bonaldo, P. (2015). Role of macrophages in Wallerian degeneration and axonal regeneration after peripheral nerve injury. *Acta Neuropathol.* 130, 605–618. doi: 10.1007/s00401-015-1482-4

Chen, B.-J., Yang, B., and Janitz, M. (2018). Region-specific expression of circular RNAs in the mouse brain. *Neurosci. Lett.* 666, 44–47. doi: 10.1016/j.neulet.2017.12.022

Chen, Z., Wang, H., Zhong, J., Yang, J., Darwazeh, R., Tian, X., et al. (2018). Significant changes in circular RNA in the mouse cerebral cortex around an injury site after traumatic brain injury. *Exp. Neurol.* 313, 37–48. doi: 10.1016/j.expneurol.2018.12.003

Damas, N. D., Marcatti, M., Côme, C., Christensen, L. L., Nielsen, M. M., Baumgartner, R., et al. (2016). SNHG5 promotes colorectal cancer cell survival by counteracting STAU1-mediated mRNA destabilization. *Nat. Commun.* 7:13875. doi: 10.1038/ncomms13875

Ding, Y., Song, Z., and Liu, J. (2016). Aberrant LncRNA expression profile in a contusion spinal cord injury mouse model. *Biomed. Res. Int.* 2016:9249401. doi: 10.1155/2016/9249401

Djebali, S., Davis, C. A., Merkel, A., Dobin, A., Lassmann, T., Mortazavi, A., et al. (2012). Landscape of transcription in human cells. *Nature* 489, 101–108. doi: 10.1038/nature11233

Duran, R. C., Yan, H., Zheng, Y., Huang, X., Grill, R., Kim, D. H., et al. (2017). The systematic analysis of coding and long non-coding RNAs in the sub-chronic and chronic stages of spinal cord injury. *Sci. Rep.* 7:41008. doi: 10.1038/srep41008

Estrada, V., and Müller, H. W. (2014). Spinal cord injury—there is not just one way of treating it. *F1000Prime Rep.* 6:84. doi: 10.12703/p6-84

Fatica, A., and Bozzoni, I. (2014). Long non-coding RNAs: new players in cell differentiation and development. *Nat. Rev. Genet.* 15, 7–21. doi: 10.1038/nrg3606

Ghislain, J., Desmarquet-Trin-Dinh, C., Jaegle, M., Meijer, D., Charnay, P., and Frain, M. (2002). Characterisation of cis-acting sequences reveals a biphasic, axon-dependent regulation of Krox20 during Schwann cell development. *Development* 129, 155–166.

Glenn, T. D., and Talbot, W. S. (2013). Signals regulating myelination in peripheral nerves and the Schwann cell response to injury. *Curr. Opin. Neurobiol.* 23, 1041–1048. doi: 10.1016/j.conb.2013.06.010

Gu, S. X., Xie, R., Liu, X. D., Shou, J. J., Gu, W. T., and Che, X. M. (2017). Long coding RNA XIST contributes to neuronal apoptosis through the downregulation of AKT phosphorylation and is negatively regulated by miR-494 in rat spinal cord injury. *Int. J. Mol. Sci.* 18:E732. doi: 10.3390/ijms18040732

Han, B., Chao, J., and Yao, H. (2018). Circular RNA and its mechanisms in disease: from the bench to the clinic. *Pharmacol. Ther.* 187, 31–44. doi: 10.1016/j.pharmthera.2018.01.010

He, B., Bai, Y., Kang, W., Zhang, X., and Jiang, X. (2017). LncRNA SNHG5 regulates imatinib resistance in chronic myeloid leukemia *via* acting as a CeRNA against MiR-205–5p. *Am. J. Cancer Res.* 7, 1704–1713. doi: 10.1089/dna.2016.3533

He, Z., and Jin, Y. (2016). Intrinsic control of axon regeneration. *Neuron* 90, 437–451. doi: 10.1016/j.neuron.2016.04.022

Jankowski, M. P., McIlwrath, S. L., Jing, X., Cornuet, P. K., Salerno, K. M., Koerber, H. R., et al. (2009). Sox11 transcription factor modulates peripheral nerve regeneration in adult mice. *Brain Res.* 1256, 43–54. doi: 10.1016/j.brainres.2008.12.032

Jessen, K. R., and Mirsky, R. (2016). The repair Schwann cell and its function in regenerating nerves. *J. Physiol.* 594, 3521–3531. doi: 10.1113/jp270874

Jiang, Z. S., and Zhang, J. R. (2018). LncRNA SNHG5 enhances astrocytes and microglia viability *via* upregulating KLF4 in spinal cord injury. *Int. J. Biol. Macromol.* 120, 66–72. doi: 10.1016/j.ijbiomac.2018.08.002

Johnson, R. (2012). Long non-coding RNAs in Huntington's disease neurodegeneration. *Neurobiol. Dis.* 46, 245–254. doi: 10.1016/j.nbd.2011.12.006

Keefe, K. M., Sheikh, I. S., and Smith, G. M. (2017). Targeting neurotrophins to specific populations of neurons: NGF, BDNF, and NT-3 and their relevance for treatment of spinal cord injury. *Int. J. Mol. Sci.* 18:E548. doi: 10.3390/ijms18030548

Kleaveland, B., Shi, C. Y., Stefano, J., and Bartel, D. P. (2018). A network of noncoding regulatory RNAs acts in the mammalian brain. *Cell* 174, 350.e17–362.e17. doi: 10.1016/j.cell.2018.05.022

Le, N., Nagarajan, R., Wang, J. Y. T., Araki, T., Schmidt, R. E., and Milbrandt, J. (2005). Analysis of congenital hypomyelinating Egr2(Lo/Lo) nerves identifies Sox2 as an inhibitor of Schwann cell differentiation and myelination. *Proc. Natl. Acad. Sci. U S A* 102, 2596–2601. doi: 10.1073/pnas.0407836102

Lee, B. B., Cripps, R. A., Fitzharris, M., and Wing, P. C. (2014). The global map for traumatic spinal cord injury epidemiology: update 2011, global incidence rate. *Spinal Cord* 52, 110–116. doi: 10.1038/sc.2012.158

Legnini, I., Di Timoteo, G., Rossi, F., Morlando, M., Briganti, F., Sthandier, O., et al. (2017). Circ-ZNF609 is a circular RNA that can be translated and functions in myogenesis. *Mol. Cell* 66, 22.e9–37.e9. doi: 10.1016/j.molcel.2017.02.017

Li, Z., Li, X., Chen, X., Li, S., Ho, I. H. T., Liu, X., et al. (2019). Emerging roles of long non-coding RNAs in neuropathic pain. *Cell Prolif.* 52:e12528. doi: 10.1111/cpr.12528

Lv, H. R. (2017). lncRNA-Map2k4 sequesters miR-199a to promote FGF1 expression and spinal cord neuron growth. *Biochem. Biophys. Res. Commun.* 490, 948–954. doi: 10.1016/j.bbrc.2017.06.145

Lyu, D., and Huang, S. (2017). The emerging role and clinical implication of human exonic circular RNA. *RNA Biol.* 14, 1000–1006. doi: 10.1080/15476286.2016.1227904

Marchese, F. P., Raimondi, I., and Huarte, M. (2017). The multidimensional mechanisms of long noncoding RNA function. *Genome Biol.* 18:206. doi: 10.1186/s13059-017-1348-2

Martinez-Moreno, M., O'Shea, T. M., Zepecki, J. P., Olaru, A., Ness, J. K., Langer, R., et al. (2017). Regulation of peripheral myelination through transcriptional buffering of Egr2 by an antisense long non-coding RNA. *Cell Rep.* 20, 1950–1963. doi: 10.1016/j.celrep.2017.07.068

Memczak, S., Jens, M., Elefsinioti, A., Torti, F., Krueger, J., Rybak, A., et al. (2013). Circular RNAs are a large class of animal RNAs with regulatory potency. *Nature* 495, 333–338. doi: 10.1038/nature11928

Navarro, X., Vivã, M., and Valero-Cabré, A. (2007). Neural plasticity after peripheral nerve injury and regeneration. *Prog. Neurobiol.* 82, 163–201. doi: 10.1016/j.pneurobio.2007.06.005

Ning, B., Gao, L., Liu, R. H., Liu, Y., Zhang, N.-S., and Chen, Z.-Y. (2014). microRNAs in spinal cord injury: potential roles and therapeutic implications. *Int. J. Biol. Sci.* 10, 997–1006. doi: 10.7150/ijbs.9058

Noh, J. H., Kim, K. M., McClusky, W. G., Abdelmohsen, K., and Gorospe, M. (2018). Cytoplasmic functions of long noncoding RNAs. *Wiley Interdiscip. Rev. RNA* 9:e1471. doi: 10.1002/wrna.1471

Pamudurti, N. R., Bartok, O., Jens, M., Ashwal-Fluss, R., Stottmeister, C., Ruhe, L., et al. (2017). Translation of CircRNAs. *Mol. Cell* 66, 9.e7–21.e7. doi: 10.1016/j.molcel.2017.02.021

Pan, Z., Li, G. F., Sun, M. L., Xie, L., Liu, D., Zhang, Q., et al. (2019). MicroRNA-1224 splicing circularRNA-filip1l in an ago2-dependent manner regulates chronic inflammatory pain *via* targeting Ubr5. *J. Neurosci.* 39, 2125–2143. doi: 10.1523/JNEUROSCI.1631-18.2018

Pan, B., Shi, Z. J., Yan, J. Y., Li, J. H., and Feng, S. Q. (2017a). Long non-coding RNA NONMMUG014387 promotes Schwann cell proliferation after peripheral nerve injury. *Neural Regen. Res.* 12, 2084–2091. doi: 10.4103/1673-5374.221168

Pan, B., Zhou, H. X., Liu, Y., Yan, J. Y., Wang, Y., Yao, X., et al. (2017b). Time-dependent differential expression of long non-coding RNAs following peripheral nerve injury. *Int. J. Mol. Med.* 39, 1381–1392. doi: 10.3892/ijmm.2017.2963

Peng, Z., Liu, C., and Wu, M. (2018). New insights into long noncoding RNAs and their roles in glioma. *Mol. Cancer* 17:61. doi: 10.1186/s12943-018-0812-2

Perry, R. B., Hezroni, H., Goldrich, M. J., and Ulitsky, I. (2018). Regulation of neuroregeneration by long noncoding RNAs. *Mol. Cell* 72, 553.e5–567.e5. doi: 10.1016/j.molcel.2018.09.021

Ponting, C. P., Oliver, P. L., and Reik, W. (2009). Evolution and functions of long noncoding RNAs. *Cell* 136, 629–641. doi: 10.1016/j.cell.2009.02.006

Qin, C., Liu, C. B., Yang, D. G., Gao, F., Zhang, X., Zhang, C., et al. (2018). Circular RNA expression alteration and bioinformatics analysis in rats after traumatic spinal cord injury. *Front. Mol. Neurosci.* 11:497. doi: 10.3389/fnmol.2018.00497

Qu, S., Yang, X., Li, X., Wang, J., Gao, Y., Shang, R., et al. (2015). Circular RNA: a new star of noncoding RNAs. *Cancer Lett.* 365, 141–148. doi: 10.1016/j.canlet.2015.06.003

Rinn, J. L., and Chang, H. Y. (2012). Genome regulation by long noncoding RNAs. *Annu. Rev. Biochem.* 81, 145–166. doi: 10.1146/annurev-biochem-051410-092902

Rybak-Wolf, A., Stottmeister, C., Glažar, P., Jens, M., Pino, N., Giusti, S., et al. (2015). Circular RNAs in the mammalian brain are highly abundant, conserved, and dynamically expressed. *Mol. Cell* 58, 870–885. doi: 10.1016/j.molcel.2015.03.027

Saijilafu, Zhang, B. Y., and Zhou, F. Q. (2013). Signaling pathways that regulate axon regeneration. *Neurosci. Bull.* 29, 411–420. doi: 10.1007/s12264-013-1357-4

Shi, Z., Ning, G., Zhang, B., Yuan, S., Zhou, H., Pan, B., et al. (2019). Signatures of altered long noncoding RNAs and messenger RNAs expression in the early acute phase of spinal cord injury. *J. Cell. Physiol.* 234, 8918–8927. doi: 10.1002/jcp.27560

Silva, N. A., Sousa, N., Reis, R. L., and Salgado, A. J. (2014). From basics to clinical: a comprehensive review on spinal cord injury. *Prog. Neurobiol.* 114, 25–57. doi: 10.1016/j.pneurobio.2013.11.002

Silver, J., and Miller, J. H. (2004). Regeneration beyond the glial scar. *Nat. Rev. Neurosci.* 5, 146–156. doi: 10.1038/nrn1326

Sofroniew, M. V., and Vinters, H. V. (2010). Astrocytes: biology and pathology. *Acta Neuropathol.* 119, 7–35. doi: 10.1007/s00401-009-0619-8

St Laurent, G., Wahlestedt, C., and Kapranov, P. (2015). The Landscape of long noncoding RNA classification. *Trends Genet.* 31, 239–251. doi: 10.1016/j.tig.2015.03.007

Tian, X., and Xu, G. (2015). Clinical value of lncRNA MALAT1 as a prognostic marker in human cancer: systematic review and meta-analysis. *BMJ Open* 5:e008653. doi: 10.1136/bmjopen-2015-008653

Tran, A. P., Warren, P. M., and Silver, J. (2018). The biology of regeneration failure and success after spinal cord injury. *Physiol. Rev.* 98, 881–917. doi: 10.1152/physrev.00017.2017

Tsai, M. J., Tsai, S. K., Huang, M. C., Liou, D. Y., Huang, S. L., Hsieh, W. H., et al. (2015). Acidic FGF promotes neurite outgrowth of cortical neurons and improves neuroprotective effect in a cerebral ischemic rat model. *Neuroscience* 305, 238–247. doi: 10.1016/j.neuroscience.2015.07.074

Vicens, Q., and Westhof, E. (2014). Biogenesis of circular RNAs. *Cell* 159, 13–14. doi: 10.1016/j.cell.2014.09.005

Wahid, F., Shehzad, A., Khan, T., and Kim, Y. Y. (2010). MicroRNAs: synthesis, mechanism, function, and recent clinical trials. *Biochim. Biophys. Acta* 1803, 1231–1243. doi: 10.1016/j.bbamcr.2010.06.013

Wan, P., Su, W., and Zhuo, Y. (2017). The role of long noncoding RNAs in neurodegenerative diseases. *Mol. Neurobiol.* 54, 2012–2021. doi: 10.1007/s12035-016-9793-6

Wang, J., Hu, B., Cao, F., Sun, S., Zhang, Y., and Zhu, Q. (2015). Down regulation of lncSCIR1 after spinal cord contusion injury in rat. *Brain Res.* 1624, 314–320. doi: 10.1016/j.brainres.2015.07.052

Wang, H., Wu, J., Zhang, X., Ding, L., and Zeng, Q. (2018). Microarray analysis of the expression profile of lncRNAs reveals the key role of lncRNA BC088327 as an agonist to heregulin-1β-induced cell proliferation in peripheral nerve injury. *Int. J. Mol. Med.* 41, 3477–3484. doi: 10.3892/ijmm.2018.3571

Wang, Y.-H., Yu, X. H., Luo, S. S., and Han, H. (2015). Comprehensive circular RNA profiling reveals that circular RNA100783 is involved in chronic CD28-associated CD8(+)T cell ageing. *Immun. Ageing* 12:17. doi: 10.1186/s12979-015-0042-z

Weng, J., Zhang, P., Yin, X., and Jiang, B. (2018). The whole transcriptome involved in denervated muscle atrophy following peripheral nerve injury. *Front. Mol. Neurosci.* 11:69. doi: 10.3389/fnmol.2018.00069

Wu, S., Bono, J., and Tao, Y. X. (2019). Long noncoding RNA (lncRNA): a target in neuropathic pain. *Expert Opin. Ther. Targets* 23, 15–20. doi: 10.1080/14728222.2019.1550075

Wu, D., and Murashov, A. K. (2013). Molecular mechanisms of peripheral nerve regeneration: emerging roles of microRNAs. *Front. Physiol.* 4:55. doi: 10.3389/fphys.2013.00055

Wu, H., Yang, L., and Chen, L. L. (2017). The diversity of long noncoding RNAs and their generation. *Trends Genet.* 33, 540–552. doi: 10.1016/j.tig.2017.05.004

Wu, P., Zuo, X., Deng, H., Liu, X., Liu, L., and Ji, A. (2013). Roles of long noncoding RNAs in brain development, functional diversification and neurodegenerative diseases. *Brain Res. Bull.* 97, 69–80. doi: 10.1016/j.brainresbull.2013.06.001

Xie, F., Zhao, Y., Wang, S. D., Ma, J., Wang, X., and Qian, L. J. (2018). Identification, characterization, and functional investigation of circular RNAs in subventricular zone of adult rat brain. *J. Cell. Biochem.* 120, 3428–3437. doi: 10.1002/jcb.27614

Xiong, D. D., Feng, Z. B., Cen, W. L., Zeng, J. J., Liang, L., Tang, R. X., et al. (2017). The clinical value of lncRNA NEAT1 in digestive system malignancies: a comprehensive investigation based on 57 microarray and RNA-seq datasets. *Oncotarget* 8, 17665–17683. doi: 10.18632/oncotarget.14756

Xu, S. M., Ao, J. P., Gu, H. H., Wang, X. Q., Xie, C., Meng, D. P., et al. (2017). IL-22 impedes the proliferation of schwann cells: transcriptome sequencing and bioinformatics analysis. *Mol. Neurobiol.* 54, 2395–2405. doi: 10.1007/s12035-016-9699-3

Yao, C., Shi, X., Zhang, Z., Zhou, S., Qian, T., Wang, Y., et al. (2016). Hypoxia-induced upregulation of miR-132 promotes schwann cell migration after sciatic nerve injury by targeting PRKAG3. *Mol. Neurobiol.* 53, 5129–5139. doi: 10.1007/s12035-015-9449-y

Yao, C., Wang, Y., Zhang, H., Feng, W., Wang, Q., Shen, D., et al. (2018). lncRNA TNXA-PS1 modulates schwann cells by functioning as a competing endogenous RNA following nerve injury. *J. Neurosci.* 38, 6574–6585. doi: 10.1523/jneurosci.3790-16.2018

Yao, C., Wang, J., Zhang, H., Zhou, S., Qian, T., Ding, F., et al. (2015). Long non-coding RNA uc.217 regulates neurite outgrowth in dorsal root ganglion neurons following peripheral nerve injury. *Eur. J. Neurosci.* 42, 1718–1725. doi: 10.1111/ejn.12966

Yu, B., Zhou, S., Hu, W., Qian, T., Gao, R., Ding, G., et al. (2013). Altered long noncoding RNA expressions in dorsal root ganglion after rat sciatic nerve injury. *Neurosci. Lett.* 534, 117–122. doi: 10.1016/j.neulet.2012.12.014

Yu, B., Zhou, S., Yi, S., and Gu, X. (2015). The regulatory roles of non-coding RNAs in nerve injury and regeneration. *Prog. Neurobiol.* 134, 122–139. doi: 10.1016/j.pneurobio.2015.09.006

Zhang, H., Li, D., Zhang, Y., Li, J., Ma, S., Zhang, J., et al. (2018a). Knockdown of lncRNA BDNF-AS suppresses neuronal cell apoptosis *via* downregulating miR-130b-5p target gene PRDM5 in acute spinal cord injury. *RNA Biol.* 15, 1071–1080. doi: 10.1080/15476286.2018.1493333

Zhang, H., Wang, W., Li, N., Li, P., Liu, M., Pan, J., et al. (2018b). LncRNA DGCR5 suppresses neuronal apoptosis to improve acute spinal cord injury through targeting PRDM5. *Cell Cycle* 17, 1992–2000. doi: 10.1080/15384101.2018.1509622

Zhao, Y., Alexandrov, P. N., Jaber, V., and Lukiw, W. J. (2016). Deficiency in the ubiquitin conjugating enzyme UBE2A in Alzheimer's disease (AD) is linked to deficits in a natural circular miRNA-7 sponge (circRNA; ciRS-7). *Genes* 7:116. doi: 10.3390/genes7120116

Zhao, L., Han, T., Li, Y., Sun, J., Zhang, S., Liu, Y., et al. (2017). The lncRNA SNHG5/miR-32 axis regulates gastric cancer cell proliferation and migration by targeting KLF4. *FASEB J.* 31, 893–903. doi: 10.1096/fj.201600994r

Zhao, X., Tang, Z., Zhang, H., Atianjoh, F. E., Zhao, J.-Y., Liang, L., et al. (2013). A long noncoding RNA contributes to neuropathic pain by silencing Kcna2 in primary afferent neurons. *Nat. Neurosci.* 16, 1024–1031. doi: 10.1038/nn.3438

Zhao, L., Yuan, Y., Li, P., Pan, J., Qin, J., Liu, Y., et al. (2018). miR-221–3p inhibits schwann cell myelination. *Neuroscience* 379, 239–245. doi: 10.1016/j.neuroscience.2018.03.019

Zhao, R.-T., Zhou, J., Dong, X. L., Bi, C. W., Jiang, R. C., Dong, J. F., et al. (2018). Circular ribonucleic acid expression alteration in exosomes from the brain extracellular space after traumatic brain injury in mice. *J. Neurotrauma* 35, 2056–2066. doi: 10.1089/neu.2017.5502

Zhou, Z.-B., Du, D., Chen, K.-Z., Deng, L., Niu, Y.-L., and Zhu, L. (2019). Differential expression profiles and functional predication of circRNA in traumatic spinal cord injury of rats. *J. Neurotrauma* doi: 10.1089/neu.2018.6366 [Epub ahead of print].

Zhou, Z.-B., Niu, Y.-L., Huang, G.-X., Lu, J.-J., Chen, A., and Zhu, L. (2018). Silencing of circRNA.2837 plays a protective role in sciatic nerve injury by sponging the miR-34 family *via* regulating neuronal autophagy. *Mol. Ther. Nucleic Acids* 12, 718–729. doi: 10.1016/j.omtn.2018.07.011

Zhou, H.-J., Wang, L.-Q., Wang, D.-B., Yu, J.-B., Zhu, Y., Xu, Q.-S., et al. (2018). Long noncoding RNA MALAT1 contributes to inflammatory response of microglia following spinal cord injury *via* the modulation of a miR-199b/IKKβ/NF-κB signaling pathway. *Am. J. Physiol. Cell Physiol.* 315, C52–C61. doi: 10.1152/ajpcell.00278.2017

Zhou, J., Xiong, Q., Chen, H., Yang, C., and Fan, Y. (2017). Identification of the spinal expression profile of non-coding RNAs involved in neuropathic pain following spared nerve injury by sequence analysis. *Front. Mol. Neurosci.* 10:91. doi: 10.3389/fnmol.2017.00091

Conflict of Interest Statement: The authors declare that the research was conducted in the absence of any commercial or financial relationships that could be construed as a potential conflict of interest.

frontiers in Molecular Neuroscience

ORIGINAL RESEARCH
published: 17 July 2019
doi: 10.3389/fnmol.2019.00170

The Role of TRESK in Discrete Sensory Neuron Populations and Somatosensory Processing

Greg A. Weir[1]†, Philippa Pettingill[1†], Yukyee Wu[1], Galbha Duggal[1], Andrei-Sorin Ilie[2], Colin J. Akerman[2] and M. Zameel Cader[1]**

[1]*Nuffield Department of Clinical Neurosciences, University of Oxford, Oxford, United Kingdom,* [2]*Department of Pharmacology, University of Oxford, Oxford, United Kingdom*

Two-pore domain K^+ (K_{2P}) channels generate K^+ leak current, which serves a vital role in controlling and modulating neuronal excitability. This diverse family of K^+ channels exhibit distinct expression and function across neuronal tissues. TWIK-related spinal cord K^+ channel (TRESK) is a K_{2P} channel with a particularly enriched role in sensory neurons and *in vivo* pain pathways. Here, we explored the role of TRESK across molecularly distinct sensory neuron populations and assessed its contribution to different sensory modalities. We found TRESK mRNA only in select populations of C- and A-δ nociceptors, in addition to low threshold D-hair afferents. Neurons from mice in which TRESK has been ablated demonstrated marked hyperexcitability, which was amplified under inflammatory challenge. Detailed behavioral phenotyping of TRESK knockout mice revealed specific deficits in somatosensory processing of noxious and non-noxious stimuli. These results demonstrate novel roles of TRESK in somatosensory processing and offer important information to those wishing to target the channel for therapeutic means.

Keywords: TRESK, sensory neuron, pain, touch, somatosensory

OPEN ACCESS

Edited by:
Felix Viana, Institute of Neurosciences of Alicante (IN), Spain

Reviewed by:
Johannes Oberwinkler, University of Marburg, Germany
Guillaume Eric Sandoz, INSERM U1091 Institut de Biologie de Valrose, France

****Correspondence:***
Greg A. Weir
gregory.weir@glasgow.ac.uk
M. Zameel Cader
zameel.cader@ndcn.ox.ac.uk

†These authors have contributed equally to this work

Received: *18 February 2019*
Accepted: *19 June 2019*
Published: *17 July 2019*

Citation:
Weir GA, Pettingill P, Wu Y, Duggal G, Ilie A-S, Akerman CJ and Cader MZ (2019) The Role of TRESK in Discrete Sensory Neuron Populations and Somatosensory Processing. Front. Mol. Neurosci. 12:170. doi: 10.3389/fnmol.2019.00170

INTRODUCTION

Two-pore domain K^+ (K_{2P}) channels are the molecular mediators of K^+ leak, which is essential for proper neuronal function. The conductance associated with K_{2P} activity stabilizes the resting membrane potential and attenuates depolarizing stimuli. As such, K_{2P} channels are becoming increasingly recognized as critical gatekeepers of neuronal excitability; important in controlling the initiation and form of the action potential (Enyedi and Czirják, 2010). Once considered passive ion conductors, K_{2P} channels are now known to be highly dynamic and regulated by a variety of factors, leading to an appreciation of their involvement in a range of physiological and pathological processes of the nervous system (Honoré, 2007; Plant, 2012; Steinberg et al., 2015).

TWIK-related spinal cord K^+ channel (TRESK) is a K_{2P} channel with a prominent role in pain pathways. While expression data is somewhat conflicted, it is consistently reported that TRESK is highly expressed in sensory ganglia and that loss of channel activity results in enhanced sensory neuron excitability and increased activation of *in vivo* pain pathways (Dobler et al., 2007; Yoo et al., 2009; Tulleuda et al., 2011). TRESK expression is down-regulated following traumatic nerve injury and conversely, viral overexpression can ameliorate injury-induced pain hypersensitivity (Tulleuda et al., 2011; Zhou et al., 2013). Pharmacological inhibition of channel activity induces spontaneous pain behaviors in rodents (Tulleuda et al., 2011). There is also genetic evidence for a

role of TRESK in human pain. A dominant negative frameshift mutation in *KCNK18*, the gene that encodes TRESK, was found to segregate in a pedigree of patients with typical migraine with aura (MA; Lafrenière et al., 2010). Activation of trigeminal nociceptors innervating the dural meninges likely underlies the headache phase of migraine (Weir and Cader, 2011), offering a plausible locus of action of the mutation due to the enrichment of TRESK in these afferents (Lafrenière et al., 2010). Such data is leading to increased efforts to target channel activity as an analgesic strategy (Wright et al., 2013; Bruner et al., 2014; Sehgal et al., 2014; Mathie and Veale, 2015).

A previous study characterizing functional TRESK knockout mice reported that channel activity accounts for 20% of the background K^+ leak and limits the excitability of dorsal root ganglion (DRG) neurons (Dobler et al., 2007). A second TRESK knockout mouse has been shown to have a 20% increase in sensitivity to noxious thermal stimuli, as well as an enhanced susceptibility to volatile anesthetics (Chae et al., 2010). The relatively small effect sizes in these studies contrast with the fact that TRESK is the most abundant K_{2P} channel in sensory neurons (Dobler et al., 2007) and the aforementioned preclinical and genetic data implicating a substantive role in pain signaling. Sensory neurons are highly heterogeneous in their transcriptomes and perform distinct roles in sensory detection and processing (Cavanaugh et al., 2009; Usoskin et al., 2015). We do not yet have a clear understanding of which sensory neuron populations express TRESK. Furthermore, previous studies of mice with genetic ablation of TRESK have not evaluated function across the different neuronal populations, and have restricted behavioral analysis to noxious thermal sensitivity, but not other sensory modalities. In particular, no efforts have been made to assess TRESK KO mice for phenotypes that mirror the sensory dysfunctions common to migraineurs.

Given the clinical potential of therapies targeting TRESK, there is a need to better characterize the channels presence and role in different classes of sensory neurons. Here, we have followed up on detailed expression analysis of the sensory ganglia to define the consequence of TRESK ablation to select sensory neuron populations and the consequence of specific sensorimotor and nociceptive functions. We defined that TRESK is selectively expressed in sub-populations of nociceptors and low threshold D-hair afferents. Recordings from trigeminal ganglion (TG) neurons from TRESK knockout (TRESK [KO]) mice indicated enhanced neuronal excitability and an increased propensity to sensitize under inflammatory challenge. Finally, using behavioral studies, we found that TRESK [KO] mice display modality-specific deficits in tests of sensory function. Collectively, these results demonstrate a previously unappreciated specificity to the role of TRESK in somatosensory processing.

MATERIALS AND METHODS

Animals

Mice were housed at the University of Oxford in holding rooms on a 12/12-h light/dark cycle (lights on at 07:00 h and off at 19:00 h) in single-sex groups of 2–6 with *ad libitum* food and water. Behavioral experiments were performed on mixed-sex naïve adult mice (14- to 20-week-old). This study was carried out in accordance with the principles of the United Kingdom Home Office Animals in Scientific Procedures Act (1986). The protocol was approved by the clinical medicine animal care and ethical review body, University of Oxford. TRESK KO and WT mice used in comparison studies were littermates. TRESK (GenBank accession number NM332396, Ensembl identification number ENSMUSG40901) knockout mice were obtained from the KOMP repository[1]. The VelociGene targeting system (Valenzuela et al., 2003) ablates *KCNK18* by replacing the majority of the coding region with a LacZ-neomycin cassette. Knockout mice were initially crossed with wild-type C57Bl/6J (Harlan, United Kingdom). Offspring from F5 heterozygous littermates were used in this study.

RNA Isolation and Quantitative Real Time PCR

Mice were sacrificed using a CO_2 chamber and TG was rapidly dissected and processed for RNA by RNeasy Mini Kit (QIAGEN) following the manufacturer's instructions. RNA was reverse transcribed to cDNA by MutiScribe reverse transcriptase (Life Technologies, Carlsbad, CA, USA) following manufacturer's instructions. Five microliter of template cDNA (20 ng/μl) was used for each 20 μl PCR reaction. Reaction utilized SYBER Green chemistry (Applied Biosystems, Foster City, CA, USA) and a StepOne Plus real-time PCR (RT-PCR) machine (Applied Biosystems, Foster City, CA, USA). Primers used in this study were: KCNK18 Fwd: 5′ CTCTCTTCTCCGCTGTCGAG 3′, KCNK18 Rev: 5′ AAGAGAGCGCTCAGGAAGG 3′, RPL19 Fwd: 5′ AGCCTGTGACTGTCCATTCC 3′, RPL19 Rev: 5′ GGCAGTACCCTTCCTCTTCC 3′. Relative expression of target genes was calculated using the comparative Ct (ΔΔCt) method.

In situ Hybridization (ISH) and Immunohistochemistry

For tissue collection, animals were deeply anesthetized with pentobarbital and perfused with ice-cold 0.9% NaCl solution through the vascular system. TG were collected, post-fixed for 1–2 h in 4% paraformaldehyde (PFA) and stored in 30% sucrose for a minimum of 48 h before being embedded and sectioned by a cryostat (15 μm thick sections). *In situ* hybridization (ISH) was performed using the RNAScope 2.5 RED chromogenic assay kit, following the manufacturer's instructions (Advanced Cell Diagnostics). Briefly, sectioned TG tissue was re-hydrated in PBS at RT followed by treatment with hydrogen peroxide at RT and a subsequent protease treatment in a hybridization oven at 40°C. Slides were then incubated with *KCNK18* mRNA probes (Advanced Cell Diagnostics) at 40°C for 2 h. Slides were then subjected to six rounds of amplification before the signal was developed by reaction with fast red. Samples were incubated at room temperature for 1 h in blocking solution (PBS + 0.3% Triton™ X-100 + 10% normal goat serum), before overnight

[1]www.komp.org

incubation with primary antibody at 4°C. Antibodies used in this study were as follows: NeuN (1:500, rabbit, ab177487, Abcam), NF200 (1:1,000, chicken, ab4680, Abcam), CGRP (1:1,000, rabbit, T-4032.0050, Peninsula Laboratories, San Carlos, CA, USA) IB4 (1:50, streptavidin conjugated, L2140, Sigma-Aldrich), parvalbumin (1:200, guinea pig, AF1000, Frontier Institute), TrkB (1:200, goat, R & D Systems, AF1494), TH (1:100, sheep, Millipore, AB1542), calbindin (1:200, rabbit, Swant, CB38) and TrkC (1:200, goat, R & D Systems, AF1404). Samples were then incubated with a corresponding fluorophore-conjugated secondary antibodies (1:1,000, Alexa Fluor® 488), diluted in blocking solution for 2 h at RT. Samples were mounted and viewed by a Zeiss LSM-700 confocal microscope and ZEN software. Image analysis was performed using ImageJ (NIH). For image quantification, data were averaged from at least three sections per tissue and sampled from at least three animals per group. Only neurons with a clear nucleus were included in the analysis of TG cell size distribution. The intensity of red signal for each neuronal soma, manually defined as being positive for the sub-population marker, was measured. On each sample, background red signal was calculated by averaging the signal from three randomly selected regions that did not include neuronal somas. A neuron was defined as positive for TRESK expression if red signal intensity was >3 fold higher than mean background value.

TG Dissociation

Mouse TG neuron cultures were prepared as outlined (Weir et al., 2017). Adult mice of either gender (4–12 weeks) were sacrificed and TG rapidly excised into ice-cold HBSS without Ca^{2+}/Mg^{2+}. Ganglia were diced into small pieces and incubated in Papain (20 U/ml—Worthington Biochemicals) solution for 20 min at 37°C. Further enzymatic dissociation involved a second 20 min incubation in Dispase type II/Collagenase solution (Worthington Biochemicals). Cells were washed to remove the residual enzyme and mechanically dissociated through a fire-polished glass pipette. Cells were plated onto laminin/poly-D lysine treated coverslips in Neurobasal media supplemented with 2% (v/v) B27, 1% (v/v) P/S (ThermoFisher), 50 ng/ml mouse NGF (Preprotech) and 10 ng/ml GDNF (Preprotech). Cells were used for recordings 24–72 h after plating.

CGRP Release ELISA

Primary TG neurons from WT (n = 3) and TRESK-KO mice (n = 3) were plated in technical duplicates in a 24-well plate format as above. Neurons were stimulated for 30 min with 50 mM KCl and the media was collected, centrifuged at 200 g for 5 min and supernatants were frozen at −80°C. Basal media was collected prior to KCl-stimulation from each well to serve as a baseline. CGRP ELISA was conducted using Rat CGRP Enzyme Immunoassay Kit as per manufacturer's instruction (Bioquote). Plates were read on a Wallac Victor 1420 Multilabel counter at 405 nm for 0.1 s and data was analyzed on GraphPad Prism 7 software.

Electrophysiology

Patch-clamp experiments were performed in whole-cell configuration at room temperature using an Axopatch 200D amplifier controlled by pClamp 10 software (Molecular Devices). Patch pipettes had resistances between 2 MΩ and 4 MΩ. Extracellular solution contained (in mM): 140 NaCl, 4.7 KCl, 2.5 $CaCl_2$, 1.2 $MgCl_2$, 10 HEPES and 10 glucose; pH was adjusted to 7.4 with NaOH. The pipette was filled with a solution containing (in mM): 130 KCl, 1 $MgCl_2$, 5 MgATP, 10 HEPES and 0.5 EGTA; pH was adjusted to 7.3 with KOH. The osmolarity of all solutions was maintained at 315 mOsm/L for extracellular solution and 305 mOsm/L for intracellular solutions. Cell capacitance and series resistance were constantly monitored throughout the recording. Data were analyzed with Clampfit 10 (Molecular Devices). To assess IB4 binding, cells were incubated with 10 μg/ml Fluorescein labeled isolectin B4 (Vector Laboratories) for 30 min prior to recording. Such labeling has previously been shown to not alter electrophysiological properties of small diameter DRG neurons (Stucky and Lewin, 1999).

Current Clamp

Two minutes after establishing whole-cell access baseline biophysical properties such as cell capacitance, resting membrane resistance and input resistance were measured. R_{input} was calculated by measuring the membrane potential change induced by hyperpolarizing current injection from 20 pA to 100 pA. R_{input} and all evoked firing protocols were performed from a holding potential of −60 mV. For analysis of rheobase, short (50 ms) injections of depolarizing current were increased incrementally (Δ10 pA) until an action potential was fired. To assess repetitive firing, response to prolonged (500 ms) depolarizing current injection (25–350 pA) were monitored. Spontaneous firing was recorded in bridge mode while zero current was inputted. For sensitization experiments inflammatory soup (IS) contained; 50 nM bradykinin, 500 nM PGE_2, 2 μM ATP, 500 nM noradrenaline and 1 μM histamine (Sigma Aldrich).

Calcium Imaging

Cell media was supplemented with 2 μM Fura-2 AM and 80 μM pluronic acid (ThermoFisher Scientific) for 1 h at 37°C, before being transferred to the recording solution, which contained (in mM): 145 NaCl, 5 KCl, 10 HEPES, 10 glucose, 2 $CaCl_2$ and 1 $MgCl_2$, pH was adjusted to 7.4. A 10× objective, dichroic LP 409 mirror and BP 510/90 emitter filter were used for all imaging. Pairs of images using excitation filters BP 340/30 and BP 387/15, respectively, were captured every 2 s. Ratiometric 340/380 calculation was performed with a background subtraction. $IB4^+$ TG were labeled as above and identified using a BP 480/30 excitation filter, dichroic LP 505 mirror and BP 535/40 emission filter. Recording solution was perfused with time-locked addition of IS/50 mM KCl by a gravity-driven application system with remotely controlled pinch valves. Cells exhibiting a Ca^{2+} transient >0.2 ΔF/F directly following treatment were defined as having responded.

Behavioral Protocols

All behavioral studies were performed by an experimenter blinded to genotype and at consistent time of day. Prior to testing, mice were acclimatized to the testing equipment and values

were obtained by averaging data from two to three sessions for each test.

Locomotor Function

Balance and coordination were examined *via* the locomotor test. Mice were placed on the rotarod (#7650, Ugo Basile) from 2 to 40 rpm over a period of 300 s and the speed at which the mouse fell was recorded.

Non-anxiogenic Open Field

The open field consists of a dark arena (dimensions height × width, 50 × 30 cm) divided into 10 cm squares. Mice were placed into the arena for 3 min and the number of squares entered, the number of rears and the latency to rear recorded.

Von Frey

Static mechanical thresholds in freely-moving awake animals were examined *via* von Frey hair application (0.008–1 g; Touch Test; Stoelting) to the plantar surface of the hindpaw using the "up–down" method (Chaplan et al., 1994). Before testing, mice were randomly assigned into individual Plexiglas cubicles (8 × 5 × 10 cm) for 1 h on an elevated wire mesh floor to enable access to the paw surface. Calibrated von Frey hairs were applied to the left and right hind paws, starting with the 0.6 g filament, until the fiber bowed. A positive withdrawal response is followed by a lower force hair and vice versa for a negative withdrawal response until a change in behavior occurs. Using this up–down sequence, four subsequent hairs were assessed and the 50% paw-withdrawal threshold (PWT) was calculated as described by Dixon (1980). Data presented are from both left and right hind paws averaged together as no laterality effects were observed.

Hargreaves

Thermal thresholds in freely-moving awake mice were assessed with the Hargreaves method using the plantar test (37370, UgoBasile). Before testing, mice were assigned to testing cubicles at random and habituated to the apparatus for 1 h in individual cubicles (8 × 5 × 10 cm) placed on a glass plate. An infrared light source was applied to the plantar surface of hind-paws through the glass plate. Withdrawal reflexes were recorded from both left and right-paws, on three occasions, leaving at least 2 min between stimuli.

Hot Plate

Noxious-thermal thresholds of the hind-paws were examined *via* the hot plate test using an incremental hot/cold plate (35150, UgoBasile) set at a temperature of 53°C ± 0.2°C. Mice were placed in the center of the hot plate in a 10 cm diameter testing box; licking, jumping or stamping reflex responses were recorded. A maximum latency of 20 s was permitted to prevent tissue damage.

Photophobia

Mice were individually tested in a light/dark box (Crawley, 1981), which consisted of a dark enclosed compartment with a removable lid (15 × 20 × 20 cm, 0 lux) and a brightly-lit white-compartment (30 × 20 × 20 cm, 900 lux). A small opening (3 × 3 cm) connects the two compartments allowing animals to move freely. Prior to testing mice were acclimatized for at least 30 min in their home cages to the testing room. Each mouse was gently placed into the center of the light compartment, facing away from the opening. Behaviors were scored for 5 min, including the latency to cross into the dark compartment (defined by all four paws in that area), time spent in each compartment and the number of transitions through compartments were scored. The light/dark box was thoroughly cleaned with 95% EtOH between animals.

Cotton Swab

Mice were housed in plexiglass cubicles on elevated wire-mesh floor as per the Von frey test. A "puffed out" cotton swab was stroked over the plantar surface of the hindpaw at a consistent speed (∼0.5 s) five times. The number of withdrawals in response to five strokes per paw were recorded and averaged between the two paws.

Back Tape Test

A 3 cm piece of sticky tape (Starlab autoclave tape, 25 mm × 50 mm) was placed firmly to the back of each mouse. The number of bouts (scratching and licking) directed at the tape was recorded over a 5 min period while the mouse was housed in a plexiglass cubile.

Statistics

The data are expressed as mean ± standard error of the mean (SEM). In cases where data did not fit the conditions of parametric testing (homogeneity of variance and normality of sampling), nonparametric tests were used. Statistical analysis was performed using GraphPad PRISM and the significance level was set at $p < 0.05$.

RESULTS

TRESK Is Selectively Expressed in Discrete Populations Within the Trigeminal Ganglion

In human and rodent tissue, TRESK is highly enriched in sensory ganglia of the DRG and TG (Dobler et al., 2007; Lafrenière et al., 2010). Previous studies report that >90% of sensory neurons in the DRG express TRESK (Dobler et al., 2007; Yoo et al., 2009), however single-cell RNA sequencing data challenges the assertion that expression is as widespread (Usoskin et al., 2015). We used RNA ISH to define TRESK expression in the TG and found expression to be highly heterogeneous across neurons. TRESK mRNA was present in 51.14 ± 4.56% of all neurons. Size-frequency analysis revealed that TRESK was present in neurons of all soma diameters (**Figure 1A**). We combined ISH with immunohistochemistry to examine expression across molecularly defined sub-populations. Within small diameter neurons (≤25 μm) that likely represent unmyelinated C-fibers, TRESK was present in 72.43 ± 1.25% of neurons that bound the lectin IB_4 (non-peptidergic nociceptors), but only 29.43 ± 8.50% of calcitonin gene related peptide (CGRP) positive neurons (peptidergic nociceptors; Nagy and Hunt, 1982;

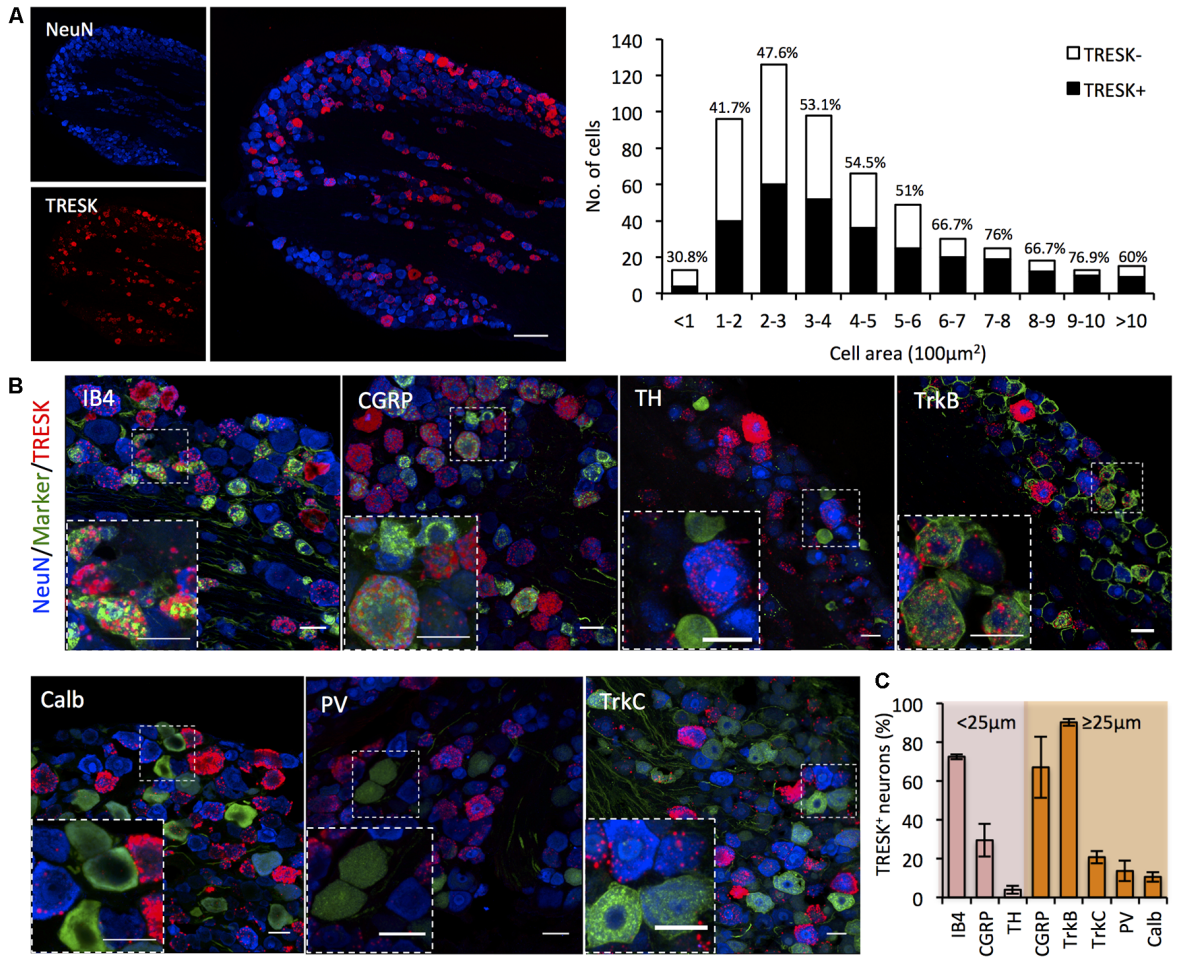

FIGURE 1 | *KCNK18* mRNA in mouse trigeminal ganglion (TG). *In situ* hybridization for *KCNK18* mRNA combined with immunocytochemistry for molecular markers of canonical sensory neuron populations. **(A)** *Left*, Overview image of *KCNK18* mRNA (red) in TG stained for NeuN (blue). Scale bar represents 100 μm. *Right*, size-frequency distribution of *KCNK18* positive neurons. Expression was defined as any neuron with signal >3-fold mean background. Data pooled from three animals and from at least three sections per animals (total of 521 neurons). **(B)** Representative images of *KCNK18* mRNA (red) with population markers (green) and all neurons marked by NeuN (blue). Insets show magnified view of selected region. All scale bars represent 25 μm. **(C)** Quantification of *KCNK18* mRNA expression in different populations. Neurons are categorized as small diameter (≤25 μm) or medium/large (>25 μm). Data represents mean ± standard error of the mean (SEM) from $n = 3$ animals and at least three section per marker and animal. PV, Parvalbumin, Calb, calbindin; TH, tyrosine hydroxylase; and CGRP, calcitonin gene related peptide.

Silverman and Kruger, 1990). Expression was virtually absent in tyrosine hydroxylase (TH) positive, C-low threshold mechanoreceptors (3.98 ± 2.03%; Li et al., 2011). Within medium/large diameter neurons (≥25 μm), we observed expression in a large proportion of CGRP$^+$ neurons (66.98 ± 15.70%) and neurons highly expressing TRKB$^+$ (90.15 ± 1.74%), representing a subset of Aδ-nociceptors and D-hairs respectively (Lawson et al., 2002; Li et al., 2011). In contrast, we saw minimal expression in Calbindin$^+$ (10.62 ± 2.51%) or TRKC$^+$ (20.74 ± 3.27%) neurons, representing populations of Aβ-low threshold mechanoreceptors (Usoskin et al., 2015). Few proprioceptors, classified as large-diameter neurons expressing parvalbumin, expressed TRESK (13.62 ± 5.25%; **Figures 1B,C**). In sum, these results demonstrate the heterogeneity of TRESK expression across different TG populations and highlight the need to study protein function in specific sub-populations.

TRESK Selectively Modulates Non-peptidergic Small Diameter Nociceptor Excitability

When sensory neurons from TRESK knockout mice have been assessed non-selectively, the channel has been shown to act as a molecular brake on excitability (Dobler et al., 2007). Given our expression data, we sought to explore whether global loss of TRESK activity had population-specific effects on excitability. The majority of the coding region of *KCNK18*, the gene that encodes TRESK, was targeted for deletion (**Figure 2A**), resulting in TRESK KO animals with no TRESK transcripts (**Figure 2B**).

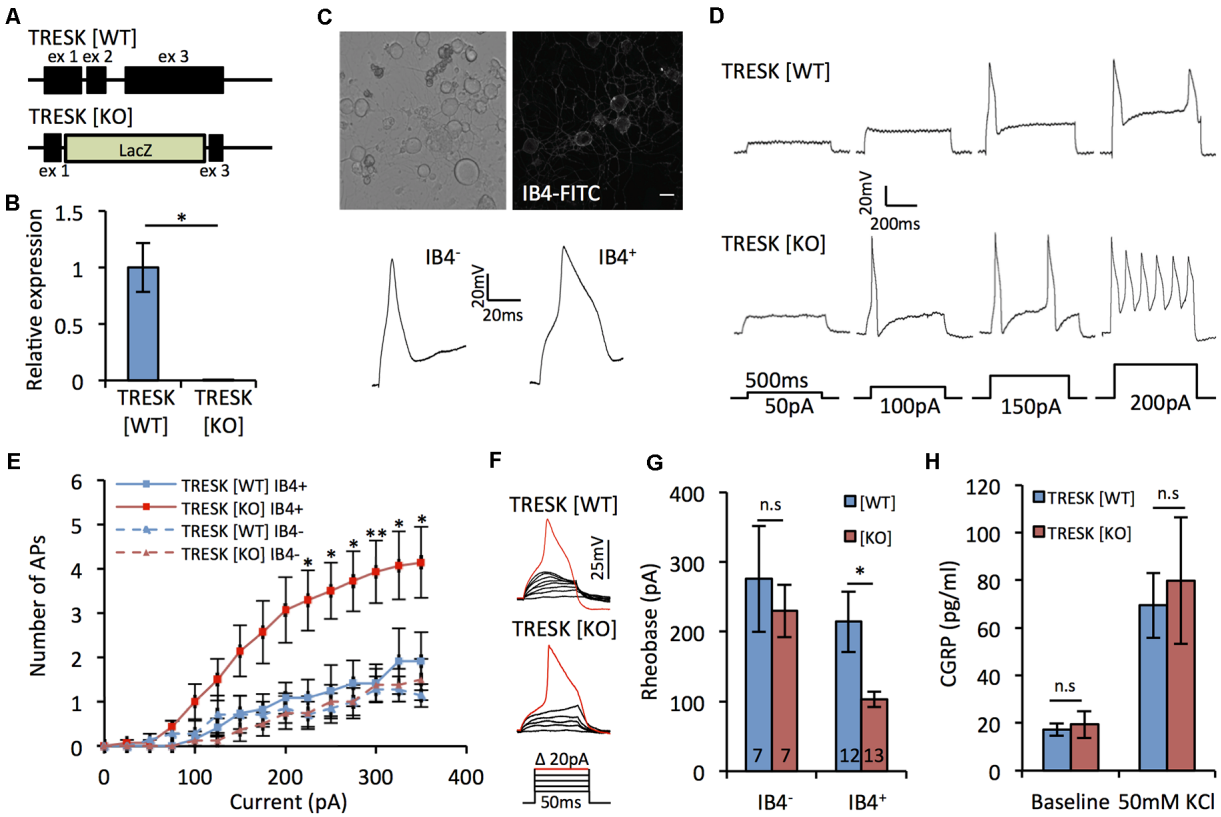

FIGURE 2 | TRESK selectively modulates non-peptidergic C-fiber excitability. **(A)** Targeted ablation of *KCNK18* gene. Allele describes neomycin/lacZ cassette, which replaces 3′ of exon 1, all of exon 2 and 5′ exon 3. **(B)** Real time PCR (RT-PCR) for TRESK expression in dorsal root ganglion (DRG) mRNA. Data derived from $n = 3$ animals. $^*p < 0.05$, student's unpaired *t*-test. **(C)** Neurons dissociated 24–48 h previously from TRESK [WT] and TRESK [KO] TG were used for patch clamp recordings. Example image of neurons live stained for IB4-FITC binding and typical action potential waveforms generated from $IB4^+$ and $IB4^-$ neurons. Note the prolonged duration of the action potential of $IB4^+$ neurons. **(D)** Example evoked firing profiles of $IB4^+$ TG neurons of both genotypes in response to prolonged (500 ms) depolarizing steps. **(E)** Quantification of TG neuron firing in response to prolonged (500 ms) suprathreshold current stimulation. $^{**}p < 0.01$, $^*p < 0.05$, RM two-way analysis of variance (ANOVA) with Sidak multiple testing comparing TRESK [KO] $IB4^+$ and TRESK [WT] $IB4^+$ groups. Data represents mean ± SEM from 12 (TRESK [WT] $IB4^+$), 7 (TRESK [WT] $IB4^-$), 13 (TRESK [KO] $IB4^+$) and 7 (TRESK [KO] $IB4^-$) neurons. Recordings were pooled from TG obtained from two mice (per genotype) cultured independently on two separate days. **(F)** Example evoked firing profiles of $IB4^+$ TG neurons of both genotypes in response to short (50 ms) depolarizing steps. **(G)** Rheobase of TG neurons, defined as the minimum current of 50 ms duration required to generate an action potential. $^*p < 0.05$, Kruskal-Wallis followed by Dunn's multiple comparisons test. Same sample sizes as **(E)**, **(H)** CGRP released into culture media at baseline and during activation with 50 mM KCl containing media. Data derived from $n = 3$ animals, each with technical triplicates. n.s, $p > 0.05$. One-way ANOVA comparing genotypes for each condition.

As a population in which TRESK is abundantly expressed, we performed recordings of small-diameter TG neurons live-stained for IB_4 binding, which demarks non-peptidergic nociceptors. Small neurons that do not bind IB4 will comprise peptidergic nociceptors and C-low threshold mechanoreceptors, two populations in which our *in situ* data would suggest that TRESK expression is minimal. IB_4^+ neurons exhibited broadened action potentials (**Figure 2C**), consistent with high levels of $Na_V1.9$ (Fjell et al., 1999; Stucky and Lewin, 1999). Excitability, both in terms of the number of action potentials fired in response to suprathreshold stimuli and the current threshold for initial action potential generation, was enhanced in TRESK [KO] IB_4^+ neurons, but not IB_4^- TRESK [KO] neurons, in comparison to TRESK [WT] (**Figures 2D–G**). We observed no difference between the genotypes for resting membrane potential ([WT] −47.2 ± 2.3 mV vs. [KO] −48.1 ± 1.8 mV; $p > 0.05$ Mann-Whitney *U* test) or input resistance ([WT] 245.8 ± 28.5 MΩ vs. [KO] 275.1 ± 24.8 MΩ; $p > 0.05$ Student's *t*-test). Further supporting a limited role in peptidergic neurons, there was no difference in release of CGRP from TRESK [KO] cultures during basal or stimulated (50 mM KCl) conditions (**Figure 2H**). These results align with the expression data and suggest that within small diameter nociceptors, TRESK selectively operates in non-peptidergic neurons to provide substantial inhibitory tone.

Lack of TRESK Exaggerates Inflammatory Sensitization

TRESK has been demonstrated to be both positively and negatively regulated by inflammatory factors (Callejo et al., 2013; Kollert et al., 2015). To address the role TRESK plays in nociceptor sensitization, we acutely applied

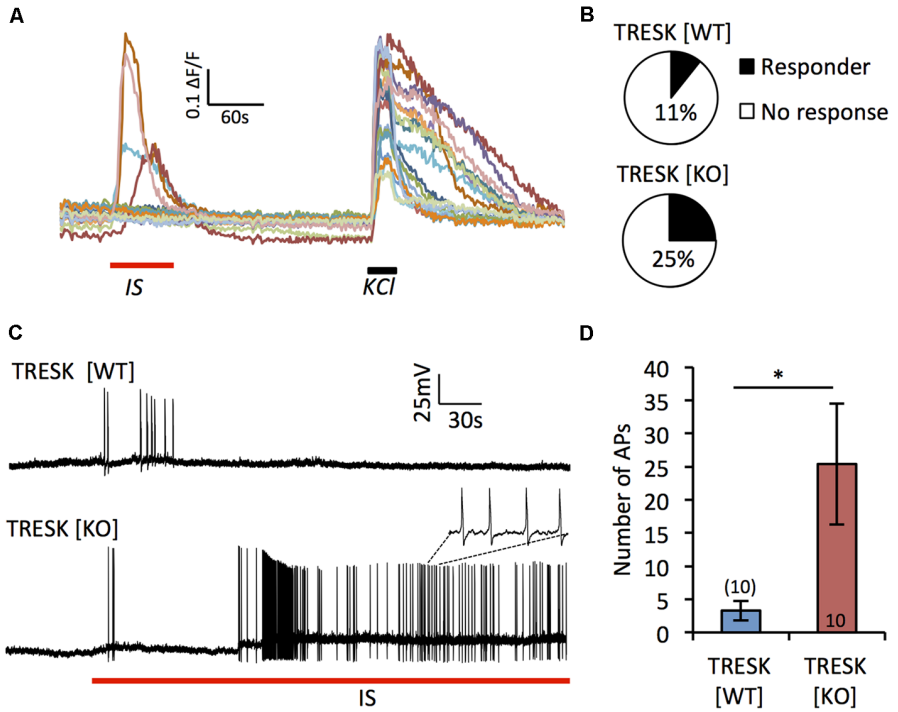

FIGURE 3 | Loss of TRESK increases activation in response to inflammatory stimulation. **(A)** Representative traces of Ca^{2+} signals in TRESK [KO] TG neurons exposed to inflammatory soup (IS; 1 min) followed by a 5 min wash out and then 50 mM KCl to depolarize all neurons (30 s). **(B)** Proportion of $IB4^{+}$ TG neurons from each genotype responding to IS with a Ca^{2+} peak >0.2 ΔF/F (TRESK [WT] $n = 45$, TRESK [KO] $n = 97$ cells). **(C)** Patch clamp recordings of TG neuron firing in response to acute (5 min) exposure to IS. **(D)** Quantification of action potential discharge during the 5 min of inflammatory challenge. Data represents mean ± SEM from 10 recordings per group. Recordings were pooled from TG obtained from three mice (per genotype), cultured independently on three separate days. *$p < 0.05$, student's unpaired *t*-test.

IS (bradykinin, PGE_2, noradrenaline, ATP and histamine) to TG neurons (**Figure 3A**). In response to IS, a greater proportion of TRESK [KO] $IB4^{+}$ nociceptors demonstrated a Ca^{2+} influx compared to TRESK [WT] $IB4^{+}$ neurons (**Figure 3B**; TRESK [WT] 4/45 cells vs. TRESK [KO] 30/97 cells, $p = 0.0053$ Fischer's exact *t*-test). Paired-patch clamp recordings confirmed the greater propensity for TRESK [KO] neurons to activate when challenged with IS. In response to acute IS treatment, $IB4^{+}$ TRESK [KO] neurons fired >7-fold more action potentials than TRESK [WT] neurons (**Figures 3C,D**; TRESK [WT] 3.3 ± 0.1.48 vs. TRESK [KO] 25.4 ± 9.16 action potentials, $p = 0.039$ student's unpaired *t*-test). These results indicate that TRESK activity reduces *in vitro* inflammatory sensitization of nociceptors.

Sensorimotor Testing of TRESK Knockout Mice

Previous assessment of mice lacking TRESK has been restricted to testing thermal nociception and has not assessed mechanical, or non-nociceptive sensitivity (Chae et al., 2010). We examined the behavior of TRESK [KO] mice in response to a range of sensory challenges. TRESK [KO] mice had normal growth and showed no structural abnormalities; body weight was normal compared to TRESK [WT] littermates ([♂ WT] 25.81 ± 0.4 g vs. [♂ KO] 25.67 ± 0.6 g and [♀ WT] 18.85 ± 0.5 g vs. [♀ KO] 18.93 ± 0.8 g; $p > 0.05$ unpaired student's *t*-test, $n = 6$, 8–10 week old littermate mice per group). TRESK [KO] mice exhibited normal punctate mechanical sensitivity as assessed by Von Frey filaments (**Figure 4A**). Plantar thermal sensitivity was normal when measured by Hargreaves (**Figure 4B**), but TRESK [KO] mice demonstrated a 14% decrease in time to respond on the nociceptive 53°C hot-plate test (**Figure 4C**, [WT] 7.7 ± 0.7 s vs. [KO] 6.6 ± 0.7 s; $p = 0.039$, Mann-Whitney *U* test). Genotype had no effect on motor performance or locomotor activity, as assayed by the Rotarod and Open field tests respectively (**Figures 4D,E**).

Given the enriched expression of TRESK in the D-hair population, which are low-threshold mechanoreceptors that activate to extremely light touch, we tested whether TRESK [KO] mice exhibited heightened sensitivity during a light touch behavioral assay (Garrison et al., 2012). TRESK [KO] mice were more likely to respond to light brushing of the hindpaw with a cotton swab (**Figure 4F**, [WT] 26.7 ± 4.1% responding vs. [KO] 57.8 ± 5.2%; $p = 0.002$ Mann-Whitney *U* test). In a test of dynamic mechanical sensitivity, TRESK [KO] mice exhibited an exaggerated response to adhesive tape placed on the back (Ranade et al., 2014; **Figure 4G**, [WT] 4.2 ± 0.7 bouts vs. [KO] 10.8 ± 0.8; $p = 0.0004$ Mann-Whitney *U* test). These results illustrate that TRESK expression regulates

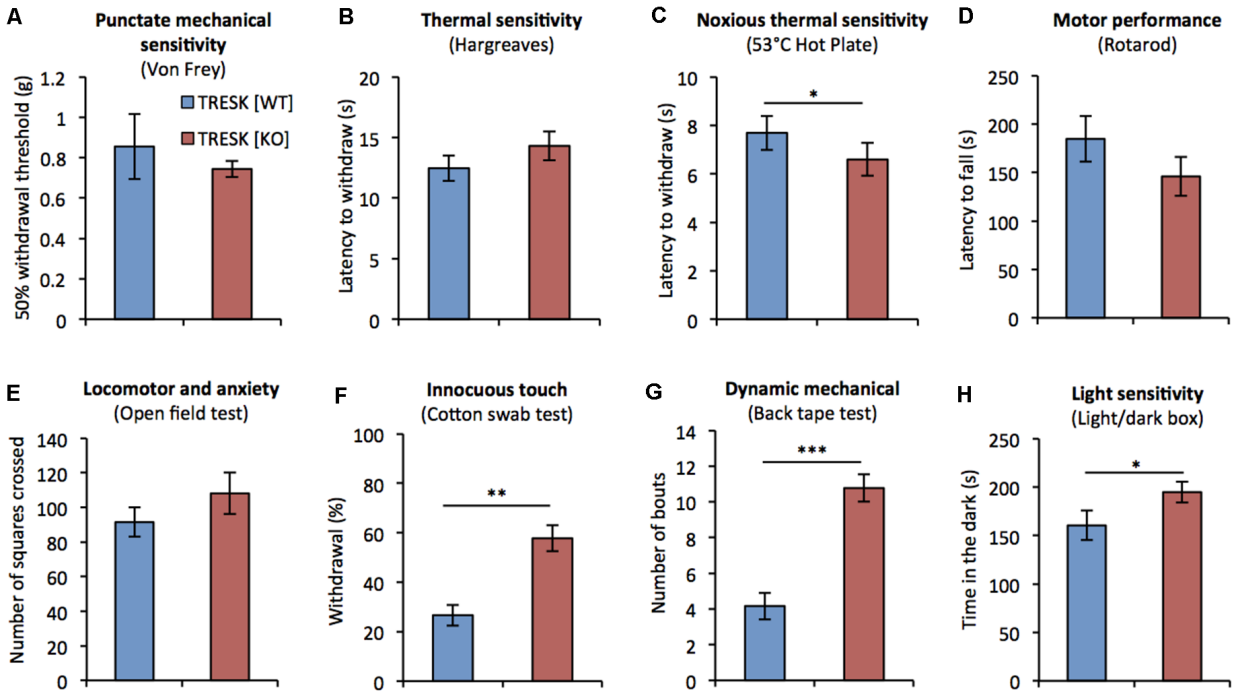

FIGURE 4 | TRESK [KO] mice exhibit selective deficits in sensory behavior. Sensorimotor testing of adult TRESK [KO] mice (red bars) and TRESK [WT] littermate controls (blue bars). **(A)** Punctate mechanical sensitivity as assessed by withdrawal to Von Frey filaments of different force. Data represents mean ± SEM from 16 TRESK [WT] and 11 TRESK [KO] animals. **(B)** Latency to withdraw hindpaw to radiant thermal stimuli (Hargreaves test). Cut-off was 30 s. **(C)** 53°C hot plate test of noxious thermal sensitivity. Cut-off was 20 s. **(D)** Latency of mice to fall on a rotating beam (rotarod test). **(E)** Number of squares crossed by mice in the open field test of locomotion and anxiety. **(F)** Number of scratches/bites in response to 5 cm sticky tape applied to the back of mice over a 5 min period. Data represents mean ± SEM from six TRESK [WT] and nine TRESK [KO] animals. **(G)** Number of withdrawals to five gentle brushes of the hindpaw with a "fluffed" cotton bud. Data represents mean ± SEM from six TRESK [WT] and nine TRESK [KO] animals. **(H)** Time spent in the dark during 5 min of testing in the light/dark box test. Unless otherwise specified, data represent mean ± SEM from 15 (TRESK [WT]) and 14 (TRESK [KO]) animals and statistical comparisons between genotypes were performed by a Mann-Whitney-*U* test. ***$p < 0.001$, **$p < 0.01$, *$p < 0.05$.

behavioral responses to extremely light static, and dynamic mechanical stimuli.

Migraine patients have higher sensitivity to light than non-migraneurs, even during migraine-free periods (Drummond, 1986). We sought to evaluate photophobia in TRESK [KO] mice under basal conditions. TRESK [KO] mice spent significantly more time compared to TRESK [WT] mice (**Figure 4H**, [WT] 160 ± 15.37 s vs. [KO] 194.8 ± 10.85 s; $p = 0.0412$ unpaired Student's *t*-test) in the dark enclosed-compartment of the light/dark box, suggestive of heightened light sensitivity.

DISCUSSION

The enriched expression of TRESK in sensory ganglia and the role of TRESK in moderating neuronal excitability suggest an important function in nociceptive transmission. In support, preclinical injury models and human genetic studies suggest that loss of TRESK activity can contribute to pathological pain (Lafrenière et al., 2010; Tulleuda et al., 2011; Zhou et al., 2013). We have performed a detailed analysis of TRESK expression within sensory ganglia and define striking heterogeneity across sub-populations. In populations in which TRESK is enriched, genetic ablation leads to marked hyperexcitability, which is exacerbated by *in vitro* nociceptor sensitization following inflammatory challenge. At the behavioral level, mice lacking TRESK exhibit very specific sensory deficits, which correlate well with the known function of populations in which TRESK is enriched.

Reports of TRESK expression are conflicted, but consistent through all studies is high expression in sensory ganglia (Sano et al., 2003; Dobler et al., 2007; Yoo et al., 2009; Lafrenière et al., 2010). Sensory neurons are highly heterogeneous and distinct sub-populations likely perform specialized roles in somatosensation. Information on expression across sub-populations is therefore very important to understand gene function. Our data contradict previous assertions that TRESK is homogenously expressed in the sensory ganglia (Dobler et al., 2007; Yoo et al., 2009), and instead demonstrates that expression is restricted to select sub-populations. We believe that the contradictory results may be a result of refined ISH technologies used in this study, which allow for more sensitive and specific detection of mRNA expression and are being increasingly exploited in sensory biology (Wang et al., 2012; Dawes et al., 2018; Dembo et al., 2018). Our data is highly congruous with recent single-cell RNA-sequencing studies which describe TRESK to be enriched primarily in non-peptidergic

nociceptors (NP1 and NP2), but also present in Aδ-nociceptors (PEP2) and D-hair afferents (NF1) and to a lesser extent in C-LTMRs (TH; which we did not observe; Usoskin et al., 2015; Zeisel et al., 2018). We cannot rule out the possibility that by setting a specific threshold of expression that we are finding false negatives. However, we observed no functional effect of genetic ablation in populations that we defined to lack TRESK expression, suggesting that even if very low levels of TRESK is present in these populations, it does not have a functional role.

TRESK has recently been demonstrated to heterodimerize with TREK1/2 channels in heterologous expression systems (Royal et al., 2019). In elegant studies, the same authors describe a mechanism by which the migraine-associated frameshift mutation (F139WfsX24) leads to production of a novel secondary protein product that selectively inhibits TREK1/2 channels and proposed that this effect of the mutation underlies migraine pathogenicity. Intriguingly, the study found that overexpression of a mutant protein product with strong dominant negative effects on wildtype TRESK channels had no effect on TG excitability. This is in contrast to previous studies and our own, which describe large changes in sensory neuron excitability upon loss of TRESK current (Dobler et al., 2007). Our results suggest that the negative findings described by the authors could in part be explained by recording from many neurons lacking endogeneous TRESK. Single-cell data suggests a degree of overlap of TRESK and TREK2 in sub-populations of non-peptidergic neurons (NP2) and Aδ-nociceptors (PEP2), however TREK1 expression shows little overlap (Zeisel et al., 2018). Future studies will be needed to confirm the profile of TREK1/2 co-expression in TRESK$^+$ populations as this may help define primary afferent subtypes important in migraine pathogenesis.

Given the prominent role TRESK plays in dampening neuronal activity, loss of channel function could be expected to enhance hyperexcitability in pathological states. We show that TG neurons lacking TRESK exhibit increased action potential discharge in response to an inflammatory challenge commonly used in experimental models of migraine and pain. Inflammatory factors have been shown to both inhibit and activate TRESK (Callejo et al., 2013; Kollert et al., 2015), and as such it is not clear whether increased neuronal activation is due to a direct modulatory effect of IS on TRESK currents, or whether loss of the inhibitory drive of TRESK activity is simply additive to the excitatory drive of IS treatment. Irrespective of this, our data suggest that TRESK activity plays a role in nociceptor sensitization by inflammation.

TRESK [KO] mice were hypersensitive to noxious thermal stimuli, which is proposed to be encoded by peptidergic afferents (McCoy et al., 2013; Cowie et al., 2018). While we did not observe significant TRESK expression in small diameter peptidergic fibers, we did see high expression in medium/large sized peptidergic neurons. These neurons likely represent Aδ-nociceptors, some of which are capable of responding to noxious thermal stimuli (Koltzenburg et al., 1997). A second population of peptidergic Aδ-nociceptors has been shown recently to respond to high-threshold mechanical stimuli induced by pulling of a single hair (Ghitani et al., 2017). Dysfunction in this population could be linked to the exaggerated response to sticky tape applied to the hairy skin of the back that we observed in TRESK KO mice. Of our sensory behavioral assays, we observed the biggest deficiency in TRESK KO animals when innocuous touch was assessed. We used a cotton swab to assess response to light stroke, an assay which has been shown sensitive to detect dysfunction in light-touch cutaneous afferents (Garrison et al., 2012). D-hair afferents are the most sensitive mechanoreceptors of the skin (Lechner and Lewin, 2013), can be marked by high TrkB expression, and we found to express TRESK abundantly. Mice in which TrkB$^+$ afferents have been ablated are less responsive to cotton swab, implicating this population in our TRESK KO phenotype. Aberrant D-hair afferent transmission has been associated recently with mechanical hypersensitivity following nerve injury (Peng et al., 2017; Dhandapani et al., 2018), which may help explain the link between loss of TRESK and enhanced mechanical hypersensitivity following traumatic nerve injury (Tulleuda et al., 2011; Zhou et al., 2013).

We cannot rule out the possibility that the method of genetic ablation (targeted insertion of a lacZ/neomycin cassette into *KCNK18* locus) disrupts the expression of genes other than *KCNK18* and contributes to the behavioral phenotype documented. However, the *in vitro* and *in vivo* phenotypes we observed are entirely consistent with predicted TRESK function, giving us confidence that they are mediated through the loss of the channel. In KO animals, TRESK is ablated globally rather than in a tissue-specific manner. Therefore, loss of TRESK function in structures other than primary afferents could be expected to influence behavioral phenotypes. TRESK expression has been noted in regions of rat brain and spinal cord (Yoo et al., 2009; Hwang et al., 2015). However, recent single-cell sequencing data profiling the mouse nervous system describes TRESK expression to be restricted to primary afferents and some neurons of the sympathetic nervous system (Zeisel et al., 2018) and to be absent from all neuronal subtypes in the dorsal horn of the spinal cord (Häring et al., 2018). We did not observe obvious signs of cognitive dysfunction in TRESK KO mice and animals performed normally in the Open Field Test. These data, in conjunction with the specific deficits in sensory behavior that we observed, strongly suggest that the phenotypes we describe following TRESK ablation are mediated by primary afferent dysfunction.

Taken together, our data show that contrary to prior assumptions, TRESK is selectively expressed in distinct sensory sub-populations and that it underlies very specific roles in somatosensory processing. TRESK is actively being pursued as a promising therapeutic target, given its important role in sensory neuron excitability. Its influence on non-nociceptive afferents has relevance for drug design. Under basal conditions these afferents code for innocuous light touch. However, in pathological conditions, their altered profile may mediate mechanical hypersensitivity- a prominent symptom of neuropathic pain and migraine. Thus, TRESK is an important mediator of nociceptive transmission and future studies investigating its role in pathological pain states may be fruitful.

DATA AVAILABILITY

All datasets generated for this study are included in the manuscript.

ETHICS STATEMENT

The maintenance and testing of these animals were performed in accordance with the United Kingdom Home Office Animals in Scientific Procedures Act (1986), at a licensed facility within the University of Oxford and following institutional review board approval.

AUTHOR CONTRIBUTIONS

GW, PP and MC: conceptualization. GW, PP, YW, GD, A-SI, CA and MC: methodology, writing—review and editing. GW, PP, YW and GD: investigation. GW: writing—original draft. GW, PP and YW: visualization. MC and CA: supervision and funding acquisition.

FUNDING

The research leading to these results has received funding from LifeArc and the European Research Council (ERC; Grant Agreement 617670).

REFERENCES

Bruner, J. K., Zou, B., Zhang, H., Zhang, Y., Schmidt, K., and Li, M. (2014). Identification of novel small molecule modulators of K_{2P}18.1 two-pore potassium channel. *Eur. J. Pharmacol.* 740, 603–610. doi: 10.1016/j.ejphar.2014.06.021

Callejo, G., Giblin, J. P., and Gasull, X. (2013). Modulation of TRESK background K^+ channel by membrane stretch. *PLoS One* 8:e64471. doi: 10.1371/journal.pone.0064471

Cavanaugh, D. J., Lee, H., Lo, L., Shields, S. D., Zylka, M. J., Basbaum, A. I., et al. (2009). Distinct subsets of unmyelinated primary sensory fibers mediate behavioral responses to noxious thermal and mechanical stimuli. *Proc. Natl. Acad. Sci. U S A* 106, 9075–9080. doi: 10.1073/pnas.0901507106

Chae, Y. J., Zhang, J., Au, P., Sabbadini, M., Xie, G. X., and Yost, C. S. (2010). Discrete change in volatile anesthetic sensitivity in mice with inactivated tandem pore potassium ion channel TRESK. *Anesthesiology* 113, 1326–1337. doi: 10.1097/aln.0b013e3181f90ca5

Chaplan, S. R., Bach, F. W., Pogrel, J. W., Chung, J. M., and Yaksh, T. L. (1994). Quantitative assessment of tactile allodynia in the rat paw. *J. Neurosci. Methods* 53, 55–63.

Crawley, J. N. (1981). Neuropharmacologic specificity of a simple animal model for the behavioral actions of benzodiazepines. *Pharmacol. Biochem. Behav.* 15, 695–699.

Cowie, A. M., Moehring, F., O'Hara, C., and Stucky, C. L. (2018). Optogenetic inhibition of CGRPα sensory neurons reveals their distinct roles in neuropathic and incisional pain. *J. Neurosci.* 38, 5807–5825. doi: 10.1523/JNEUROSCI.3565-17.2018

Dawes, J. M., Weir, G. A., Middleton, S. J., Patel, R., Chisholm, K. I., Pettingill, P., et al. (2018). Immune or genetic-mediated disruption of CASPR2 causes pain hypersensitivity due to enhanced primary afferent excitability. *Neuron* 97, 806.e10–822.e10. doi: 10.1016/j.neuron.2018.01.033

Dembo, T., Braz, J. M., Hamel, K. A., Kuhn, J. A., and Basbaum, A. I. (2018). Primary afferent-derived BDNF contributes minimally to the processing of pain and itch. *eNeuro* 5:ENEURO.0402–18.2018. doi: 10.1523/eneuro.0402-18.2018

Dhandapani, R., Arokiaraj, C. M., Taberner, F. J., Pacifico, P., Raja, S., Nocchi, L., et al. (2018). Control of mechanical pain hypersensitivity in mice through ligand-targeted photoablation of TrkB-positive sensory neurons. *Nat. Commun.* 9:1640. doi: 10.1038/s41467-018-04049-3

Dobler, T., Springauf, A., Tovornik, S., Weber, M., Schmitt, A., Sedlmeier, R., et al. (2007). TRESK two-pore-domain K^+ channels constitute a significant component of background potassium currents in murine dorsal root ganglion neurones. *J. Physiol.* 585, 867–879. doi: 10.1113/jphysiol.2007.145649

Drummond, P. D. (1986). A quantitative assessment of photophobia in migraine and tension headache. *Headache* 26, 465–469. doi: 10.1111/j.1526-4610.1986.hed2609465.x

Dixon, W. J. (1980). Efficient analysis of experimental observations. *Annu. Rev. Pharmacol. Toxicol* 20, 441–462. doi: 10.1146/annurev.pa.20.040180.002301

Enyedi, P., and Czirják, G. (2010). Molecular background of leak K^+ currents: two-pore domain potassium channels. *Physiol. Rev.* 90, 559–605. doi: 10.1152/physrev.00029.2009

Fjell, J., Cummins, T. R., Dib-Hajj, S. D., Fried, K., Black, J. A., and Waxman, S. G. (1999). Differential role of GDNF and NGF in the maintenance of two TTX-resistant sodium channels in adult DRG neurons. *Mol. Brain Res.* 67, 267–282. doi: 10.1016/s0169-328x(99)00070-4

Garrison, S. R., Dietrich, A., and Stucky, C. L. (2012). TRPC1 contributes to light-touch sensation and mechanical responses in low-threshold cutaneous sensory neurons. *J. Neurophysiol.* 107, 913–922. doi: 10.1152/jn.00658.2011

Ghitani, N., Barik, A., Szczot, M., Thompson, J. H., Li, C., Le Pichon, C. E., et al. (2017). Specialized mechanosensory nociceptors mediating rapid responses to hair pull. *Neuron* 95, 944.e4–954.e4. doi: 10.1016/j.neuron.2017.07.024

Häring, M., Zeisel, A., Hochgerner, H., Rinwa, P., Jakobsson, J. E. T., Lönnerberg, P., et al. (2018). Neuronal atlas of the dorsal horn defines its architecture and links sensory input to transcriptional cell types. *Nat. Neurosci.* 21, 869–880. doi: 10.1038/s41593-018-0141-1

Honoré, E. (2007). The neuronal background K_{2P} channels: focus on TREK1. *Nat. Rev. Neurosci.* 8, 251–261. doi: 10.1038/nrn2117

Hwang, H. Y., Zhang, E., Park, S., Chung, W., Lee, S., Kim, D. W., et al. (2015). TWIK-related spinal cord K^+ channel expression is increased in the spinal dorsal horn after spinal nerve ligation. *Yonsei Med. J.* 56, 1307–1315. doi: 10.3349/ymj.2015.56.5.1307

Kollert, S., Dombert, B., Döring, F., and Wischmeyer, E. (2015). Activation of TRESK channels by the inflammatory mediator lysophosphatidic acid balances nociceptive signalling. *Sci. Rep.* 5:12548. doi: 10.1038/srep12548

Koltzenburg, M., Stucky, C. L., and Lewin, G. R. (1997). Receptive properties of mouse sensory neurons innervating hairy skin. *J. Neurophysiol.* 78, 1841–1850. doi: 10.1152/jn.1997.78.4.1841

Lafrenière, R. G., Cader, M. Z., Poulin, J. F., Andres-Enguix, I., Simoneau, M., Gupta, N., et al. (2010). A dominant-negative mutation in the TRESK potassium channel is linked to familial migraine with aura. *Nat. Med.* 16, 1157–1160. doi: 10.1038/nm.2216

Lawson, S. N., Crepps, B., and Perl, E. R. (2002). Calcitonin gene-related peptide immunoreactivity and afferent receptive properties of dorsal root ganglion neurone in guinea-pigs. *J. Physiol.* 540, 989–1002. doi: 10.1113/jphysiol.2001.013086

Lechner, S. G., and Lewin, G. R. (2013). Hairy sensation. *Physiology* 28, 142–150. doi: 10.1152/physiol.00059.2012

Li, L., Rutlin, M., Abraira, V. E., Cassidy, C., Kus, L., Gong, S., et al. (2011). The functional organization of cutaneous low-threshold mechanosensory neurons. *Cell* 147, 1615–1627. doi: 10.1016/j.cell.2011.11.027

Mathie, A., and Veale, E. L. (2015). Two-pore domain potassium channels: potential therapeutic targets for the treatment of pain. *Pflugers Arch.* 467, 931–943. doi: 10.1007/s00424-014-1655-3

McCoy, E. S., Taylor-Blake, B., Street, S. E., Pribisko, A. L., Zheng, J., and Zylka, M. J. (2013). Peptidergic CGRPα primary sensory neurons encode heat and itch and tonically suppress sensitivity to cold. *Neuron* 78, 138–151. doi: 10.1016/j.neuron.2013.01.030

Nagy, J. I., and Hunt, S. P. (1982). Fluoride-resistant acid phosphatase-containing neurones in dorsal root ganglia are separate from those containing substance P or somatostatin. *Neuroscience* 7, 89–97. doi: 10.1016/0306-4522(82)90155-5

Peng, C., Li, L., Zhang, M. D., Bengtsson Gonzales, C., Parisien, M., Belfer, I., et al. (2017). MIR-183 cluster scales mechanical pain sensitivity by regulating basal and neuropathic pain genes. *Science* 356, 1168–1172. doi: 10.1126/science.aam7671

Plant, L. D. (2012). A role for K2P channels in the operation of somatosensory nociceptors. *Front. Mol. Neurosci.* 5:21. doi: 10.3389/fnmol.2012.00021

Ranade, S. S., Woo, S. H., Dubin, A. E., Moshourab, R. A., Wetzel, C., Petrus, M., et al. (2014). Piezo2 is the major transducer of mechanical forces for touch sensation in mice. *Nature* 516, 121–125. doi: 10.1038/nature13980

Royal, P., Andres-Bilbe, A., Ávalos Prado, P., Verkest, C., Wdziekonski, B., Schaub, S., et al. (2019). Migraine-associated TRESK mutations increase neuronal excitability through alternative translation initiation and inhibition of TREK. *Neuron* 101, 232.e6–245.e6. doi: 10.1016/j.neuron.2018.11.039

Sano, Y., Inamura, K., Miyake, A., Mochizuki, S., Kitada, C., Yokoi, H., et al. (2003). A novel two-pore domain K^+ channel, TRESK, is localized in the spinal cord. *J. Biol. Chem.* 278, 27406–27412. doi: 10.1074/jbc.m206810200

Sehgal, S. A., Hassan, M., and Rashid, S. (2014). Pharmacoinformatics elucidation of potential drug targets against migraine to target ion channel protein KCNK18. *Drug Des. Devel. Ther.* 8, 571–581. doi: 10.2147/dddt.s63096

Silverman, J. D., and Kruger, L. (1990). Selective neuronal glycoconjugate expression in sensory and autonomic ganglia: relation of lectin reactivity to peptide and enzyme markers. *J. Neurocytol.* 19, 789–801. doi: 10.1007/bf01188046

Steinberg, E. A., Wafford, K. A., Brickley, S. G., Franks, N. P., and Wisden, W. (2015). The role of K_2P channels in anaesthesia and sleep. *Pflugers Arch.* 467, 907–916. doi: 10.1007/s00424-014-1654-4

Stucky, C. L., and Lewin, G. R. (1999). Isolectin B_4-positive and -negative nociceptors are functionally distinct. *J. Neurosci.* 19, 6497–6505. doi: 10.1523/JNEUROSCI.19-15-06497.1999

Tulleuda, A., Cokic, B., Callejo, G., Saiani, B., Serra, J., and Gasull, X. (2011). TRESK channel contribution to nociceptive sensory neurons excitability: modulation by nerve injury. *Mol. Pain* 7:30. doi: 10.1186/1744-8069-7-30

Usoskin, D., Furlan, A., Islam, S., Abdo, H., Lönnerberg, P., Lou, D., et al. (2015). Unbiased classification of sensory neuron types by large-scale single-cell RNA sequencing. *Nat. Neurosci.* 18, 145–153. doi: 10.1038/nn.3881

Valenzuela, D. M., Murphy, A. J., Frendewey, D., Gale, N. W., Economides, A. N., Auerbach, W., et al. (2003). High-throughput engineering of the mouse genome coupled with high-resolution expression analysis. *Nat. Biotechnol.* 21, 652–659. doi: 10.1038/nbt822

Wang, F., Flanagan, J., Su, N., Wang, L. C., Bui, S., Nielson, A., et al. (2012). RNAscope: a novel in situ RNA analysis platform for formalin-fixed, paraffin-embedded tissues. *J. Mol. Diagn.* 14, 22–29. doi: 10.1016/j.jmoldx.2011.08.002

Weir, G. A., and Cader, M. Z. (2011). New directions in migraine. *BMC Med.* 9:116. doi: 10.1186/1741-7015-9-116

Weir, G. A., Middleton, S. J., Clark, A. J., Daniel, T., Khovanov, N., McMahon, S. B., et al. (2017). Using an engineered glutamate-gated chloride channel to silence sensory neurons and treat neuropathic pain at the source. *Brain* 140, 2570–2585. doi: 10.1093/brain/awx201

Wright, P. D., Weir, G., Cartland, J., Tickle, D., Kettleborough, C., Cader, M. Z., et al. (2013). Cloxyquin (5-chloroquinolin-8-ol) is an activator of the two-pore domain potassium channel TRESK. *Biochem. Biophys. Res. Commun.* 441, 463–468. doi: 10.1016/j.bbrc.2013.10.090

Yoo, S., Liu, J., Sabbadini, M., Au, P., Xie, G. X., and Yost, C. S. (2009). Regional expression of the anesthetic-activated potassium channel TRESK in the rat nervous system. *Neurosci. Lett.* 465, 79–84. doi: 10.1016/j.neulet.2009.08.062

Zeisel, A., Hochgerner, H., Lönnerberg, P., Johnsson, A., Memic, F., van der Zwan, J., et al. (2018). Molecular architecture of the mouse nervous system. *Cell* 174, 999.e22–1014.e22. doi: 10.1016/j.cell.2018.06.021

Zhou, J., Yang, C. X., Zhong, J. Y., and Wang, H. B. (2013). Intrathecal TRESK gene recombinant adenovirus attenuates spared nerve injury-induced neuropathic pain in rats. *Neuroreport* 24, 131–136. doi: 10.1097/wnr.0b013e32835d8431

Conflict of Interest Statement: MC has received honoraria and consultancy from Novartis, TEVA, Orion and Daichii Sankyo.

The remaining authors declare that the research was conducted in the absence of any commercial or financial relationships that could be construed as a potential conflict of interest.

frontiers in Molecular Neuroscience

ORIGINAL RESEARCH
published: 19 July 2019
doi: 10.3389/fnmol.2019.00178

PIEZO1 Is Selectively Expressed in Small Diameter Mouse DRG Neurons Distinct From Neurons Strongly Expressing *TRPV1*

*Jigong Wang, Jun-Ho La and Owen P. Hamill**

Department of Neuroscience, Cell Biology and Anatomy, The University of Texas Medical Branch, Galveston, TX, United States

Using a high resolution *in situ* hybridization technique we have measured *PIEZO1*, *PIEZO2,* and *TRPV1* transcripts in mouse dorsal root ganglion (DRG) neurons. Consistent with previous studies, *PIEZO2* transcripts were highly expressed in DRG neurons of all sizes, including most notably the largest diameter neurons implicated in mediating touch and proprioception. In contrast, *PIEZO1* transcripts were selectively expressed in smaller DRG neurons, which are implicated in mediating nociception. Moreover, the small neurons expressing *PIEZO1* were mostly distinct from those neurons that strongly expressed *TRPV1*, one of the channels implicated in heat-nociception. Interestingly, while *PIEZO1*- and *TRPV1*- expressing neurons form essentially non-overlapping populations, *PIEZO2* showed co-expression in both populations. Using an *in vivo* functional test for the selective expression, we found that Yoda1, a PIEZO1-specific agonist, induced a mechanical hyperalgesia that displayed a significantly prolonged time course compared with that induced by capsaicin, a TRPV1-specific agonist. Taken together, our results indicate that PIEZO1 should be considered a potential candidate in forming the long sought channel mediating mechano-nociception.

Keywords: *PIEZO1*, *PIEZO2*, *TRPV1*, Yoda1, mechanically gated channel, mechano-nociception, pain

OPEN ACCESS

Edited by:
Volker Eulenburg,
University Hospital Leipzig, Germany

Reviewed by:
Gehoon Chung,
Seoul National University, South Korea
Tibor Rohacs,
Rutgers New Jersey Medical School, United States

***Correspondence:**
Owen P. Hamill
ohamill@utmb.edu

Received: *08 February 2019*
Accepted: *04 July 2019*
Published: *19 July 2019*

Citation:
Wang J, La J-H and Hamill OP (2019) PIEZO1 Is Selectively Expressed in Small Diameter Mouse DRG Neurons Distinct From Neurons Strongly Expressing TRPV1. Front. Mol. Neurosci. 12:178. doi: 10.3389/fnmol.2019.00178

INTRODUCTION

Mechanical forces can evoke many different types of sensation beginning in the peripheral nervous system, including discriminative touch, proprioception, and mechano-nociception. Recent studies have provided strong evidence that the mechanically gated channel PIEZO2 mediates discriminative touch and proprioception, but not mechano-nociception (Coste et al., 2010; Ranade et al., 2014; Woo et al., 2014, 2015; Florez-Paz et al., 2016). In particular, transgenic mice lacking PIEZO2 show a profound loss of touch and proprioception, but show little or no impairment in their normal ability to detect painful mechanical stimuli (Ranade et al., 2014; Woo et al., 2015; Murthy et al., 2018). The mouse results have recently been confirmed in human patients that display a genetic loss of PIEZO2. In particular, these patients show a general loss of vibration detection, touch discrimination and joint proprioception, while retaining almost normal thresholds for mechanical pain (Chesler et al., 2016; Mahmud et al., 2016; Vedove et al., 2016; Szczot et al., 2018). Therefore, one of most critical sensory mechanisms involved in determining how an animal

senses and responds to its surroundings, namely the mechano-nociceptive channel, remains to be identified (Hu et al., 2006; Woolf and Ma, 2007; Dubin and Patapoutian, 2010; Murthy et al., 2018; Szczot et al., 2018). One possible candidate may be the closely related mechanically gated channel PIEZO1 (Coste et al., 2010). However, initial *PIEZO* expression studies using RT-PCR indicated that while *PIEZO2* was highly expressed in mouse DRG neurons, *PIEZO1* transcripts were barely detectable (Coste et al., 2010). Moreover, this apparent *PIEZO1* absence was confirmed by *in situ* hybridization (ISH) measurements (Ranade et al., 2014). However, another group studying the mechanosensory facial organ of the star-nosed mole, found using qPCR that *PIEZO1* was detected at significant levels in both the mole's trigeminal ganglia (TG) and DRG. Moreover, *PIEZO1* was enriched over *PIEZO2* in neurons, not only in the star-nosed mole TG, but also in the mouse TG (Gerhold et al., 2013). Interestingly, other evidence suggesting a PIEZO role in mechano-nociception has come from studies of *Drosophila* where knockout of the single *PIEZO* homolog blocks mechano-nociception (Kim et al., 2012). What remains unclear is whether this ancestral function has been conserved in vertebrates. Because the issue of *PIEZO1* expression and its somatosensory function in vertebrates remains unclear, we decided to reinvestigate *PIEZO1* expression in mouse DRG, taking special notice of its possible expression in small diameter DRG neurons that are generally implicated as mediating nociception (Lee et al., 1986; Lawson and Waddell, 1991; Le Pichon and Chesler, 2014). In brief, our results indicate that *PIEZO1* is selectively expressed in small diameter neurons and these neurons are mostly distinct from those neurons strongly expressing *TRPV1*, a channel implicated in mediating heat nociception (Caterina et al., 1997). Moreover, we found that Yoda1, a highly specific agonist for PIEZO1 over PIEZO2 (Syeda et al., 2015), induced a nociceptive response (hyperalgesia) in mice that was significantly prolonged in time course compared with the hyperalgesia induced by capsaicin, a TRPV1 agonist (Caterina et al., 1997). Taken together these results implicate PIEZO1 in forming the long sought mechano-nociceptor channel. In direct support of this idea and while this manuscript was under review, a Finnish group (Mikhailov et al., 2019) reported that PIEZO1 proteins are expressed in mouse trigeminal cultured neurons and that Yoda1 induces rapid Ca^{2+} transients in isolated trigeminal neurons. Even more compelling, Yoda1 was shown to induce, in a rat hemi-skull preparation, a pronounced and sustained firing of trigeminal mechanosensory nerve fibers innervating the meninges. Based on these results it was concluded that PIEZO1 plays a crucial role in triggering pulsating migraine related nociception (Mikhailov et al., 2019).

MATERIALS AND METHODS

Preparation of Mouse Dorsal Root Ganglia

All experimental protocols were approved by the Animal Care and Use Committee at the UTMB and are in accordance with the NIH *Guide for the Care and Use of Laboratory Animals*. Young adult FVB/NJ male mice 4–5-week old, 20–25 g body weight, (The Jackson Laboratory, Bar Harbor, ME, United States) were used for both in ISH and behavioral studies (see also Schwartz et al., 2008). For the ISH studies, the mice were deeply anesthetized with isoflurane and perfused through the aorta, firstly with cold heparinized and then 10% formalin in phosphate-buffered saline (PBS). Their DRG were harvested from all spinal levels and fixed in 10% formalin overnight. The DRG were then dehydrated through an ethanol series/xylene and embedded in paraffin.

In situ Hybridization

Ten micrometer sections of DRG were cut and *in situ* hybridization was carried out using the RNAscope assay according to the manufacturer's instructions (Advanced Cell Diagnostics, Hayward, CA, United States). The RNAscope technique is able to assess cellular RNA content with single molecule resolution within individual cells through the use of a novel probe design strategy and a hybridization-based signal amplification system that simultaneously amplifies signals and suppresses background (Wang et al., 2012). Development of signal was done using the RNAscope 2.0 HD brown detection kit. Probes for *mPIEZO1* (cat number: 400181) and *mPIEZO2* (cat number: 400191) and *mTRPV1* (cat number: 313331) were purchased from ACD (Hayward, CA, United States). The *PIEZO1* probe involved NT 5477-6623 (corresponding to amino acids 1825-2207). The *PIEZO2 in situ* probe involved NT 983-1920 (amino acids 328-64). As a positive control for RNA integrity, an RNAscope probe specific to the house keeping gene for peptidyl-prolyl isomerase B (*PPIB*) RNA (cat number: 313911) was used. *PPIB* has been recommended by RNAscope because it is expressed at a sufficiently low level in all cell types so as to provide a rigorous control for sample quality and technical performance. As a negative control, a probe specific to bacterial dihydrodipicolinate reductase (*dapB)* RNA (cat number: 310043) was used. The negative control ensured that there was no background staining related to the assay and DRG specimen. The ISH results are based on detailed analysis of 891 neurons from ∼50 DRG isolated from three different mice.

Slides were mounted with Cytoseal and imaged under a bright field Olympus BX51 microscope (10×, 40×, and 60× objectives) with Olympus DP imaging software. The cross sectional area of neurons was measured using the Image J software[1]. Bright puncta (or dots) rather than a diffuse staining pattern represent true RNA transcript signals and *PIEZO1* transcripts were counted within each defined cell area. Both *PIEZO1* and *PPIB* staining most typically appeared as single puncta, or less frequently as clusters of 2–3 puncta distributed throughout the neurons, enabling the direct count of transcripts. *PIEZO2* and *TRPV1* staining more often appeared in clumps, presumably representing many superimposed stained transcripts. In these cases in order to obtain an estimate of the transcript density within the clumps, Image J was used to measure the clump area, which was then divided by the area of individual punctate stains in relatively

[1]https://imagej.nih.gov/ij/

low transcript density regions. This method may underestimate density because of overlying transcripts. In order to estimate expression of *PIEZO1*, *PIEZO1,* and/or *TRPV1* within the same DRG neuron, sequential DRG slices were stained by different probes (i.e., there was no re-staining of a slice with multiple probes) and the same neuron was identified by its similar size, shape and neighbors, allowing for some cell distortion and reorientation caused by the slicing.

Testing the Behavioral Response to Yoda1 and Capsaicin Injections

Mice were housed in groups of four to five in plastic cages with soft bedding and free access to food and water under a 12-12-h light–dark cycle. All animals were acclimated for 1 week before any experimental procedures. To compare Yoda1 (Tocris, Minneapolis, MN, United States) with well-established nociceptive responses caused by capsaicin injections (Schwartz et al., 2008, 2009), each chemical was injected into the footpads of different mice. One micromole of Yoda1 was dissolved in 1 ml dimethyl sulfoxide and three micromole capsaicin in 1 ml of vehicle containing 20% alcohol and 10% Tween 80 in saline, immediately before injection.

For behavioral experiments each mouse was anesthetized with isoflurane (4% for induction and 1.5% for maintenance) in a flow of O_2 and placed in a prone position, and then 5 μl of either Yoda1 (i.e., 5 nanomole) or capsaicin (i.e., 15 nanomole) solutions was injected intra-dermally using a 30 gauge needle attached to a Hamilton syringe (i.e., to give maximum local dermal concentrations of 1 mM Yoda1 and 3 mM capsaicin). As a control for the vehicle and the injection, the same volume of vehicle alone (i.e., used for Yoda1 or capsaicin) was injected in different mice. In each case, the needle was inserted near the heel of the left hind foot and advanced to the middle of the plantar surface (**Figure 9A**). The insertion site was pressed for 1 min to prevent leakage of the solution after removal of the needle. Anesthesia was discontinued and the mice were aroused within 5 min and then returned to their cages. For behavioral testing the mice were placed on an elevated metal grid and mechanically stimulated by applying punctate stimulation on the hind paw plantar with a von Frey filament (VFF) which was equivalent to 0.1 g force. Foot withdrawal frequencies in response to the VFF stimuli were measured as an indicator of mechanical hyperalgesia. To assess primary hyperalgesia the VFF was applied to a site <3 mm distal from the injection site. For secondary hyperalgesia, the VFF was applied at the base and/or proximal part of the third and fourth toes (see **Figure 9A**, Schwartz et al., 2008). This area is considered an adequate distance from the injection site, and thus should not be directly affected by the injection. Effects of Yoda1 or capsaicin on foot withdrawal responses were assessed before and 0.5, 1, 2, 3, 4, 6, 24, and 48 h after intradermal injection for both chemicals (tested blindly against the vehicle alone) and for Yoda1 also after 72 and 96 h that was necessary to observe full recovery. The Mann–Whitney *U* test was used to compare Yoda1 or capsaicin against vehicle at each time point.

RESULTS

PIEZO1 and *PIEZO2* Expression Patterns in Mouse DRG

Figure 1 shows microscopic images of slices from the same DRG examined at low (**Figures 1A,B**) and higher magnification (**Figures 1C,D**) stained with RNA probes for *PIEZO1* and *PIEZO2*. Whereas the *PIEZO2* probe stained many neurons dark brown, the *PIEZO1* probe showed much fainter punctate staining. At the higher magnification (40× objective) some larger diameter neurons showed minimal or no staining by the *PIEZO1* probe but displayed light to heavy staining by the *PIEZO2* probe (red arrows in **Figures 1C,D**). In comparison, smaller neurons (i.e., see within red circle in **Figure 1C**) showed clear punctate staining by the *PIEZO1* probe while larger neurons in the same region (see red circle in **Figure 1D**) showed strong *PIEZO2* probe staining.

The difference in *PIEZO1* and *PIEZO2* probe staining is shown even more clearly in **Figure 2** for adjacent slices taken from another DRG and examined at still higher magnification (60× objective). Again, there appeared to be zero *PIEZO1* expression in some of the largest neurons but clear punctate staining in smaller neurons (**Figure 2A**). In comparison, *PIEZO 2* expression was evident in close to all of the largest neurons (i.e., ∼95%) and in most (i.e., >80%) of the smaller neurons (**Figure 2B**). The apparent ubiquity in *PIEZO2* expression meant that a significant proportion (>50%) of *PIEZO1*-expressing neurons also showed *PIEZO2* co-expression (see below).

PIEZO1 Expression as a Function of Cell Size

In order to measure the cross sectional area and *PIEZO1* expression of specific neurons, each neuron within a microscopic field had its membrane perimeter traced and its enclosed area numbered for identification (e.g., **Figures 3A,B**). Following this procedure, individual neurons could be clearly seen to be ringed by one or more darkly stained cells that were consistent with cell bodies of satellite glial cells (SGCs). For example, the neuron designated # 6 is ringed by at least 3 SGCs densely stained by the *PIEZO1* probe, whereas neuron #24 is associated with at least one darkly stained SGC and one unstained SGC that appears light blue from the hematoxylin counterstain. This heterogeneity in SGC staining by the *PIEZO1* probe may indicate a stochastic, all-or-none process regulates *PIEZO1* expression in SGCs. In comparison, the *PIEZO2* probe failed to stain SGCs (e.g., see all blue SGCs in **Figure 2B**). **Figure 3** also confirms that specific large DRG neuron were either unstained by the *PIEZO1* probe (neurons 5, 7, 11, 19, and 23) or only showed relatively low density punctuate staining (neuron 4, 9 and 24). In contrast, several smaller neurons in the same field showed high density *PIEZO1* probe staining (neurons 1, 2, 3, 14, and 15). **Figure 3C** quantifies this dependence of *PIEZO1* expression on neuron size by plotting *PIEZO1* transcript density as function of neuronal cross-sectional area. The larger neurons ranging from ∼700 to over 2000 μm^2 showed a very similar very low *PIEZO1* transcript density (0.006 ± 0.0005, $n = 96$). In contrast,

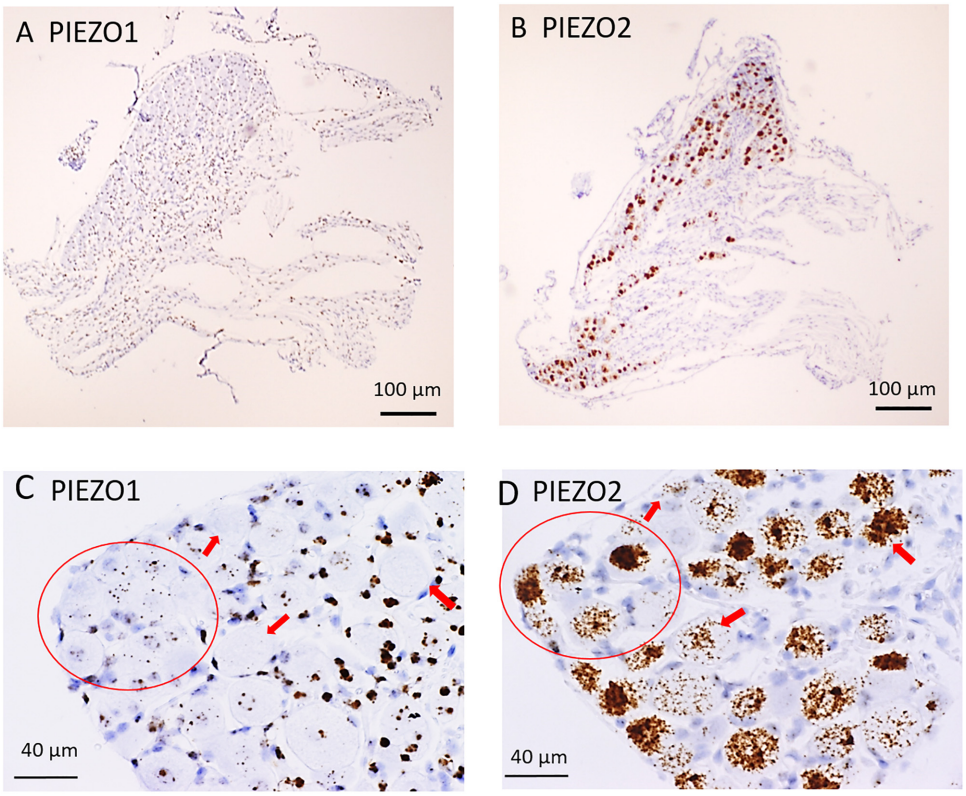

FIGURE 1 | *PIEZO1* and *PIEZO2* expression in mouse DRG. **(A,B)** Adjacent DRG slices viewed at low magnification (10× objective) showing faint brown punctuate staining by the *PIEZO1* RNA probe **(A)** and dark brown staining with the *PIEZO2* probe **(B)**. **(C,D)** Specific DRG regions examined at higher magnification (40× objective). The red circles circumscribe several (∼10) small DRG neurons with punctuate *PIEZO1* probe staining **(C)** as well as five larger neurons with denser *PIEZO2* probe staining **(D)**. The red arrows indicate large neurons with variable densities of *PIEZO2* probe staining **(D)** but no staining by the *PIEZO1* probe **(C)**.

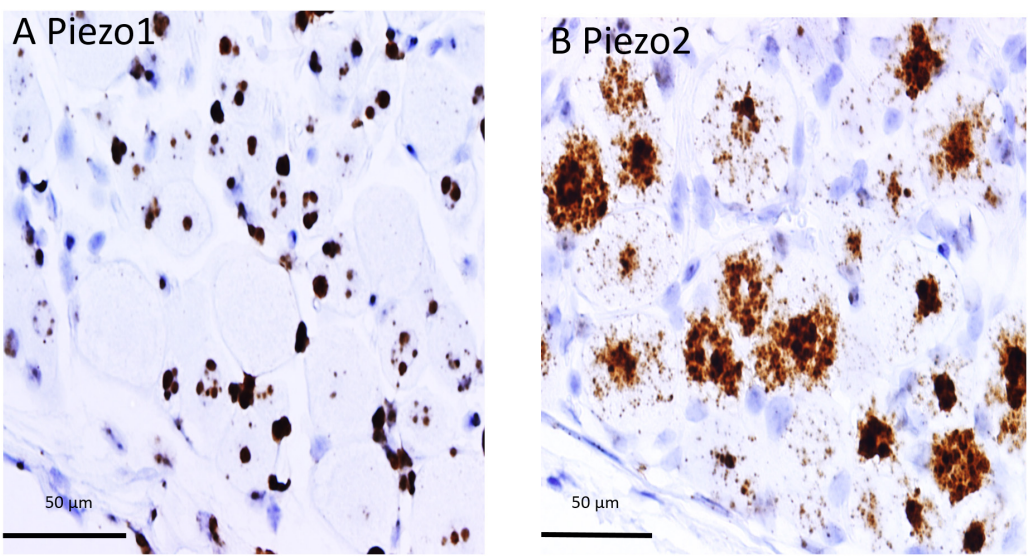

FIGURE 2 | Comparison of *PIEZO1* and *PIEZO2* expression examined at high magnification (60× objective). Adjacent DRG slices stained with *PIEZO1* and *PIEZO2* probes indicating while most neurons express *PIEZO2* **(B)** several of the large neurons show zero or minimal *PIEZO1* expression **(A)**. Also the several small cells in **(B)** that surround neurons and appear universally stained blue with the hematoxylin counterstain are unstained by the *PIEZO2* probe **(B)** but at least some are heavily stained by the *PIEZO1* probe **(A)**.

smaller neurons from 500 to ∼100 μm^2 showed a progressively increasing transcript density with the smallest (≤150 μm^2) expressing a *PIEZO1* transcript density (0.19 ± 0.043, n = 23, P < 0.0001) that was more than 30-fold higher than measured in the larger neurons.

In marked contrast to the cell size-dependent PIEZO1 expression, the housekeeper gene peptidylprolyl isomerase B (*PPIB*) expression shows little cell size-dependence [e.g., compare designated large (*) and small (*) neurons in **Figure 4A**] with a less than 1.5-fold change in transcript density over the same neuronal size range (see **Figure 4B**). This difference between *PIEZO1 and PPIB* probe staining as a function of cell size is evident in the spreads of their data sets (c.f., **Figures 3C**, **4B**) around the dashed red lines

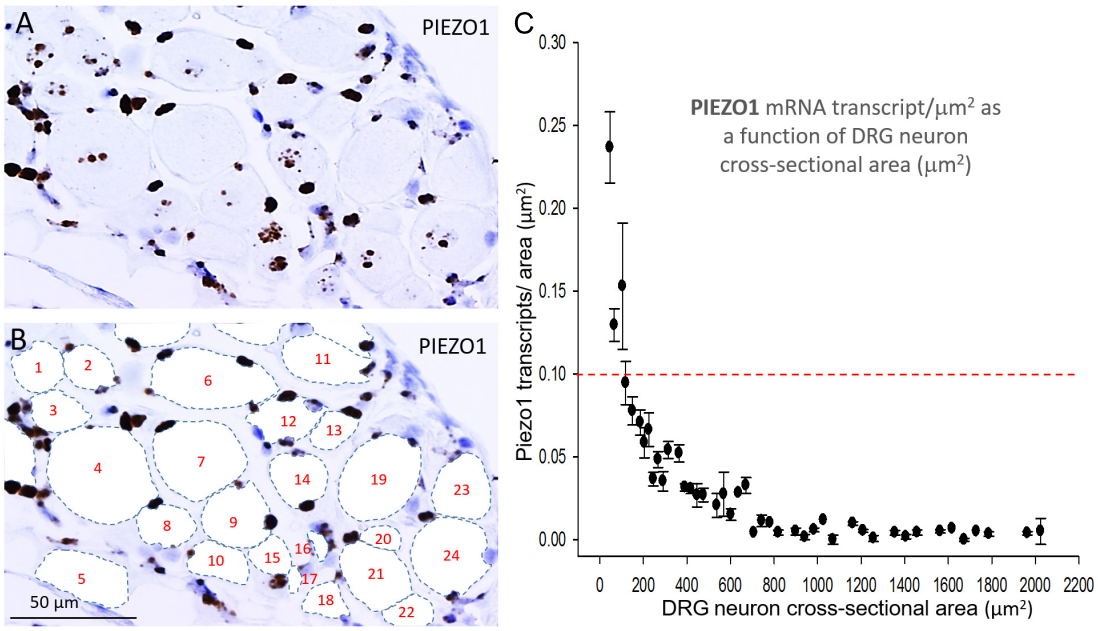

FIGURE 3 | *PIEZO1* expression varies with DRG cell size. **(A)** DRG cells stained with the PIEZO1 RNA probe. Note the absence of *PIEZO1* expression in many of the largest neurons in contrast to relatively high expression in some of the smallest neurons. **(B)** The same microscopic field in which each neuron's perimeter has been traced out to better define their cross-sectional area which has been numbered for identification. Following this procedure, individual neurons can be seen to be "ringed" by several smaller cells, consistent with satellite glial cells, that are heavily stained by the *PIEZO1* probe. **(C)** A plot showing the relationship between *PIEZO1* transcript densities normalized for neuronal cross-sectional area (transcripts/μm^2) plotted as a function of DRG neuronal cross sectional area (μm^2). The data represent transcripts counted in 167 neurons with each data points representing the mean ± SEM for 2–7 neurons. The red dashed line at 0.1 transcript/μm^2 is drawn for comparison with the median expression of the house keeper gene PPIB (e.g., see **Figure 4**).

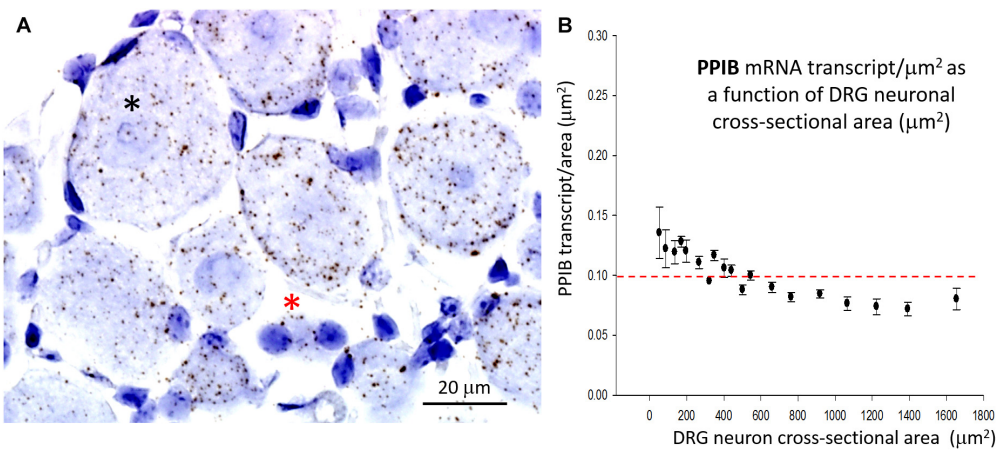

FIGURE 4 | Expression of the housekeeper gene PPIB varies little with cell size. **(A)** DRG section showing qualitatively similar densities of PPIB transcripts in the largest (*) and smallest (*) neurons. PPIB transcripts at a similar density were also evident in the blue stained SGCs that surround neurons. **(B)** Plot of PPIB transcript density (transcripts/μm^2) in neurons measured as a function of neuronal cross sectional area (μm^2).

at 0.10 transcripts/μm^2 that represents the ∼median *PPIB* transcript density. Finally, examination of **Figure 4A** also indicates that SGCs showed qualitatively similar *PPIB* transcript densities as their neighboring neurons.

Comparing *PIEZO1, PIEZO2,* and *TRPV1* Expression and Co-expression

Figures 5A–C shows analysis of *PIEZO2* expression as a function of neuron size, and indicates that *PIEZO2* is more widely and highly expressed in both small and large neurons than *PIEZO1* (c.f., **Figures 5C,D**). Indeed, the very high expression of *PIEZO2*, particularly in small and medium sized neurons, indicates significant *PIEZO2* co-expression (>50%) in those neurons that selectively express either *PIEZO1* (**Figure 5C**) or *TRPV1* (**Figure 5E**). TRPV1 is one of the channels strongly implicated in mediating heat-nociception (Caterina et al., 2000; Vandewauw et al., 2018) and is highly expressed in small and medium sized neurons but poorly expressed in large neurons (**Figure 5E**). This expression pattern appears similar to *PIEZO1*, although with overall greater expression in medium-sized neurons (c.f., **Figures 5D,E**). However, as described below the *PIEZO1*-expressing and *TRPV1*-expressing neurons represent essentially non-overlapping populations. It is evident that the expression density plots for the three genes (**Figures 5C–E**) show similar neuronal size distributions, indicating that the exclusive *PIEZO1* expression in the smaller SGCs did not bias the estimation of *PIEZO1* expression in neurons.

In order to determine co-expression of specific genes, individual neurons identified across adjacent DRG slices (i.e., stained with *PIEZO1*, *PIEZO2,* or *TRPV1* probes) were identified and analyzed. **Figure 6** shows high magnified images of adjacent slices stained with the *PIEZO1* (6A) and *TRPV1* (6B) probes. The *TRPV1* probe stained very darkly several smaller and medium sized DRG neurons (e.g., see neurons enclosed within the red oval in **Figure 6B**). In contrast, neurons enclosed in the same region in **Figure 6A** showed little or no detectable staining by the *PIEZO1* probe even though many of the SGCs within the same region were strongly stained. Although most neurons that showed *TRPV1* staining did not show significant *PIEZO1* staining, at least one neuron in the same microscopic field (see the black arrow designated neuron in **Figures 6A,B**) darkly stained by the *TRPV1* probe also showed punctate staining by the *PIEZO1* probe. On the other hand, specific neurons that showed clear punctuate staining by the *PIEZO1* probe (e.g., within the blue circle in **Figure 6A**) showed little or no apparent staining by the *TRPV1* probe (see same region in **Figure 6B**). **Figure 6C** shows a plot describing the co-expression of *PIEZO1*

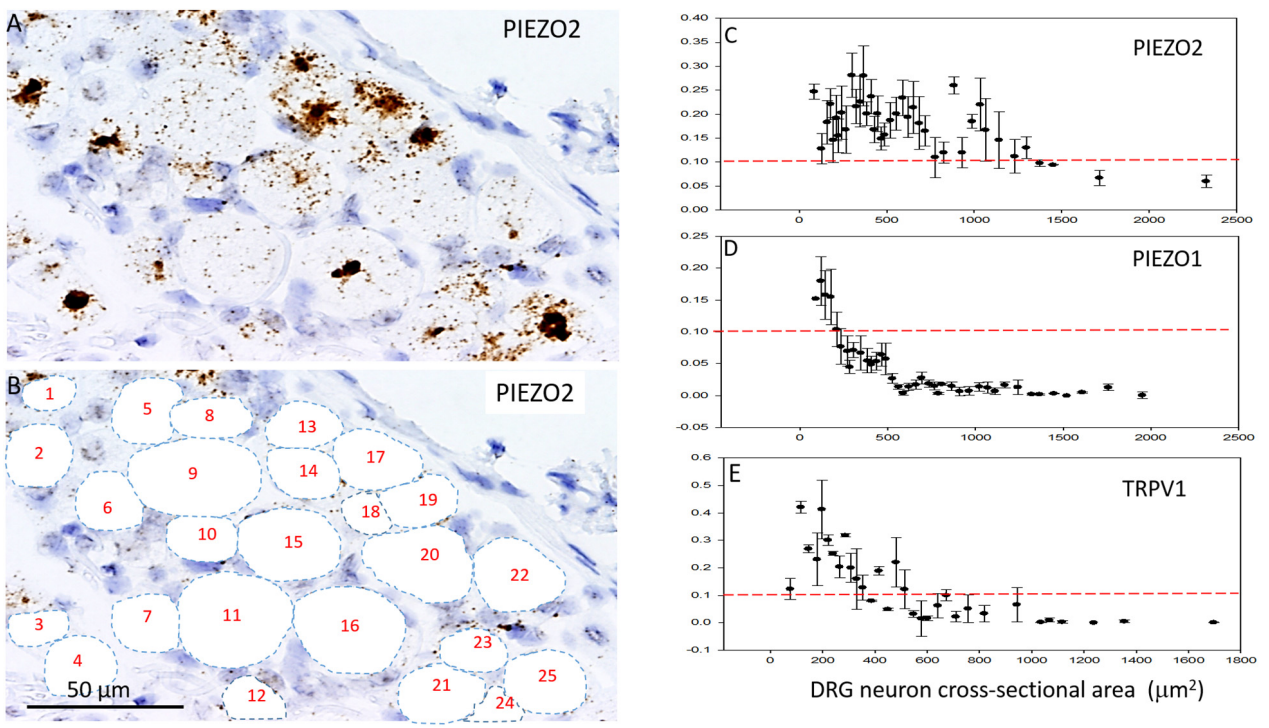

FIGURE 5 | Comparison of *PIEZO1*, *PIEZO2,* and *TRPV1* expression in DRG. **(A,B)** A DRG slice stained with the *PIEZO2* probe with specific neurons identified and numbered for analysis. Note the variable density in *PIEZO2* probe staining with medium to smaller neurons showing stronger staining than larger neurons. **(C)** A plot showing the relationship between *PIEZO2* transcript densities normalized for neuronal cross-sectional area (transcripts/μm^2) plotted as a function of DRG neuronal cross sectional area (μm^2). The data represent transcripts counted in 200 neurons with each data points representing the mean ± SEM for 3–10 neurons. The red dashed line at 0.1 transcript/μm^2 is drawn for comparison with the median expression of the housekeeper gene *PPIB*. **(D,E)** Similar plots as in **(B)** from the same DRG of *PIEZO1* and *TRPV1* probe staining. Note that the expression of *TRPV1* is similar to *PIEZO1* in that the larger neurons weakly express these genes. However, *PIEZO1* differs in that it is more selectively expressed in the smallest neurons compared with *TRPV1*.

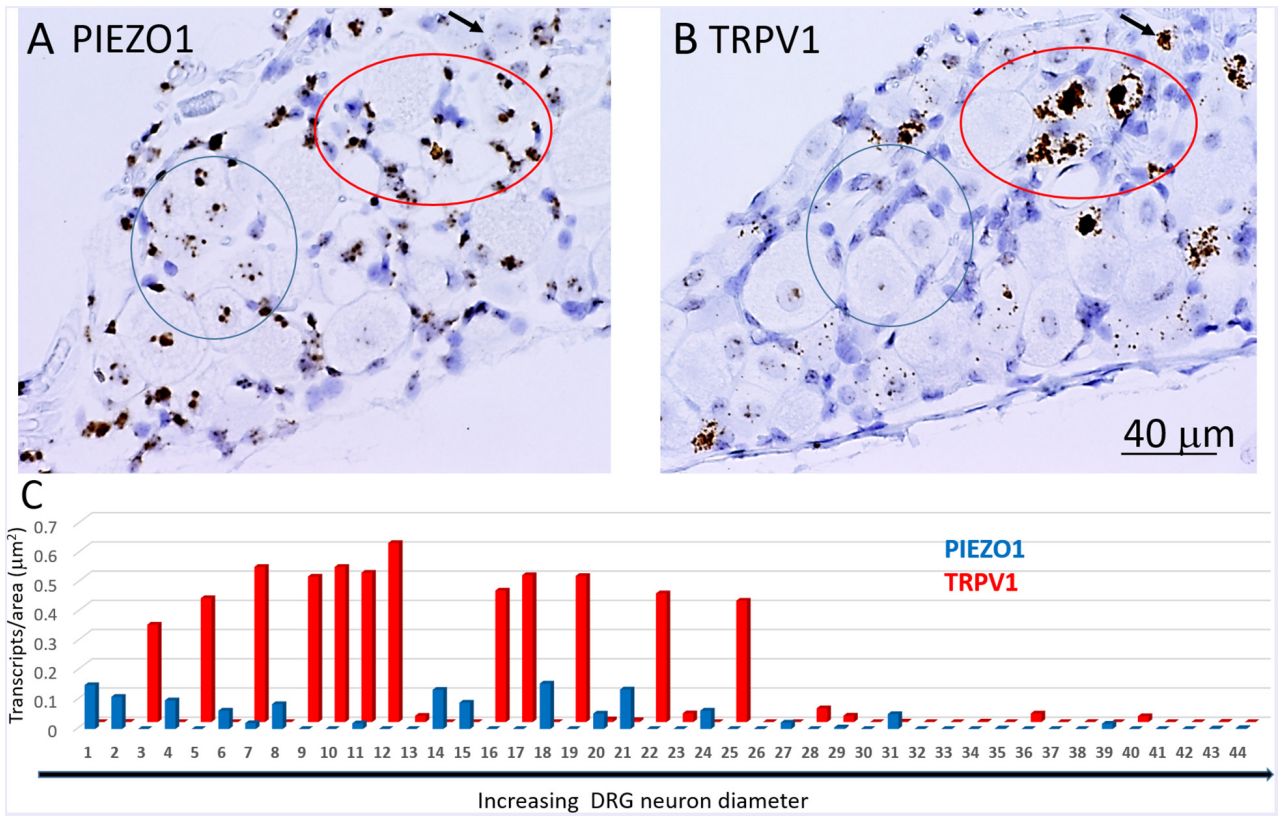

FIGURE 6 | Co-expression of *PIEZO1* and *TRPV1* in a DRG. **(A)** DRG slices stained with the *PIEZO1* RNA probe. **(B)** The adjacent DRG slice stained with the *TRPV1* probe. The red oval designate a region in which at least three neurons are heavily stained with the *TRPV1* probe **(B)** whereas in the same region the *PIEZO1* probe stains only SGCs **(A)**. The blue ovals designates another region in which there is clear punctate staining by the *PIEZO1* probe **(A)** but no staining by the *TRPV1* probe **(B)**. The black arrow in the upper right quadrant in each panel designates on neuron that does show strong expression of *TRPV1* **(B)** and also punctate expression of *PIEZO1* **(A)**. Note the *TRPV1* probe, unlike the *PIEZO1* probe, does not stain SGCs. **(C)** A plot of 44 neurons identified in adjacent slices that were analyzed for *PIEZO1* and *TRPV1* co-expression. The 44 neurons are number according to increasing cross-sectional area with a range of 90-2070 μm^2. Neuron #26 that showed no expression of *PIEZO1* or *TRPV1* had an area 565 μm^2.

and *TRPV1* in 44 neurons of progressively increasing cell size (range 150–1800 μm^2 indicated by the extended black arrow). Again, the larger DRG neurons showed little or no expression of either *PIEZO1* or *TRPV1*, whereas, most of the smaller neurons expressed either *PIEZO1* or *TRPV1*. For example, some of the smaller neurons expressed only *PIEZO1* (neurons 1, 2, 4, 6, and 8), whereas of the 12 neurons that strongly expressed *TRPV1* (3, 5, 7, 9, 10, 11, 12, 16, 17, 19, 22, 25) only two neurons (7 and 11, 16%) showed detectable co-expression of *PIEZO1*.

Figure 7 shows another slice stained with *PIEZO2* and *TRPV1* probes. The microscopic fields indicate that many of the larger neurons that expressed *PIEZO2* showed either very little or no detectable *TRPV1* expression (c.f. green arrowed neurons in **Figures 7A,B**). In comparison, at least one identified neuron in the field that showed very high *TRPV1* expression (**Figure 7B**, red arrow) did not appear to express *PIEZO2* (**Figure 7A**). However, given the wide expression of *PIEZO2* in small and medium sized neurons (e.g., ∼85%) some neurons were seen that co-expressed *PIEZO2* and *TRPV1*. For example, of 33 neurons specifically analyzed for co-expression (**Figure 7C**), 12 of the smaller neurons showed *TRPV1* expression, and of these, eight neurons (i.e., 67%) showed at least some co-expression of *PIEZO2* (i.e., neurons 4, 6, 7, 8, 10, 14, 15, 17). Moreover, three neurons (i.e., 8, 15, and 17) showed high transcript density of both genes (i.e., ≥0.2 transcripts/μm^2) consistent with multi-modal neurons. The numbered neurons analyzed in **Figure 7C** were in different DRG slices from the neurons analyzed in **Figure 6C**.

Estimation of Specific Gene Expression Indices (ε) in Small and Large DRG Neurons

In order to estimate the possible contribution of specific genes to DRG neuron function, an expression index (ε) was calculated as the product of the percentage of neurons expressing the gene (i.e., ≥1 transcript) multiplied by the average transcript density (transcripts/μm^2). For convenience, we arbitrarily divided DRG neurons into large (≥600 μm^2, **Figures 8A–C**) and small neurons (≤500 μm^2, **Figures 8D,E**). As expected, 100% of both large and small neurons expressed the housekeeper gene *PPIB,* but with only moderate average expression levels (∼0.1 transcripts/μm^2) to give an average ε value of ∼10 in both small and large neurons.

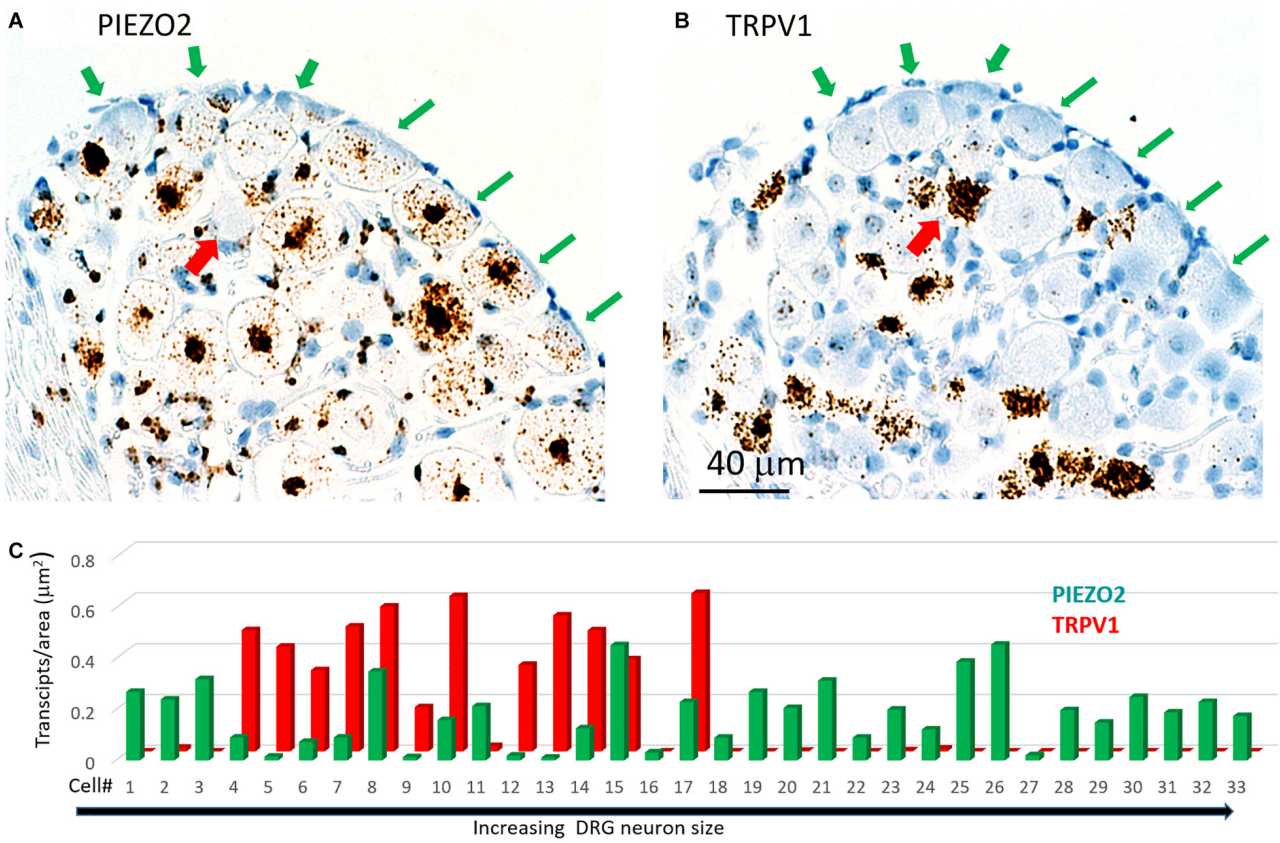

FIGURE 7 | Co-expression of *PIEZO2* and *TRPV1* in DRG cells. **(A)** A DRG section stained by the *PIEZO2* probe. **(B)** The adjacent DRG section stained with the *TRPV1* probe. Note the selective expression of *PIEZO2* over *TRPV1*, particularly in the neurons indicated by the green arrows. Whereas almost all neurons in this section showed some staining by the *PIEZO2* probe (≥90%) less than 50% were stained by the *TRPV1* probe and these were the smaller neurons. The red arrow indicates at least one neuron heavily stained by the *TRPV1* probe that was not stained by the *PIEZO2* probe. **(C)** Analysis of co-expression of *PIEZO2* and *TRPV1* in 33 neurons identified in adjacent slices. The neurons were numbered in increasing cross-sectional area with a range of 100–1900 μm^2. Neuron #18 had an area of 648 μm^2 (Note these neurons are not the same as in **Figure 6C**).

In comparison, 96% of large neurons and 83% of small neurons expressed *PIEZO2*, with respective high expression indices of 21 and 25, due to the relatively high transcript densities (0.22 and 0.3 transcripts/μm^2). Therefore, based on ε values alone, *PIEZO2* would be expected to play a significant functional role in both small and large DRG neurons, and is consistent with a recent study showing that complete *PIEZO2* knock-out, in addition to abolishing touch and proprioception (see also references in section "Introduction") also partially impairs nociception (Murthy et al., 2018). On the other hand, the relatively large ε value for *PIEZO1* in small (7.2) versus large (0.26) neurons, indicates that *PIEZO1* may be capable of providing functional redundancy in small but not large neurons when *PIEZO 2* is genetically removed (or absent as in humans). Finally, in the case of TRPV1, the high ε value (19) in a mostly non-overlapping population of neurons distinct from the neurons expressing *PIEZO1,* is at least consistent with the idea that these two channels may participate in different forms of nociception. However, as already mentioned a proportion of *TRPV1*-expressing neurons (∼70 %) also expressed significant *PIEZO 2* (**Figure 7**) implying the existence of multimodal neurons capable of transducing both heat and mechanical stimuli. This demonstration of co-expression of *PIEZO2* and *TRPV1* also provides a cellular basis for the finding that capsaicin can strongly inhibit PIEZO2-mediated mechanosensitive currents in TRPV1-expressing neurons (Borbiro et al., 2015).

Yoda1 Injection Causes a Prolonged Hyperalgesia in Mice

As an *in vivo* assay to determine the functional significance of the DRG neuronal specific expression of *PIEZO1* and *TRPV1*, we tested the responses in mice to injections of either capsaicin, a TRPV1 specific agonist (Caterina et al., 1997, 2000) or Yoda1, a PIEZO1 channel specific agonist and modulator (Syeda et al., 2015). In particular, Yoda1 is known to increase the mechanosensitivity of PIEZO1 channels, by both lowering their threshold and reducing their rapid inactivation in response to mechanical stimuli. Therefore, we tested mice for mechanical hyperalgesia, by measuring the nocifensive response to a mechanical stimulus, at a primary site (i.e., close ≤ 3 mm to the Yoda1 injection site) and at a secondary site that was

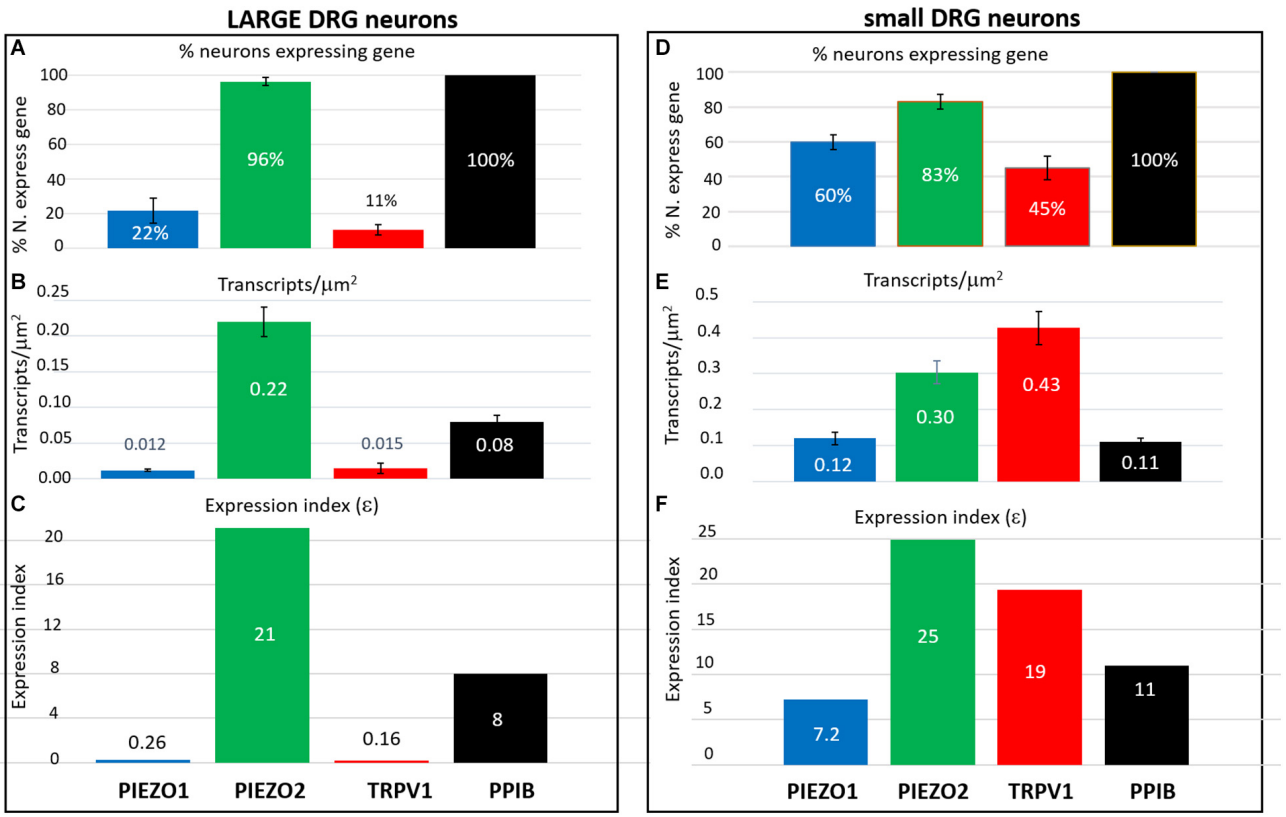

FIGURE 8 | Expression index (ε) estimated for different genes in larger versus smaller DRG neurons. Left, Gene expression parameters estimated in analysis of 257 larger neurons (≥600 μm^2). **(A)** Histograms showing the percentage of neurons expressing *PIEZO1, PIEZO2, TRPV1,* and *PPIB* genes. **(B)** Histograms showing the measured average gene transcript density (transcripts/μm^2) in neurons that expressed the specific gene. **(C)** Histograms of the expression index calculated as the product of the % of neurons expressing the gene and their average transcript density (transcripts/μm^2). Right, Expression parameters for 354 smaller neurons (≤500 μm^2). **(D)** Histograms showing the percentage of neurons expressing *PIEZO1, PIEZO2, TRPV1,* and *PPIB* genes. **(E)** Histograms showing their average transcript density (transcripts/μm^2) in neurons that expressed the specific gene. **(F)** Histogram of the expression index calculated as the product of the percentage of neurons expressing the gene and their average gene density transcripts/μm^2.

relatively distant from the Yoda1 injection site (**Figure 9A**, and see section "Materials and Methods"). It has already been established in both mice and humans that capsaicin injections can induce mechanical hyperalgesia, as well as heat hyperalgesia, at the primary site, but only mechanical hyperalgesia at the secondary site (see Torebjörk et al., 1992; Schwartz et al., 2008, 2009). **Figure 9** shows the results of 5 µl (5 nanomole) injections of Yoda1 (**Figures 9B,C**) and 5 µl (15 nanomole) capsaicin (**Figures 9D,E**) compared with 5 µl injections of vehicle alone. For Yoda1, significant mechanical hyperalgesia was evident 30 min after injection at both the primary (**Figure 9B**) and secondary sites (**Figure 9C**). However, from the early initial peak in hyperalgesia there was a significant decrease evident at 1 h, followed by return to even higher levels of hyperalgesia by 2 h. Most dramatically, this second phase of elevated hyperalgesia was still evident 72 h after the Yoda1 injection, and only fully recovered 96 h after the injection. All five mice tested with Yoda1 showed this response pattern of prolonged hyperalgesia with full recovery after only 96 h. The capsaicin response was different (**Figures 9D,E**) but similar to previously published capsaicin results (i.e., see Figure 2 in Schwartz et al., 2008). In particular, there was a progressive increase to a maximum hyperalgesia by 2 h at both the primary and secondary sites, but with capsaicin there was no early transient decline within the first hour. After the 2 h peak, the capsaicin-induced hyperalgesia progressively declined so that there was partial recovery at 24 h (unlike with Yoda1) but full recovery at both sites was only evident after 48 h. It is possible that the mechanical hyperalgesia caused by Yoda1 and capsaicin injections arises because of neurogenic inflammation (Richardson and Vasko, 2002). However, although Yoda1 did cause initial redness at the injection site, it was less pronounced than that caused by capsaicin. Furthermore, by 24 h after injection there was no sign of inflammation in either the Yoda1 and capsaicin injected groups. This observation alone may indicate that the mechanical hyperalgesia arises from central sensitization due to increased afferent nerve activity induced by Yoda1 in *PIEZO1*- expressing afferents (Mikhailov et al., 2019) or by capsaicin in TRPV1-expressing afferents (Banik and Brennan, 2009). However, a further possible complication is that keratinocytes, which are located in the epidermal layer of the skin, express PIEZO1 (Maksimovic et al., 2014) and TRPV1 (Ko et al., 1998). In this

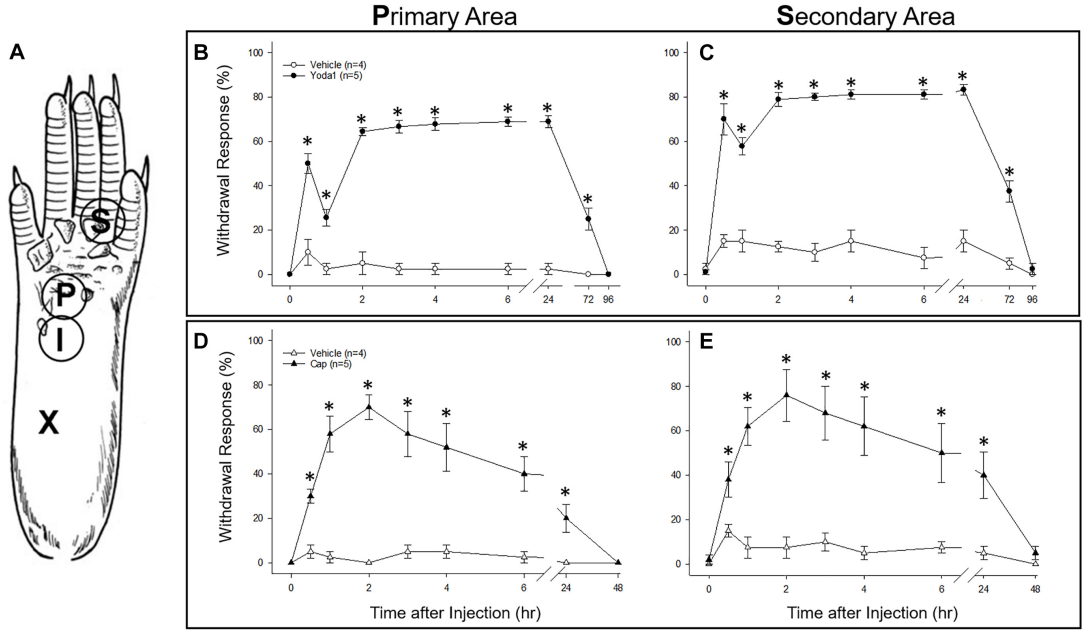

FIGURE 9 | Comparison of nociceptive responses (mechanical hyperalgesia) induced in mice injected with Yoda1, capsaicin and vehicle alone. **(A)** A schematic showing sites of injection and behavioral testing in the mouse hind foot. For injection, a 30-gauge needle was inserted at the heel of the foot (X) and advanced to the injection site (I), where a 5 μl intradermal injection of Yoda1 (5 nanomole), capsaicin (15 nanomole) or vehicle alone was carried out. Foot withdrawal frequencies in response to von Frey filament stimuli were measured at the primary site (P) for hyperalgesia and at the secondary site (S) for hyperalgesia. **(B)** Primary and **(C)** secondary mechanical hyperalgesia measured in response to Yoda1 and vehicle alone. **(D)** Primary and **(E)** secondary mechanical hyperalgesia measured in response to capsaicin and vehicle alone. The data points represent mean ± SEM for 4–5 mice under each condition. The Mann–Whitney *U* test was used to compare Yoda1 or capsaicin against vehicle alone at each time point.

case, activation of keratinocytes could somehow contribute to the hyperalgesia by, for example, inducing an abnormal wound healing/inflammatory response (Pastar et al., 2008). However again, the absence of visible redness and inflammation 24 h after injection does not favor this as the major underlying mechanism for the prolonged hyperalgesia.

DISCUSSION

The key finding of this study is that *PIEZO1* expression shows a strong dependence on DRG neuron size, with a high expression index in small neurons (ε = 7.2) compared with large neurons (ε = 0.26). This contrasts with *PIEZO2,* which is highly expressed in most DRG neurons (∼90%) including both small (ε = 25) and large neurons (ε = 21). Consequently, a significant proportion of small neurons (∼60%) that express *PIEZO1* also co-express *PIEZO2*. This co-expression, may allow for chimeras of PIEZO1/PIEZO2 subunits to form a high threshold slow-inactivating channel that transduces painful stimuli, similar to the chimeric channels proposed to confer high-strain mechanosensitivity on articular cartilage (Lee et al., 2014). However, whereas knockout of either *PIEZO1* or *PIEZO2* abolishes chondrocyte mechanosensitivity (Lee et al., 2014) complete knockout of *PIEZO2* only partly impairs mechano-nociception (Murthy et al., 2018). Interestingly, a recent study of *PIEZO1* and *PIEZO2* expression in baroreceptor neurons of mouse visceral ganglia indicates an equal percentage of neurons (∼40%) expressed either *PIEZO1* or *PIEZO2*, but only a small percentage (∼15%) showed co-expression (Zeng et al., 2018). Significantly, double knockout of both *PIEZOs* was required to suppress the baroreflex-mediated heart rate changes (Zeng et al., 2018). Our results predict that a double knockout of *PIEZO1* and *PIEZO2* will also be required to block mechano-nociception.

While *PIEZO2* knockout does not abolish mechano-nociception, there is substantial evidence for PIEZO2 involvement in transducing specific chronic pain states including hyperalgesia and allodynia (Dubin et al., 2012; Eijkelkamp et al., 2013; Singhmar et al., 2016; Yang et al., 2016; Murthy et al., 2018; Szczot et al., 2018). Whereas mechanical hyperalgesia, in the strict sense, involves an increased sensitivity to normally noxious mechanical stimuli, mechanical allodynia occurs when a normally non-noxious mechanical stimulus causes pain (Sandkühler, 2009). Two recent studies focused on mechanical allodynia – one involving *PIEZO2* knockout mice (Murthy et al., 2018), the other human patients deficient in *PIEZO2* expression (Szczot et al., 2018) – have shown that the absence of PIEZO2 completely eliminates the mechanical allodynia induced by capsaicin injection. Several mechanisms may underlie allodynia, including peripheral and central sensitization of nociceptive neurons (Sandkühler, 2009). In particular, allodynia may arise because of induced cross talk between touch and nociceptor labeled lines (see **Figure 10**) via induced gap junction communication between small and large DRG neurons (e.g., see

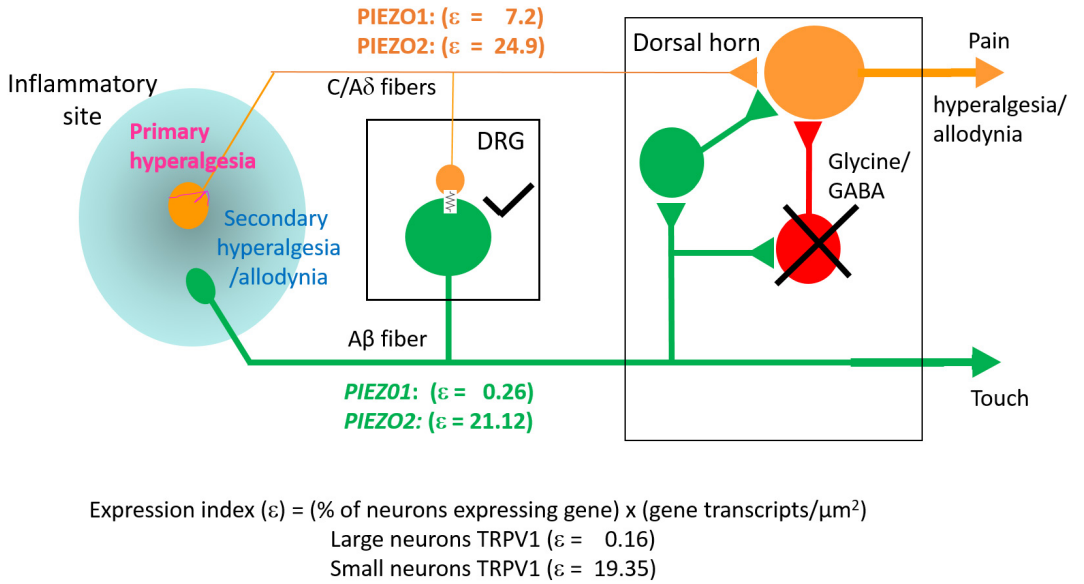

FIGURE 10 | Schematic illustrating differential *PIEZO1* and *PIEZO2* expression in nociceptive and touch labeled lines and their predicted contributions to normal and abnormal pain states (allodynia and hyperalgesia). Touch is mediated by large cell body/thick axon myelinated DRG neurons (Aβ fibers) that express predominately *PIEZO2* with minimal expression of *PIEZO1*. Nociception is mediated by small body/thin axon unmyelinated (C) fibers and thinly myelinated (Aδ) fibers that express *PIEZO2* and relatively high levels of *PIEZO1*. As discussed in the text, hyperalgesia and allodynia are pathological pain states that may arise from crosstalk between the nociceptive and touch lines in addition to possible sensitization of peripheral nerve endings. Different mechanisms may promote this cross talk. One mechanism may occur within the DRG where inflammation, nerve damage and/or elevated neural activity induces gap junction connections (indicated by the electrical resistance symbol) between large and small diameter neurons. Another mechanism may occur within the dorsal horn in which the normal inhibitory synaptic input (indicated by the cross) that suppresses the influence of excitatory inputs on projecting neurons that transmit pain signals to the brain is reduced. In both cases, signals generated by *PIEZO2* activation in the "touch line" may also be transmitted to the "nociceptive line" (see text).

Kim et al., 2016; Spray and Hanani, 2019). Another non-exclusive mechanism may arise via the removal of the inhibitory drive that normally suppresses excitatory synaptic inputs linking touch inputs to the pain projection neurons within the dorsal horn of the spinal cord (e.g., see Torsney and MacDermott, 2006; Arcourt et al., 2017). In terms of these mechanisms, one can see how genetic knockout of *PIEZO2* would eliminate allodynia while only partly impairing normal nociception because PIEZO1 may serve a redundant role (**Figure 10**). On the other hand, complete *PIEZO1* knockout should leave allodynia intact unless it occurs via sensitization of PIEZO1 channels in nociceptive nerve endings, while normal nociception may be only partly impaired, since in this case PIEZO2 serves redundant roles in both touch and mechano-nociception. Interestingly, a recent *PIEZO2* knockout study has reported that not only is there an impairment in touch but also an actual increase in normal mechanical nociception (Zhang et al., 2019). This paradoxical result is consistent with the idea that touch normally suppresses pain (Torsney and MacDermott, 2006; Arcourt et al., 2017). Moreover, following ectopic expression of *PIEZO1* in the *PIEZO2* knockout, not only was defective touch rescued, but mechanical pain was also suppressed, indicating that ectopic PIEZO1 can take over PIEZO2 function in large neurons (Zhang et al., 2019). These combined studies, considered from an evolutionary perspective, indicate how the *PIEZO* gene duplication that occurred in vertebrates – invertebrates like *Drosophila* express only one *PIEZO* and this forms the mechano-nociceptive channel (Coste et al., 2010; Kim et al., 2012) – may have given vertebrates an added selective advantage by introducing more redundancy and flexibility in transducing different forms of somatosensory stimulation.

Our ISH results indicate that the small DRG neurons that selectively express *PIEZO1* are part of a non-overlapping population mostly distinct from those neurons that strongly express *TRPV1*, one of the channels implicated in heat-nociception. This idea of distinct nociceptor populations for mechano- and heat-nociception in the DRG is consistent with several previous studies that used genetic and pharmacological approaches to selectively ablate TRPV1+ neurons and G-protein coupled receptor MRGPRD+ neurons, and demonstrate these neurons mediate heat- and mechano-nociception, respectively (Cavanaugh et al., 2009, see also Beaudry et al., 2017). Our results also agree qualitatively, if not quantitatively, with the single cell RNA-sequencing dissection of mouse DRG neurons[2] (Usoskin et al., 2015). In this study, DRG neurons were classified into four distinct clusters: An NF cluster that expressed the neurofilament heavy chain associated with myelinated neurons. A PEP cluster that expressed substance P and calicitonin gene-related peptide associated with peptidergic nociceptors. An NP non-peptidergic cluster that was also *TRPV1*-negative, associated with mechano-nociceptors, and a TH cluster that expressed tyrosine hydroxylase (*Th*), and is associated with unmyelinated neurons (type C)

[2]http://linnarssonlab.org/drg/

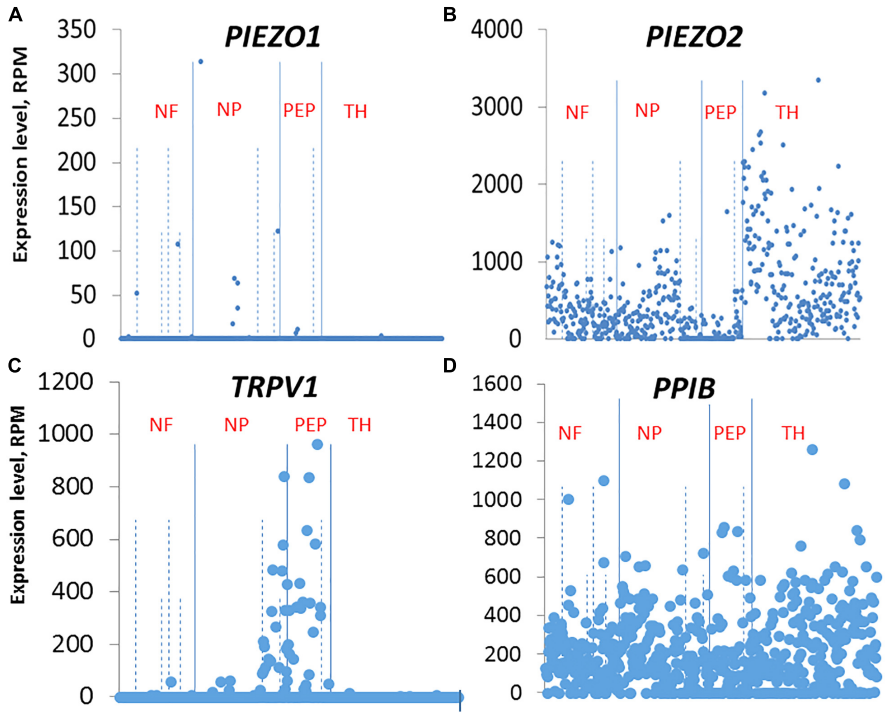

FIGURE 11 | Single cell RNA-sequencing scatter plots for *PIEZO1* **(A)**, *PIEZO2* **(B)**, *TRPV1* **(C)**, and *PPIB* **(D)** taken from Usoskin et al. (2015) (see http://linnarssonlab.org/drg/). The vertical axis represents the normalized gene expression levels in reads per million (RPM) for individual cells. The RPM counts are grouped along the horizontal axis according to identified populations separated by the solid vertical lines in the order: NF, NP, PEP, TH populations (NF, Neurofilament; NP, Non-Peptidergic; PEP, Peptidergic; and TH, tyrosine hydroxylase). The dashed vertical lines separate major populations into further subtypes, for example NF1 to NF5 for NF major type.

involved in mediating pleasant or emotional touch. In terms of these four clusters, *PIEZO1* was expressed mainly, although at very low levels in the NP cluster (**Figure 11** shows the relevant gene scatter plots taken from http://linnarssonlab.org/drg/ see also External resource Table 1). Specifically, seven of the 19 neurons that expressed *PIEZO1* (out of 622 neurons) were in the NP cluster (**Figure 11A**), and of those 19, 16 co-expressed *PIEZO2*. *PIEZO2* was widely expressed in all DRG neurons, but most predominately in the *Th* cluster (**Figure 11B**). As expected, *TRPV1* expressed almost exclusively in the PEP cluster involved in sensing noxious heat, although with some overlap into the NP cluster (**Figure 11C**). Moreover, of the 66 neurons that expressed *TRPV1,* 50 neurons co-expressed *PIEZO2.* In the case of non-neuronal cells, Usoskin et al. (2015) reported that only three out of ∼100 non-neuronal cells analyzed expressed *PIEZO1*. However, in two of these the *PIEZO1* transcript counts were several orders of magnitude higher than the counts in any neurons. At this time, we have no explanation for the quantitative differences in *PIEZO1* expression in mouse DRG seen between the ISH and scRNA-seq studies. However, our ISH analysis did appear to include more small DRG neurons (i.e., ≤10 μm in diameter e.g., see **Figure 3B**) than those analyzed in the scRNA-seq study (i.e., ≥15 μm in diameter).

A specific prediction from our ISH results is that Yoda1, a chemical identified as a highly selective agonist/modulator of PIEZO1 channels versus PIEZO2 channels (Syeda et al., 2015; Lacroix et al., 2018) should also produce some form of nociceptive response in mice. Indeed, the mechanical hyperalgesia we observed is consistent with a prolonged increase in mechanosensitivity and reduction in rapid channel inactivation of PIEZO1 channels that would tend to increase afferent nerve firing (Syeda et al., 2015; Lacroix et al., 2018). In direct support of this idea, a Finnish group (Mikhailov et al., 2019) has recently shown that Yoda1 induces rapid and large Ca^{2+} transients in isolated trigeminal *PIEZO1*-expressing neurons. Even more compelling, Yoda1 also induced, in a rat hemi-skull preparation, a pronounced and sustained firing of trigeminal mechanosensory nerve fibers innervating the meninges (Mikhailov et al., 2019). The last result may directly contribute to mechanical hyperalgesia we observe, since sustained firing of afferents alone can induce central sensitization and chronic pain states in both rodents and humans (Xie et al., 2005; Sandkühler, 2009; Pfau et al., 2011). Nevertheless, at this time off-target effects of Yoda1 cannot be excluded (Dela Paz and Frangos, 2018). A further added complication is that epidermal keratinocytes also express relatively high levels of PIEZO1 (Maksimovic et al., 2014). In this case, Yoda1 activation of keratocytes may induce an abnormal inflammatory response (Pastar et al., 2008; Shipton, 2013) that could underlie the resurgence in mechanical hyperalgesia (i.e., after ∼1 h) as well as the delayed recovery of hyperalgesia to

baseline levels (i.e., >72 h, see **Figure 8**). However, again although Yoda1 did cause initial redness at the injection site, it was less pronounced than that caused by capsaicin. Furthermore, by 24 h after injection, there was no sign of inflammation in either the Yoda1 and capsaicin injected groups.

In conclusion, our DRG study and the recently published TG study (Mikhailov et al., 2019) directly implicates PIEZO1 in mechano-nociception. Obviously, further genetic manipulations of both *PIEZO1* and *PIEZO2* and will be required to confirm their individual and combined roles, as has been recently demonstrated for baroreception (Zeng et al., 2018). Interestingly, while in mice global knock-out of *PIEZO1* is embryonically lethal, in humans a PIEZO1 loss-of-function mutation has been reported to cause mainly a loss of lymphatic function (Lukacs et al., 2015) while a PIEZO1 gain-of-function mutation results in a red blood cell dehydration (e.g., see Ma et al., 2018). Although nociception changes were not reported, these disorders may not be associated with either impairment or enhancement of nociception because of the redundant role played by PIEZO2. Finally, from a biophysical perspective, a mechanism is required to explain how PIEZO channels, characterized by their very rapid inactivation (<10 ms), can mediate the slow inactivating currents that transduce mechano-nociceptive stimuli. Interestingly, in a variety of cells types that express PIEZO-like mechanically gated cation channels, the channel can be switched permanently from a transient to a sustained gating mode (i.e., TM →SM) by strong mechanical stimulation (Hamill and McBride, 1997; Maroto et al., 2012; Bae et al., 2013). On the other hand, a switch in PIEZO1 channel gating in the reverse direction (i.e., SM → TM) also occurs with differentiation of mouse embryonic stem cells (Del Marmol et al., 2018 see also Soria et al., 2013). Understanding the basis of these gating switches could provide a novel approach to manipulating how mechanotransducers including mechano-nociceptors respond to mechanical stimuli.

ETHICS STATEMENT

This study was carried out in accordance with the recommendations of the Animal Care and Use Committee at the UTMB and are in accordance with the NIH Guide for the Care and Use of Laboratory Animals. All experimental protocols were approved by the Animal Care and Use Committee at the UTMB and are in accordance with the NIH Guide for the Care and Use of Laboratory Animals.

AUTHOR CONTRIBUTIONS

OH conceived the study and carried out the ISH experiments. JW surgically isolated the DRG and carried out the Yoda1/capsaicin injections and behavioral assays. J-HL analyzed the behavioral results. OH wrote the manuscript. All authors read and approved the final manuscript.

FUNDING

JW was supported by NIH Grant RO1 NS03168 to Dr. Jin Mo Chung. J-HL was supported by JSMEF data Acquisition Grant CON2273.

ACKNOWLEDGMENTS

We thank Dr. Jin Mo Chung for providing financial support and helpful comments on early versions of the manuscript. We also thank Drs. Richard Coggeshall and Agenor Limon for their helpful input. We also appreciate the assistance from the UTMB Neuropathology core facility and its staff, Kerry Graves, and Kenneth Escobar in preparing the DRG slices and providing microscopy facilities.

REFERENCES

Arcourt, A., Gorham, L., Dhandapani, R., Prato, V., Taberner, F. J., Wende, H., et al. (2017). Touch receptor-derived sensory information alleviates acute pain signaling and fine-tunes nociceptive reflex coordination. *Neuron* 93, 179–193. doi: 10.1016/j.neuron.2016.11.027

Bae, C., Gottlieb, P. A., and Sachs, F. (2013). Human PIEZO1: removing inactivation. *Biophys. J.* 105, 880–886. doi: 10.1016/j.bpj.2013.07.019

Banik, R. K., and Brennan, T. J. (2009). TRPV1 mediates spontaneous firing and heat sensitization of cutaneous primary afferents after plantar incision. *Pain* 141, 41–51. doi: 10.1016/j.pain.2008.10.004

Beaudry, H., Daou, I., Ase, A. R., Ribeiro-da-Silva, A., and Seguela, P. (2017). Distinct behavioral response evoked by selective optogenetic stimulation of the major TRPV1+ and MrgD+ subsets of C-fibers. *Pain* 158, 2329–2339. doi: 10.1097/j.pain.0000000000001016

Borbiro, I., Badheka, D., and Rohacs, T. (2015). Activation of TRPV1 channels inhibits mechanosensitive PIEZO channel activity by depleting membrane phosphoinositides. *Sci. Signal.* 8:ra15. doi: 10.1126/scisignal.2005667

Caterina, M. J., Leffler, A., Malmberg, A. B., Martin, W. J., Trafton, J., Petersen-Zeitz, K., et al. (2000). Impaired nociception and pain sensation in mice lacking the capsaicin receptor. *Science* 288, 306–313. doi: 10.1126/science.288.5464.306

Caterina, M. J., Schumacher, M. A., Tominaga, M., Rosen, T. A., Levine, J. D., and Julius, D. (1997). The capsaicin receptor: a heat-activated ion channel in the pain pathway. *Nature* 389, 816–824. doi: 10.1038/39807

Cavanaugh, D. J., Lee, H., Lo, L., Shields, S. D., Zylka, M. J., Basbaum, A. I., et al. (2009). Distinct subsets of unmyelinated primary sensory fibers mediate behavioral responses to noxious thermal and mechanical stimuli. *Proc. Natl. Acad. Sci. U.S.A.* 106, 9075–9080. doi: 10.1073/pnas.0901507106

Chesler, A. T., Marcin, S., Bharucha-Goebel, D., Ceko, M., Donkervoort, S., Laubacher, C., et al. (2016). The role of PIEZO2 in human mechanosensation. *N. Eng. J. Med.* 375, 1355–1364. doi: 10.1056/nejmoa1602812

Coste, B., Mathur, J., Schmidt, M., Taryn, J., Earley, T. J., Ranade, S., et al. (2010). PIEZO1 and PIEZO2 are essential components of distinct mechanically activated cation channels. *Science* 330, 55–60. doi: 10.1126/science.1193270

Del Marmol, J. I., Touhara, K. K., Croft, G., and MacKinnon, R. (2018). PIEZO1 forms a slowly-inactivating mechanosensory channel in mouse embryonic stem cells. *eLife* 7:e33149. doi: 10.7554/eLife.33149

Dela Paz, N. G., and Frangos, J. A. (2018). Yoda1-induced phosphorylation of Akt and ERK1/2 does not require PIEZO1 activation. *Biochem. Biophys. Res. Commun.* 497, 220–225. doi: 10.1016/j.bbrc.2018.02.058

Dubin, A. E., and Patapoutian, A. (2010). Nociceptors: the sensors of the pain pathway. *J. Clin. Invest.* 120, 3760–3772. doi: 10.1172/JCI42843

Dubin, A. E., Schmidt, M., Mathur, J., Petrus, M. J., Xiao, B., Coste, B., et al. (2012). Inflammatory signals enhance PIEZO2-mediated mechanosensitive currents. *Cell Rep.* 2, 511–517. doi: 10.1016/j.celrep.2012.07.014

Eijkelkamp, N., Linley, J. E., Torres, J. M., Bee, L., Dickenson, A. H., Gringhuis, M., et al. (2013). A role for PIEZO2 in EPAC1-dependent mechanical allodynia. *Nat. Commun.* 4:1682. doi: 10.1038/ncomms2673

Florez-Paz, D., Bali, K. K., Kuner, R., and Gomis, A. (2016). A critical role for PIEZO2 channels in the mechanotransduction of mouse proprioceptive neurons. *Sci. Rep.* 6:25923. doi: 10.1038/srep25923

Gerhold, K. A., Pellegrino, M., Tsunozaki, M., Morita, T., Leitch, D. B., Tsuruda, P. R., et al. (2013). The star-nosed mole reveals clues to the molecular basis of mammalian touch. *PLos One* 8:e55001. doi: 10.1371/journal.pone.0055001

Hamill, O. P., and McBride, D. W. (1997). Mechano-gated channels in *Xenopus* oocytes: different gating modes enable a channel to switch from a phasic to a tonic mechanotransducer. *Biol. Bull.* 192, 121–122. doi: 10.2307/1542583

Hu, J., Milenkovic, N., and Lewin, G. R. (2006). The high threshold mechanotransducer: a status report. *Pain* 120, 3–7. doi: 10.1016/j.pain.2005.11.002

Kim, S. E., Coste, B., Chadha, A., Cook, B., and Patapoutian, A. (2012). The role of *Drosophila* PIEZO in mechanical nociception. *Nature* 483, 209–212. doi: 10.1038/nature10801

Kim, Y. S., Anderson, M., Park, K., Zeng, Q., Agarwal, A., Gong, C., et al. (2016). Coupled activation of primary sensory neurons contributes to chronic pain. *Neuron* 91, 1085–1096. doi: 10.1016/j.neuron.2016.07.044

Ko, F., Diaz, M., Smith, P., Emerson, E., Kim, Y. J., Krizek, T. J., et al. (1998). Toxic effect of capsaicin on keratinocytes and fibroblasts. *J. Burn Care Rehabil.* 19, 409–413. doi: 10.1097/00004630-199809000-00010

Lacroix, J. L., Botello-Smith, W. M., and Luo, Y. (2018). Probing the gating mechanism of the mechanosensitive channel PIEZO1 with the small molecule yoda1. *Nat. Commun.* 9:2029. doi: 10.1038/s41467-018-04405-3

Lawson, S. N., and Waddell, P. J. (1991). Soma neurofilament immunoreactivity is related to cell size and fibre conduction velocity in rat primary sensory neurons. *J. Physiol.* 435, 41–63. doi: 10.1113/jphysiol.1991.sp018497

Le Pichon, C. E., and Chesler, A. T. (2014). The functional and anatomical dissection of somatosensory subpopulations using mouse genetics. *Front. Neuroanat.* 8:21. doi: 10.3389/fnana.2014.00021

Lee, K. H., Chung, K., Chung, J. M., and Coggeshall, R. E. (1986). Correlation of cell body size, axon size, and signal conduction velocity for individually labeled dorsal root ganglion cells in the cat. *J. Comp. Neurol.* 243, 335–346. doi: 10.1002/cne.902430305

Lee, W., Leddy, H. A., Chen, Y., Lee, S. H., Zelenski, N. A., McNulty, A. L., et al. (2014). Synergy between PIEZO1 and PIEZO2 channels confers high-strain mechanosensitivity to articular cartilage. *Proc. Natl. Acad. Sci. U.S.A.* 111, E5114–E5122. doi: 10.1073/pnas.1414298111

Lukacs, V., Mathur, J., Mao, R., Bayrak-Toydemir, P., Procter, M., Cahalan, S. M., et al. (2015). Impaired PIEZO1 function in patients with a novel autosomal recessive congenital lymphatic dysplasia. *Nat. Commun.* 6:8329. doi: 10.1038/ncomms9329

Ma, S., Cahalan, S., LaMonte, G., Grubaugh, N. D., Zeng, W., Murth, S. E., et al. (2018). Common PIEZO1 allele in african populations causes RBC dehydration and attenuates plasmodium infection. *Cell* 173, 443–455. doi: 10.1016/j.cell.2018.02.047

Mahmud, A. A., Nahid, N. A., Nassif, C., Sayeed, M. S. B., Ahmed, M. U., Parveen, M., et al. (2016). Loss of the proprioception and touch sensation channel PIEZO2 in siblings with a progressive form of contractures. *Clin. Genet.* 91, 470–475. doi: 10.1111/cge.12850

Maksimovic, S., Nakatani, M., Baba, Y., Nelson, A. M., Marshall, K. L., Wellnitz, S. A., et al. (2014). Epidermal merkel cells are mechanosensory cells that tune mammalian touch receptors. *Nature* 509, 617–621. doi: 10.1038/nature13250

Maroto, R., Kurosky, A., and Hamill, O. P. (2012). Mechanosensitive channels in human prostate tumor cells. *Channels* 6, 290–307. doi: 10.4161/chan.21063

Mikhailov, N., Leskinenb, J., Fagerlunda, I., Poguzhelskayaa, E., Giniatullinaa, R., Gafurovc, O., et al. (2019). MS meningeal nociception via PIEZO channels: implications for pulsatile pain in migraine? *Neuropharm.* 149, 113–123. doi: 10.1016/j.neuropharm.2019.02.015

Murthy, S. E., Loud, M. C., Daou, I., Marshall, K. L., Schwaller, F., Kühnemund, J., et al. (2018). The mechanosensitive ion channel PIEZO2 mediates sensitivity to mechanical pain in mice. *Sci Transl. Med.* 10:eaat9897. doi: 10.1126/scitranslmed.aat9897

Pastar, I., Stojadinovic, O., and Tomic-Canic, M. (2008). Role of keratinocytes in healing of chronic wounds. *Surg. Tech. Int.* 17, 105–112.

Pfau, D. A., Klein, T., Putzer, D., Pogatzki-Zahn, E. M., Treede, R. D., and Mager, W. (2011). Analysis of hyperalgesia time courses in humans after painful electrical high-frequency stimulation identifies a possible transition from early to late LTP-like pain plasticity. *Pain* 152, 1532–1539. doi: 10.1016/j.pain.2011.02.037

Ranade, S. S., Woo, S. H., Dubin, A. E., Moshourab, R. A., Wetzel, C., Petrus, M., et al. (2014). PIEZO2 is the major transducer of mechanical forces for touch sensation in mice. *Nature* 516, 121–125. doi: 10.1038/nature13980

Richardson, J. D., and Vasko, M. R. (2002). Cellular mechanisms of neurogenic inflammation. *J. Pharmaol. Exp. Therap.* 302, 839–845. doi: 10.1124/jpet.102.032797

Sandkühler, J. (2009). Models and mechanisms of hyperalgesia and allodynia. *Physiol. Rev.* 89, 707–758. doi: 10.1152/physrev.00025.2008

Schwartz, E. S., Kim, H. Y., Wang, J., Lee, I., Klann, E., Chung, J. M., et al. (2009). Persistent pain is dependent on spinal mitochondrial antioxidant levels. *J. Neurosci.* 29, 159–168. doi: 10.1523/JNEUROSCI.3792-08.2009

Schwartz, E. S., Lee, I., Chung, K., and Chung, J. M. (2008). Oxidative stress in the spinal cord is an important contributor in capsaicin-induced mechanical secondary hyperalgesia in mice. *Pain* 138, 514–524. doi: 10.1016/j.pain.2008.01.029

Shipton, E. A. (2013). Skin Matters: identifying pain mechanisms and predicting treatment outcomes. *Neurol. Res. Internat.* 2013, 329–364. doi: 10.1155/2013/329364

Singhmar, P., Huo, X., Eijkelkamp, N., Berciano, S. R., Baameur, F., Mei, F. C., et al. (2016). Critical role for epac1 in inflammatory pain controlled by GRK2-mediated phosphorylation of epac1. *Proc. Nat. Acad. Sci. U.S.A.* 113, 3036–3041. doi: 10.1073/pnas.1516036113

Soria, B., Navas, S., Hmadcha, A., and Hamill, O. P. (2013). Single mechanosensitive and Ca2+-sensitive channel currents recorded from mouse and human embryonic stem cells. *J. Memb. Biol.* 246, 215–230. doi: 10.1007/s00232-012-9523-6

Spray, D. C., and Hanani, M. (2019). Gap junctions, pannexins and pain. *Neurosci. Lett.* 695, 46–52. doi: 10.1016/j.neulet.2017.06.035

Syeda, R., Xu, J., Dubin, A. E., Coste, B., Mathur, J., Huynh, T., et al. (2015). Chemical activation of the mechanotransduction channel PIEZO1. *eLife* 4:e07369.

Szczot, M., Liljencrantz, J., Ghitani, N., Barik, A., Lam, R., Thompson, J. H., et al. (2018). PIEZO2 mediates injury-induced tactile pain in mice and humans. *Sci. Transl. Med.* 10:eaat9892. doi: 10.1126/scitranslmed.aat9892

Torebjörk, H. E., Lundberg, L. E., and LaMotte, R. H. (1992). Central changes in processing of mechanoreceptive input in capsaicin-induced secondary hyperalgesia in humans. *J. Physiol.* 448, 765–780. doi: 10.1113/jphysiol.1992.sp019069

Torsney, C., and MacDermott, A. B. (2006). Disinhibition opens the gate to pathological pain signaling in superficial neurokinin 1 receptor-expressing neurons in rat spinal cord. *J. Neurosci.* 26, 1833–1843. doi: 10.1523/jneurosci.4584-05.2006

Usoskin, D., Furlan, A., Islam, S., Abdo, H., Lönnerberg, P., Lou, D., et al. (2015). Unbiased classification of sensory neuron types by large-scale single-cell RNA sequencing. *Nat. Neuro.* 18, 145–153. doi: 10.1038/nn.3881

Vandewauw, I., De Clercq, K., Mulier, M., Held, K., Pinto, S., Van Ranst, N., et al. (2018). A TRP channel trio mediates acute noxious heat sensing. *Nature* 555, 662–666. doi: 10.1038/nature26137

Vedove, A. D., Storbeck, M., Heller, R., Hölker, I., Hebbar, M., Shukla, A., et al. (2016). Biallelic loss of proprioception-related PIEZO2 causes muscular atrophy with perinatal respiratory distress, arthrogryposis, and scoliosis. *Am. J. Hum. Gen.* 99, 1206–1216. doi: 10.1016/j.ajhg.2016.09.019

Wang, F., Flanagan, J., Su, N., Wang, L. C., Bui, S., Nielson, A., et al. (2012). RNAscope: a novel in situ RNA analysis platform for formalin-fixed, paraffin-embedded tissues. *J. Mol. Diagn.* 14, 22–29. doi: 10.1016/j.jmoldx.2011.08.002

Woo, S. H., Lukacs, V., de Nooij, J. C., Zaytseva, D., Criddle, C. R., Francisco, A., et al. (2015). PIEZO2 is the principal mechanotransduction channel for proprioception. *Nat. Neurosci.* 18, 1756–1762. doi: 10.1038/nn.4162

Woo, S. H., Ranade, S., Weyer, A. D., Dubin, A. E., Baba, Y., Qiu, Z., et al. (2014). PIEZO2 is required for Merkel-cell mechanotransduction. *Nature* 509, 622–626. doi: 10.1038/nature13251

Woolf, C. J., and Ma, Q. (2007). Nociceptors–noxious stimulus detectors. *Neuron* 55, 353–364. doi: 10.1016/j.neuron.2007.07.016

Xie, W., Strong, J. A., Meij, J. T. A., Zhang, J. M., and Yu, L. (2005). Neuropathic pain: early spontaneous afferent activity is the trigger. *Pain* 116, 243–256. doi: 10.1016/j.pain.2005.04.017

Yang, H., Li, K., Lei, X., Xu, J., Yang, J., and Zhang, J. (2016). The potential role of PIEZO2 in the mediation of visceral sensation. *Neurosci. Lett.* 630, 158–163. doi: 10.1016/j.neulet.2016.07.058

Zeng, W. Z., Marshall, K. L., Min, S., Daou, I., Chapleau, M. W., Abboud, F. M., et al. (2018). PIEZOs mediate neuronal sensing of blood pressure and the baroreceptor reflex. *Science* 362, 464–467. doi: 10.1126/science.aau6324

Zhang, M., Wang, Y., Geng, J., Zhou, S., and Xiao, B. (2019). Mechanically-activated PIEZO2 channels mediate touch and suppress acute mechanical pain response in mice. *Cell Rep.* 26, 1419–1431. doi: 10.1016/j.celrep.2019.01.056

Conflict of Interest Statement: The authors declare that the research was conducted in the absence of any commercial or financial relationships that could be construed as a potential conflict of interest.

frontiers in Molecular Neuroscience

ORIGINAL RESEARCH
published: 22 November 2019
doi: 10.3389/fnmol.2019.00283

Tissue Specific Reference Genes for MicroRNA Expression Analysis in a Mouse Model of Peripheral Nerve Injury

Theodora Kalpachidou†, Kai K. Kummer†, Miodrag Mitrić and Michaela Kress*

Institute of Physiology, Department of Physiology and Medical Physics, Medical University of Innsbruck, Innsbruck, Austria

MicroRNAs (miRNAs) have emerged as master switch regulators in many biological processes in health and disease, including neuropathy. miRNAs are commonly quantified by reverse transcription quantitative real-time polymerase chain reaction (RT-qPCR), usually estimated as relative expression through reference genes normalization. Different non-coding RNAs (ncRNAs) are used for miRNA normalization; however, there is no study identifying the optimal reference genes in animal models for peripheral nerve injury. We evaluated the stability of eleven ncRNAs, commonly used for miRNA normalization, in dorsal root ganglia (DRG), dorsal horn of the spinal cord (dhSC), and medial prefrontal cortex (mPFC) in the mouse spared nerve injury (SNI) model. After RT-qPCR, the stability of each ncRNA was determined by using four different methods: BestKeeper, the comparative delta-Cq method, geNorm, and NormFinder. The candidates were rated according to their performance in each method and an overall ranking list was compiled. The most stable ncRNAs were: sno420, sno429, and sno202 in DRG; sno429, sno202, and U6 in dhSC; sno202, sno420, and sno142 in mPFC. We provide the first reference genes' evaluation for miRNA normalization in different neuronal tissues in an animal model of peripheral nerve injury. Our results underline the need for careful selection of reference genes for miRNA normalization in different tissues and experimental conditions. We further anticipate that our findings can be used in a broad range of nerve injury related studies, to ensure validity and promote reproducibility in miRNA quantification.

Keywords: miRNA normalization, ncRNA, spared nerve injury, dorsal root ganglia, spinal dorsal horn, medial prefrontal cortex

OPEN ACCESS

Edited by:
Sung Jun Jung,
Hanyang University, South Korea

Reviewed by:
Qiwei Yang,
The Second Affiliated Hospital of Jilin University, China
Eva Maria Jimenez-Mateos,
Trinity College Dublin, Ireland

****Correspondence:***
Theodora Kalpachidou
theodora.kalpachidou@i-med.ac.at;
tkalpachidou@gmail.com

† These authors have contributed equally to this work and share first authorship

Received: *25 June 2019*
Accepted: *06 November 2019*
Published: *22 November 2019*

Citation:
Kalpachidou T, Kummer KK, Mitrić M and Kress M (2019) Tissue Specific Reference Genes for MicroRNA Expression Analysis in a Mouse Model of Peripheral Nerve Injury. Front. Mol. Neurosci. 12:283. doi: 10.3389/fnmol.2019.00283

INTRODUCTION

MicroRNAs (miRNAs) are small non-coding RNAs (ncRNAs) of approximately 22 nucleotides length, which can regulate gene expression by translational inhibition or promotion of degradation of their target mRNAs (Eulalio et al., 2008). miRNAs play fundamental roles in biological processes, such as cell proliferation, differentiation, and survival and are crucial for normal developmental processes, homeostasis, as well as a plethora of diseases and pathologies (Vidigal and Ventura, 2015). Accumulating data suggest that miRNA expression patterns are

deregulated following peripheral nerve injury (Kress et al., 2013; Sakai and Suzuki, 2015; Jiangpan et al., 2016; Lopez-Gonzalez et al., 2017). Furthermore, several studies have identified miRNAs that are upregulated upon peripheral nerve injury and can promote regeneration (Strickland et al., 2011; Zhou et al., 2012; Wu and Murashov, 2013; Motti et al., 2017), rendering miRNAs attractive potential targets for therapeutic interventions (Jiangpan et al., 2016; Ghibaudi et al., 2017; Zhang J. et al., 2018). To this end, in depth mechanistic understanding of the role of up- and downregulated miRNAs in human pathologies and mouse models of the respective disorders is increasing, which in turn necessitates the reliable and reproducible quantification of miRNA expression levels.

miRNA expression is commonly assessed by reverse transcription quantitative real-time polymerase chain reaction (RT-qPCR), either as a primary method or for the validation of miRNA profiling results (e.g., miRNA microarrays, small RNA sequencing). RT-qPCR highly relies on appropriate normalization procedures, usually achieved by means of relative expression to one or multiple reference genes (Bustin et al., 2009). In order to qualify as reference genes, the expression of such genes needs to remain stable when exposed to specific experimental conditions (Kozera and Rapacz, 2013). It is commonly accepted that no gene exists for which expression levels remain unaltered under every experimental condition and in every tissue or cell line. The importance of using appropriate reference genes is stressed in the Minimum Information for publication of Quantitative real-time PCR Experiments (MIQE) guidelines, which state that "normalization against a single reference gene is not acceptable unless the investigators present clear evidence for the reviewers that confirms its invariant expression under the experimental conditions described. The optimal number and choice of reference genes must be experimentally determined and the method reported" (Bustin et al., 2009).

Based on these considerations, several publications have analyzed the stability of potential reference genes for miRNA expression normalization in different human, animal, and plant studies (Bouhaddioui et al., 2014; Matouskova et al., 2014; Ferdous et al., 2015; Wu et al., 2016; Babion et al., 2017; Mase et al., 2017). To our knowledge, the present study for the first time evaluated potential reference genes in the mouse spared nerve injury (SNI) model, a commonly used, robust and reproducible animal model of peripheral nerve injury (Decosterd and Woolf, 2000). We analyzed the expression of 11 ncRNAs, which are frequently used as reference genes, with commercially available assays in the dorsal root ganglia (DRG) and dorsal horn of the spinal cord (dhSC) ipsilateral to the injury as well as the medial prefrontal cortex (mPFC) contralateral to the injury, using four different statistical methods: BestKeeper (Pfaffl et al., 2004), the comparative delta-Cq method (Silver et al., 2006), geNorm (Vandesompele et al., 2002), and NormFinder (Andersen et al., 2004). Upon rating each ncRNA according to its performance in the different methods, we compiled an overall ranking list and propose the most appropriate reference genes for assessing miRNA expression in the SNI mouse model in three neuronal tissues.

MATERIALS AND METHODS

Animals

In total, 16 male, 8–12 weeks old C57Bl/6J mice (Janvier Labs, France) were used for the experiments. Animals were kept under standard pathogen free (SPF) conditions, at 24°C on a 12 h light/dark cycle and had free access to autoclaved pelleted food and water. All mice were treated in accordance with the Ethics Guidelines of Animal Care (Medical University of Innsbruck), the European Communities Council Directive of 22nd September 2010 on the protection of animals used for scientific purposes (2010/63/EU) and all procedures were approved by the Austrian National Animal Experiment Ethics Committee of the Austrian Bundesministerium für Wissenschaft und Forschung (permit number BMWF-66.011/0054-WF/V/3b/2015).

Spared Nerve Injury Model

Mice were divided in three groups, non-treated (n = 5), sham (n = 6), and SNI (n = 5). The SNI model was adopted from Decosterd and Woolf (2000). Briefly, mice were anesthetized with a mixture of xylazine (10 mg/kg, AniMedica, Germany) and ketamine (100 mg/kg, Graeub, Switzerland). The skin of the lateral surface of the left thigh was incised and the sciatic nerve was exposed. For the SNI procedure, the common peroneal and the tibial nerves were ligated with 4-0 vicryl (Sh-1 plus, Ethicon, Austria) and a portion of approximately 1–2 mm length was excised, leaving the sural nerve intact. Mice subjected to sham surgery had their sciatic nerve exposed but not lesioned. After surgery, the skin was sutured using 4-0 vicryl and mice were placed on a heat block adjusted to 37°C until recovery. Non-treated mice were not subjected to any treatment.

Tissue Collection

Non-treated, sham and SNI mice 7 days post-surgery (only for sham and SNI mice) were deeply anesthetized with isoflurane (Forane, Abbott, United Kingdom) and euthanized by decapitation. Lumbar ipsilateral L3-L5 DRG and dhSC as well as contralateral mPFC were microdissected, snap-frozen in liquid nitrogen, and stored at –80°C until use.

RNA Extraction

RNA extraction was performed using peqGOLD TriFast reagent (Peqlab Biotechnologie, Germany), according to the protocol provided by the manufacturer [chloroform (C2432) and absolute ethanol (107017) were obtained from Merck, United States]. The air-dried RNA pellets were diluted in nuclease free water (R0582, ThermoFisher Scientific, United States). RNA quantity was estimated using Nanodrop 2000 (ThermoFisher Scientific) and RNA integrity [RNA integrity number (RIN)] was assessed using 2100 Bioanalyzer (Agilent Technologies, United States) in the deep-sequencing core facility of the Medical University of Innsbruck.

Reverse Transcription and Quantitative Real-Time PCR

We evaluated the stability of all ncRNAs, suggested as controls and available by Thermo Fisher Scientific. The expression of small nucleolar (snoRNA) and small nuclear (snRNA) RNAs, as potential reference genes, was quantified using Taqman MicroRNA Control Assays, which through a two-step protocol ensure high specificity and sensitivity and do not require prior DNase treatment of the RNA template, since the stem-loop transcription amplifies only the mature sequence (Mestdagh et al., 2008). Reverse transcription and qPCR reactions were prepared according to the protocol provided by the supplier. Briefly, each reverse transcription reaction contained 10 ng of total RNA, 1X reverse transcription buffer, 5.5 mM $MgCl_2$ (GeneAmp® 10X PCR Buffer II and $MgCl_2$, #N8080130), 1 mM dNTPs, RNase inhibitor (#N8080119), 50 units of MultiScribe™ Reverse Transcriptase (#4311235), and 1X RT specific primers (**Table 1**), in a final volume of 15 μL, adjusted with nuclease free water (#R0582). The RT program was: 30 min at 16°C, 30 min at 42°C, 5 min at 85°C, followed by a holding step at 4°C. After reverse transcription, reactions were stored at –20°C until next day. Each qPCR reaction contained 1.33 μL of the RT product, 1X TaqMan® Universal Master Mix II, no UNG (#44440049), 1X of the appropriate assay (**Table 1**), and nuclease free water up to a final volume of 20 μL. Reactions for each sample were prepared as technical duplicates, alongside reverse transcription non-template controls, loaded on MicroAmp Fast Optical 96-well reaction plates (#4346906) and placed in the 7500 Fast RT-PCR system (all reagents for RT-qPCR were from ThermoFisher Scientific). The PCR cycle protocol was: 10 min at 95°C, 40 two-step cycles of 15 s at 95°C, and 1 min at 60°C. In order to account for potential methodological variabilities, all RT (day 1) and qPCR reactions (day 2) per tissue assessed were processed on the same day. The MIQE checklist for authors, reviewers, and editors can be found in **Supplementary Table S1**.

Data Analysis

Results were extracted from the 7500 Software v2.3 (ThermoFisher Scientific), by manually setting the threshold at 0.1 (single threshold method) for all amplicons and keeping the automatic baseline (baseline start cycle: 3, baseline end cycle: 15). Additionally, raw amplification data were imported to LinRegPCR program (Ramakers et al., 2003; Ruijter et al., 2009, 2015; Tuomi et al., 2010), which performs a baseline correction of the amplification data, determines a window of linearity, and through a linear regression analysis determines the qPCR efficiency and the Cq value per reaction, in order to estimate the mean PCR efficiency per primer set or assay [52]. The efficiencies for each amplicon were calculated using LinRegPCR (v2014) for hydrolysis probes with the following parameters: window of linearity: four points; exclude no plateau samples; include efficiency outlier samples; log-linear phase criterion: strictly continuous log-linear phase. Mean Cq values for each sample and ncRNA were calculated as the average of the technical duplicates. The stability of all evaluated ncRNAs was estimated based on the Cq values obtained from single threshold settings and LinRegPCR program adjustments, by using four different statistical approaches that are commonly used for stability assessment of reference genes: BestKeeper (Pfaffl et al., 2004), the comparative delta-Cq method (Silver et al., 2006), geNorm (Vandesompele et al., 2002), and NormFinder (Andersen et al., 2004).

For BestKeeper (Pfaffl et al., 2004), the appropriate reference genes need to exhibit low variability and comparable levels of expression. Variability was defined by the standard deviation (SD) of mean Cq values and low SD values corresponded to stable ncRNAs. Candidates with SD > 1 were considered inappropriate for normalization. Similar levels of expression were explored using Pearson's linear correlation, by comparing each ncRNA with the BestKeeper index (BKI), which was the geometric mean of the mean Cq values of all evaluated ncRNAs. The closer the correlation was to 1, the more stably an ncRNA was considered to be expressed. A mean ranking score for each ncRNA was calculated by averaging the scores obtained by SD and correlation with the BKI rankings.

In the comparative delta-Cq method (Silver et al., 2006), all pairs of ncRNAs were compared with each other, according to their Cq differences (ΔCq). Variability was determined by calculating the average SD between the pairwise comparisons of all ncRNAs and a low average SD indicated increased stability.

GeNorm (Vandesompele et al., 2002) calculated the average expression stability M, which represents the average pairwise variation of each evaluated ncRNA compared to all the rest. Low M values suggested that the ncRNAs expression was stable. Subsequently, geNorm performed repeated stepwise exclusions (by repeatedly omitting the candidate with the worst M value) and identified the most stable pair of ncRNAs. Additionally, geNorm identified the optimal number of reference genes, by calculating the pairwise variation coefficient (V value).

NormFinder (Andersen et al., 2004), besides calculating the variation of expression, estimated the variation between groups. Specifically, for each ncRNA the stability value ρ was estimated as well as the intra- and inter-group variations. The lowest ρ values represented more stably expressed candidates. Furthermore, a stably expressed ncRNA needed to exhibit intra- and inter-group variations as close as possible to zero.

Each ncRNA was subsequently ranked according to its performance in each of the four different methods (with 1 indicating the most stable ncRNA). The overall stability of each candidate was estimated by calculating the mean of the rankings provided by each statistical approach.

The expression levels of miR-21a-5p were quantified in the DRG of non-treated, sham, and SNI mice and expressed as fold changes relative to the respective expression in the non-treated mice using the $2^{-\Delta\Delta Cq}$ method. ncRNAs were assessed for their suitability for the quantification of miR-21a-5p in DRG by using as a reference gene(s): (1) three (sno420, sno429, and sno202) and two (sno420 and sno429) most stable ncRNAs from the overall ranking, (2) two most stable pair of ncRNAs as suggested by geNorm (sno202 and sno420) and Normfinder (sno234 and sno429), and (3) each ncRNA as a single normalizer.

For statistical data analyses, GraphPad Prism 7.00 and IBM SPSS Statistics 21 were used. Statistical tests used were specified in

TABLE 1 | Details of the ncRNA assays used.

Assay name	Assay ID	Official symbol	Official name	Also known as	RNA class
snoRNA55	001228	Snord110	small nucleolar RNA, C/D box 110	MBII-55	Small nucleolar RNA
snoRNA135	001230	Snord65	small nucleolar RNA, C/D box 65	MBII-135; snoRNA135	Small nucleolar RNA
snoRNA142	001231	Snord66	small nucleolar RNA, C/D box 66	MBII-142; snoRNA142	Small nucleolar RNA
snoRNA202	001232	Snord68	small nucleolar RNA, C/D box 68	MBII-202	Small nucleolar RNA
snoRNA234	001234	Snord70	small nucleolar RNA, C/D box 70	MBII-234; snoRNA234	Small nucleolar RNA
snoRNA251	001236	Snord85	small nucleolar RNA, C/D box 85	Z50; MBII-251	Small nucleolar RNA
snoRNA292	001242	Snord42a	small nucleolar RNA, C/D box 42A	U42A; MBII-292	Small nucleolar RNA
snoRNA412	001243	Snord45b	small nucleolar RNA, C/D box 45B	MBII-412	Small nucleolar RNA
snoRNA420	001239	Snord99	small nucleolar RNA, C/D box 99	MBII-420	Small nucleolar RNA
snoRNA429	001240	Snord100	small nucleolar RNA, C/D box 100	Z51; MBII-429	Small nucleolar RNA
U6 snRNA	001973	Rnu6	U6 small nuclear RNA	–	Small nuclear RNA
hsa-miR-21	000397	Mir21a	microRNA 21a miRBase: MIMAT0000530	mmu-miR21a-5p	Small non-coding RNA

the text or in their respective figures or tables. Statistical analysis for miR-21a-5p expression was performed using one-way analysis of variance (ANOVA) with the group of animals (non-treated, sham, and SNI) as the independent factor, followed by Tukey's multiple comparison test, when appropriate, in order to identify differences between groups. The level of statistical significance was predefined at $p < 0.05$. Graphs were plotted in GraphPad Prism 7.00 and illustrated in CorelDRAW X7.

RESULTS

RNA Quantity and Integrity

RNA quantity and integrity varied in between samples and tissues (**Supplementary Table S2**). For DRG the median total RNA concentration was 102.3 ng/μL with an interquartile range (IQR) of 88.85–122.6 ng/μL, for dhSC the median RNA concentration was 127.8 ng/μL with an IQR of: 106.2–176.2 ng/μL, and for mPFC the median RNA concentration was 68.35 ng/μL with an IQR of: 58.43–88.95 ng/μL. Analysis of integrity provided median values of RIN = 6.85 (IQR: 6.45–7.55) in DRG, RIN = 7.55 (IQR: 6.825–8.0) in dhSC, and RIN = 7.35 (IQR: 7.1–7.75) in mPFC.

qPCR Efficiencies

Mean qPCR efficiencies for all evaluated ncRNAs were calculated by the LinRegPCR program (**Supplementary Table S3**). R^2 values for all amplicons, as calculated by LinRegPCR, were > 0.998. Correlation coefficients for RIN values and amplicons' efficiencies were not statistically significant (**Supplementary Table S4**). Furthermore, no statistically significant difference was observed for individual assay performance on different experimental days (**Supplementary Table S5A**) or in different experimental groups (**Supplementary Table S5B**), suggesting that all assays performed similarly in all experimental groups, experimental days, and tissues.

Cq Values Distribution

After setting the common threshold at 0.1 and after importing the raw amplification data into LinRegPCR, we assessed the raw Cq values (**Figures 1A–C**). All ncRNAs were successfully amplified and both settings provided similar results in DRG, dhSC, and mPFC. In all three tissues, the most abundantly expressed ncRNA was sno202, followed by U6, whereas the least abundant ncRNA was sno412 (**Figures 1A–C** and **Supplementary Table S6**). We further analyzed the SDs of the technical duplicates per sample and amplicon, since reproducibility is critically important for RT-qPCR quantification (**Figures 1D–F** and **Supplementary Table S6**). SDs for technical replicates ≤0.167 are required to detect a 2-fold change of expression in 99.7% of cases (Applied Biosystems, 2016). Since sno55 exhibited SDs > 0.167 in the technical duplicates in all three tissues, it was excluded from further analysis. Likewise, sno412 was excluded from assessment in the mPFC. In DRG and dhSC, U6 also showed SDs > 0.167 according to LinRegPCR settings, however, was kept for further analysis, since the common threshold setting suggested appropriate variability in technical replicates.

Bestkeeper

Data extracted using both the common threshold and LinRegPCR adjustments, provided similar results in BestKeeper evaluation (**Figure 2** and **Supplementary Table S7**). In DRG (**Figure 2A** and **Supplementary Table S7A**), U6 showed the lowest SD (SD = 0.336 for the common threshold and 0.341 for LinRegPCR) across non-treated, sham, and SNI mice, whereas sno251 showed the highest SD (SD = 0.602 for the common threshold and 0.604 for LinRegPCR). All SDs were below the proposed cut-off value of < 1 for the exclusion of a candidate. Correlation analysis between each ncRNA and BKI revealed $r > 0.92$ for sno202, sno420, and sno429, whereas sno135, sno292, and U6 had r values <0.67. In the dhSC (**Figure 2B** and **Supplementary Table S7B**), sno429 exhibited the lowest SD (0.138 and 0.113, according to the common threshold and LinRegPCR, respectively) and sno234 the highest SD (0.333 using the common threshold and 0.325 according to LinRegPCR). r values for most ncRNAs were surprisingly low and p values were not significant for sno135, sno142, sno251, sno412, and sno429, indicating no correlation with the BKI. Out of the ncRNAs, which significantly correlated with the BKI, the best

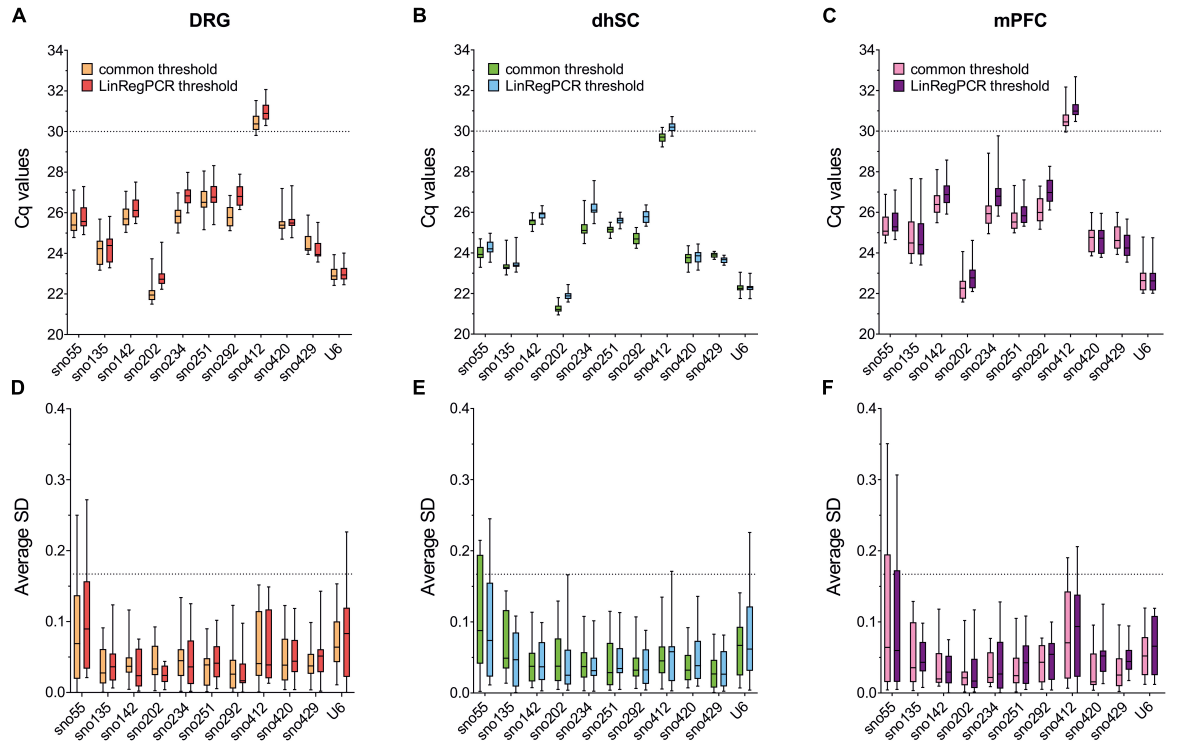

FIGURE 1 | Raw Cq values and average standard deviations of technical duplicates for all evaluated ncRNAs in DRG **(A,D)**, dhSC **(B,E)**, and mPFC **(C,F)** of non-treated (n = 5), sham (n = 6), and SNI (n = 5) mice, as estimated by setting a common threshold (0.1) and by using LinRegPCR software. Values are presented as boxplots, representing upper quartile, median, and lower quartile, whereas whiskers depict minimum and maximum values. The dotted line in **A–C** is set at Cq = 30 and in **D–F** at 0.167. DRG: dorsal root ganglia, dhSC: dorsal horn of the spinal cord, mPFC: medial prefrontal cortex, Cq: quantitation cycle, SD: standard deviation.

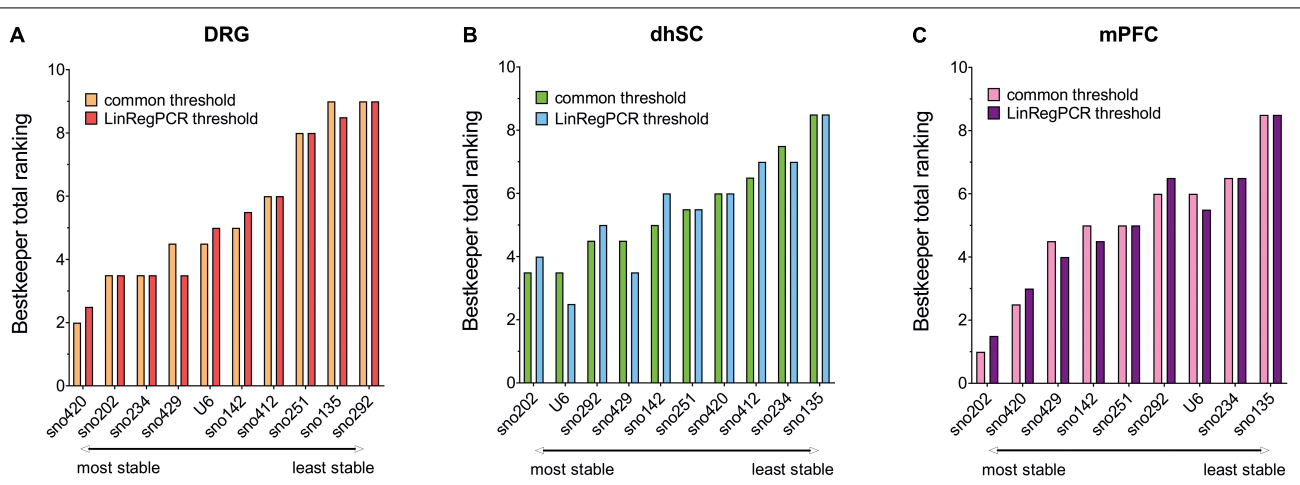

FIGURE 2 | Total ranking obtained from Bestkeeper for each evaluated ncRNA **(A)**, dhSC **(B)**, and mPFC **(C)** of non-treated (n = 5), sham (n = 6), and SNI (n = 5) mice, as estimated by setting a common threshold (0.1) and by using LinRegPCR software. Total ranking was calculated by averaging the rankings achieved by each ncRNA in SD and BKI correlation coefficient. DRG: dorsal root ganglia, dhSC: dorsal horn of the spinal cord, mPFC: medial prefrontal cortex.

correlation was determined for sno292 (r = 0.738), followed by U6 (r = 0.732) for the common threshold, whereas for LinRegPCR processed data, the best correlation was observed for U6 (r = 0.777), followed by sno292 (r = 0.735). In the mPFC (**Figure 2C** and **Supplementary Table S7C**), sno202 showed the lowest SD (0.494 for the common threshold and 0.498 for LinRegPCR) and sno135 the highest SD (0.900 for the common threshold and 0.905 for LinRegPCR). Furthermore, in the data normalized with the common threshold, sno202 exhibited the highest correlation (r = 0.918) with the BKI, whereas in the

LinRegPCR processed data, the best correlation was observed for sno429 ($r = 0.923$).

Comparative Delta-Cq Method

The comparative delta-Cq method provided similar results for both common threshold and LinRegPCR processed data (see **Figure 3** and **Supplementary Table S8** for details). In DRG, the most stable ncRNA was sno429 (with a ΔCq SD = 0.398 in the common threshold and 0.388 in LinRegPCR), whereas sno135 was the least stable, with ΔCq SD > 0.66 (**Figure 3A** and **Supplementary Table S8A**). In dhSC, sno429 showed the lowest ΔCq SD (0.322 in the common threshold and 0.332 in LinRegPCR) and sno234 the highest (0.529 in the common threshold and 0.524 in LinRegPCR; **Figure 3B** and **Supplementary Table S8B**). Overall, in the mPFC all ncRNAs had higher ΔCq SDs (**Figure 3C** and **Supplementary Table S8C**). Among them, sno202 displayed the highest stability (with a ΔCq SD = 0.521 in the common threshold and equal to 0.522 in LinRegPCR processed data) and sno135 the lowest (ΔCq SD = 0.947 in the common threshold and 0.956 in LinRegPCR data).

GeNorm

According to the developers' recommendations, the M values should not exceed 1.5 and all ncRNAs in all tissues analyzed with both common threshold and LinRegPCR settings met this requirement. Initial M values (with all ncRNAs included in the analysis), as computed by geNorm are reported in **Supplementary Table S9**. After step-wise exclusion of the worst ncRNA and pairwise variation for the determination of the optimal number of ncRNAs for normalization, the average expression stability of the remaining candidates was determined (**Figure 4**). In DRG, sno135 was identified as the least stable ncRNA; whereas the sno202/sno420 pair was the most stable (**Figure 4A**). In the dhSC, sno234 showed the lowest and the sno251/sno429 pair the highest stability (**Figure 4B**). In the mPFC, sno135 was determined as the least stable ncRNA and the sno142/sno202 pair as the most stable (**Figure 4C**). Pairwise variation analysis showed that in all cases the V values were below 0.15, suggesting that the best pair of ncRNAs would already be sufficient for appropriate normalization (**Figures 4D–F**).

NormFinder

Stability values ρ, inter- and intra-group variability for all ncRNAs, were evaluated (**Figure 5**; detailed data are provided in **Supplementary Table S10**). Both threshold settings provided similar ranking results: In DRG, the lowest ρ value was observed for sno420 when using the common threshold (ρ = 0.121) and sno429 when using LinRegPCR (ρ = 0.090; **Figures 5A,B**). The highest ρ value was observed for sno292 (ρ = 0.306 for the common threshold and ρ = 0.265 with LinRegPCR). The sno234/sno429 pair was identified as the best pair combination (ρ = 0.069 and ρ = 0.048, respectively for the common threshold and LinRegPCR settings; **Table 2**). In the dhSC, the most stable ncRNA was sno429 (ρ = 0.071 using the common threshold and ρ = 0.077 using LinRegPCR; **Figures 5C,D**) and the best pair combination sno429/U6 (ρ = 0.062 for both settings; **Table 2**), whereas sno234 exhibited the worst performance (ρ = 0.158 for both settings). In the mPFC, the setting of a common threshold revealed that sno142 was the most stable ncRNA (ρ = 0.113), whereas sno420 showed the best performance when using LinRegPCR (ρ = 0.088; **Figures 5E,F**). The most stable pair was sno202/sno420 (ρ = 0.078) for the common threshold and sno142/sno420 (ρ = 0.070) for LinRegPCR (**Table 2**). Both the common threshold and LinRegPCR settings identified sno135 as the least stable ncRNA (ρ = 0.374 for the common threshold and ρ = 0.317 for LinRegPCR).

Overall Ranking of Potential Reference Genes for the Different Neuronal Tissues

Each potential reference gene was assigned a rank, according to its performance (1 was assigned to the most stable ncRNA) in each analysis. For BestKeeper analysis, ncRNAs were ranked based on both their SD and correlation with the BKI. Finally,

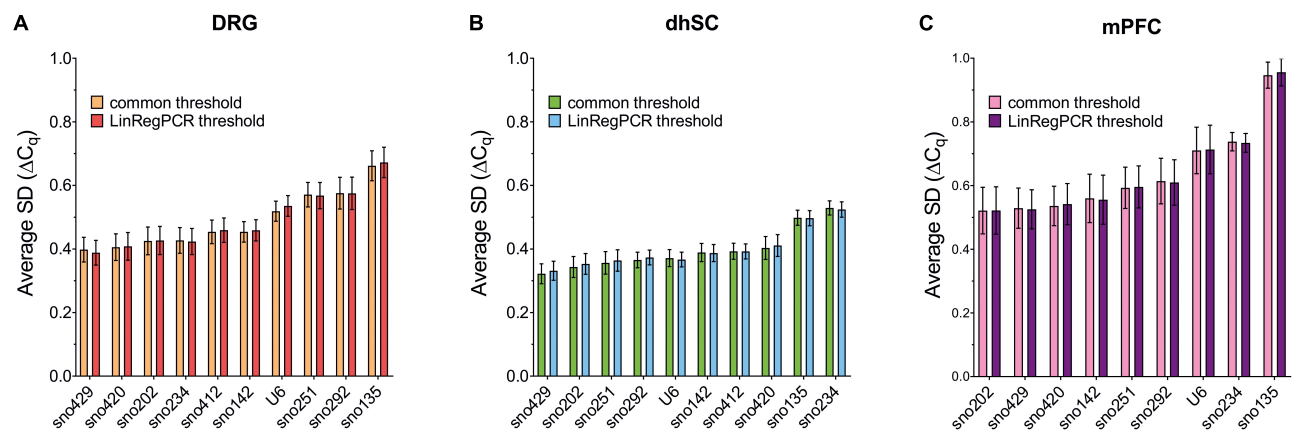

FIGURE 3 | Average standard deviation (SD) of the Cq differences (ΔCq) computed for each evaluated ncRNA vs all the remaining ncRNAs (comparative delta-Cq method) in DRG **(A)**, dhSC **(B)**, and mPFC **(C)** of non-treated ($n = 5$), sham ($n = 6$), and SNI ($n = 5$) mice, as estimated by setting a common threshold (0.1) and by using LinRegPCR software. DRG: dorsal root ganglia, dhSC: dorsal horn of the spinal cord, mPFC: medial prefrontal cortex, SD: standard deviation.

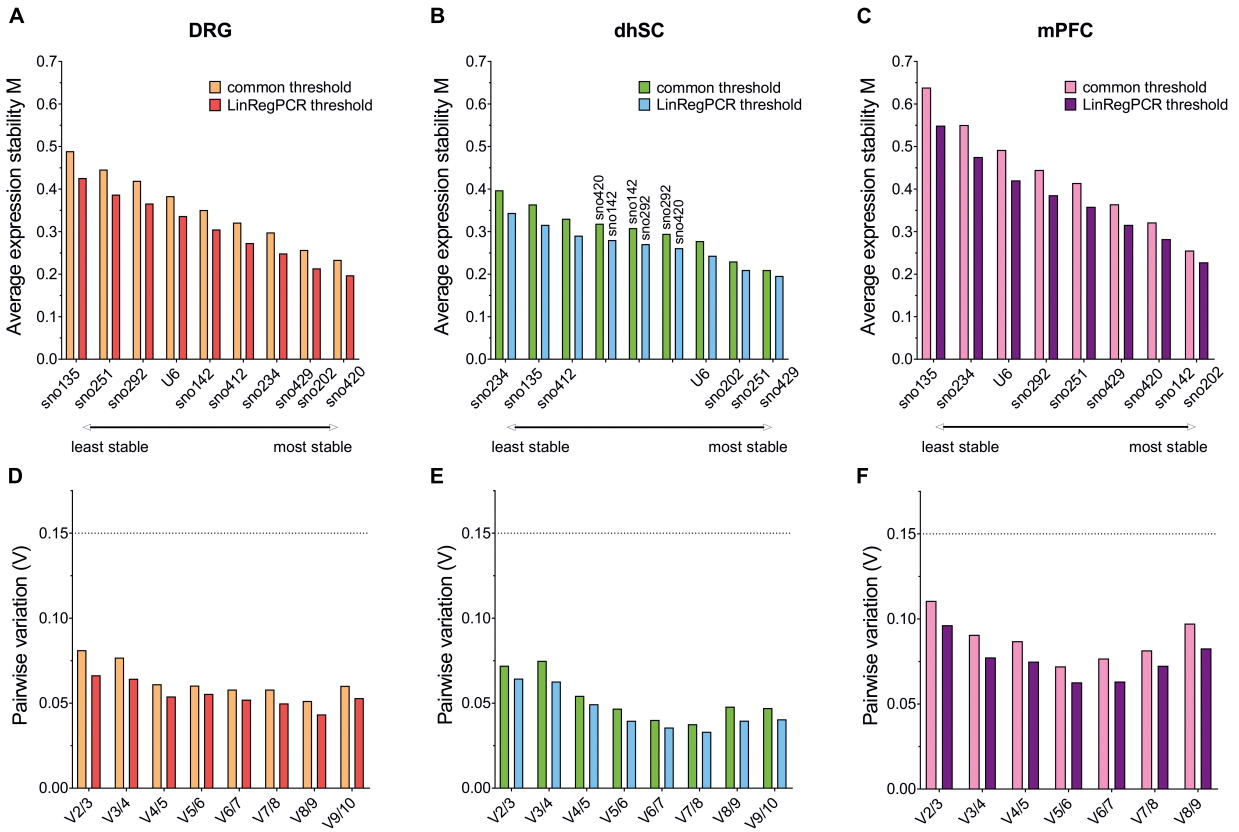

FIGURE 4 | Average expression stability of the remaining ncRNAs after stepwise exclusion of the least stable candidate (upper panel) and pairwise variation analysis (lower panel), as calculated by geNorm for all ncRNAs in DRG **(A,D)**, dhSC **(B,E)**, and mPFC **(C,F)** of non-treated (n = 5), sham (n = 6), and SNI (n = 5) mice, as estimated by setting a common threshold (0.1) and by using LinRegPCR software. The dotted line represents a pairwise variability of 0.15. DRG: dorsal root ganglia, dhSC: dorsal horn of the spinal cord, mPFC: medial prefrontal cortex.

we calculated the arithmetic mean and compiled an overall ranking list (**Figure 6** and **Table 3**). Since all four methods employed for assessing the stability of the ncRNAs, and their potential as reference genes, were taken into account as of equal importance, we did not use the geometric mean as it indicates the tendency of a set of values and dampens the effect of extreme values. Nevertheless, the rating was also calculated using the geometric mean and only sno251 in the dhSC for the common threshold exhibited a slightly different ranking (one rank higher), compared to the ranking obtained by using the arithmetic mean (**Supplementary Table S11**). Both the common threshold and LinRegPCR settings revealed the same three ncRNAs as the most stable and the same two candidates as the least stable, which, however, were different between the three neuronal tissues. Specifically, in DRGs, sno420, sno429, and sno202 ranked as the top three stable ncRNAs, whereas the lowest stability was observed for sno135, sno292, and sno251 (**Figure 6A**). In the dhSC, sno429, sno202, and U6 had the best stability, whereas sno234 and sno135 were the most variably expressed ncRNAs (**Figure 6B**). In the mPFC, the best three candidates were sno202, sno420, and sno142, whereas the least stable ncRNAs were sno135, sno234, and U6 (**Figure 6C**). The overall ranking for DRG and mPFC resembled the ranking provided by geNorm analysis. Furthermore, the overall ranking did not substantially differ between the common threshold and LinRegPCR datasets.

Reference Gene Selection Affects Outcome of miR-21a-5p Quantification

The ranked ncRNAs were assessed for their suitability to quantify miR-21a-5p, which is upregulated in DRG after peripheral nerve injury (Strickland et al., 2011; Zhou et al., 2015; Hori et al., 2016; Chang et al., 2017; Karl et al., 2017; Simeoli et al., 2017; Zhang Z. J. et al., 2018). miR-21a-5p was found upregulated in the SNI group when three (sno420/sno429/sno202; $F_{2,9}$ = 10.72, p = 0.0042; non-treated vs. SNI p = 0.0058, sham vs. SNI p = 0.0110; **Figure 7A**, left panel) or two (sno420/sno429; $F_{2,9}$ = 12.05, p = 0.0028; non-treated vs. SNI p = 0.0035, sham vs. SNI p = 0.0097; **Figure 7A**, right panel) most stable ncRNAs from the overall ranking list were used as reference genes. The most stable pair of genes as computed by geNorm (sno202/sno420; $F_{2,9}$ = 9.781, p = 0.0055; non-treated vs. SNI p = 0.0086, sham vs. SNI p = 0.0121; **Figure 7B**) and NormFinder (sno234/sno429; $F_{2,9}$ = 24.34, p = 0.0002; non-treated vs. SNI p = 0.0003, sham vs. SNI p = 0.0009; **Figure 7C**) provided similar results. However, when U6 was used as a normalizer,

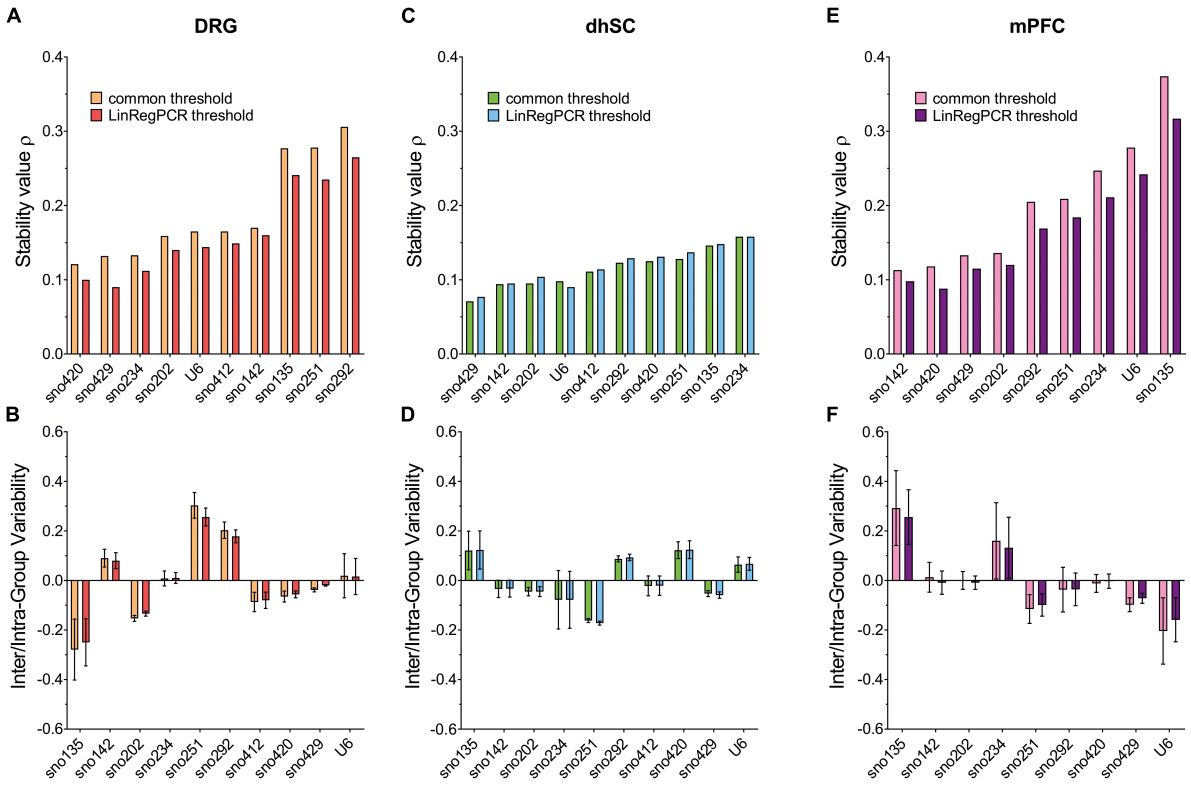

FIGURE 5 | Stability value ρ (upper panel), inter- (box) and intra- (whiskers) group variability (lower panel), as evaluated by NormFinder for all evaluated ncRNAs in DRG **(A,B)**, dhSC **(C,D)**, and mPFC **(E,F)** of non-treated (n = 5), sham (n = 6), and SNI (n = 5) mice, as estimated by setting a common threshold (0.1) and by using LinRegPCR software. DRG: dorsal root ganglia, dhSC: dorsal horn of the spinal cord, mPFC: medial prefrontal cortex.

TABLE 2 | The best combination of two ncRNAs and their stability values as computed by NormFinder in DRG, dhSC, and mPFC of non-treated, sham, and SNI mice, calculated by setting a common threshold (0.1) and by using LinRegPCR software.

	DRG		dhSC		mPFC	
	0.1	**LinReg**	**0.1**	**LinReg**	**0.1**	**LinReg**
Best combination of two genes	sno234/sno429	sno234/sno429	sno429/U6	sno429/U6	sno202/sno420	sno142/sno420
Stability value for best pair	0.069	0.048	0.062	0.062	0.078	0.070

DRG, dorsal root ganglia; dhSC, dorsal horn of the spinal cord; mPFC, medial prefrontal cortex; SNI, spared nerve injury.

miR-21a-5p expression was different only between non-treated vs. SNI ($F_{2,9}$ = 5.72, p = 0.0249; non-treated vs. SNI p = 0.0321; **Figure 7D**), whereas the use of sno135 completely abolished the significance ($F_{2,9}$ = 1.048, p = 0.3897; **Figure 7E**). The use of single reference genes revealed that the five most stable ncRNAs, namely, sno420 ($F_{2,9}$ = 11.06, p = 0.0038; non-treated vs. SNI p = 0.0052, sham vs. SNI p = 0.0104; **Supplementary Figure S1A**), sno429 ($F_{2,9}$ = 11.21, p = 0.0036; non-treated vs. SNI p = 0.0039, sham vs. SNI p = 0.0153; **Supplementary Figure S1B**), sno202 ($F_{2,9}$ = 8.319, p = 0.0090; non-treated vs. SNI p = 0.0160, sham vs. SNI p = 0.0158; **Supplementary Figure S1C**), sno234 ($F_{2,9}$ = 33.09, p < 0.0001; non-treated vs. SNI p = 0.0001, sham vs. SNI p = 0.0002; **Supplementary Figure S1D**), and sno412 ($F_{2,9}$ = 17.07, p = 0.0009; non-treated vs. SNI p = 0.0023, sham vs. SNI p = 0.0014; **Supplementary Figure S1E**) could also detect the upregulation of miR-21a-5p in the SNI mice in comparison to non-treated and sham mice. Normalization to sno142 showed a significant difference only between non-treated vs. SNI mice ($F_{2,9}$ = 8.652, p = 0.0080; non-treated vs. SNI p = 0.0071; **Supplementary Figure S1F**), whereas sno251 ($F_{2,9}$ = 16.63, p = 0.0010; non-treated vs. SNI p = 0.0010, sham vs. SNI p = 0.0058; **Supplementary Figure S1G**) and sno292 ($F_{2,9}$ = 48.52, p < 0.0001; non-treated vs. SNI and sham vs. SNI p < 0.0001; **Supplementary Figure S1H**) exaggerated the upregulation of miR-21a-5p, indicating that these two ncRNAs likely were regulated by the treatment.

DISCUSSION

This study for the first time identified suitable reference genes for the normalization of miRNA expression in the SNI mouse model

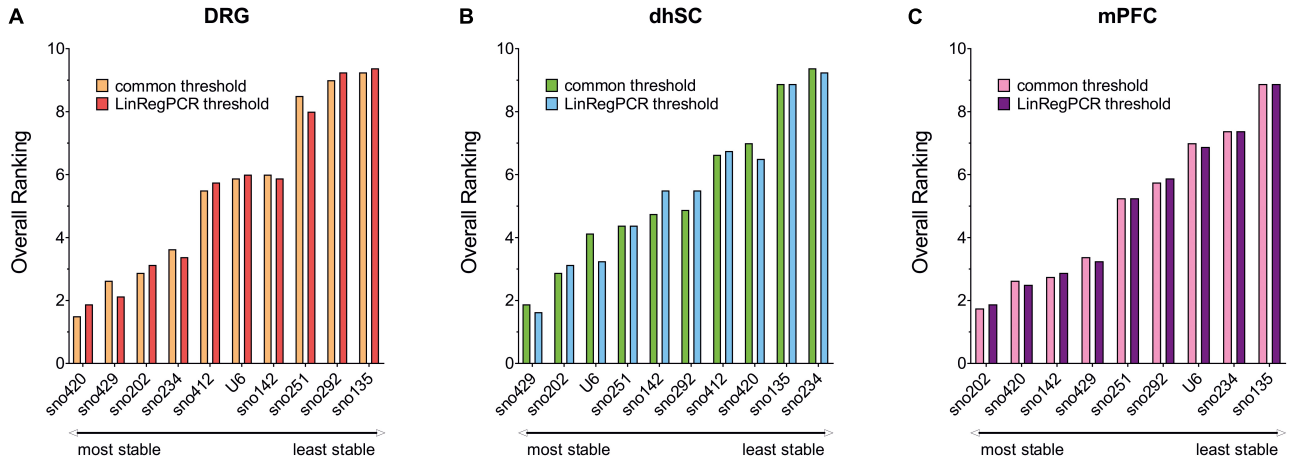

FIGURE 6 | Overall ranking of all evaluated ncRNAs, as obtained by calculating the mean of the separate rankings achieved in BestKeeper, comparative delta-Cq method, geNorm, and NormFinder, in DRG **(A)**, dhSC **(B)**, and mPFC **(C)** of non-treated (n = 5), sham (n = 6), and SNI (n = 5) mice, as estimated by setting a common threshold (0.1) and by using LinRegPCR software. DRG: dorsal root ganglia, dhSC: dorsal horn of the spinal cord, mPFC: medial prefrontal cortex.

TABLE 3 | Overall ranking of all evaluated ncRNAs expressed as the arithmetic mean of the ranks achieved in Bestkeeper, delta-Cq method, geNorm, and NormFinder in DRG, dhSC, and mPFC of non-treated, sham, and SNI mice, calculated by setting a common threshold (0.1) and by using LinRegPCR software.

DRG			dhSC			mPFC			
ncRNA	0.1	LinReg	ncRNA	ncRNA	0.1	LinReg	ncRNA	ncRNA	0.1	LinReg
	Mean score				Mean score				Mean score	
sno420	1.50	1.88	**sno420**	**sno429**	1.88	1.63	**sno429**	**sno202**	1.75	1.88
sno429	2.63	2.13	**sno429**	**sno202**	2.88	3.13	**U6**	**sno420**	2.63	2.50
sno202	2.88	3.13	**sno202**	**U6**	4.13	3.25	**sno202**	**sno142**	2.75	2.88
sno234	3.63	3.38	sno234	sno251	4.38	4.38	sno251	sno429	3.38	3.25
sno412	5.50	5.75	sno412	sno142	4.75	5.50	sno292	sno251	5.25	5.25
U6	5.88	5.88	sno142	sno292	4.88	5.50	sno142	sno292	5.75	5.88
sno142	6.00	6.00	U6	sno412	6.63	6.50	sno420	U6	7.00	6.88
sno251	8.50	8.00	sno251	sno420	7.00	6.75	sno412	sno234	7.38	7.38
sno292	9.00	9.25	sno292	sno135	8.88	8.88	sno135	sno135	8.88	8.88
sno135	9.25	9.38	sno135	sno234	9.38	9.25	sno234			

DRG, dorsal root ganglia; dhSC, dorsal horn of the spinal cord; mPFC, medial prefrontal cortex; SNI, spared nerve injury; the three most stable ncRNAs are depicted in bold.

of peripheral nerve injury by employing four commonly used statistical tools, BestKeeper (Pfaffl et al., 2004), the comparative delta-Cq method (Silver et al., 2006), geNorm (Vandesompele et al., 2002), and NormFinder (Andersen et al., 2004), and two Cq datasets (one with a common threshold set at 0.1, in which qPCR efficiency for all amplicons was assumed to be 2 and the second one with LinRegPCR corrected baselines and efficiencies). We compiled a mean score ranking list, evaluating the expression stability of eleven ncRNAs regularly used for miRNA normalization in DRG, dhSC, and mPFC of naive, sham, and SNI mice. In DRG, the most stable ncRNAs were sno420, sno429, and sno202. In the dhSC, the best ncRNAs were sno429, sno202, and U6, whereas in the mPFC, the three superior ncRNAs were sno202, sno420, and sno142. sno55 was found unsuitable for further analysis due to its high variability and sno135 consistently ranked in the two least stable candidates. Overall, there were minor differences between the two Cq datasets and the final ranking indicated a general agreement on the most and least stable ncRNAs with minimal differences.

The efficiency of a qPCR reaction is regularly considered to be 2 (Bustin et al., 2013; Bustin and Nolan, 2017), particularly when commercially available hydrolysis probes are used. Through experimental examples, at least for mRNA expression, application manuals suggest that measuring efficiency is not required when using, e.g., Taqman® gene expression assays, since they should perform at ∼100% ± 10% (Applied Biosystems, 2004, 2015). The gold standard for measuring the efficiency of assays and primer sets is the standard curve approach, in which Cq values are determined for reactions containing serial dilutions of the target template (Hellemans and Vandesompele, 2011). Although we did not run a standard curve in our experiments, we addressed the potential issue of variable efficiencies by

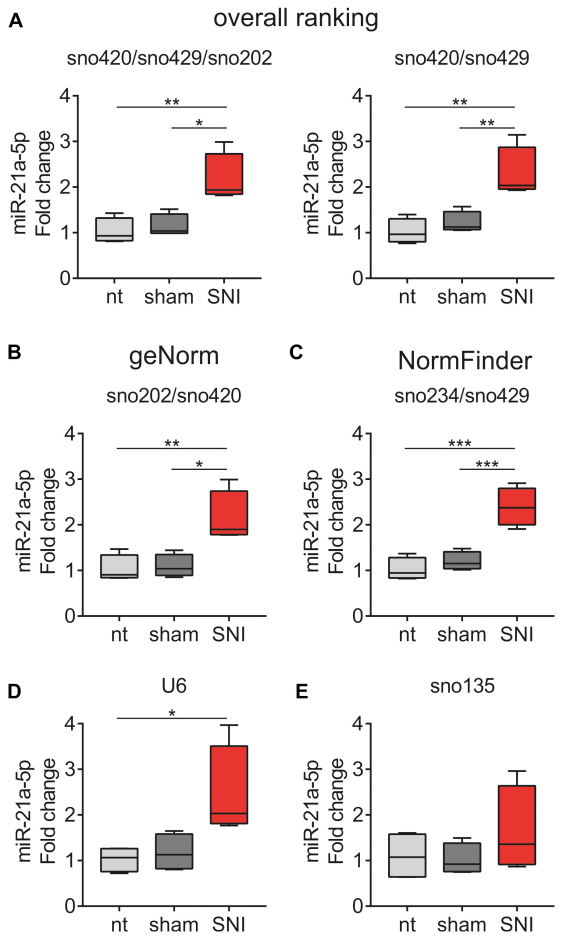

FIGURE 7 | miR-21a-5p quantification in the DRG of non-treated (nt), sham and SNI mice using **(A)** three (sno420/sno429/sno202, left panel) or two (sno420/sno429, right panel) most stable ncRNAs from the overall ranking list, the most stable pair of ncRNAs as computed by **(B)** geNorm (sno202/sno420) and **(C)** NormFinder (sno234/sno429), **(D)** U6, and **(E)** sno135. miR-21a-5p levels were expressed as fold changes relative to the respective expression levels in the non-treated group using the $2^{-\Delta\Delta Cq}$ method. Values are presented as boxplots, representing upper quartile, median, and lower quartile, whereas whiskers depict minimum and maximum values.*$p < 0.05$, **$p < 0.01$, ***$p < 0.001$.

analyzing individual amplifications with the LinRegPCR software (Ramakers et al., 2003; Ruijter et al., 2009, 2015; Tuomi et al., 2010) and compared the results with the results obtained by setting the threshold manually at 0.1, under the assumption that the efficiency was 2. Efficiencies obtained from LinRegPCR ranged between 1.765 and 1.888 and were slightly below the expected values. However, correlation analyses of efficiencies and initial template integrity as well as comparison of efficiencies vs different tissues and vs experimental groups were not statistically significant. Additionally, the overall ranking of all the candidates was similar when the efficiency was set to 2 vs. using the efficiencies calculated by LinRegPCR. The MIQE guidelines do not provide recommendations for appropriate PCR efficiency values and we cannot exclude that the lower efficiencies obtained from LinRegPCR could be attributed to the strict parameters set by the program or the presence of inhibitors in the reactions, even though all protocols were strictly implemented (Bustin et al., 2009). Nevertheless, the efficiencies did not correlate with RNA integrity or differ between experimental days and experimental groups, indicating that the obtained data were highly reliable.

Although there are other methods, such as miRNA sequencing and microarray analyses, RT-qPCR remains the most commonly used method to quantify miRNA expression due to its high sensitivity and specificity (Bustin and Nolan, 2017). However, appropriate normalization strategies are critically important for acquiring reliable results and ensuring reproducibility (Bustin et al., 2009; Bustin and Nolan, 2017). A suggested approach for normalization relies on multiple validated reference genes (Vandesompele et al., 2002; D'Haene et al., 2012). It is proposed that before initiating an RT-qPCR experiment, the most appropriate reference genes need to be determined for a given experimental setup using a representative set of samples (Hellemans and Vandesompele, 2011). However, RT-qPCR data are frequently normalized with only one reference gene (Bustin and Nolan, 2017). Despite their frequent use, the stability of these reference genes is not always documented for the particular experimental conditions and they may have even been reported to be unsuitable normalizers in specific experimental setups, e.g., U6 for miRNA expression in neuronal differentiation (Lim et al., 2011; Schwarzenbach et al., 2015). miRNAs are currently being explored as potential biomarkers for various diseases as well as tools for therapeutic interventions (Hayes et al., 2014; Ramanathan and Ajit, 2016; Lopez-Gonzalez et al., 2017; Zhou et al., 2018; Martinez and Peplow, 2019). Therefore, the establishment of appropriate reference genes for reliable and reproducible quantification of miRNA expression levels is of critical importance.

Neuropathic pain resulting from nerve injury is a serious health problem, which greatly decreases patients' life quality and inflicts a high economic burden on society (Pain Proposal Steering Committee, 2010). It is considered to be one of the least manageable pain syndromes for which available treatment and medication is suboptimal (Van Hecke et al., 2014). Furthermore, due to the complex mechanisms involved in the development and maintenance of neuropathic pain, the use of animal models for elucidating the pain pathways is apparent (Jaggi et al., 2011; Gregory et al., 2013). Nerve injury and consecutive neurodegeneration or other complex pathophysiological reactions of the nervous system have been associated with miRNA deregulation both in humans and animal models (Bai et al., 2007; Kress et al., 2013; McDonald et al., 2014; Gong et al., 2015; Zhou et al., 2017) and several studies have addressed the suitability of deregulated miRNAs as potential biomarkers or targets for neurodegeneration and neuropathic treatments (Jiangpan et al., 2016; Ramanathan and Ajit, 2016; Lopez-Gonzalez et al., 2017; Birklein et al., 2018). However, the validity of studies quantifying miRNA expression in rodent pain models may be hampered by the use of suboptimal reference controls for miRNA normalization.

In the present study, we systematically evaluated the suitability of eleven ncRNAs for miRNA normalization in the SNI

mouse model for peripheral nerve injury and neuropathy. Coding mRNA genes were excluded from our analysis as their much larger size adds variability in RNA extraction, reverse transcription, and qPCR efficiency. We assessed the stability of snoRNA and snRNA. Although these two classes of small RNAs have been extensively used for normalizing miRNAs, they differ from miRNAs in size, transcription, processing, and expression patterns (Meyer et al., 2010; Chugh and Dittmer, 2012). Moreover, both snRNAs and snoRNAs have been found deregulated in various human pathologies, such as different types of cancers, liver, heart and cardiovascular diseases, and disorders of the central nervous system (Madadi et al., 2019; Watson et al., 2019). The causes for differential expression of snRNAs and snoRNAs in health and disease are poorly understood (Didychuk et al., 2018; Kufel and Grzechnik, 2019). In humans, deletions in SNORD116C/D box (Duker et al., 2010) and HBII-85C/D box (Sahoo et al., 2008) are associated with Prader–Willi syndrome, whereas duplications within the same chromosome region (15q11-q13) are related to autism spectrum disorder (Hogart et al., 2009; Nakatani et al., 2009). Mutations in the gene encoding for RNA polymerase III deregulate snRNA and snoRNA expression (Azmanov et al., 2016). Adding to this complexity, snoRNAs have functions beyond ribosomal modification, e.g., they can act like miRNAs (Ender et al., 2008; Patterson et al., 2017) or as indirect transcriptional inhibitors by modifying RNA-binding proteins (Wang et al., 2008). Therefore, the use of these ncRNAs as reference genes for miRNA quantification is recommended only after validation of their stability in the specific experimental settings. The alternative to snoRNAs and snRNAs for the normalization of miRNAs is the global mean normalization or the use of miRNAs that mimic the global mean expression (Mestdagh et al., 2009; D'Haene et al., 2012). However, both of these approaches rely on the analysis of very large numbers of miRNAs, resulting in disproportionally high costs, particularly for small-scale studies.

The most commonly used ncRNA for normalizing miRNA expression levels in rodent nerve injury models is the snRNA U6 (Chen et al., 2018; Norcini et al., 2018; Pan et al., 2018; Yan et al., 2018; Jiang et al., 2019). Other ncRNAs that have been used as reference genes are the snoRNAs sno202 (Imai et al., 2011; Kusuda et al., 2011; Karl et al., 2017), sno135 (Norcini et al., 2018), and sno55 (Willemen et al., 2012). In most of the studies, the aforementioned controls are used as single normalizers. In our analysis, U6 was found in the top three stable ncRNAs only in the dhSC, whereas it ranked in the medium-to-low range in DRG and mPFC. In DRG, although U6 showed the smallest SD among the samples, it scored at the low end when it was compared to the BKI and average or below average in the delta-Cq method, geNorm, and NormFinder, thus representing an ncRNA of medium–low expression stability. In the mPFC, the rank of U6 was similar to DRG. Overall, among all candidates investigated in the present study, U6 consistently ranked slightly below average, suggesting that it may not be the most suitable candidate for miRNA normalization, in particular when used as a single normalizer. Interestingly, U6 has already been documented to be unsuitable for normalizing miRNAs in serum (Benz et al., 2013), plasma (Tang et al., 2015; Gevaert et al., 2018), different types of cancers (Lou et al., 2015; Popov et al., 2015), and in neuronal differentiation (Lim et al., 2011; Schwarzenbach et al., 2015).

sno55 (Snord110) and sno135 (Snord65) showed considerable variability and this confirmed previous reports suggesting that both snoRNAs do not represent stable reference genes for miRNA normalization (Karl et al., 2017). In contrast, sno202 (Snord68) and sno234 (Snord70) have been reported to be stably expressed across 12 different naive mouse tissues (Applied Biosystems, 2010). In line with these findings, the overall ranking for sno202 in our analysis was in the top 30% for all three tissues assessed, suggesting that sno202 is one of the most suitable candidates for normalizing miRNA expression. Additionally, sno202 was the only candidate that ranked in the three most stable ncRNAs in all tissues assessed. sno202 has been stated to be stable in the chronic inflammatory (Kusuda et al., 2011), axotomy (Kusuda et al., 2011), acute noxious stimulation (Kusuda et al., 2011), and SNI pain models (Kusuda et al., 2011; Karl et al., 2017), whereas it is highly unstable in the livers of mice subjected to an obesity model (Matouskova et al., 2014). On the other hand, in our analysis, sno234 ranked fourth in DRG, last in dhSC, and second to last in the mPFC, although it was documented as one of the most stable ncRNAs in the aforementioned study on obesity (Matouskova et al., 2014).

The differences in the stability of the evaluated ncRNAs were further demonstrated by normalizing miR-21a-5p, a miRNA that is upregulated in the DRG after peripheral nerve injury, including spinal nerve ligation (Sakai and Suzuki, 2013; Chang et al., 2017; Zhang Z. J. et al., 2018), sciatic nerve transection (Zhou et al., 2015), partial sciatic nerve ligation (Hori et al., 2016), sciatic nerve dissection (Strickland et al., 2011), and SNI (Karl et al., 2017; Simeoli et al., 2017). The ncRNAs possibly suitable as single normalizers, demonstrating significant deregulation of miR-21a-5p in the DRG of SNI mice belonged to the five most stable ncRNAs (sno420, sno429, sno202, sno234, and sno412). ncRNAs with lower ranking either detected a significant regulation only when the non-treated vs. SNI groups were compared (U6 and sno142) or exaggerated the effect (sno251 and sno292), indicating that the latter ncRNAs are regulated by SNI; or in the case of sno135 failed to reveal any significant upregulation. These findings further support guidelines discouraging the use of single reference genes (Vandesompele et al., 2002; Bustin et al., 2009; D'Haene et al., 2012). In addition, the four methods indicate relative stability since they rely on the comparison between the analyzed ncRNAs. In order to address this issue, we quantified miR-21a-5p by using as reference genes three or two very stable ncRNAs as well as the pairs of ncRNAs proposed as most stable by geNorm and Normfinder, which provided similar results. Therefore, the use of at least two of the top four-to-five most stably expressed ncRNAs significantly improves reliability of miRNA quantification in the DRG. Our results, alongside the literature, provide further support that the stability of reference genes may dramatically vary between different tissues and different experimental conditions. The ncRNAs we have identified as stable should be considered stable in the assessed tissues, under the specific conditions used for RNA extraction, cDNA preparation and qPCR reactions, and the employed animal

model. Thus, in other animal models for nerve lesion or under different sample handling procedures, these ncRNAs may not be the most appropriate for miRNA normalization and their stability should be re-evaluated. Nevertheless, our results provide a firm indication on which of these ncRNAs could be stably expressed and pilot experiments to select the most stable ncRNAs for specific experimental settings are highly recommended.

We for the first time identify highly stable reference genes suitable for miRNA quantification in the DRG, dhSC, and mPFC of non-treated, sham, and SNI mice. Our results underline the need for thorough validation of reference genes for miRNA normalization in different tissues and experimental settings. We expect that the ncRNAs reported here could be suitable for miRNA quantification in nervous tissues in other nerve lesion models, thus promoting validity and reproducibility in miRNA expression analyses.

DATA AVAILABILITY STATEMENT

All datasets generated for this study are included in the article/**Supplementary Material**.

ETHICS STATEMENT

The animal study was reviewed and approved by the Austrian National Animal Experiment Ethics Committee of the Austrian Bundesministerium für Wissenschaft und Forschung (permit number BMWF-66.011/0054-WF/V/3b/2015).

AUTHOR CONTRIBUTIONS

TK, KK, and MK designed the study. TK, KK, and MM performed the sample collection and experiments. TK and KK performed the data analysis and interpreted the data. TK and MK wrote the manuscript. KK and MM critically reviewed the contents of the manuscript and suggested substantial improvements. All authors have approved the final version of the manuscript.

FUNDING

This study was supported by the Austrian Science Fund (FWF): DK-SPIN W1206-06, P25345, and P28611 to MK, and P30809 to KK; the Austrian Research Promotion Agency (FFG): D-150700-013-017 to MK; and the European Commission under FP7: GA nr. 602133 to MK.

ACKNOWLEDGMENTS

We would like to thank Theresa Martha and Federica Vercelli for expert technical assistance.

SUPPLEMENTARY MATERIAL

The Supplementary Material for this article can be found online at: https://www.frontiersin.org/articles/10.3389/fnmol.2019.00283/full#supplementary-material

FIGURE S1 | miR-21a-5p quantification in the DRG of non-treated (nt), sham, and SNI mice using each assessed ncRNA as a single reference gene **(A)** sno420, **(B)** sno429, **(C)** sno202, **(D)** sno234, **(E)** sno412, **(F)** sno142, **(G)** sno251, and **(H)** sno292. miR-21a-5p levels were expressed as fold changes relative to the respective expression levels in the non-treated group using the $2^{-\Delta\Delta Cq}$ method. Values are presented as boxplots, representing upper quartile, median, and lower quartile, whereas whiskers depict minimum and maximum values. $^{*}p < 0.05$, $^{**}p < 0.01$, $^{***}p < 0.001$, $^{****}p < 0.0001$.

TABLE S1 | MIQE checklist for authors, reviewers, and editors.

TABLE S2 | Quantity and integrity of RNA extracted from DRG, dhSC, and mPFC of non-treated, sham, and SNI mice.

TABLE S3 | Mean qPCR efficiencies for all amplified ncRNAs calculated by LinRegPCR.

TABLE S4 | Spearman's correlation between RNA integrity and qPCR efficiency per reaction.

TABLE S5 | Kruskal–Wallis test for differences in efficiencies vs. experimental day **(A)** and vs. experimental groups **(B)**.

TABLE S6 | Descriptive statistics of the Cq values for all evaluated ncRNAs in DRG **(A)**, dhSC **(B)**, and mPFC **(C)** of non-treated, sham, and SNI mice, calculated by setting a common threshold (0.1) and by using LinRegPCR software.

TABLE S7 | Descriptive statistics of the Cq values and correlation analysis obtained from BestKeeper for all evaluated ncRNAs in DRG **(A)**, dhSC **(B)**, and mPFC **(C)** of non-treated, sham, and SNI mice, calculated by setting a common threshold (0.1) and by using LinRegPCR software.

TABLE S8 | Comparison of all evaluated ncRNAs using the comparative delta-Cq method in DRG **(A)**, dhSC **(B)**, and mPFC **(C)** of non-treated, sham, and SNI mice, calculated by setting a common threshold (0.1) and by using LinRegPCR software.

TABLE S9 | Initial M values of all evaluated ncRNAs as computed by geNorm in DRG, dhSC, and mPFC of non-treated, sham, and SNI mice, calculated by setting a common threshold (0.1) and by using LinRegPCR software.

TABLE S10 | ρ values, inter- and intra-group variations for all evaluated ncRNAs as obtained from NormFinder in DRG **(A)**, dhSC **(B)**, and mPFC **(C)** of non-treated, sham, and SNI mice, calculated by setting a common threshold (0.1) and by using LinRegPCR software.

TABLE S11 | Overall ranking of all evaluated ncRNAs expressed as the geometric mean of the ranks achieved in Bestkeeper, delta-Cq method, geNorm, and NormFinder in DRG, dhSC, and mPFC of non-treated, sham, and SNI mice, calculated by setting a common threshold (0.1) and by using LinRegPCR software.

REFERENCES

Andersen, C. L., Jensen, J. L., and Orntoft, T. F. (2004). Normalization of real-time quantitative reverse transcription-PCR data: a model-based variance estimation approach to identify genes suited for normalization, applied to bladder and colon cancer data sets. *Cancer Res.* 64, 5245–5250. doi: 10.1158/0008-5472.can-04-0496

Applied Biosystems (2004). *Amplification Efficiency of TaqMan§Gene Expression Assays*. Available: https://pdfs.semanticscholar.org/190c/9c97484c3f8fa168b9b0910338f31da25bbd.pdf (accessed June 20, 2019).

Applied Biosystems (2010). *Endogenous Controls for Real-Time Quantitation of miRNA Using TaqMan® MicroRNA Assays*. Available: http://tools.thermofisher.com/content/sfs/brochures/cms_044972.pdf (accessed June 20, 2019).

Applied Biosystems (2015). *Gene Expression Assay Performance Guaranteed With the TaqMan® Assays QPCR Guarantee Program*. Available: https://www.thermofisher.com/content/dam/LifeTech/Documents/PDFs/PG1500-PJ9167-CO017361-TaqMan-Guarantee-WhitePaper-Global-FHR.pdf (accessed June 20, 2019).

Applied Biosystems (2016). *Real-Time PCR: Understanding Ct*. Available: https://www.thermofisher.com/content/dam/LifeTech/Documents/PDFs/PG1503-PJ9169-CO019879-Re-brand-Real-Time-PCR-Understanding-Ct-Value-Americas-FHR.pdf (accessed June 20, 2019).

Azmanov, D. N., Siira, S. J., Chamova, T., Kaprelyan, A., Guergueltcheva, V., Shearwood, A. J., et al. (2016). Transcriptome-wide effects of a POLR3A gene mutation in patients with an unusual phenotype of striatal involvement. *Hum. Mol. Genet.* 25, 4302–4314. doi: 10.1093/hmg/ddw263

Babion, I., Snoek, B. C., Van De Wiel, M. A., Wilting, S. M., and Steenbergen, R. D. M. (2017). A strategy to find suitable reference genes for miRNA quantitative PCR analysis and its application to cervical specimens. *J. Mol. Diagn.* 19, 625–637. doi: 10.1016/j.jmoldx.2017.04.010

Bai, G., Ambalavanar, R., Wei, D., and Dessem, D. (2007). Downregulation of selective microRNAs in trigeminal ganglion neurons following inflammatory muscle pain. *Mol. Pain* 3:15.

Benz, F., Roderburg, C., Vargas Cardenas, D., Vucur, M., Gautheron, J., Koch, A., et al. (2013). U6 is unsuitable for normalization of serum miRNA levels in patients with sepsis or liver fibrosis. *Exp. Mol. Med.* 45:e42. doi: 10.1038/emm.2013.81

Birklein, F., Ajit, S. K., Goebel, A., Perez, R. S. G. M., and Sommer, C. (2018). Complex regional pain syndrome – phenotypic characteristics and potential biomarkers. *Nat. Rev. Neurol.* 14:272. doi: 10.1038/nrneurol.2018.20

Bouhaddioui, W., Provost, P. R., and Tremblay, Y. (2014). Identification of most stable endogenous control genes for microRNA quantification in the developing mouse lung. *PLoS One* 9:e111855. doi: 10.1371/journal.pone.0111855

Bustin, S., and Nolan, T. (2017). Talking the talk, but not walking the walk: RT-qPCR as a paradigm for the lack of reproducibility in molecular research. *Eur. J. Clin. Invest.* 47, 756–774. doi: 10.1111/eci.12801

Bustin, S. A., Benes, V., Garson, J., Hellemans, J., Huggett, J., Kubista, M., et al. (2013). The need for transparency and good practices in the qPCR literature. *Nat. Methods* 10, 1063–1067. doi: 10.1038/nmeth.2697

Bustin, S. A., Benes, V., Garson, J. A., Hellemans, J., Huggett, J., Kubista, M., et al. (2009). The MIQE guidelines: minimum information for publication of quantitative real-time PCR experiments. *Clin. Chem.* 55, 611–622. doi: 10.1373/clinchem.2008.112797

Chang, H. L., Wang, H. C., Chunag, Y. T., Chou, C. W., Lin, I. L., Lai, C. S., et al. (2017). miRNA expression change in dorsal root ganglia after peripheral nerve injury. *J. Mol. Neurosci.* 61, 169–177. doi: 10.1007/s12031-016-0876-7

Chen, M. L., Lin, K., and Lin, S. K. (2018). NLRP3 inflammasome signaling as an early molecular response is negatively controlled by miR-186 in CFA-induced prosopalgia mice. *Braz. J. Med. Biol. Res.* 51:e7602. doi: 10.1590/1414-431X20187602

Chugh, P., and Dittmer, D. P. (2012). Potential pitfalls in microRNA profiling. *Wiley Interdiscip. Rev. RNA* 3, 601–616. doi: 10.1002/wrna.1120

Decosterd, I., and Woolf, C. J. (2000). Spared nerve injury: an animal model of persistent peripheral neuropathic pain. *Pain* 87, 149–158. doi: 10.1016/s0304-3959(00)00276-1

D'Haene, B., Mestdagh, P., Hellemans, J., and Vandesompele, J. (2012). miRNA expression profiling: from reference genes to global mean normalization. *Methods Mol. Biol.* 822, 261–272. doi: 10.1007/978-1-61779-427-8_18

Didychuk, A. L., Butcher, S. E., and Brow, D. A. (2018). The life of U6 small nuclear RNA, from cradle to grave. *RNA* 24, 437–460. doi: 10.1261/rna.065136.117

Duker, A. L., Ballif, B. C., Bawle, E. V., Person, R. E., Mahadevan, S., Alliman, S., et al. (2010). Paternally inherited microdeletion at 15q11.2 confirms a significant role for the SNORD116 C/D box snoRNA cluster in Prader-Willi syndrome. *Eur. J. Hum. Genet.* 18, 1196–1201. doi: 10.1038/ejhg.2010.102

Ender, C., Krek, A., Friedlander, M. R., Beitzinger, M., Weinmann, L., Chen, W., et al. (2008). A human snoRNA with microRNA-like functions. *Mol. Cell.* 32, 519–528. doi: 10.1016/j.molcel.2008.10.017

Eulalio, A., Huntzinger, E., and Izaurralde, E. (2008). Getting to the root of miRNA-mediated gene silencing. *Cell* 132, 9–14. doi: 10.1016/j.cell.2007.12.024

Ferdous, J., Li, Y., Reid, N., Langridge, P., Shi, B. J., and Tricker, P. J. (2015). Identification of reference genes for quantitative expression analysis of microRNAs and mRNAs in barley under various stress conditions. *PLoS One* 10:e0118503. doi: 10.1371/journal.pone.0118503

Gevaert, A. B., Witvrouwen, I., Vrints, C. J., Heidbuchel, H., Van Craenenbroeck, E. M., Van Laere, S. J., et al. (2018). MicroRNA profiling in plasma samples using qPCR arrays: Recommendations for correct analysis and interpretation. *PLoS One* 13:e0193173. doi: 10.1371/journal.pone.0193173

Ghibaudi, M., Boido, M., and Vercelli, A. (2017). Functional integration of complex miRNA networks in central and peripheral lesion and axonal regeneration. *Prog. Neurobiol.* 158, 69–93. doi: 10.1016/j.pneurobio.2017.07.005

Gong, Q., Lu, Z., Huang, Q., Ruan, L., Chen, J., Liang, Y., et al. (2015). Altered microRNAs expression profiling in mice with diabetic neuropathic pain. *Biochem. Biophys. Res. Commun.* 456, 615–620. doi: 10.1016/j.bbrc.2014.12.004

Gregory, N. S., Harris, A. L., Robinson, C. R., Dougherty, P. M., Fuchs, P. N., and Sluka, K. A. (2013). An overview of animal models of pain: disease models and outcome measures. *J. Pain* 14, 1255–1269. doi: 10.1016/j.jpain.2013.06.008

Hayes, J., Peruzzi, P. P., and Lawler, S. (2014). MicroRNAs in cancer: biomarkers, functions and therapy. *Trends Mol. Med.* 20, 460–469. doi: 10.1016/j.molmed.2014.06.005

Hellemans, J., and Vandesompele, J. (2011). "qPCR data analysis – unlocking the secret to successful results," in *Troubleshooting, Optimization, The Essential, and Guide* eds S. Kennedy, and N. Oswald (Norfolk: Caister Academic Press), 139–150.

Hogart, A., Leung, K. N., Wang, N. J., Wu, D. J., Driscoll, J., Vallero, R. O., et al. (2009). Chromosome 15q11-13 duplication syndrome brain reveals epigenetic alterations in gene expression not predicted from copy number. *J. Med. Genet.* 46, 86–93. doi: 10.1136/jmg.2008.061580

Hori, N., Narita, M., Yamashita, A., Horiuchi, H., Hamada, Y., Kondo, T., et al. (2016). Changes in the expression of IL-6-Mediated MicroRNAs in the dorsal root ganglion under neuropathic pain in mice. *Synapse* 70, 317–324. doi: 10.1002/syn.21902

Imai, S., Saeki, M., Yanase, M., Horiuchi, H., Abe, M., Narita, M., et al. (2011). Change in microRNAs associated with neuronal adaptive responses in the nucleus accumbens under neuropathic pain. *J. Neurosci.* 31, 15294–15299. doi: 10.1523/JNEUROSCI.0921-11.2011

Jaggi, A. S., Jain, V., and Singh, N. (2011). Animal models of neuropathic pain. *Fundam. Clin. Pharmacol.* 25, 1–28. doi: 10.1111/j.1472-8206.2009.00801.x

Jiang, W., Wang, Q., Yu, X., Lu, T., and Zhang, P. (2019). MicroRNA-217 relieved neuropathic pain through targeting toll-like receptor 5 expression. *J. Cell. Biochem.* 120, 3009–3017. doi: 10.1002/jcb.27269

Jiangpan, P., Qingsheng, M., Zhiwen, Y., and Tao, Z. (2016). Emerging role of microRNA in neuropathic pain. *Curr. Drug Metab.* 17, 336–344. doi: 10.2174/1389200216666151015113400

Karl, F., Grießhammer, A., Üçeyler, N., and Sommer, C. (2017). Differential impact of miR-21 on pain and associated affective and cognitive behavior after spared nerve injury in B7-H1 ko mouse. *Front. Mol. Neurosci.* 10:219. doi: 10.3389/fnmol.2017.00219

Kozera, B., and Rapacz, M. (2013). Reference genes in real-time PCR. *J. Appl. Genet.* 54, 391–406.

Kress, M., Huttenhofer, A., Landry, M., Kuner, R., Favereaux, A., Greenberg, D., et al. (2013). microRNAs in nociceptive circuits as predictors of future clinical applications. *Front. Mol. Neurosci.* 6:33. doi: 10.3389/fnmol.2013.00033

Kufel, J., and Grzechnik, P. (2019). Small nucleolar RNAs tell a different tale. *Trends Genet.* 35, 104–117. doi: 10.1016/j.tig.2018.11.005

Kusuda, R., Cadetti, F., Ravanelli, M. I., Sousa, T. A., Zanon, S., De Lucca, F. L., et al. (2011). Differential expression of microRNAs in mouse pain models. *Mol. Pain* 7:17. doi: 10.1186/1744-8069-7-17

Lim, Q. E., Zhou, L., Ho, Y. K., Wan, G., and Too, H. P. (2011). snoU6 and 5S RNAs are not reliable miRNA reference genes in neuronal differentiation. *Neuroscience* 199, 32–43. doi: 10.1016/j.neuroscience.2011.10.024

Lopez-Gonzalez, M. J., Landry, M., and Favereaux, A. (2017). MicroRNA and chronic pain: from mechanisms to therapeutic potential. *Pharmacol. Ther.* 180, 1–15. doi: 10.1016/j.pharmthera.2017.06.001

Lou, G., Ma, N., Xu, Y., Jiang, L., Yang, J., Wang, C., et al. (2015). Differential distribution of U6 (RNU6-1) expression in human carcinoma

tissues demonstrates the requirement for caution in the internal control gene selection for microRNA quantification. *Int. J. Mol. Med.* 36, 1400–1408. doi: 10.3892/ijmm.2015.2338

Madadi, S., Schwarzenbach, H., Lorenzen, J., and Soleimani, M. (2019). MicroRNA expression studies: challenge of selecting reliable reference controls for data normalization. *Cell Mol. Life. Sci.* 76, 3497–3514. doi: 10.1007/s00018-019-03136-y

Martinez, B., and Peplow, P. V. (2019). MicroRNAs as diagnostic and therapeutic tools for Alzheimer's disease: advances and limitations. *Neural Regen. Res.* 14, 242–255. doi: 10.4103/1673-5374.244784

Mase, M., Grasso, M., Avogaro, L., D'amato, E., Tessarolo, F., Graffigna, A., et al. (2017). Selection of reference genes is critical for miRNA expression analysis in human cardiac tissue. A focus on atrial fibrillation. *Sci. Rep.* 7:41127.

Matouskova, P., Bartikova, H., Bousova, I., Hanusova, V., Szotakova, B., and Skalova, L. (2014). Reference genes for real-time PCR quantification of messenger RNAs and microRNAs in mouse model of obesity. *PLoS One* 9:e86033. doi: 10.1371/journal.pone.0086033

McDonald, M. K., Tian, Y., Qureshi, R. A., Gormley, M., Ertel, A., Gao, R., et al. (2014). Functional significance of macrophage-derived exosomes in inflammation and pain. *Pain* 155, 1527–1539. doi: 10.1016/j.pain.2014.04.029

Mestdagh, P., Feys, T., Bernard, N., Guenther, S., Chen, C., Speleman, F., et al. (2008). High-throughput stem-loop RT-qPCR miRNA expression profiling using minute amounts of input RNA. *Nucleic Acids Res.* 36:e143. doi: 10.1093/nar/gkn725

Mestdagh, P., Van Vlierberghe, P., De Weer, A., Muth, D., Westermann, F., Speleman, F., et al. (2009). A novel and universal method for microRNA RT-qPCR data normalization. *Genome Biol.* 10:R64. doi: 10.1186/gb-2009-10-6-r64

Meyer, S. U., Pfaffl, M. W., and Ulbrich, S. E. (2010). Normalization strategies for microRNA profiling experiments: a 'normal' way to a hidden layer of complexity? *Biotechnol. Lett.* 32, 1777–1788. doi: 10.1007/s10529-010-0380-z

Motti, D., Lerch, J. K., Danzi, M. C., Gans, J. H., Kuo, F., Slepak, T. I., et al. (2017). Identification of miRNAs involved in DRG neurite outgrowth and their putative targets. *FEBS Lett.* 591, 2091–2105. doi: 10.1002/1873-3468.12718

Nakatani, J., Tamada, K., Hatanaka, F., Ise, S., Ohta, H., Inoue, K., et al. (2009). Abnormal behavior in a chromosome-engineered mouse model for human 15q11-13 duplication seen in autism. *Cell* 137, 1235–1246. doi: 10.1016/j.cell.2009.04.024

Norcini, M., Choi, D., Lu, H., Cano, M., Piskoun, B., Hurtado, A., et al. (2018). Intrathecal injection of miR-133b-3p or miR-143-3p prevents the development of persistent cold and mechanical allodynia following a peripheral nerve injury in rats. *Neuroscience* 386, 223–239. doi: 10.1016/j.neuroscience.2018.06.040

Pain Proposal Steering Committee (2010). *Pain Proposal - Improving the Current and Future Management of Chronic Pain*. Available: https://www.europeanpainfederation.eu/wp-content/uploads/2016/06/pain_proposal (accessed June 20, 2019).

Pan, Z., Shan, Q., Gu, P., Wang, X. M., Tai, L. W., Sun, M., et al. (2018). miRNA-23a/CXCR4 regulates neuropathic pain via directly targeting TXNIP/NLRP3 inflammasome axis. *J. Neuroinflamm.* 15:29. doi: 10.1186/s12974-018-1073-0

Patterson, D. G., Roberts, J. T., King, V. M., Houserova, D., Barnhill, E. C., Crucello, A., et al. (2017). Human snoRNA-93 is processed into a microRNA-like RNA that promotes breast cancer cell invasion. *NP J. Breast Cancer* 3:25. doi: 10.1038/s41523-017-0032-8

Pfaffl, M. W., Tichopad, A., Prgomet, C., and Neuvians, T. P. (2004). Determination of stable housekeeping genes, differentially regulated target genes and sample integrity: BestKeeper–Excel-based tool using pair-wise correlations. *Biotechnol. Lett.* 26, 509–515. doi: 10.1023/b:bile.0000019559.84305.47

Popov, A., Szabo, A., and Mandys, V. (2015). Small nucleolar RNA U91 is a new internal control for accurate microRNAs quantification in pancreatic cancer. *BMC Cancer* 15:774. doi: 10.1186/s12885-015-1785-9

Ramakers, C., Ruijter, J. M., Deprez, R. H., and Moorman, A. F. (2003). Assumption-free analysis of quantitative real-time polymerase chain reaction (PCR) data. *Neurosci. Lett.* 339, 62–66. doi: 10.1016/s0304-3940(02)01423-4

Ramanathan, S., and Ajit, S. K. (2016). MicroRNA-Based Biomarkers in Pain. *Adv. Pharmacol.* 75, 35–62. doi: 10.1016/bs.apha.2015.12.001

Ruijter, J. M., Ramakers, C., Hoogaars, W. M., Karlen, Y., Bakker, O., Van Den Hoff, M. J., et al. (2009). Amplification efficiency: linking baseline and bias in the analysis of quantitative PCR data. *Nucleic Acids Res.* 37:e45. doi: 10.1093/nar/gkp045

Ruijter, J. M., Ruiz Villalba, A., Hellemans, J., Untergasser, A., and Van Den Hoff, M. J. B. (2015). Removal of between-run variation in a multi-plate qPCR experiment. *Biomol. Detect. Quantif.* 5, 10–14. doi: 10.1016/j.bdq.2015.07.001

Sahoo, T., Del Gaudio, D., German, J. R., Shinawi, M., Peters, S. U., Person, R. E., et al. (2008). Prader-Willi phenotype caused by paternal deficiency for the HBII-85 C/D box small nucleolar RNA cluster. *Nat. Genet.* 40, 719–721. doi: 10.1038/ng.158

Sakai, A., and Suzuki, H. (2013). Nerve injury-induced upregulation of miR-21 in the primary sensory neurons contributes to neuropathic pain in rats. *Biochem. Biophys. Res. Commun.* 435, 176–181. doi: 10.1016/j.bbrc.2013.04.089

Sakai, A., and Suzuki, H. (2015). microRNA and Pain. *Adv. Exp. Med. Biol.* 888, 17–39. doi: 10.1007/978-3-319-22671-2_3

Schwarzenbach, H., Da Silva, A. M., Calin, G., and Pantel, K. (2015). Data normalization strategies for MicroRNA quantification. *Clin. Chem.* 61, 1333–1342. doi: 10.1373/clinchem.2015.239459

Silver, N., Best, S., Jiang, J., and Thein, S. L. (2006). Selection of housekeeping genes for gene expression studies in human reticulocytes using real-time PCR. *BMC Mol. Biol.* 7:33.

Simeoli, R., Montague, K., Jones, H. R., Castaldi, L., Chambers, D., Kelleher, J. H., et al. (2017). Exosomal cargo including microRNA regulates sensory neuron to macrophage communication after nerve trauma. *Nat. Commun.* 8:1778. doi: 10.1038/s41467-017-01841-5

Strickland, I. T., Richards, L., Holmes, F. E., Wynick, D., Uney, J. B., and Wong, L. F. (2011). Axotomy-induced miR-21 promotes axon growth in adult dorsal root ganglion neurons. *PLoS One* 6:e23423. doi: 10.1371/journal.pone.0023423

Tang, G., Shen, X., Lv, K., Wu, Y., Bi, J., and Shen, Q. (2015). Different normalization strategies might cause inconsistent variation in circulating microRNAs in patients with hepatocellular carcinoma. *Med. Sci. Monit.* 21, 617–624. doi: 10.12659/msm.891028

Tuomi, J. M., Voorbraak, F., Jones, D. L., and Ruijter, J. M. (2010). Bias in the Cq value observed with hydrolysis probe based quantitative PCR can be corrected with the estimated PCR efficiency value. *Methods* 50, 313–322. doi: 10.1016/j.ymeth.2010.02.003

Van Hecke, O., Austin, S. K., Khan, R. A., Smith, B. H., and Torrance, N. (2014). Neuropathic pain in the general population: a systematic review of epidemiological studies. *Pain* 155, 654–662. doi: 10.1016/j.pain.2013.11.013

Vandesompele, J., De Preter, K., Pattyn, F., Poppe, B., Van Roy, N., De Paepe, A., et al. (2002). Accurate normalization of real-time quantitative RT-PCR data by geometric averaging of multiple internal control genes. *Genome Biol.* 3:Research0034.

Vidigal, J. A., and Ventura, A. (2015). The biological functions of miRNAs: lessons from in vivo studies. *Trends Cell Biol.* 25, 137–147. doi: 10.1016/j.tcb.2014.11.004

Wang, X., Arai, S., Song, X., Reichart, D., Du, K., Pascual, G., et al. (2008). Induced ncRNAs allosterically modify RNA-binding proteins in cis to inhibit transcription. *Nature* 454, 126–130. doi: 10.1038/nature06992

Watson, C. N., Belli, A., and Di Pietro, V. (2019). Small non-coding RNAs: new class of biomarkers and potential therapeutic targets in neurodegenerative disease. *Front. Genet.* 10:364. doi: 10.3389/fgene.2019.00364

Willemen, H. L., Huo, X. J., Mao-Ying, Q. L., Zijlstra, J., Heijnen, C. J., and Kavelaars, A. (2012). MicroRNA-124 as a novel treatment for persistent hyperalgesia. *J. Neuroinflamm.* 9:143. doi: 10.1186/1742-2094-9-143

Wu, D., and Murashov, A. K. (2013). MicroRNA-431 regulates axon regeneration in mature sensory neurons by targeting the Wnt antagonist Kremen1. *Front. Mol. Neurosci.* 6:35. doi: 10.3389/fnmol.2013.00035

Wu, W., Deng, Q., Shi, P., Yang, J., Hu, Z., and Zhang, M. (2016). Identification of appropriate reference genes for normalization of miRNA expression in grafted watermelon plants under different nutrient stresses. *PLoS One* 11:e0164725. doi: 10.1371/journal.pone.0164725

Yan, T., Zhang, F., Sun, C., Sun, J., Wang, Y., Xu, X., et al. (2018). miR-32-5p-mediated dusp5 downregulation contributes to neuropathic pain. *Biochem. Biophys. Res. Commun.* 495, 506–511. doi: 10.1016/j.bbrc.2017.11.013

Zhang, J., Liu, Y., and Lu, L. (2018). Emerging role of MicroRNAs in peripheral nerve system. *Life Sci.* 207, 227–233. doi: 10.1016/j.lfs.2018.06.011

Zhang, Z. J., Guo, J. S., Li, S. S., Wu, X. B., Cao, D. L., Jiang, B. C., et al. (2018). TLR8 and its endogenous ligand miR-21 contribute to neuropathic pain in murine DRG. *J. Exp. Med.* 215, 3019–3037. doi: 10.1084/jem.20180800

Zhou, J., Xiong, Q., Chen, H., Yang, C., and Fan, Y. (2017). Identification of the spinal expression profile of non-coding RNAs involved in neuropathic pain following spared nerve injury by sequence analysis. *Front. Mol. Neurosci.* 10:91.

Zhou, S., Shen, D., Wang, Y., Gong, L., Tang, X., Yu, B., et al. (2012). microRNA-222 targeting PTEN promotes neurite outgrowth from adult dorsal root ganglion neurons following sciatic nerve transection. *PLoS One* 7:e44768. doi: 10.1371/journal.pone.0044768

Zhou, S., Zhang, S., Wang, Y., Yi, S., Zhao, L., Tang, X., et al. (2015). MiR-21 and miR-222 inhibit apoptosis of adult dorsal root ganglion neurons by repressing TIMP3 following sciatic nerve injury. *Neurosci. Lett.* 586, 43–49. doi: 10.1016/j.neulet.2014.12.006

Zhou, S. S., Jin, J. P., Wang, J. Q., Zhang, Z. G., Freedman, J. H., Zheng, Y., et al. (2018). miRNAS in cardiovascular diseases: potential biomarkers, therapeutic targets and challenges. *Acta Pharmacol. Sin.* 39, 1073–1084. doi: 10.1038/aps.2018.30

Conflict of Interest: The authors declare that the research was conducted in the absence of any commercial or financial relationships that could be construed as a potential conflict of interest.

frontiers in Molecular Neuroscience

BRIEF RESEARCH REPORT
published: 22 November 2019
doi: 10.3389/fnmol.2019.00280

Modulation of Glycine Receptor-Mediated Pain Signaling *in vitro* and *in vivo* by Glucose

Rama Ashraf Hussein, Marwa Ahmed, Hans-Georg Breitinger and Ulrike Breitinger**

Department of Biochemistry, German University in Cairo, New Cairo, Egypt

The inhibitory glycine receptor (GlyR) plays an important role in rapid synaptic inhibition in mammalian spinal cord, brainstem, higher brain centers, and is involved in transmission of nociceptive signals. Glucose and related mono- and disaccharides potentiate currents mediated by recombinant α1, α1-β, and α3 GlyRs. Here, we confirmed the specific potentiation of α3 GlyR signaling by glucose through: (i) patch-clamp electrophysiology on recombinant receptors; and (ii) by verifying *in vitro* data in a mouse model *in vivo*. Mice were intraperitoneally (IP) injected with glucose (2 g/kg) or vehicle, and then challenged with sublethal doses of strychnine (0.2 mg/kg and 0.5 mg/kg). Pain-related behavior was assessed using two established models: (i) touch sensitivity tests using von Frey filaments; and (ii) hotplate assay. We observed a reduction of pain sensitivity in glucose-treated mice relative to vehicle-treated control mice. Injection of strychnine resulted in an increased sensitivity to tactile and heat stimuli, which was reversed in the presence of glucose. Analgesic effects of glucose were more pronounced in von Frey experiments, consistent with the established use of this model for neuropathic pain. Overall, glucose showed mild analgesic effects and was able to compensate for strychnine-induced allodynia in mice. Since the action of strychnine is specific for GlyR, these experiments show for the first time an *in vivo* potentiation of GlyR activity by glucose and suggest a molecular mechanism for glucose-mediated analgesia.

Keywords: nociception, spinal α3 glycine receptors, glycinergic transmission, glucose modulation, patch-clamp recording, pain-related behavior, tactile sensitivity, hotplate assay

OPEN ACCESS

Edited by:
Robert J. Harvey, University of the Sunshine Coast, Australia

Reviewed by:
Argel Estrada-Mondragon, Linköping University, Sweden
Francesco Fazio, Albert Einstein College of Medicine, United States

****Correspondence:***
Hans-Georg Breitinger
hans.breitinger@guc.edu.eg
Ulrike Breitinger
ulrike.breitinger@guc.edu.eg

Received: *24 July 2019*
Accepted: *01 November 2019*
Published: *22 November 2019*

Citation:
Hussein RA, Ahmed M, Breitinger H-G and Breitinger U (2019) Modulation of Glycine Receptor-Mediated Pain Signaling in vitro and in vivo by Glucose. Front. Mol. Neurosci. 12:280. doi: 10.3389/fnmol.2019.00280

INTRODUCTION

The inhibitory glycine receptor (GlyR) is one of the principal mediators of rapid synaptic inhibition in the mammalian spinal cord, brainstem, and higher brain centers. It is a member of the Cys-loop family of ligand-gated ion channel receptors, which includes nicotinic acetylcholine; $GABA_A$ and serotonin type 3 ($5\text{-}HT_3$) receptors. Cys-loop receptors are pentameric transmembrane complexes that surround a central ion pore which opens transiently upon binding of the activating ligand. In the case of the GlyR, five subunits (α1–4, β) have been identified. GLRA4, encoding the α4 subunit is a pseudogene in humans, while α2 receptors are predominant in neonatal tissue and their abundance decreases dramatically in most adult tissues (Breitinger, 2014). α1-β receptors are mainly located in brainstem and spinal cord, where they mediate muscle tone and movement; they have also been found in numerous other tissues including the mesolimbic system (Munoz et al., 2018), while α3 subunits are found in higher brain centers and spinal cord where their prominent contribution to nociceptive signal

transmission has been well established (Harvey et al., 2004, 2009; Lynch and Callister, 2006; Zeilhofer et al., 2012). In the last years, several high-resolution structures became available that provide important information about binding sites on the receptor, including electron microscopy studies on Zebrafish α1 GlyR bound to strychnine, glycine, and ivermectin (Du et al., 2015), the crystal structure of GlyR α3 exhibiting the binding site of strychnine (Huang et al., 2015), and recently the structure of α3 receptor bound to a novel class of analgesic GlyR potentiators (Huang et al., 2017; **Figure 1**). This study identified a novel binding site for analgesics near the N-terminus of the receptor protein. In addition to well-defined sites from GlyR structures, binding sites for ethanol and anesthetics—both enhancing GlyR function—had been postulated earlier. Using chimeric receptor constructs and subsequent mutagenesis studies identified Ser267 as a crucial amino acid residue for their action (Mihic et al., 1997). Specific amino acids enhancing the effects of alcohol and anesthetics were suggested to border a water-filled cavity between transmembrane domains 2–3 (Mihic et al., 1997; Lobo et al., 2004). This binding pocket was thought to be present in all cys-loop receptors, yet the modulatory effects of alcohols and anesthetics vary between different members of this receptor family (Dupre et al., 2007). Glucose, a polyalcohol, may indeed be able to access this cavity on the receptor.

Loss-of-function mutations in GlyR genes underlie complex motor disorders, such as human hyperekplexia (STHE, startle disease, OMIM 149400), stiff-man syndrome, bovine myoclonus, and other neuromuscular diseases. GlyR function is inhibited specifically by strychnine but also by other compounds including brucine (Pullan and Powel, 1992), ginkgolide B (Kondratskaya et al., 2004) or flavonoids (Huang and Dillon, 2000; Zhu et al., 2003; Raafat et al., 2010). Biphasic modulation is observed for Zn^{2+} (Bloomenthal et al., 1994). Positive modulation has been described for glutamate (Liu et al., 2010), ethanol and anesthetics (Mascia et al., 1996). Glucose and related mono- and disaccharides were recently identified as positive modulators of recombinant α1, α1-β (Breitinger et al., 2015), and α3 (Breitinger and Breitinger, 2016) GlyRs in HEK293 cells, reducing EC_{50} value 2–4 fold. When glucose was present in the cell culture medium for 2–24 h prior to the experiments, positive modulation was observed even in the absence of sugar during experiments (Breitinger et al., 2015, 2016). Other sugars, including fructose, mannose, and the disaccharides lactose and sucrose also potentiate GlyR currents (Breitinger et al., 2016). EC_{50} of glucose and fructose for augmentation of glycine-mediated responses was ∼6–7 mM. At sugar concentrations >10 mM, the maximum of current enhancement was reached within ∼30 min, corresponding on-rates were <0.5 h for saturating concentrations of monosaccharides (glucose and fructose) and ∼1.5 h for disaccharides (sucrose and lactose). Off-rates were considerably slower (>24 h). Kinetics and concentration dependence of receptor potentiation are similar to those of protein glycation, suggesting a possible mechanism for GlyR modulation by sugars (Breitinger et al., 2016).

After overnight preincubation with 10 mM of glucose, we observed the maximum potentiation of recombinant α1 (Breitinger et al., 2016) and α3 (Breitinger and Breitinger, 2016) GlyRs. Fasting glucose levels in healthy individuals are ≤ 5.6 mM (≤100 mg/dl), levels of 5.6–7.9 mM (100–125 mg/dl) are considered prediabetic, and 7 mM (126 mg/dl) or higher indicate diabetes[1]. Thus, GlyR modulation is observed at physiological levels of glucose.

Since α3 GlyRs are involved in pain signaling pathways, we investigated the influence of glucose on *in vivo* pain-related behavior in two different mouse models, namely von Frey filaments and hotplate tests. Both experiments demonstrated a significant reduction of touch and pain sensitivity of mice after glucose treatment.

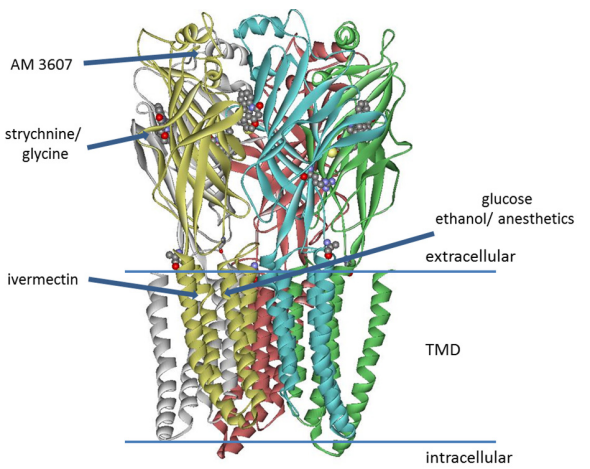

FIGURE 1 | Model of glycine receptor (GlyR), adapted from pdb data of the zebrafish α1 electron cryo-microscopy structure (Du et al., 2015). The binding site of AM-3607 was identified for GlyR α3 (Huang et al., 2017). Strychnine and the side chain of residue Lys143 (not fully resolved in the structure) are represented as ball and stick structures. Binding of strychnine, glycine, ivermectin and AM-3607 was determined from high-resolution structures, while the sites for ethanol, anesthetics (Mihic et al., 1997; Lobo et al., 2004), as well as the putative glucose binding site (Breitinger et al., 2016) were postulated from mutagenesis studies and functional analysis.

MATERIALS AND METHODS

Cell Culture and Transfection

HEK293 cells were grown, passaged and transfected using PEI as described (see **Supplementary Materials**).

Electrophysiological Recordings and Data Analysis

Current responses from GlyR-transfected HEK293 cells were measured at room temperature (21–23°C) at a holding potential of −50 mV using a HEKA EPC10 amplifier (HEKA Electronics, Lambrecht, Germany) controlled by Pulse software (HEKA Electronics). Recording pipettes were pulled from borosilicate glass (World Precision Instruments, Berlin, Germany) using a Sutter P-97 horizontal puller (Sutter, Novato, CA, USA). Solutions were applied using an Octaflow system (NPI

[1]https://www.mayoclinic.org/diseases-conditions/diabetes/diagnosis-treatment/drc-20371451

electronics, Tamm, Germany). The external buffer consisted of 135 mM NaCl, 5.5 mM KCl, 2 mM $CaCl_2$, 1.0 mM $MgCl_2$, and 10 mM Hepes (pH adjusted to 7.4 with NaOH); the internal buffer was 140 mM CsCl, 1.0 mM $CaCl_2$, 2.0 mM $MgCl_2$, 5.0 mM EGTA, and 10 mM Hepes (pH adjusted to 7.2 with CsOH). Glucose (Sigma-Aldrich, Munich, Germany) was added to the growth medium on the day before experiments to give a pre-exposure to 50 mM of glucose for 16–20 h. Dose-response data were fitted to the Hill equation (see **Supplementary Material**) to determine EC_{50} and IC_{50}. Significance of differences between EC_{50} values were determined using one-way ANOVA with $p \leq 0.05$ (*) and $p \leq 0.01$ (**) taken as significant.

Animal Housing

All animal experiments were performed according to ARRIVE guidelines and approved by the Ethics committee of the German University in Cairo. Animals were not sacrificed during or after any experiment. Male Swiss Webster mice weighing 20–45 g were used in this experiment. Four to eight animals were housed together in standard mouse cages with free access to chow and water with a 12 h light/dark cycle. Littermates were divided equally between experimental groups.

Tactile and Heat Sensitivity Tests

See **Supplementary Material S1** for experimental details. On the day of the experiment, mice were weighed and then fasted for 5–6 h to reduce variability in initial blood glucose levels (BGL). Mice had been accustomed to the test apparatus for 2–3 h on two separate days before experiments. Two hours before testing, mice were acclimatized to the measuring apparatus. For hotplate tests, mice were accustomed to the testing condition by placing them one by one on a switched off hotplate at room temperature for the set cut off time of 30 s. One hour before testing, baseline measurements for touch sensitivity were recorded. For both experiments, mice were then injected according to protocol. Blood glucose level was measured before and after injections (**Figure 3A**).

Mice were divided into four experimental groups (see main text). The investigator performing the measurements was blinded to treatment groups and to the blood glucose readings. All mice were measured for their Paw withdrawal threshold (PWT) using von Frey filaments on at least one occasion before the testing day to reduce the stress or surprise from the experiment. We used the up-and-down method to determine pain withdrawal thresholds (PWT; Bradman et al., 2015) with 8 mN as the starting value (see **Supplementary Material** for details). Baseline PWT values for each mouse were determined before treatment. Indices of tactile sensitivity were calculated by dividing 50% PWT values of each mouse by the baseline values that had been before treatment. Measurements were limited to the time window of 5 min after the second injection (strychnine or vehicle) due to the fast elimination kinetics of low doses of strychnine.

For hotplate tests, mice were placed in a 500 ml glass beaker set on the hotplate at 55°C. Mice were placed one by one on the hotplate, the time for the first nocifensive response was recorded using a stopwatch then the animal was immediately removed from the hotplate. The cut off time for the test was 30 s. Recorded responses were either licking or shaking of the hind paw, vocalization, or attempting to escape. Time until the first response was normalized to a control time taken 1 h before the injection protocol was started; ratios of response times were reported and given as average ± SEM.

See **Supplementary Material** for full details of experiments.

RESULTS

Glucose-Potentiated α3 Glycine Receptors Are Strychnine Sensitive

Initially, we verified the augmentation of recombinant α3L GlyRs expressed in HEK293 cells by glucose (Glc) and investigated the inhibition of the receptor by strychnine. In this set of experiments, the EC_{50} of control currents (no glucose) was 106 ± 16 μM, in comparison to 49.9 ± 5.3 μM after preincubation with 50 mM glucose (**Figures 2A–C**). The shift of EC_{50} was significant ($p = 0.0046$, one-Way ANOVA).

Strychnine is a highly specific antagonist with nanomolar affinity for the receptor. For inhibition experiments, glycine concentration was kept constant at 60 μM, which represents ∼EC_{25} in control cells, and ∼EC_{50} in glucose-treated cells. We tested $n = 7$ cells for each condition (**Figure 2B**). Strychnine inhibition at 60 μM of glycine gave IC_{50} values of 30.7 ± 2.8 nM and 46.2 ± 5.8 nM in the absence or presence of 50 mM glucose, respectively. This shift was statistically significant ($p = 0.034$). K_i values were calculated using the Cheng-Prusoff equation (Cer et al., 2009) to account for the different effective EC_{50} of glycine in the absence and presence of glucose, giving K_i of 18.8 ± 1.4 nM for control cells and 19.8 ± 1.6 nM for cells pretreated with 50 mM glucose. After correcting for the glucose-induced left-shift of the EC_{50} curve, the difference in the Ki of strychnine was below statistical significance ($p = 0.66$, one-way ANOVA). We thus concluded that inhibition of α3 GlyRs by strychnine is independent of the absence or presence of glucose (**Figure 2D**).

Glucose Reduces Tactile and Heat Sensitivity in Mice

In vivo tests were carried out in accordance with GUC Ethics and Animal care regulations. The LD_{50} of strychnine on mice is reported to be 0.98 mg/kg for intraperitoneal (IP) injection (Prasad et al., 1981; Patocka, 2009) and 2 mg/kg for oral administration (Setnikar et al., 1960; Patocka, 2009), while 2 mg/kg of IP administered strychnine was found to be lethal in 85% of Swiss Webster mice (Maher et al., 2014). In our study, non-lethal doses of strychnine of 0.2 mg/kg and 0.5 mg/kg were used, while the glucose dose was 2 g/kg in all experiments.

Tactile Sensitivity (von Frey) Tests

Tactile sensitivity was assessed using calibrated von Frey filaments (Department of Physiology, University of Erlangen, Germany). The protocol used was as follows (**Figure 3A**):

(i) Baseline PWT determination for each mouse, 30 min prior to the experiment;

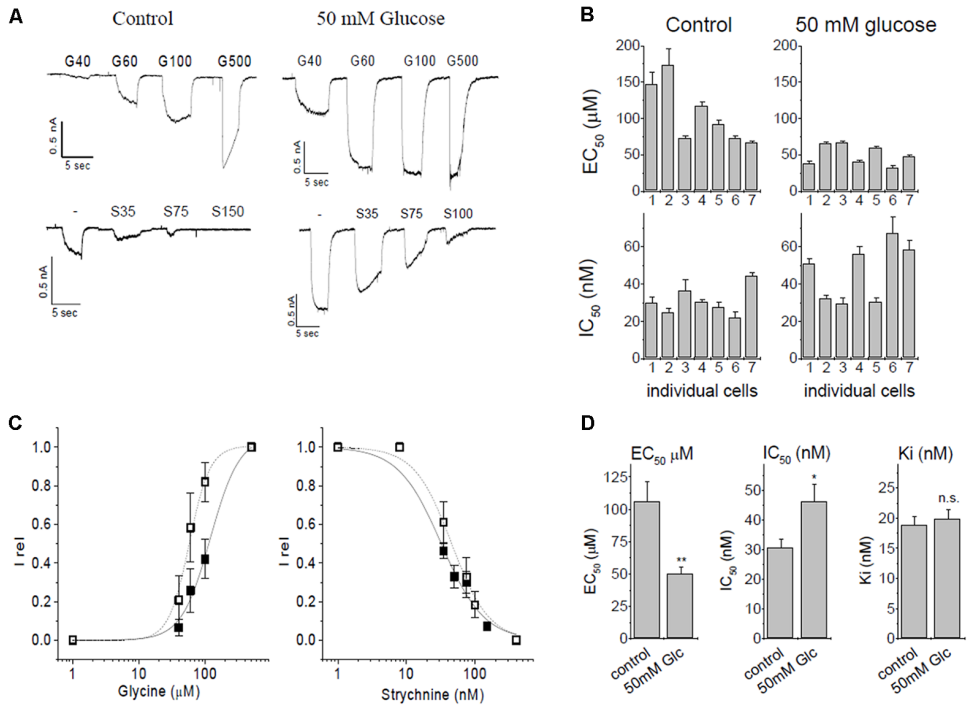

FIGURE 2 | Patch-clamp studies of α3 GlyR modulation by glucose and strychnine. **(A)** Glycine induced currents in HEK293 cells transfected with GlyR α3L constructs. Top panels: currents from untreated controls (5.5 mM glucose) and after overnight preincubation in 50 mM glucose. Bottom panels: inhibition by strychnine in the presence of 60 μM glycine of untreated cells, or cells preincubated with 50 mM glucose. **(B)** EC_{50}- and IC_{50} values of seven individual cells without (control) and with glucose preincubation. **(C)** EC_{50} and IC_{50} curves for control conditions (solid squares, solid line) and after preincubation with 50 mM glucose (open squares, dashed line). **(D)** Summary of changes of ion channel parameters before (left bar) and after (right bar) pretreatment with 50 mM glucose. Left panel: EC_{50} values for glycine. Middle panel: IC_{50}, values of strychnine at 60 μM glycine. Right panel: K_i for strychnine at 60 μM glycine. K_i was calculated using the Cheng-Prusoff correction, significance was tested using one-way ANOVA with $p < 0.05$ considered significant. Note that the observed IC_{50} for strychnine increases after receptors were preincubated with 50 mM glucose because glucose left-shifts concentration-response curve of glycine. The Cheng-Prusoff correction considers this change in EC_{50}, and K_i for strychnine is independent of the glucose concentration. $n = 7$ cells were used in all experiments. All data are means ± SEM; significance levels (relative to control) are indicated: $^*p \leq 0.5$; $^{**}p \leq 0.01$; ns, not significant.

(ii) at time $t = 0$, mice were injected with glucose (2 g/kg) or vehicle
(iii) at $t = 30$ min, mice were injected with strychnine (0.2 or 0.5 mg/kg) or vehicle;
(iv) at $t = 35$ min pain-related behavior was assessed.

Whenever glucose was injected, we observed a robust increase in BGL (**Figure 3B**, **Supplementary Tables S1–S3**). The timing of the strychnine injection was critical since our initial experiments showed that sub-lethal amounts of strychnine, as used here, are metabolized quickly, and after >5 min notable effects on pain sensitivity were gone. Effects of glucose on pain-related behavior were fully developed after 20 min and stable until at least 60 min post-injection (**Figure 3C**), in agreement with the time course for changes in BGL after IP injection (Xu et al., 2016). Thirty minutes after injection, BGL level was found to be increased by 2.2 ± 0.6 and 2.0 ± 0.8-fold in glucose and (Glc+Str) groups, respectively. There was no correlation between the magnitude of increase in BGL and the extent of glucose effect on pain hypersensitivity in Glc group mice (see **Supplementary Tables S1–S3**).

In agreement with previous studies (Yaksh, 1989; Lim and Lee, 2010) strychnine injected mice showed a significant increase in tactile sensitivity relative to control (**Figure 3D**). Upon glucose injection, PWT increased ∼2-fold relative to control (**Supplementary Tables S1–S3**). Increasing concentrations of strychnine led to increasing touch sensitivity in both, glucose-treated mice and vehicle-treated control animals (**Figure 3D**). Glucose treatment compensated hypersensitivity and allodynic effects of 0.2 and 0.5 mg/kg of strychnine (**Supplementary Tables S1–S3**). This indicates that increased blood glucose could indeed lower pain sensitivity in mice. Furthermore, glucose counteracted strychnine-induced touch sensitivity, indicating that at least part of the analgesic effect of glucose was mediated through the glycinergic pathway.

Hotplate Test

Hotplate tests were performed as a second assessment of pain-related behavior. Here, we measured the latency time of mice until pain-related reaction on a 55°C hotplate. Groups and injection protocols were as described for tactile sensitivity tests. Following the second injection, the latency time on the hotplate was recorded and normalized to baseline time. Glucose exhibited an analgesic effect with a significant increase of the average normalized latency time from 0.99 ± 0.10 (control)

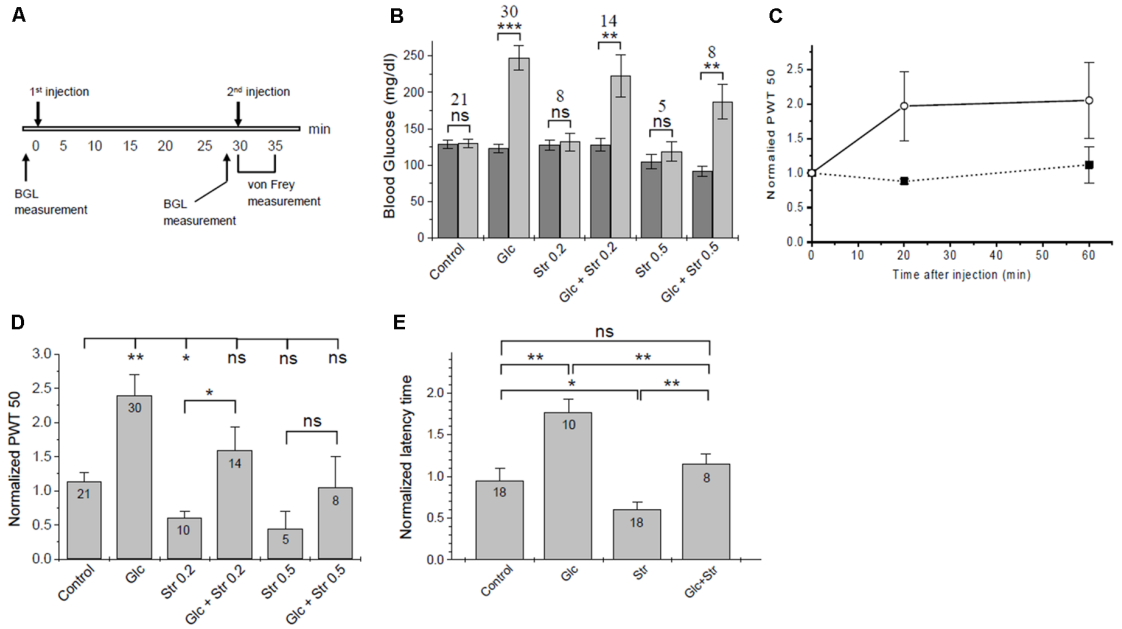

FIGURE 3 | Touch- and heat sensitivity tests. **(A)** Time course of *in vivo* tests. **(B)** Changes in blood glucose. Blood glucose levels (BGL) at time 0 (dark bars) and 30 min after 1st injection (light bars) are plotted for the experimental groups. The number of animals in each group and the significance of differences in BGL before/after injection are given. Significance was tested using one-way ANOVA with $^{*}p < 0.05$, $^{**}p < 0.01$, $^{***}p < 0.005$, ns, not significant. See **Supplementary Material S2** for a list of blood glucose values. **(C)** Time course of tactile sensitivity after glucose administration. Paw withdrawal threshold (PWT), normalized to baseline, was measured 20 min and 60 min after glucose injection (open circles, dashed line, $n = 4$) or PBS control (solid squares, solid line, $n = 3$). Analgesic effects of glucose persisted for >60 min. **(D)** Summary of normalized PWT values after treatment of mice with glucose/vehicle and different doses of strychnine. Data are given as means ± SEM, see **Supplementary Material S2** for details. Significance of differences (one-way ANOVA) is indicated with $^{*}p < 0.05$, $^{**}p < 0.01$, ns, not significant. The number of animals for each condition is given. **(E)** Hotplate test—normalized latency time until heat-related behavior (means ± SEM). Significance is indicated (one-way ANOVA); $^{*}p < 0.05$, $^{**}p < 0.01$, ns, not significant. The number of animals in each experimental group is indicated.

to 1.79 ± 0.18 (+glucose). Strychnine decreased the thermal pain threshold, causing a statistically significant decrease in the average normalized latency time of mice on the hotplate compared to control (**Figure 3E**). Normalized time to response was 0.63 ± 0.10 for mice injected with 0.2 mg/kg strychnine. Mice who received glucose pretreatment followed by 0.2 mg/kg of strychnine had a normalized response time of 1.72 ± 0.44. Mice who received 0.5 mg/kg strychnine showed a further reduction of normalized response time (0.30 ± 0.07), which was increased to 0.74 ± 0.15 in mice who received 2 g/kg of glucose prior to the strychnine challenge. Thus, increased heat sensitivity caused by strychnine was offset after pretreatment of mice with glucose in a dose-dependent manner, in agreement with the results from von Frey tactile tests (**Figure 3D**). Changes in heat sensitivity by glucose (reduced) and strychnine (increased) were statistically significant, while heat-related behavior of mice receiving both compounds was not different from control animals (**Figure 3E**).

DISCUSSION

Glycinergic interneurons control the transmission of these afferent nerve fibers to the projection neurons that ascends to the brain thereby controlling pain transmission (Zeilhofer and Zeilhofer, 2008; Imlach et al., 2016). Alpha3 GlyRs inhibit Aβ fibers from amplifying nociceptive signal pathways (Lynch and Callister, 2006; Harvey et al., 2009; Zeilhofer et al., 2012). Inhibition of α3 GlyR activity removes this block, the resulting "disinhibition" allows non-noxious signals from Aβ fibers to enter pain circuitry, and these signals are then transmitted to the brain as noxious, causing allodynia and hypersensitivity (Zeilhofer et al., 2012). This type of allodynia is observed in some forms of neuropathy or caused by specific GlyR blockers such as strychnine (Imlach et al., 2016), or prostaglandins which reduce α3 GlyR activity through EP2 receptors and protein kinase A (Harvey et al., 2004). The increase in sensitivity to tactile stimuli after administration of strychnine is well documented in the literature. Our results agree well with reports showing that strychnine injection increased pain hypersensitivity in von Frey test due to its blockade of synaptic GlyR ion channels (Lim and Lee, 2010). Moreover, it is well established that spinal glycinergic interneurons are important in controlling and processing tactile sensation. In many studies investigating neuropathic pain, loss of glycinergic inhibition on Aβ afferent fibers was implicated in perceiving tactile (non-painful) sensation as pain (Sivilotti and Woolf, 1994; Lim and Lee, 2010; Imlach et al., 2016).

The opposite effect, analgesia, is observed upon GlyR stimulation by cannabinoids (Ahrens et al., 2009; Xiong et al., 2011, 2012), showing that α3 receptor activity is an essential component of both, augmentation and suppression of nociceptive signals. The ability of glucose to offset

strychnine-induced hypersensitivity is consistent with a direct augmentation of α3 GlyR function by glucose, as was observed *in vitro* by patch-clamp studies (Breitinger and Breitinger, 2016). Notably, glucose was shown to potentiate not only α3 but also α1 and α1-β GlyRs (Breitinger et al., 2015, 2016). Indeed, similar effects were reported for cannabinoids (Ahrens et al., 2009; Wells et al., 2015). Indeed, cannabinoid-related ligands for α1 receptors were used for a virtual screening approach in search of novel analgesics (Wells et al., 2015). The dependence of glucose-mediated analgesia on strychnine concentration that we observed is a strong argument in favor of a specific action of glucose on α3 GlyRs *in vivo*. The observed analgesic effects of glucose would thus be the result of: (i) a reduced efficiency of strychnine because of the left-shift of the EC_{50} of glycine at higher glucose concentrations; and (ii) a potentiation of uninhibited GlyR currents, compensating the loss of strychnine-inhibited receptors. Apparently, glucose binding generates a more active receptor with decreased apparent strychnine sensitivity when measurements are performed at the same concentration of glycine. Converting IC_{50} values into K_i binding constants—thereby correcting for the reduced EC_{50} values in presence of 50 mM glucose—shows that strychnine inhibition is not affected by glucose.

An interplay between glucose and neuronal ion channels, as well as crosstalk between glucose and glycine metabolism has been reported. Indirect effects of glucose concentration on leptin-induced IPSCS and GABAergic modulation in insular cortex cells were described (Murayama et al., 2019). Indeed, $GABA_A$ receptors contribute to the activity of pancreatic beta cells (Korol et al., 2018), but no direct modulation of the receptor by glucose was reported. Glycine itself was reported to be an antioxidant and protective of pancreatic cells in diabetic rats (Chen et al., 2018), the effects of glycine on glucose homeostasis (but not vice versa) have recently been reviewed (Yan-Do and MacDonald, 2017). Ketone bodies have been shown to modulate ligand-gated in channel function, with β-hydroxybutyrate at physiological concentrations being an inhibitor of GlyRs expressed on Xenopus oocytes (Pflanz et al., 2019).

Structural data reveal the binding sites of strychnine, glycine, ivermectin and a new class of analgesic potentiators AM-3607 (Du et al., 2015; Huang et al., 2015, 2017). Considering these structures, the distance between residue Lys143—putatively involved in glucose binding—and the glycine- or strychnine pocket is too large for direct interaction. For the same reason, there is no direct evidence to suggest a newly discovered analgesic binding site close to the N-terminal α-helix (Huang et al., 2017) as glucose binding pocket. However, the binding cavity of ivermectin from electron cryo-microscopy data (Du et al., 2015) is close to Lys143. The key residue postulated for the action of alcohol and anesthetics is Ser267 (Mihic et al., 1997; Lobo et al., 2004), which is also involved in ivermectin binding (Du et al., 2015), suggesting that these sites overlap. Ivermectin and volatile anesthetics are hydrophobic, yet hydrophilic alcohols are also postulated to bind to the same pocket (Mihic et al., 1997; Lobo et al., 2004), which appears to accommodate both, hydrophilic and hydrophobic compounds. It is noted, that the side chain of Lys143 was not resolved in two high-resolution structures (Du et al., 2015; Huang et al., 2015). This is indicative of high conformational flexibility, which is generally considered a good prerequisite for binding (Najmanovich et al., 2000; Zavodszky and Kuhn, 2005). While the interaction of ivermectin with the receptor has been resolved, structural data of the glucose-bound receptor are not yet available. Similar interactions between M3 of the (+) subunit, M1 of the (−) subunit, and contacts with M2 and M2/M3 loop can be inferred, but require experimental proof.

Diabetic neuropathy (DN) is a common complication of diabetes, where the patients' pain threshold can be increased or decreased. Non-painful DN represents a clinical and diagnostic challenge, often going unnoticed until irreversible nerve damage has occurred (Gylfadottir et al., 2019). Over time, at least 50% of patients with diabetes develop DN. Although overall understanding of the complexities of DN has substantially evolved over the past decade, the distinct mechanisms underlying neuropathy in type 1 and type 2 diabetes remains unknown (Feldman et al., 2019). Tight control of hyperglycemia reduces the incidence of DN in type 1 diabetes mellitus but its role in type 2 diabetes is less clear. The cause of DN remains controversial, focused on the impact of metabolic abnormalities, polyol flux, microvascular changes, mitochondria, oxidative stress, lipid biology and others (Zochodne, 2019). Glycemic control is known to reduce diabetic neuropathic pain. However, it was observed that too severe reduction of BGL increases the risk of hypoglycemic episodes, which are themselves linked to painful neuropathy (Zhang et al., 2016). This phenomenon, known as "insulin neuritis" or "treatment-induced neuropathy," has been reported in both type 1 and type 2 diabetic patients treated with insulin or oral hypoglycemic agents, who typically had a history of poor glycemic control (Gibbons and Freeman, 2010; Knopp et al., 2013). The involvement of GlyR α3 signaling in pain regulation could explain these phenomena. In the case of non-treated diabetes, BGL are usually elevated, thereby increasing GlyR function and one would expect reduced pain sensitivity. Under hypoglycemic conditions, GlyR activity would be decreased and pain sensitivity increased.

To our knowledge, a direct effect of glucose-induced GlyR potentiation (Breitinger et al., 2015, 2016) on pain sensitivity *in vivo* has not been described before. However, a recent study has shown that morphine-mediated analgesia in rats is enhanced upon intraperitoneal administration of glucose, and is not related to glucose "taste or gustation" (Yamamoto et al., 2014), suggesting a "molecular" effect of glucose, similar to our observations. Indeed, potentiation of α3 GlyR activity by glucose could enhance other mechanisms of analgesia. Combined evidence from *in vitro* and *in vivo* studies suggests that glucose has a direct effect on nociceptive signaling *via* potentiation of spinal α3 GlyRs, and modulation of neuronal ion channels by glucose may indeed be a relevant physiological mechanism. Data suggest the α3 GlyR signaling pathway as a possible player in DN.

DATA AVAILABILITY STATEMENT

All datasets generated for this study are included in the article/**Supplementary Material**.

ETHICS STATEMENT

The animal study was reviewed and approved by Ethics Committe, German University in Cairo.

AUTHOR CONTRIBUTIONS

UB and H-GB devised the study and wrote the manuscript. RH, MA and UB devised and performed experiments. RH, MA, UB and H-GB analyzed the data.

ACKNOWLEDGMENTS

Expert laboratory assistance by Mousa Abdalla Mousa is gratefully acknowledged.

SUPPLEMENTARY MATERIAL

The Supplementary Material for this article can be found online at: https://www.frontiersin.org/articles/10.3389/fnmol.2019.00280/full#supplementary-material.

REFERENCES

Ahrens, J., Demir, R., Leuwer, M., de la Roche, J., Krampfl, K., Foadi, N., et al. (2009). The nonpsychotropic cannabinoid cannabidiol modulates and directly activates alpha-1 and alpha-1-Beta glycine receptor function. *Pharmacology* 83, 217–222. doi: 10.1159/000201556

Bloomenthal, A. B., Goldwater, E., Pritchett, D. B., and Harrison, N. L. (1994). Biphasic modulation of the strychnine-sensitive glycine receptor by Zn^{2+}. *Mol. Pharmacol.* 46, 1156–1159.

Bradman, M. J., Ferrini, F., Salio, C., and Merighi, A. (2015). Practical mechanical threshold estimation in rodents using von Frey hairs/Semmes-Weinstein monofilaments: towards a rational method. *J. Neurosci. Methods* 255, 92–103. doi: 10.1016/j.jneumeth.2015.08.010

Breitinger, H. (2014). "*Glycine receptors*", in eLS (electronic Library of Science) (Chichester, UK: John Wiley & Sons, Ltd.). doi: 10.1002/9780470015902.a0000236.pub2

Breitinger, U., and Breitinger, H. G. (2016). Augmentation of glycine receptor α3 currents suggests a mechanism for glucose-mediated analgesia. *Neurosci. Lett.* 612, 110–115. doi: 10.1016/j.neulet.2015.11.051

Breitinger, U., Raafat, K. M., and Breitinger, H. G. (2015). Glucose is a positive modulator for the activation of human recombinant glycine receptors. *J. Neurochem.* 134, 1055–1066. doi: 10.1111/jnc.13215

Breitinger, U., Sticht, H., and Breitinger, H. G. (2016). Modulation of recombinant human a1 glycine receptors by mono- and disaccharides: a kinetic study. *ACS Chem. Neurosci.* 7, 1077–1087. doi: 10.1021/acschemneuro.6b00044

Cer, R. Z., Mudunuri, U., Stephens, R., and Lebeda, F. J. (2009). IC50-to-K_i: a web-based tool for converting IC50 to K_i values for inhibitors of enzyme activity and ligand binding. *Nucleic Acids Res.* 37, W441–W445. doi: 10.1093/nar/gkp253

Chen, L., Zhang, J., Li, C., Wang, Z., Li, J., Zhao, D., et al. (2018). Glycine transporter-1 and glycine receptor mediate the antioxidant effect of glycine in diabetic rat islets and INS-1 cells. *Free Radic. Biol. Med.* 123, 53–61. doi: 10.1016/j.freeradbiomed.2018.05.007

Du, J., Lü, W., Wu, S., Cheng, Y., and Gouaux, E. (2015). Glycine receptor mechanism elucidated by electron cryo-microscopy. *Nature* 526, 224–229. doi: 10.1038/nature14853

Dupre, M. L., Broyles, J. M., and Mihic, S. J. (2007). Effects of a mutation in the TM2-TM3 linker region of the glycine receptor alpha1 subunit on gating and allosteric modulation. *Brain Res.* 1152, 1–9. doi: 10.1016/j.brainres.2007.03.031

Feldman, E. L., Callaghan, B. C., Pop-Busui, R., Zhang, D. W., Wright, D. E., Bennett, D. L., et al. (2019). Diabetic neuropathy. *Nat. Rev. Dis. Primers* 5:41. doi: 10.1038/s41572-019-0092-1

Gibbons, C. H., and Freeman, R. (2010). Treatment-induced diabetic neuropathy: a reversible painful autonomic neuropathy. *Ann. Neurol.* 67, 534–541. doi: 10.1002/ana.2195

Gylfadottir, S. S., Weeracharoenkul, D., Andersen, S. T., Niruthisard, S., Suwanwalaikorn, S., and Jensen, T. S. (2019). Painful and non-painful diabetic polyneuropathy: clinical characteristics and diagnostic issues. *J. Diabetes Investig.* 10, 1148–1157. doi: 10.1111/jdi.13105

Harvey, R. J., Depner, U. B., Wassle, H., Ahmadi, S., Heindl, C., Reinold, H., et al. (2004). GlyR alpha3: an essential target for spinal PGE2-mediated inflammatory pain sensitization. *Science* 304, 884–887. doi: 10.1126/science.1094925

Harvey, V. L., Caley, A., Müller, U. C., Harvey, R. J., and Dickenson, A. H. (2009). A selective role for alpha3 subunit glycine receptors in inflammatory pain. *Front. Mol. Neurosci.* 2:14. doi: 10.3389/neuro.02.014.2009

Huang, X., Chen, H., Michelsen, K., Schneider, S., and Shaffer, P. L. (2015). Crystal structure of human glycine receptor-alpha3 bound to antagonist strychnine. *Nature* 526, 277–280. doi: 10.1038/nature14972

Huang, R. Q., and Dillon, G. H. (2000). Direct inhibition of glycine receptors by genistein, a tyrosine kinase inhibitor. *Neuropharmacology* 39, 2195–2204. doi: 10.1016/s0028-3908(00)00046-0

Huang, X., Shaffer, P. L., Ayube, S., Bregman, H., Chen, H., Lehto, S. G., et al. (2017). Crystal structures of human glycine receptor α3 bound to a novel class of analgesic potentiators. *Nat. Struct. Mol. Biol.* 24, 108–113. doi: 10.1038/nsmb.3329

Imlach, W. L., Bhola, R. F., Mohammadi, S. A., and Christie, M. J. (2016). Glycinergic dysfunction in a subpopulation of dorsal horn interneurons in a rat model of neuropathic pain. *Sci. Rep.* 6:37104. doi: 10.1038/srep37104

Knopp, M., Srikantha, M., and Rajabally, Y. A. (2013). Insulin neuritis and diabetic cachectic neuropathy: a review. *Curr. Diabetes Rev.* 9, 267–274. doi: 10.2174/1573399811309030007

Kondratskaya, E. L., Fisyunov, A. I., Chatterjee, S. S., and Krishtal, O. A. (2004). Ginkgolide B preferentially blocks chloride channels formed by heteromeric glycine receptors in hippocampal pyramidal neurons of rat. *Brain Res. Bull.* 63, 309–314. doi: 10.1016/j.brainresbull.2004.03.007

Korol, S. V., Jin, Z., Jin, Y., Bhandage, A. K., Tengholm, A., Gandasi, N. R., et al. (2018). Functional characterization of native, high-affinity $GABA_A$ receptors in human pancreatic β cells. *EBioMedicine* 30, 273–282. doi: 10.1016/j.ebiom.2018.03.014

Lim, E. S., and Lee, I. O. (2010). Effect of intrathecal glycine and related amino acids on the allodynia and hyperalgesic action of strychnine or bicuculline in mice. *Korean J. Anesthesiol.* 58, 76–86. doi: 10.4097/kjae.2010.58.1.76

Liu, J., Wu, D. C., and Wang, Y. T. (2010). Allosteric potentiation of glycine receptor chloride currents by glutamate. *Nat. Neurosci.* 13, 1225–1232. doi: 10.1038/nn.2633

Lobo, I. A., Mascia, M. P., Trudell, J. R., and Harris, R. A. (2004). Channel gating of the glycine receptor changes accessibility to residues implicated in receptor potentiation by alcohols and anesthetics. *J. Biol. Chem.* 279, 33919–33927. doi: 10.1074/jbc.M313941200

Lynch, J. W., and Callister, R. J. (2006). Glycine receptors: a new therapeutic target in pain pathways. *Curr. Opin. Investig. Drugs* 7, 48–53.

Maher, A., Radwan, R., and Breitinger, H. G. (2014). *In vivo* protection against strychnine toxicity in mice by the glycine receptor agonist ivermectin. *Biomed Res. Int.* 2014:640790. doi: 10.1155/2014/640790

Mascia, M. P., Machu, T. K., and Harris, R. A. (1996). Enhancement of homomeric glycine receptor function by long-chain alcohols and anaesthetics. *Br. J. Pharmacol.* 119, 1331–1336. doi: 10.1111/j.1476-5381.1996.tb16042.x

Mihic, S. J., Ye, Q., Wick, M. J., Koltchine, V. V., Krasowski, M. D., Finn, S. E., et al. (1997). Sites of alcohol and volatile anaesthetic action on $GABA_A$ and glycine receptors. *Nature* 389, 385–389. doi: 10.1038/38738

Munoz, B., Yevenes, G. E., Forstera, B., Lovinger, D. M., and Aguayo, L. G. (2018). Presence of inhibitory glycinergic transmission in medium spiny neurons in the nucleus accumbens. *Front Mol. Neurosci.* 11, 228. doi: 10.3389/fnmol.2018.00228

Murayama, S., Yamamoto, K., Fujita, S., Takei, H., Inui, T., Ogiso, B., et al. (2019). Extracellular glucose-dependent IPSC enhancement by leptin in fast-spiking to pyramidal neuron connections via JAK2-PI3K pathway in the rat insular cortex. *Neuropharmacology* 149, 133–148. doi: 10.1016/j.neuropharm.2019.02.021

Najmanovich, R., Kuttner, J., Sobolev, V., and Edelman, M. (2000). Side-chain flexibility in proteins upon ligand binding. *Proteins* 39, 261–268. doi: 10.1002/(sici)1097-0134(20000515)39:3<261::aid-prot90>3.0.co;2-4

Patocka, J. (2009). "Strychnine," in *Handbook of Toxicology of Chemical Warfare Agents*, ed. R. C. Ghupta (London: Academic Press), 1168.

Pflanz, N. C., Daszkowski, A. W., James, K. A., and Mihic, S. J. (2019). Ketone body modulation of ligand-gated ion channels. *Neuropharmacology* 148, 21–30. doi: 10.1016/j.neuropharm.2018.12.013

Prasad, C. R., Patnaik, G. K., Gupta, R. C., Anand, N., and Dhawan, B. N. (1981). Central nervous system stimulant activity of n-(delta 3-chromene-3-carbonyl)-4 iminopyridine (compound 69/224). *Indian J. Exp. Biol.* 19, 1075–1076.

Pullan, L. M., and Powel, R. J. (1992). Comparison of binding at strychnine-sensitive (inhibitory glycine receptor) and strychnine-insensitive (N-methyl-D-aspartate receptor) glycine binding sites. *Neurosci. Lett.* 148, 199–201. doi: 10.1016/0304-3940(92)90838-x

Raafat, K., Breitinger, U., Mahran, L., Ayoub, N., and Breitinger, H. G. (2010). Synergistic inhibition of glycinergic transmission *in vitro* and *in vivo* by flavonoids and strychnine. *Toxicol. Sci.* 118, 171–182. doi: 10.1093/toxsci/kfq245

Setnikar, I., Murmann, W., Magistretti, M. J., and Da Re, P. (1960). Amino-methylchromones, brain stem stimulants and pentobarbital antagonists. *J. Pharmacol. Exp. Ther.* 128, 176–181.

Sivilotti, L., and Woolf, C. J. (1994). The contribution of $GABA_A$ and glycine receptors to central sensitization: disinhibition and touch-evoked allodynia in the spinal cord. *J. Neurophysiol.* 72, 169–179. doi: 10.1152/jn.1994.72.1.169

Wells, M. M., Tillman, T. S., Mowrey, D. D., Sun, T., Xu, Y., and Tang, P. (2015). Ensemble-based virtual screening for cannabinoid-like potentiators of the human glycine receptor α1 for the treatment of pain. *J. Med. Chem.* 58, 2958–2966. doi: 10.1021/jm501873p

Xiong, W., Cheng, K., Cui, T., Godlewski, G., Rice, K. C., Xu, Y., et al. (2011). Cannabinoid potentiation of glycine receptors contributes to cannabis-induced analgesia. *Nat. Chem. Biol.* 7, 296–303. doi: 10.1038/nchembio.552

Xiong, W., Cui, T., Cheng, K., Yang, F., Chen, S. R., Willenbring, D., et al. (2012). Cannabinoids suppress inflammatory and neuropathic pain by targeting alpha3 glycine receptors. *J. Exp. Med.* 209, 1121–1134. doi: 10.1084/jem.20120242

Xu, X., Pang, J., Chen, Y., Bucala, R., Zhang, Y., and Ren, J. (2016). Macrophage migration inhibitory factor (MIF) deficiency exacerbates aging-induced cardiac remodeling and dysfunction despite improved inflammation: role of autophagy regulation. *Sci. Rep.* 6:22488. doi: 10.1038/srep22488

Yaksh, T. L. (1989). Behavioral and autonomic correlates of the tactile evoked allodynia produced by spinal glycine inhibition: effects of modulatory receptor systems and excitatory amino acid antagonists. *Pain* 37, 111–123. doi: 10.1016/0304-3959(89)90160-7

Yamamoto, R. T., Foulds-Mathes, W., and Kanarek, R. B. (2014). Antinociceptive actions of peripheral glucose administration. *Pharmacol. Biochem. Behav.* 117, 34–39. doi: 10.1016/j.pbb.2013.12.002

Yan-Do, R., and MacDonald, P. E. (2017). Impaired "Glycine"-mia in type 2 diabetes and potential mechanisms contributing to glucose homeostasis. *Endocrinology* 158, 1064–1073. doi: 10.1210/en.2017-00148

Zavodszky, M. I., and Kuhn, L. A. (2005). Side-chain flexibility in protein-ligand binding: the minimal rotation hypothesis. *Protein Sci.* 14, 1104–1114. doi: 10.1110/ps.041153605

Zeilhofer, H. U., Wildner, H., and Yévenes, G. E. (2012). Fast synaptic inhibition in spinal sensory processing and pain control. *Physiol. Rev.* 92, 193–235. doi: 10.1152/physrev.00043.2010

Zeilhofer, H. U., and Zeilhofer, U. B. (2008). Spinal dis-inhibition in inflammatory pain. *Neurosci. Lett.* 437, 170–174. doi: 10.1016/j.neulet.2008.03.056

Zhang, Y. P., Mei, S., Yang, J., Rodriguez, Y., and Candiotti, K. A. (2016). Acute hypoglycemia induces painful neuropathy and the treatment of coenzyme Q10. *J. Diabetes Res.* 2016:4593052. doi: 10.1155/2016/4593052

Zhu, L., Jiang, Z. L., Krnjević, K., Wang, F. S., and Ye, J. H. (2003). Genistein directly blocks glycine receptors of rat neurons freshly isolated from the ventral tegmental area. *Neuropharmacology* 45, 270–280. doi: 10.1016/s0028-3908(03)00151-5

Zochodne, D. W. (2019). The challenges of diabetic polyneuropathy: a brief update. *Curr. Opin. Neurol.* 32, 666–675. doi: 10.1097/WCO.0000000000000723

Conflict of Interest: The authors declare that the research was conducted in the absence of any commercial or financial relationships that could be construed as a potential conflict of interest.

frontiers in Molecular Neuroscience

ORIGINAL RESEARCH
published: 26 November 2019
doi: 10.3389/fnmol.2019.00284

Transcriptional Profiling of Non-injured Nociceptors After Spinal Cord Injury Reveals Diverse Molecular Changes

Jessica R. Yasko[1], *Isaac L. Moss*[2] *and Richard E. Mains*[1]*

[1]*Department of Neuroscience, University of Connecticut Health Center, Farmington, CT, United States,* [2]*Department of Orthopedic Surgery and the Comprehensive Spine Center, University of Connecticut Health Center, Farmington, CT, United States*

Traumatic spinal cord injury (SCI) has devastating implications for patients, including a high predisposition for developing chronic pain distal to the site of injury. Chronic pain develops weeks to months after injury, consequently, patients are treated after irreparable changes have occurred. Nociceptors are central to chronic pain; however, the diversity of this cellular population presents challenges to understanding mechanisms and attributing pain modalities to specific cell types. To begin to address how peripheral sensory neurons below the injury level may contribute to the below-level pain reported by SCI patients, we examined SCI-induced changes in gene expression in lumbar dorsal root ganglia (DRG) below the site of injury. SCI was performed at the T10 vertebral level, with injury produced by a vessel clip with a closing pressure of 15 *g* for 1 min. Alterations in gene expression produce long-term sensory changes, therefore, we were interested in studying SCI-induced transcripts before the onset of chronic pain, which may trigger changes in downstream signaling pathways and ultimately facilitate the transmission of pain. To examine changes in the nociceptor subpopulation in DRG distal to the site of injury, we retrograde labeled sensory neurons projecting to the hairy hindpaw skin with fluorescent dye and collected the corresponding lumbar (L2–L6) DRG 4 days post-injury. Following dissociation, labeled neurons were purified by fluorescence-activated cell sorting (FACS). RNA was extracted from sorted sensory neurons of naïve, sham, or SCI mice and sequenced. Transcript abundances validated that the desired population of nociceptors were isolated. Cross-comparisons to data sets from similar studies confirmed, we were able to isolate our cells of interest and identify a unique pattern of gene expression within a subpopulation of neurons projecting to the hairy hindpaw skin. Differential gene expression analysis showed high expression levels and significant transcript changes 4 days post-injury in SCI cell populations relevant to the onset of chronic pain. Regulatory interrelationships predicted by pathway analysis implicated changes within the synaptogenesis signaling pathway as well as networks related to inflammatory signaling mechanisms, suggesting a role for synaptic plasticity and a correlation with pro-inflammatory signaling in the transition from acute to chronic pain.

Keywords: DRG, pain, inflammation, von Frey, hypersensitivity, FACS

OPEN ACCESS

Edited by:
Ildikó Rácz,
Universitätsklinikum Bonn, Germany

Reviewed by:
Edgar T. Walters,
University of Texas Health Science Center at Houston, United States
Rainer Viktor Haberberger,
Flinders University, Australia

***Correspondence:**
Richard E. Mains
mains@uchc.edu

Received: *21 August 2019*
Accepted: *08 November 2019*
Published: *26 November 2019*

Citation:
Yasko JR, Moss IL and Mains RE (2019) Transcriptional Profiling of Non-injured Nociceptors After Spinal Cord Injury Reveals Diverse Molecular Changes. Front. Mol. Neurosci. 12:284. doi: 10.3389/fnmol.2019.00284

INTRODUCTION

While spinal cord injury (SCI) is typically associated with loss of locomotor function, it can also result in chronic pain, affecting nearly 70% of patients with SCI (Finnerup et al., 2001). There are many categories of pain types affecting this population, however, studies indicate that neuropathic pain below, or distal, to the level of injury is among the most common and difficult to treat (Defrin et al., 2001; Finnerup et al., 2001; Siddall and Loeser, 2001; Yezierski, 2005; Nees et al., 2016). Of those patients reporting below-level neuropathic pain, half described their pain as severe or excruciating, causing significant disability in patients already disabled from loss of motor function (Defrin et al., 2001; Siddall et al., 2003). With few patients able to achieve complete relief with current treatment options, research has focused on mechanisms responsible for SCI pain at the site of injury, with the intention of treating the injury itself to prevent subsequent development of pain.

Considerable advances have been made in understanding changes within the spinal cord, including how spinally mediated alterations contribute to SCI-induced pain by increasing spinal cord excitability, and by establishing a variety of factors that impact how incoming sensory stimulation is processed (Bruce et al., 2002; You et al., 2008; Meisner et al., 2010). However, this approach has not translated into successful pain management. This may be attributed to an incomplete understanding of the differential functions of specific afferent subtypes in SCI, and how afferents distal to the site of injury become sensitized in patients with chronic below-level pain (Thakur et al., 2014). The sensory system receives inputs from multiple cell types, and peripheral cell bodies within the dorsal root ganglia (DRG) are important targets for assessing sensory function and pain (Usoskin et al., 2015). Persistent activity from injured and non-injured afferent fibers contributes to development and maintenance of many types of chronic pain (Devor, 2009; Gold and Gebhart, 2010; Walters, 2012).

Each sensory neuron has a unique pattern of gene expression that influences its modality-specific contribution to injury-induced pain (Le Pichon and Chesler, 2014). To better understand the underlying pathophysiology of below-level pain following SCI, it is necessary to identify changes in cells impacted by the injury. The skin is heavily innervated by a broad range of nociceptors, and previous work using a model of spared nerve injury (SNI) has shown that the function of cutaneous nociceptors can be impacted by injury (Berta et al., 2017). This has also been demonstrated in models of SCI by sustained spontaneous activity in peripheral terminals and in cell bodies of sensory neurons projecting to the skin after initial SCI (Carlton et al., 2009; Bedi et al., 2010; Wu et al., 2013; Yang et al., 2014; Ritter et al., 2015). Additional work has demonstrated that blockade of peripheral afferents into the central nervous system (CNS) can effectively mitigate patient discomfort and chronic pain (Campbell et al., 1988; Basbaum et al., 2009; Gold and Gebhart, 2010; Vaso et al., 2014; Haroutounian et al., 2018; Buch et al., 2019). These data support the idea that the mechanisms generating and maintaining prolonged pain reside within the peripheral nervous system.

In the present study, we identify specific transcriptional alterations in non-injured DRG distal to the site of injury. Using retrograde labeling from hairy hindpaw skin and flow cytometry, we isolated a nociceptor population projecting to sites distal to the spinal injury, free of surrounding neuronal and glial cells. This enabled identification of novel cutaneous nociceptor genes and predicted pathways not discernible by whole DRG tissue analyses.

MATERIALS AND METHODS

Animals

Experiments were conducted with adult (8–12 weeks) female C57BL/6J mice (Jackson Laboratory, Bangor, ME, USA). Several chronic pain conditions have a higher prevalence in females, and numerous studies have reported higher pain prevalence in the SCI population among female patients (Cardenas et al., 2004). Women also report greater frequency, severity, and longer-lasting pain, as well as neuropathic pain below the level of injury, in comparison to men (Cardenas et al., 2004). The majority of research examines SCI in male rodents and this study will add to what is known in the literature by focusing on female mice (Cardenas et al., 2004). Naïve animals were group-housed; sham and spinal cord injured animals were individually caged. All animals were maintained on a 12:12-h light-dark cycle with a temperature-controlled environment, and given food and water *ad libitum*. All treatments and testing were approved by the University of Connecticut Health Center Institutional Animal Care and Use Committee.

Spinal Cord Injury (SCI) Procedure

Animals were anesthetized by inhalation of isoflurane and a 1.0-cm dorsal midline skin sterile incision was made over T8–T11, as per Ma et al. (2001). Connective and muscle tissue were removed to expose the bone from T9–T10, and a laminectomy was performed at the T10 vertebral level. SCI was produced by compression of the vertical plane of the spinal cord using a vessel clip with a closing pressure of 15 *g* (WPI, Sarasota, FL, USA) for 1 min, exerting pressure from side to side on the spinal cord. Sudden impact is produced by the rapid release of the vessel clip (Tator and Poon, 2008). After removal of the clip a hemorrhagic ring at the site of compression is present. This injury is analogous to the majority of lesions in humans, as the model constitutes both contusion and compression (Marques et al., 2014). The injury resulted in paralysis of the hindpaws below the level of injury and was considered mild-moderate based on the ability of animals to exhibit slight ankle movement 24 h following injury (a score of 1 on the Basso Mouse Scale for locomotion), their ability to recover additional ankle movement by day 4, but the inability of mice to recover complete bladder control by day 4 (Basso et al., 2006). The wound is closed with coated vicryl absorbable sutures (Ethicon, Somerville, NJ, USA). Mice were allowed to recover in warm cages for 24 h. All animals were administered antibiotics once immediately following surgery (5 mg/kg gentamicin), as well as subcutaneous saline for 4 days following surgery, without analgesics. Sham control mice received the same treatment excluding the vessel

clip. Manual bladder expression on SCI mice was performed twice daily until mice were sacrificed. Mortality was less than 10% and typically occurred during the laminectomy due to excessive blood loss, or when postinjury weight loss required the animal to be sacrificed. Spinal cords collected at 4 days post-injury were most notably characterized by minimal cavitation and scar tissue that progressively diminished with increasing distance distal to the site of injury (∼L1–2 vertebral level), analogous to previous studies that have characterized this injury model (Joshi and Fehlings, 2002; Marques et al., 2014).

Behavioral Tests

Tail-Flick Test for Thermal Sensitivity

Mice were acclimated in 50 ml tubes for 2 days prior to testing, 20 min per day. On testing days, mice were left in their home cage to acclimate to the test room for 30 min before testing (Bannon and Malmberg, 2007). Latency to respond to thermal stimuli was measured by dipping the distal 1.5 cm of the tail into a 50°C water bath (Ramabadran et al., 1989). The tail was removed from the water upon response, or after 15 s to prevent tissue damage. The stimulus was conducted three times, at 20 s intervals or less (Zhou et al., 2014). The first response was dropped, and the average latency to respond from two trials was used for analysis. Video recording and VLC software were used to determine tail-flick responses in milliseconds. Mice were tested for thermal sensitivity 1 day prior to surgery for baseline response thresholds, and at days 1, 3, 5, and 7 post-surgery. $N = 6$ per group for each time point.

Mechanical Sensitivity

To assess mechanical sensitivity, mice were confined in clear plastic containers placed on an elevated wire mesh platform. Prior to testing, mice were acclimated to the apparatus for 60 min. Mechanical reactivity was assessed on the plantar surface of the hindpaw using a series of calibrated von Frey filaments according to the up-down method as described (Dixon, 1980), and 50% response thresholds were compared across all conditions. Both hindpaws were tested for mechanical sensitivity and collapsed across each group of mice per condition. Mice were tested for mechanical hypersensitivity 1 day prior to surgery for baseline response thresholds and at days 1, 3, 5, and 7 post-surgery. $N = 6$ per group for each time point.

Open Field Test

The open field test was conducted using a 16" × 16" open-field container subdivided by infrared beams to track movement (San Diego Instruments, San Diego, CA, USA). Data were acquired using the manufacturer's tracking software, which records ambulation movements based on beam breaks as well as central vs. peripheral beam break counts. All mice were placed in the same corner of the box before testing and allowed to freely explore for 10 min. Mice were tested 1 day prior to surgery for baseline locomotor behavior, and at days 1, 3, 5, and 7 post-surgery. Spinally injured mice were tested 1 day prior to surgery and 1 day post-surgery. Naive $N = 4$ for each time point; Sham $N = 3$–10 for each time point (within-group design, tissue was collected for ELISAs for corresponding time points); $N = 4$ SCI day 1.

Cuprizone Treated Mice

Female C57BL/6 mice (6–10 weeks old) were fed powdered milled chow mixed to contain a final concentration of 0.2% bis (cyclohexanone) oxaldihydrazone (cuprizone; Sigma-Aldrich, St. Louis, MO, USA), with food and water available *ad libitum*. Each mouse received approximately 5 g of chow per day, fresh cuprizone containing chow was prepared every 7 days. Cuprizone feeding was maintained for 35 days, and tissue was collected for protein analyses on day 35. Digitized, non-overlapping electron micrographs of the corpus callosum were analyzed for unmyelinated axon frequency and g-ratios to assess effectiveness of cuprizone treatment (Wasko et al., 2019; $N = 5$).

Cytokine ELISAs

Spinal cord segments at the level of laminectomy (T8–T11) were collected from naïve, sham, SCI, or cuprizone-treated mice immediately following perfusion with ice-cold 0.9% NaCl. Spinal cord segments were homogenized in ice-cold buffer containing 20 mM TES, pH 7.4, 10 mM mannitol, 0.3 mg/ml phenylmethylsulfonyl fluoride, 2 μg/ml leupeptin, 2 μg/ml pepstatin, 2 μg/ml benzamidine, 16 μg/ml benzamidine, and 50 μg/ml lima bean trypsin inhibitor at a concentration of 0.1 *g* tissue per 1 ml buffer (Mains et al., 2018). Homogenates were freeze-thawed three times, centrifuged (20 min, 17,400 *g*), and supernatants were collected. Approximately 60 μg of protein per sample was used for each ELISA. The ELISA assays were performed according to the manufacturer's instructions (R&D systems mouse duo-sets IL-10, IL-6, IL-1β, TNF-α, completed with Ancillary Reagent Kit 2, Minneapolis, MN, USA). The sample absorbance was read with an ELISA plate reader at 450 nm; readings were also taken at 570 nm to subtract optical background. The concentration was determined based on a standard curve. All results were normalized to amount of protein added per sample and graphed as pg/mg. Naïve, 1 day Sham, 4 days Sham, and 1 day SCI $N = 4$ mice; 5 days and 7 days Sham conditions $N = 3$ mice.

Backlabeling Procedure

To backlabel DRG L2-L6 projecting to the hairy hindpaw skin, mice were anesthetized with isoflurane. 0.3% wheat germ agglutinin conjugated to an AF-488 dye (WGA-488, Thermo Fisher Scientific, Waltham, MA, USA) in sterile PBS was injected into the sural, common peroneal, and saphenous nerve skin territories for retrograde labeling of DRG neurons (da Silva Serra et al., 2016; Berta et al., 2017). A total of 6 μl of WGA-488 was injected 2 days prior to surgery by three 2 μl injections in the lateral zones of each hindpaw (2 μl per nerve territory) using a 10 μl Hamilton Syringe and 30G needle. This was performed on both hindpaws of each mouse. This technique does not cause significant injury to the sensory afferents being studied.

Primary DRG Neuron Dissociation

Mice were anesthetized 4 days post-surgery with an intraperitoneal injection of ketamine (100 mg/kg) plus xylazine (10 mg/kg) and perfused with ice-cold 0.9% NaCl. A laminectomy was performed and L2-L6 DRG from both sides of the spinal column were collected into cold HBSS (KCl 5.4 mM,

NaCl 137 mM, Glucose 5.6 mM, Hepes 20 mM, pH 7.35 NaOH), after which the mice were sacrificed by decapitation. Sensory neuron dissociation was performed as described (Malin et al., 2007). Briefly, following collection, tissue was treated with 60U papain (Worthington), 1 mg of cysteine, and 6 μl of $NaHCO_3$ in 1.5 ml HBSS at 37°C for 10 min. Tissue was then treated with 12 mg collagenase II (Worthington, Lakewood, NJ, USA) and 14 mg dispase (Roche, Basel, Switzerland) in 3 ml HBSS at 37°C for 20 min, washed, and triturated with fire-polished glass Pasteur pipettes in 1 ml of DMEM (Gibco Thermo Fisher Scientific, Waltham, MA, USA) supplemented with FBS (Hyclone, Logan, UT, USA) and pen/strep (Gibco). The cell suspension was pelleted (1 min, 80 *g*), DMEM was removed, and cells were re-suspended in a modified solution (Citri et al., 2011) containing 140 mM NaCl, 5 mM KCl, 10 mM Hepes, 10 mM glucose, 0.1% Bovine Serum Albumin, pH 7.4. After re-suspension, cells were strained through a 70 μm cell strainer and placed on ice in the modified solution until fluorescence-activated cell sorting (FACS).

Imaging Flow Cytometry

Single cell suspensions of cells isolated from *in situ* WGA-488 labeled DRG were live-stained using Hoechst 33342 (10 μg/ml, Thermo Fisher Scientific, Waltham, MA, USA) and propidium iodide (PI; 1 μg/ml), and analyzed on an Amnis ImageStreamX Mark II imaging flow cytometer (Luminex Company, Austin, TX, USA). Fluorescent cell images were captured using a 60× objective lens with excitation from a 405 nm laser at 20 mW power and a 488 nm laser at 200 mW power. Images of in-focus nucleated WGA AF488-positive cells were identified and electronically gated using IDEAS software (Amnis, v6.2.183, Seattle, WA, USA).

Flow Cytometry and Cell Sorting

Neurons labeled with WGA-488 dye *in situ* in the DRG were purified by FACS 4 days post-surgery. Following primary dissociation of DRGs L2-L6, single cell suspensions were analyzed and sorted using a BD FACS Aria II cell sorter (Becton Dickinson) set up with a 130 μm nozzle at 12 PSI in order to gently isolate cells between 10 and 30 μm. Single live neurons were defined by electronic gating in FACS DIVA software (BD, ver. 8.01) using forward and side-angle light scatter, omission of PI (1 μg/ml), and AF488 fluorescence. All fluorescence gates were confirmed using fluorescence minus one controls (e.g., a sample of cells from unlabeled DRG was used to gate for AF488 positive cells and a sample of cells not treated with PI was used to set the live cell gate). WGA-488 positive cells were sorted directly into lysis buffer (NucleoSpin RNA XS Kit, Machery-Nagel, Bethlehem, PA, USA) and immediately placed on dry ice until RNA extraction. Cell sorting took 5–10 min per sample and was performed at 4°C before placement of samples on dry ice.

RNA Extraction and RNA Sequencing

RNA from FACS sorted cells was isolated using NucleoSpin RNA XS Kit, including a DNA digestion step but without carrier RNA step. Before library preparation, RNA quality and integrity was tested for each sample using the Agilent High Sensitivity RNA Screen Tape on the Agilent Tapestation 2200 (Agilent Technologies, Santa Clara, CA, USA). RNA with RIN values ≥6.7 (minimum 6.7, maximum 9.9, average 7.3) was further processed for RNA sequencing. It is important to note that these RIN values are based on relatively low RNA sample concentrations (RNA extracted from approximately 3,000 single cells per sample) and that the Agilent Tapestation software may have issues accurately calling RIN scores from sample concentrations below 50 ng/μl (Schroeder et al., 2006; Mueller et al., 2016). Because of this, RIN scores as low as 6.7 were considered suitable for RNA sequencing based on additional comparisons from the gel electrophoresis run on the Agilent Tapestation software that showed little to no RNA degradation, and previous work that has shown RNA samples with RIN scores below 7 are sufficient to identify differentially expressed genes (Gallego Romero et al., 2014). Library preparation was performed using the Illumina sequencing kit for high output 75-cycles for 25–30 M total single-end reads per sample. DESeq2 analyses[1] of differential expression were performed, and outliers beyond 30%–50% of the mean for each group of animals were eliminated (Love et al., 2014; Conesa et al., 2016; Labaj and Kreil, 2016; Wu and Wu, 2016).

Pathway Analysis

Data were analyzed by Ingenuity Pathway Analysis (IPA; Qiagen, Germantown, MD, USA). An overlap of significance for DEseq2 comparisons plus an RPKM cut-off >10 were required for transcripts to be included for IPA analysis. We analyzed 125 transcripts for comparisons between SCI and naïve groups, and 560 transcripts for comparisons between SCI and sham groups.

qPCR Validation

Pre-amplification of cDNA for Gene Expression

cDNA was generated from RNA samples from FACS sorted cells with the iScript Reverse Transcription Supermix (#1708840 Bio-Rad, Hercules, CA, USA), $N = 6$ per condition. Target-specific preamplification was performed on cDNA generated from RNA samples using SsoAdvanced PreAmp Supermix (#1725160 Bio-Rad) containing Sso7d fusion polymerase. Briefly, 20 μl of cDNA was pre-amplified in a total volume of 50 μl containing 25 μl of 2× SsoAdvanced PreAmp Supermix and 21 primer pairs, 50 nM of each primer. Preamplification was performed at 95°C for 3 min followed by 12 cycles of amplification at 95°C for 15 s and 58°C for 4 min. The samples were moved directly to ice and stored at −80°C. Pre-amplified cDNA was diluted 1:5 with H_2O. Controls performed for pre-amplification include qPCR and gel electrophoresis analysis of RNA extracted from both whole DRG tissue and FACS isolated DRG neurons from naïve mice. Following qPCR and gel analysis, all pre-amplified samples had no double bands and ran at expected weights based on product size.

qPCR

Following cDNA synthesis and preamplification, qPCR was performed using the primers listed in **Supplementary Figure S6**. All primers had calculated melt temperatures of 59.5–63.5°C,

[1] https://bioconductor.org/packages/release/bioc/html/DESeq2.html

and all products were 111–143 bp in length, as verified by agarose gel electrophoresis. Individual primers were analyzed by qPCR and gel electrophoresis from both whole DRG tissue and FACS isolated DRG neurons from naïve mice before pre-amplification was performed, to ensure proper primer efficiency. Following qPCR and gel analysis, all pre-amplified samples had no double bands, ran at expected weights based on product size, and had a maximum rate of amplification of 1.80/cycle or higher for all of the transcripts examined. qPCR was performed at 95°C, 2 min; 95°C, 10 s; 55°C, 15 s; and 72°C, 40 s, repeating the second through fourth steps for a total of 40 cycles in a Bio-Rad CFX Connect Optics Module machine. iQ SYBR Green Supermix (#1708882 Bio-Rad) was used for linear detection of qPCR results. Hypoxanthine phosphoribosyltransferase (Hprt) was used as the most constant normalizer transcript, based on the RPKM data (Klenke et al., 2016; Lima et al., 2016).

Statistical Analyses

Differences between groups were compared using student's *t*-test or ANOVA, followed by Tukey's post-test, Bonferroni's multiple comparisons test, or by unpaired student's *t*-test. *P*-values < 0.05 were considered statistically significant. Statistics on PCR data were conducted using delta CT values. Heat maps were generated by Microsoft software (Excel), hierarchical clustering was generated by Gene Cluster 3.0 and visualized using Java TreeView (de Hoon et al., 2004; Baek et al., 2017). All other data were plotted using Prism 6 (GraphPad Software, San Diego, CA, USA). R studio was utilized for differential expression analysis; Prism software was used for all other statistical tests.

RESULTS

Characterization of Behavioral and Inflammatory Phenotypes of Sham Mice

To determine an optimal time point to observe transcriptional changes contributing to the transition from acute to chronic pain, we tested behavioral differences between naïve and sham-operated mice. The objective of this was to ensure that changes within the DRG were due to injury to the spinal cord itself, not to the laminectomy performed in both injured and sham mice. It is likely that early effects of sham surgery involve changes in gene expression that overlap with a subset of genes that also change following SCI. It is important to define how long the functional effects of sham surgery persist to better discern the effects of SCI. Specifically, we tested naïve and sham mice for open field locomotor differences 1, 3, 5, and 7 days post-surgery (**Figure 1A1**). Naïve and sham mice did not differ significantly at any of the time points tested, including as early as 1 day post-surgery. To ensure that SCI mice (T10 compression-clip injury) did exhibit behavioral differences and locomotor deficits following injury, we compared SCI mice to naïve and sham mice for open field behavior 1 day post-injury (**Figure 1A2**). SCI mice exhibited substantially decreased total ambulation (one-way ANOVA, $p = 0.0059$, Tukey's multiple comparisons test, naïve $^{**}p < 0.005$, sham $^{*}p < 0.05$) following

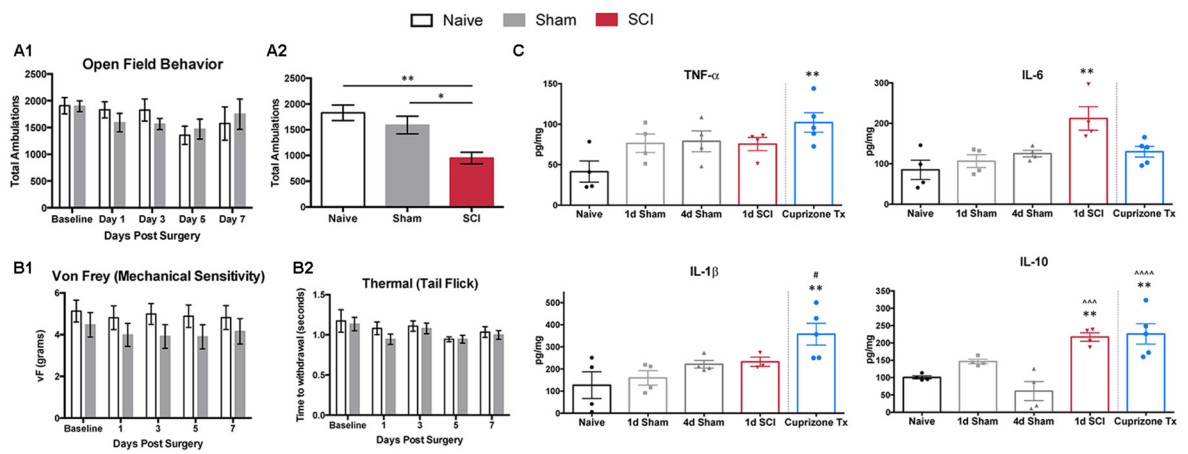

FIGURE 1 | Behavioral responses and cytokines. **(A1)** Open field behavior (10 min trials) in naïve or sham mice 0, 1, 3, 5 and 7 days post-surgery does not differ significantly at any time point in total ambulation, $N = 3$–10 sham, 4 naïve. **(A2)** Total ambulation differs significantly 1 day post-spinal cord injury (SCI) in both SCI vs. naïve (one-way ANOVA, $p = 0.0059$, Tukey's multiple comparisons test, $^{**}p < 0.005$) and SCI vs. sham ($^{*}p < 0.05$) mice. **(B1)** Mechanical and **(B2)** thermal sensitivity do not differ significantly 0, 1, 3, 5, and 7 days post-surgery in naïve and sham mice, $N = 6$ each. **(C)** Cytokine ELISAs on spinal cord segments at the level of laminectomy (T8–T11) show no significant differences between naïve and sham mice 1 or 4 days post-surgery. One-day post-operation, SCI mice have significantly increased levels of IL-6 and IL-10 compared to naïve controls (one-way ANOVA, Bonferroni's multiple comparisons test; $^{*}p < 0.05$, $^{**}p < 0.005$, respectively) and significantly increased levels of IL-10 in comparison to 4 days sham condition (one-way ANOVA, Bonferroni's multiple comparisons test; $^{\wedge\wedge\wedge}p < 0.001$). Cuprizone-treated mice as positive control, with significantly increased TNF-α, IL-1β, and IL-10 compared to naïve controls (one-way ANOVA, Bonferroni's multiple comparisons test; $^{*}p < 0.05$, $^{**}p < 0.005$, $^{\wedge\wedge\wedge}p < 0.001$, respectively) after 5 weeks of cuprizone treatment and significant increases in IL-1β at the 1 day sham time point, and IL-10 at the 4 days sham time point (one-way ANOVA, Bonferroni's multiple comparisons test; $^{*}p < 0.05$, $^{\wedge\wedge\wedge\wedge}p < 0.0001$, respectively). *Represents comparisons to naïve conditions, #represents comparisons to 1 day sham conditions, ^represents comparisons to 4 days sham conditions.

injury, as expected, although time spent in the periphery did not differ (**Supplementary Figure S1A**). Additional tests for mechanical (von Frey) and thermal (hot water tail-flick) hypersensitivity showed that naïve and sham conditions did not differ significantly at any time point (**Figures 1B1,B2**). Previous literature has demonstrated analogous results when testing hindpaw thermal sensitivity by radiant heat stimulus on sham animals at multiple time points (Christensen and Hulsebosch, 1997; Bedi et al., 2010; Gaudet et al., 2017). We did not examine SCI mice for thermal or mechanical sensitivity, as paralysis below the level of injury prohibited below-level sensitivity testing at the time points studied. Previous work using the clip-compression model has shown varying results regarding the occurrence of above-level sensitivity following SCI (Bruce et al., 2002; Densmore et al., 2010). While above-level pain may occur following injury, below-level pain is one of the most prevalent, and most difficult, pain types to treat, and is the focus of these studies (Yezierski, 2005). The development of chronic pain at later time points following clip-compression models of SCI (in addition to several other models) has already been well characterized. Therefore, we focused on early time points after injury, to identify contributions to the onset of pain, rather than changes after chronic pain has already developed (Bruce et al., 2002; Nakae et al., 2011; Gaudet et al., 2017).

Previous work has highlighted the importance of inflammatory cytokines within the CNS to facilitate the transduction of noxious stimuli in neuropathic pain (Cook et al., 2018). Thus, we examined post-surgical changes in inflammation, using ELISAs to analyze common cytokine markers to ensure that sham mice did not differ significantly from naïve mice following the removal of bone and muscle. We did not observe significant differences in inflammatory cytokine levels (TNF-α, IL-6, IL-1β, IL-10) in extracts of spinal cord segments (T8-T11) among naïve or sham mice at 1, 4, 5, and 7 days post-surgery (**Figure 1C**, **Supplementary Figure S1B**), similar to previous studies (Stammers et al., 2012). Spinal cords from SCI mice had significantly increased levels of IL-6 and IL-10 in comparison to naïve controls (one-way ANOVA, Bonferroni's multiple comparisons test; $^{*}p < 0.05$, $^{**}p < 0.005$, respectively). When compared to sham conditions, spinal cords from SCI mice had significantly increased levels of IL-10 in comparison to 4 days, 5 days, and 7 days sham conditions (one-way ANOVA, Bonferroni's multiple comparisons test; $^{***}p < 0.001$, $^{**}p < 0.005$, $^{**}p < 0.005$, respectively.

As a positive control, we tested cuprizone-treated mice (a model of multiple sclerosis), which are known to secrete proinflammatory cytokines at the end of 5 weeks of treatment (Mukhamedshina et al., 2017). Cuprizone-treated mice showed expected increases in levels of TNF-α, IL-1β, and IL-10 in comparison to naïve controls (one-way ANOVA, Bonferroni's multiple comparisons test; $^{*}p < 0.05$, $^{**}p < 0.005$, $^{**}p < 0.005$, respectively; Schmitz and Chew, 2008). Similarly, in comparison to sham mice, spinal cord extracts from cuprizone-treated mice had significant increases in IL-1β at the 1 day sham timepoint, and IL-10 at the 4 days, 5 days, and 7 days sham timepoints (one-way ANOVA, Bonferroni's multiple comparisons test; $^{*}p < 0.05$, $^{****}p < 0.0001$, $^{**}p < 0.005$, $^{***}p < 0.001$, respectively). Behavioral testing and cytokine analyses did not reveal differences between naïve and sham mice at any time point.

Confirmation of Cell Population Specific Labeling of Cutaneous Nociceptors

Because the laminectomy did not significantly affect behavior or inflammatory responses in sham mice, we determined an optimal time point to study the transition of acute to chronic pain based upon established characteristics of nociceptors following SCI. The inflammatory cytokine assays demonstrated significant increases in inflammation 1 day post-SCI compared to 4 days sham controls (**Figure 1C**, **Supplementary Figure S1B**). We did not observe significant differences in inflammatory cytokine levels (TNF-α, IL-6, IL-1β, IL-10) in extracts of spinal cord segments (T8-T11) among naïve or sham mice at 1, 4, 5, and 7 days post-surgery (**Figure 1C**, **Supplementary Figure S1B**); this is similar to previous studies (Stammers et al., 2012). In addition, previous studies have documented onset of spontaneous activity in nociceptors distal to the site of SCI as early as 3 days post-injury in rats; increased activity persisted for at least 8 months (Bedi et al., 2010). Thus, it is possible that the transition to chronic pain begins around 3 days after SCI in rats and mice, and this transition is not due to laminectomy, as nociceptors isolated from sham rats show either no significant changes in spontaneous activity (Bedi et al., 2010; Yang et al., 2014) or only a minor increase compared to the effect of SCI (Odem et al., 2018). Subsequently, we chose 4 days post-injury to assess transcriptional changes in nociceptors below the level of injury in mice.

To perform transcriptional profiling on nociceptors that project to the cutaneous skin after injury, we injected wheat germ agglutinin conjugated to an AF-488 dye (WGA-488) into the sural, common peroneal, and saphenous nerve skin territories for retrograde labeling of DRG neurons. Next, we performed compression-clip SCI or sham surgeries at the T10 vertebral level 2 days post-WGA injection and collected L2-L6 DRG for dissociation 4 days post-injury (**Figure 2A**). Based on the vertebral level at which we performed SCI, the DRG collected were located below the level of injury, thus our analysis was comprised of non-injured nociceptors that do not project directly to the lesion site. Flow cytometry confirmed that our cell population of interest (cutaneous nociceptors) was positively labeled with WGA-488 (**Figure 2B**). We also observed non-labeled (WGA-488) cells and dead cells (propidium iodide, PI+), to be excluded from cell sorting and analysis (**Figure 2B**). As expected, a significant number of viable small nociceptor cells were excluded in this analytical approach, to avoid including RNAs from non-nociceptor cells or attached fragments of dead cells (examples in **Figure 2C**; Thakur et al., 2014; Lopes et al., 2017; Megat et al., 2019).

FACS Purification of DRG Nociceptors Projecting to the Cutaneous Hind Paw

We performed FACS purification of nociceptor populations from naïve, sham, and SCI adult (8–12 weeks old) female

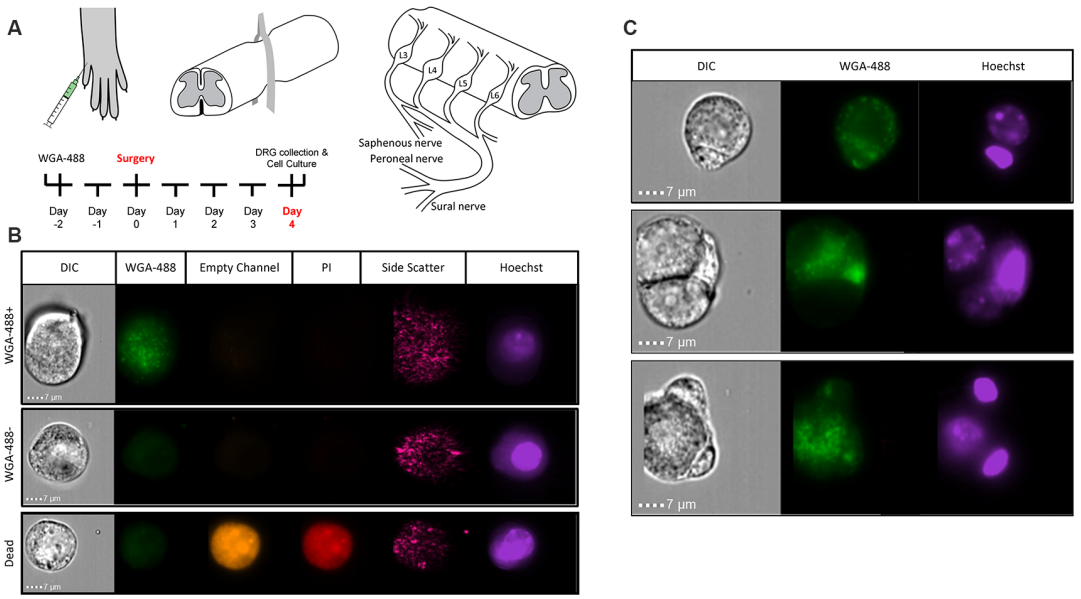

FIGURE 2 | Identifying sensory neurons. **(A)** Diagram of WGA-488 injection under the hairy hindpaw skin of a mouse, how the SCI was conducted with a vessel clip, and projections to the corresponding dorsal root ganglia (DRG). **(B)** Fluorescent cell images taken by Amnis ImageStreamX Mark II imaging flow cytometer (Luminex Corporation, Austin, TX, USA) using a 60x objective lens with excitation from a 405 nm laser and a 488 nm laser to identify propidium iodide (PI; red) positive (dead) cells and WGA (green) labeled cells, respectively. **(C)** Sample images of rejected cells because of attachment to non-nociceptor cells. Similarly, nociceptors with attached PI+ debris were eliminated.

mice (n = 5 per condition). We pooled DRGs from lumbar regions L2-L6 on either side of the spinal column to ensure all DRGs isolated would have projections to the hairy hindpaw skin. DRG cells were enzymatically dissociated and subjected to flow cytometry, to gently isolate positively labeled cells between 10 and 30 µm; PI staining was used to identify dead cells. All conditions were gated on DRG from naïve mice that did not receive WGA-488 injections, enabling purification of positively labeled cells (**Figure 3A**). Analysis of our flow cytometry data shows that, we were successful in retrogradely labeling DRG neurons projecting to hairy hindpaw skin. Many positively labeled neurons were part of cell aggregates, limiting retrieval of the single-cell population of interest to ∼2% of all dissociated cells per animal (**Figure 3B**). This percentage amounted to approximately 3,000 cells per mouse, a suitable representation of this cell population in agreement with previous studies (Shields et al., 2012; Goswami et al., 2014; Thakur et al., 2014; Usoskin et al., 2015; Berta et al., 2017). DRG populations were sorted directly into lysis buffer and placed on dry ice to preserve transcriptional profiles at the time of isolation. RNA quality was tested using the Agilent TapeStation; a representative image of an RNA sample following FACS purification is shown (**Figure 3C**).

Major Characteristics of Somatosensory Mediators in the Purified Neuron Population

We used the RNA sequencing data to evaluate the neuronal population that had been isolated. Scn10a, which encodes $Na_v1.8$, is present in 80–90% of nociceptors and Trpv1 serves as a marker for the peptidergic population of nociceptors (Basbaum et al., 2009; Harriott and Gold, 2009; Wu et al., 2013). RPKM values of 1,000 for Scn10a and 400 for Trpv1 confirm that FACS purified cells express high levels of these nociceptor markers **Figure 4A**). The low RPKM values observed for Parvalbumin (Pvalb), a glial transcript also found in large diameter proprioceptors and Aβ neurons, and glial fibrillary acidic protein (Gfap), another marker for glial cells, suggests that the non-nociceptive sensory neurons responsible for touch and proprioception (Aβ and Aδ neurons) and satellite glial cells are largely absent from our purified nociceptor population (**Figure 4B**; Huang et al., 2013; Le Pichon and Chesler, 2014); this conclusion is further supported by the somatosensory profiling of transcripts in **Figure 4C** (below). Previous studies have confirmed that intact DRG as well as unsorted dissociated DRG yield much higher levels of non-neuronal markers (Thakur et al., 2014). This highlights the importance of excluding cell aggregates during cell sorting (**Figure 3**) to avoid the analysis of transcripts from cells outside of the target population of nociceptors.

We next analyzed gene expression patterns for known functional mediators of somatosensation (Chiu et al., 2014; Le Pichon and Chesler, 2014; Usoskin et al., 2015). The purified cutaneous nociceptors displayed high expression levels of genes involved in thermosensation and nociception, such as specific Trp channels (notably Trpv1), sodium channels (Scn9a, 10a, 11a) and peripherin (Prph; **Figure 4C**). The skin is innervated by both peptidergic nociceptors and non-peptidergic neurons (Zylka et al., 2005; Lallemend and Ernfors, 2012; Kjell and Olson,

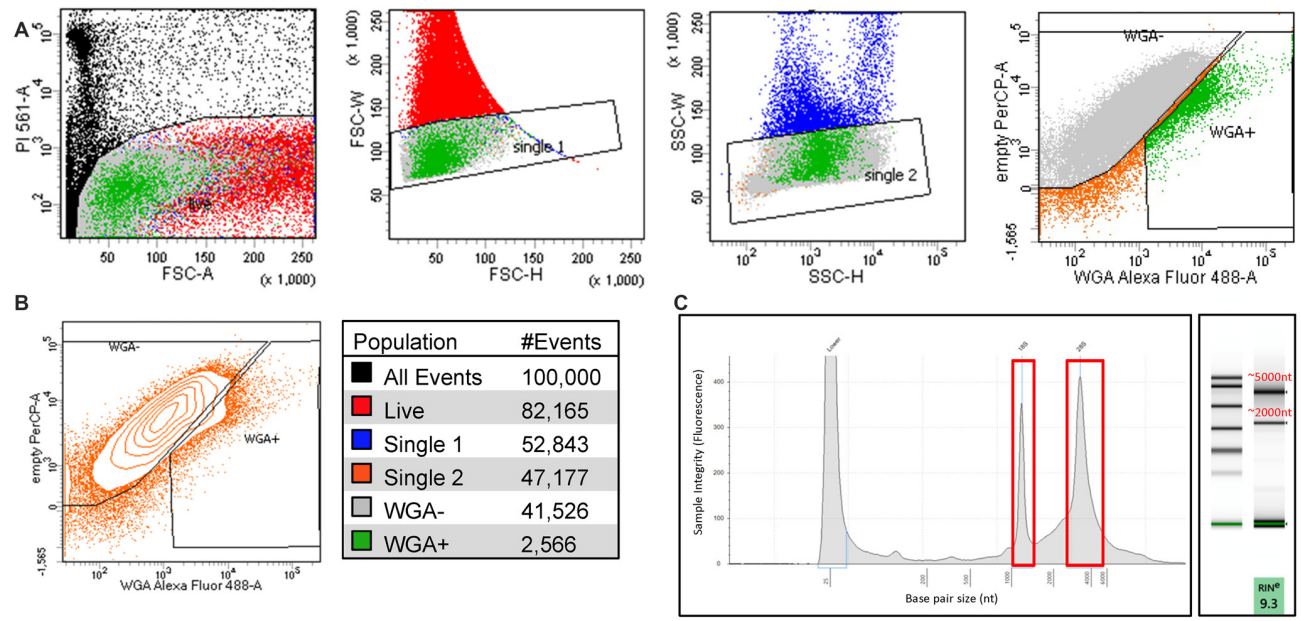

FIGURE 3 | Isolating sensory neurons. **(A)** Fluorescence-activated cell sorting (FACS) purification of cultured DRG cells based on PI staining (dead) single-cell populations by forward scatter (FSC), single-cell populations by side scatter (SSC), and cells fluorescently labeled with WGA-488 (WGA+). **(B)** Contour plot of single WGA+ cells that were sorted directly into lysis buffer for RNA extraction and color scheme for the gated populations, each condition $N = 5$; ~3,000 cells. **(C)** Representative image of RIN values run on an Agilent TapeStation before RNAseq.

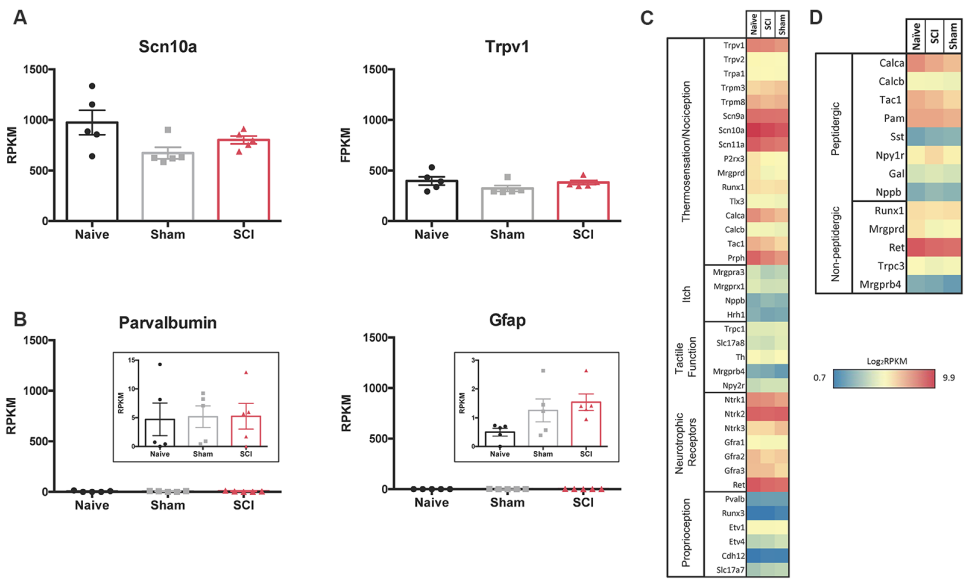

FIGURE 4 | RNAseq demonstrates specificity of cell isolation. **(A)** Average RPKM values from RNAseq dataset from genes that are known to be highly expressed in the cell population of interest or **(B)** expected to be expressed in other cell populations outside of the one being studied; larger myelinated neurons or satellite glial cells, respectively, $N = 5$ per condition. **(C)** Heatmap of functional somatosensory mediators within the isolated cell population of interest. Genes were grouped based on roles established in the literature: thermosensation and nociception, itch, tactile function, and neurotrophic factors. **(D)** Heatmap of peptidergic and non-peptidergic markers. Graph: $\log_2$ of average RPKM values within each condition, RPKM >1, $N = 5$ per condition.

2016). Markers for non-peptidergic nociceptors were abundant, such as Mas-Related G-Protein Coupled Receptor Member D (Mrgprd), Runt related transcription factor 1 (Runx1), Ret proto-oncogene (Ret), and transient receptor potential cation channel C3 (Trpc3). As expected, transcripts enriched in peptidergic nociceptors were present, such as Calca and

Calcitonin Related Polypeptides (Calcb) and Tac1 (the tachykinin precursor for peptides such as Substance P), the peptide processing enzyme peptidylglycine α-amidating monooxygenase (PAM), as well as Npy1r, one of the most abundant Npy receptors (Julius and Basbaum, 2001; Basbaum et al., 2009). However, genes encoding proteins involved in itch, such as brain natriuretic peptide (Nppb) and histamine receptor H1 (Hrh1) were only expressed at low levels (Usoskin et al., 2015). Similarly, genes responsible for proteins involved in tactile function, including Transient Receptor Potential cation channel subfamily C Member 1 (Trpc1), and those responsible for proprioception, such as Runt related transcription factor 3 (Runx3), exhibited low expression levels (Le Pichon and Chesler, 2014). In contrast, nerve growth factor receptors (Neurotrophic Receptor Tyrosine Kinases 1–3, Ntrk), which are characteristic of many subtypes of nociceptors, were expressed at high levels for each condition and did not differ significantly when comparisons were made between all conditions. It is of significance that Ntrk2 is typically used as a marker to identify myelinated sensory neurons, and relatively high levels of Ntrk2 (and Ntrk3) may indicate the presence of some proprioceptive or low threshold mechanoreceptors within the isolated population of neurons (Lallemend and Ernfors, 2012; Usoskin et al., 2015). However, this seems unlikely based on the absence of other common proprioceptor and mechanoreceptor transcripts within our dataset (**Figure 4C**). It is possible that higher levels of Ntrk2 and Ntrk3 are unique to our isolated population of neurons that project to the hairy hindpaw skin. High expression levels were also observed for some of the transcripts of the two major subpopulations of nociceptors: peptidergic and non-peptidergic (**Figure 4D**).

Gene Expression Profiling and Enrichment Patterns in Injured and Non-injured Cutaneous Nociceptors After SCI

To further assess expression profiles of the purified nociceptor population and differences among naïve, sham, and SCI conditions within this nociceptor-enriched population, we focused on expression patterns of gene families that mediate general neuronal functions (Chiu et al., 2014; Berta et al., 2017). We used differential expression analysis (DESeq2) to analyze significant changes between SCI and naïve or SCI and sham populations (Love et al., 2014). Pairwise comparisons of significant genes generated by DESeq2 analysis yielded many differentially expressed genes in each subset (**Supplementary Figures S2A,B**). We also assessed differences between sham and naïve populations. Any genes that differed significantly between the sham and naïve populations were considered significant transcript changes due to laminectomy, and thus were excluded from analysis in the SCI vs. Naïve and SCI vs. Sham comparisons (**Supplementary Figure S2C**).

We focused on expression patterns of gene families which mediate neuronal functions and contribute to pain phenotypes and found both high expression levels and significant differences within the chloride channel family, Trp channels, glutamate receptors, GABA receptors, potassium channels, sodium channels, and piezo channels (**Figures 5A–G**, *p*-values in **Table 1**). We also examined ASICs (acid-sensing ion channels), calcium channels, glycine receptors, and P2rx and P2ry families (purinergic receptors), because these are widely studied gene families known to be involved in the development or maintenance of chronic pain (**Supplementary Figures S3A–E**). Many channels and receptors were highly expressed within this cell population, but no significant changes among the transcripts were demonstrated for any condition (**Supplementary Figure S3**).

Several transcription factors were highly expressed, including signal transducer and activator of transcription 3 (Stat3), FJB osteosarcoma oncogene (Fos), and Jun Proto-Oncogene (Jun; **Supplementary Figure S4**). Evidence from various models of neuropathic pain implicates these transcription factors in the development or maintenance of chronic pain (Naranjo et al., 1991; Harris, 1998; Dominguez et al., 2008; Tsuda et al., 2011; Xue et al., 2014). Stat3 inhibitors are used to treat peripheral nerve injury-induced hyperexcitability within dorsal horn neurons, pain behaviors, chronic constriction injury, and signaling of IL-6 cytokines (Dominguez et al., 2008; Tsuda et al., 2011; Xue et al., 2014). Previous studies also show that Fos links extracellular events to long-term intracellular changes (such as noxious stimuli) and have established Fos expression as a valid tool to study nociceptive changes (Naranjo et al., 1991; Harris, 1998). Jun also contributes to persistent pain phenotypes following injury (Naranjo et al., 1991). DESeq2 analysis determined additional transcription factors to be significantly altered by SCI (**Supplementary Figure S5**). Interestingly, activating transcription factor-3 (Atf3), a cellular stress-inducible factor that also increases in non-injured neurons after axotomy, was present at similar levels as Atf4 in all conditions but did not differ significantly. This suggests that Atf3 may be upregulated by axonal injury during the DRG dissociation process, similar to other findings, but that the increases in Atf3 are not due to SCI itself (Tsujino et al., 2000; Huang et al., 2006; Seijffers et al., 2007).

Backlabeled FACS-Sorted Cutaneous Cell Transcriptome Is Distinguished by Nociceptor-Enriched Gene Patterns

To gain further insight into differentially regulated genes in our isolated population of neurons, we compared our dataset with similar studies on isolated DRGs from publicly available datasets which focused on nociceptors (expressing $Na_v1.8$) or DRG collected from the same lumbar spinal level (L2–L6; **Figure 6**; Thakur et al., 2014; Usoskin et al., 2015; Hu et al., 2016; Megat et al., 2019). Unsupervised hierarchical clustering of the top 260 genes revealed that a large number of genes display distinct patterns of expression dependent upon the technique used: isolated neurons from all DRG by translating ribosome affinity purification (TRAP) using the $Na_v1.8^{Cre}$ mouse (Megat et al., 2019); single-cell isolation from L3 to L5 DRG (Hu et al., 2016); single-cell isolation from L4-L6 DRG (Usoskin et al., 2015); and magnetic cell sorting (MACS) using the

TABLE 1 | Ion channels and synaptogenesis.

Gene	RPKM Naïve	RPKM SCI	RPKM Sham	*p*-value SCI vs. N	*p*-value SCI vs. Sham
Ion channels					
Calcb	86	83	71	-	6.5E-03
Gabrg3	12	6	17	5.3E-04	5.7E-04
Gfra2	219	166	186	1.3E-03	-
Gria4	108	131	119	5.0E-02	4.5E-02
Grik1	270	196	213	4.1E-05	-
Kcng3	20	13	18	3.3E-03	1.3E-02
Kcnh8	20	13	18	-	1.2E-02
Kcnj11	34	30	44	8.3E-04	-
Kcnk1	13	7	11	2.0E-02	1.7E-02
Kcnk13	28	19	30	-	2.2E-03
Kcnk18	19	15	23	3.2E-02	1.6E-03
Kcnn3	21	15	22	-	8.8E-03
Mrgprd	40	32	51	3.7E-07	-
Piezo2	143	82	96	1.5E-02	-
Scn3a	542	447	526	2.6E-02	1.0E-05
Scn5a	27	22	34	-	8.8E-04
Trpc3	23	17	34	5.2E-04	-
Trpc4	104	74	86	-	2.3E-03
Ttyh1	18	16	25	-	2.0E-02
Synaptogenesis pathway					
Adcy1	56	45	83	-	6.9E-05
Adcy2	120	144	140	2.9E-02	-
Ap2a2	307	305	260	-	1.6E-02
Atf4	154	147	121	-	1.3E-02
Bdnf	57	77	60	1.2E-02	3.6E-06
Cadm1	352	304	269	7.7E-02	4.5E-03
Camk2g	322	339	278	-	2.3E-02
Cdh10	35	34	46	-	9.0E-03
Dlg4	228	218	200	-	2.2E-02
Epha10	9	10	13	-	3.3E-02
Ephb2	11	9	15	-	8.4E-04
Gosr2	102	115	103	-	1.0E-02
Gria4	108	131	119	5.0E-02	4.5E-02
Nap1l1	210	203	177	-	3.1E-02
Nlgn2	202	205	185	-	9.4E-04
Plcg2	8	6	12	-	4.7E-04
Prkag2	161	169	147	-	5.7E-03
Prkar2b	182	153	147	1.5E-02	-
Rap2b	11	19	20	4.0E-03	-
Rasgrp1	364	286	303	8.1E-03	-
Rras	68	67	57	-	1.6E-02
Rras2	19	26	26	3.1E-02	-
Stxbp2	48	60	50	3.8E-02	3.0E-02
Syn3	28	27	37	-	4.0E-03
Syt4	235	231	197	-	1.1E-02

Average RPKM values that significantly differ 4 days post-spinal cord injury (SCI). DESeq2 p-Value based on SCI vs. naïve or SCI vs. sham comparisons. p-values that are not listed were >0.05. Transcripts from Ingenuity Pathway Analysis (IPA) canonical pathway analysis significantly different 4 days post-SCI. DESeq2 p-value based on SCI vs. Naïve or SCI vs. Sham comparisons.

$Na_V1.8$ TdTomato mouse (Thakur et al., 2014; **Figure 6A**). We found that, while our cutaneous nociceptor-enriched population clustered most closely with the datasets of both TRAP sorted and unsorted DRG from Megat et al. (2019), our isolated population was characterized by its own unique dataset. Notably, datasets from studies analyzing single-cell transcriptomes cluster together, while studies utilizing either TRAP or MACS cluster with their own respective unsorted DRG controls, suggesting that while techniques for isolating specific cell populations can be useful, some variations in gene expression may be attributed to individual differences in cell isolation and RNA extraction methods.

To better characterize enriched genes within our population, we graphed the expression of the 25 most significantly enriched genes in our dataset in comparison to the same datasets used for hierarchical clustering (**Figure 6B**). While many of the genes have similarly high expression levels, several genes were unique to our isolated population, including diacylglycerol kinase (Dgkh), ankyrin 2 (Ank2), PHD finger protein 24 (Phf24), serine/arginine repetitive matrix 2 (Srrm2), fatty acid synthase (Fasn), phosphoinositide-interacting regulator of transient receptor potential channels (Pirt), and pleckstrin homology domain containing, family A member 6 (Plekha6). We also compared the expression pattern of

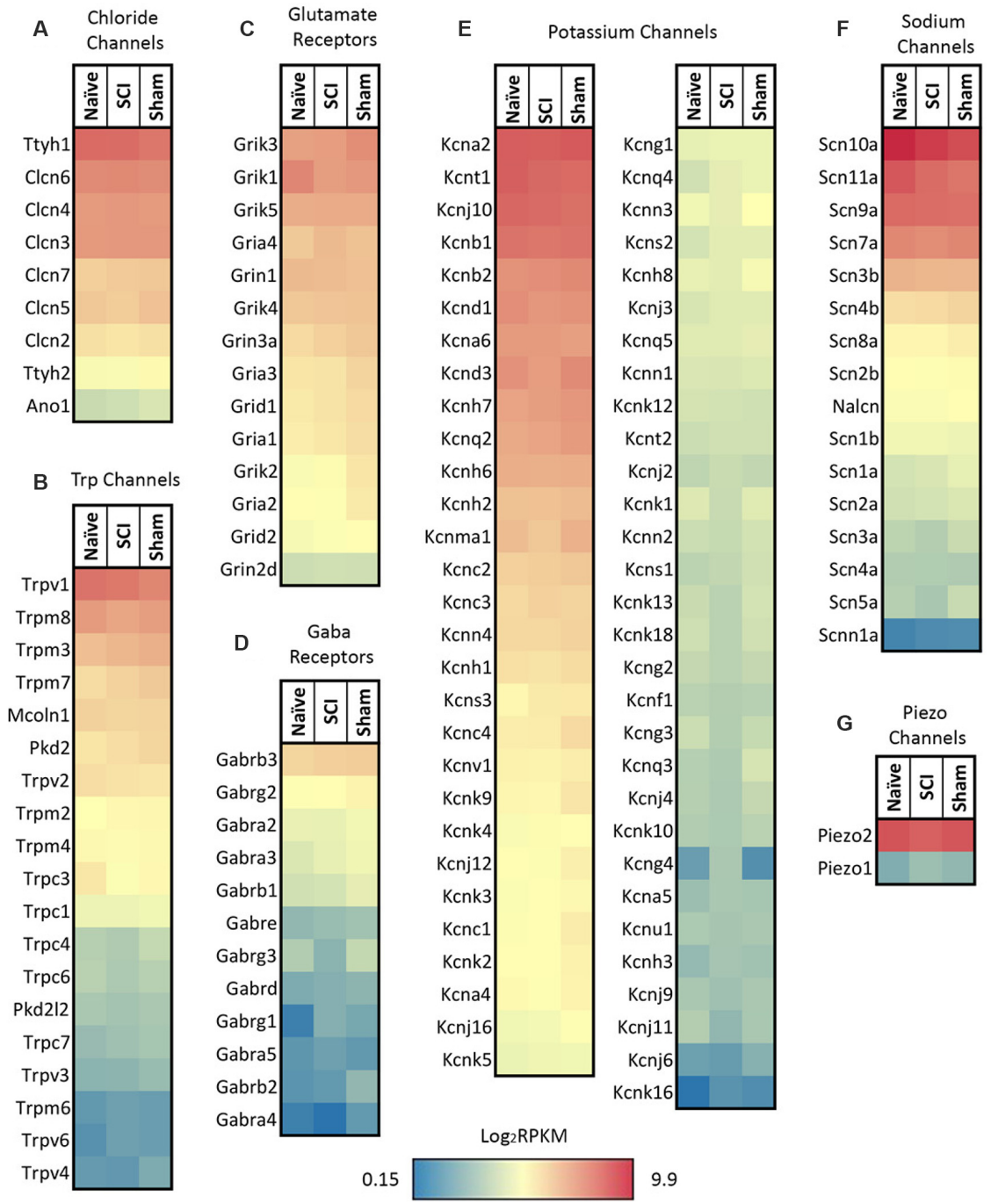

FIGURE 5 | Heatmaps of ion channel transcripts. **(A)** Chloride channels, **(B)** TRP channels, **(C)** glutamate ionotropic receptors, **(D)** GABA ionotropic receptors, **(E)** potassium channels, **(F)** sodium channels, **(G)** piezo channels. Each family of transcripts includes significant differences in at least one gene 4 days post-SCI. Channels were clustered based on SCI expression level and graphed by the $\log_2$ of average RPKM values within each condition. RPKM <1 were not included, $N = 5$ per condition.

our naïve nociceptor-enriched population to the various datasets by again examining known neuronal markers of somatosensation (**Figure 6C**). As predicted, all of the sorted populations exhibit relatively high expression levels of gene transcripts associated with thermosensation, nociception, or neurotrophic receptors, and comparatively low levels of genes associated with itch, tactile function, or proprioception. It is evident that our cutaneous, nociceptor-enriched population can be defined by its distinct gene expression patterns, in particular, high expression levels of the Trp family of genes

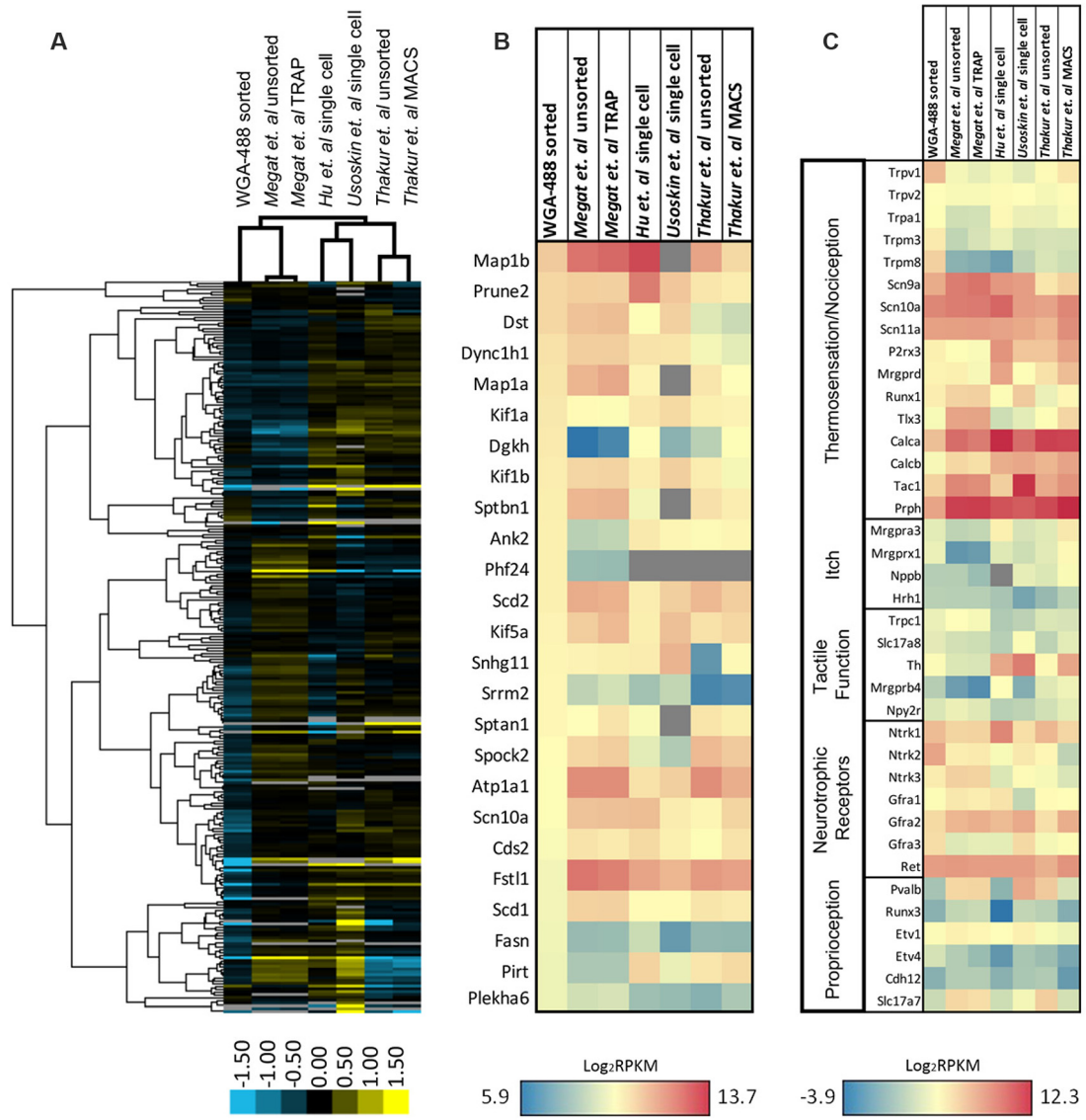

FIGURE 6 | Expression profiling of differentially sorted isolated DRG. **(A)** Heatmap of the top 260 genes from sorted isolated DRG neurons in comparison to similar studies from publicly available datasets (unsorted dissociated DRG, translating ribosome affinity purification (TRAP)-sorted, single cell, or MACS-sorted dissociated DRGs). Comparisons between conditions were made by unsupervised hierarchical clustering. **(B)** Heatmap of the 25 most significantly enriched genes in our dataset in comparison to similar studies from publicly available datasets. Transcripts were graphed by the $\log_2$ average values within each condition. Datasets that did not express transcripts (RPKM = 0) are depicted in gray. **(C)** Heatmap of functional somatosensory mediators within the isolated cell population of interest in comparison to similar studies from publicly available datasets. Transcripts were graphed by the $\log_2$ average values within each condition. Datasets that did not express transcripts (RPKM = 0) are depicted in gray.

listed in **Figure 6C**, as well as Ntrk2, Ntrk3, and Gfra3 neurotrophic receptors.

Ingenuity Pathway Analysis (IPA) Identified Significantly Different Canonical Pathways From Cutaneous Nociceptors After SCI

Based on DESeq2 analysis, levels of several hundred transcripts in the nociceptor-enriched population were altered by SCI. We restricted IPA input lists to genes that had RPKM values greater than 10 and were statistically different (SCI vs. Naïve or SCI vs. Sham) by DESeq2 analysis (**Figures 7A,B**). Transcripts that exhibited large-fold changes included Mrgprb5, Hal, Chrnb4, Cap2, Sez6l, Calb1, Prokr2, Rxfp1, Nxpe2, and Arap3 (**Figures 7A,B**). Despite the noticeable changes in these individual genes, they did not appear in any common significant canonical pathways. Instead, we chose to focus on smaller-fold changes that may result in the coordinated functions of many genes. IPA identified several pathways that are considered important for inflammatory processes, pain transduction, or

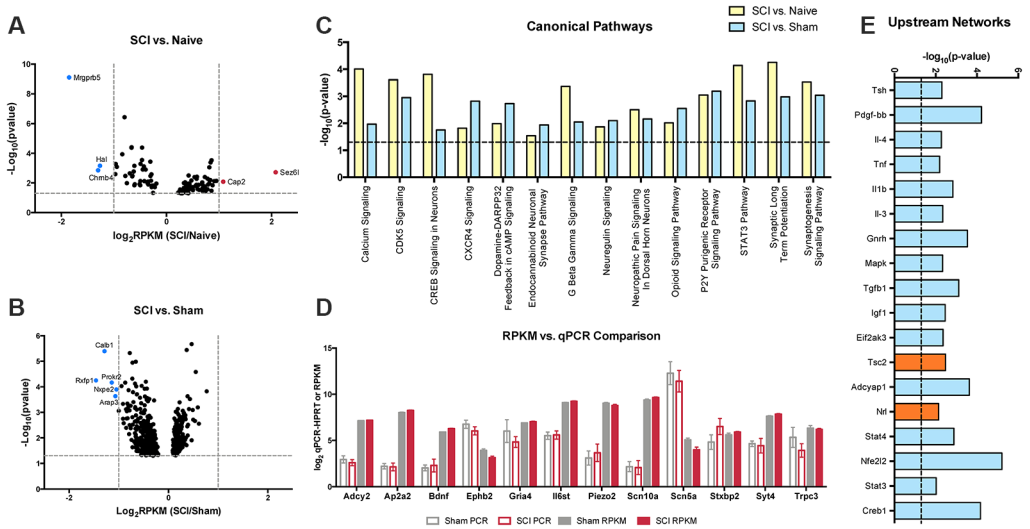

FIGURE 7 | Volcano plots and upstream analysis. **(A,B)** DESeq2 significant ($p > 0.05$) genes included in IPA analysis comparing SCI vs. naïve or SCI vs. sham conditions. **(C)** Significant ($p < 0.05$) overlapping canonical pathways predicted by analyzing genes determined by DESeq2 and outlier cut-off in IPA. **(D)** Comparisons of RPKM values generated by RNAseq and log2 transcript levels (gene-Hprt) validated by qPCR between sham and injured conditions. **(E)** IPA network analysis predicted networks based on differentially expressed genes between sham and SCI conditions. Network analysis also made predictions about the activation state of the transcript regulator; positive *z*-score (blue) indicates activation, negative *z*-score (orange) indicates inhibition.

the maintenance of chronic pain (**Figure 7C**). This includes calcium signaling, Cxcr4 signaling, neuropathic pain signaling in dorsal horn neurons, opioid signaling, purinergic receptor signaling and synaptic long term potentiation (**Figure 7C**; Julius and Basbaum, 2001; Walters, 2012, 2018). The current study focused on significant changes due to SCI pain and not due to post-surgical pain (i.e., changes between sham vs. naïve groups).

Validation of RNASeq Data Using qPCR

We used qPCR to confirm changes in transcripts of interest from our RNAseq dataset. To validate qPCR and RNAseq comparisons, we compared qPCR or RPKM Log_2 transcript levels of SCI and sham genes of interest (**Figure 7D**). SCI and sham qPCR fold change results were analogous to the RNAseq fold change dataset. We focused on the synaptogenesis pathway in particular, as it includes several genes present in overlapping canonical pathways, including changes in receptors involved in organization of excitatory signaling (Ephb) and synapses which may be involved in development of chronic pain (TrkB and BDNF). We validated receptors for significant genes in the synaptogenesis pathway, and genes considered possible contributors to pain that also showed significant differences between conditions Gabrg3, Il6st, Kcng3, Piezo2, Scn5a, Trpc3; Waxman et al., 1999; Wickenden, 2002; De Jongh et al., 2003; Devor, 2006; Eijkelkamp et al., 2013; Guptarak et al., 2013; Xia et al., 2015; Deng et al., 2018; Szczot et al., 2018). Additional targets were chosen in order to validate isolation of the correct cell population (Scn10a). Samples for qPCR were collected by backlabeling cutaneous afferents and cell sorting, consistent with samples generated for RNAseq analysis. Following cDNA synthesis, samples were subjected to gene target-specific preamplification using the same primers used for qPCR (**Supplementary Figure S6**). Hprt was chosen as the housekeeping gene for qPCR analysis because it was the most constant normalizer transcript from the RPKM data across all 15 mice in the present study (Klenke et al., 2016; Lima et al., 2016).

IPA Network Analysis Revealed Several Regulatory Interrelationships After SCI

We used IPA upstream network analysis to further interpret the function of the several hundred transcripts significantly altered determined by DESeq2. This method predicted several transcriptional regulators associated with altered expression levels of downstream target genes following SCI (**Figure 7E**). The upstream regulator molecules graphed do not show a significant change in RNA expression in response to injury. However, these targets are activated by posttranslational modifications that can alter many of the downstream molecules within its network.

DISCUSSION

SCI initiates persistent molecular changes in nociceptors, similar to inflammation in models of peripheral injury (Djouhri et al., 2001; Xie et al., 2005). Several studies of SCI pain have evaluated mechanical hypersensitivity from von Frey stimulation above and below the level of thoracic injury, in addition to testing tail withdrawal from heat stimuli (Kramer et al., 2017; Shiao and Lee-Kubli, 2018). Additional behavioral studies have demonstrated that SCI animals exhibit significant increases in mechanical and thermal hypersensitivity compared to naïve and sham animals, beginning at 1 month and persisting for several months

post-injury (Carlton et al., 2009; Bedi et al., 2010). However, other studies have asserted that operant behavioral tasks, such as conditioned place preference, are required to effectively study spontaneous pain in animals with SCI (Yezierski, 2005; Davoody et al., 2011; Yang et al., 2014). The present study focused on the transition from acute to chronic pain, in the absence of early pain-related behavior, to examine transcriptional differences that occur at much earlier time points rather than a point at which chronic pain is already present. We first tested behavioral differences between naïve and sham mice to identify changes due to the laminectomy, not the SCI itself, to better determine a time point that captures the transition from acute to chronic pain following SCI. For example, removal of bone and muscle alone could trigger chronic pain-like symptoms, analogous to post-surgical pain reported in humans (Woolf, 2011). Sham surgery for SCI has also recently been reported to produce significant increases in pain-avoidance behavior in rats, which is indicative of persistent post-surgical pain (Odem et al., 2019). Surprisingly, there were no significant differences between naïve and sham mice at any time point (**Figures 1A,B**), suggesting that the laminectomy did not produce any locomotor differences or behavioral hypersensitivity 1–7 days post-surgery in mice. By contrast, the SCI produced clear locomotor differences (**Figure 1A2**).

Injury and Inflammation in SCI

We also considered post-surgical inflammation, using cytokine ELISAs to assess changes in the spinal cord at the level of laminectomy (T8–T11). We wanted to assess changes in cytokine levels for two main reasons; first, to confirm that sham mice did not exhibit differences from naïve mice at key time points in comparison to SCI mice, and second to determine whether sham mice exhibited a prolonged inflammatory response, which could potentially be correlated to the development of chronic pain (Guptarak et al., 2013; Krames, 2014). Both pro-inflammatory cytokines TNF-α and IL-1β have been studied in neuroprotection models of SCI. IL-6 has been implicated in neurodegeneration after CNS injury, and the anti-inflammatory cytokine IL-10 exhibits neuroprotective effects (Donnelly and Popovich, 2008; Schmitz and Chew, 2008; Zhang et al., 2019). However, we did not find any significant cytokine changes between naïve and sham mice within 7 days of injury, indicating that the laminectomy did not produce a significant inflammatory response at the time points tested. As a positive control for the cytokine ELISAs (Suzuki and Kikkawa, 1969), we used the cuprizone model for multiple sclerosis. Key pathological features of the treatment include secretion of proinflammatory cytokines such as TNF-α and IL-1β (Schmitz and Chew, 2008). Consistent with previous findings, mice treated with cuprizone exhibited significant increases in TNF-α, IL-1β, and IL-10 relative to naïve mice (**Figure 1C**; Schmitz and Chew, 2008).

Tissue injury can also lead to prolonged functional changes and hyperalgesia that are accompanied by behavioral changes due to increased spontaneous activity of nociceptors (Carlton et al., 2009; Bedi et al., 2010; Walters, 2012). Spontaneous activity in nociceptors following SCI begins at 3 days after injury and persists for at least 8 months (Bedi et al., 2010). This increase in nociceptor activity elicits changes within the spinal dorsal horn, which receives input from these nociceptors, ultimately contributing to spontaneous pain (Dubner and Ruda, 1992; Wu et al., 2001). However, the source of hyperexcitability of nociceptors after injury is still unknown. Because spontaneous activity in nociceptors begins by 3 days post-injury, and has been correlated with the generation of persistent pain, we chose to observe transcriptomic changes immediately after this time point at 4 days post-injury (Xie et al., 2005). We intentionally excluded large sensory afferents from our experimental model, as the response to SCI by these afferents is transient and large sensory afferents have not been directly correlated with pain transduction in other models of chronic pain (Huang et al., 2006; Hu et al., 2016). We focused on an anatomically defined population of nociceptors (projecting from below the level of SCI to hairy hindpaw skin) by backlabeling from peripheral afferent terminals and sorting based on both fluorescence and size. These neurons represent ∼10% of dissociated DRG tissue and have a distinct transcriptome (Thakur et al., 2014). Our approach to identifying anatomically defined small nociceptors is distinct from single-cell transcriptome isolation based on the expression of the sodium channel Scn10a ($Na_v1.8$) or expression of advillin (Avil, a marker for all neural crest neurons; Lopes et al., 2017; Megat et al., 2019).

Different DRG Neuronal Populations in SCI

Different types of sensory neurons are distinct in their responses to injury. It is likely that, even within an identified subpopulation, cells will nonetheless exhibit heterogeneity (Hu et al., 2016). Because injury does not impact all afferents in the same way, we analyzed gene expression changes within the population of nociceptors projecting to the skin below the level of injury. By focusing on small nociceptors innervating dermatomes below the level of injury, we begin to address what unique set of genes within a specific population may be contributing to the burning, stabbing, and shooting pain reported in SCI patients suffering from below-level neuropathic pain (Siddall et al., 2003). Our goal was to better understand how SCI affects molecular changes within a specific population of neurons, and how this may contribute to hypersensitivity following SCI. We focused our analysis on sensory neurons from lumbar DRGs (below the level of the SCI) projecting to the hairy hindpaw skin (**Figure 2A**). After confirming, we had isolated the cell population of interest (**Figures 2B**, **3**), we used RNAseq to identify changes in gene expression. The use of RNA-Seq has clear advantages over microarrays, since RNA-Seq is not limited to a set of pre-determined transcripts, has a larger dynamic range of transcript expression, and is highly reproducible (Usoskin et al., 2015). By utilizing this technology, we were able to identify transcript changes undetectable with traditional RT-PCR or microarrays (Wang and Zylka, 2009). Our RNAseq data from naïve, sham, and injured animals display distinct patterns of somatosensory genes present in this nociceptor-enriched population. In particular, RPKM values show high levels of Scn10a (a marker for nociceptors), purinergic receptor P2rx3, Mrgprd (markers for the non-peptidergic population of nociceptors), and Calca and Calcb (neuropeptide precursors), indicating that we isolated the desired nociceptor specific cell

population, and also indicating important genes within the population of sensory neurons projecting to the hairy hindpaw skin (**Figures 4A–D**). Multiple gene transcripts important for itch, tactile function, and proprioception all had relatively low RPKM values, indicating again that we isolated the desired target cell population, and that injury did not induce modifications in the type of stimuli nociceptors transduce (**Figure 4C**). Our population-level analysis revealed significant changes after SCI in a number of ion channels and receptors that are already known to play a role in pain or hypersensitivity, such as Piezo2, and transcripts involved in excitatory signaling, such as Grik1 (**Figure 5C**, **Table 1**). However, there were also many genes whose expression and functional roles in persistent pain have yet to be characterized, including Trpc4 and Ttyh1 (**Figures 5A,B**, **Table 1**).

Transcriptome Profiling in Studies of DRG

Many studies have utilized RNA-seq technology to gain insight into nociceptor transcriptomes within the DRG and how it changes relative to different pain models (Thakur et al., 2014; Usoskin et al., 2015; Hu et al., 2016; Megat et al., 2019). Although previous screens have yielded various nociceptor-specific genes, we have identified a unique pattern of gene expression within a population of nociceptors projecting to the periphery (**Figure 6**). By cross-comparing our dataset with similar studies, we were able to identify our cells of interest and confirm that, we obtained cell-type specificity. Notably, many of the current technologies require a transgenic mouse with a cell-type specific reporter. However, by taking advantage of the anatomical organization of the mouse, we were able to use backlabeling and FACS sorting in non-transgenic animals to isolate a nociceptor-enriched population with a low degree of contamination with other cell types. We further implemented this methodology to identify candidate genes in a specific population of neurons below the level of injury in a model of SCI to better understand the heterogeneous injury response among the many subtypes of DRG neurons.

Among these comparisons, we observed large fold changes in several genes (**Figures 7A,B**, highlighted in red and blue). However, instead of focusing on larger changes in a small subset of genes with individual functions, we concentrated our analysis on the interaction of many transcripts that were significantly altered after SCI and how these influenced intracellular signaling pathways (**Figure 7C**). Ingenuity Pathway Analysis implicated numerous pathways associated with the progression to persistent pain. We took particular interest in the synaptogenesis signaling pathway as a key player at this 4-day time point, suggesting a role for synaptic plasticity in the transition from acute to chronic pain after SCI. In addition to its relevance within our model, many of the transcripts involved in synaptic plasticity overlapped with several other pathways (**Figure 7C**) and had RPKM values that could be validated by qPCR (**Figure 7D**). Synaptogenesis is typically associated with developmental processes, including axon guidance and synapse formation (Klein, 2004; Price and Inyang, 2015). However, activation of various signaling pathways involved in synaptogenesis may also contribute to pain; for example persistent pain is supported *via* changes in synaptic signaling, neuronal plasticity, and long term potentiation, and may form memory-like networks for painful signals that allow persistent pain to occur long after the initial injury (Kobayashi et al., 2007; Khangura et al., 2019).

Included in the many of the genes of interest within the synaptogenesis pathway, Ephb2 was significantly down-regulated post-injury (**Table 1**). The gene transcript is part of the Ephrin tyrosine kinase receptor protein family that is expressed in laminae I-III of the spinal dorsal horn on small and medium-sized DRG neurons (presumably nociceptors; Bundesen et al., 2003). Ephb receptors regulate synaptic activity in the spinal cord and contribute to persistent pain associated with NMDA activity (Khangura et al., 2019). Numerous receptor tyrosine kinases localize to synapses and contribute to synaptogenesis in addition to EphB receptors, including Trk receptors (Biederer and Stagi, 2008). Ntrk2, the receptor for BDNF, was highly expressed in this cell population; commensurately, BDNF transcript levels were significantly upregulated in the injured population (**Table 1**). Camk2g transcript levels were significantly increased in the SCI population of cutaneous nociceptors as well, and recent work has shown phosphorylation of Camk2g induces Bdnf mRNA transcription (Melemedjian et al., 2013; Yan et al., 2016). This parallels increasing evidence that neuronal activity (such as increased activity or hyperexcitability) activates alternative neuronal circuits through activity-regulated genes, such as *BDNF* (Lu et al., 2009; Melemedjian et al., 2013). Many of the genes significantly altered in the synaptogenesis pathway may function together to generate neuropathic pain (**Supplementary Figure S7**).

Networks of Genes Coordinating Responses to SCI

Regulatory interrelationships predicted by the IPA program were also examined (**Figure 7E**). Many of these networks are related to inflammatory signaling mechanisms, suggesting a link between pro-inflammatory signaling and synaptic transmission (Alexander and Popovich, 2009; Walters, 2014; Medelin et al., 2018). Previous work has associated inflammatory mechanisms to diseases of the CNS, including multiple sclerosis, Alzheimer's disease, and Parkinson's disease (Medelin et al., 2018). The mechanisms through which inflammation prompts changes in synaptic transmission are not fully understood, but several of the classic pro-inflammatory cytokines (including TNF-α, IL-6, IL-1β) have been shown to contribute to a decrease in hippocampal neurogenesis, and could be playing a similar role within the spinal cord following injury (Kohman and Rhodes, 2013). Overall, pro-inflammatory conditions have been associated with increases in post-synaptic NMDA and AMPA receptors, and inhibition of GABAergic receptors (Medelin et al., 2018).

CONCLUSION

Molecular changes typically reflect phenotypic characteristics, and our data show changes in gene expression 4 days after injury, suggesting that many of these genes may be responsible for the

development of spontaneous activity reported elsewhere (Bedi et al., 2010; Yang et al., 2014). We recognize that RNA-Seq of batched neurons elucidated changes in gene targets in a subpopulation of cells, but averaging occurred when pooling large numbers of cells, precluding analysis at the level of the single cell (Haque et al., 2017). Further analysis at the single-cell level of cutaneous nociceptors will clarify the contributions of specific subpopulations (non-peptidergic vs. peptidergic) to chronic pain after SCI. Functional studies are also needed to analyze the roles of this specific cell population, to better understand the connectivity and plasticity of the CNS and PNS. While our results begin to address prospective gene networks that may contribute to the development of chronic pain, additional behavioral testing in conjunction with targeting of specific biological mechanisms until the chronic pain phase is necessary in order to attribute specific transcriptional changes to pain phenotypes. The DRG nociceptor preparation isolated by backlabeling with WGA-488 and FACS has many applications in molecular studies. However, it is important to note that while this methodology is beneficial in gaining knowledge of changes in gene expression at the transcriptional level, additional studies would need to be done to corroborate similar changes in protein levels. Previously mentioned isolation methods such as TRAP-seq are able to elucidate functional changes at the translational level. We have demonstrated how the cutaneous nociceptor transcriptome is altered following SCI to gain novel biological insight into disease mechanisms in a cell-type-specific approach. It is evident that the transition from acute to chronic pain occurs in distinct steps that involve numerous signaling pathways, providing a host of potential new drug targets.

DATA AVAILABILITY STATEMENT

The datasets generated during and/or analyzed during the current study are available in Gene Expression Omnibus (GEO) repository under the series record number GSE132552, all other data generated during this study are included in this published article (and its **Supplementary Material**).

ETHICS STATEMENT

The animal study was reviewed and approved by University of Connecticut health Center Institutional Animal Care and Use Committee.

AUTHOR CONTRIBUTIONS

JY and RM designed the research. JY performed the research. JY and RM analyzed the data. JY, IM and RM wrote the article.

FUNDING

This work was supported by National Institutes of Health (NIH) DK032948 (RM) and the University of Connecticut Graduate School. Both played no role in the any decisions about scientific direction or judgments.

ACKNOWLEDGMENTS

We thank Dr. Nicholas Wasko and Dr. Robert Clarke for providing us with cuprizone-treated mice, and Dr. Evan Jellison for his help and expertise with flow cytometry. We acknowledge Dr. Bo Reese and the Center for Genome Innovation, Institute for Systems Genomics, University of Connecticut for library construction and RNA sequencing services. We also acknowledge Dr. Vijender Singh and the Computational Biology Core, Institute for Systems Genomics, University of Connecticut for base-calling, read alignment, and assembly of individual transcripts to align to the genome.

SUPPLEMENTARY MATERIAL

The Supplementary Material for this article can be found online at: https://www.frontiersin.org/articles/10.3389/fnmol.2019.00284/full#supplementary-material.

REFERENCES

Alexander, J. K., and Popovich, P. G. (2009). Neuroinflammation in spinal cord injury: therapeutic targets for neuroprotection and regeneration. *Prog. Brain Res.* 175, 125–137. doi: 10.1016/s0079-6123(09)17508-8

Baek, A., Cho, S. R., and Kim, S. H. (2017). Elucidation of gene expression patterns in the brain after spinal cord injury. *Cell Transplant.* 26, 1286–1300. doi: 10.1177/0963689717715822

Bannon, A. W., and Malmberg, A. B. (2007). Models of nociception: hot-plate, tail-flick, and formalin tests in rodents. *Curr. Protoc. Neurosci.* 8:8.9. doi: 10.1002/0471142301.ns0809s41

Basbaum, A. I., Bautista, D. M., Scherrer, G., and Julius, D. (2009). Cellular and molecular mechanisms of pain. *Cell* 139, 267–284. doi: 10.1016/j.cell.2009.09.028

Basso, D. M., Fisher, L. C., Anderson, A. J., Jakeman, L. B., McTigue, D. M., and Popovich, P. G. (2006). Basso mouse scale for locomotion detects differences in recovery after spinal cord injury in five common mouse strains. *J. Neurotrauma* 23, 635–659. doi: 10.1089/neu.2006.23.635

Bedi, S. S., Yang, Q., Crook, R. J., Du, J., Wu, Z., Fishman, H. M., et al. (2010). Chronic spontaneous activity generated in the somata of primary nociceptors is associated with pain-related behavior after spinal cord injury. *J. Neurosci.* 30, 14870–14882. doi: 10.1523/JNEUROSCI.2428-10.2010

Berta, T., Perrin, F. E., Pertin, M., Tonello, R., Liu, Y. C., Chamessian, A., et al. (2017). Gene expression profiling of cutaneous injured and non-injured nociceptors in SNI animal model of neuropathic pain. *Sci. Rep.* 7:9367. doi: 10.1038/s41598-017-08865-3

Biederer, T., and Stagi, M. (2008). Signaling by synaptogenic molecules. *Curr. Opin. Neurobiol.* 18, 261–269. doi: 10.1016/j.conb.2008.07.014

Bruce, J. C., Oatway, M. A., and Weaver, L. C. (2002). Chronic pain after clip-compression injury of the rat spinal cord. *Exp. Neurol.* 178, 33–48. doi: 10.1006/exnr.2002.8026

Buch, N. S., Ahlburg, P., Haroutounian, S., Andersen, N. T., Finnerup, N. B., and Nikolajsen, L. (2019). The role of afferent input in postamputation pain: a randomized, double-blind, placebo-controlled crossover study. *Pain* 160, 1622–1633. doi: 10.1097/j.pain.0000000000001536

Bundesen, L. Q., Scheel, T. A., Bregman, B. S., and Kromer, L. F. (2003). Ephrin-B2 and EphB2 regulation of astrocyte-meningeal fibroblast interactions in response to spinal cord lesions in adult rats. *J. Neurosci.* 23, 7789–7800. doi: 10.1523/JNEUROSCI.23-21-07789.2003

Campbell, J. N., Raja, S. N., Meyer, R. A., and Mackinnon, S. E. (1988). Myelinated afferents signal the hyperalgesia associated with nerve injury. *Pain* 32, 89–94. doi: 10.1016/0304-3959(88)90027-9

Cardenas, D. D., Bryce, T. N., Shem, K., Richards, J. S., and Elhefni, H. (2004). Gender and minority differences in the pain experience of people with spinal cord injury. *Arch. Phys. Med. Rehabil.* 85, 1774–1781. doi: 10.1310/kg8c-tjcp-95a5-n949

Carlton, S. M., Du, J., Tan, H. Y., Nesic, O., Hargett, G. L., Bopp, A. C., et al. (2009). Peripheral and central sensitization in remote spinal cord regions contribute to central neuropathic pain after spinal cord injury. *Pain* 147, 265–276. doi: 10.1016/j.pain.2009.09.030

Chiu, I. M., Barrett, L. B., Williams, E. K., Strochlic, D. E., Lee, S., Weyer, A. D., et al. (2014). Transcriptional profiling at whole population and single cell levels reveals somatosensory neuron molecular diversity. *Elife* 3:e04660. doi: 10.7554/eLife.04660

Christensen, M. D., and Hulsebosch, C. E. (1997). Chronic central pain after spinal cord injury. *J. Neurotrauma* 14, 517–537. doi: 10.1089/neu.1997.14.517

Citri, A., Pang, Z. P., Sudhof, T. C., Wernig, M., and Malenka, R. C. (2011). Comprehensive qPCR profiling of gene expression in single neuronal cells. *Nat. Protoc.* 7, 118–127. doi: 10.1038/nprot.2011.430

Conesa, A., Madrigal, P., Tarazona, S., Gomez-Cabrero, D., Cervera, A., McPherson, A., et al. (2016). A survey of best practices for RNA-seq data analysis. *Genome Biol.* 17:13. doi: 10.1186/s13059-016-0881-8

Cook, A. D., Christensen, A. D., Tewari, D., McMahon, S. B., and Hamilton, J. A. (2018). Immune cytokines and their receptors in inflammatory pain. *Trends Immunol.* 39, 240–255. doi: 10.1016/j.it.2017.12.003

da Silva Serra, I., Husson, Z., Bartlett, J. D., and Smith, E. S. (2016). Characterization of cutaneous and articular sensory neurons. *Mol. Pain* 12:1744806916636387. doi: 10.1177/1744806916636387

Davoody, L., Quiton, R. L., Lucas, J. M., Ji, Y., Keller, A., and Masri, R. (2011). Conditioned place preference reveals tonic pain in an animal model of central pain. *J. Pain* 12, 868–874. doi: 10.1016/j.jpain.2011.01.010

de Hoon, M. J., Imoto, S., Nolan, J., and Miyano, S. (2004). Open source clustering software. *Bioinformatics* 20, 1453–1454. doi: 10.1093/bioinformatics/bth078

De Jongh, R. F., Vissers, K. C., Meert, T. F., Booij, L. H., De Deyne, C. S., and Heylen, R. J. (2003). The role of interleukin-6 in nociception and pain. *Anesth. Analg.* 96, 1096–1103. doi: 10.1213/01.ane.0000055362.56604.78

Defrin, R., Ohry, A., Blumen, N., and Urca, G. (2001). Characterization of chronic pain and somatosensory function in spinal cord injury subjects. *Pain* 89, 253–263. doi: 10.1016/s0304-3959(00)00369-9

Deng, X., Wang, D., Wang, S., Wang, H., and Zhou, H. (2018). Identification of key genes and pathways involved in response to pain in goat and sheep by transcriptome sequencing. *Biol. Res.* 51:25. doi: 10.1186/s40659-018-0174-7

Densmore, V. S., Kalous, A., Keast, J. R., and Osborne, P. B. (2010). Above-level mechanical hyperalgesia in rats develops after incomplete spinal cord injury but not after cord transection and is reversed by amitriptyline, morphine and gabapentin. *Pain* 151, 184–193. doi: 10.1016/j.pain.2010.07.007

Devor, M. (2006). Sodium channels and mechanisms of neuropathic pain. *J. Pain* 7, S3–S12. doi: 10.1016/j.jpain.2005.09.006

Devor, M. (2009). Ectopic discharge in Aβ afferents as a source of neuropathic pain. *Exp. Brain Res.* 196, 115–128. doi: 10.1007/s00221-009-1724-6

Dixon, W. J. (1980). Efficient analysis of experimental observations. *Annu. Rev. Pharmacol. Toxicol.* 20, 441–462. doi: 10.1146/annurev.pa.20.040180.002301

Djouhri, L., Dawbarn, D., Robertson, A., Newton, R., and Lawson, S. N. (2001). Time course and nerve growth factor dependence of inflammation-induced alterations in electrophysiological membrane properties in nociceptive primary afferent neurons. *J. Neurosci.* 21, 8722–8733. doi: 10.1523/JNEUROSCI.21-22-08722.2001

Dominguez, E., Rivat, C., Pommier, B., Mauborgne, A., and Pohl, M. (2008). JAK/STAT3 pathway is activated in spinal cord microglia after peripheral nerve injury and contributes to neuropathic pain development in rat. *J. Neurochem.* 107, 50–60. doi: 10.1111/j.1471-4159.2008.05566.x

Donnelly, D. J., and Popovich, P. G. (2008). Inflammation and its role in neuroprotection, axonal regeneration and functional recovery after spinal cord injury. *Exp. Neurol.* 209, 378–388. doi: 10.1016/j.expneurol.2007.06.009

Dubner, R., and Ruda, M. A. (1992). Activity-dependent neuronal plasticity following tissue injury and inflammation. *Trends Neurosci.* 15, 96–103. doi: 10.1016/0166-2236(92)90019-5

Eijkelkamp, N., Linley, J. E., Torres, J. M., Bee, L., Dickenson, A. H., Gringhuis, M., et al. (2013). A role for Piezo2 in EPAC1-dependent mechanical allodynia. *Nat. Commun.* 4:1682. doi: 10.1038/ncomms2673

Finnerup, N. B., Johannesen, I. L., Sindrup, S. H., Bach, F. W., and Jensen, T. S. (2001). Pain and dysesthesia in patients with spinal cord injury: a postal survey. *Spinal Cord* 39, 256–262. doi: 10.1038/sj.sc.3101161

Gallego Romero, I., Pai, A. A., Tung, J., and Gilad, Y. (2014). RNA-seq: impact of RNA degradation on transcript quantification. *BMC Biol.* 12:42. doi: 10.1186/1741-7007-12-42

Gaudet, A. D., Ayala, M. T., Schleicher, W. E., Smith, E. J., Bateman, E. M., Maier, S. F., et al. (2017). Exploring acute-to-chronic neuropathic pain in rats after contusion spinal cord injury. *Exp. Neurol.* 295, 46–54. doi: 10.1016/j.expneurol.2017.05.011

Gold, M. S., and Gebhart, G. F. (2010). Nociceptor sensitization in pain pathogenesis. *Nat. Med.* 16, 1248–1257. doi: 10.1038/nm.2235

Goswami, S. C., Mishra, S. K., Maric, D., Kaszas, K., Gonnella, G. L., Clokie, S. J., et al. (2014). Molecular signatures of mouse TRPV1-lineage neurons revealed by RNA-Seq transcriptome analysis. *J. Pain* 15, 1338–1359. doi: 10.1016/j.jpain.2014.09.010

Guptarak, J., Wanchoo, S., Durham-Lee, J., Wu, Y., Zivadinovic, D., Paulucci-Holthauzen, A., et al. (2013). Inhibition of IL-6 signaling: a novel therapeutic approach to treating spinal cord injury pain. *Pain* 154, 1115–1128. doi: 10.1016/j.pain.2013.03.026

Haque, A., Engel, J., Teichmann, S. A., and Lonnberg, T. (2017). A practical guide to single-cell RNA-sequencing for biomedical research and clinical applications. *Genome Med.* 9:75. doi: 10.1186/s13073-017-0467-4

Haroutounian, S., Ford, A. L., Frey, K., Nikolajsen, L., Finnerup, N. B., Neiner, A., et al. (2018). How central is central poststroke pain? The role of afferent input in poststroke neuropathic pain: a prospective, open-label pilot study. *Pain* 159, 1317–1324. doi: 10.1097/j.pain.0000000000001213

Harriott, A. M., and Gold, M. S. (2009). Contribution of primary afferent channels to neuropathic pain. *Curr. Pain Headache Rep.* 13, 197–207. doi: 10.1007/s11916-009-0034-9

Harris, J. A. (1998). Using c-fos as a neural marker of pain. *Brain Res. Bull.* 45, 1–8. doi: 10.1016/s0361-9230(97)00277-3

Hu, G., Huang, K., Hu, Y., Du, G., Xue, Z., Zhu, X., et al. (2016). Single-cell RNA-seq reveals distinct injury responses in different types of DRG sensory neurons. *Sci. Rep.* 6:31851. doi: 10.1038/srep31851

Huang, L. Y., Gu, Y., and Chen, Y. (2013). Communication between neuronal somata and satellite glial cells in sensory ganglia. *Glia* 61, 1571–1581. doi: 10.1002/glia.22541

Huang, W. L., Robson, D., Liu, M. C., King, V. R., Averill, S., Shortland, P. J., et al. (2006). Spinal cord compression and dorsal root injury cause up-regulation of activating transcription factor-3 in large-diameter dorsal root ganglion neurons. *Eur. J. Neurosci.* 23, 273–278. doi: 10.1111/j.1460-9568.2005.04530.x

Joshi, M., and Fehlings, M. G. (2002). Development and characterization of a novel, graded model of clip compressive spinal cord injury in the mouse: Part 1. Clip design, behavioral outcomes and histopathology. *J. Neurotrauma* 19, 175–190. doi: 10.1089/08977150252806947

Julius, D., and Basbaum, A. I. (2001). Molecular mechanisms of nociception. *Nature* 413, 203–210. doi: 10.1038/35093019

Khangura, R. K., Sharma, J., Bali, A., Singh, N., and Jaggi, A. S. (2019). An integrated review on new targets in the treatment of neuropathic pain. *Korean J. Physiol. Pharmacol.* 23, 1–20. doi: 10.4196/kjpp.2019.23.1.1

Kjell, J., and Olson, L. (2016). Rat models of spinal cord injury: from pathology to potential therapies. *Dis. Model. Mech.* 9, 1125–1137. doi: 10.1242/dmm.025833

Klein, R. (2004). Eph/ephrin signaling in morphogenesis, neural development and plasticity. *Curr. Opin. Cell Biol.* 16, 580–589. doi: 10.1016/j.ceb.2004.07.002

Klenke, S., Renckhoff, K., Engler, A., Peters, J., and Frey, U. H. (2016). Easy-to-use strategy for reference gene selection in quantitative real-time PCR experiments. *Naunyn Schmiedebergs. Arch. Pharmacol.* 389, 1353–1366. doi: 10.1007/s00210-016-1305-8

Kobayashi, H., Kitamura, T., Sekiguchi, M., Homma, M. K., Kabuyama, Y., Konno, S., et al. (2007). Involvement of EphB1 receptor/EphrinB2 ligand in neuropathic pain. *Spine* 32, 1592–1598. doi: 10.1097/brs.0b013e318074d46a

Kohman, R. A., and Rhodes, J. S. (2013). Neurogenesis, inflammation and behavior. *Brain Behav. Immun.* 27, 22–32. doi: 10.1016/j.bbi.2012.09.003

Kramer, J. L., Minhas, N. K., Jutzeler, C. R., Erskine, E. L., Liu, L. J., and Ramer, M. S. (2017). Neuropathic pain following traumatic spinal cord injury: models, measurement, and mechanisms. *J. Neurosci. Res.* 95, 1295–1306. doi: 10.1002/jnr.23881

Krames, E. S. (2014). The role of the dorsal root ganglion in the development of neuropathic pain. *Pain Med.* 15, 1669–1685. doi: 10.1111/pme.12413

Labaj, P. P., and Kreil, D. P. (2016). Sensitivity, specificity and reproducibility of RNA-Seq differential expression calls. *Biol. Direct* 11:66. doi: 10.1186/s13062-016-0169-7

Lallemend, F., and Ernfors, P. (2012). Molecular interactions underlying the specification of sensory neurons. *Trends Neurosci.* 35, 373–381. doi: 10.1016/j.tins.2012.03.006

Le Pichon, C. E., and Chesler, A. T. (2014). The functional and anatomical dissection of somatosensory subpopulations using mouse genetics. *Front. Neuroanat.* 8:21. doi: 10.3389/fnana.2014.00021

Lima, L., Gaiteiro, C., Peixoto, A., Soares, J., Neves, M., Santos, L. L., et al. (2016). Reference genes for addressing gene expression of bladder cancer cell models under hypoxia: a step towards transcriptomic studies. *PLoS One* 11:e0166120. doi: 10.1371/journal.pone.0166120

Lopes, D. M., Denk, F., and McMahon, S. B. (2017). The molecular fingerprint of dorsal root and trigeminal ganglion neurons. *Front. Mol. Neurosci.* 10:304. doi: 10.3389/fnmol.2017.00304

Love, M. I., Huber, W., and Anders, S. (2014). Moderated estimation of fold change and dispersion for RNA-seq data with DESeq2. *Genome Biol.* 15:550. doi: 10.1186/s13059-014-0550-8

Lu, B., Wang, K. H., and Nose, A. (2009). Molecular mechanisms underlying neural circuit formation. *Curr. Opin. Neurobiol.* 19, 162–167. doi: 10.1016/j.conb.2009.04.004

Ma, M., Basso, D. M., Walters, P., Stokes, B. T., and Jakeman, L. B. (2001). Behavioral and histological outcomes following graded spinal cord contusion injury in the C57Bl/6 mouse. *Exp. Neurol.* 169, 239–254. doi: 10.1006/exnr.2001.7679

Mains, R. E., Blaby-Haas, C., Rheaume, B. A., and Eipper, B. A. (2018). Changes in corticotrope gene expression upon increased expression of peptidylglycine α-amidating monooxygenase. *Endocrinology* 159, 2621–2639. doi: 10.1210/en.2018-00235

Malin, S. A., Davis, B. M., and Molliver, D. C. (2007). Production of dissociated sensory neuron cultures and considerations for their use in studying neuronal function and plasticity. *Nat. Protoc.* 2, 152–160. doi: 10.1038/nprot.2006.461

Marques, S. A., de Almeida, F. M., Mostacada, K., and Martinez, A. M. (2014). A highly reproducible mouse model of compression spinal cord injury. *Methods Mol. Biol.* 1162, 149–156. doi: 10.1007/978-1-4939-0777-9_12

Medelin, M., Giacco, V., Aldinucci, A., Castronovo, G., Bonechi, E., Sibilla, A., et al. (2018). Bridging pro-inflammatory signals, synaptic transmission and protection in spinal explants *in vitro*. *Mol. Brain* 11:3. doi: 10.1186/s13041-018-0347-x

Megat, S., Ray, P. R., Tavares-Ferreira, D., Moy, J. K., Sankaranarayanan, I., Wanghzou, A., et al. (2019). Differences between dorsal root and trigeminal ganglion nociceptors in mice revealed by translational profiling. *J. Neurosci.* 39, 6829–6847. doi: 10.1523/jneurosci.2663-18.2019

Meisner, J. G., Marsh, A. D., and Marsh, D. R. (2010). Loss of GABAergic interneurons in laminae I-III of the spinal cord dorsal horn contributes to reduced GABAergic tone and neuropathic pain after spinal cord injury. *J. Neurotrauma* 27, 729–737. doi: 10.1089/neu.2009.1166

Melemedjian, O. K., Tillu, D. V., Asiedu, M. N., Mandell, E. K., Moy, J. K., Blute, V. M., et al. (2013). BDNF regulates atypical PKC at spinal synapses to initiate and maintain a centralized chronic pain state. *Mol. Pain* 9:12. doi: 10.1186/1744-8069-9-12

Mueller, O., Lightfoot, S., and Schroeder, A. (2016). *RNA Integrity Number (RIN)—Standardization of RNA Quality Control.* Waldbronn: Agilent Technologies.

Mukhamedshina, Y. O., Akhmetzyanova, E. R., Martynova, E. V., Khaiboullina, S. F., Galieva, L. R., and Rizvanov, A. A. (2017). Systemic and local cytokine profile following spinal cord injury in rats: a multiplex analysis. *Front. Neurol.* 8:581. doi: 10.3389/fneur.2017.00581

Nakae, A., Nakai, K., Yano, K., Hosokawa, K., Shibata, M., and Mashimo, T. (2011). The animal model of spinal cord injury as an experimental pain model. *J. Biomed. Biotechnol.* 2011:939023. doi: 10.1155/2011/939023

Naranjo, J. R., Mellstrom, B., Achaval, M., and Sassone-Corsi, P. (1991). Molecular pathways of pain: Fos/Jun-mediated activation of a noncanonical AP-1 site in the prodynorphin gene. *Neuron* 6, 607–617. doi: 10.1016/0896-6273(91)90063-6

Nees, T. A., Tappe-Theodor, A., Sliwinski, C., Motsch, M., Rupp, R., Kuner, R., et al. (2016). Early-onset treadmill training reduces mechanical allodynia and modulates calcitonin gene-related peptide fiber density in lamina III/IV in a mouse model of spinal cord contusion injury. *Pain* 157, 687–697. doi: 10.1097/j.pain.0000000000000422

Odem, M. A., Bavencoffe, A. G., Cassidy, R. M., Lopez, E. R., Tian, J., Dessauer, C. W., et al. (2018). Isolated nociceptors reveal multiple specializations for generating irregular ongoing activity associated with ongoing pain. *Pain* 159, 2347–2362. doi: 10.1097/j.pain.0000000000001341

Odem, M. A., Lacagnina, M. J., Katzen, S. L., Li, J., Spence, E. A., Grace, P. M., et al. (2019). Sham surgeries for central and peripheral neural injuries persistently enhance pain-avoidance behavior as revealed by an operant conflict test. *Pain* 160, 2440–2455. doi: 10.1097/j.pain.0000000000001642

Price, T. J., and Inyang, K. E. (2015). Commonalities between pain and memory mechanisms and their meaning for understanding chronic pain. *Prog. Mol. Biol. Transl. Sci.* 131, 409–434. doi: 10.1016/bs.pmbts.2014.11.010

Ramabadran, K., Bansinath, M., Turndorf, H., and Puig, M. M. (1989). Tail immersion test for the evaluation of a nociceptive reaction in mice. *J. Pharmacol. Methods* 21, 21–31. doi: 10.1016/0160-5402(89)90019-3

Ritter, D. M., Zemel, B. M., Lepore, A. C., and Covarrubias, M. (2015). Kv3.4 channel function and dysfunction in nociceptors. *Channels* 9, 209–217. doi: 10.1080/19336950.2015.1056949

Schmitz, T., and Chew, L. J. (2008). Cytokines and myelination in the central nervous system. *ScientificWorldJournal* 8, 1119–1147. doi: 10.1100/tsw.2008.140

Schroeder, A., Mueller, O., Stocker, S., Salowsky, R., Leiber, M., Gassmann, M., et al. (2006). The RIN: an RNA integrity number for assigning integrity values to RNA measurements. *BMC Mol. Biol.* 7:3. doi: 10.1186/1471-2199-7-3

Seijffers, R., Mills, C. D., and Woolf, C. J. (2007). ATF3 increases the intrinsic growth state of DRG neurons to enhance peripheral nerve regeneration. *J. Neurosci.* 27, 7911–7920. doi: 10.1523/JNEUROSCI.5313-06.2007

Shiao, R., and Lee-Kubli, C. A. (2018). Neuropathic pain after spinal cord injury: challenges and research perspectives. *Neurotherapeutics* 15, 635–653. doi: 10.1007/s13311-018-0633-4

Shields, S. D., Ahn, H. S., Yang, Y., Han, C., Seal, R. P., Wood, J. N., et al. (2012). Nav1.8 expression is not restricted to nociceptors in mouse peripheral nervous system. *Pain* 153, 2017–2030. doi: 10.1016/j.pain.2012.04.022

Siddall, P. J., and Loeser, J. D. (2001). Pain following spinal cord injury. *Spinal Cord* 39, 63–73. doi: 10.1038/sj.sc.3101116

Siddall, P. J., McClelland, J. M., Rutkowski, S. B., and Cousins, M. J. (2003). A longitudinal study of the prevalence and characteristics of pain in the first 5 years following spinal cord injury. *Pain* 103, 249–257. doi: 10.1016/s0304-3959(02)00452-9

Stammers, A. T., Liu, J., and Kwon, B. K. (2012). Expression of inflammatory cytokines following acute spinal cord injury in a rodent model. *J. Neurosci. Res.* 90, 782–790. doi: 10.1002/jnr.22820

Suzuki, K., and Kikkawa, Y. (1969). Status spongiosus of CNS and hepatic changes induced by cuprizone (biscyclohexanone oxalyldihydrazone). *Am. J. Pathol.* 54, 307–325.

Szczot, M., Liljencrantz, J., Ghitani, N., Barik, A., Lam, R., Thompson, J. H., et al. (2018). PIEZO2 mediates injury-induced tactile pain in mice and humans. *Sci. Transl. Med.* 10:eaat9892. doi: 10.1126/scitranslmed.aat9892

Tator, C. P., and Poon, P. (2008). "Acute clip impact-compression model," in *Animal Models of Acute Neurological Injuries*, eds J. Chen, Z. C. Xu, X.-M. Xu and J. H. Zhang (New York, NY and Totowa, NJ: Humana Press), 449–460.

Thakur, M., Crow, M., Richards, N., Davey, G. I., Levine, E., Kelleher, J. H., et al. (2014). Defining the nociceptor transcriptome. *Front. Mol. Neurosci.* 7:87. doi: 10.3389/fnmol.2014.00087

Tsuda, M., Kohro, Y., Yano, T., Tsujikawa, T., Kitano, J., Tozaki-Saitoh, H., et al. (2011). JAK-STAT3 pathway regulates spinal astrocyte proliferation and neuropathic pain maintenance in rats. *Brain* 134, 1127–1139. doi: 10.1093/brain/awr025

Tsujino, H., Kondo, E., Fukuoka, T., Dai, Y., Tokunaga, A., Miki, K., et al. (2000). Activating transcription factor 3 (ATF3) induction by axotomy in sensory and motoneurons: a novel neuronal marker of nerve injury. *Mol. Cell. Neurosci.* 15, 170–182. doi: 10.1006/mcne.1999.0814

Usoskin, D., Furlan, A., Islam, S., Abdo, H., Lonnerberg, P., Lou, D., et al. (2015). Unbiased classification of sensory neuron types by large-scale single-cell RNA sequencing. *Nat. Neurosci.* 18, 145–153. doi: 10.1038/nn.3881

Vaso, A., Adahan, H. M., Gjika, A., Zahaj, S., Zhurda, T., Vyshka, G., et al. (2014). Peripheral nervous system origin of phantom limb pain. *Pain* 155, 1384–1391. doi: 10.1016/j.pain.2014.04.018

Walters, E. T. (2012). Nociceptors as chronic drivers of pain and hyperreflexia after spinal cord injury: an adaptive-maladaptive hyperfunctional state hypothesis. *Front. Physiol.* 3:309. doi: 10.3389/fphys.2012.00309

Walters, E. T. (2014). Neuroinflammatory contributions to pain after SCI: roles for central glial mechanisms and nociceptor-mediated host defense. *Exp. Neurol.* 258, 48–61. doi: 10.1016/j.expneurol.2014.02.001

Walters, E. T. (2018). How is chronic pain related to sympathetic dysfunction and autonomic dysreflexia following spinal cord injury? *Auton. Neurosci.* 209, 79–89. doi: 10.1016/j.autneu.2017.01.006

Wang, H., and Zylka, M. J. (2009). Mrgprd-expressing polymodal nociceptive neurons innervate most known classes of substantia gelatinosa neurons. *J. Neurosci.* 29, 13202–13209. doi: 10.1523/jneurosci.3248-09.2009

Wasko, N. J., Kulak, M. H., Paul, D., Nicaise, A. M., Yeung, S. T., Nichols, F. C., et al. (2019). Systemic TLR2 tolerance enhances central nervous system remyelination. *J. Neuroinflammation* 16:158. doi: 10.1186/s12974-019-1540-2

Waxman, S. G., Dib-Hajj, S., Cummins, T. R., and Black, J. A. (1999). Sodium channels and pain. *Proc. Natl. Acad. Sci. U S A* 96, 7635–7639. doi: 10.1073/pnas.96.14.7635

Wickenden, A. (2002). K(+) channels as therapeutic drug targets. *Pharmacol. Ther.* 94, 157–182. doi: 10.1016/s0163-7258(02)00201-2

Woolf, C. J. (2011). Central sensitization: implications for the diagnosis and treatment of pain. *Pain* 152, S2–S15. doi: 10.1016/j.pain.2010.09.030

Wu, G., Ringkamp, M., Hartke, T. V., Murinson, B. B., Campbell, J. N., Griffin, J. W., et al. (2001). Early onset of spontaneous activity in uninjured C-fiber nociceptors after injury to neighboring nerve fibers. *J. Neurosci.* 21:RC140. doi: 10.1523/jneurosci.21-08-j0002.2001

Wu, Z., and Wu, H. (2016). Experimental design and power calculation for RNA-seq experiments. *Methods Mol. Biol.* 1418, 379–390. doi: 10.1007/978-1-4939-3578-9_18

Wu, Z., Yang, Q., Crook, R. J., O'Neil, R. G., and Walters, E. T. (2013). TRPV1 channels make major contributions to behavioral hypersensitivity and spontaneous activity in nociceptors after spinal cord injury. *Pain* 154, 2130–2141. doi: 10.1016/j.pain.2013.06.040

Xia, M., Liu, D., and Yao, C. (2015). TRPC3: a new target for therapeutic strategies in chronic pain-DAG-mediated activation of non-selective cation currents and chronic pain (Mol. Pain 2014;10:43). *J. Neurogastroenterol. Motil.* 21, 445–447. doi: 10.5056/jnm15078

Xie, W., Strong, J. A., Meij, J. T., Zhang, J. M., and Yu, L. (2005). Neuropathic pain: early spontaneous afferent activity is the trigger. *Pain* 116, 243–256. doi: 10.1016/j.pain.2005.04.017

Xue, Z. J., Shen, L., Wang, Z. Y., Hui, S. Y., Huang, Y. G., and Ma, C. (2014). STAT3 inhibitor WP1066 as a novel therapeutic agent for bCCI neuropathic pain rats. *Brain Res.* 1583, 79–88. doi: 10.1016/j.brainres.2014.07.015

Yan, X., Liu, J., Ye, Z., Huang, J., He, F., Xiao, W., et al. (2016). CaMKII-mediated CREB phosphorylation is involved in Ca^{2+}-induced BDNF mRNA transcription and neurite outgrowth promoted by electrical stimulation. *PLoS One* 11:e0162784. doi: 10.1371/journal.pone.0162784

Yang, Q., Wu, Z., Hadden, J. K., Odem, M. A., Zuo, Y., Crook, R. J., et al. (2014). Persistent pain after spinal cord injury is maintained by primary afferent activity. *J. Neurosci.* 34, 10765–10769. doi: 10.1523/JNEUROSCI.5316-13.2014

Yezierski, R. P. (2005). Spinal cord injury: a model of central neuropathic pain. *Neurosignals* 14, 182–193. doi: 10.1159/000087657

You, H. J., Colpaert, F. C., and Arendt-Nielsen, L. (2008). Long-lasting descending and transitory short-term spinal controls on deep spinal dorsal horn nociceptive-specific neurons in response to persistent nociception. *Brain Res. Bull.* 75, 34–41. doi: 10.1016/j.brainresbull.2007.07.015

Zhang, D., Mou, J. Y., Wang, F., Liu, J., and Hu, X. (2019). CRNDE enhances neuropathic pain *via* modulating miR-136/IL6R axis in CCI rat models. *J. Cell. Physiol.* 234, 22234–22241. doi: 10.1002/jcp.28790

Zhou, Q., Bao, Y., Zhang, X., Zeng, L., Wang, L., Wang, J., et al. (2014). Optimal interval for hot water immersion tail-flick test in rats. *Acta Neuropsychiatr.* 26, 218–222. doi: 10.1017/neu.2013.57

Zylka, M. J., Rice, F. L., and Anderson, D. J. (2005). Topographically distinct epidermal nociceptive circuits revealed by axonal tracers targeted to Mrgprd. *Neuron* 45, 17–25. doi: 10.1016/j.neuron.2004.12.015

Conflict of Interest: The authors declare that the research was conducted in the absence of any commercial or financial relationships that could be construed as a potential conflict of interest.

frontiers in Molecular Neuroscience

ORIGINAL RESEARCH
published: 10 January 2020
doi: 10.3389/fnmol.2019.00326

Differential Expression Profiles and Functional Prediction of tRNA-Derived Small RNAs in Rats After Traumatic Spinal Cord Injury

Chuan Qin[1,2,3,4,5†], *Hao Feng*[1,2,3,4,5†], *Chao Zhang*[1,2,3,4,5], *Xin Zhang*[1,2,3,4,5], *Yi Liu*[1,2,3,4,5], *De-Gang Yang*[1,2,3,4,5], *Liang-Jie Du*[1,2,3,4,5], *Ying-Chun Sun*[1,6], *Ming-Liang Yang*[1,2,3,4,5], *Feng Gao*[1,2,3,4,5*] *and Jian-Jun Li*[1,2,3,4,5*]

[1]School of Rehabilitation Medicine, Capital Medical University, Beijing, China, [2]Department of Spinal and Neural Functional Reconstruction, China Rehabilitation Research Center, Beijing, China, [3]Center of Neural Injury and Repair, Beijing Institute for Brain Disorders, Beijing, China, [4]Chinese Institute of Rehabilitation Science, Beijing, China, [5]Beijing Key Laboratory of Neural Injury and Rehabilitation, Beijing, China, [6]TCM Treatment Center, China Rehabilitation Research Center, Beijing, China

OPEN ACCESS

Edited by:
Michele Papa,
University of Campania Luigi Vanvitelli, Italy

Reviewed by:
Daniele Bottai,
University of Milan, Italy
Muddanna Sakkattu Rao,
Kuwait University, Kuwait

***Correspondence:**
Feng Gao
gaofeng5960@126.com
Jian-Jun Li
crrclijj@163.com

[†]These authors have contributed equally to this work

Received: 19 August 2019
Accepted: 17 December 2019
Published: 10 January 2020

Citation:
Qin C, Feng H, Zhang C, Zhang X, Liu Y, Yang D-G, Du L-J, Sun Y-C, Yang M-L, Gao F and Li J-J (2020) Differential Expression Profiles and Functional Prediction of tRNA-Derived Small RNAs in Rats After Traumatic Spinal Cord Injury. Front. Mol. Neurosci. 12:326. doi: 10.3389/fnmol.2019.00326

Spinal cord injury (SCI) is mostly caused by trauma. As the primary mechanical injury is unavoidable, a focus on the underlying molecular mechanisms of the SCI-induced secondary injury is necessary to develop promising treatments for patients with SCI. Transfer RNA-derived small RNA (tsRNA) is a novel class of short, non-coding RNA, possessing potential regulatory functions in various diseases. However, the functional roles of tsRNAs in traumatic SCI have not been determined yet. We used a combination of sequencing, quantitative reverse transcription-polymerase chain reaction (qRT-PCR), bioinformatics, and luciferase reporter assay to screen the expression profiles and identify the functional roles of tsRNAs after SCI. As a result, 297 differentially expressed tsRNAs were identified in rats' spinal cord 1 day after contusion. Of those, 155 tsRNAs were significantly differentially expressed: 91 were significantly up-regulated, whereas 64 were significantly down-regulated after SCI (fold change > 1.5; $P < 0.05$). Bioinformatics analyses revealed candidate tsRNAs (tiRNA-Gly-GCC-001, tRF-Gly-GCC-012, tRF-Gly-GCC-013, and tRF-Gly-GCC-016) that might play regulatory roles through the mitogen-activated protein kinase (MAPK) and neurotrophin signaling pathways by targeting brain-derived neurotrophic factor (BDNF). We validated the candidate tsRNAs and found opposite trends in the expression levels of the tsRNAs and BDNF after SCI. Finally, tiRNA-Gly-GCC-001 was identified to target BDNF using the luciferase reporter assay. In summary, we found an altered tsRNA expression pattern

Abbreviations: SCI, spinal cord injury; tRNA, transfer RNA; tsRNA, tRNA-derived small RNA; qRT-PCR, quantitative reverse transcription-polymerase chain reaction; MAPK, mitogen-activated protein kinase; BDNF, brain-derived neurotrophic factor; ncRNAs, noncoding RNAs; lncRNAs, long non-coding RNAs; miRNAs, microRNAs; circRNAs, circular RNAs; mRNAs, messenger RNAs; tRFs, tRNA-derived fragments; tiRNAs, tRNA-derived stress-induced RNAs; FC, fold change; CPMs, counts per million; GO, Gene Ontology; KEGG, Kyoto Encyclopedia of Genes and Genomes database; FC, fold change.

and predicted tiRNA-Gly-GCC-001 might be involved in the MAPK and neurotrophin pathways by targeting the BDNF, thus regulating the post-SCI pathophysiologic processes. This study provides novel insights for future investigations to explore the mechanisms and therapeutic targets for SCI.

Keywords: tRNA-derived small RNA, spinal cord injury, sequencing, bioinformatics, BDNF

INTRODUCTION

With the economic and social development, spinal cord injury (SCI) has become a growing public health concern worldwide. It is estimated that there are approximately 11,000 new patients with SCI in America each year, and currently, there are approximately 250,000 people with SCI (Qin et al., 2018; Hall et al., 2019; Liu et al., 2019). SCI is mostly caused by trauma, including the primary mechanical injury due to a rapid direct compression and contusion of the cord, and the subsequent secondary pathophysiological changes, such as edema, ischemia, apoptosis, autophagy, and oxidative stress, which usually lead to a permanent neurological impairment (Kang et al., 2018; Alizadeh et al., 2019; Vawda et al., 2019). The primary injury is in fact mostly unavoidable. Thus, there is an urgent need to attenuate the undesirable pathophysiological changes caused by the secondary injury in order to develop promising diagnostic and treatment methods for SCI in the clinical practice (Carelli et al., 2019).

However, the controversy about scientific evidence of neuroprotective and regenerative therapies for SCI has raged unabated for ages. Recently, extensive evidence related to the noncoding RNAs (ncRNAs), including long non-coding RNAs (lncRNAs; Zhang et al., 2018a,b), microRNAs (miRNAs; Liu et al., 2018), and circular RNAs (circRNAs; Qin et al., 2019), maybe at the point of breaking this impasse. The existing research has identified the critical role of these ncRNAs in alleviating the secondary pathophysiological damage after SCI (Jiang and Zhang, 2018; Wang et al., 2019).

Furthermore, with the help of next-generation sequencing techniques, many researchers found a heterogeneous population of small ncRNAs with lengths of 18–40 nucleotides cleaved from transfer RNA (tRNA), known as tRNA-derived small RNAs (tsRNAs; Lee et al., 2009; Li et al., 2018). Generally, there are two types of tsRNAs based on the length and cleavage sites of the tRNAs: tRNA-derived fragments (tRFs) and tRNA-derived stress-induced RNAs (tiRNAs). Interestingly, mounting evidence has shown that they are not merely byproducts of a random tRNA cleavage, but rather have critical functional roles as regulatory factors in the pathophysiologic processes of various diseases, such as tumor proliferation in ovarian cancer cells (Zhou et al., 2017) and cell cycle regulation in non-small cell lung cancer (Shao et al., 2017), and are potential biomarkers in prostate cancer (Olvedy et al., 2016). Nevertheless, to date, there are no studies focusing on the relationship between tsRNAs and traumatic SCI, and their molecular and intermolecular interactions and key signaling pathways remain to be elucidated. In addition, there is a growing body of evidence that various tsRNAs are generated under stress conditions and act as miRNAs in gene expression regulation by targeting the messenger RNAs (mRNAs; Kumar et al., 2014; Gebetsberger et al., 2017). As a result, it is rational to speculate that tsRNAs may be involved in the progression of the pathophysiological changes after SCI.

Therefore, the aim of this investigation was to explore the tsRNAs' expression profiles and preliminarily determine the potential functional roles of candidate tsRNAs in the pathophysiology after traumatic SCI. The study design is presented in **Figure 1**. These findings may provide new clues for studying the mechanisms underlying SCI and novel molecular targets for the clinical therapy of SCI.

In our study, we explored the relationship between tsRNAs and SCI. First, we examined the expression profiles of tsRNAs in rats' spinal cords after SCI using next-generation sequencing. Second, bioinformatics methods were used to perform tsRNA/mRNA interaction networks and predict the potential role of the target genes of chosen tsRNAs in the process after SCI. Third, four candidate tsRNAs and their potential target mRNAs were further validated by quantitative reverse transcription-polymerase chain reaction (qRT-PCR) to reveal their trends of expression level alteration after SCI. Finally, we used the luciferase reporter assay to detect the direct combination between the selected tsRNA and its target gene.

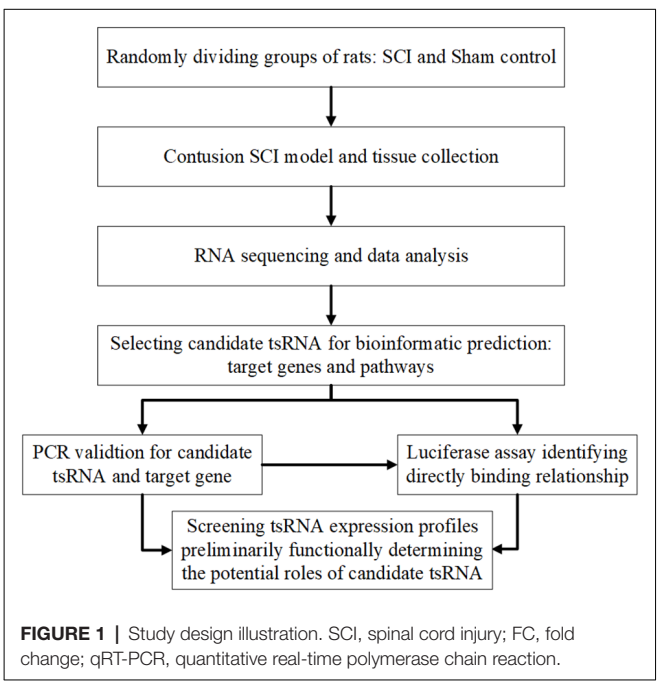

FIGURE 1 | Study design illustration. SCI, spinal cord injury; FC, fold change; qRT-PCR, quantitative real-time polymerase chain reaction.

MATERIALS AND METHODS

Animals and Experimental Groups

This study was performed in accordance with the principles of the Basel Declaration and the recommendations of the National Institute of Health Guide for the Care and Use of Laboratory Animals (NIH Publications No. 8023, revised 1978). The protocol was approved by the Institutional Animal Care and Use Committee of Capital Medical University. Male Sprague–Dawley rats (250–300 g) were housed for at least 7 days before the study in a temperature- (22–25°C) and humidity-controlled (50% relative humidity) animal facility with 12-h light/dark cycles. The animals had free access to food and water. However, food was withheld overnight before surgery.

Similar as in our previous study (Qin et al., 2019), 12 rats were randomly assigned into two groups using a computer-generated randomization schedule: the rats in the sham control group ($n = 6$) underwent laminectomy alone without contusion, and the rats in the SCI group ($n = 6$) underwent laminectomy and were subjected to contusion. The operators performing the surgeries were blinded to the experimental groups. Before and after surgery, our two experienced researchers performed a behavioral test of the rats in the two groups using the Basso, Beattie, and Bresnahan (BBB) score, frequently used to access the locomotor function in rats (Scheff et al., 2002). The BBB score ranges from 0 (no hindlimb movement) to 21 (normal movement), and the final score was given by a consensus.

Contusion SCI Model and Tissue Collection

In this study, the contusion injury method was used to induce moderate injuries in the rat models, similar to our previous study (Qin et al., 2019). In brief, all rats were anesthetized by an intraperitoneal injection of sodium pentobarbital solution at 40 mg/Kg body weight, and then their backs were shaved and sterilized. After holding or fixing the rats in a stereotaxic frame, a 4-cm longitudinal midline incision was made to expose the spinous processes of the thoracic (T) 9–T11 vertebrae. Following stripping of the paraspinal muscles, laminectomy was performed at the T10 level to expose the spinal dura mater without tearing it in a sterile condition. Subsequently, the rats were clamped by the T9 and T11 spinous processes using a sterile forceps, followed by a spinal cord contusion induced by an Infinite Horizon Impactor (IH-0400 Impactor, Precision Systems and Instrumentation, LLC., Natick, MA, USA), causing a moderate injury at the T10 level. Regarding the parameter settings, a standard rat tip impactor size (2.5 mm in diameter) and programmable force levels (225 kDynes) were applied, which were similar with the NYU weight-drop device settings (2.5 mm in diameter, 10 g rod, height of 12.5 mm) according to the conversion equation (Khuyagbaatar et al., 2015). Errors greater than 3% in terms of force levels and tears of the spinal dura mater were not accepted.

After inducing contusions, the operative region was gently washed twice with a warm 0.9% normal saline (37°C, 2 ml) to avoid local infection. The cord surface showed signs of a subarachnoid hematoma and an intense dark brown/purple color. The rats with swinging tails that quickly retracted their lower limbs immediately after the SCI were regarded as eligible, as previously described (Hu et al., 2015). Finally, the wound was sutured in layers. A warm environment was established to maintain body temperature during the surgery. Notably, 4 ml of Ringer lactate solution was administered intraperitoneally for electrolyte and fluid supplementation. Penicillin (40,000 U) was administered by intramuscular injection to prevent a systemic infection. The rats were then housed in individual cages, and their bladders were emptied manually every 8 h until they were sacrificed.

At 24 h after surgery, the rats in all groups were euthanized with an overdose of 40 mg/kg sodium pentobarbital solution, and a 1-cm long segment of the spinal cord, including the injury epicenter, was quickly dissected and collected without a prior transcardial perfusion and was fresh frozen in liquid nitrogen to prevent RNA degradation, similarly to a previously reported method (Pang et al., 2016).

RNA Extraction and Quality Control

In brief, the total RNA was isolated using TRIzol reagent (Invitrogen, Carlsbad, CA, USA) based on the manufacturer's instructions. Before the sequencing experiment, the integrity and quantity of each RNA sample were checked using agarose gel electrophoresis and the NanoDrop ND-1000 (NanoDrop, Wilmington, DE, USA) instrument.

Pretreatment of tsRNA and Library Preparation

In order to prevent RNA modifications that interfere with the small RNA-seq library construction, we performed the following treatments before the library preparation for the total RNA samples: 3′-aminoacyl (charged) deacylation to 3′-OH for 3′-adaptor ligation, 3′-cP (2′,3′-cyclic phosphate) removal to 3′-OH for 3′-adaptor ligation, 5′-OH (hydroxyl group) phosphorylation to 5′-P for 5′-adaptor ligation, and m1A and m3C demethylation for efficient reverse transcription. Subsequently, sequencing libraries were size-selected for the RNA biotypes to be sequenced using an automated gel cutter. The sequencing library was determined by the Agilent 2100 Bioanalyzer using the Agilent DNA 1000 chip kit (Agilent, part # 5067-1504).

Libraries Denaturation and Sequencing

The libraries were denatured and diluted to a loading volume of 1.3 ml and a loading concentration of 1.8 pM. The diluted libraries were loaded onto a reagent cartridge and forwarded to sequencing, which was performed on an Illumina NextSeq 500 system using a NextSeq 500/550 V2 kit (#FC-404-2005, Illumina, San Diego, CA, USA), according to the manufacturer's instructions. The sequencing was performed by running 50 cycles.

Data Collection and Analysis

The raw sequencing data that passed the Illumina chastity filter were used for the following analysis. After the Illumina quality control, the sequencing reads were 5′,3′-adaptor trimmed and filtered for over 15 nucleotides by the Cutadapt software.

Using the NovoAlign software (v2.07.11), the trimmed reads were aligned to the mature tRNA sequences, allowing for one mismatch only, and the reads that did not map were aligned to the precursor tRNA sequences, allowing for one mismatch only, using the BowTie software (Langmead et al., 2009).

The differentially expressed tsRNAs were screened based on the count value using R package edgeR (Qin et al., 2019). Moreover, the tsRNA expression levels could be measured and normalized as counts per million (CPMs) of the total aligned tRNA reads. The tsRNA expression profiling and differential expression analysis were calculated by the average CPM. When comparing the two groups for profile differences (SCI group vs. sham group), the "fold change (FC)," i.e., the ratio of the group averages between the groups was computed for each tsRNA. An FC > 1.5 and a *P*-value < 0.05 were considered as a significantly different expression, and the tsRNAs with such values were chosen for the next analysis. Principal component analysis (PCA), correlation analysis, pie plots, Venn plots, hierarchical clustering, scatter plots, and volcano plots were performed in an R or a Perl environment for statistical computing and graphical presentation of the expressed tsRNAs.

Bioinformatic Prediction

The four significantly differentially expressed tsRNAs (FC > 1.5 and *P*-value < 0.05) selected from the sequencing data were analyzed using bioinformatic methods. The candidate selection was based on several points: (1) higher FC and lower *P*-value; (2) higher CPM in both groups and balanced expression

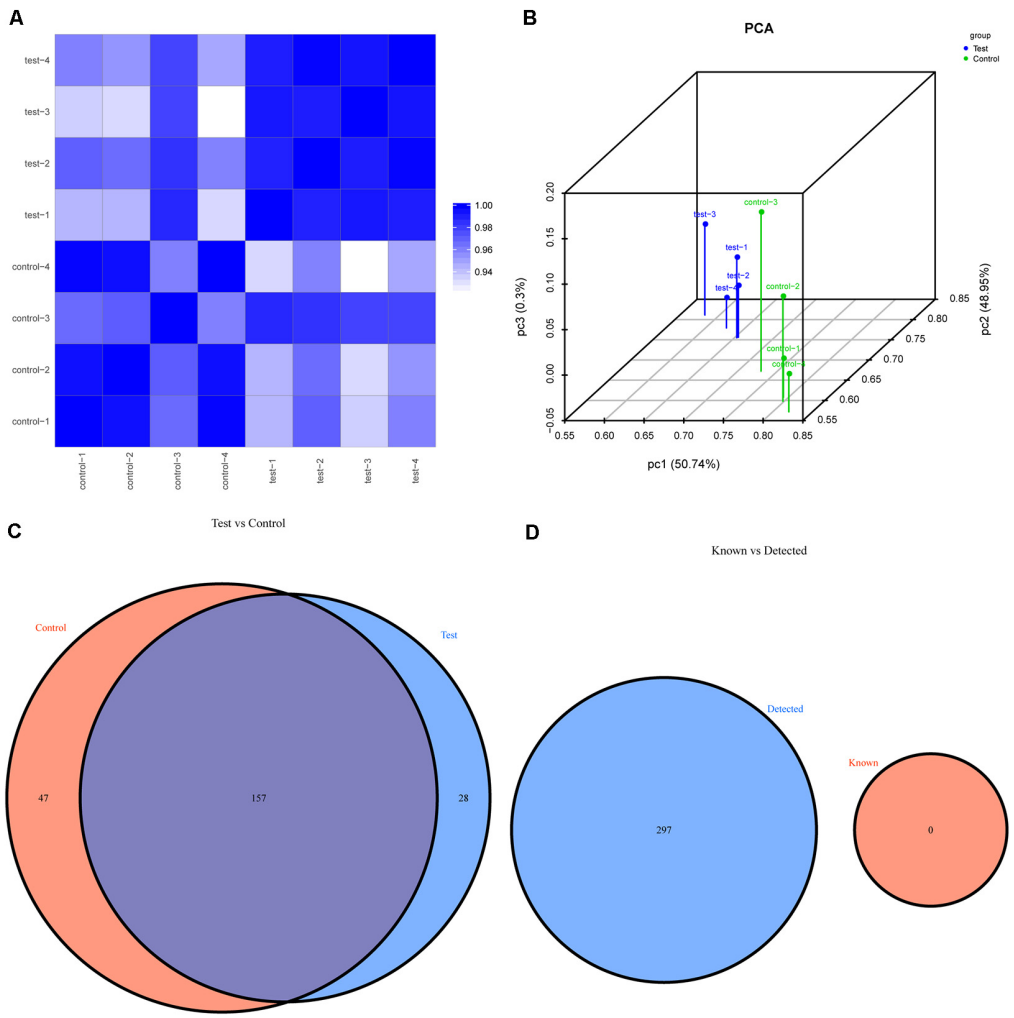

FIGURE 2 | The expression level analysis. **(A)** Heat-map of the correlation coefficient from all samples. The color in the panel represents the correlation coefficient of the two samples. The blue represents the two samples with a high correlation coefficient, and the white represents the low similarity of the two samples. **(B)** Primary component analysis: X, Y and Z axes represent the three main factors that affected the expression level of the sample. The colored point represents the corresponding sample, and its location shows the main character of the sample. The space distance represents the similarity of the data size. **(C)** Venn diagram based on the number of commonly expressed and specifically expressed tsRNAs. This diagram shows the number of tsRNAs which were expressed in both groups and also indicated the number of the specifically expressed tsRNAs. **(D)** Venn diagram based on the number of tsRNAs known and detected. This diagram shows the number of tsRNAs detected in this project and collected in the tRFdb.

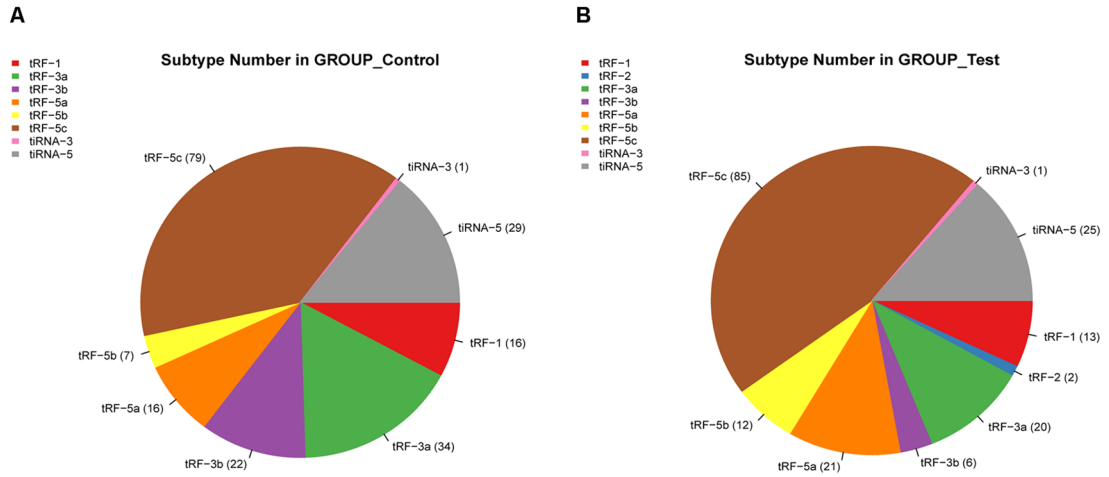

FIGURE 3 | Pie chart of each tsRNA subtype. **(A)** Pie chart of the distribution of tsRNA subtypes in the sham group. **(B)** Pie chart of the distribution of tsRNA subtypes in the SCI group.

of each rat in each group; and (3) Referring to previous publications to achieve more evidence of similar subtype of tsRNA.

First, in terms of target prediction of the candidate tsRNAs, the tsRNAs contained some seed sequences that could match the crosslink-centered regions of the target mRNAs (Kim et al., 2017). Mounting evidence has strongly suggested that tsRNAs could act as miRNAs, silencing the target mRNA *via* complementary base pairing (Kumar et al., 2014). According to a previous study (Li et al., 2019), three common algorithms were used to predict the tsRNA targets, including TargetScan[1], miRanda[2], and miRDB[3]. Notably, to reduce the false-positive results, only the genes predicted by all three software were considered as target mRNAs of the tsRNAs. A graph of the tsRNA/mRNA network was derived using the Cytoscape software (version 3.5.1, the Cytoscape Consortium, San Diego, CA, USA) to visualize these relationships.

Second, to assign the biological annotation of the targets, pathway, and process enrichment analyses were performed. We used Gene Ontology (GO[4]) to reveal the biological process, cellular component, and molecular function of the target mRNAs. Significant pathways were identified using the pathways in the Kyoto Encyclopedia of Genes and Genomes database (KEGG[5]). A $P < 0.05$ indicated the significance of the GO and KEGG pathway terms. The false discovery rate was calculated to correct the *P*-values. More specifically, *P*-values were calculated based on an accumulative hypergeometric distribution and the enrichment factor was the ratio between the observed count and the count expected by chance.

[1]http://www.targetscan.org
[2]http://www.microrna.org
[3]http://www.mirdb.org
[4]http://www.geneontology.org
[5]www.genome.jp/kegg

qRT-PCR Assay

The expression of the four tsRNAs selected through the bioinformatic analysis and that of the target mRNAs was validated using a qRT-PCR assay. The cord tissue samples from the rats in the SCI ($n = 6$) and sham groups ($n = 6$), including the tissue collected for the sequencing ($n = 4$ in both groups), as well as additional tissues ($n = 2$ in both groups) were used in the PCR experiment. As previously reported (Zhang et al., 2018), the total RNA was isolated using TRIzol reagent according to the manufacturer's standard protocols (Invitrogen, Carlsbad, CA, USA). RNA quantification and quality were assessed using NanoDrop ND-1,000, and RNA integrity was verified by electrophoresis on a denaturing agarose gel. Next, we synthesized complementary DNA (cDNA) in line with the manufacturer's instructions. qRT-PCR was performed in a ViiA 7 Real-time PCR System (Applied Biosystems, Foster City, CA, USA) using a PCR master mix (2×, Arraystar). The parameter settings were as follows: 95°C denaturation (10 min), 95°C (10 s), and 60°C (60 s), which was repeated for 40 cycles. After the amplification reaction was finished, the procedure was performed as follows: 95°C (10 s), 60°C (60 s), and 95°C (15 s). The relative tsRNA expression levels were calculated using the relative standard curve method (Larionov et al., 2005) and were normalized to U6 and β-actin, as endogenous. All reactions were performed in triplicate.

Luciferase Assay

Luciferase constructs containing either base pairs of the brain-derived neurotrophic factor (BDNF) 3′ UTR or two base-pair regions containing the predicted binding sites and a second construct, containing site-directed mutations in the predicted binding site, were prepared using methods as previously described (Arcaroli et al., 2012). The BDNF 3′ UTR, including the predicted binding sites for tiRNA-Gly-GCC-001, was cloned into a psiCheck-2

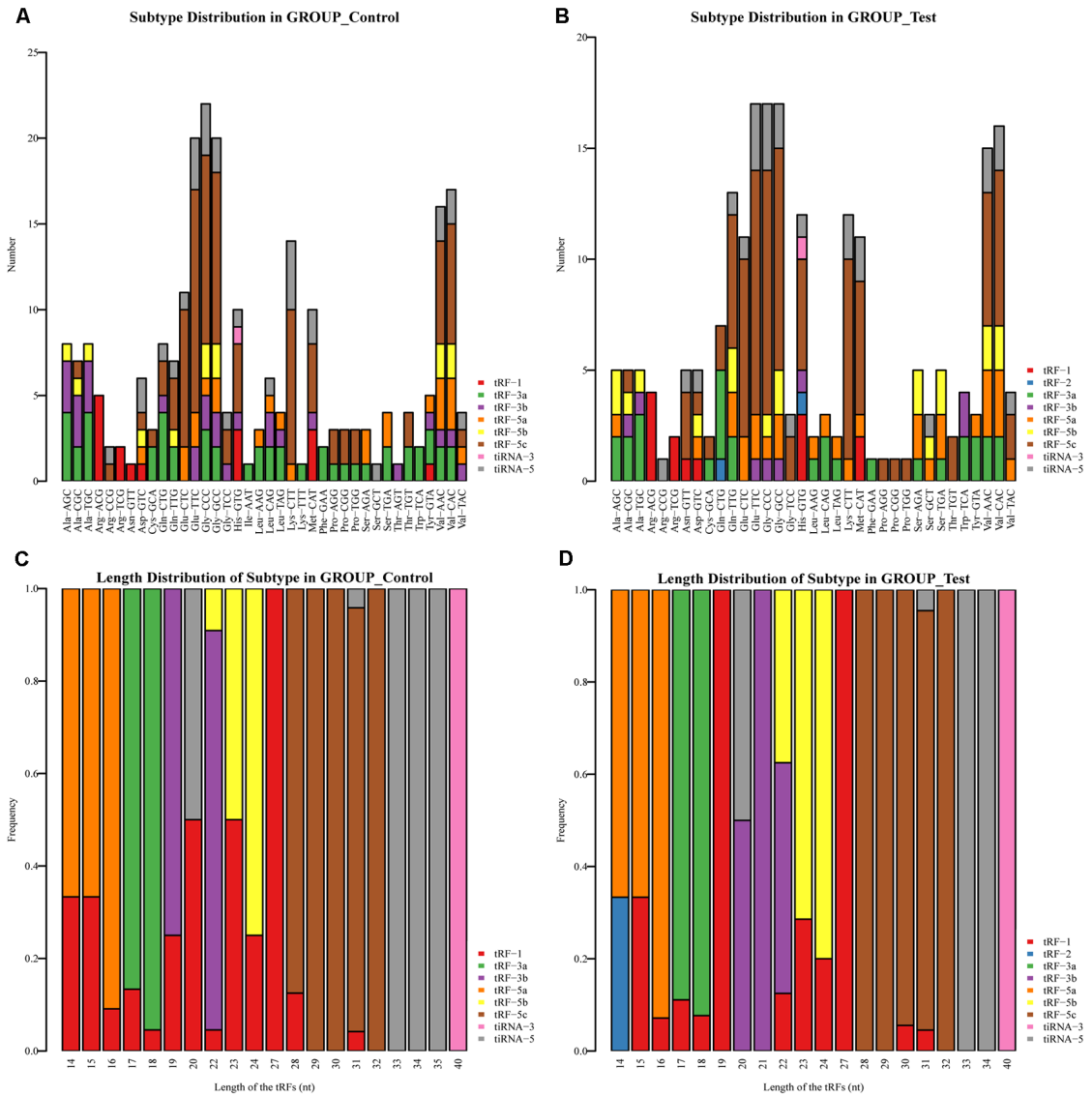

FIGURE 4 | Stacked Bar Chart. **(A)** The number of tsRNA subtypes against tRNA isodecoders in the sham group. **(B)** The number of tsRNA subtypes against tRNA isodecoders in the SCI group. **(C)** The Frequency of Subtype against Length of the tsRNAs in the sham group. **(D)** The Frequency of Subtype against Length of the tsRNAs in the SCI group.

dual-luciferase vector. Mutant BDNF 3′ UTR luciferase vectors were produced in the predicted tiRNA-Gly-GCC-001-binding regions. These plasmids and a tiRNA-Gly-GCC-001 mimic were co-transfected into HEK293T cells. Finally, luciferase assays were conducted using the dual-luciferase system (Promega, Madison, WI, USA), according to the manufacturer's instructions.

Statistical Analysis

Statistical analysis was performed using SPSS software (version 21.0, Chicago, IL, USA). The results are shown as the mean ± standard error of the mean (SEM). Student's *t*-test was used to compare the significant differences between the two groups. The level of significance was set at $P < 0.05$.

Database and Accession Numbers

The raw data of the tsRNA-Seq in our study were deposited at the NCBI Gene Expression Omnibus (GEO) under the accession number GSE133157.

RESULTS

Altered Expression Profiles of tsRNAs in Spinal Cord Tissues After SCI

Prior to injury, the BBB scores of all rats were 21. The rats in the sham group maintained a score of 21 during the experimental period, indicating the integrity of the spinal cord. However, in the SCI group, no hindlimb motor performance was observed

TABLE 1 | The top 10 up-regulated and down-regulated tsRNAs ranked by fold changes after SCI.

tsRNA	Type	Length	Fold change	*P*-value	Regulation
tiRNA-Asn-GTT-001	tiRNA-5	33	159.003645915166	1.41E-19	Up
tRF-Met-CAT-017	tRF-5c	30	122.01571606758	2.45E-15	Up
tRF-Met-CAT-051	tRF-5c	28	105.133667532338	5.65E-16	Up
tRF-Ser-AGA-016	tRF-5b	23	85.3172694348191	1.94E-40	Up
tRF-Met-CAT-016	tRF-5c	29	77.9150421396709	2.30E-15	Up
tRF-Gln-CTG-005	tRF-2	14	75.0513113045871	1.05E-20	Up
tRF-Ser-AGA-017	tRF-5b	24	57.6418498950225	2.52E-38	Up
tiRNA-Met-CAT-002	tiRNA-5	31	40.6199926628678	7.39E-14	Up
tRF-His-GTG-017	tRF-2	14	40.6053037913958	4.27E-18	Up
tRF-Asn-GTT-047	tRF-5c	32	33.3246942968211	2.66E-13	Up
tRF-Thr-AGT-022	tRF-3b	22	0.222109257777734	1.07E-05	Down
tRF-Ala-AGC-057	tRF-3b	22	0.243965889353342	1.06E-06	Down
tRF-Cys-GCA-007	tRF-3a	18	0.246922741938728	4.34E-07	Down
tRF-Ala-TGC-027	tRF-3b	22	0.274660579014769	3.43E-06	Down
tRF-Ala-TGC-035	tRF-3b	22	0.291169582918833	3.24E-04	Down
tRF-Ala-AGC-056	tRF-3b	22	0.293223504647025	4.91E-06	Down
tRF-Ala-TGC-002	tRF-3b	19	0.301367786961553	2.09E-05	Down
tRF-Leu-TAG-014	tRF-3a	17	0.30328867954121	1.77E-06	Down
tRF-Leu-CAG-023	tRF-3b	22	0.318608293880152	4.18E-06	Down
tRF-Cys-GCA-029	tRF-3a	17	0.32652518025552	8.72E-05	Down
The candidate tsRNAs selected for bioinformatics and PCR					
tiRNA-Gly-GCC-001	tiRNA-5	33	6.41547526797363	7.46E-13	Up
tRF-Gly-GCC-012	tRF-5c	28	6.05230928162583	4.36E-12	Up
tRF-Gly-GCC-013	tRF-5c	29	3.57949960289882	1.15E-06	Up
tRF-Gly-GCC-016	tRF-5c	32	3.35515175746991	4.78E-07	Up

immediately after recovery from anesthesia and before sacrifice to reduce the contusion error and heterogeneity, indicating a loss of the locomotive function due to the contusion.

The first set of questions aimed to identify the tsRNA expression levels in the two groups; thus, the tsRNA-Seq analysis was used. Prior to analysis, sequencing quality control was performed *via* the quality score plot of each sample (see **Supplementary Figures S1, S2**, and **Supplementary Table S1**). A Q score above 30 (>99.9% correct) indicated high-quality data and a very large proportion of the bases in each sample achieved a $Q \geq 30$ (all more than 92%). After the quality filtering, according to the expression level of each sample, we calculated the correlation coefficient between any two of the samples, which is an important evaluation criterion of the reliability and reasonability of the sample selection, showing that the two compared samples were quite similar (see **Figure 2A**). In addition, we used PCA, a statistical method used for an unsupervised analysis to reduce the dimension of large data sets, and it was a useful tool to explore the sample classes based on the expression, showing a distinguishable tsRNA expression profiling among eight samples (see **Figure 2B**).

We identified a dysregulated expression of all 297 tsRNAs between the SCI and sham groups. In **Figure 2C**, the Venn diagram presents a total of 157 commonly expressed tsRNAs, 47 tsRNAs specifically expressed in the sham group, and 28 tsRNAs specifically expressed in the SCI group. In **Figure 2D**, the Venn diagram shows that all 297 dysregulated tsRNAs in this study were known tRFs from tRFdb. Next, as shown in **Figures 3A,B**, a pie chart was performed of each tsRNA subtype, indicating that most tsRNAs were generated from mature tRNAs (subtypes of tsRNAs, except for tRF-1). In those tsRNAs, the expression levels of each tsRNA subtype were quite different. Overall, the expression level of tRF-5 s was increased, whereas that of other subtypes was decreased after the SCI, as compared to the sham group. Furthermore, the number of tsRNA subtypes against tRNA isodecoders and the frequency of subtypes against the length of the tsRNA were compared *via* the stacked bar charts (see **Figures 4A–D**).

In addition, we identified that a total of 155 tsRNAs were significantly differentially expressed between the two groups: 91 were significantly up-regulated, whereas 64 were significantly down-regulated (SCI vs. sham; FC $>$ 1.5; $P < 0.05$). The experimental data on the top 10 upregulated and downregulated tsRNAs ranked by fold changes are presented in **Table 1**. As shown in **Figure 5A**, hierarchical clustering was performed using the significantly differentially expressed tsRNAs, indicating a distinguishable tsRNA expression profiling among the samples. Next, scatter plots were created presenting the tsRNA expression variation (or reproducibility) between the SCI and sham control groups using the fold change (**Figure 5B**) and volcano plots were constructed using the fold change values and *P*-values to visualize the differential expression between the two different conditions (**Figure 5C**).

Bioinformatic Prediction

The four significantly differentially expressed tsRNAs, namely, tiRNA-Gly-GCC-001, tRF-Gly-GCC-012, tRF-Gly-GCC-013, and tRF-Gly-GCC-016, selected from the tsRNAs commonly expressed in both groups, were subsequently analyzed using bioinformatic tools. First, based on the knowledge that the

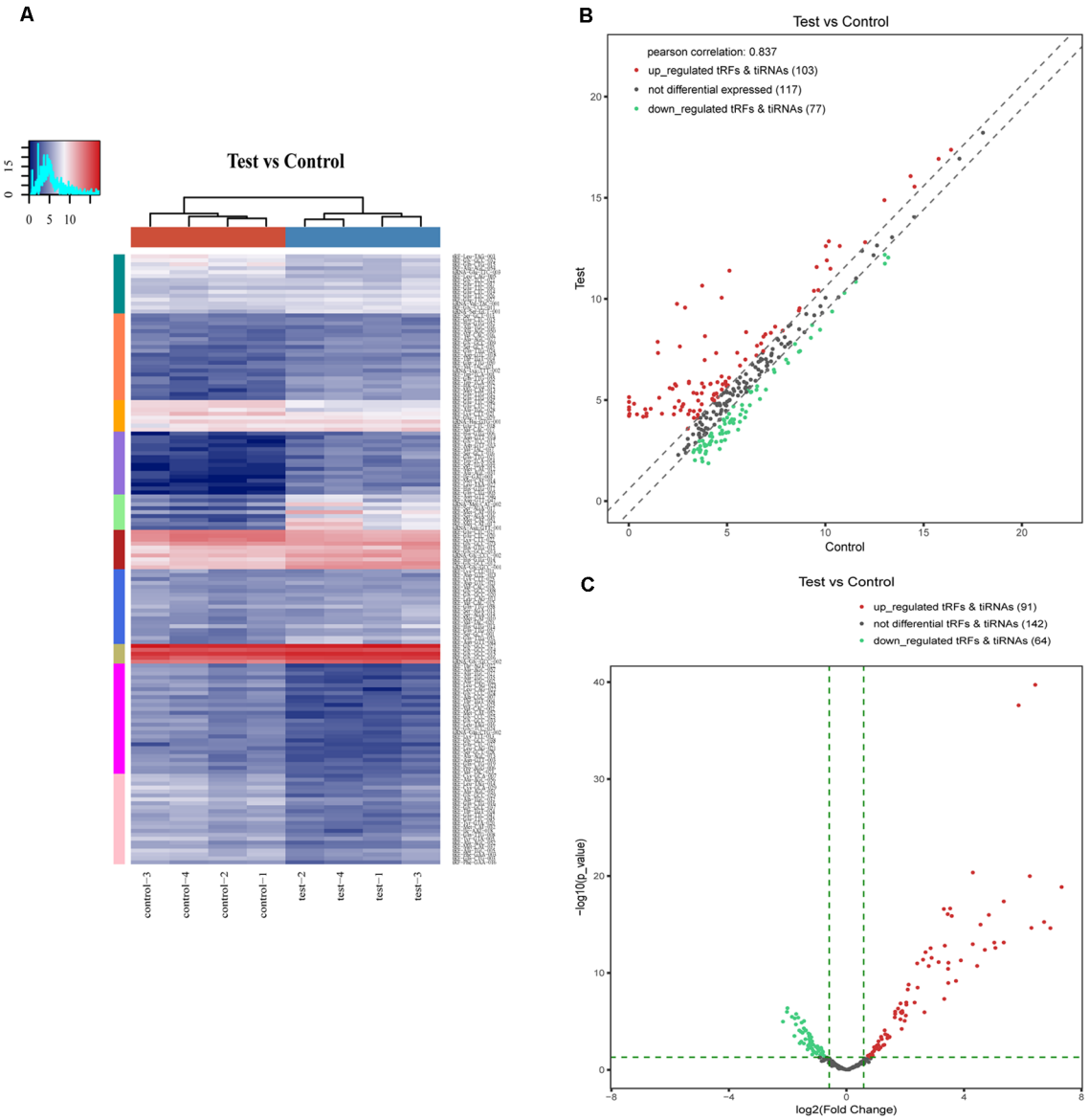

FIGURE 5 | Hierarchical clustering and difference in the tsRNA expression between the two groups. **(A)** The hierarchical clustering heat-map for the tsRNAs. The color in the panel represents the relative expression level (log2-transformed). The colored bar top at the top panel showed the sample groups, and the colored bar at the right side of the panel indicated the divisions that were performed using K-means. **(B)** The scatter plots of differentially expressed tsRNAs. tsRNAs above the top line (red dots, up-regulation) or below the bottom line (green dots, down-regulation) indicate more than 1.5-fold change between the two compared groups. Gray dots indicate non-differentially expressed tsRNAs. **(C)** The volcano plots of differentially expressed tsRNA. The values of the X and Y axes in the volcano plot are log2 transformed fold change and −log10 transformed *P*-values between the two groups, respectively. Red/Green circles indicate statistically significant differentially expressed tsRNAs with a fold change of no less than 1.5 and a *P*-value $\leq$ 0.05 (Red: up-regulated; Green: down-regulated). Gray circles indicate non-differentially expressed tsRNA, with FC and/or *q*-value that are not meeting the cut off thresholds.

tsRNAs could perform an miRNA-like mode of action, that is, recognize their mRNA targets using their seed sequence (positions 2–7nt at their 5′ ends) and inhibit the global mRNA translational activities (Kumar et al., 2014), three kinds of algorithms were used to predict the mRNA targets of the four candidate tsRNAs. As a result, we constructed tsRNA/mRNA interaction networks using the top 150 target mRNAs of each tsRNA based on the prediction score (**Figure 6**).

Second, we conducted a bioinformatic analysis of the functions of all target mRNAs of each candidate tsRNA using the KEGG pathway and GO biological processes. GO bioinformatic analysis covers three domains: biological process, cellular component, and molecular function. For each part, we performed a classification for the significantly enriched terms of each candidate tsRNA—a top 10 enrichment score with counts and *P*-values. In terms of cellular component and molecular

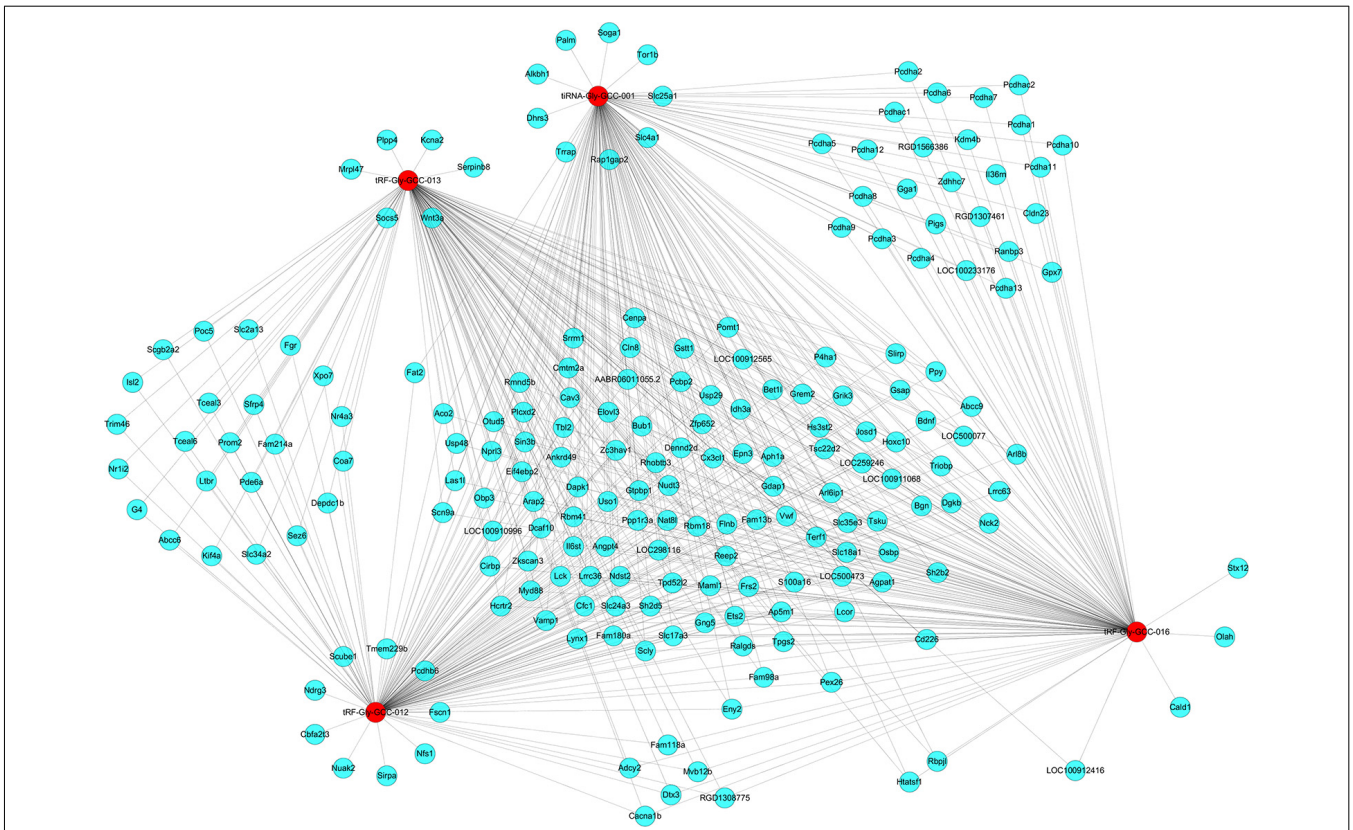

FIGURE 6 | The tsRNA/mRNA network analysis. The network included the four candidate tsRNAs and their predicted target mRNAs (Nodes in red color are tsRNAs; nodes in light-blue color are mRNAs).

function (**Figure 7**), the general results showed that the most significant enrichment and the most meaningful terms were binding (GO:0005488) and intracellular part (GO:0044424) in each of the four tsRNA predictions (**Supplementary Figures S3, S4**), suggesting a functional role of the target genes of the candidate tsRNAs at the molecular and cellular level. However, the major biological processes surveyed by GO were diverse in the four tsRNA predictions, namely, negative regulation (GO:0048519), regulation of the macromolecular metabolic process (GO:0060255), and regulation of the cellular morphogenesis, involved in differentiation (GO:0010769), suggesting their potential roles in the biological processes (**Supplementary Figure S5**).

According to the KEGG enrichment analysis, mitogen-activated protein kinase (MAPK) signaling pathway (rno04010), proteoglycans in cancer (rno05205), and neurotrophin signaling pathway (rno04722) were significantly identified in general view for each candidate tsRNA (**Figure 8**). In addition, in view of the prediction score of the target mRNAs and previous publications, it is plausible to speculate that these four tsRNAs might be involved in the regulation of the biological processes *via* the MAPK and neurotrophin signaling pathway. All tsRNA-targeted genes in both pathways are shown in **Supplementary Figures S6, S7**. Notably, BDNF is one target mRNA of the four significantly differentially expressed tsRNAs as well as a vital gene involving in MAPK and neurotrophin signaling pathway (binding sites were shown in **Supplementary Figure S8**). In addition, emerging evidence has suggested that BDNF, a substance that supports the growth and maintenance of brain cells, is closely related to the regulation of the pathophysiological processes in the acute phase of SCI, such as to attenuate the secondary injury (Keefe et al., 2017; Zhang et al., 2018a,b; Li et al., 2019). Therefore, we reasonably speculate that tiRNA-Gly-GCC-001, tRF-Gly-GCC-012, tRF-Gly-GCC-013, and tRF-Gly-GCC-016 might regulate the BDNF and thus play a vital role in the pathophysiological process *via* the MAPK and neurotrophin signaling pathway.

Verification of qRT-PCR

In this section, our aim was to validate the tsRNA-Seq results *via* detecting the expression level of the four candidate tsRNAs using a low-throughput qRT-PCR. As a result, compared with the sham control, tiRNA-Gly-GCC-001, tRF-Gly-GCC-012, tRF-Gly-GCC-013, and tRF-Gly-GCC-016 were all significantly up-regulated in the SCI group, showing a similar expression pattern in both the sequencing and PCR data, see **Figures 9A–D**. The fold change and *P*-values of each candidate tsRNA between the groups in terms of sequencing and PCR analysis are presented in **Table 2**, to make data interpretation more

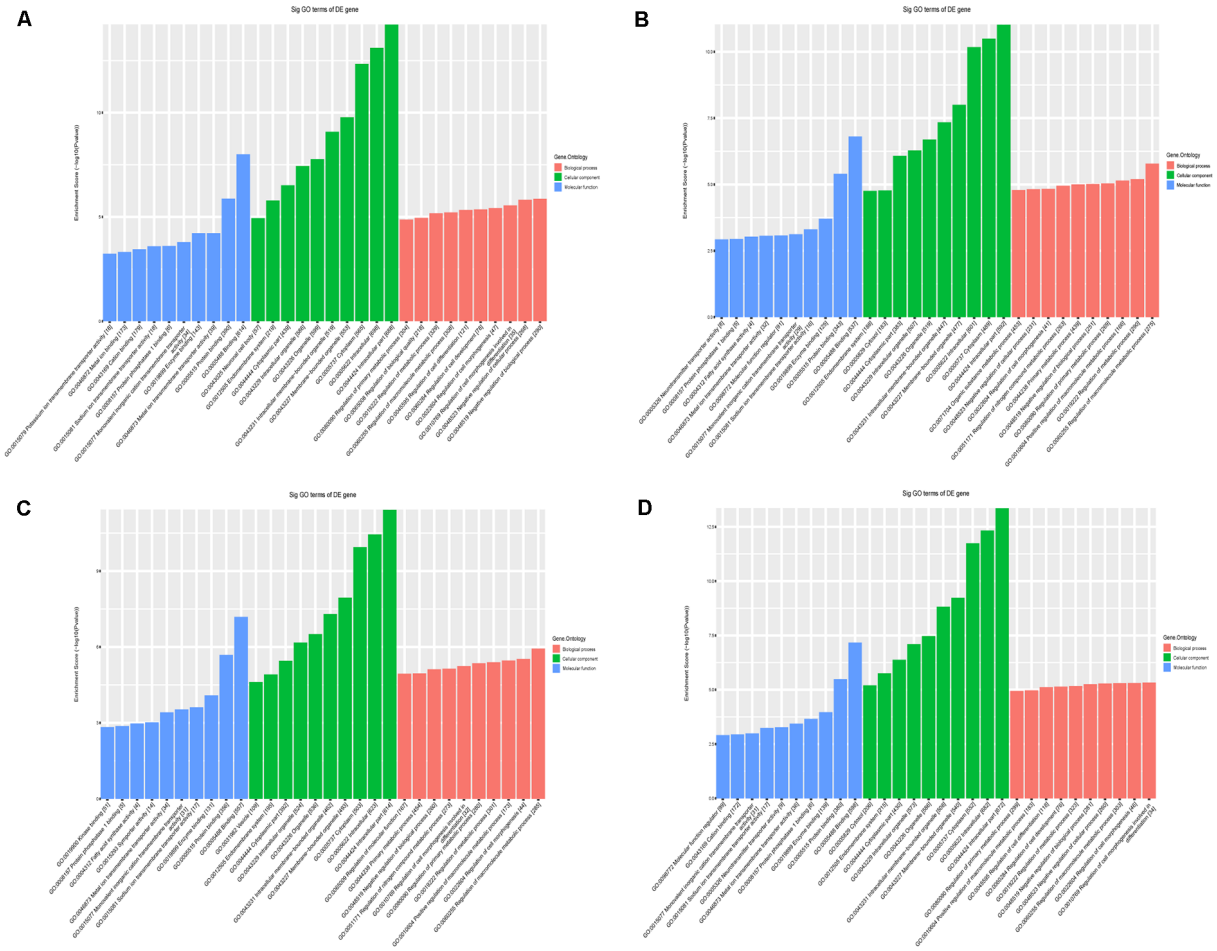

FIGURE 7 | The general GO annotations for cellular component, molecular function, and biological processes of the target mRNAs regulated by the four candidate tsRNAs. **(A)** tiRNA-Gly-GCC-001. **(B)** tRF-Gly-GCC-012. **(C)** tRF-Gly-GCC-013. **(D)** tRF-Gly-GCC-016.

straightforward. The sequences of the primers used for the qRT-PCR are listed in **Table 3**. In consideration of the FC and *P*-values, tiRNA-Gly-GCC-001 was selected for the next binding experiment.

The Relationship of tiRNA-Gly-GCC-001 and BDNF

To identify their relationship, low-throughput qRT-PCR for BDNF and luciferase assay were performed. As a result, BDNF was found to be significantly down-regulated after SCI, indicating an opposite change of expression after injury compared to that of the candidate tsRNA (see **Figures 10A,B**), which suggested that BDNF might act as a target gene negatively regulated by tiRNA-Gly-GCC-001. In terms of the luciferase reporter assay, a sequence alignment of the tiRNA-Gly-GCC-001 with the 3′UTR of the BDNF was shown and the BDNF expression was inhibited by the tiRNA-Gly-GCC-001 directly targeting its 3′UTR (**Figures 10C,D**). This lays the foundation for our future research of the mechanism of this process.

DISCUSSION

In summary, we initially revealed the expression profiles of the tsRNAs using RNA-sequencing. Second, bioinformatic analysis prompted that four tsRNAs might inhibit the BDNF, thereby regulating the pathophysiological process *via* the MAPK and neurotrophin signaling pathway. Next, using PCR, we validated the candidate tsRNAs and found the opposite trends of expression levels of the tsRNAs and BDNF in the SCI vs. the sham group. Finally, we identified tiRNA-Gly-GCC-001 directly targeted the BDNF using the luciferase reporter assay. Taken together, the striking observations from our study indicate that these candidate tsRNAs might be involved in the pathophysiologic processes after traumatic SCI. In reviewing the literature, the present study, to the best of our knowledge, offers the first comprehensive assessment of the tsRNAs expression patterns and subsequent functional prediction and preliminarily target validation after traumatic SCI, providing strong evidence for further investigation.

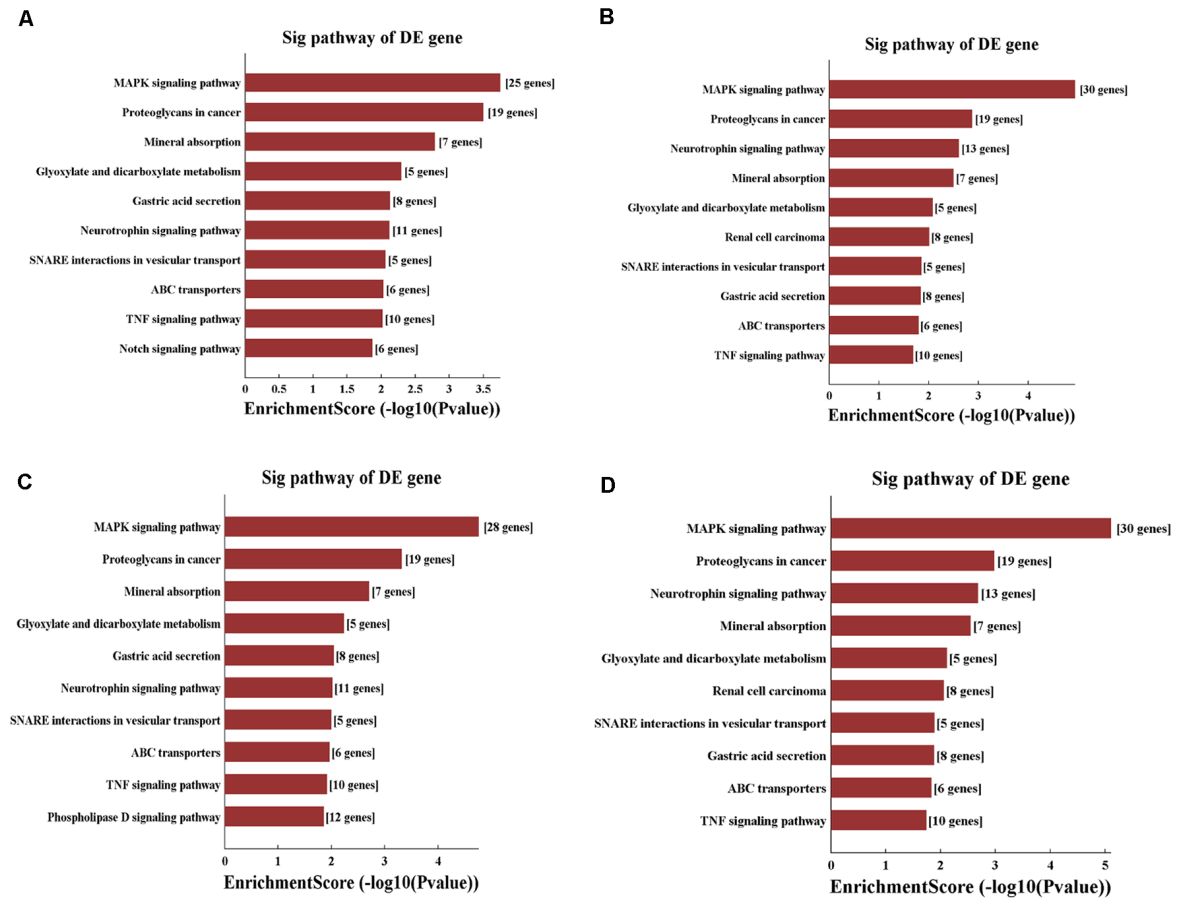

FIGURE 8 | KEGG pathway analysis of the target mRNAs regulated by the four candidate tsRNAs. **(A)** The bar plot shows the top 10 enrichment score values of the significantly enriched pathway for tiRNA-Gly-GCC-001. **(B)** The bar plot shows the top 10 enrichment score values of the significantly enriched pathway for tRF-Gly-GCC-012. **(C)** The bar plot shows the top 10 enrichment score values of the significantly enriched pathway for tRF-Gly-GCC-013. **(D)** The bar plot shows the top 10 enrichment score values of the significantly enriched pathway for tRF-Gly-GCC-016.

Most of the human genome is composed of ncRNAs, which are widely involved in physiological and pathological activities, and are closely related to many diseases (Chen et al., 2019). These universal nucleic acid entities are commonly considered as a special type of RNA that cannot be translated into proteins (Yang et al., 2019). tsRNAs are the most common type of small ncRNAs, a recently rising star of the ncRNAs, that are reported to participate in the regulation of RNA processing and protein translation (Ivanov et al., 2011). Interestingly, tsRNAs, a heterogeneous population of small ncRNAs with lengths of 18–40 nucleotides, were first considered to be the byproducts of random tRNA cleavage. Generally, tsRNAs include two main types based on the length and cleavage sites of the tRNAs: tRFs and tiRNAs. Mostly, they are generated under stress conditions (Lee and Collins, 2005).

Growing evidence has shown that tsRNAs are implicated in various biological processes and human illness, such as tumors, cardiovascular system diseases, epigenetics, and neurological diseases, that scientists are increasingly concerned with, in the recent years (Olvedy et al., 2016; Zhou et al., 2017; Elkordy et al., 2018; Zhang et al., 2018). In terms of the functional roles of the tsRNAs in neurodegeneration, as an example, tiRNAAla and tiRNACys and their DNA analogs with a G4 motif could promote neuronal survival under stress conditions and provide new chances for the treatment of neurodegenerative disorders in the future (Li et al., 2018). In addition, the transfection of a particular tRF-5 into patient-derived neurons resulted in a reduction in cell survival under oxidative stress *in vitro* (Schaffer et al., 2014). In terms of neurotrauma, Elkordy et al. (2018, 2019) found that in PC-12, the rat neuronal cell line, tRNA cleavage and tiRNA generation were initiated under stress conditions induced by arsenite and hydrogen peroxide or ischemic-reperfusion. Notably, they identified that the generation of tiRNAs occurred prior to severe cell damage, indicating their potential roles as novel biomarkers for cell damage assessment. However, no previous studies have profiled the tsRNA expression in the spinal cord after SCI. As a result, after sequencing and PCR validation, the striking results in our study indicated that the expression levels of tsRNAs were

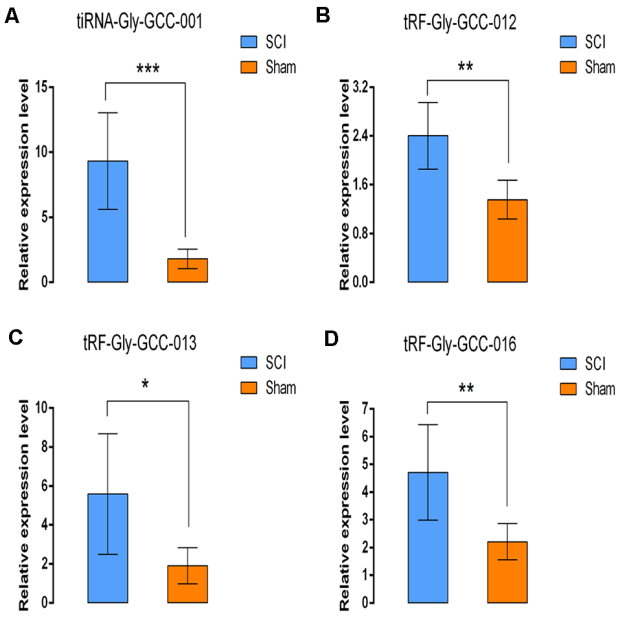

FIGURE 9 | Validation of the four selected tsRNAs using qRT-PCR. Compared with the sham control, tiRNA-Gly-GCC-001, tRF-Gly-GCC-012, tRF-Gly-GCC-013, tRF-Gly-GCC-016 were all significantly upregulated in the SCI group **(A–D)**. The data were normalized using the mean ± standard error of the mean (SEM; $n = 6$ per group). $^{*}P < 0.05$, $^{**}P < 0.01$, $^{***}P < 0.001$.

significantly altered in rats' spinal cord after SCI compared to the sham controls.

In terms of the functions of the tsRNAs, an increasing number of tRFs and tiRNAs have been reported to act as functional regulatory factors in physiological processes and the cellular metabolism, indicating their non-random processing. Namely, tsRNAs have been confirmed to act as miRNA in gene expression regulation (Shao et al., 2017), to regulate protein translation (Sobala and Hutvagner, 2013), various cellular activities (Maute et al., 2013), to mediate the immune system (Zhang et al., 2014), and the response under stress conditions (Gebetsberger et al., 2017). Notably, some tsRNAs are known to directly bind to mRNA targets in a manner similar to the canonical miRNAs (Huang et al., 2017; Zhou et al., 2017). These tsRNAs are physically related to Argonaute (AGO) proteins (Ago1–4), as stated in reference (Kumar et al., 2014), indicating that a tsRNA may contain multiple mRNA-binding sites and may have adsorptive and suppressive effects on the target genes. Based on this function, using bioinformatic tools, potential target-binding mRNAs for four candidate tsRNA were calculated and filtered to construct tsRNA/mRNA interactions for bioinformatic analysis. Next, using GO and KEGG pathway analysis, we found that the target mRNAs are involved in various biological processes, intracellular parts, and binding as well as cellular signaling pathways. As an example, the regulation of the macromolecular metabolic process was identified to be one of the most significantly enriched and most meaningful terms of biological processes, which was confirmed to closely correlate to the pathophysiological process after SCI (Kumar et al., 2015; Shakhbazau et al., 2015). In the KEGG pathway, the MAPK and neurotrophin signaling pathways were the top two signaling pathways affected by the candidate tsRNA-mRNA axes. Previous studies (Zhang et al., 2015; Hodgetts and Harvey, 2017; Fu et al., 2018) have explored the relationships between these pathways and SCI, indicating that MAPK-related molecules regulate the neuronal survival, synaptic function, and neurotransmitter release, and elicit the plasticity and growth of axons within the central nervous system after SCI. Additionally, another report (Keefe et al., 2017) described that the neurotrophins, including NGF, BDNF, and NT-3, targeted specific populations of neurons *via* their effects on the populations of neurons within diverse spinal tracts.

Finally, using PCR, we found that the four candidate tsRNAs and BDNF, one of the neurotrophins predicted by the bioinformatic analysis as a target gene, had opposite alterations of the expression level, which indirectly suggests that these specific tsRNAs could inhibit the BDNF very

TABLE 2 | Comparison for candidate tsRNAs expression in sequencing and PCR (SCI vs. Sham; FC, fold change).

tsRNAs	Sequencing			PCR		
	FC	*P*-value	Regulation	FC	*P*-value	Regulation
tiRNA-Gly-GCC-001	6.42	7.46E-13	Up	5.21	0.0007	Up
tRF-Gly-GCC-012	6.05	4.36E-12	Up	1.77	0.0023	Up
tRF-Gly-GCC-013	3.58	1.15E-06	Up	2.95	0.0187	Up
tRF-Gly-GCC-016	3.36	4.79E-07	Up	2.13	0.0076	Up

TABLE 3 | Sequences of primers used for qRT-PCR assay.

Gene name	Primer sequence	Ta Opt (°C)	Product size(bp)
U6	F:5′ GCTTCGGCAGCACATATACTAAAAT 3′ R:5′ CGCTTCACGAATTTGCGTGTCAT 3′	60	89
β-actin	F:5′ CGAGTACAACCTTCTTGCAGC 3′ R :5′ ACCCATACCCACCATCACAC 3′	60	202
tiRNA-Gly-GCC-001	F:5′ GCATGGGTGGTTCAGTGGTAG 3′ R:5′ ACGTGTGCTCTTCCGATCTCA 3′	60	52
tRF-Gly-GCC-012	F:5′ GCATGGGTGGTTCAGTGGTAG 3′ R:5′ CGTGTGCTCTTCCGATCTGA 3′	60	46
tRF-Gly-GCC-013	F:5′ GCATGGGTGGTTCAGTGGTAG 3′ R:5′ CGTGTGCTCTTCCGATCTCG 3′	60	47
tRF-Gly-GCC-016	F:5′ GCATGGGTGGTTCAGTGGTAG 3′ R:5′ ACGTGTGCTCTTCCGATCTAGG 3′	60	51
BDNF	F:5′ GCGTGTGTGACAGTATTAGCGAG 3′ R:5′ GGCATTGCGAGTTCCAGTG 3′	60	210

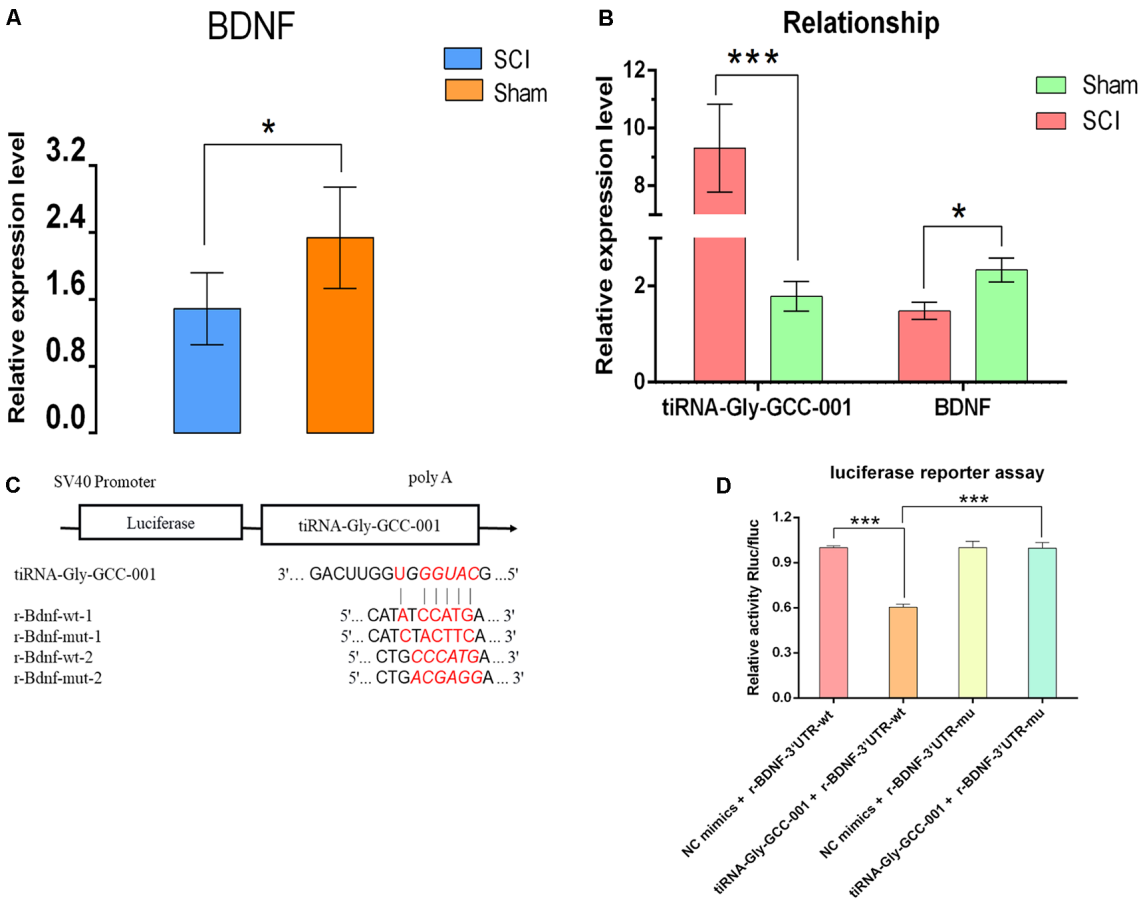

FIGURE 10 | The relationship of tiRNA-Gly-GCC-001 and brain-derived neurotrophic factor (BDNF) validated by PCR and luciferase reporter assay. **(A)** The BDNF expression in the SCI group was significantly downregulated compared with the sham control ($n = 6$ per group). *$p < 0.05$. **(B)** An opposite change of expression between tiRNA-Gly-GCC-001 and BDNF was identified after injury, indicating that BDNF might act as a target gene inhibited by tiRNA-Gly-GCC-001. **(C)** A schematic of the base pair regions of the BDNF 3′ UTR and the predicted binding site for tiRNA-Gly-GCC-001 is shown with the wild type and mutant seed sequences listed below. **(D)** The repressive effect of tiRNA-Gly-GCC-001 on the activity of the site of BDNF 3′UTR measured by luciferase reporter assay, indicating that tiRNA-Gly-GCC-001 directly targeted BDNF. ***$p < 0.001$.

likely *via* complementary base pairing. In addition, using the luciferase reporter assay we identified one candidate tsRNA, tiRNA-Gly-GCC-001, directly binding to BDNF, which indicates that tiRNA-Gly-GCC-001 might be involved in the MAPK and neurotrophin pathways *via* targeting the key gene, BDNF, thereby regulating the pathophysiological process after SCI.

However, several questions remain to be answered. First and most importantly, the reader should bear in mind that this study has finished the expression profile and functional prediction; thus, our future work is to identify the functions of the candidate tsRNAs *in vitro* and *in vivo*. Furthermore, it was beyond the scope of this study to examine the potential effect of different time points on the possible dynamic changes in the tsRNA expression patterns in the contused spinal cords of rats with SCI. Finally, we strongly recommend that future research should focus on different animal models and types of SCI to study the expression and functions of tsRNAs.

DATA AVAILABILITY STATEMENT

The raw data supporting the conclusions of this article will be made available by the authors, without undue reservation, to any qualified researcher.

ETHICS STATEMENT

The animal study was reviewed and approved by the Institutional Animal Care and Use Committee of Capital Medical University.

AUTHOR CONTRIBUTIONS

CQ and HF performed the research. J-JL and FG designed the research study. CZ, XZ and Y-CS contributed essential reagents or tools. YL, D-GY and L-JD analyzed the data. CQ wrote the article. M-LY revised the article. All authors read and approved the final manuscript.

FUNDING

This work was supported by a grant from the National Key R&D Program of China (2018YFF0301104), the National Natural Science Foundation of China (General Program 81870979), the Special Fund for Basic Scientific Research of Central Public Research Institutes (2018CZ-1; 2019CZ-1), the Basic Scientific Research Foundation of China Rehabilitation Research Center (2018ZX-30), the Beijing Municipal Science and Technology Commission (Z181100004118004; Z171100001017076), the Beijing Science and Technology Major Project (D161100002816004), and the Capital Health Research and Development of Special (2018-1-6011).

ACKNOWLEDGMENTS

We thank Meng-Yuan Li for her special support.

SUPPLEMENTARY MATERIAL

The Supplementary Material for this article can be found online at: https://www.frontiersin.org/articles/10.3389/fnmol.2019.00326/full#supplementary-material.

REFERENCES

Alizadeh, A., Dyck, S. M., and Karimi-Abdolrezaee, S. (2019). Traumatic spinal cord injury: an overview of pathophysiology, models and acute injury mechanisms. *Front. Neurol.* 10:282. doi: 10.3389/fneur.2019.00282

Arcaroli, J. J., Quackenbush, K. S., Powell, R. W., Pitts, T. M., Spreafico, A., Varella-Garcia, M., et al. (2012). Common PIK3CA mutants and a novel 3′ UTR mutation are associated with increased sensitivity to saracatinib. *Clin. Cancer Res.* 18, 2704–2714. doi: 10.1158/1078-0432.ccr-11-3167

Carelli, S., Giallongo, T., Rey, F., Colli, M., Tosi, D., Bulfamante, G., et al. (2019). Neuroprotection, recovery of function and endogenous neurogenesis in traumatic spinal cord injury following transplantation of activated adipose tissue. *Cells* 8:E329. doi: 10.3390/cells8040329

Chen, R., Xu, X., Huang, L., Zhong, W., and Cui, L. (2019). The regulatory role of long noncoding RNAs in different brain cell types involved in ischemic stroke. *Front. Mol. Neurosci.* 12:61. doi: 10.3389/fnmol.2019.00061

Elkordy, A., Mishima, E., Niizuma, K., Akiyama, Y., Fujimura, M., Tominaga, T., et al. (2018). Stress-induced tRNA cleavage and tiRNA generation in rat neuronal PC12 cells. *J. Neurochem.* 146, 560–569. doi: 10.1111/jnc.14321

Elkordy, A., Rashad, S., Shehabeldeen, H., Mishima, E., Niizuma, K., Abe, T., et al. (2019). tiRNAs as a novel biomarker for cell damage assessment in *in vitro* ischemia-reperfusion model in rat neuronal PC12 cells. *Brain Res.* 1714, 8–17. doi: 10.1016/j.brainres.2019.02.019

Fu, X., Shen, Y., Wang, W., and Li, X. (2018). MiR-30a-5p ameliorates spinal cord injury-induced inflammatory responses and oxidative stress by targeting Neurod 1 through MAPK/ERK signalling. *Clin. Exp. Pharmacol. Physiol.* 45, 68–74. doi: 10.1111/1440-1681.12856

Gebetsberger, J., Wyss, L., Mleczko, A. M., Reuther, J., and Polacek, N. (2017). A tRNA-derived fragment competes with mRNA for ribosome binding and regulates translation during stress. *RNA Biol.* 14, 1364–1373. doi: 10.1080/15476286.2016.1257470

Hall, O. T., McGrath, R. P., Peterson, M. D., Chadd, E. H., DeVivo, M. J., Heinemann, A. W., et al. (2019). The burden of traumatic spinal cord injury in the united states: disability-adjusted life years. *Arch. Phys. Med. Rehabil.* 100, 95–100. doi: 10.1016/j.apmr.2018.08.179

Hodgetts, S. I., and Harvey, A. R. (2017). Neurotrophic factors used to treat spinal cord injury. *Vitam. Horm.* 104, 405–457. doi: 10.1016/bs.vh.2016.11.007

Hu, A., Li, J., Sun, W., Yang, D., Yang, M., Du, L., et al. (2015). Myelotomy reduces spinal cord edema and inhibits aquaporin-4 and aquaporin-9 expression in rats with spinal cord injury. *Spinal Cord* 53, 98–102. doi: 10.1038/sc.2014.209

Huang, B., Yang, H., Cheng, X., Wang, D., Fu, S., Shen, W., et al. (2017). tRF/miR-1280 suppresses stem cell-like cells and metastasis in colorectal cancer. *Cancer Res.* 77, 3194–3206. doi: 10.1158/0008-5472.can-16-3146

Ivanov, P., Emara, M. M., Villen, J., Gygi, S. P., and Anderson, P. (2011). Angiogenin-induced tRNA fragments inhibit translation initiation. *Mol. Cell* 43, 613–623. doi: 10.1016/j.molcel.2011.06.022

Jiang, Z., and Zhang, J. (2018). LncRNA SNHG5 enhances astrocytes and microglia viability *via* upregulating KLF4 in spinal cord injury. *Int. J. Biol. Macromol.* 120, 66–72. doi: 10.1016/j.ijbiomac.2018.08.002

Kang, Y., Ding, H., Zhou, H., Wei, Z., Liu, L., Pan, D., et al. (2018). Epidemiology of worldwide spinal cord injury: a literature review. *J. Neurorestoratol.* 6, 1–9. doi: 10.2147/jn.s143236

Keefe, K., Sheikh, I., and Smith, G. (2017). Targeting neurotrophins to specific populations of neurons: NGF, BDNF, and NT-3 and their relevance for treatment of spinal cord injury. *Int. J. Mol. Sci.* 18:E548. doi: 10.3390/ijms18030548

Khuyagbaatar, B., Kim, K., and Kim, Y. H. (2015). Conversion equation between the drop height in the new york university impactor and the impact force in the infinite horizon impactor in the contusion spinal cord injury model. *J. Neurotrauma* 32, 1987–1993. doi: 10.1089/neu.2015.3875

Kim, H. K., Fuchs, G., Wang, S., Wei, W., Zhang, Y., Park, H., et al. (2017). A transfer-RNA-derived small RNA regulates ribosome biogenesis. *Nature* 552, 57–62. doi: 10.1038/nature25005

Kumar, P., Anaya, J., Mudunuri, S. B., and Dutta, A. (2014). Meta-analysis of tRNA derived RNA fragments reveals that they are evolutionarily conserved and associate with AGO proteins to recognize specific RNA targets. *BMC Biol.* 12:78. doi: 10.1186/s12915-014-0078-0

Kumar, P., Choonara, Y. E., Modi, G., Naidoo, D., and Pillay, V. (2015). Multifunctional therapeutic delivery strategies for effective neuro-regeneration following traumatic spinal cord injury. *Curr. Pharm. Des.* 21, 1517–1528. doi: 10.2174/1381612821666150115152323

Langmead, B., Trapnell, C., Pop, M., and Salzberg, S. L. (2009). Ultrafast and memory-efficient alignment of short DNA sequences to the human genome. *Genome Biol.* 10:R25. doi: 10.1186/gb-2009-10-3-r25

Larionov, A., Krause, A., and Miller, W. (2005). A standard curve based method for relative real time PCR data processing. *BMC Bioinformatics* 6:62. doi: 10.1186/1471-2105-6-62

Lee, S. R., and Collins, K. (2005). starvation-induced cleavage of the trna Anticodon loop inTetrahymena thermophila. *J. Biol. Chem.* 280, 42744–42749. doi: 10.1074/jbc.m510356200

Lee, Y. S., Shibata, Y., Malhotra, A., and Dutta, A. (2009). A novel class of small RNAs: tRNA-derived RNA fragments (tRFs). *Genes Dev.* 23, 2639–2649. doi: 10.1101/gad.1837609

Li, P., Tang, T., Liu, T., Zhou, J., Cui, H., He, Z., et al. (2019). Systematic analysis of tRNA-derived small RNAs reveals novel potential therapeutic targets of traditional chinese medicine (buyang-huanwu-decoction) on intracerebral hemorrhage. *Int. J. Biol. Sci.* 15, 895–908. doi: 10.7150/ijbs.29744

Li, X., Wu, Q., Xie, C., Wang, C., Wang, Q., Dong, C., et al. (2019). Blocking of BDNF-TrkB signaling inhibits the promotion effect of neurological function recovery after treadmill training in rats with spinal cord injury. *Spinal Cord* 57, 65–74. doi: 10.1038/s41393-018-0173-0

Li, S., Xu, Z., and Sheng, J. (2018). tRNA-derived small RNA: a novel regulatory small non-coding RNA. *Genes* 9:E246. doi: 10.3390/genes9050246

Liu, R., Wang, W., Wang, S., Xie, W., Li, H., and Ning, B. (2018). microRNA-21 regulates astrocytic reaction post-acute phase of spinal cord injury through modulating TGF-β signaling. *Aging* 10, 1474–1488. doi: 10.18632/aging.101484

Liu, S., Xie, Y., and Wang, B. (2019). Role and prospects of regenerative biomaterials in the repair of spinal cord injury. *Neural Regen. Res.* 14, 1352–1363. doi: 10.4103/1673-5374.253512

Maute, R. L., Schneider, C., Sumazin, P., Holmes, A., Califano, A., Basso, K., et al. (2013). tRNA-derived microRNA modulates proliferation and the DNA damage response and is down-regulated in B cell lymphoma. *Proc. Natl. Acad. Sci. U S A* 110, 1404–1409. doi: 10.1073/pnas.1206761110

Olvedy, M., Scaravilli, M., Hoogstrate, Y., Visakorpi, T., Jenster, G., and Martens-Uzunova, E. S. (2016). A comprehensive repertoire of tRNA-derived fragments in prostate cancer. *Oncotarget* 7, 24766–24777. doi: 10.18632/oncotarget.8293

Pang, X., Tang, Y., and Zhang, D. (2016). Role of miR-145 in chronic constriction injury in rats. *Exp. Ther. Med.* 12, 4121–4127. doi: 10.3892/etm.2016.3900

Qin, C., Liu, C., Yang, D., Gao, F., Zhang, X., Zhang, C., et al. (2019). Circular RNA expression alteration and bioinformatics analysis in rats after traumatic spinal cord injury. *Front. Mol. Neurosci.* 11:497. doi: 10.3389/fnmol.2018.00497

Qin, C., Zhang, W., Yang, D., Yang, M., Du, L., and Li, J. (2018). Myelotomy promotes locomotor recovery in rats subjected to spinal cord injury: a meta-analysis of six randomized controlled trials. *Neural Regen. Res.* 13, 1096–1106. doi: 10.4103/1673-5374.233454

Schaffer, A. E., Eggens, V. R. C., Caglayan, A. O., Reuter, M. S., Scott, E., Coufal, N. G., et al. (2014). CLP1 founder mutation links tRNA splicing and maturation to cerebellar development and neurodegeneration. *Cell* 157, 651–663. doi: 10.1016/j.cell.2014.03.049

Scheff, S. W., Saucier, D. A., and Cain, M. E. (2002). A statistical method for analyzing rating scale data: the BBB locomotor score. *J. Neurotrauma* 19, 1251–1260. doi: 10.1089/08977150260338038

Shakhbazau, A., Mishra, M., Chu, T., Brideau, C., Cummins, K., Tsutsui, S., et al. (2015). Fluorescent phosphorus dendrimer as a spectral nanosensor for macrophage polarization and fate tracking in spinal cord injury. *Macromol. Biosci.* 15, 1523–1534. doi: 10.1002/mabi.201500150

Shao, Y., Sun, Q., Liu, X., Wang, P., Wu, R., and Ma, Z. (2017). tRF-Leu-CAG promotes cell proliferation and cell cycle in non-small cell lung cancer. *Chem. Biol. Drug Des.* 90, 730–738. doi: 10.1111/cbdd.12994

Sobala, A., and Hutvagner, G. (2013). Small RNAs derived from the 5′ end of tRNA can inhibit protein translation in human cells. *RNA Biol.* 10, 553–563. doi: 10.4161/rna.24285

Vawda, R., Badner, A., Hong, J., Mikhail, M., Lakhani, A., Dragas, R., et al. (2019). Early intravenous infusion of mesenchymal stromal cells exerts a tissue source age-dependent beneficial effect on neurovascular integrity and neurobehavioral recovery after traumatic cervical spinal cord injury. *Stem Cells Transl. Med.* 8, 639–649. doi: 10.1002/sctm.18-0192

Wang, Y., Jiao, J., Ren, P., and Wu, M. (2019). Upregulation of miRNA-223–3p ameliorates RIP3-mediated necroptosis and inflammatory responses *via* targeting RIP3 after spinal cord injury. *J. Cell. Biochem.* 120, 11582–11592. doi: 10.1002/jcb.28438

Yang, L., Yang, L., Zhu, J., Chen, J., Wang, Y., and Xiong, K. (2019). Expression signatures of long non-coding RNA and mRNA in human traumatic brain injury. *Neural Regen. Res.* 14, 632–641. doi: 10.4103/1673-5374.247467

Zhang, Y., Cai, F., Liu, J., Chang, H., Liu, L., Yang, A., et al. (2018). Transfer RNA-derived fragments as potential exosome tRNA-derived fragment biomarkers for osteoporosis. *Int. J. Rheum. Dis.* 21, 1659–1669. doi: 10.1111/1756-185x.13346

Zhang, Y., Hu, H., Tian, T., Zhang, L., Zhao, D., Wu, Q., et al. (2015). Mst3b promotes spinal cord neuronal regeneration by promoting growth cone branching out in spinal cord injury rats. *Mol. Neurobiol.* 51, 1144–1157. doi: 10.1007/s12035-014-8785-7

Zhang, H., Li, D., Zhang, Y., Li, J., Ma, S., Zhang, J., et al. (2018a). Knockdown of lncRNA BDNF-AS suppresses neuronal cell apoptosis *via* downregulating miR-130b-5p target gene PRDM5 in acute spinal cord injury. *RNA Biol.* 15, 1071–1080. doi: 10.1080/15476286.2018.1493333

Zhang, H., Wang, W., Li, N., Li, P., Liu, M., Pan, J., et al. (2018b). LncRNA DGCR5 suppresses neuronal apoptosis to improve acute spinal cord injury through targeting PRDM5. *Cell Cycle* 17, 1992–2000. doi: 10.1080/15384101.2018.1509622

Zhang, Y., Zhang, Y., Shi, J., Zhang, H., Cao, Z., Gao, X., et al. (2014). Identification and characterization of an ancient class of small RNAs enriched in serum associating with active infection. *J. Mol. Cell Biol.* 6, 172–174. doi: 10.1093/jmcb/mjt052

Zhou, K., Diebel, K. W., Holy, J., Skildum, A., Odean, E., Hicks, D. A., et al. (2017). A tRNA fragment, tRF5-Glu, regulates BCAR3 expression and proliferation in ovarian cancer cells. *Oncotarget* 8, 95377–95391. doi: 10.18632/oncotarget.20709

Conflict of Interest: The authors declare that the research was conducted in the absence of any commercial or financial relationships that could be construed as a potential conflict of interest.

frontiers in Molecular Neuroscience

ORIGINAL RESEARCH
published: 05 May 2020
doi: 10.3389/fnmol.2020.00071

Identification of Differentially Expressed Genes and Key Pathways in the Dorsal Root Ganglion After Chronic Compression

*Zhanhui Du[1,2], Sen Yin[3], Xiuhui Song[4], Lechi Zhang[5], Shouwei Yue[1], Xiaofeng Jia[6,7,8] and Yang Zhang[1,6]**

[1]Department of Physical Medicine & Rehabilitation, Qilu Hospital, Shandong University, Jinan, China, [2]Heart Center, Qingdao Women and Children's Hospital, Qingdao, China, [3]Department of Neurology, Qilu Hospital, Shandong University, Jinan, China, [4]Department of Neurosurgery, The People's Hospital of Jimo City, Qingdao, China, [5]Department of Physical Medicine & Rehabilitation, Suzhou Hospital Affiliated to Nanjing Medical University, Suzhou, China, [6]Department of Neurosurgery, University of Maryland School of Medicine, Baltimore, MD, United States, [7]Department of Orthopaedics, Anatomy & Neurobiology, University of Maryland School of Medicine, Baltimore, MD, United States, [8]Departments of Biomedical Engineering, Anesthesiology and Critical Care Medicine, The Johns Hopkins University School of Medicine, Baltimore, MD, United States

Neuropathic pain (NP) is caused by primary or secondary impairment of the peripheral or central nervous systems. Its etiology is complex and involves abnormal patterns of gene expression and pathway activation. Using bioinformatics analysis, we aimed to identify NP-associated changes in genes and pathways in L4 and L5 dorsal root ganglia (DRG) in a rat model of NP induced by chronic compression of the DRG (CCD). Genome-wide transcriptional analyses were used to elucidate the molecular mechanisms underlying NP. We screened differentially expressed genes (DEGs) 7 days after CCD in comparison with sham-operated controls. Quantitative real-time polymerase chain reaction (RT-qPCR) and western blotting were used to confirm the presence of key DEGs. Kyoto Encyclopedia of Genes and Genomes (KEGG)-pathway analysis of DEGs and global signal transduction network analysis of DEGs were also conducted. The CCD group developed clear mechanical and thermal allodynia in the ipsilateral hind paw compared with the sham group. This comparison identified 1,887 DEGs, with 1156 upregulated and 731 downregulated DEGs, and 123 DEG-enriched pathways. We identified the key candidate genes that might play a role in the development of NP, namely *syndecan 1* (*Sdc1*), *phosphatidylinositol-4,5-bisphosphate 3-kinase*, *catalytic subunit gamma* (*Pi3k*), *Janus kinase 2* (*Jak2*), *jun proto-oncogene, AP-1 transcription factor subunit* (*Jun*), and *interleukin 6* (*IL-6*) by analyzing the global signal transduction network. RT-qPCR and western blot analysis confirmed the microarray results. The DEGs *Sdc1*, *Pi3k*, *Jak2*, *Jun*, and *IL-6*, and the cytokine signaling pathway, the neuroactive ligand-receptor interaction, the toll-like receptor signaling pathway, and the PI3K-Akt signaling pathway may have decisive modulatory roles in both nerve regeneration and NP. These results provide deeper insight into the mechanism underlying NP and promising therapeutic targets for its treatment.

Keywords: neuropathic pain, bioinformatic analysis, differentially expressed gene, gene ontology analysis, pathway analysis, KEGG database, CCD

OPEN ACCESS

Edited by:
Aurelio Galli,
University of Alabama at Birmingham, United States

Reviewed by:
Heinrich J. G. Matthies,
University of Alabama at Birmingham, United States
Kai K. Kummer,
Innsbruck Medical University, Austria

****Correspondence:***
Yang Zhang
zhangyang982003@163.com

Received: *23 January 2020*
Accepted: *14 April 2020*
Published: *05 May 2020*

Citation:
Du Z, Yin S, Song X, Zhang L, Yue S, Jia X and Zhang Y (2020) Identification of Differentially Expressed Genes and Key Pathways in the Dorsal Root Ganglion After Chronic Compression. Front. Mol. Neurosci. 13:71. doi: 10.3389/fnmol.2020.00071

INTRODUCTION

Neuropathic pain (NP; or spontaneous pain) lacks organic causes and usually arises from a primary lesion or dysfunction of the nervous system (Woolf and Mannion, 1999). It has a global incidence of 7–10% (van Hecke et al., 2014). Patients present with varying degrees of mechanical and heat hyperalgesia and sleep and anxiety disorders, which impair their quality of life (Attal et al., 2011; Finnerup et al., 2016). The efficacy of pharmacotherapy for treating NP is limited, owing to undesirable side effects and poor responsiveness (Jacobs, 2017). Although several novel therapies have been developed for NP, the mechanism underlying NP remains unclear. Clarifying the molecular mechanism underlying NP remains an unresolved issue in the field of medical research, and a solution could lead to better clinical management of NP.

Neuronal sensitization is thought to play a key role in the development and maintenance of NP (Teixeira et al., 2015). Inflammation is inevitable during this process, and allodynia and hyperalgesia are common features. Gene expression is altered in the spinal cord and dorsal root ganglion (DRG), as evidenced by inconsistent results in different animal models of peripheral nerve injury (Wang et al., 2017; Liu et al., 2018; Zhao et al., 2020). The chronic compression of the DRG (CCD) model mimics clinical radicular pain, such as spontaneous pain, hyperalgesia, and allodynia. In comparison with other models, there are distinct properties of the CCD model, such as maintenance of peripheral input, absence of motor disorders, and ectopic discharge of neurons. Studies on CCD are essential to improve understanding of comprehensive neuropathic pain; they will also provide an opportunity to compare the results with other models.

The DRG has been proven to be involved in NP and nerve regeneration as a modulatory locus, and it may be the most important therapeutic target. Several studies have reported that the expression of ion channels, chemokines, and receptors changed after CCD (Oh et al., 2001). However, these studies focused on individual genes and failed to provide insight into the overall changes and the networks between the target genes. New insights have been achieved into the diagnosis and treatment of several diseases, with the development of high-throughput gene screening technology such as microarrays. The use of microarrays has rendered gene expression profiling a robust and straightforward process for studying the molecular features of diseases at the systemic level. Therefore, research on the molecular mechanism of NP based on the CCD model using microarrays may be useful for the development of appropriate clinical therapies for NP. This study aimed to explore the central genes that are dysregulated and the signaling pathways that are activated in a rat CCD model of NP using bioinformatics analysis.

MATERIALS AND METHODS

Experimental Animals

A total of 34 Wistar rats (adult male, weighing 180–200 g) were purchased from the Experimental Animal Center of Shandong University and housed in a room with pathogen-free air at $20 \pm 2°C$, with two rats in a cage, at a 12-h light/dark cycle. Water and food were available *ad libitum*. The experimental operation began on the 8th day so that the animals were habituated to their environment. The rats were divided into the sham and CCD groups randomly, in which 18 rats were used for microarray analysis (eight in the CCD group; 10 in the sham group) and 16 rats were used for behavioral studies and molecular experiments (eight in each group). Each behavioral study began 10 min after the animal entered the experimental environment. All experimental procedures were approved by the Animal Care and Use Committee of Shandong University.

CCD Model

CCD was induced as described earlier (Jia et al., 2018). In summary, after the rats were anesthetized, the paraspinal muscles were separated to unilaterally expose the transverse processes and intervertebral foramina of L4 and L5. Two L-shaped stainless steel rods (diameter = 0.63 mm and length = 4 mm) were implanted into the intervertebral foramina of L4 and L5 at an oblique angle of 30° with the spinal column to compress the DRGs. The other end of the bar was maintained out of the intervertebral foramen. Rats in the sham-operated group underwent the same procedure without steel rod insertion. Those exhibiting autophagy, tactile sensory deficiencies, or disabilities were excluded. The rats were administered deep anesthesia with isoflurane and were sacrificed after behavioral testing on the 7th-day post-surgery. The L4 and L5 DRG were then harvested for microarray analysis and validation tests.

Nociceptive Behavioral Testing

Mechanical hypersensitivity was determined by the same experimenter before the procedure and on the 1st, 3rd, 5th, and 7th days after CCD induction, respectively (Qu et al., 2016). The paw withdrawal threshold was automatically recorded by the BEM-404 mechanical analgesia tester [Chinese Academy of Medical Sciences (CAMS), Beijing, China] and the cutoff force was set at 50 g. Tests were started 10 min after the rats entered the test environment. A rigid tip was applied perpendicularly to the mid-plantar surface of the hind paw. Brisk withdrawal or paw flinching was considered a positive response. The number displayed on the digital monitor was recorded as the paw withdrawal mechanical threshold (PWMT). Three successive stimuli were applied. The mean of three successive measurements was recorded as the PWMT of each animal.

Thermal paw withdrawal latency (TPWL) was measured using the BME-410C thermal analgesia tester (CAMS) as described previously (Jia et al., 2018). The light source was a 12 V/10 W halogen lamp and the thermal intensity was set at 60°C. Radiant light was focused on the center of the hind paw at about 1 cm, and TPWL was recorded when the rat lifted or licked the hind paw. A 25-s cutoff period was used to avoid tissue damage. The test was repeated three times for each rat with a 5-min interval between successive measurements; the mean of three successive measurements was recorded as the TPWL of each animal.

Total RNA Extraction and Microarray Assay

One sample for each group (sham and CCD) was collected by pooling the L4 and L5 DRG of two rats. Total RNA was extracted and purified with an RNeasy Mini Kit (Qiagen, Hilden, Germany) according to the manufacturer's instructions. The quality and amount of RNA were measured using NanoDrop 2000 (Thermo, USA). mRNA expression profiling was performed using Affymetrix Clariom D Rat array (Affymetrix; Thermo Fisher Scientific Inc., Waltham, MA, USA), which contains 46,800 gene-level probe sets. GeneChips were washed, stained, and subsequently scanned using the 3000 7G GeneChip Scanner. Raw data were analyzed using the Robust Multichip Analysis (RMA) algorithm with the Affymetrix Expression Console Software (version 1.2.1). The values were presented as $\log_2$ RMA signal intensities. The microarray data discussed in this article have been submitted to the NCBI Gene Expression Omnibus and can be accessed through the GSE accession number (GSE145222).

Data Analysis

Differentially expressed genes (DEGs) were identified using the random variance model *t*-test and false discovery rate (FDR) analysis for comparisons between two groups. DEGs were considered to be present if $p < 0.05$ and the absolute value of fold change (FC) >2. DEGs were considered up or down-regulated if there was at least a 2-fold change in the positive or negative direction, respectively. Hierarchical clustering was performed using Cluster Treeview software (Palo Alto, CA, USA) to observe the DEG-expression pattern.

Gene ontology (GO) analysis was used to classify DEGs into different hierarchical categories based on the biological process and molecular function and reveal the gene regulatory network. Pathway analyses of DEGs were determined according to the Kyoto Encyclopedia of Genes and Genomes (KEGG) database. The significance of the pathway was determined using Fisher's exact test. The *P*-value was corrected by FDR analysis and a *p*-value < 0.05 was considered statistically significant.

A global signal transduction network was constructed using Cytoscape V3.6.0 based on the KEGG database to illustrate the inter-gene signaling of DEGs and discover the core genes playing an important role in this network. The nodes and lines in the network graphs represented the genes and the interactions between the nodes, respectively, such as inhibition of phosphorylation. "In-degree," "out-degree," or "degree" represented the number of links of a single node with its upstream genes, downstream genes, or all binding genes, respectively. The hub gene was selected based on the degrees. Genes with higher degrees had a more crucial position in the network.

Real-Time Polymerase Chain Reaction Analysis

Quantitative real-time polymerase chain reaction (RT-qPCR) was performed as described previously (Du et al., 2018). The total RNA was extracted and reverse-transcribed into cDNA. qPCR was performed on an iQ5 Real-Time PCR cycler (Bio-Rad, Hercules, CA, USA). All samples were normalized to Gapdh values. Data are shown as fold changes ($2^{-\Delta\Delta CT}$). The primer sequence used is shown in **Table 1**.

Western Blotting

Total proteins were extracted from tissues using RIPA Lysis Buffer (Beyotime, Haimen, Jiangsu, China). Equal amounts of the protein were separated using sodium dodecyl sulfate-polyacrylamide gel electrophoresis and transferred to a polyvinylidene fluoride membrane, followed by overnight incubation with primary antibodies at 4°C. Primary antibodies against the following proteins were used: Pi3k (1:300, 20584-1-AP, Proteintech), Jak2 (1:4,000, ab108596, Abcam), Gng7 (1:800, GTX65584, GeneTex), Jun (1:1,500, 66313-1-Ig, Proteintech), IL-6 (1:1,000, ab9324, Abcam), Met (1:1,500, ab51067, Abcam), Pdgfra (1:1,000, ab203491, Abcam), Camk2b (1:1,000, ab34703, Abcam), Ptgs2 (1:1,000, ab15191, Abcam), Sdc1 (1:1,000, ab128936, Abcam), and Gapdh (1:10,000; SAB2100894; Sigma–Aldrich; Merck KGaA). Target protein expression was normalized to Gapdh expression.

Statistical Analysis

All data are presented as mean ± SEM. The repeated measures two-way ANOVA test was used for the statistical analysis of the sham and CCD groups using SPSS 20.0 software (IBM Company, Armonk, NY, USA). Significant GO categories and pathways were selected based on Fisher's exact test, and all *p*-values

TABLE 1 | Primers used in Quantitative real-time polymerase chain reaction (RT-PCR) analysis.

Gene	Sequence 5′-3′
Pi3k	F: TCTCTGGACCTGTGCCTTCT
	R: GCCTGTCACCTATCCCAAGA
Jak2	F: AGATATGCAAGGGCATGGAG
	R: GTCAAGGATTCGGGAGCATA
Gng7	F: ACTTTGTCTCCGAAGCCTGA
	R: AGAAAATGGCCACAGTCCAC
Jun	F: CAGGTGGCACAGCTTAAACA
	R: CGCAACCAGTCAAGTTCTCA
IL6	F: CCGGAGAGGAGACTTCACAG
	R: ACAGTGCATCATCGCTGTTC
Met	F: CAGCGGCAATTCTAGACACA
	R:CTGAAGCTGCTTGTCACTCG
Pdgfra	F: CACAATAACGGGAGGCTGGT
	R: GTTCTGACGTGGCTTTCAAGG
Camk2b	F: GGAGTCAAGCCCCAGACAAAC
	R: GTGTTGGTGCTGTCGGAAGATT
Ptgs2	F: GTGGGATGACGAGCGACTG
	R: CCGTGTTCAAGGAGGATGG
Sdc1	F: ACCATCAGCCTCCAAGTGTG
	R: TGAAGTCTTGTTCTCCAGAGCC
Gapdh	F: AGGTCGGAGTCA ACGGATTTGGT
	R: CATGTGGGCCATGAGGTCCACCAC

Pi3k, phosphatidylinositol-4,5-bisphosphate 3-kinase catalytic subunit gamma; Jak2, Janus kinase 2; Gng7, G protein subunit gamma 7; Jun, Jun proto-oncogene, AP-1 transcription factor subunit; IL6, interleukin 6; Met, MET proto-oncogene, receptor tyrosine kinase; Pdgfra, platelet-derived growth factor receptor alpha; Camk2b, calcium/calmodulin-dependent protein kinase II beta; Ptgs2, prostaglandin-endoperoxide synthase 2; Sdc1, syndecan 1; F, forward; R, reverse.

were FDR adjusted p-values. A p-value < 0.05 was considered statistically significant.

RESULTS

PWMT and TPWL Changes After CCD Operation

The CCD group developed clear mechanical allodynia in the ipsilateral hind paw, compared with the sham group (**Figure 1A**). The PWMT decreased significantly 3rd ($p = 0.008$), 5th ($p = 0.002$), and 7th ($p = 0.001$) days after CCD operation ($n = 8$ in each group).

Thermal hyperalgesia was determined using the TPWL test. As indicated in **Figure 1B**, the TPWL decreased significantly (similar to the PWMT) from the 1st to 7th-day post-surgery (all $p \leq 0.001$), when compared to the sham-operated rats ($n = 8$ in each group).

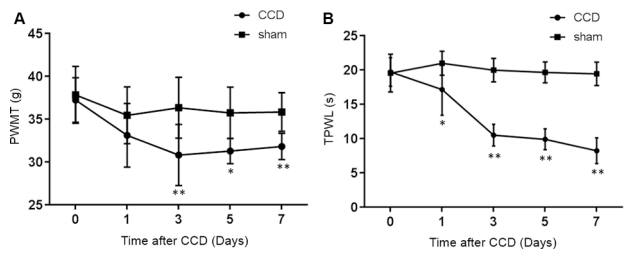

FIGURE 1 | PWMT and TPWL changes after chronic compression of the DRG (CCD) operation. **(A)** The PWMT decreased significantly 3rd, 5th, and 7th days after CCD surgery when compared with the sham group. **(B)** Compared to the sham group, TPWL decreased from the 1st to 7th-day post-surgery; $n = 8$ in both groups. PWMT, the paw withdrawal mechanical threshold; TPWL, thermal paw withdrawal latency. $^{*}P < 0.05$ and $^{**}P < 0.01$ compared with the sham group.

Analysis of mRNA With Differential Expression

Microarray analysis identified 1,887 differentially expressed genes (DEGs) in comparing the CCD and sham groups. A volcano plot was applied to visualize the genes identified (**Figure 2A**). Among all these genes, 1,156 were upregulated and 731 were downregulated (**Figure 2B**). **Figure 2C** shows a heatmap of DEG expression; it demonstrates that the mRNA expression profiles of the two groups were distinct ($n = 4$ in the CCD group, $n = 5$ in the sham group).

GO-Term Enrichment Analysis of DEGs

GO analysis was performed to explore the main cell functions of DEGs. The top five GO terms among the CCD-upregulated genes (upGOs) were as follows: response to lipopolysaccharide, inflammatory response, cellular response to lipopolysaccharide, integrin-mediated signaling pathway, and chemotaxis (**Figure 3A**). The GO terms for CCD-downregulated genes (downGOs) included regulation of ionic transmembrane transport, potassium ion transmembrane transport, regulation of potassium transmembrane transport, chemical synaptic transmission, and positive regulation of synapse assembly (**Figure 3B**).

KEGG-Pathway Analysis of DEGs

The DEGs were subjected to pathway analysis based on the KEGG database. The analysis revealed 123 enriched pathways for both upregulated and downregulated DEGs. As shown in **Figure 4**, several important pathways were altered in our NP model, including cytokine-cytokine receptor interaction, neuroactive ligand-receptor interaction, cell adhesion molecules, toll-like receptor signaling pathway, phagosome, lysosome, PI3K-Akt signaling pathway, cell cycle, TNF signaling pathway, Jak-STAT signaling pathway, and apoptosis.

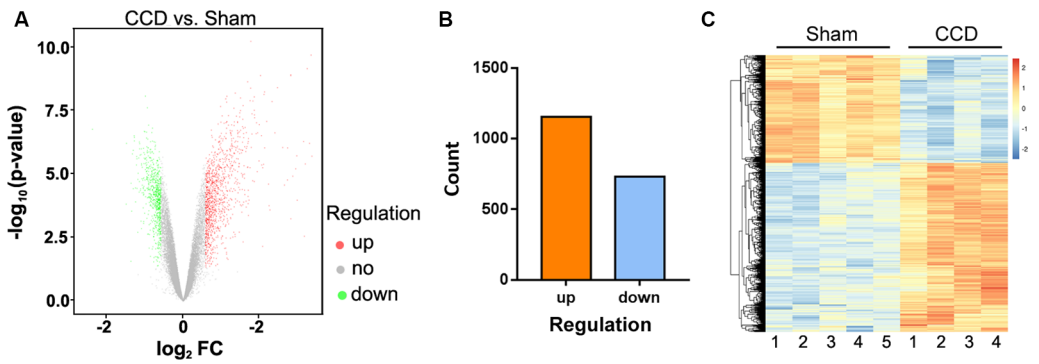

FIGURE 2 | DEGs between the CCD group and the sham group. **(A)** Volcano plot of the $-\log_{10}$(p-value) against the $\log_2$FC of each gene. Red dot indicates an upregulated DEG, whereas green dot indicates a downregulated gene. Gray indicates that there is no statistically significant difference in gene expression. **(B)** There were 1,887 DEGs identified between the CCD group and the sham group. Of these genes, 1,156 were upregulated and 731 were downregulated. **(C)** Hierarchical clustering shows the DEGs between the two groups. The number at the bottom represents the name of the samples. The color scale at the top right represents the normalized expression data, which represents the degree of gene clustering. The upregulated genes are indicated in red, and the downregulated genes are indicated in blue. DEGs, differentially expressed genes; CCD, chronic compression of the dorsal root ganglion surgery group; FC, fold change; sham, compression of the dorsal root ganglion sham group. The p-value was corrected by false discovery rate (FDR).

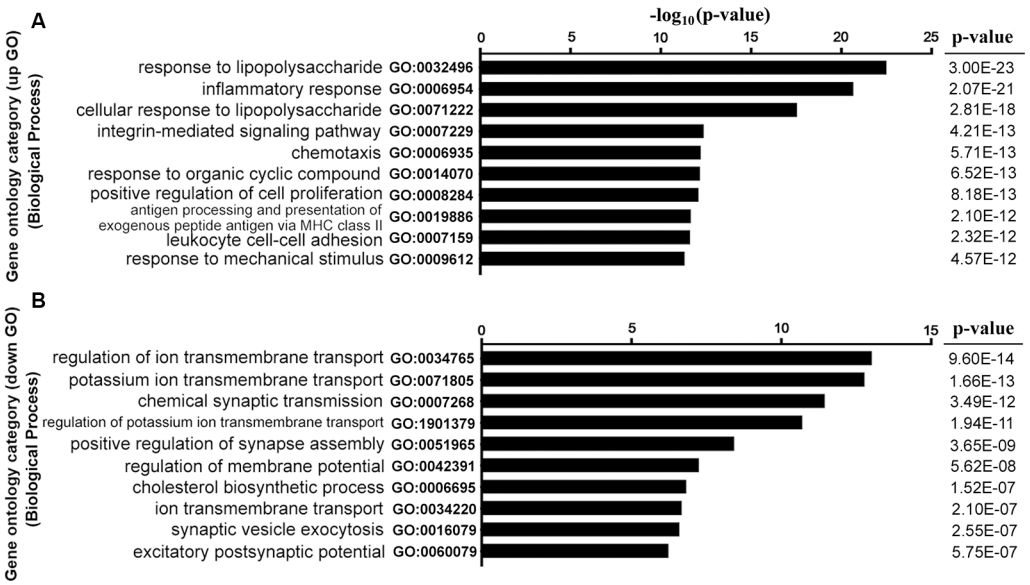

FIGURE 3 | Functional enrichment analysis for DEGs. GO terms enriched by upregulated (upGOs) and downregulated genes (downGOs) are shown as **(A)** and **(B)**, respectively. The horizontal axis represents the value of $-\log_{10}$ (*p*-value), and the vertical axis represents the category of GO biological processes. *P*-value was adjusted by FDR. GO, gene ontology. BP, biological process.

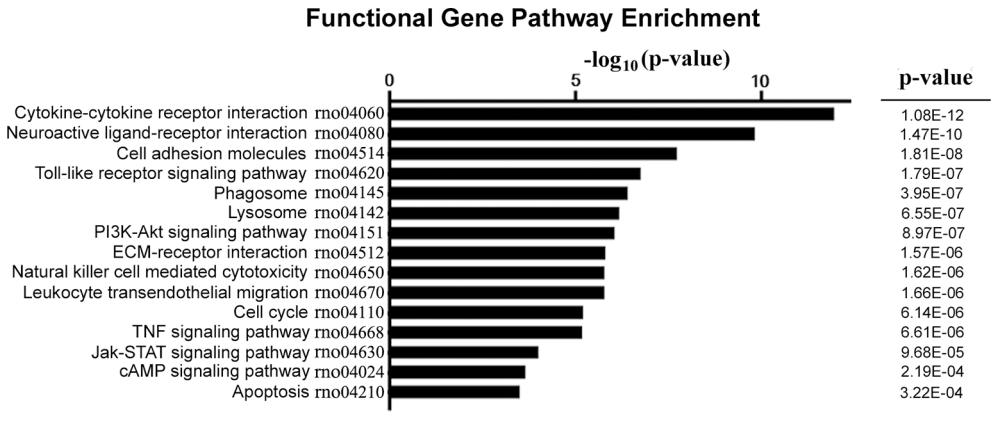

FIGURE 4 | KEGG pathway enrichment analysis for DEGs. The vertical axis on the left side represents the name of the pathway, and the horizontal axis at the top represents the value of $-\log_{10}$ (*p*-value). *P*-value was adjusted by FDR. KEGG, Kyoto Encyclopedia of Genes and Genomes.

Global Signal Transduction Network Analysis of DEGs

The candidate genes that could play a key role in the development of NP were screened using global signal transduction network analysis. As illustrated in **Figure 5**, the high-degree genes were: *phosphatidylinositol-4,5-bisphosphate 3-kinase, catalytic subunit gamma* (*Pi3k*), *Janus kinase 2* (*Jak2*), *G protein subunit gamma 7* (*Gng7*), *Jun proto-oncogene* aka *AP-1 transcription factor subunit* (*Jun*), *interleukin 6* (*IL-6*), *MET proto-oncogene* aka *receptor tyrosine kinase* (*Met*), *platelet-derived growth factor receptor alpha* (*Pdgfa*), *calcium/calmodulin-dependent protein kinase II beta* (*Camk2b*), *prostaglandin-endoperoxide synthase 2* (*Ptgs2*), and *syndecan 1* (*Sdc1*). *Gng7* and *Camk2b* were downregulated while the others were upregulated (**Table 2**).

qPCR was performed to validate the mRNA levels of the ten DEGs. *Gng7* and *Camk2b* were found to be downregulated and the remaining genes were upregulated (**Figure 6A**), supporting the microarray results. Moreover, western blotting confirmed that the protein levels of *Pi3k*, *Jak2*, *Jun*, *IL-6*, and *Sdc1* were markedly higher in the CCD group than in the sham group (**Figure 6B**). However, there was no difference in protein expression of *Gng7*, *Met*, *Pdgfra*, *Camk2b*, and *Ptgs2* (data are not shown in the figure).

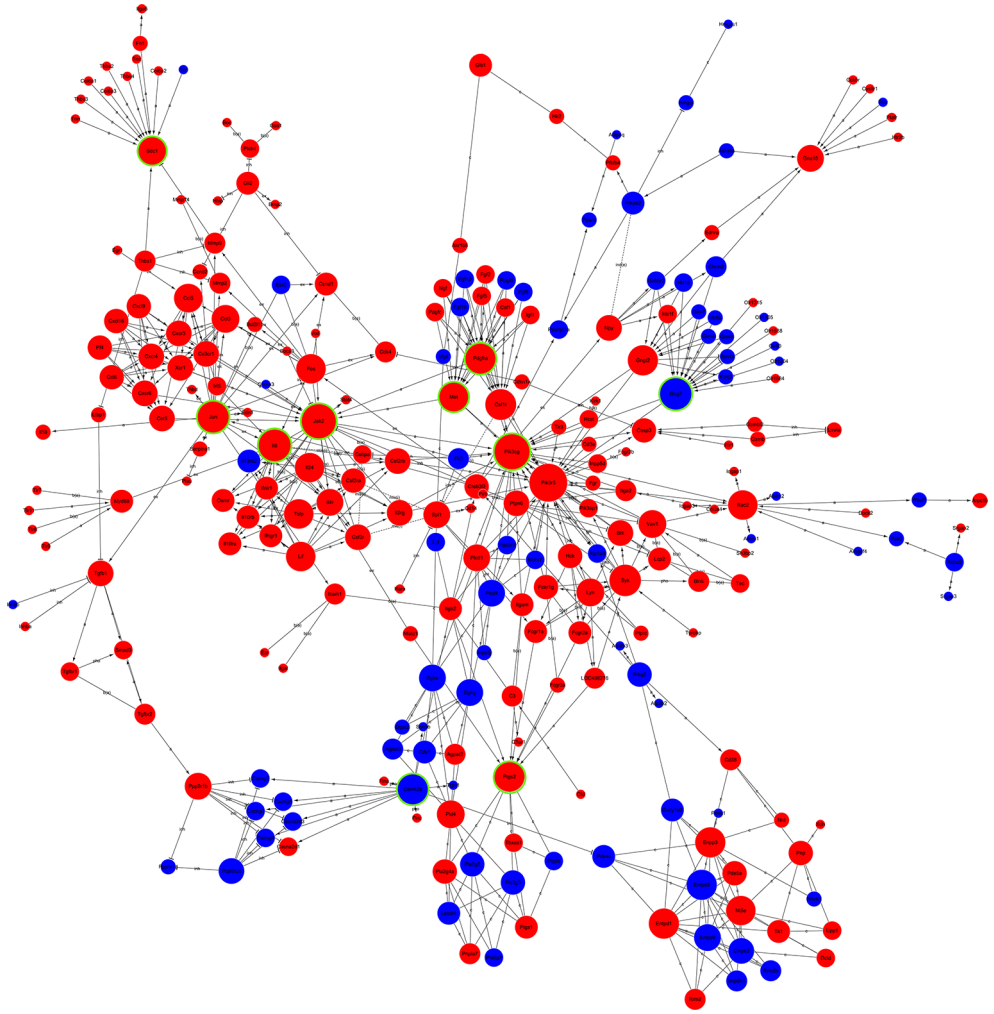

FIGURE 5 | Global signal transduction network of DEGs. The red node represents an upregulated gene, and the blue node represents the downregulated gene. The lines exhibit the interaction between the genes. The size of the node indicates the degree of interacting with other genes. The more important the genes are, the larger the node is. Nodes with green rings were the genes that were selected to be experimentally validated.

TABLE 2 | Ten key genes identified by global signal transduction network analysis.

Gene symbol	Offical full name	Style	Degree	Indegree	Outdegree	*p*-value	Fold change
Pi3k	phosphatidylinositol-4,5-bisphosphate 3-kinase catalytic subunit gamma	up	30	24	6	0.003	1.79
Jak2	Janus kinase 2	up	26	23	3	0.0008	1.75
Gng7	G protein subunit gamma 7	down	18	14	4	0.002	−1.65
Jun	Jun proto-oncogene, AP-1 transcription factor subunit	up	18	2	16	0.0005	1.89
IL6	interleukin 6	up	16	5	11	0.001	2.24
Met	MET proto-oncogene, receptor tyrosine kinase	up	13	10	3	7.321E-0.5	2.34
Pdgfra	platelet derived growth factor receptor alpha	up	13	10	3	0.0006	1.65
Camk2b	calcium/calmodulin-dependent protein kinase II beta	down	12	0	12	0.0006	−1.51
Ptgs2	prostaglandin-endoperoxide synthase 2	up	12	10	2	0.014	2.51
Sdc1	syndecan 1	up	12	12	0	8.327E-0.5	1.96

P-value was corrected by FDR.

DISCUSSION

NP is a commonly encountered neurological condition wherein patients feel pain in the absence of external stimuli; this is termed "spontaneous pain." Alterations in gene and protein expression characterize the development and maintenance of NP (Gold and Gebhart, 2010; Wang et al., 2017). In the present study, we analyzed the mRNA expression patterns after CCD

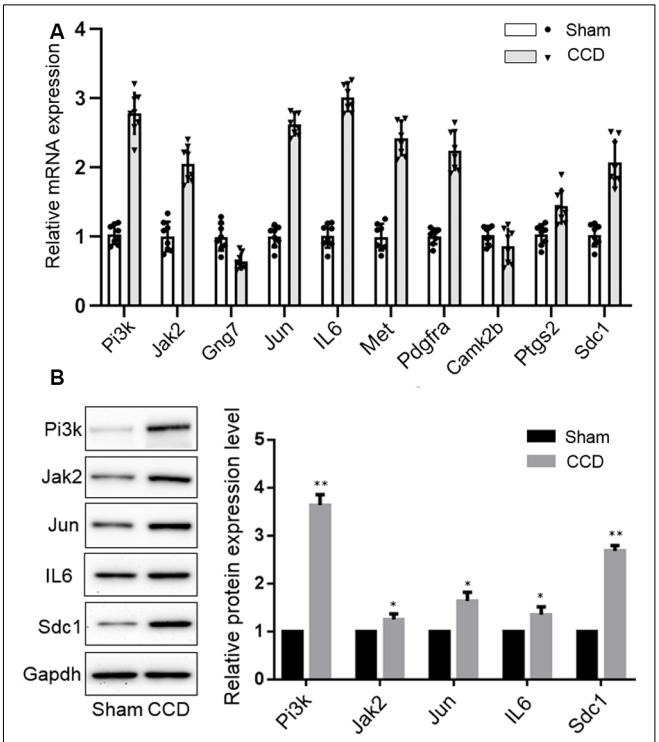

FIGURE 6 | Experimental validation of key genes. **(A)** Reverse-transcription quantitative chain reaction was performed to detect the mRNA expression of 10 key genes. **(B)** Western blotting validation of the protein expression changes of key genes in the CCD and sham group. Gapdh was used as a loading control. $^{*}p < 0.05$ and $^{**}p < 0.01$ compared with the sham group.

in the L4 and L5 DRG, which are important sites of pain regulation, synaptic plasticity, and NP treatment. Comparisons of sham-operated and CCD rats revealed expression changes in 1,887 genes. GO term enrichment analysis-term enrichment analysis of DEGs showed that the top GO terms among upGOs included a response to inflammation, integrin-mediated signaling pathway, and chemotaxis; those among downGOs included regulation of ionic transmembrane transport.

Recent bioinformatic analysis has explored the genetic processes and molecular mechanisms underlying NP, and several DEGs have been identified (Wang et al., 2017; Liu et al., 2018; Yang et al., 2018; Tang et al., 2020). Cobos et al. (2018) obtained a PPI network consisting of 31 nodes and 442 edges, which revealed certain key signaling molecules such as ATF3, JUN, BDNF, and MAPK1/3 in the sciatic nerve injury (SNI) model. Using the same dataset, Tang et al. (2020) identified additional 10 major DEGs, such as *Npy, Atf3*, and *Gpr151*, that were predominantly associated with cytokine-cytokine receptor interactions and the p53 signaling pathway. CCL2, NF-κB1, and C1Q in the dorsal horns (Wang et al., 2017), p53 and active caspase-3 in the DRG (Gao et al., 2018), Ccl3, Atf3, and Tgif1 in the spinal cord (Zhang and Yang, 2017) were separately considered to contribute to the generation of NP after SNI, chronic constriction injury (CCI), and spinal cord injury (SCI). Our study showed that *Jun* and *IL-6* may evoke the progression of NP after CCD; this was consistent with other bioinformatics analysis (Liu et al., 2018; Yang et al., 2018; Tang et al., 2020). Therefore, the genetic targets differed with the pathological conditions and analytical methods. The CCD model mimics the effects of protrusion of an intervertebral disc through the injuring of both sensory neurons and spinal nerves; this distinguishes it different from other animal models. Moreover, the steel rods used in the protocol could potentially induce sterile inflammation and damage spinal segmental vessels passing through the intervertebral foramina. Hence, spinal compression and the accompanying inflammation may contribute to the behavioral and physiological consequences of CCD and greater complexity in the local microenvironments (Yang et al., 2018). This is consistent with our observation that the upGO terms enriched by DEGs after CCD were the inflammatory response and integrin-mediated signaling pathway, that were associated with mechanotransduction.

Meanwhile, the main downGOs categories of DEGs were the regulation of ion transmembrane transport, potassium ion transmembrane transport, and regulation of membrane potential. It is well known that potassium ion channels, inward rectifying potassium channels (Kir) in particular, maintain strongly negative resting membrane potential (Rosenhouse-Dantsker, 2019). Thus, downGOs of potassium ion transmembrane transport and regulation of membrane potential may be associated with neuronal somal hypeand peripheral axotomyrexcitability and spontaneous action potentials after CCD. However, Gao et al. (2018) reported that the DEGs associated with the regulation of transmembrane transport and regulation of membrane potential were upregulated after CCI. This further demonstrates the importance of research in different pathological conditions. Interestingly, the downGOs included the cholesterol biosynthetic process. It has been demonstrated that many ion channels including Kir channels, in particular, are modulated by cholesterol (Rosenhouse-Dantsker, 2019). Therefore, our findings provide a new insight into the understanding of the mechanism of cellular excitability and ion channel rearrangements after CCD.

We found that the expression of *Sdc1* was significantly increased 7 days after CCD. Sdc1 is expressed in C-fiber sensory neurons distributed in peripheral and central axons. It was demonstrated that *Sdc1* could reduce neurite extension in primary cultured DRG neurons in both, the proximal region and distal regions of the injured sciatic nerve (Murakami et al., 2015). Sciatic nerve axotomy and infraorbital nerve axotomy induced *Sdc1* in primary sensory neurons, which may contribute to the development of abnormal nociception (Couchman, 2003). Moreover, *Sdc1* expression plays a functional role in nerve regeneration and synaptic plasticity in injured primary sensory neurons (Edwards and Hammarlund, 2014; Bray et al., 2019). The increased expression of *Sdc1* may have multiple functions in nerve regeneration and the development of abnormal nociception after CCD; this needs further research.

As shown in **Figure 5**, the expression of *Jun* and *IL-6* increased significantly 7 days after CCD; this was consistent with findings from previous studies (Ding et al., 2016; Zhao et al., 2020). *Jun* is expressed at lower levels in normal nervous

systems; however, it is upregulated in response to harmful stimuli such as dorsal column transection, root rhizotomy, and peripheral axotomy, et cetera (Kenney and Kocsis, 1998; Li et al., 2013). Notably, the c-Jun N-terminal kinase (JNK) signaling pathway is essential for chronic inflammatory pain (Sanna and Galeotti, 2018). Inhibition of JNK signaling was effective in relieving inflammatory pain and NP in several animal models (Li et al., 2017). The upregulation of *Jun* also showed protective and nerve-regenerative roles in DRG and Schwann cells in a nerve injury model (Yang et al., 2012; Zhao et al., 2014). JNK inhibitors may enhance the expression of activated transcription factor 3 and decrease the expression of multiple neurotrophic factors secreted by the DRG (Tu et al., 2016). Thus, an increase in the expression of *Jun* may be correlated with post-CCD pain and nerve regeneration.

The role of *IL-6* in nociceptive processing and regulation of pathological pain is well established (Schaper and Rose-John, 2015). *IL-6* was shown to induce the JAK-mediated phosphorylation of STAT proteins (Schaper and Rose-John, 2015) and participate in the later maintenance of NP by activating the JAK/STAT3 signaling pathway (Ding et al., 2016). Although the pain caused by *IL-6* is subjectively unpleasant, several studies suggest that IL-6 is beneficial to the nervous system. *IL-6* is rapidly expressed in the retina and promotes the regeneration of the optic nerve by activating the JAK/STAT3 and PI3K/AKT signaling pathways following optic nerve injury (Leibinger et al., 2013). In general, *IL-6* has detrimental and beneficial effects on the nervous system.

The upregulation of JAK/STAT3 signaling has been observed after nerve injury in animal models of neuropathic pain (Dominguez et al., 2008, 2010). Activation of the JAK/STAT3 cascade is induced by both pro-nociceptive (IL-6) and anti-nociceptive (IL-10) factors. These two forms of activation lead to the transcription of different pools of genes affecting the state of polarization of the microglia. The PI3K/AKT signaling pathway is also involved in the IL-6–mediated regulation of pathological pain (Ding et al., 2018). Plantar incisions have been found to induce time-dependent activation of the PI3K/Akt pathway in the spinal cord and DRG (Xu et al., 2014). As shown in **Figure 4** and **Table 2**, the key candidate genes *JAK*, *IL-6*, *Jun*, and *PI3K* are vertices of a global signal transduction network and act synergistically; this is consistent with the findings of other studies. They are also involved in a complex physiological response that involves the termination of inflammation, promotion of the M2 state of microglial polarization, and synaptic plasticity (Nicolas et al., 2013; Xue et al., 2014).

Our study has several limitations. First, tissue samples obtained from rats differ from those of humans and may not show the same target genes after nerve injury. Second, we detected the DEGs 7 days after CCD, which may reveal genes involved in the development, but not in the maintenance of NP. Third, the analysis of a larger number of tissue samples is required to improve the reliability of these results.

In conclusion, we found that *Sdc1*, *Pi3k*, *Jak2*, *Jun*, *IL-6*, and the signaling pathways cytokine-cytokine receptor interaction, neuroactive ligand-receptor interaction, toll-like receptor signaling pathway, and PI3K-Akt signaling pathway have key roles in both nerve regeneration and NP. These results may provide deeper insight into the understanding of the mechanism of NP after CCD, and help to identify promising therapeutic targets. Further studies are needed to confirm the role of cytokines and signaling pathways in the development of neuropathic pain, both individually and in cooperation.

DATA AVAILABILITY STATEMENT

The microarray data discussed in this article have been submitted to the NCBI Gene Expression Omnibus and can be accessed through the GSE accession number (GSE145222).

ETHICS STATEMENT

Procedures were approved by the Chinese Institutional Animal Care Committee of Shandong University.

AUTHOR CONTRIBUTIONS

ZD, SYi, and XS performed the experiments and analyzed the data. YZ and LZ wrote the manuscript. XJ revised the manuscript and provided critical appraisal. SYu and YZ conceived the original idea and designed the experiments for this study. All authors read and approved the final manuscript.

FUNDING

This work was supported by the National Natural Science Foundation of China (Nos. 81101453 and 81472159, both to YZ).

ACKNOWLEDGMENTS

We appreciate the technical assistance of the cardiovascular research center of Qilu Hospital.

REFERENCES

Attal, N., Lanteri-Minet, M., Laurent, B., Fermanian, J., and Bouhassira, D. (2011). The specific disease burden of neuropathic pain: results of a French nationwide survey. *Pain* 152, 2836–2843. doi: 10.1016/j.pain.2011.09.014

Bray, E. R., Yungher, B. J., Levay, K., Ribeiro, M., Dvoryanchikov, G., Ayupe, A. C., et al. (2019). Thrombospondin-1 mediates axon regeneration in retinal ganglion cells. *Neuron* 103, 642.e7–657.e7. doi: 10.1016/j.neuron.2019.05.044

Cobos, E. J., Nickerson, C. A., Gao, F., Chandran, V., Bravo-Caparros, I., Gonzalez-Cano, R., et al. (2018). Mechanistic differences in neuropathic pain modalities revealed by correlating behavior with global expression profiling. *Cell Rep.* 22, 1301–1312. doi: 10.1016/j.celrep.2018.01.006

Couchman, J. R. (2003). Syndecans: proteoglycan regulators of cell-surface microdomains? *Nat. Rev. Mol. Cell Biol.* 4, 926–937. doi: 10.1038/nrm1257

Ding, C. P., Guo, Y. J., Li, H. N., Wang, J. Y., and Zeng, X. Y. (2018). Red nucleus interleukin-6 participates in the maintenance of neuropathic pain

through JAK/STAT3 and ERK signaling pathways. *Exp. Neurol.* 300, 212–221. doi: 10.1016/j.expneurol.2017.11.012

Ding, C. P., Xue, Y. S., Yu, J., Guo, Y. J., Zeng, X. Y., and Wang, J. Y. (2016). The red nucleus interleukin-6 participates in the maintenance of neuropathic pain induced by spared nerve injury. *Neurochem. Res.* 41, 3042–3051. doi: 10.1007/s11064-016-2023-9

Dominguez, E., Mauborgne, A., Mallet, J., Desclaux, M., and Pohl, M. (2010). SOCS3-mediated blockade of JAK/STAT3 signaling pathway reveals its major contribution to spinal cord neuroinflammation and mechanical allodynia after peripheral nerve injury. *J. Neurosci.* 30, 5754–5766. doi: 10.1523/jneurosci.5007-09.2010

Dominguez, E., Rivat, C., Pommier, B., Mauborgne, A., and Pohl, M. (2008). JAK/STAT3 pathway is activated in spinal cord microglia after peripheral nerve injury and contributes to neuropathic pain development in rat. *J. Neurochem.* 107, 50–60. doi: 10.1111/j.1471-4159.2008.05566.x

Du, Z., Song, X., Yan, F., Wang, J., Zhao, Y., and Liu, S. (2018). Genome-wide transcriptional analysis of BRD4-regulated genes and pathways in human glioma U251 cells. *Int. J. Oncol.* 52, 1415–1426. doi: 10.3892/ijo.2018.4324

Edwards, T. J., and Hammarlund, M. (2014). Syndecan promotes axon regeneration by stabilizing growth cone migration. *Cell Rep.* 8, 272–283. doi: 10.1016/j.celrep.2014.06.008

Finnerup, N. B., Haroutounian, S., Kamerman, P., Baron, R., Bennett, D. L., Bouhassira, D., et al. (2016). Neuropathic pain: an updated grading system for research and clinical practice. *Pain* 157, 1599–1606. doi: 10.1097/j.pain.0000000000000492

Gao, Y., Sun, N., Wang, L., Wu, Y., Ma, L., Hong, J., et al. (2018). Bioinformatics analysis identifies p53 as a candidate prognostic biomarker for neuropathic pain. *Front. Genet.* 9:320. doi: 10.3389/fgene.2018.00320

Gold, M. S., and Gebhart, G. F. (2010). Nociceptor sensitization in pain pathogenesis. *Nat. Med.* 16, 1248–1257. doi: 10.1038/nm.2235

Jacobs, D. S. (2017). Diagnosis and treatment of ocular pain: the ophthalmologist's perspective. *Curr. Ophthalmol. Rep.* 5, 271–275. doi: 10.1007/s40135-017-0152-1

Jia, L., Zhang, Y., Qu, Y. J., Huai, J., Wei, H., and Yue, S. W. (2018). Gene therapy by lentivirus-mediated RNA interference targeting extracellular-regulated kinase alleviates neuropathic pain *in vivo*. *J. Cell. Biochem.* doi: 10.1002/jcb.28090 [Epub ahead of print]

Kenney, A. M., and Kocsis, J. D. (1998). Peripheral axotomy induces long-term c-Jun amino-terminal kinase-1 activation and activator protein-1 binding activity by c-Jun and junD in adult rat dorsal root ganglia *in vivo*. *J. Neurosci.* 18, 1318–1328.

Leibinger, M., Andreadaki, A., Diekmann, H., and Fischer, D. (2013). Neuronal STAT3 activation is essential for CNTF- and inflammatory stimulation-induced CNS axon regeneration. *Cell Death Dis.* 4:e805. doi: 10.1038/cddis.2013.310

Li, H., Li, Q., Xie, K., Feng, S., Wang, P., and Ma, X. (2013). Expression of c-Fos and c-Jun in adjacent cervical spinal cord segments following C_7 nerve root rhizotomy in rats: Indication of a neural pathway between adjacent cervical spinal cord segments. *Exp. Ther. Med.* 6, 373–377. doi: 10.3892/etm.2013.1136

Li, J., Zhao, P. P., Hao, T., Wang, D., Wang, Y., Zhu, Y. Z., et al. (2017). Urotensin II inhibitor eases neuropathic pain by suppressing the JNK/NF-κB pathway. *J. Endocrinol.* 232, 165–174. doi: 10.1530/joe-16-0255

Liu, H., Xia, T., Xu, F., Ma, Z., and Gu, X. (2018). Identification of the key genes associated with neuropathic pain. *Mol. Med. Rep.* 17, 6371–6378. doi: 10.3892/mmr.2018.8718

Murakami, K., Tanaka, T., Bando, Y., and Yoshida, S. (2015). Nerve injury induces the expression of syndecan-1 heparan sulfate proteoglycan in primary sensory neurons. *Neuroscience* 300, 338–350. doi: 10.1016/j.neuroscience.2015.05.033

Nicolas, C. S., Amici, M., Bortolotto, Z. A., Doherty, A., Csaba, Z., Fafouri, A., et al. (2013). The role of JAK-STAT signaling within the CNS. *JAKSTAT* 2:e22925. doi: 10.4161/jkst.22925

Oh, S. B., Tran, P. B., Gillard, S. E., Hurley, R. W., Hammond, D. L., and Miller, R. J. (2001). Chemokines and glycoprotein120 produce pain hypersensitivity by directly exciting primary nociceptive neurons. *J. Neurosci.* 21, 5027–5035. doi: 10.1523/jneurosci.21-14-05027.2001

Qu, Y. J., Zhang, X., Fan, Z. Z., Huai, J., Teng, Y. B., Zhang, Y., et al. (2016). Effect of TRPV4–p38 MAPK pathway on neuropathic pain in rats with chronic compression of the dorsal root ganglion. *Biomed. Res. Int.* 2016:6978923. doi: 10.1155/2016/6978923

Rosenhouse-Dantsker, A. (2019). Cholesterol binding sites in inwardly rectifying potassium channels. *Adv. Exp. Med. Biol.* 1135, 119–138. doi: 10.1007/978-3-030-14265-0_7

Sanna, M. D., and Galeotti, N. (2018). The HDAC1/c-JUN complex is essential in the promotion of nerve injury-induced neuropathic pain through JNK signaling. *Eur. J. Pharmacol.* 825, 99–106. doi: 10.1016/j.ejphar.2018.02.034

Schaper, F., and Rose-John, S. (2015). Interleukin-6: biology, signaling and strategies of blockade. *Cytokine Growth Factor Rev.* 26, 475–487. doi: 10.1016/j.cytogfr.2015.07.004

Tang, S., Jing, H., Huang, Z., Huang, T., Lin, S., Liao, M., et al. (2020). Identification of key candidate genes in neuropathic pain by integrated bioinformatic analysis. *J. Cell. Biochem.* 121, 1635–1648. doi: 10.1002/jcb.29398

Teixeira, M. J., da Paz, M. G., Bina, M. T., Santos, S. N., Raicher, I., Galhardoni, R., et al. (2015). Neuropathic pain after brachial plexus avulsion—central and peripheral mechanisms. *BMC Neurol.* 15:73. doi: 10.1186/s12883-015-0329-x

Tu, N. H., Katano, T., Matsumura, S., Pham, V. M., Muratani, T., Minami, T., et al. (2016). Role of c-Jun N-terminal kinase in late nerve regeneration monitored by *in vivo* imaging of thy1-yellow fluorescent protein transgenic mice. *Eur. J. Neurosci.* 43, 548–560. doi: 10.1111/ejn.13139

van Hecke, O., Austin, S. K., Khan, R. A., Smith, B. H., and Torrance, N. (2014). Neuropathic pain in the general population: a systematic review of epidemiological studies. *Pain* 155, 654–662. doi: 10.1016/j.pain.2013.11.013

Wang, J., Ma, S. H., Tao, R., Xia, L. J., Liu, L., and Jiang, Y. H. (2017). Gene expression profile changes in rat dorsal horn after sciatic nerve injury. *Neurol. Res.* 39, 176–182. doi: 10.1080/01616412.2016.1273590

Woolf, C. J., and Mannion, R. J. (1999). Neuropathic pain: aetiology, symptoms, mechanisms, and management. *Lancet* 353, 1959–1964. doi: 10.1016/s0140-6736(99)01307-0

Xu, B., Guan, X. H., Yu, J. X., Lv, J., Zhang, H. X., Fu, Q. C., et al. (2014). Activation of spinal phosphatidylinositol 3-kinase/protein kinase B mediates pain behavior induced by plantar incision in mice. *Exp. Neurol.* 255, 71–82. doi: 10.1016/j.expneurol.2014.02.019

Xue, Z. J., Shen, L., Wang, Z. Y., Hui, S. Y., Huang, Y. G., and Ma, C. (2014). STAT3 inhibitor WP1066 as a novel therapeutic agent for bCCI neuropathic pain rats. *Brain Res.* 1583, 79–88. doi: 10.1016/j.brainres.2014.07.015

Yang, J. A., He, J. M., Lu, J. M., and Jie, L. J. (2018). Jun, Gal, Cd74, and C1qb as potential indicator for neuropathic pain. *J. Cell. Biochem.* 119, 4792–4798. doi: 10.1002/jcb.26673

Yang, D. P., Kim, J., Syed, N., Tung, Y. J., Bhaskaran, A., Mindos, T., et al. (2012). p38 MAPK activation promotes denervated Schwann cell phenotype and functions as a negative regulator of Schwann cell differentiation and myelination. *J. Neurosci.* 32, 7158–7168. doi: 10.1523/JNEUROSCI.5812-11.2012

Zhang, G., and Yang, P. (2017). Bioinformatics genes and pathway analysis for chronic neuropathic pain after spinal cord injury. *Biomed. Res. Int.* 2017:6423021. doi: 10.1155/2017/6423021

Zhao, H., Duan, L. J., Sun, Q. L., Gao, Y. S., Yang, Y. D., Tang, X. S., et al. (2020). Identification of key pathways and genes in L4 dorsal root ganglion (DRG) after sciatic nerve injury *via* microarray analysis. *J. Invest. Surg.* 33, 172–180. doi: 10.1080/08941939.2018.1452996

Zhao, L., Qu, W., Wu, Y., Ma, H., and Jiang, H. (2014). Dorsal root ganglion-derived Schwann cells combined with poly(lactic-co-glycolic acid)/chitosan conduits for the repair of sciatic nerve defects in rats. *Neural Regen. Res.* 9, 1961–1967. doi: 10.4103/1673-5374.145374

Conflict of Interest: The authors declare that the research was conducted in the absence of any commercial or financial relationships that could be construed as a potential conflict of interest.

frontiers in Molecular Neuroscience

ORIGINAL RESEARCH
published: 30 June 2020
doi: 10.3389/fnmol.2020.00105

Inhibition of M/K_v7 Currents Contributes to Chloroquine-Induced Itch in Mice

Dong Zhang[1,2,3,4,5†], Hongchao Men[1,2,3,4,5†], Ludi Zhang[1,2,3,4], Xiangxin Gao[1,2,3,4], Jingjing Wang[1,2,3,4], Leying Li[1,2,3,4], Qiaoying Zhu[1,2,3,4], Hailin Zhang[1,2,3,4] and Zhanfeng Jia[1,2,3,4*]*

[1] Department of Pharmacology, Hebei Medical University, Shijiazhuang, China, [2] Center for Innovative Drug Research and Evaluation, Institute of Medical Science and Health, Hebei Medical University, Shijiazhuang, China, [3] The Key Laboratory of Neural and Vascular Biology, Ministry of Education, Shijiazhuang, China, [4] The Key Laboratory of New Drug Pharmacology and Toxicology, Shijiazhuang, China, [5] Department of Anesthesiology, Hebei General Hospital, Shijiazhuang, China

M/K_v7 potassium channels play a key role in regulation of neuronal excitability. Modulation of neuronal excitability of primary sensory neurons determines the itch sensation induced by a variety of itch-causing substances including chloroquine (CQ). In the present study, we demonstrate that suppression of M/K_v7 channel activity contributes to generation of itch in mice. CQ enhances excitability of the primary sensory neurons through inhibiting M/K_v7 potassium currents in a Ca^{2+} influx-dependent manner. Specific M/K_v7 channel opener retigabine (RTG) or tannic acid (TA) not only reverses the CQ-induced enhancement of neuronal excitability but also suppresses the CQ-induced itch behavior. Systemic application of RTG or TA also significantly inhibits the itch behavior induced by a variety of pruritogens. Taken together, our findings provide novel insight into the molecular basis of CQ-induced itch sensation in mammals that can be applied to the development of strategies to mitigate itch behavior.

Keywords: M/K_v7 potassium currents, dorsal root ganglion neurons, inhibition, chloroquine, itch

OPEN ACCESS

Edited by:
Wolfgang Liedtke, Duke University, United States

Reviewed by:
Hyosang Lee, Daegu Gyeongbuk Institute of Science and Technology (DGIST), South Korea
Hongzhen Hu, Washington University in St. Louis, United States

***Correspondence:**
Hailin Zhang
zhanghl@hebmu.edu.cn
Zhanfeng Jia
jiazf@hebmu.edu.cn;
jia_zf75@hotmail.com

† These authors have contributed equally to this work

Received: *28 December 2019*
Accepted: *20 May 2020*
Published: *30 June 2020*

Citation:
Zhang D, Men H, Zhang L, Gao X, Wang J, Li L, Zhu Q, Zhang H and Jia Z (2020) Inhibition of M/K_v7 Currents Contributes to Chloroquine-Induced Itch in Mice. Front. Mol. Neurosci. 13:105. doi: 10.3389/fnmol.2020.00105

INTRODUCTION

M/K_v7 channels are extensively distributed in central and peripheral nerve system (Brown and Passmore, 2009) and play a crucial role in the stabilization of membrane potential and modulation of neuronal excitability (Jentsch, 2000). For example, M/K_v7 channels determine the resting membrane potential (RMP) of dorsal root ganglion (DRG) neurons (Du et al., 2014) and the firing patterns of action potentials (APs) in superior cervical ganglion (SCG) sympathetic neurons (Jia et al., 2008); loss-of-function mutations of M/K_v7 channel subunits located in the brain result in epilepsy (Biervert et al., 1998; Singh et al., 1998; Allen et al., 2014).

Importance of M/K_v7 channels have been demonstrated in a variety of pathological conditions. In the brain, inhibition of M/K_v7 channels by M1 muscarinic receptor in basolateral amygdala promotes fear memory consolidation (Young and Thomas, 2014); augmentation of M/K_v7 channels reduces cerebral ischemic stroke-induced brain injury (Bierbower et al., 2015). In the peripheral nerve system, inhibition of M/K_v7 currents of DRG neurons contributes to acute inflammatory pain induced by pro-inflammatory factors such as proteases (Linley et al., 2008) and bradykinin (Liu et al., 2010); down-regulation of M/K_v7 expression in DRG neurons mediates chronic inflammatory pain (Mucha et al., 2010), neuropathic pain (Rose et al., 2011;

King et al., 2014; Zhang et al., 2019), and cancer pain (Zheng et al., 2013). Activation of peripheral M/K_v7 channels significantly relives gout pain (Zheng et al., 2015). Thus, suppression of neuronal excitability via augmentation of peripheral M/K_v7 currents is a valuable analgesic strategy.

Itch, also known as pruritus, is an uncomfortable everyday experience that evokes a desire to scratch (Dong and Dong, 2018). Itch is commonly caused by chemical pruritogens (Dong and Dong, 2018); meanwhile, itch is also a prominent symptom of many diseases, such as dry skin (Pereira and Ständer, 2018), psoriasis (Elewski et al., 2019), and atopic/allergic dermatitis (Bieber, 2008), as well as patients with system disease such as chronic cholestatic liver disease (Carey et al., 2015) and renal disease (Simonsen et al., 2017). Understanding the neural basis of itch at the molecular, cellular, and circuit levels can identify new therapeutic targets to treat this devastating symptom (Meixiong and Dong, 2017). Mammals appear to have evolved two forms of itch: (i) chemical itch, which is activated by chemical mediators such as histamine (HIS) and chloroquine (CQ) and can be effectively gated by noxious painful stimuli (Han and Dong, 2014), and (ii) mechanical itch, which is evoked by light mechanical stimuli such as when insects or parasites come in contact with the skin (Bourane et al., 2015; Dong and Dong, 2018). Mechanical itch transmission is gated by a population of spinal inhibitory interneurons that expressed neuropeptide Y (NPY) (Bourane et al., 2015). Loss of Merkel cells and associated mechanosensitive Piezo2 channels in the skin alleviates the activity of these inhibitory NPY interneurons and leads to mechanical itch (Feng et al., 2018). TRP channels such as TRPV1 and TRPA1 expressed in peripheral DRG pruritic neurons can be activated by G-protein-coupled pruriceptors (i.e., HIS-H1 receptor/H4 receptor, Serotonin-H7 receptor, CQ-MrgprA3 receptor), hence initiate itch sensation (Dong and Dong, 2018).

The fundamental step for different sensation generation including pain and itch is that irritants excite sensory neurons through the corresponding receptors and/or ion channels. Given the crucial role of M/K_v7 currents in controlling neuronal excitability of sensory neurons, we hypothesize that M/K_v7 may be involved in pruritogen-induced itch sensation. In the present study, itch-like behavior induced by several pruritogens such as CQ, serotonin (5-hydroxytryptamine, 5-HT), capsaicin (CAP), HIS, carvacrol (CAR), and β-alanine (β-ALA) have been measured. We demonstrate that CQ acts as a novel inhibitor of M/K_v7 currents and its inhibition of M/K_v7 currents at least partially contributes to CQ-induced itch in mice.

MATERIALS AND METHODS

Animals

Male C57B/J mice (6–8 weeks old; 20–25 g) were used. Mice were purchased from Beijing Vital River Laboratory Animal Technology Co., Ltd. (Beijing, China) and housed with a stable humidity (55 ± 15%) with free access to food/water in a 12/12 h light–dark cycle at room temperature (22–24°C), according to the guidelines of the local Animal Care and Use Committee at Hebei Medical University (Shijiazhuang, China).

Chemicals and Antibodies

All chemicals except β-ALA were purchased from Sigma (Sigma-Aldrich LLC, St. Louis, MO, United States). β-ALA was purchased from Beijing Brinway Technology Co. (Beijing, China). Antibodies specific to mouse K_v7.2 subunit and mouse MrgprA were purchased from Abcam (Ambridge, United Kingdom). Goat anti-rabbit (Fluorescein 5-isothiocyanate, FITC) and Goat anti-mouse (Tetramethylrhodamine, TRITC) were purchased from Jackson ImmunoResearch Inc. (Baltimore, United States). 4′,6-Diamidino-2-phenylindole (DAPI) was purchased from Protein Tech Group, Inc. (Wu Han, China).

Itch Behavior Test

The itch-like behavior test was performed as previously described (Shimada and LaMotte, 2008; Wilson et al., 2011). Briefly, for assessing CQ-evoked itch behavior, mice received a subcutaneous injection into the cheek (20 μl) or neck (50 μl), with 200 μg CQ dissolved in saline (the concentrations were 20 and 8 mM, respectively). Mice were videotaped for 30 min following the injection. The number of scratch bouts were quantified over a 30-min period. One bout of scratching was defined as an episode in which a mouse lifted its hind paw and scratched continuously for any length of time, until the hind paw was returned to the floor or to the mouth. For assessing XE991 (a specific M/K_v7 channel blocker)-evoked itch-like behaviors, mice received a subcutaneous injection into the cheek (0.1 or 1 mM, 20 μl) or neck (0.1 or 1 mM, 50 μl). Pruritogen such as 5-HT (1 mM, 50 μl)-, CAP (10 μM, 50 μl)-, HIS (90 mM, 50 μl)-, CAR (70 mM, 50 μl)-, and β-ALA (50 mM, 50 μl)-induced itch-like behaviors by subcutaneous injection into the neck were measured, respectively.

Rota-Rod Test

Rota-rod test was performed as previously described (Chindo et al., 2014) to assess motor coordination in mice. Briefly, mice were trained to remain on a treadmill device (Jixing Rota-Rod, Hebei, China) with slowly revolving rods of 5 cm diameter at 20 rpm for 180 s. Mice that were able to remain on the rod for 180 s or longer were selected and divided into three groups of five mice per group. Group I received saline, while groups II and III received RTG (20 mg/kg) and TA (16 mg/kg) by intraperitoneal injection, respectively. Thirty minutes after the treatment, mice were placed individually on the rod at intervals of 30 min, up to 60 min. If an animal failed more than once to remain on the rod for 3 min, the test was considered positive, meaning there was a lack of motor coordination.

Immunostaining

Mice were transcardially perfused with 4% PFA under depth of anesthesia (2% sodium pentobarbital, 30 mg/kg). DRGs were removed and stored in 4% PFA followed by embedding in OCT (SAKURA, Japan). Ten-micrometer DRG sections were cut using a freezing microtome (Leica, Germany). Sections were washed once with 0.1 mol/L PBS (Beijing Solarbio Science & Technology

Co., Ltd.) and punched for 30 min in 37°C with 0.3% Triton X-100/PBS buffer and blocked for 1 h with blocking buffer (10% goat serum in 0.1 mol/L PBS). Primary antibodies were diluted in 0.1% Triton X-100/PBS buffer before overnight incubation at 4°C. The second day, sections received three additional washes in PBS before incubation with secondary antibodies for 2 h at 37°C. Sections were washed three times with PBS and placed on microscope slides in Vectashield with DAPI (Southern Biotech). Staining was visualized and captured using a laser scanning confocal microscope (Leica SP5, Leica, Germany).

Cell Culture

Primary cultures of DRG neurons were prepared from 6- to 8-week-old male mice (20–25 g). Briefly, mice were anesthetized with isoflurane and sacrificed by decapitation. DRGs were rapidly dissected out bilaterally and incubated with 0.2% collagenase and 0.5% dispase for 1 h at 37°C in minimum essential medium for suspension culture (Thermo Fisher Scientific, Inc., Waltham, MA, United States). After digestion and trituration to dissociate neurons, DRG neurons were plated on glass coverslips pre-coated with poly-D-lysine (12.5 μg/ml) and laminin (20 μg/ml in Hanks' buffered salt solution, BD Biosciences). The cells were cultured in minimum essential medium (Thermo Fisher Scientific, Inc., Waltham, MA, United States) that contained 2.5S NGF (10 ng/ml; Roche Applied Science, Indianapolis, IN, United States), 5% heat-inactivated horse serum (JRH Biosciences, Lenexa, KS, United States), uridine/5-fluoro-2′-deoxyuridine (10 μM), 8 mg/ml glucose, and 1% vitamin solution (Thermo Fisher Scientific, Inc., Waltham, MA, United States). The cultures were maintained in an incubator at 37°C with a humidified atmosphere of 95% air + 5% CO_2. Cells were used for patch clamp recordings after culturing for 2 days.

Electrophysiology

Whole-cell mode patch recordings in voltage- and current-clamp configurations were performed at room temperature (22–24°C). Coverslips with cultured neurons were placed in a 0.5-ml recording chamber. The recording chamber was mounted on a stage of an Olympus IX71 inverted microscope (Olympus Corporation, Tokyo, Japan) and cells were continuously perfused at 2 ml/min with bath solution. CQ was applied through bath solution perfusion. The bath solution contained (in mM): 145 NaCl, 5 KCl, 2 $MgCl_2$, 2 $CaCl_2$, 10 glucose, and 10 HEPES, with an osmolarity of 320 mOsm and a pH of 7.35. The intracellular solution contained (in mM): 150 KCl, 2.4 $MgCl_2$, 0.5 $CaCl_2$, 5 EGTA, 10 HEPES, 5.0 Na_2ATP, and 0.33 GTP-Tris salt, with a pH of 7.35 and an osmolarity of 320 mOsm. The recording electrodes were fabricated from thin wall borosilicate glass capillaries using a Flaming P-97 puller (Sutter Instrument Co., Novato, CA, United States) and had resistances of 3–5 MΩ. Signals were recorded with an Axonpatch 700B amplifier, filtered at 2 kHz, and sampled at 5 kHz using pCLAMP 10.7 (Axon Instruments; Molecular Devices, LLC, Sunnyvale, CA, United States). The protocol used to study M/K_v7 currents of DRG neurons was as follows: the cells were held at −20 mV following a 1-s hyperpolarizing step to −60 mV every 4 s (Jia et al., 2008). We used the current-clamp method to record the APs of DRG neurons. Continuous current-clamp recording with no current injection was used for monitoring of membrane potential (Vm). For recording of APs, cells were held at 0 pA and the APs were elicited by current injection at near the twofold rheobase for 0.5 s. The bath solution and internal solution used to record neuronal APs was the same as that used for M/K_v7 current recordings. Whole-cell patch clamp recording data were analyzed using Clampfit 10.7 software (Axon Instruments; Molecular Devices, LLC, Sunnyvale, CA, United States).

Calcium Imaging

DRG neurons were loaded with 2 μM fluo-4-acetoxymethyl ester (fluo-4-AM; Molecular Probes; Thermo Fisher Scientific, Inc.) at 37°C for 30 min. After loading, the cells were washed three times with Dulbecco's PBS to remove the extracellular dye, and then placed in a chamber mounted on the stage of laser scanning confocal microscope (Leica TCS SP5; Leica Microsystems GmbH, Wetzlar, Germany). The cells were incubated with the same bath solution as the patch clamp experiment. Fluo-4-AM loaded calcium signals were excited at a wavelength of 488 nm, and the emission fluorescence was measured at 530 nm. The calcium signals induced by drug application in bath solution were measured. Dynamic signals were recorded at an interval of 2 s and normalized to the initial fluorescence value.

Statistics

Data were presented as the mean ± SEM for the indicated number of independently conducted experiments, and analyzed with Origin 9.1 software (OriginLab Corporation, Northampton, MA, United States) and SPSS 13.0 (SPSS Inc., Chicago, IL, United States). Statistical significance was evaluated using either a Student's *t*-test or a one-way analysis of variance followed by Dunnett's *post-hoc* test for multiple groups. For the behavioral data that were not in normal distribution, Mann–Whitney *U* test was used to evaluate the statistical significance. $p < 0.05$ was considered to indicate a statistically significant difference.

RESULTS

Inhibition of M/K_v7 Channel Activity Induces Itch-Like Behavior in Mice

To determine the role of M/K_v7 channel in the generation of itch sensation, itch-like behavior test *in vivo* was performed in mice. Intracutaneous injection of 1 mM XE991, a selective M/K_v7 channel blocker (Wang et al., 1998) into the nape of neck, elicited obvious scratching behavior (**Figure 1A**). The scratching behavior induced by XE991 was significantly suppressed by the specific M/K_v7 channel opener retigabine (RTG) (Tatulian et al., 2001; **Figure 1B**). These results suggest that inhibition of M/K_v7 channel activity induces itch-like behavior in mice.

To distinguish the itch-like behavior from the painful behavior that could also be induced by inhibition of M/K_v7 channel activity (Liu et al., 2010; Du et al., 2014), agents were intracutaneously injected into the cheek (known as "cheek model of itch"). In this case, the itch-like behavior will be demonstrated

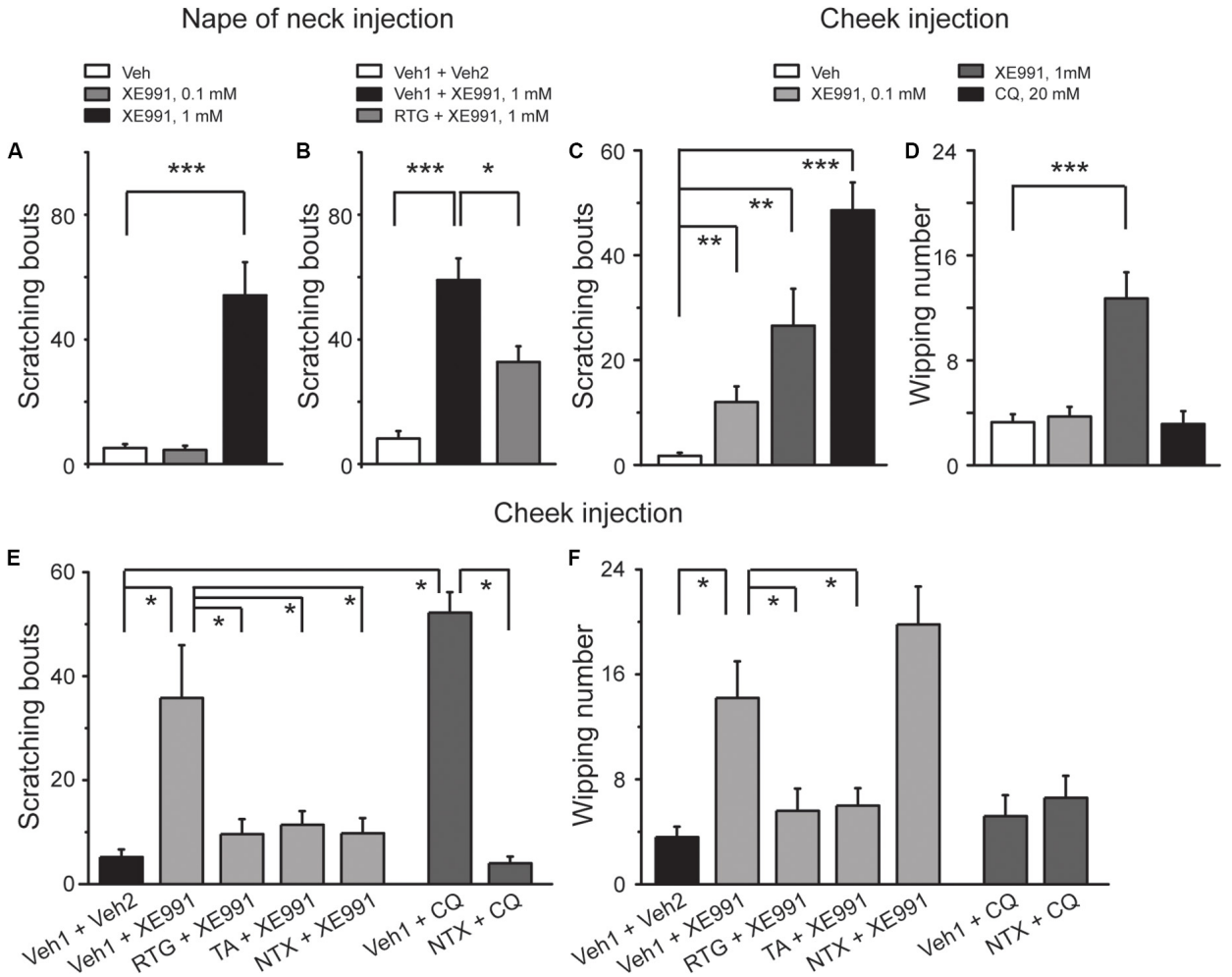

FIGURE 1 | Inhibition of M/K_v7 channel activity induces itch in mice. **(A)** Intracutaneous injection of XE991 (1 mM, 50 μl) into the nape of neck induces scratching behavior. **(B)** Intracutaneous pre-injection of M/K_v7 channel opener retigabine (RTG, 10 mg/kg, 100 μl) suppresses XE991-induced scratching behavior. **(C,D)** Intracutaneous injection of XE991 into the cheek induces scratching **(C)** and pain behavior **(D)**, respectively. As a positive control, pruritogen CQ (20 mM, 20 μl) only induces itch **(C)** but not pain behavior **(D)**. **(E,F)** Intracutaneous pre-injection of RTG (15 mM, 25 μl) and tannic acid (TA, 5 mM, 25 μl) significantly suppresses XE991 (1 mM)-induced scratching **(E)** and pain behavior **(F)** in cheek model. Intracutaneous pre-injection of naltrexone (1 mg/kg, 25 μl) only inhibits XE991 (1 mM)-induced scratching **(E)** but not pain behavior **(F)**. As a positive control, CQ (20 mM, 20 μl) only induces itch behavior **(E)**, and it can be reversed by naltrexone. Data are shown as mean ± SEM (n = 8 per group in **A–D** and n = 5 per group in **E** and **F**). The statistical significance was evaluated using Student's t-test. $^*p < 0.05$, $^{**}p < 0.01$, $^{***}p < 0.001$.

by hindpaw scratching, whereas the painful behavior will be demonstrated by forepaw wiping, respectively (Shimada and LaMotte, 2008; Wilson et al., 2011). Indeed, cheek injection of 0.1 and 1 mM XE991 both induced significant scratching behavior (**Figure 1C**). However, only 1 mM XE991 induced pain behavior (**Figure 1D**). As a positive control, cheek injection of CQ (20 mM) elicited obvious scratching (**Figure 1C**) but not pain behavior (**Figure 1D**). In the cheek model, RTG and another M/K_v7 channel opener tannic acid (TA) (Zhang et al., 2015) were used to further determine the role of M/K_v7 channel in itch and pain. XE991 (1 mM)-induced scratching and pain behavior were significantly suppressed by intracutaneous pre-injection of RTG (15 mM) and TA (5 mM) (**Figures 1E,F**). Naltrexone (1 mg/kg), a well-known itch antagonist (Spradley et al., 2012), significantly inhibited 1 mM XE991-induced scratching but not pain behavior by intracutaneous pre-injection (**Figures 1E,F**). CQ-induced scratching behavior was also significantly suppressed by intracutaneous pre-injection of naltrexone (1 mg/kg) (**Figures 1E,F**). On the other hand, rota-rod test was performed to exclude the possibility that M/K_v7 channel inhibition-induced itch and pain were suppressed by M/K_v7 channel openers through inhibiting the central nervous system (CNS) and motor function. As shown in **Table 1**, intraperitoneal injection of RTG (20 mg/kg) or TA (16 mg/kg) did not affect CNS and motor function at the time points when the itch behavior tests were performed (**Table 1**). Taken together, these results indicate that inhibition of M/K_v7 channel activity contributes to not only pain but also itch sensation generation.

TABLE 1 | Effects of intraperitoneal injection of RTG and TA on rota-rod test in mice.

Treatment	Post-treatment (min)			
	30		60	
	Time on rod %	Fail.%	Time on rod %	Fail.%
Saline	>180.0 s	0.0	>180.0 s	0.0
RTG 20 mg/kg	>180.0 s	0.0	>180.0 s	0.0
TA 16 mg/kg	>180.0 s	0.0	>180.0 s	0.0

Agents were administrated by intraperitoneal (i.p.) injection. Rota-rod test was performed after treatment for 30 and 60 min, respectively. Thirty minutes was used because it was the start time to observe the effects of CQ after i.p. administration of RTG or TA in the experiments. Results are presented as mean ± SEM. No significant difference between saline and treated groups; one-way analysis of variance (ANOVA) followed by Dunnett's post-hoc test for multiple comparisons; n = 5 in each group.

M/K_v7 Channel Openers Selectively Suppress CQ-induced Itch-Like Behavior in Mice

To determine the role of M/K_v7 channel in CQ-induced itch sensation, the *in vivo* behavioral test was performed in mice whose nape of neck was intradermally injected with CQ; the itch sensation was identified by the scratching on the skin with hindpaws. RTG and TA were tested in the scratching behavioral measurement. Intradermal injection of CQ significantly increased the scratching bouts to 263 ± 24 (n = 8) from 23 ± 8 (n = 8, $p < 0.001$) in control group mice (**Figure 2A**). Intraperitoneal pre-administration of RTG or TA effectively prevented CQ-induced scratching behavior in a dose-dependent manner (**Figures 2A,C**). For example, pre-administration of RTG at 5, 10, and 20 mg/kg significantly reduced the scratching bouts of CQ group from 263 ± 24 to 185 ± 20 (n = 8, $p < 0.05$), 151 ± 33 (n = 8, $p < 0.05$), and 112 ± 30 (n = 8, $p < 0.01$), respectively (**Figure 2A**). Pre-administration of TA at 4, 8, and 16 mg/kg also significantly reduced CQ-induced scratching bouts from 236 ± 35 (n = 8) to 104 ± 16 (n = 8, $p < 0.05$), 73 ± 21 (n = 8, $p < 0.01$), and 18 ± 6 (n = 8, $p < 0.001$), respectively (**Figure 2C**). Furthermore, intradermal pre-injection of RTG and TA at the nape of neck significantly reduced the scratching bouts induced by CQ injected at the same site from 252 ± 22 (n = 8) and 211 ± 44 (n = 8) to 143 ± 23 (n = 8, $p < 0.01$) and 103 ± 13 (n = 8, $p < 0.01$), respectively (**Figures 2B,D**). These results indicate that the M/K_v7 channel is involved in the CQ-induced itch sensation.

We then examined whether the M/K_v7 channel is also involved in itch sensation induced by other pruritogens. For this, 5-HT, CAP, HIS, CAR, and β-ALA were intradermally injected into the nape of neck, respectively. All the above compounds elicited obvious itch-like scratching behavior (**Figures 3A–E**). Intraperitoneal pre-administration of RTG or TA significantly prevented this compound-induced scratching behavior in a dose-dependent manner (**Figures 3A–E**). Taken together, these results indicate that augmentation of M/K_v7 channel activity significantly suppresses the itch sensation induced by the above compounds.

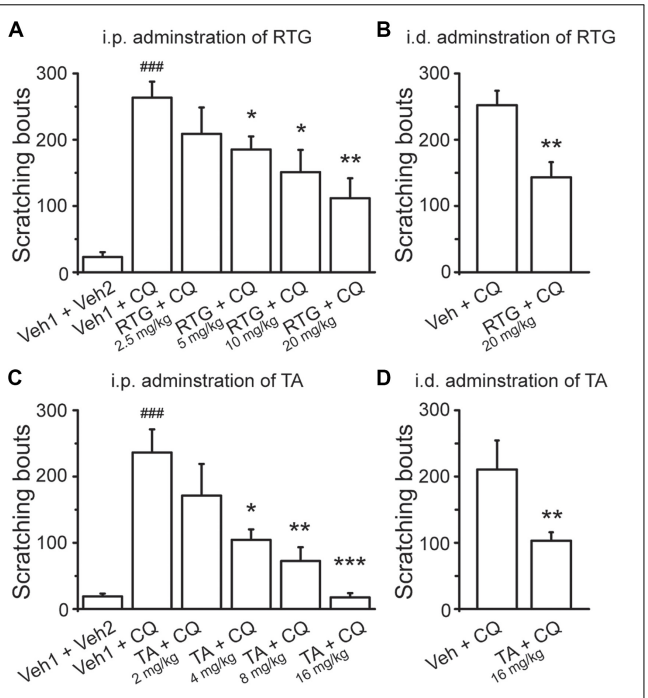

FIGURE 2 | Activation of M/K_v7 channel suppresses CQ-evoked itch. Intraperitoneal (i.p.) pre-injection of RTG **(A)** and TA **(C)** suppresses CQ (8 mM, 50 μl)-evoked scratching behavior in a dose-dependent manner. Intradermal (i.d.) pre-injection of RTG (20 mg/kg, 100 μl) **(B)** and TA (16 mg/kg, 100 μl) **(D)** reduces the same site injection of CQ (8 mM, 50 μl)-evoked scratching behavior. Data are shown as mean ± SEM (n = 8 per group). The statistical significance was evaluated using one-way analysis of variance followed by Dunnett's *post-hoc* test for comparation among multiple groups and Student's t-test between two groups. $^{*}p < 0.05$, $^{**}p < 0.01$, $^{***/\#\#\#}p < 0.001$.

CQ Inhibits M/K_v7 Currents Through Increasing Intracellular Ca^{2+} in Mouse DRG Neurons

To determine the effect of CQ on M/K_v7 currents, whole-cell patch-clamp recordings were performed in cultured mouse DRG neurons. Bath application of CQ significantly inhibited M/K_v7 currents in a concentration-dependent manner (**Figures 4A,B**). CQ initiated its inhibition on M/K_v7 currents at 0.01 mM and reached its maximal inhibition at 100 mM (**Figure 4B**). The half maximum inhibitory concentration (IC_{50}) was at 1.0 ± 0.4 mM (**Figure 4B**). However, the current–voltage (I–V) curve of M/K_v7 was not affected by CQ (**Figure 4C**). In addition, immunostaining assay showed that M/K_v7 channel subunit K_v7.2 was co-localized with MrgprA receptor (CQ receptor) in mouse DRG neurons (**Supplementary Figure 1**).

For the signaling molecules involved in M/K_v7 current inhibition, three mechanisms have been proposed, PIP_2 depletion, increment of intracellular Ca^{2+}, and PKC phosphorylation, which are the downstream signals of phospholipase C (PLC) activation (Gamper and Shapiro, 2015; Du et al., 2018). Previous studies have demonstrated that CQ increases intracellular concentration of Ca^{2+} through

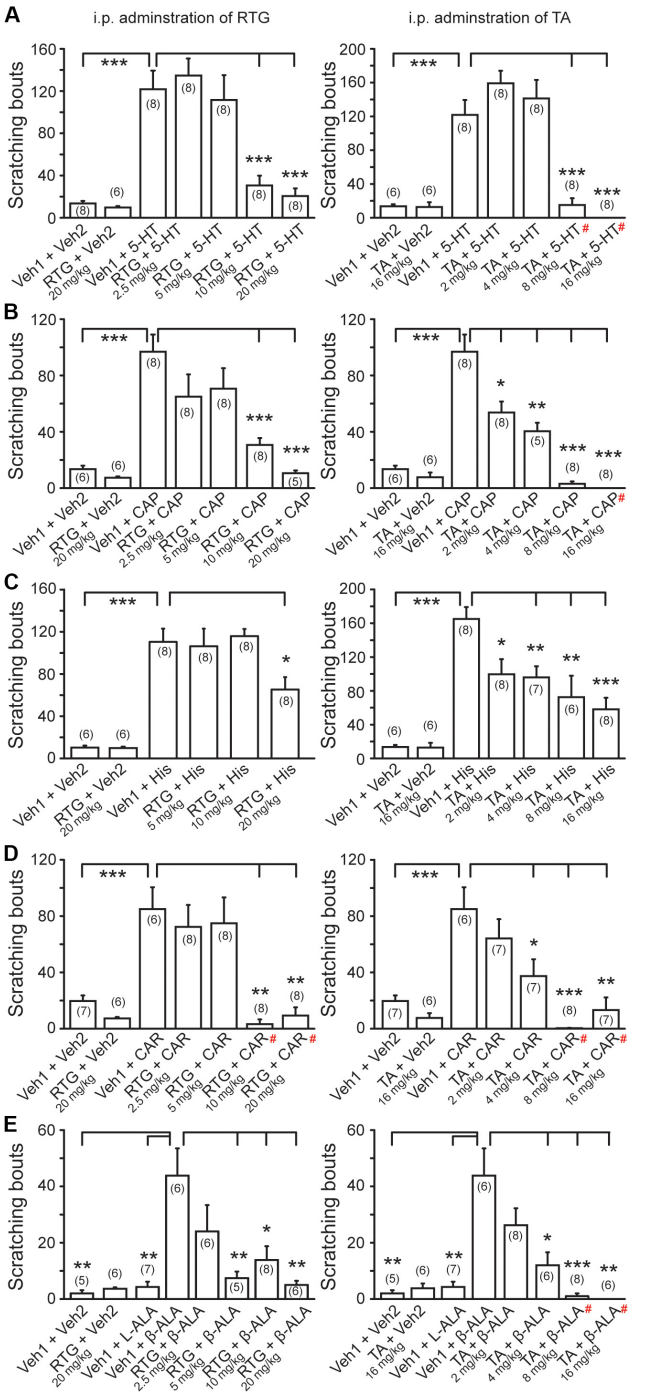

FIGURE 3 | Effects of M/K_v7 channel activation in several pruritogens-evoked itch. I.p. pre-injection of RTG (left) and TA (right) suppresses serotonin (5-HT, 1 mM, 50 μl) **(A)**, capsaicin (CAP, 10 μM, 50 μl) **(B)**, histamine (His, 90 mM, 50 μl) **(C)**, carvacrol (CAR, 70 mM, 50 μl) **(D)**, and β-alanine (β-ALA, 50 mM, 50 μl) **(E)**-evoked scratching behavior in a dose-dependent manner, respectively. Data are shown as mean ± SEM (the *n* number in each group is indicated). For the data that exhibited normal distribution, the statistical significance was evaluated using Student's *t*-test between two groups; for the data that were not in normal distribution (#), the statistical significance was evaluated using Mann–Whitney *U* test between two groups. $^*p < 0.05$, $^{**}p < 0.01$, $^{***}p < 0.001$.

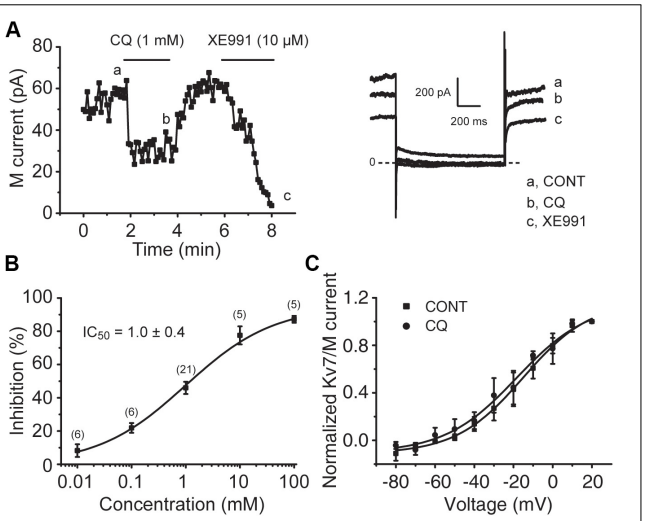

FIGURE 4 | CQ inhibits M/K_v7 currents in mice DRG neurons. **(A)** Representative time course of CQ (1 mM)-induced inhibition of M/K_v7 currents (left). Current traces are shown (right). XE991 (10 μM) was used as positive control to inhibit M/K_v7 currents. **(B)** The concentration–effect relationship curve for CQ-induced inhibition of M/K_v7 currents is shown. IC_{50} = 1.0 ± 0.4 mM (*n* = 6, 6, 21, 5, 5 at each concentration of CQ, respectively). **(C)** CQ (1 mM) has no significant effect on current–voltage (*I–V*) curve of M/K_v7 channel. The statistical significance was evaluated using one-way analysis of variance followed by Dunnett's *post-hoc* test for multiple comparations.

activation of TRPA1 channels (Wilson et al., 2011; Than et al., 2013). We examined the effect of CQ on mouse DRG neurons using Ca^{2+}-imaging assay. Specific TRPA1 agonist allyl isothiocyanate (AITC) was used to indicate the DRG neurons with TRPA1-positive response. As shown in **Figure 5**, CQ significantly increased intracellular Ca^{2+} in mouse DRG neurons (**Figure 5A**). Eighty-three percent (44 out of 53) of mouse DRG neurons that responded to CQ were TRPA1-positive DRG neurons (**Figures 5A,B**). Excluding the Ca^{2+} from the bath solution eliminated CQ-induced increase of intracellular Ca^{2+} (**Figures 5C,D,F**). HC-030031, a specific TRPA1 channel blocker, significantly inhibited CQ-induced increase of intracellular Ca^{2+} (**Figures 5E,F**). These results indicate that CQ-induced intracellular Ca^{2+} increase in mouse DRG neurons is due to the TRPA1 activation-induced Ca^{2+} influx.

Consistently, CQ-induced inhibition of M/K_v7 currents was significantly attenuated by perfusing cells with Ca^{2+}-free bath solution and HC-030031, respectively (**Figures 6A–C,F**). For example, Ca^{2+}-free bath solution significantly reduced the CQ (1 mM)-induced inhibition of M/K_v7 current from 45% (*n* = 15) to 24% (*n* = 8, $p < 0.01$), while HC-030031 significantly reduced the inhibition to 23% (*n* = 5, $p < 0.05$) (**Figure 6F**). However, bath application of U73122, a PLC inhibitor, showed no obvious effects on CQ-induced inhibition of M/K_v7 currents (36%; *n* = 5, $p > 0.05$) (**Figures 6D,F**). Furthermore, activation of TRPA1 with AITC (1 mM) significantly inhibited M/K_v7 currents by 41% (*n* = 4), and this effect was reduced to 17% (*n* = 4, $p < 0.01$) by 10 μM RTG (**Figures 6E,F**). Taken together, these results suggest

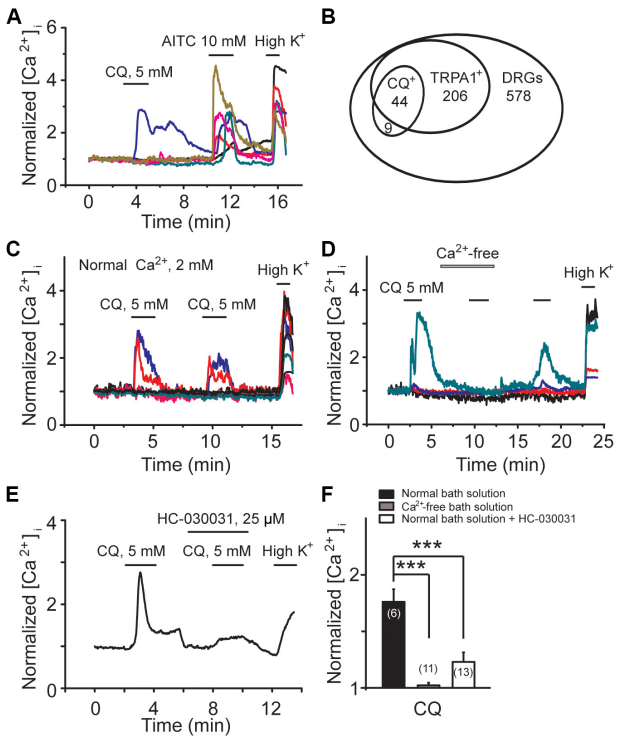

FIGURE 5 | CQ increases intracellular Ca^{2+} through TRPA1-mediated Ca^{2+} influx in mice DRG neurons. **(A)** Representative traces from six different DRG neurons with calcium-imaging assay. Allyl isothiocyanate (AITC, 10 mM)-responsive DRG neurons indicate TRPA1-positive neurons. **(B)** The Venn diagram illustrates the relationships of CQ-, AITC (TRPA1$^+$)-responsive neurons in adult DRG. The sizes of the circles are proportional to the sizes of the cell populations. CQ can increase intracellular Ca^{2+} in the presence **(C)** but not in the absence **(D)** of extracellular Ca^{2+} (2 mM). **(E)** Selective inhibition of TRPA1 by HC-030031 reduces CQ-induced increase of intracellular Ca^{2+}. **(F)** Summary data of CQ-induced increase of intracellular Ca^{2+} in normal bath solution, Ca^{2+}-free solution, and normal bath solution contained HC-030031, respectively. Data are shown as mean ± SEM (the *n* number in each group is indicated). The statistical significance was evaluated using Student's *t*-test for comparison between two groups. ***$p < 0.001$.

that CQ-induced inhibition of M/K_v7 currents in mouse DRG neurons is due to the CQ-induced increase of intracellular Ca^{2+}, which is through TRPA1 activation-mediated Ca^{2+} influx. PIP_2 depletion and PKC phosphorylation, the downstream signals of PLC, may not be involved in CQ-mediated inhibition of M/K_v7 currents.

CQ Enhances the Excitability of Mouse DRG Neurons

M/K_v7 currents play a key role in regulation of neuronal excitability. As a result, inhibition of M/K_v7 currents causes membrane depolarization and reduces the threshold and rheobase of action potentials (Du et al., 2018). We next tested whether CQ increased the excitability of mouse DRG neurons through inhibition of M/K_v7 currents as demonstrated above. The membrane potential of mouse DRG neurons was first recorded using the current clamp method (**Figures 7A–C**). CQ depolarized the membrane potential in a concentration-dependent manner (**Figures 7A,B**). At 1 mM, CQ significantly depolarized the membrane potential from −59 ± 1 mV ($n = 31$) to −49.5 ± 1.2 mV ($n = 37$, $p < 0.001$) (**Figures 7C,D**). Furthermore, the CQ-induced depolarization of membrane potential could be reversed (to 59 ± 1.2 mV, $n = 14$, $p < 0.001$) by the M/K_v7 channel opener RTG (**Figures 7C,D**). Then, the effect of CQ on action potentials (APs) of mouse DRG neurons was tested; APs were induced by different levels of current injection. For this, the threshold (the distance from resting membrane potential to threshold membrane potential) and the rheobase for eliciting APs and AP fire numbers was addressed. The threshold was significantly reduced from 28.8 ± 1.4 mV ($n = 7$) of control group to 19.3 ± 0.9 mV ($n = 5$, $p < 0.001$) by CQ (**Figures 8A,B**), which was mostly reversed by RTG (30 ± 1.1mV, $n = 4$, $p < 0.001$) (**Figures 8A,B**). Similarly, CQ reduced the rheobase from 73 ± 11 pA ($n = 7$) to 39 ± 9 pA ($n = 5$, $p < 0.05$), and RTG reversed this CQ-induced reduction of the rheobase (to 79 ± 15 pA, $n = 6$, $p < 0.05$) (**Figure 8C**). Finally, numbers of APs induced by a 120-pA current injection were increased from 3.3 ± 1.3 ($n = 6$) to 9.0 ± 1.2 by CQ ($n = 4$, $p < 0.05$) (**Figures 8A,D**), which was again reversed by RTG (to 2.2 ± 0.5, $n = 6$, $p < 0.01$) (**Figures 8A,D**). These results indicate that CQ enhances the excitability of mouse DRG neurons through its inhibition of M/K_v7 currents.

DISCUSSION

For chemical itch, a better understanding of peripheral mechanisms is emerging (Dong and Dong, 2018), and to this we add a new mechanism of M/K_v7 channels. The major findings of this study are as follows: (1) inhibition of M/K_v7 potassium currents causes itch sensation; (2) CQ is an inhibitor of M/K_v7 currents, and inhibitory mechanism involves TRPA1-mediated Ca^{2+} influx; (3) CQ-induced inhibition of M/K_v7 induces hyper-excitability of DRG neurons, which is likely the mechanism for CQ-induced itch sensation. It is well-known that peripheral M/K_v7 channels play a key role in pain sensation. Augmentation of its expression or activity is an effective analgesic strategy (Du et al., 2018). Interestingly, we found in this study that inhibition of M/K_v7 also leads to itch generation under the "cheek model of itch" and "neck model of itch" measurements, and activators of M/K_v7 channels alleviate itch behavior caused by CQ and other pruritogens. This is the first time, to our best knowledge, to describe the relationship between M/K_v7 channel and itch. In the peripheral sensory system, increasing the expression and/or the activity of M/K_v7 channels may have great benefit for anti-pruritus.

Among the pruritogens we tested in this study, CQ is a drug that has long been used in the treatment and prevention of malaria. One major side effect of CQ is HIS-independent itch (Ezeamuzie et al., 1990; Abila et al., 1994; Green et al., 2006). Recently, the molecular mechanisms for CQ-induced itch has been studied. One subpopulation of dorsal horn neurons in the spinal cord that specifically expresses gastrin-releasing peptide receptor (GRPR) mediates CQ- and other chemical-induced itch (Sun and Chen, 2007). In the primary DRG sensory

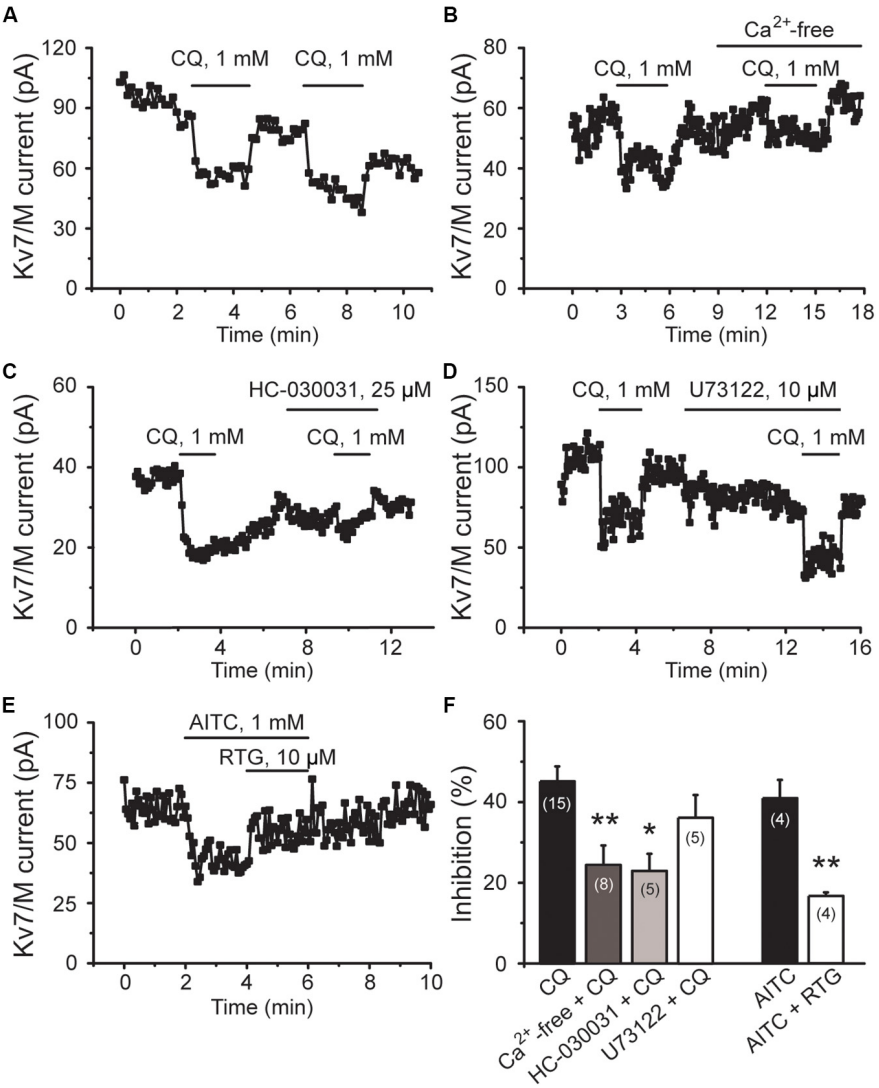

FIGURE 6 | CQ inhibits M/K_v7 currents through TRPA1-mediated Ca^{2+} influx in mice DRG neurons. **(A)** Representative time course of CQ (1 mM)-induced inhibition of M/K_v7 currents. **(B)** Excluding the Ca^{2+} from the bath solution eliminates CQ-induced inhibition of M/K_v7 currents. **(C)** Selective inhibition of TRPA1 by HC-030031 suppresses CQ-induced inhibition of M/K_v7 currents. **(D)** Inhibition of phospholipase C by U73122 does not suppress CQ-induced inhibition of M/K_v7 currents. **(E)** Selective activation of TRPA1 by AITC inhibits M/K_v7 currents, and this effect can be reduced by RTG. **(F)** Summary data from **(A–E)**. Data are shown as mean ± SEM (the *n* number in each group is indicated). The statistical significance was evaluated using Student's *t*-test for comparison between two groups. $^*p < 0.05$, $^{**}p < 0.01$.

neurons, mouse MrgprA3 and human MrgprX1 are functioned as the predominant receptors for CQ (Liu et al., 2009). Mrgprs (known as the Mas-related G protein-coupled receptors) are a family of orphan GPCRs that are restricted to express in the subsets of small-diameter sensory neurons in DRG (Dong et al., 2001). Since all of the molecular correlates of M/K_v7 channel, KCNQ2/3/5, were widely expressed in DRG neurons including small- and large-diameter sensory neurons (Passmore et al., 2003; Du et al., 2018), it will be not surprised to find that M/K_v7 channels are co-localized with CQ receptors. Indeed, our results show that MrgprA receptors are co-localized with K_v7.2 subunit in mouse DRG neurons. CQ activates TRPA1 channel through the activation of the MrgprA3-$G_{\beta\gamma}$ pathway, which evokes itch (Wilson et al., 2011). Consistent with the previous study, our results demonstrate that CQ increases intracellular Ca^{2+} concentration by Ca^{2+} influx in a TRPA1-dependent manner in mouse DRG neurons. Furthermore, it is likely that CQ uses this mechanism but not MrgprA3/PLC pathway to inhibit M/K_v7 currents, because removing extracellular Ca^{2+} or blocking TRPA1 channel both significantly suppresses the CQ-induced inhibition of M/K_v7 currents, whereas blocking PLC activity does not affect CQ-mediated inhibition of M/K_v7 currents. Interestingly, TRPA1 activation is likely sufficient to inhibit M/K_v7 currents directly. It is well-known that increase of intracellular Ca^{2+} induces M/K_v7 inhibition (Cruzblanca et al., 1998; Gamper and Shapiro, 2003; Kosenko and Hoshi, 2013).

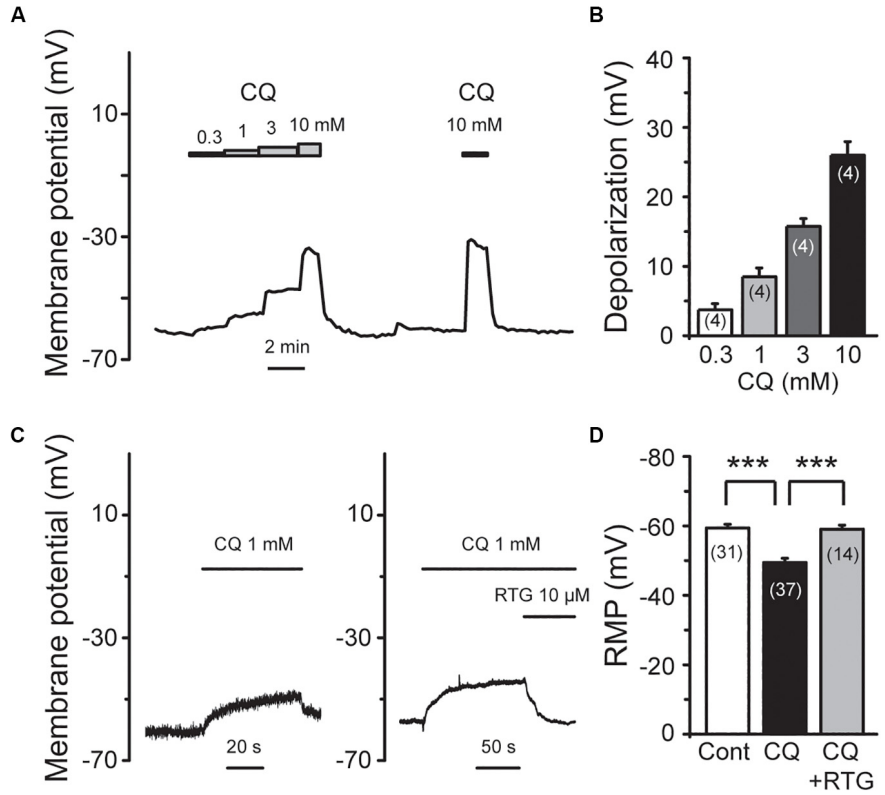

FIGURE 7 | RTG reverses CQ-induced depolarization of the membrane potential in DRG neurons. **(A)** Representative trace shows that CQ depolarizes membrane potential (Vm) in a concentration-dependent manner. **(B)** Summary data of depolarization of membrane potential by different concentration of CQ. **(C)** RTG reverses CQ (1 mM)-induced depolarization of membrane potential. **(D)** Summary data of resting membrane potential (RMP). Data are shown as mean ± SEM (the *n* number in each group is indicated). The statistical significance was evaluated using Student's *t*-test for comparison between two groups. ***$p < 0.001$.

Consistent with our observation, TRPV1-mediated Ca^{2+} influx has been shown to inhibit M/K_v7 currents (Zhang et al., 2011). It is worth noting that CQ still inhibited M/K_v7 currents in Ca^{2+}-free bath solution or in the presence of TRPA1 blocker. This phenomenon indicates that CQ may exhibit non-specific, direct inhibition on M/K_v7 currents in mouse DRG neurons. Similar to CQ, 5-HT activates TRPA1 channels but through HT receptor 7 (HTR7)–Adenylyl Cyclase (AC)–cAMP pathway that evokes itch sensation (Morita et al., 2015). Genetic knockout of HTR7 completely abolished low dose of 5-HT-induced itch and partially reduced scratching in mouse model of atopic dermatitis (Morita et al., 2015). Thus, both CQ and 5-HT target to activate TRPA1 channel and thereby enhance neuronal excitability to evoke itch sensation (Wilson et al., 2011; Morita et al., 2015). However, whether 5-HT/HTR7/TRPA1-mediated Ca^{2+} influx inhibits M/K_v7 currents and then contributes to 5-HT-induced itch remains to be determined.

HIS-induced itch sensation is due to exciting sensory neurons through the activation of H1 or H4 receptor (Dunford et al., 2007; Simons and Simons, 2011). Direct activation of TRPV1 channel by HIS-H1R underlies HIS induced itch (Shim et al., 2007). HIS also inhibits M/K_v7 currents through H1R–PLC pathway-induced membrane PI(4,5)P_2 hydrolysis in rat SCG neurons (Liu et al., 2008). Moreover, TRPV1 channel-mediated Ca^{2+} influx inhibits M/K_v7 currents (Zhang et al., 2011). Thus, involvement of M/K_v7 inhibition in HIS-induced itch sensation is a logical explanation. TRPV1, when activated by its agonist CAP (Caterina et al., 1997, 2000), also evokes moderate itch (Sikand et al., 2009, 2011), besides its being well-known as a nociceptive receptor (Caterina et al., 1997, 2000).

β-ALA is reported to inhibit M/K_v7 currents through MrgprD receptor in rat DRG neurons (Crozier et al., 2007); also, this may not be the case in mice DRG neurons (Rau et al., 2009). Indeed, β-ALA can evoke HIS-independent itch sensation and increase intracellular Ca^{2+} concentration, both through MrgprD receptor in mice, but whether M/K_v7 channels are involved remains unclear (Liu et al., 2012). Nonetheless, we show in this study that activation of M/K_v7 channels also alleviates the β-ALA-induced itch behavior.

CAR is a natural compound that can specifically activate TRPV3 channels (Nilius and Szallasi, 2014; Wang and Wang, 2017). TRPV3 is most abundantly expressed in skin keratinocytes and in cells surrounding hair follicles, where it plays an essential role in cutaneous sensation including thermal sensation, nociception, and itch, in addition to maintenance of the skin barrier and hair growth (Peier et al., 2002; Cheng et al., 2010; Cui et al., 2018). In human, gain-of-function mutations of TRPV3 are associated with Olmsted syndrome, which is characterized

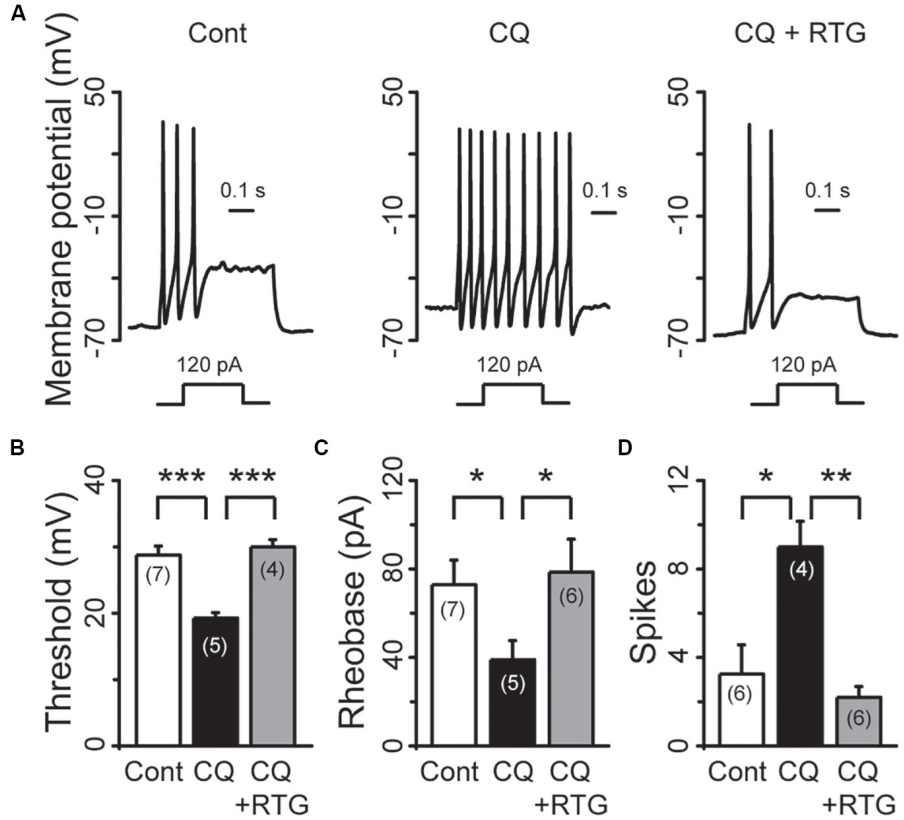

FIGURE 8 | RTG reverses CQ-induced hyperexcitability of DRG neurons. **(A)** Representative samples show that CQ induces hyperexcitability (middle) compared with control (Cont, left), while RTG reverses CQ-induced the neuronal hyperexcitability (right). **(B)** RTG increases CQ (1 mM)-induced reduction of the threshold (n = 7, Cont group; n = 5, CQ group; and n = 4, CQ + RTG group). **(C)** RTG increases CQ (1 mM)-induced reduction of the rheobase. n = 7, 5, and 6 in Cont, CQ, and CQ + RTG group, respectively. **(D)** RTG reduces CQ (1 mM)-induced increase of action potentials (spikes) number. n = 6, 4, and 6 in Cont, CQ, and CQ + RTG group, respectively. Data are shown as mean ± SEM (the n number in each group is indicated). The statistical significance was evaluated using Student's t-test for comparison between two groups. $^*p < 0.05$, $^{**}p < 0.01$, $^{***}p < 0.001$.

by severe itch and palmoplantar and periorificial keratoderma (Lai-Cheong et al., 2012; Lin et al., 2012). In rodents, gain-of-function mutations of TRPV3 are associated with skin inflammation and pruritus (Asakawa et al., 2006; Yoshioka et al., 2009). In addition, itching behavior is suppressed in TRPV3 knockout mice (Yamamoto-Kasai et al., 2012). TRPV3 is unlikely to be distributed in sensory neurons of rodents (Peier et al., 2002). Thus, systemic application of M/K_v7 opener, RTG, and TA, may indirectly reduce CAR/TRPV3-induced itch by suppressing the excitability of sensory neurons.

In conclusion, the results of this study strongly demonstrate that inhibition of M/K_v7 currents induces itch. TRPA1-dependent inhibition of M/K_v7 currents by CQ contributes to CQ-induced itch. These findings provide novel insight into the molecular basis of chemical itch that can be used to develop strategies to mitigate itch sensation.

DATA AVAILABILITY STATEMENT

All datasets generated for this study are included in the article/**Supplementary Material**.

ETHICS STATEMENT

The animal study was reviewed and approved by the Animal Care and Use Committee of the Hebei Medical University.

AUTHOR CONTRIBUTIONS

HZ and ZJ designed the study and wrote the manuscript. DZ, HM, LZ, XG, JW, LL, and QZ performed the experiments. ZJ, DZ, and HM analyzed the data. All authors contributed to the article and approved the submitted version.

FUNDING

This work was supported by the National Natural Science Foundation of China (No. 81571080 to ZJ and Nos. 91732108 and 81871075 to HZ), the Natural Science Foundation of Hebei Province (No. H2015206240 to ZJ), and the Science and Technology Research Project of Hebei Colleges (No. ZD2017053 to ZJ).

SUPPLEMENTARY MATERIAL

The Supplementary Material for this article can be found online at: https://www.frontiersin.org/articles/10.3389/fnmol.2020.00105/full#supplementary-material

FIGURE S1 | Co-localization of K_v7.2 and MrgprA in mouse DRG neurons. **(A)** Representative images show that M/K_v7 channel subunit K_v7.2 is co-localized with MrgprA receptor (arrows, bottom merged) in mouse DRG neurons. Images in the bottom row are extended from the square regions in the up row./break Scale bar in each panel in up and bottom row is 75 and 25 μm, respectively.

REFERENCES

Abila, B., Ezeamuzie, I. C., Igbigbi, P. S., Ambakederemo, A. W., and Asomugha, L. (1994). Effects of two antihistamines on chloroquine and histamine induced weal and flare in healthy African volunteers. *Afr. J. Med. Med. Sci.* 23, 139–142.

Allen, N. M., Mannion, M., Conroy, J., Lynch, S. A., Shahwan, A., Lynch, B., et al. (2014). The variable phenotypes of KCNQ-related epilepsy. *Epilepsia* 55, e99–e105. doi: 10.1111/epi.12715

Asakawa, M., Yoshioka, T., Matsutani, T., Hikita, I., Suzuki, M., Oshima, I., et al. (2006). Association of a mutation in TRPV3 with defective hair growth in rodents. *J. Invest. Dermatol.* 126, 2664–2672. doi: 10.1038/sj.jid.5700468

Bieber, T. (2008). Atopic dermatitis. *N. Engl. J. Med.* 358, 1483–1494. doi: 10.1056/NEJMra074081

Bierbower, S. M., Choveau, F. S., Lechleiter, J. D., and Shapiro, M. S. (2015). Augmentation of M-type (KCNQ) potassium channels as a novel strategy to reduce stroke-induced brain injury. *J. Neurosci.* 35, 2101–2011. doi: 10.1523/JNEUROSCI.3805-14.2015

Biervert, C., Schroeder, B. C., Kubisch, C., Berkovic, S. F., Propping, P., Jentsch, T. J., et al. (1998). A potassium channel mutation in neonatal human epilepsy. *Science* 279, 403–406. doi: 10.1126/science.279.5349.403

Bourane, S., Duan, B., Koch, S. C., Dalet, A., Britz, O., Garcia-Campmany, L., et al. (2015). Gate control of mechanical itch by a subpopulation of spinal cord interneurons. *Science* 350, 550–554. doi: 10.1126/science.aac8653

Brown, D. A., and Passmore, G. M. (2009). Neural KCNQ (Kv7) channels. *Br. J. Pharmacol* 156, 1185–1195. doi: 10.1111/j.1476-5381.2009.00111.x

Carey, E. J., Ali, A. H., and Lindor, K. D. (2015). Primary biliary cirrhosis. *Lancet* 386, 1565–1575. doi: 10.1016/S0140-6736(15)00154-3

Caterina, M. J., Leffler, A., Malmberg, A. B., Martin, W. J., Trafton, J., Petersen-Zeitz, K. R., et al. (2000). Impaired nociception and pain sensation in mice lacking the capsaicin receptor. *Science* 288, 306–313. doi: 10.1126/science.288.5464.306

Caterina, M. J., Schumacher, M. A., Tominaga, M., Rosen, T. A., Levine, J. D., and Julius, D. (1997). The capsaicin receptor: a heat-activated ion channel in the pain pathway. *Nature.* 389, 816–824. doi: 10.1038/39807

Cheng, X., Jin, J., Hu, L., Shen, D., Dong, X. P., Samie, M. A., et al. (2010). TRP channel regulates EGFR signaling in hair morphogenesis and skin barrier formation. *Cell* 141, 331–343. doi: 10.1016/j.cell.2010.03.013

Chindo, B. A., Ya'U, J., Danjuma, N. M., Okhale, S. E., Gamaniel, K. S., and Becker, A. (2014). Behavioral and anticonvulsant effects of the standardized extract of Ficus platyphylla stem bark. *J. Ethnopharmacol.* 154, 351–360. doi: 10.1016/j.jep.2014.03.061

Crozier, R. A., Ajit, S. K., Kaftan, E. J., and Pausch, M. H. (2007). MrgD activation inhibits KCNQ/M-currents and contributes to enhanced neuronal excitability. *J. Neurosci.* 27, 4492–4496. doi: 10.1523/JNEUROSCI.4932-06.2007

Cruzblanca, H., Koh, D. S., and Hille, B. (1998). Bradykinin inhibits M current via phospholipase C and Ca^{2+} release from IP3-sensitive Ca^{2+} stores in rat sympathetic neurons. *Proc. Natl. Acad. Sci. U.S.A.* 95, 7151–7156. doi: 10.1073/pnas.95.12.7151

Cui, T. T., Wang, G. X., Wei, N. N., and Wang, K. (2018). A pivotal role for the activation of TRPV3 channel in itch sensations induced by the natural skin sensitizer carvacrol. *Acta Pharmacol. Sin.* 39, 331–335. doi: 10.1038/aps.2017.152

Dong, X., and Dong, X. (2018). Peripheral and Central Mechanisms of Itch. *Neuron* 98, 482–494. doi: 10.1016/j.neuron.2018.03.023

Dong, X., Han, S., Zylka, M. J., Simon, M. I., and Anderson, D. J. (2001). A diverse family of GPCRs expressed in specific subsets of nociceptive sensory neurons. *Cell* 106, 619–632. doi: 10.1016/s0092-8674(01)00483-4

Du, X., Gao, H., Jaffe, D., Zhang, H., and Gamper, N. (2018). M-type K^+ channels in peripheral nociceptive pathways. *Br. J. Pharmacol.* 175, 2158–2172. doi: 10.1111/bph.13978

Du, X., Hao, H., Gigout, S., Huang, D., Yang, Y., Li, L., et al. (2014). Control of somatic membrane potential in nociceptive neurons and its implications for peripheral nociceptive transmission. *Pain* 155, 2306–2322. doi: 10.1016/j.pain.2014.08.025

Dunford, P. J., Williams, K. N., Desai, P. J., Karlsson, L., McQueen, D., and Thurmond, R. L. (2007). Histamine H4 receptor antagonists are superior to traditional antihistamines in the attenuation of experimental pruritus. *J. Allergy Clin. Immunol.* 119, 176–183. doi: 10.1016/j.jaci.2006.08.034

Elewski, B., Alexis, A. F., Lebwohl, M., Stein Gold, L., Pariser, D., Del Rosso, J., et al. (2019). Itch: an under-recognized problem in psoriasis. *J. Eur. Acad. Dermatol. Venereol.* 33, 1465–1476. doi: 10.1111/jdv.15450

Ezeamuzie, C. I., Igbigbi, P. S., Asomugha, L., Ambakederemo, A. W., Abila, B., and Assem, E. S. (1990). Urine methylhistamine concentrations before and after chloroquine in healthy black subjects. *J. Trop. Med. Hyg.* 93, 423–425.

Feng, J., Luo, J., Yang, P., Du, J., Kim, B. S., and Hu, H. (2018). Piezo2 channel-Merkel cell signaling modulates the conversion of touch to itch. *Science* 360, 530–533. doi: 10.1126/science.aar5703

Gamper, N., and Shapiro, M. S. (2003). Calmodulin mediates Ca^{2+}-dependent modulation of M-type K^+ channels. *J. Gen. Physiol.* 122, 17–31. doi: 10.1085/jgp.200208783

Gamper, N., and Shapiro, M. S. (2015). "KCNQ Channels," in *Handbook of Ion Channels*, 1st Edn, eds J. Zheng and M. C. Trudeau (Boca Raton, FL: CRC Press), 275–306. doi: 10.1201/b18027-24

Green, A. D., Young, K. K., Lehto, S. G., Smith, S. B., and Mogil, J. S. (2006). Influence of genotype, dose and sex on pruritogen-induced scratching behavior in the mouse. *Pain* 124, 50–58. doi: 10.1016/j.pain.2006.03.023

Han, L., and Dong, X. (2014). Itch mechanisms and circuits. *Annu. Rev. Biophys.* 43, 331–355. doi: 10.1146/annurev-biophys-051013-022826

Jentsch, T. J. (2000). Neuronal KCNQ potassium channels: physiology and role in disease. *Nat. Rev. Neurosci.* 1, 21–30. doi: 10.1038/35036198

Jia, Z., Bei, J., Rodat-Despoix, L., Liu, B., Jia, Q., Delmas, P., et al. (2008). NGF inhibits M/KCNQ currents and selectively alters neuronal excitability in subsets of sympathetic neurons depending on their M/KCNQ current background. *J. Gen. Physiol.* 131, 575–587. doi: 10.1085/jgp.200709924

King, C. H., Lancaster, E., Salomon, D., Peles, E., and Scherer, S. S. (2014). Kv7.2 regulates the function of peripheral sensory neurons. *J. Comp. Neurol.* 522, 3262–3280. doi: 10.1002/cne.23595

Kosenko, A., and Hoshi, N. (2013). A change in configuration of the calmodulin-KCNQ channel complex underlies Ca^{2+}-dependent modulation of KCNQ channel activity. *PLoS One* 8:e82290. doi: 10.1371/journal.pone.0082290

Lai-Cheong, J. E., Sethuraman, G., Ramam, M., Stone, K., Simpson, M. A., and McGrath, J. A. (2012). Recurrent heterozygous missense mutation, p.Gly573Ser, in the TRPV3 gene in an Indian boy with sporadic Olmsted syndrome. *Br. J. Dermatol.* 167, 440–442. doi: 10.1111/j.1365-2133.2012.11115.x

Lin, Z., Chen, Q., Lee, M., Cao, X., Zhang, J., Ma, D., et al. (2012). Exome sequencing reveals mutations in TRPV3 as a cause of Olmsted syndrome. *Am. J. Hum. Genet.* 90, 558–564. doi: 10.1016/j.ajhg.2012.02.006

Linley, J. E., Rose, K., Patil, M., Robertson, B., Akopian, A. N., and Gamper, N. (2008). Inhibition of M current in sensory neurons by exogenous proteases: a signaling pathway mediating inflammatory nociception. *J. Neurosci.* 28, 11240–11249. doi: 10.1523/JNEUROSCI.2297-08.2008

Liu, B., Liang, H., Liu, L., and Zhang, H. (2008). Phosphatidylinositol 4,5-bisphosphate hydrolysis mediates histamine-induced KCNQ/M current inhibition. *Am. J. Physiol. Cell Physiol.* 295, C81–C91. doi: 10.1152/ajpcell.00028.2008

Liu, B., Linley, J. E., Du, X., Zhang, X., Ooi, L., Zhang, H., et al. (2010). The acute nociceptive signals induced by bradykinin in rat sensory neurons are mediated by inhibition of M-type K^+ channels and activation of Ca^{2+}-activated Cl^- channels. *J. Clin. Invest.* 120, 1240–1252. doi: 10.1172/JCI41084

Liu, Q., Sikand, P., Ma, C., Tang, Z., Han, L., Li, Z., et al. (2012). Mechanisms of itch evoked by b-alanine. *J. Neurosci.* 32, 14532–14537. doi: 10.1523/JNEUROSCI.3509-12.2012

Liu, Q., Tang, Z., Surdenikova, L., Kim, S., Patel, K. N., Kim, A., et al. (2009). Sensory neuron-specific GPCR Mrgprs are itch receptors mediating chloroquine-induced pruritus. *Cell* 139, 1353–1365. doi: 10.1016/j.cell.2009.11.034

Meixiong, J., and Dong, X. (2017). Mas-related G protein-coupled receptors and the biology of itch sensation. *Annu. Rev. Genet.* 51, 103–121. doi: 10.1146/annurev-genet-120116-024723

Morita, T., McClain, S. P., Batia, L. M., Pellegrino, M., Wilson, S. R., Kienzler, M. A., et al. (2015). HTR7 mediates serotonergic acute and chronic itch. *Neuron* 87, 124–138. doi: 10.1016/j.neuron.2015.05.044

Mucha, M., Ooi, L., Linley, J. E., Mordaka, P., Dalle, C., Robertson, B., et al. (2010). Transcriptional control of KCNQ channel genes and the regulation of neuronal excitability. *J. Neurosci.* 30, 13235–13245. doi: 10.1523/JNEUROSCI.1981-10.2010

Nilius, B., and Szallasi, A. (2014). Transient receptor potential channels as drug targets: from the science of basic research to the art of medicine. *Pharmacol. Rev.* 66, 676–814. doi: 10.1124/pr.113.008268

Passmore, G. M., Selyanko, A. A., Mistry, M., Al-Qatari, M., Marsh, S. J., Matthews, E. A., et al. (2003). KCNQ/M currents in sensory neurons: significance for pain therapy. *J. Neurosci.* 23, 7227–7236. doi: 10.1523/JNEUROSCI.23-18-07227

Peier, A. M., Reeve, A. J., Andersson, D. A., Moqrich, A., Earley, T. J., Hergarden, A. C., et al. (2002). A heat-sensitive TRP channel expressed in keratinocytes. *Science* 296, 2046–2049. doi: 10.1126/science.1073140

Pereira, M. P., and Ständer, S. (2018). Therapy for pruritus in the elderly: a review of treatment developments. *Expert Opin. Pharmacother.* 19, 443–450. doi: 10.1080/14656566.2018.1444752

Rau, K. K., McIlwrath, S. L., Wang, H., Lawson, J. J., Jankowski, M. P., Zylka, M. J., et al. (2009). Mrgprd enhances excitability in specific populations of cutaneous murine polymodal nociceptors. *J. Neurosci.* 29, 8612–8619. doi: 10.1523/JNEUROSCI.1057-09.2009

Rose, K., Ooi, L., Dalle, C., Robertson, B., Wood, I. C., and Gamper, N. (2011). Transcriptional repression of the M channel subunit Kv7.2 in chronic nerve injury. *Pain* 152, 742–754. doi: 10.1016/j.pain.2010.12.028

Shim, W. S., Tak, M. H., Lee, M. H., Kim, M., Kim, M., Koo, J. Y., et al. (2007). TRPV1 mediates histamine-induced itching via the activation of phospholipase A2 and 12-lipoxygenase. *J. Neurosci.* 27, 2331–2337. doi: 10.1523/JNEUROSCI.4643-06.2007

Shimada, S. G., and LaMotte, R. H. (2008). Behavioral differentiation between itch and pain in mouse. *Pain* 139, 681–687. doi: 10.1016/j.pain.2008.08.002

Sikand, P., Shimada, S. G., Green, B. G., and LaMotte, R. H. (2009). Similar itch and nociceptive sensations evoked by punctate cutaneous application of capsaicin, histamine and cowhage. *Pain* 144, 66–75. doi: 10.1016/j.pain.2009.03.001

Sikand, P., Shimada, S. G., Green, B. G., and LaMotte, R. H. (2011). Sensory responses to injection and punctate application of capsaicin and histamine to the skin. *Pain* 152, 2485–2494. doi: 10.1016/j.pain.2011.06.001

Simons, F. E., and Simons, K. J. (2011). Histamine and H1-antihistamines: celebrating a century of progress. *J. Allergy Clin. Immunol.* 128, 1139–1150.e4. doi: 10.1016/j.jaci.2011.09.005

Simonsen, E., Komenda, P., Lerner, B., Askin, N., Bohm, C., Shaw, J., et al. (2017). Treatment of uremic pruritus: a systematic review. *Am. J. Kidney Dis.* 70, 638–655. doi: 10.1053/j.ajkd.2017.05.018

Singh, N. A., Charlier, C., Stauffer, D., DuPont, B. R., Leach, R. J., Melis, R., et al. (1998). A novel potassium channel gene. KCNQ2, is mutated in an inherited epilepsy of newborns. *Nat. Genet.* 18, 25–29. doi: 10.1038/ng0198-25

Spradley, J. M., Davoodi, A., Carstens, M. I., and Carstens, E. (2012). Opioid modulation of facial itch- and pain-related responses and grooming behavior in rats. *Acta Derm. Venereol.* 92, 515–520. doi: 10.2340/00015555-1364

Sun, Y. G., and Chen, Z. F. (2007). A gastrin-releasing peptide receptormediates the itch sensation in the spinal cord. *Nature* 448, 700–703. doi: 10.1038/nature06029

Tatulian, L., Delmas, P., Abogadie, F. C., and Brown, D. A. (2001). Activation of expressed KCNQ potassium currents and native neuronal M-type potassium currents by the anti-convulsant drug retigabine. *J. Neurosci.* 21, 5535–5545. doi: 10.1523/JNEUROSCI.21-15-05535.2001

Than, J. Y., Li, L., Hasan, R., and Zhang, X. (2013). Excitation and modulation of TRPA1, TRPV1, and TRPM8 channel-expressing sensory neurons by the pruritogen chloroquine. *J. Biol. Chem.* 288, 12818–12827. doi: 10.1074/jbc.M113.450072

Wang, G., and Wang, K. (2017). The Ca^{2+}-permeable cation transient receptor potential TRPV3 channel: An emerging pivotal target for itch and skin diseases. *Mol. Pharmacol.* 92, 193–200. doi: 10.1124/mol.116.107946

Wang, H. S., Pan, Z., Shi, W., Brown, B. S., Wymore, R. S., Cohen, I. S., et al. (1998). KCNQ2 and KCNQ3 potassium channel subunits: molecular correlates of the M-channel. *Science* 282, 1890–1893. doi: 10.1126/science.282.5395.1890

Wilson, S. R., Gerhold, K. A., Bifolck-Fisher, A., Liu, Q., Patel, K. N., Dong, X., et al. (2011). TRPA1 is required for histamine-independent, Mas-related G protein-coupled receptor-mediated itch. *Nat. Neurosci.* 14, 595–602. doi: 10.1038/nn.2789

Yamamoto-Kasai, E., Imura, K., Yasui, K., Shichijou, M., Oshima, I., Hirasawa, T., et al. (2012). TRPV3 as a therapeutic target for itch. *J. Invest. Dermatol.* 132, 2109–2112. doi: 10.1038/jid.2012.97

Yoshioka, T., Imura, K., Asakawa, M., Suzuki, M., Oshima, I., Hirasawa, T., et al. (2009). Impact of the Gly573Ser substitution in TRPV3 on the development of allergic and pruritic dermatitis in mice. *J. Invest. Dermatol.* 129, 714–722. doi: 10.1038/jid.2008.245

Young, M. A., and Thomas, S. A. (2014). M1-muscarinic receptors promote fear memory consolidation via phospholipase C and the M-current. *J. Neurosci.* 34, 1570–1578. doi: 10.1523/JNEUROSCI.1040-13.2014

Zhang, F., Gigout, S., Liu, Y., Wang, Y., Hao, H., Buckley, N. J., et al. (2019). Repressor element 1-silencing transcription factor drives the development of chronic pain states. *Pain* 160, 2398–2408. doi: 10.1097/j.pain.0000000000001633

Zhang, X., Zhang, H., Zhou, N., Xu, J., Si, M., Jia, Z., et al. (2015). Tannic acid modulates excitability of sensory neurons and nociceptive behavior and the Ionic mechanism. *Eur. J. Pharmacol.* 764, 633–642. doi: 10.1016/j.ejphar.2015.06.048

Zhang, X. F., Han, P., Neelands, T. R., McGaraughty, S., Honore, P., Surowy, C. S., et al. (2011). Coexpression and activation of TRPV1 suppress the activity of the KCNQ2/3 channel. *J. Gen. Physiol.* 138, 341–352. doi: 10.1085/jgp.201110618

Zheng, Q., Fang, D., Liu, M., Cai, J., Wan, Y., Han, J. S., et al. (2013). Suppression of KCNQ/M (Kv7) potassium channels in dorsal root ganglion neurons contributes to the development of bone cancer pain in a rat model. *Pain* 154, 434–448. doi: 10.1016/j.pain.2012.12.005

Zheng, Y., Xu, H., Zhan, L., Zhou, X., Chen, X., and Gao, Z. (2015). Activation of peripheral KCNQ channels relieves gout pain. *Pain* 156, 1025–1035. doi: 10.1097/j.pain.0000000000000122

Conflict of Interest: The authors declare that the research was conducted in the absence of any commercial or financial relationships that could be construed as a potential conflict of interest.

Advantages of publishing in Frontiers

OPEN ACCESS
Articles are free to read for greatest visibility and readership

FAST PUBLICATION
Around 90 days from submission to decision

HIGH QUALITY PEER-REVIEW
Rigorous, collaborative, and constructive peer-review

TRANSPARENT PEER-REVIEW
Editors and reviewers acknowledged by name on published articles

Frontiers
Avenue du Tribunal-Fédéral 34
1005 Lausanne | Switzerland

Visit us: www.frontiersin.org
Contact us: frontiersin.org/about/contact

REPRODUCIBILITY OF RESEARCH
Support open data and methods to enhance research reproducibility

DIGITAL PUBLISHING
Articles designed for optimal readership across devices

FOLLOW US
@frontiersin

IMPACT METRICS
Advanced article metrics track visibility across digital media

EXTENSIVE PROMOTION
Marketing and promotion of impactful research

LOOP RESEARCH NETWORK
Our network increases your article's readership